Physics of the Solid State, Vol. 45, No. 5, 2003, pp. 1002–1003. Translated from Fizika Tverdogo Tela, Vol. 45, No. 5, 2003, pp. 954–955.

FULLERENES AND ATOMIC CLUSTERS

Metastable Quasi-One-Dimensional Ensembles of C_8 Clusters

N. N. Degtyarenko, V. F. Elesin, N. E. L'vov, L. A. Openov, and A. I. Podlivaev

Moscow State Institute of Engineering Physics (Technical University), Kashirskoe sh. 31, Moscow, 115409 Russia

Received June 18, 2002

Abstract—The geometric and energy characteristics of quasi-one-dimensional ensembles of metastable carbon clusters C_8 are calculated using the molecular dynamics method with an empirical interatomic potential. The decay activation energy and the lifetime of the metastable state are determined. © *2003 MAIK "Nauka/Interperiodica".*

1. INTRODUCTION

Since the discovery of fullerene C_{60} [1] in 1985, interest in small-sized atomic clusters has increased significantly. This is associated with both the necessity of investigating the fundamental characteristics of atomic clusters and the prospects for their practical applications. Carbon clusters and macrosamples prepared from these clusters [2] are a new type of material (cluster matter). Many properties of this material differ essentially from those of bulk carbon forms (graphite, diamond, carbyne). It can be expected that these differences will become all the more evident with a decrease in the size of C_n clusters, i.e., with a decrease in the number n of atoms in a carbon cluster.

Among the three-dimensional (cagelike) clusters experimentally observed to date, C_{20} is the smallest sized cluster [3]. It seems likely that the binding (cohesion) energy E_{coh} of atoms in a C_{20} cluster [$E_{coh}(n) = nE(1) - E(n)$, where $E(n)$ is the total energy of an n-atom cluster] is higher than the binding energy of one-dimensional or two-dimensional C_n clusters with $n = 20$. Consequently, a C_{20} three-dimensional cluster is stable in the absence of interaction with the environment (this cluster was revealed in the gaseous phase). It remains unclear whether C_{20} three-dimensional clusters are capable of forming macrostructures (ensembles), i.e., whether the interaction between the clusters can lead to loss of their individuality and to a transition to another state with a lower total energy.

Earlier [4], we performed tight-binding molecular dynamics (TBMD) calculations and predicted the possible existence of an eight-atom three-dimensional carbon cluster, namely, the C_8 prismane. This cluster has the form of a triangular prism with two carbon atoms located in the vicinity of the centers of the prism bases. Unlike the C_{20} three-dimensional cluster, the C_8 prismane is a metastable cluster. In actual fact, the calculated binding energy of the C_8 prismane is 0.45 eV/atom less than those of the one-dimensional (chain) and two-dimensional (ring) C_8 clusters, which are energetically close to each other. However, the energy U needed to overcome the barrier for the decay of the C_8 metastable state is rather high ($U \approx 0.44$ eV [5]). Therefore, it can be assumed that the lifetime of the C_8 prismane even at room temperature is long enough for this cluster to be observed in the experiment. In [6], the TBMD calculations of the interaction between the C_8 prismanes demonstrated the possibility of forming a $(C_8)_2$ molecule in which two C_8 prismanes are bound by covalent bonds.

The goal of the present work was to investigate theoretically the geometric and energy characteristics of ensembles composed of a large number of C_8 prismanes and to analyze their stability.

2. COMPUTATIONAL TECHNIQUE

In this work, we used the molecular dynamics method with a classical interatomic potential [7]. On the one hand, the molecular dynamics method offers an adequate description of ordered, defect, and amorphous carbon structures [7]. On the other hand, this method allows one to obtain statistics large enough to estimate the decay activation energy E_a and the lifetime τ of the metastable state to sufficient accuracy even for relatively large-sized systems composed of several hundreds of atoms. The activation energy E_a was determined from the relationship $\tau(T) = \tau_0 \exp(E_a/k_B T)$, where $\tau_0 \sim 10^{-15}$ s is the characteristic time of the order of the vibration period of the system (the dependence of the lifetime τ on the temperature T was obtained by direct modeling of the dynamics of the heat-insulated system at $T = 800$–3000 K, and the quantities τ_0 and E_a played the role of adjustable parameters for the approximation of the curve $\tau(T)$ by an exponential function). The minimum height U of the barrier separating a particular metastable configuration from other metastable configurations with a higher binding energy and/or from a stable configuration was determined by searching for the saddle points on the generalized surface of the total energy as a function of the atomic coordinates when the number of atoms in the system was fixed [5].

1063-7834/03/4505-1002$24.00

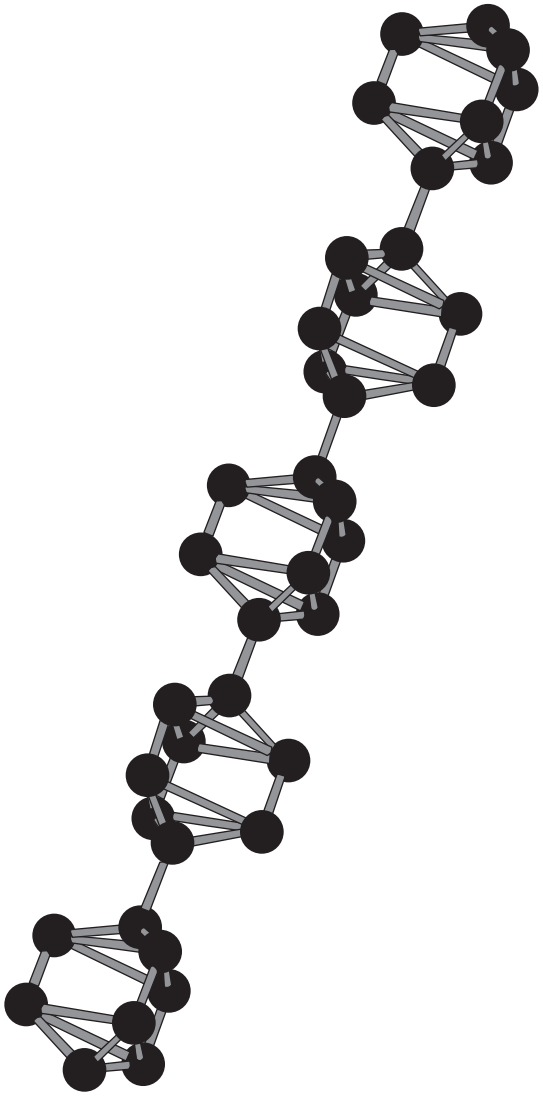

A $(C_8)_5$ ensemble consisting of 5 C_8 prismanes.

3. RESULTS AND DISCUSSION

For an isolated C_8 prismane, the calculated values of the cohesion energy E_{coh} and the length of covalent bonds are consistent with the results obtained by the TBMD method [4] with an accuracy of 5–10%. The activation energy $E_a = 1.2 \pm 0.1$ eV and the energy barrier $U = 1.36$ eV agree qualitatively with the TBMD data ($E_a = 0.8 \pm 0.1$ eV [4] and $U = 0.44$ eV [5]) but disagree quantitatively with them due to the sensitivity of the studied system to the specific computational procedure.

We demonstrated that the C_8 prismanes can form quasi-one-dimensional ensembles in which the adjacent clusters of C_8 are linked to each other via a single covalent bond (see figure). The decay activation energies for the $(C_8)_2$, $(C_8)_3$, and $(C_8)_5$ ensembles were determined to be as follows: $E_a = 0.8 \pm 0.1$, 0.9 ± 0.1, and 0.8 ± 0.1 eV, respectively. The ensemble begins to decay with one of the C_8 prismanes constituting the ensemble due to the breaking of a covalent bond. A drastic increase in the temperature leads to the decay of other prismanes.

After extrapolating the calculated dependences $\tau(T)$ to the low-temperature range, we found that, for example, at $T = 200$ K, the lifetime τ is approximately equal to 10^6 s for an isolated C_8 prismane and $\tau \sim 0.1$–1 s for $(C_8)_2$, $(C_8)_3$, and $(C_8)_5$ ensembles. We numerically simulated quasi-one-dimensional ensembles $(C_8)_m$ with $m \leq 20$. The metastable state was observed in all the ensembles studied. Although the statistics at $m > 5$ is not sufficient to reliably estimate the decay activation energy of the ensemble and its lifetime, it can be stated that the quantities E_a and τ as functions of m approach the corresponding constants even at $m \sim 2$.

4. CONCLUSION

The above results demonstrated the possible existence of a new type of cluster form of carbon, namely, ensembles of C_8 three-dimensional clusters.

ACKNOWLEDGMENTS

N. E. L'vov would like to thank K. Nordlund for presenting the data on the parameters of the interatomic potential.

This work was carried out in the framework of Contract DSWA01-98-C-0001 and supported by the Russian Federal Program "Integration," project AO133.

REFERENCES

1. H. W. Kroto, J. R. Heath, S. C. O'Brien, *et al.*, Nature **318** (6042), 162 (1985).
2. W. Kratschmer, L. D. Lamb, K. Fostiropoulos, and D. R. Huffman, Nature **347** (6291), 354 (1990).
3. H. Prinzbach, A. Weller, P. Landenberger, *et al.*, Nature **407** (6800), 60 (2000).
4. L. A. Openov and V. F. Elesin, Pis'ma Zh. Éksp. Teor. Fiz. **68** (9), 695 (1998) [JETP Lett. **68**, 726 (1998)].
5. V. F. Elesin, A. I. Podlivaev, and L. A. Openov, Phys. Low-Dimens. Semicond. Struct. **11/12**, 91 (2000).
6. L. A. Openov and V. F. Elesin, Mol. Mater. **13** (1–4), 391 (2000).
7. K. Nordlund, J. Keinonen, and T. Mattila, Phys. Rev. Lett. **77** (4), 699 (1996).

Translated by O. Moskalev

Physics of the Solid State, Vol. 45, No. 5, 2003, pp. 809–811. Translated from Fizika Tverdogo Tela, Vol. 45, No. 5, 2003, pp. 771–773.

PERSONALIA

Celebrating the 75th Birthday of Boris Petrovich Zakharchenya

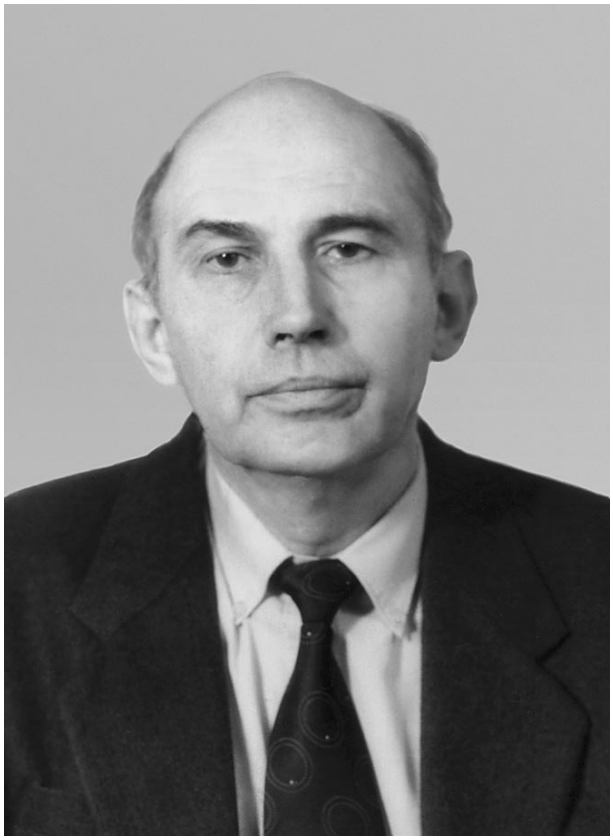

On May 1, 2003, Academician Boris Petrovich Zakharchenya, a prominent scientist in the field of solid-state physics, director of the Division of solid-state physics at Ioffe Physicotechnical Institute of the Russian Academy of Sciences, and editor-in-chief of the journal *Physics of the Solid State*, will celebrate his 75th Birthday.

B.P. Zakharchenya was born in the town of Orsha, Byelorussia (Belarus), into a military engineering family. The family soon moved to Leningrad (St. Petersburg), where in 1947 Boris Petrovich finished secondary school and entered the Faculty of Physics at the Leningrad (St. Petersburg) State University.

In 1952, upon graduating from university, he was admitted to the Leningrad Physicotechnical Institute for post-graduate studies. His scientific supervisor was Corresponding Member of the Academy of Sciences E.F. Gross, an outstanding scientist in the field of spectroscopy. In 1951, before Zakharchenya entered the Physicotechnical Institute, E.F. Gross and N.A. Karryev discovered the hydrogen-like spectrum of excitons in crystals of Cu_2O. Boris Petrovich was immediately involved into the actively ongoing experimental studies on the properties of this quasiparticle, which had been theoretically predicted by Ya.I. Frenkel in 1937. A series of experiments conducted by Zakharchenya on crystals of Cu_2O led to the discovery of a number of new phenomena. The observation of two exciton series in the spectra of Cu_2O demonstrated opportunities to investigate the complicated band structure of semiconductors by using the spectra of excitons. In external fields, the Zeeman and Stark effects in the spectra of excitons were observed experimentally for the first time. These results made a substantial contribution to the physics of excitons and the development of fine methods of semiconductor spectroscopy.

Research on the exciton spectra of semiconductors in a magnetic field was continued and intensively pursued by B.P. Zakharchenya, together with E.F. Gross, after having defended his candidate dissertation in 1955. Among the results obtained are the first observation of a strong diamagnetic shift in the levels of exci-

1063-7834/03/4505-0809$24.00

tons, caused by the large exciton radius (1956), and the discovery of magnetoabsorption oscillations, which are connected with Landau levels and occur beyond the scope of exciton series (1957). These observations of exciton effects in the spectra of Cu_2O, as well as independent observations of magnetoabsorption oscillations in Ge (Lax and Zwerdling) and in InSb (Burstein and Picus) marked the beginning of semiconductor magnetooptics. The investigations carried out by Zakharchenya in the 1960s were also devoted to excitons in a magnetic field; they proved the existence of quasi-one-dimensional magnetic excitons (work performed together with R.P. Seisyan) and, independently of but simultaneously with the work of Thomas and Hopfield, discovered (1961) an effect of magnetic-field inversion in the spectra of noncentrosymmetrical CdS crystals closely associated with the existence of the exciton momentum. In 1966, a group of scientists, including Zakharchenya, was awarded the Lenin Prize for research on excitons in semiconductors. The same year, Zakharchenya successfully defended his doctorate dissertation.

In 1970, based on analogous symmetry properties of the magnetic field and circularly polarized light, as well as on results obtained using atomic-spectroscopy methods, Zakharchenya suggested the possibility of electronic-spin orientation in semiconductors under the influence of circularly polarized light. The experimental and theoretical studies into the optical orientation of electronic and nuclear spins in semiconductors, initiated by Boris Petrovich in the Physicotechnical Institute, led to the understanding of many important dynamical electronic and electronic–nuclear processes in semiconductors. In the course of the work carried out by B.P. Zakharchenya and V.G. Fleisher, they managed to achieve optical cooling of the nuclear-spin system down to 10^{-6} K and discovered multi-quantum nuclear resonances under optical-orientation conditions, optical orientation of holes, and other phenomena. In 1976, for a number of studies on optical orientation in semiconductors, Zakharchenya and other research workers of the Physicotechnical Institute were awarded the State Prize of the USSR. The joint monograph *Optical Orientation* edited by B.P. Zakharchenya and F. Maier was published in English in 1984 and reissued in Russian in 1989; this monograph summarized the achievements made around the world in this new area of solid-state physics.

The observation of hot luminescence of high-energy photoelectrons and of optical aligning of their momenta under the influence of circularly polarized light performed by B.P. Zakharchenya and D.N. Mirlin and other coworkers in 1976 opened up another important area of the physics of semiconductors. Experimental and theoretical studies (V.I. Perel', M.I. D'yakonov) demonstrated ample opportunities available in the stationary research of hot luminescence (in a magnetic field in particular) for the investigation of energy and momentum relaxation of carriers, including fast femtosecond processes, in semiconductors and semiconductor structures. Those studies gained wide recognition and had a great impact on developments in research abroad.

Over the last years, research into spin phenomena in quantum-confinement semiconductor structures has been successfully carried out under the supervision of Zakharchenya by employing the spectroscopic and magnetooptics methods developed by him earlier for bulk semiconductors. Optical orientation has been observed in quantum wells and quantum dots. In these nanoscale objects, fine and hyperfine structures of exciton states have been studied. A giant anisotropy of the hole g factor in quantum well and electron spin quantum beats in quantum dots have been discovered. In studying bulk semiconductors, emphasis was placed on the properties of magnetically mixed semiconductors (magnetic-polaron optics). The works of Zakharchenya and his colleagues made a significant contribution to the forming of modern ideas concerning the use of spin phenomena in electronics (spin electronics or "spintronics").

Zakharchenya's accomplishments in the development of optical spectroscopy and magnetooptics of semiconductors were recognized in his being elected Corresponding Member of the USSR Academy of Sciences (1976) and then Member of the Russian Academy of Sciences (1992). His achievements have been honored with a number of state and foreign rewards and prizes. In 1996, the Russian Academy of Sciences awarded Zakharchenya the P.N. Lebedev Grand Golden Medal. His works in optical orientation in semiconductors have been marked with the Hanle Prize, awarded in Germany, and the works in semiconductor–ferromagnet hybrid structures, with the A.G. Aronov Prize. Zakharchenya has also won support from the Abramovich and Deripaska Fund.

Over many years, Zakharchenya has been director of the division of solid-state physics at the Ioffe Physicotechnical Institute of the Russian Academy of Sciences. In this post of high responsible, he devotes a lot of his efforts to developing an experimental base in the laboratory of the division (the cryogen equipment, in particular), supporting new prospective scientific directions, and creating a favorable work and research atmosphere.

Zakharchenya is a professor of the St. Petersburg State University of Electrical Engineering. The lectures on optics of semiconductors read by Boris Petrovich have been a success; in addition, they attract a new generation of physicists to the Physicotechnical Institute.

For many years, Academician Zakharchenya has been editor-in-chief of the journal "Physics of the Solid State." He plays an inestimable role in shaping the journal's editorial policy and in ensuring timely publication of its English version.

Academician Zakharchenya contributes greatly to strengthening international ties at the Physicotechnical Institute. He has collected unique material on close links between scientists of the Physicotechnical Institute and physicists from Germany. The materials date back to the works of A.F. Ioffe in the laboratory of Roentgen. They roused keen interest in the scientific community and promoted the raising of funds to repair the Physicotechnical Institute. This money was supplied by the German "Messerschmidt Fund," which sponsors foreign institutions that have historical ties with Germany. During 2001–2002, Zakharchenya worked as a professor at the Vuerzburg University (in the framework of the Mercator personal professorship); there has been a close cooperation between this university and the Physicotechnical Institute in the joint research of semiconductors.

Zakharchenya's talent has displayed itself not only in physics. His essays and memoirs on meeting interesting people from the world of science and art have been published in journals of fiction, such as *Our Heritage*, *Aurora*, and *Neva*. Boris Petrovich is an outstanding narrator, his stories, which are very emotional and original in form, stay in the memory of his listeners (and recently TV viewers) for a long time. Those publications and pieces of performance feature Boris Petrovich as an all-round educated person and a genuine intellectual in the true sense of the word.

We congratulate Boris Petrovich on the occasion of his 75th birthday and wish him good health and every success in his scientific endeavors.

Editorial Board
of the Journal *Physics of the Solid State*

Physics of the Solid State, Vol. 45, No. 5, 2003, pp. 812–815. Translated from Fizika Tverdogo Tela, Vol. 45, No. 5, 2003, pp. 774–777.

METALS AND SUPERCONDUCTORS

Resonance Attenuation of Ultrasonic Waves in a Superconductor with a Moving Vortex Structure

E. D. Gutliansky

Research Institute of Physics, Rostov State University, pr. Stachki 194, Rostov-on-Don, 344090 Russia

e-mail: gutlian@ip.rsu.ru

Received September 26, 2002

Abstract—Equations describing the interaction of ultrasonic waves with a moving vortex structure are derived. The addition to attenuation and the relative change in the velocity of longitudinal ultrasonic waves due to this interaction are calculated. It is found that when a longitudinal ultrasonic wave propagates along the direction of motion of the vortex structure and the velocity V of the structure is equal to half the velocity of the wave, then anomalous acoustic attenuation occurs and the contribution from the ultrasound–vortex interaction to the velocity of the ultrasonic wave vanishes. It is shown that if the vortex structure moves at a sufficiently high velocity, then (in contrast to the case of the structure at rest) a weakly damping collective mode propagating with velocity $2V$ arises in the structure. It is this mode that is responsible for anomalous attenuation of longitudinal ultrasonic waves. *© 2003 MAIK "Nauka/Interperiodica".*

1. Ultrasonic methods for investigating a mixed state of superconductors offer few advantages over the more widely used electromagnetic methods. One of these advantages is that an ultrasonic wave interacts with a vortex structure everywhere over the superconductor bulk. The current theory of interaction between ultrasonic waves and a vortex structure enables one to calculate the effect of the ultrasound–vortex interaction on the acoustic attenuation and on the velocity of ultrasonic waves [1–13], as well as the electric field resulting from this interaction (acoustoelectric effect) [3, 4, 6, 7]. In all the papers indicated above, the interaction with a vortex structure at rest as a unit was considered. In this paper, we investigate the interaction with a moving vortex structure.

The objective of this work is to show that, in a vortex structure moving as a whole with a velocity V, a collective mode arises propagating with velocity $2V$. This mode causes two observable phenomena: the acoustic attenuation anomalously increases and the effect of the vortex structure on the velocity of longitudinal ultrasonic waves changes sign when the velocity of the vortex structure becomes equal to half the velocity of longitudinal ultrasonic waves c_l.

We will represent a superconductor as two interacting subsystems: the ionic lattice and the electron superfluid possessing a vortex structure. The normal electrons outside the cores of vortices are ignored; these are assumed to move with the ionic lattice and partially screen its ions. This assumption limits the ultrasound-frequency range of interest, because the relaxation time of the normal electrons must be much shorter than the period of an ultrasonic wave. The interaction of the normal vortex core with the ionic lattice is included by using phenomenological viscosity η [4–7], which can depend on the velocity of the vortex lattice [14, 15]. This possible dependence does not affect the results obtained in this paper.

2. Let us derive the equations of motion of the vortex structure of a superconductor. The current density $\mathbf{J}_s$ of the electron superfluid in the laboratory frame is given by the gradient-invariant expression

$$\mathbf{J}_s = \frac{1}{\lambda_L^2 \mu_0}\left(\frac{\phi_0}{2\pi}\nabla\Phi - \mathbf{A}\right). \quad (1)$$

Here, Φ is the phase of the order parameter, $\mathbf{A}$ is the vector potential ($\mathbf{B} = \nabla \times \mathbf{A}$, with $\mathbf{B}$ being the magnetic induction), λ_L is the London penetration depth, ϕ_0 is the flux quantum, and μ_0 is the permeability of free space. Let us find the vector product of Eq. (1) and the ∇ operator:

$$\nabla \times \mathbf{J}_s = \frac{1}{\lambda_L^2 \mu_0}\left(\frac{\phi_0}{2\pi}\nabla \times \nabla\Phi - \nabla \times \mathbf{A}\right). \quad (2)$$

Now, we introduce the magnetic induction $\mathbf{B}_v$ of the vortex lattice; its magnitude is equal to $\phi_0 n_v$, where n_v is the two-dimensional vortex density (the number of vortices per unit area in a plane perpendicular to the vortex lines), and its direction is determined by the tangent to the vortex line. In the presence of vortices, the phase of the order parameter is a multivalued function and the circulation of this phase around a closed loop l is determined by the number of vortices enclosed by the loop:

$$\frac{\phi_0}{2\pi}\int \nabla\Phi d\mathbf{l} = \int \mathbf{B}_v d\mathbf{s},$$

1063-7834/03/4505-0812$24.00

where $\int d\mathbf{s}$ is an integral over a surface bounded by the loop l. According to Stokes's theorem, this expression can be rewritten as

$$\frac{\phi_0}{2\pi}\int \nabla\times\nabla\Phi d\mathbf{s} = \int \mathbf{B}_\nu d\mathbf{s};$$

therefore, since the loop is chosen arbitrarily, we have

$$\frac{\phi_0}{2\pi}\nabla\times\nabla\Phi = \mathbf{B}_\nu.$$

For the sake of further analysis, Eq. (2) should be expressed in terms of macroscopic electrodynamics. For this purpose, we write the total current density in the laboratory frame; under the basis assumptions made above, this current density is

$$\mathbf{j} = \mathbf{j}_s - qn_s\dot{\mathbf{U}}. \tag{3}$$

Here, $-qn_s\dot{\mathbf{U}}$ is the current density associated with the moving ionic lattice in the laboratory frame and $\mathbf{U}$ is the strain vector of the ionic lattice.

Substituting Eq. (3) into Eq. (1) and taking into account the Maxwell equations

$$\nabla\times\mathbf{E} = -\frac{\partial\mathbf{B}}{\partial t}, \tag{4}$$

$$\nabla\times\mathbf{H} = \mathbf{j}, \tag{5}$$

we obtain, after simple algebra,

$$\mathbf{B} - \lambda_L^2\nabla^2\mathbf{B} + \frac{m}{q}\nabla\times\dot{\mathbf{U}} = \mathbf{B}_\nu. \tag{6}$$

By differentiating Eq. (6) with respect to time and using the continuity equation for $\mathbf{B}_\nu$

$$\frac{\partial\mathbf{B}_\nu}{\partial t} = \nabla\times(\dot{\mathbf{W}}\times\mathbf{B}_\nu),$$

we represent Eq. (6) in the form

$$\frac{\partial}{\partial t}\left(-\lambda_L^2\nabla^2\mathbf{B} + \mathbf{B} + \frac{m}{q}\nabla\times\dot{\mathbf{U}}\right) = \nabla\times(\dot{\mathbf{W}}\times\mathbf{B}_\nu). \tag{7}$$

Here, $\dot{\mathbf{W}}$ is the local velocity of the vortex lattice. This equation (derived in a different way) was used by us in [3–7] to construct a theory of the acoustoelectric effect.

For definiteness, we consider a homogeneous isotropic superconductor in an external magnetic field applied in the negative direction of the z axis and producing a magnetic induction $\mathbf{B}_\nu = \mathbf{B}_0$ in the superconductor (in the absence of an ultrasonic wave). We assume that a longitudinal ultrasonic wave propagates in the positive direction of the y axis ($\mathbf{U} = \mathbf{U}_0\exp(i\mathbf{k}\mathbf{y} - i\omega t)$, where $\mathbf{k}$ is the wave vector, $\omega = 2\pi f$, f is the frequency of the ultrasonic wave) and that there is a vortex structure which moves at a velocity $\mathbf{V}$ in the same direction. The ultrasonic wave causes oscillations $\Delta\mathbf{B}_\nu$ in the flux density of the vortex structure relative to its equilibrium value $\mathbf{B}_0$, which is determined by the external magnetic field. We assume that $\mathbf{B}_0$ is independent of the spatial coordinates.[1] Thus, we have $\mathbf{B}_\nu = \mathbf{B}_0 + \Delta\mathbf{B}_\nu$ and the local velocity of the vortex structure can be written as $\dot{\mathbf{W}} = \mathbf{V} + \dot{\mathbf{W}}'$, where $\mathbf{V}$ is the time-independent velocity characterizing the motion of the vortex structure as a whole and $\dot{\mathbf{W}}'$ is the variable part of the vortex-structure velocity. Substituting these expressions into Eq. (7) and taking into account that only harmonic waves will be considered in what follows, we obtain

$$\begin{aligned}\mathbf{B} - \lambda_L^2\nabla^2\mathbf{B} &= -\frac{q}{m}\nabla\times\dot{\mathbf{U}} + \nabla\times(\mathbf{W}'\times\mathbf{B}_0)\\ &+ \frac{1}{-i\omega}\nabla\times(\mathbf{V}\times\Delta\mathbf{B}_\nu).\end{aligned} \tag{8}$$

By solving Eq. (8) for $\mathbf{B}$ and using Eq. (5), we find the current density produced by the moving vortex structure and the vibrating ionic lattice of the superconductor:

$$\begin{aligned}\mathbf{J} &= \frac{1}{\mu_0[1 + (\lambda_L k)^2]}\\ &\times\left[(\mathbf{W}\times\mathbf{B}_0)k^2 - \frac{1}{i\omega}(\mathbf{V}\times\Delta\mathbf{B}_y)k^2\right].\end{aligned} \tag{9}$$

Now, we will write the local equation of motion of the vortex structure (neglecting the inertial mass of a vortex). This equation follows from the balance $\mathbf{F}_{\rm fr} = \mathbf{F}_L$ between the Lorentz force $\mathbf{F}_L = \mathbf{J}_s'\times\mathbf{B}_\nu$ and the friction force $\mathbf{F}_{\rm fr} = \eta(\dot{\mathbf{W}} - \dot{\mathbf{U}}) - \tilde{\eta}(\dot{\mathbf{W}} - \dot{\mathbf{U}})\times\mathbf{B}_\nu$ exerted on the vortex structure by the crystal lattice of the superconductor, where $\mathbf{J}_s'$ is the current density in the local frame attached to the vortex structure. Using the relation $\mathbf{J}_s' = (\mathbf{J}_s - qn_s\dot{\mathbf{W}})$, we obtain

$$\eta(\dot{\mathbf{W}} - \dot{\mathbf{U}}) - \tilde{\eta}(\dot{\mathbf{W}} - \dot{\mathbf{U}})\times\mathbf{B}_\nu = (\mathbf{j}_s - qn_s\dot{\mathbf{W}})\times\mathbf{B}_\nu, \tag{10}$$

where η and $\tilde{\eta}$ are the longitudinal and transverse viscosities of the vortex structure, respectively: $\tilde{\eta} = (q/h)\eta'$, with η' being the transverse viscosity for a vortex. Equations (3), (4), (9), and (10) completely describe the motion of the vortex structure. To solve the problem under study, these equations should be combined with the equation of motion of the ionic lattice:

$$\begin{aligned}\rho\ddot{\mathbf{U}} &= \rho c_t^2\Delta\mathbf{U} + \rho(c_l^2 - c_t^2)\,\mathrm{graddiv}\,\mathbf{U}\\ &- qn_s\dot{\mathbf{U}}\times\mathbf{B} - qn_s\mathbf{E} + \mathbf{F}_{\rm fr}.\end{aligned} \tag{11}$$

[1] For a bulk superconductor, the criterion for the independence of $\mathbf{B}_0$ from the coordinate y is that $\mu_0 Jc_l/B_0 f \ll 1$. In a film, the vortex structure is accelerated by London currents; therefore, the film thickness should not exceed λ_L.

Here, ρ is the density of the superconductor and c_l and c_t are the velocities of longitudinal and transverse ultrasonic waves, respectively, in the absence of the vortex structure. In Eq. (11), the third and fourth terms are the forces exerted on the ionic lattice by the magnetic and electric fields, respectively, and the fifth term is the friction force. In order to solve the problem of the interaction between the moving vortex structure and ionic-lattice vibrations, we have to find the relation between the strain of the ionic lattice and the deformation of the vortex lattice. We will solve this problem by linearizing Eq. (10). In what follows, we consider the case of a "dirty" superconductor and assume that the Magnus force is balanced by the transverse friction force, $qn_s - \tilde{\eta} = 0$, which means that the Hall effect is ignored. In this case, we obtain two equations:

$$\eta \mathbf{V} = \mathbf{J}_0 \times \mathbf{B}_0, \tag{12}$$

$$\eta(\dot{\mathbf{W}}' - \dot{\mathbf{U}}) = \mathbf{J} \times \mathbf{B}_0 + \mathbf{J}_0 \times \Delta\mathbf{B}_\nu. \tag{13}$$

Equation (12) allows one to find the current density that needs to be passed through the superconductor in order to accelerate the vortex structure to the velocity V. Equation (13) describes vibrations of the vortex lattice and their interaction with an ultrasonic wave. Using the local continuity equation, we find $\Delta\mathbf{B}_\nu$:

$$\Delta\mathbf{B}_\nu = -\frac{i\omega\mathbf{k}(\mathbf{W}' - \mathbf{U})}{\omega - Vk}\mathbf{B}_0. \tag{14}$$

Substituting Eq. (9) and then Eq. (14) into Eq. (13) yields

$$\eta(\dot{\mathbf{W}}' - \dot{\mathbf{U}}) = -Dk^2\mathbf{W}' + \frac{1}{i\omega}\frac{Vk}{\omega - Vk}(Dk^2 + i\omega\eta)(\dot{\mathbf{W}}' - \dot{\mathbf{U}}). \tag{15}$$

Here, $D = B_0^2/\mu_0(1 + \lambda_L^2 k^2)$. We note that $D \approx C_{11}$, where C_{11} is the longitudinal elastic modulus of the vortex structure [9]. In the case of $V = 0$, Eq. (15) reduces to the equation of motion of a vortex structure proposed in [10].

By solving Eq. (15), in combination with linearized equation (11) and Eqs. (3)–(5), we find the velocity change $\Delta c_l/c_l$ and the additional attenuation α due to the interaction with the vortex structure:

$$\frac{\Delta c_l}{c_l} = \frac{1}{2}\left(1 - \frac{V}{c_l}\right)\left(1 - 2\frac{V}{c_l}\right)\frac{\omega^2}{\rho c_l^2}\frac{D}{\left(1 - 2\frac{V}{c_l}\right)^2\omega^2 + X^2}, \tag{16}$$

$$\alpha = \frac{1}{2}\frac{\omega^2}{\rho c_l^3}\left(1 - \frac{V}{c_l}\right)D\frac{X}{\left(1 - 2\frac{V}{c_l}\right)^2\omega^2 + X^2}. \tag{17}$$

Here, $X = \frac{D}{\eta}k^2$ and $D = B_0^2/\mu_0(1 + \lambda_L^2 k^2)$.

In Eqs. (16) and (17) for the attenuation and the relative change in the velocity of sound, two values of the vortex-structure velocity are of special interest: $V = c_l/2$ and $V = c_l$. The physical consequences of the latter relation were discussed by us in [16, 17]. At $V = c_l/2$, the contribution from the vortex structure to the velocity of sound changes sign and the attenuation of sound due to its interaction with the vortex structure increases anomalously, which is associated with the formation of a new collective mode in the vortex structure; this type of mode arises only in a moving vortex structure.

3. In order to make certain that this mode exists, we consider the equation of motion of the vortex structure, which is obtained by putting $\dot{\mathbf{U}} = 0$ in Eq. (15):

$$\eta\dot{\mathbf{W}}' = -Dk^2\mathbf{W}' + \frac{1}{i\omega}\frac{Vk}{\omega - Vk}(Dk^2 + i\omega\eta)\dot{\mathbf{W}}'. \tag{18}$$

The dispersion relation for vortex-lattice vibrations has the form

$$zik'^2 - k' + 1 = 0, \tag{19}$$

where $k = k'k_0$, $k_0 = \omega/2V$, and $z = Dk_0^2/\eta\omega$.

We consider the following two extreme cases where the solution to Eq. (19) has a clear physical interpretation:

$$k_1' = 1 + 2z^2 - z^2 i, \qquad k_2' = -1 - 2z^2 - z^{-1}i, \quad z \ll 1, \tag{20}$$

$$k_{1,2}' = \pm\frac{\sqrt{2}}{2}z^{-\frac{1}{2}}(1 + i), \quad z \gg 1. \tag{21}$$

It follows from Eq. (20) that at a sufficiently large vortex-structure velocity satisfying the condition $D\omega/4\eta V^2 \ll 1$, a well-defined, weakly damping collective mode with the wave vector k_1' exists that propagates with velocity $2V$ in the direction of motion of the vortex structure. When the velocity of the vortex structure becomes equal to $c_l/2$, the velocity of this collective mode coincides with the velocity of ultrasound and, hence, resonance depletion of acoustic power into the moving vortex structure occurs. This resonance is manifested in the relative velocity change and attenuation of ultrasound described by Eqs. (16) and (17): attenuation of longitudinal ultrasonic waves anomalously increases and the contribution from the vortex lattice to their velocity vanishes when the velocity of the vortex structure becomes equal to half the velocity of the longitudinal ultrasonic waves.

The root k_2' of Eq. (19) corresponds to the same mode propagating in the direction opposite to that of the vortex-structure motion. In this case, the mode is

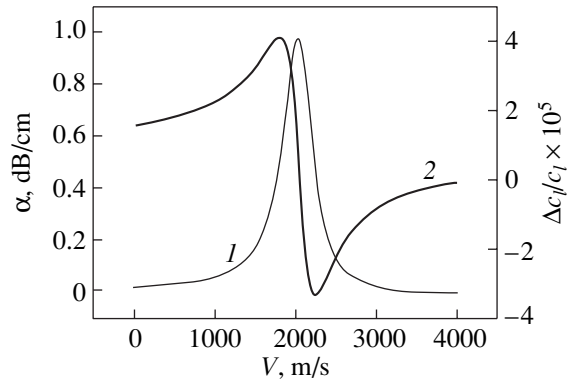

Calculated (*1*) attenuation and (*2*) relative change in the velocity of ultrasonic waves as a function of the vortex-structure velocity of the superconductor. The external magnetic field equals 2 T, the ultrasound frequency is 100 MHz, and the temperature $T = 0.989T_c$.

not well-defined, because the real part of k_2' is much smaller than its imaginary part.

The solution to Eq. (19) given by Eq. (21) for small velocities of the vortex structure indicates that there are no well-defined modes in this case.

4. Now, we estimate the effect numerically. The figure shows the attenuation (curve *1*) and the relative change in the velocity (curve *2*) of ultrasonic waves as a function of the vortex-structure velocity. These quantities are calculated for the following material parameters typical of high-temperature superconductors: $\rho = 6 \times 10^3$ kg/m^3, $c_l = 4.1 \times 10^3$ m/s, $t = T/T_c = 0.989$, $B_{c2}(t) = B_{c2}(0)(1-t)$, $B_{c2}(0) = 184.47$ T, and $r_0 = 10^{-8}\,\Omega$ m. The viscosity is calculated using the Stefan formula in the FF regime $\eta = BB_{c2}/r_0$ [18]. The frequency of ultrasonic waves is 100 MHz, and the external magnetic field is $B = 2$ T. As is seen from the figure, the effect is easily observable. Indeed, the attenuation is 0.022 dB/cm for $V = 0$ and increases by 50 times for $V = 2000$ m/s.

5. Thus, we have shown that, at velocities of the vortex structure satisfying the condition $D\omega/4\eta V^2 \ll 1$, a collective mode exists that propagates at velocity $2V$ along the direction of the vortex-structure motion. This mode can cause, for example, anomalous attenuation of longitudinal ultrasonic waves propagating through a superconductor with a moving vortex structure when the direction of their propagation coincides with that of the vortex-structure motion and the velocity of the vortex structure is half that of these waves.

ACKNOWLEDGMENTS

The author is grateful to V.P. Sakhnenko for helpful discussions of the results of this work.

This paper was supported by the Russian Foundation for Basic Research (project no. 17037) and the Ministry of Education of the Russian Federation (project no. E00-3.4-288).

REFERENCES

1. J. Pankert, Physica C (Amsterdam) **168**, 335 (1990).
2. E. D. Gutlyanskiĭ, Fiz. Nizk. Temp. **18** (4), 428 (1992) [Sov. J. Low Temp. Phys. **18**, 290 (1992)].
3. E. D. Gutlyanskiĭ, Pis'ma Zh. Éksp. Teor. Fiz. **59** (7), 459 (1994) [JETP Lett. **59**, 480 (1994)].
4. E. D. Gutliansky, Physica C (Amsterdam) **235–240**, 2080 (1994).
5. E. D. Gutliansky and T. V. Kolesnikova, Physica C (Amsterdam) **235–240**, 2078 (1994).
6. E. D. Gutlyanskiĭ, Fiz. Tverd. Tela (St. Petersburg) **38** (5), 1341 (1996) [Phys. Solid State **38**, 743 (1996)].
7. E. D. Gutlyanskiĭ, Pis'ma Zh. Éksp. Teor. Fiz. **67** (3), 222 (1998) [JETP Lett. **67**, 239 (1998)].
8. D. Dominguez, B. Bulaevskii, B. Ivlev, *et al.*, Phys. Rev. Lett. **74** (13), 2579 (1995).
9. E. B. Sonin, Phys. Rev. Lett. **76** (15), 2794 (1996).
10. J. Pankert, G. Marbach, A. Comberg, *et al.*, Phys. Rev. Lett. **65** (24), 3052 (1990).
11. D. Dominguez, B. Bulaevskii, B. Ivlev, *et al.*, Phys. Rev. B **53** (10), 6682 (1996).
12. G. Blatter and B. Ivlev, Phys. Rev. B **52** (6), 4588 (1995).
13. D. Dominguez, B. Bulaevskii, B. Ivlev, *et al.*, Phys. Rev. B **51** (21), 15649 (1995).
14. M. Sugahara, Phys. Rev. B **6** (1), 130 (1972).
15. A. I. Larkin and Yu. N. Ovchinnikov, Zh. Éksp. Teor. Fiz. **68** (5), 1915 (1975) [Sov. Phys. JETP **41**, 960 (1975)].
16. E. D. Gutlyanskiĭ, Izv. Ross. Akad. Nauk, Ser. Fiz. **66** (6), 779 (2002).
17. E. D. Gutliansky, Phys. Rev. B **66** (5), 52511 (2002).
18. P. Nozieres and W. F. Vinen, Philos. Mag. **14** (2), 667 (1966).

Translated by Yu. Epifanov

Physics of the Solid State, Vol. 45, No. 5, 2003, pp. 816–824. Translated from Fizika Tverdogo Tela, Vol. 45, No. 5, 2003, pp. 778–785.

SEMICONDUCTORS AND DIELECTRICS

Electronic Band Structure and X-ray Spectra of Boron Nitride Polytypes

V. V. Ilyasov, T. P. Zhdanova, and I. Ya. Nikiforov

Don State Technical University, Rostov-on-Don, 344010 Russia

e-mail: victor.ilyasov@rost.ru

Received June 4, 2002

Abstract—The electronic band structures of boron nitride crystal modifications of the graphite (*h*-BN), wurtzite (*w*-BN), and sphalerite (*c*-BN) types are calculated using the local coherent potential method in the cluster muffin-tin approximation within the framework of the multiple scattering theory. The specific features of the electronic band structure of 2*H*, 4*H*, and 3*C* boron nitride polytypes are compared with those of experimental x-ray photoelectron, x-ray emission, and *K* x-ray absorption spectra of boron and nitrogen. The features of the experimental x-ray spectra of boron nitride in different crystal modifications are interpreted. It is demonstrated that the short-wavelength peak revealed in the total densities of states (TDOS) in the boron nitride polytypes under consideration can be assigned to the so-called outer collective band formed by 2*p* electrons of boron and nitrogen atoms. The inference is made that the decrease observed in the band gap when changing over from wurtzite and sphalerite to hexagonal boron nitride is associated with the change in the coordination number of the components, which, in turn, leads to a change in the energy location of the conduction band bottom in the crystal. *© 2003 MAIK "Nauka/Interperiodica".*

1. INTRODUCTION

Considerable progress achieved in solid-state electronics has brought problems concerning local compositions, structures, and physicochemical properties of solid surfaces to the forefront. Increased interest in wide-gap semiconductor materials (GaN, BN, GaAs, SiC, etc.) has been stimulated by their use in the design of optoelectronic devices operating, in particular, in the short-wavelength range [1]. As was noted in recent papers [1–3], the possibility exists of preparing heterostructures of the type GaN/SiC, *h*-BN/*r*-BN, etc. Interpretation of the optical properties of semiconductor materials requires detailed knowledge of the specific features of their electronic band structure. Hexagonal crystal modifications of boron nitride, namely, graphite-like (*h*-BN), wurtzite (*w*-BN), and sphalerite (*c*-BN) forms, have been studied in sufficient detail. In particular, Aleshin *et al.* [4] and Nemoshkalenko *et al.* [5] measured the experimental x-ray photoelectron spectra (XPS) of valence electrons for these modifications of boron nitride with a resolution of 0.9–1.2 eV. However, in our opinion, these spectra cannot exhibit all features inherent in the fine structure of the density of states due to small photoionization cross sections σ_s and σ_p for *s* and *p* valence electrons of boron and nitrogen atoms. Since the ratio $\sigma_s(\mathrm{N})/\sigma_p(\mathrm{N})$ is equal to 10.5 and the photoionization cross sections for valence electrons of nitrogen are larger than those for valence electrons of boron, the x-ray photoelectron spectrum predominantly reflects the energy distributions of nitrogen *s* electrons and, to some extent, nitrogen *p* electrons. For example, the intense maximum observed at an energy of 20 eV in the vicinity of the valence band bottom is associated primarily with nitrogen 2*s* electrons. Nitrogen *p* and boron *p* electrons are localized near the valence band top. In this region, the contribution of the former electrons to the x-ray photoelectron spectrum is considerably larger than that of the latter electrons. As a rule, the structure of the valence band in solids has been investigated using photoelectron and *K* emission spectroscopies simultaneously.

X-ray emission spectra of boron and nitrogen in boron nitride were analyzed earlier in [6–9]. Fomichev [6] recorded the boron emission band in the third diffraction order with a wavelength resolution of 0.1 Å and an instrumental distortion of 0.6 eV. The nitrogen emission spectrum of the *c*-BN modification was measured in the fourth diffraction order with an instrumental distortion of 0.6 eV. These results made it possible to estimate the valence band width (15.3 eV) and the band gap (4.5 eV). Mansour and Schnatterly [9] succeeded in separating *K* emission bands into σ and π components. It was demonstrated that anisotropy of the hexagonal lattice affects the *K* emission band. According to [9], π excitons manifest themselves in the B *K* emission band and the double peak can be attributed to phonons. Muramatsu *et al.* [10] examined the boron *K* x-ray emission spectra of hexagonal, wurtzite, and sphalerite modifications of boron nitride. It was shown that the high-energy satellites observed in the B *K* emission spectrum are caused by x-ray Raman scattering and correlate well with the coordination number of boron atoms in the structures of boron nitride modifications.

1063-7834/03/4505-0816$24.00 © 2003 MAIK "Nauka/Interperiodica"

The electronic band structure of BN polytypes in the region of the x-ray absorption near-edge structure (XANES) is of special interest. In the boron *K* absorption (quantum yield) spectra of hexagonal [8] and sphalerite [11] modifications of boron nitride, the clear maxima can be associated both with the appearance of an excited state upon expulsion of a boron 1*s* electron (an x-ray exciton) [8] or a Wannier exciton [11] and with the transfer of a boron 1*s* electron to a free state arising from a vacancy [12]. Moreover, a number of important features in the fine structure of the *K* absorption spectra of boron and nitrogen in the 2*H* BN polytype have hitherto defied explanation. The necessity of interpreting a great body of available x-ray spectral data lent impetus to theoretical investigations into the specific features of the electronic band structure of boron nitride polytypes. The electron energy spectra have been theoretically analyzed using the orthogonalized plane wave (OPW) [13–15], linearized augmented-plane wave (FLAPW) [16], orthogonalized linear combination of atomic orbitals (OLCAO) [17–19], linearized muffin-tin orbital (LMTO) [20, 21], pseudopotential [2, 22], and local coherent potential (within the cluster approximation) [23–25] methods. However, up to now, there has been no complete consistent description of all available experimental data for graphite-like *h*-BN [2] (and other boron nitride polytypes) and more complex heterostructures [20].

Furthermore, a unified theory of polytypism of boron nitride has not been proposed to date. The thermodynamic factors that account for the dependence of the polytypism on macroparameters (temperature and pressure) [26] and on the stoichiometry of the composition [27, 28] have been studied most extensively. Although these polytypes have long been known, the contribution of the electronic subsystem to their relatively high stability has not been considered in terms of the features revealed in the electronic band structure and chemical bonding.

In our recent works [25], we analyzed the specific features in the electronic band structures of 4*H* and 3*C* boron nitride polytypes. A comparison with the x-ray spectra revealed both the similarities and differences in their electronic structures. However, we failed to interpret all the features observed in the boron *K* emission bands of the 4*H* and 3*C* boron nitride polytypes. This can be explained by the small size of the computational cluster (five coordination spheres) used in [25]. In the present work, the electronic band structures of 2*H*, 4*H*, and 3*C* boron nitride polytypes were computed with the use of a larger sized cluster (containing more than 30 coordination spheres) in the framework of the multiple scattering theory. This model can be considered to be a fairly good approximation for calculating an infinite crystal. The calculations performed in this work provide new insight into the origin of the fine structure of the boron *K* emission spectra in the high-energy range of the valence band.

2. COMPUTATIONAL TECHNIQUE

The electronic band structure of the boron nitride crystal modifications under investigation (see Table 1) was calculated within a unified approach using the local coherent potential method [23]. The effective crystal potential for each of the boron nitride polytypes was determined as the sum of the Coulomb potential, the exchange component, and the Madelung potential. The crystal muffin-tin potential was calculated for an equilibrium state with the lattice parameters listed in Table 1.

The contributions of nearest neighbor atoms to the density of states and the Coulomb potential of 33 coordination spheres were also included in the calculation. The exchange component of the crystal potential was determined in the Slater X_α-approximation with the exchange correction $\alpha = 2/3$. The computational unit cell was chosen with due regard for the fact that the wurtzite crystal structure can be considered to consist of four built-in hexagonal unit cells. For simplicity, as in [25], the ratio between the lattice parameters was taken to be equal to $c/a = 1.633$ instead of $c/a = 1.67$. Within this approximation, two nearest coordination spheres (containing one and three atoms, respectively) are combined into a single sphere, which significantly simplifies the calculation without a significant loss in accuracy. The structure of graphite-like boron nitride consists of a system of plane-parallel layers arranged just above one another. In this case, boron and nitrogen atoms alternate along the *c* axis. The layers are composed of regular hexagons of the benzene-ring type with an angle of 120° between the bonds in such a way that each atom of one sort is surrounded by three nearest neighbor atoms of the other sort. The unit cell was chosen in the form of a hexagonal prism containing four atoms (two boron and two nitrogen atoms) with the coordinates B1 = a (0, 0, 0), B2 = a (0.5, $\sqrt{3}/6$, $c/2a$), N1 = a (0.5, $\sqrt{3}/6$, 0), N2 = a (0.5, $\sqrt{3}/2$, $c/2a$). The Madelung potential was calculated using the Ewald method and accounted for the electrostatic contribution made by different sublattices to the crystal potential:

$$\varphi_{11} = \varphi_{22} = -4.5849q/a,$$
$$\varphi_{12} = \varphi_{21} = -0.80194q/a$$

for sphalerite-type boron nitride;

$$\varphi_{11} = \varphi_{22} = -3.242q/a,$$
$$\varphi_{12} = \varphi_{21} = -0.91568q/a$$

for wurtzite-type boron nitride; and

$$\varphi_{11} = \varphi_{22} = -3.701q/a,$$
$$\varphi_{12} = \varphi_{21} = -0.3839q/a$$

for hexagonal graphite-type boron nitride.

Here, φ_{ii} is the potential produced by the *i*th boron ($i = 1$) or nitrogen ($i = 2$) atom at atoms of the *i*th sub-

Table 1. Crystal chemical characteristics and crystal potentials of the studied compounds

Characteristic	Lattice type					
	sphalerite		wurtzite		graphite	
	B	N	B	N	B	N
Unit cell parameter, nm	0.3615		a = 0.2551, c/a = 1.633		a = 0.2504, c/a = 2.67	
Coordination number	4		4		3	
Number of atoms per unit cell	8		4		4	
Radius of the muffin-tin sphere, au	1.449	1.449	1.327	1.327	1.367	1.367
Radius of the Wigner–Seitz sphere, au	2.121	2.121	1.898	1.898	1.849	1.849
Number of valence electrons in the muffin-tin sphere	2.97	5.19	3.076	4.864	2.844	4.979
Potential between the muffin-tin spheres, Ry	0.00985		−0.10626		−1.48600	
Charge density between the muffin-tin spheres	0.07061		0.10770		0.13229	
B–N interatomic distance, nm	0.1565331		0.1562156		0.1445684	
	0.2997413		0.2603627		0.2891368	
B–B or N–N interatomic distance, nm	0.3993378		0.2991303		0.334284	
	0.2556203		0.2551000		0.2504000	
	0.3615000		0.3607675		0.3642068	

lattice and φ_{ij} is the potential produced by atoms of the ith sublattice at atoms of the jth sublattice.

The crystal muffin-tin potentials thus obtained were used in solving the Schrödinger radial equation at $l = 0$ and 1 (for light elements such as boron and nitrogen, the d electron states were disregarded) in the energy range from 0.02 to 2.5 Ry. The local partial densities of states (PDOS) for boron and nitrogen in boron nitride were calculated with a cluster containing 250 atoms in 30 coordination spheres for c-BN, 253 atoms in 31 coordination spheres for w-BN, and 251 atoms in 33 coordination spheres for hexagonal graphite-like BN according to the relationship

$$n_l^A(E) = \frac{\sqrt{E}}{\pi}\int_0^{r_{ws}} [R_l^A(r, E)r]^2 dr \frac{\mathrm{Im}\,\mathrm{Tr}\,T_{L,L'}^{A,00}(E)}{\mathrm{Im}\,t_l^A(E)}.$$

Here, l is the orbital quantum number, $R_l^A(r)$ stands for the radial wave functions of the A-type atom in the cluster, and $T_{lm,l_1m_1}^{A,00}$ is the matrix element of the scattering operator. The total density of states (TDOS) of valence electrons per unit cell for one spin projection was determined as the sum of the local densities of states (LDOS) according to the procedure described in [25].

3. RESULTS AND DISCUSSION

A detailed analysis of the calculated electron energy spectra of 2*H*, 4*H*, and 3*C* boron nitride polytypes and a comparison with the experimental x-ray photoelectron and x-ray emission spectra of valence electrons and *K* x-ray absorption spectra of boron and nitrogen in these polytypes demonstrate that their spectra contain three groups of bands separated by wide energy gaps. Figure 1 shows the total densities of occupied and free states according to the results of our calculations in comparison with the experimental x-ray photoelectron spectra [4] and the theoretical TDOS curves obtained using the OLCAO method [19] for sphalerite, wurtzite, and graphite-like modifications of boron nitride. The experimental boron *K* x-ray absorption spectra are also displayed in this figure. It is worth noting that there are wide energy gaps between the valence band top and the conduction band bottom in the *h*-BN (3.4 eV), *c*-BN (4.5 eV), and *w*-BN (5.2 eV) modifications, which suggests semiconductor behavior of these compounds. In this respect, it is interesting to note that crystallization of nitrides, for example, NbN, in a simple hexagonal crystal system (with a WC-type structure) can lead to a manifestation of semimetallic properties [29]. The structure of the valence band (VB) consisting of two subbands is well represented (with due regard for the van Hove singularities) by the specific features in the x-ray photoelectron spectra of boron nitride polytypes.

The lower subband (**II**-VB) is predominantly formed by the boron 2*s* states. This is a common feature of the polytypes observed for nitrides of boron, niobium [29], and other elements. The energy location of subband **II**-VB corresponds to the *A* peak in the x-ray photoelectron spectra of boron nitride. The band gap between subband **II**-VB and the upper broad valence subband **I**-VB (formed primarily by the 2*p* states of boron and nitrogen) is maximum in the 2*H* polytype (4.4 eV [19]), which agrees with the data obtained by Boev and Kul'kova [21]. Thus, the band gap in the 2*H* BN polytype appears to be 2 eV larger than that in the hexagonal niobium nitride 2*H* NbN. This can be associated with the deeper potential well of niobium atoms. A comparison of the experimental and theoretical data on the widths of subbands **I**-VB and **II**-VB and the band gaps E_g presented in Table 2 shows that the results of our calculations are in reasonable agreement with the data available in the literature. It should be noted that the total width of the valence band in the polytypes under investigation increases in the following order: 2*H* BN < 3*C* BN < 4*H* BN. As can be seen from the calculated total and local partial densities of states (Figs. 2–4), the densities of boron 2*p* and nitrogen 2*p* states are primarily responsible for the structure of subband **I**-VB in the aforementioned boron nitride polytypes. The contributions of the *s* and *p* states to the upper valence subband can be judged from the partial charge distributions of valence electrons (Table 3). Earlier [25], we revealed the specific features in the electronic structure of the valence band in the 4*H* and 3*C* BN polytypes from a comparison with the x-ray emission spectra of boron and nitrogen. These features manifest themselves more clearly in the TDOS and PDOS curves calculated in the present work (Figs. 3, 4). An analysis of the results demonstrates that the broad subband **I**-VB, which is formed by the *s*–*p*-hybridized states of boron and the *p* states of nitrogen, is characteristic of the studied crystals.

As follows from our calculations (Figs. 2–4), the electronic band structure of the 2*H*, 4*H*, and 3*C* BN polytypes in the region of the x-ray absorption near-edge structure is predominantly formed by free 2*p* states of boron atoms. This is consistent with the universally accepted concept that the near-edge fine structure (for example, in 2*H* BN) is governed by the narrow π band (in the vicinity of the conduction band bottom) and two broad σ bands (lying 10–20 eV above the π band) weakly overlapping with the high-energy tail of the π band [31]. The most smeared spectrum of free states is observed for the 4*H* BN polytype. By contrast, for the 2*H* BN polytype, the *a*, *b*, *c*, and *d* peaks attributed to the boron *p* states are characterized by oscillations with an energy period of 0.5 Ry. The features observed in the energy spectrum can be assigned to strongly localized excited states of the crystal, which is in agreement with the concepts proposed by Vinogradov *et al.* [31]. According to [31], the dominant absorption bands *a* and *b* in the boron and nitrogen x-ray absorption spectra of 2*H* BN, which correspond to the first two peaks *a* and *b* in Fig. 2, are associated with the transitions of B *K* and N *K* electrons to the aforementioned excited states with π and σ symmetries in the crystal.

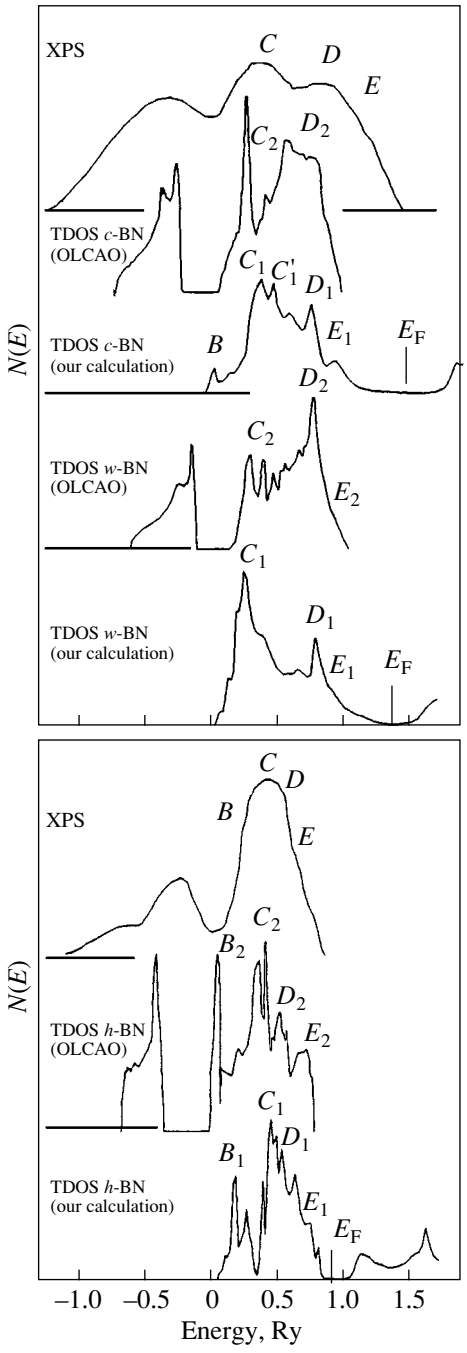

Fig. 1. Experimental x-ray photoelectron spectra (XPS) [23] and the total densities of states (TDOS) of valence electrons according to the results of our calculations and the OLCAO method [19] for sphalerite- (*c*-BN), wurtzite- (*w*-BN), and graphite-type (*h*-BN) boron nitrides, respectively.

Closer examination of the valence band top in the *h*-BN crystal revealed that the boron and nitrogen elec-

Table 2. Experimental and theoretical valence subband widths and band gaps in BN crystals (in eV)

Phase	Reference	VB	**II**-VB	**I**-VB	E_g
c-BN	[6]*	20.2	5.2	16.1	4.6
		22.0	–	15.4	6.0
		–	–	13.5	6.4
	[30]*	21.1	6.0	11.8	–
	[13]	23.4	6.1	11.8	3.4
	[19]	21.1	6.92	10.94	5.18
	[23]	23.3	8.6	12.0	5.7
	This work	–	–	14.5	5.6
w-BN	[19]	21.0	6.28	11.76	5.81
	This work	–	–	15.9	5.2
h-BN	[6]*	19.4	4.6	14.0	3.6
	[14]	29.0	4.1	15.5	5.8
	[2]	26.6	4.0	13.2	5.2
	[19]	18.8	4.02	10.40	4.07
	This work	–	–	11.1	3.4

* Experimental data.

Table 3. Partial charge distributions of valence electrons in subband **I**-VB

	c-BN		*w*-BN		*h*-BN	
	B	N	B	N	B	N
S	0.37254	0.13217	0.58604	0.16162	0.17338	0.05744
P	2.28626	3.70713	2.47006	3.71152	2.11073	2.91180
Σ	2.65879	3.83930	3.05610	3.87314	2.28411	2.96954

tron states contribute equally to the formation of subband **I**-VB. This correlates with the boron and nitrogen *K* x-ray emission spectra [6–8] and the calculated local partial densities of states of boron and nitrogen in the *h*-BN modification (see Fig. 2). The 2*H* BN polytype is characterized by a decrease in the valence band width and the band gap (as compared to those for other polytypes), which is confirmed by the available experimental data [4, 6–8] and theoretical estimates (Table 2). The only exception is represented by the theoretical results obtained in [2, 14], which, in our opinion, can be explained by the limitations of the computational methods used in these works. A decrease in the valence band width in the *h*-BN modification leads to a change in the energy separation between the principal peaks *C* and *D* by a factor of more than two (as compared to those observed for *c*-BN and *w*-BN crystals). This is supported by the fact that the x-ray photoelectron spectrum of the 2*H* BN polytype does not contain the high-energy peak *D* at 0.75 Ry (Fig. 1), which is clearly seen in the x-ray photoelectron spectra of the 4*H* and 3*C* BN polytypes. The observed features can be caused by the decrease in the coordination number (Table 1) and a manifestation of the atomic character of the states due to geometric properties of the 2*H* BN polytype. Specifically, the number of atoms in the first three coordination shells of the *h*-BN crystal is 2.5 times smaller than that in the *c*-BN crystal. In the 2*H* BN polytype, the occupied states of *s* and *p* electrons are associated with the formation of localized states, which results in splitting of the *B* and *C* peaks in the TDOS curve. The electron states responsible for the *B* peak at 0.12 Ry can be treated as quasi-core states with a binding energy of the order of 8.8 eV. This value is 1.7 times less than that for the relevant states in the *c*-BN crystal. The principal peak *C* in the theoretical TDOS curve has a fine structure whose features manifest themselves in the experimental x-ray photoelectron and *K* x-ray emission spectra of boron and nitrogen. For subband **I**-VB of graphite-like boron nitride, the binding energy in the ground state is equal to 4.4 eV, which is also 1.7 times less than that of the 3*C* BN polytype.

The fine structure of the features in the TDOS curve for the 2*H* BN polytype is noteworthy. Reasoning from the results of analyzing this structure, we can interpret the specific features in the experimental *K* x-ray emis-

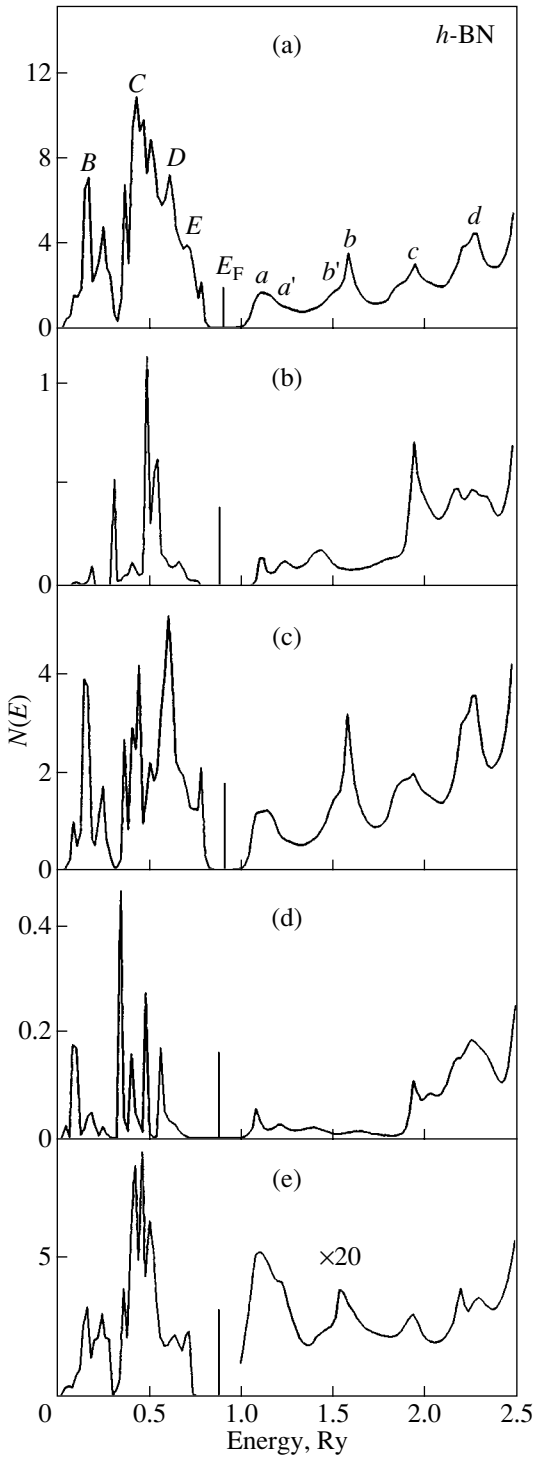

Fig. 2. (a) Total density of states and the local partial densities of (b) B 2*s*, (c) B 2*p*, (d) N 2*s*, and (e) N 2*p* states in hexagonal graphite-type boron nitride.

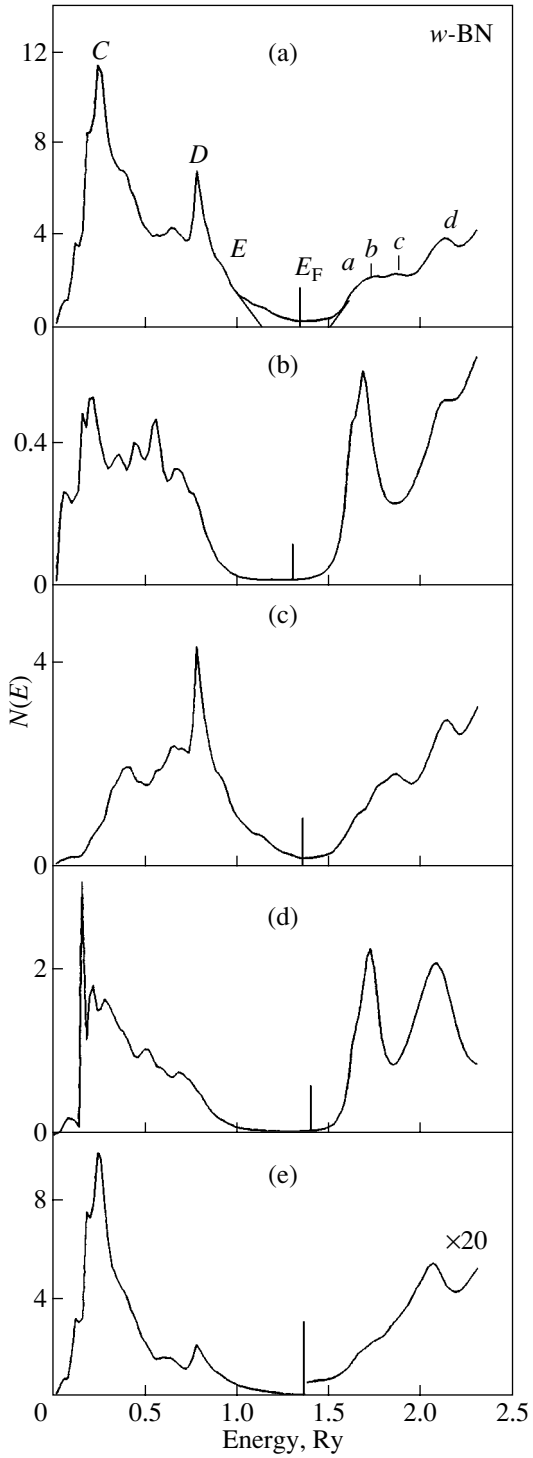

Fig. 3. (a) Total density of states and the local partial densities of (b) B 2*s*, (c) B 2*p*, (d) N 2*s*, and (e) N 2*p* states in wurtzite-type boron nitride.

sion and x-ray absorption spectra of boron and nitrogen. In particular, the short-wavelength peak *E* in the TDOS curve can be assigned to the boron 2*p* and nitrogen 2*p* states with a small admixture of the boron 3*s* states, whereas the short-wavelength peak *E*' is attributed to the boron 2*p* states alone. A comparison of the calculated local partial densities of boron 2*p* and nitrogen 2*p* states with the *K* x-ray emission spectra of boron (Fig. 5) and nitrogen (Fig. 6) allows us to draw some inferences regarding the origin of the specific features

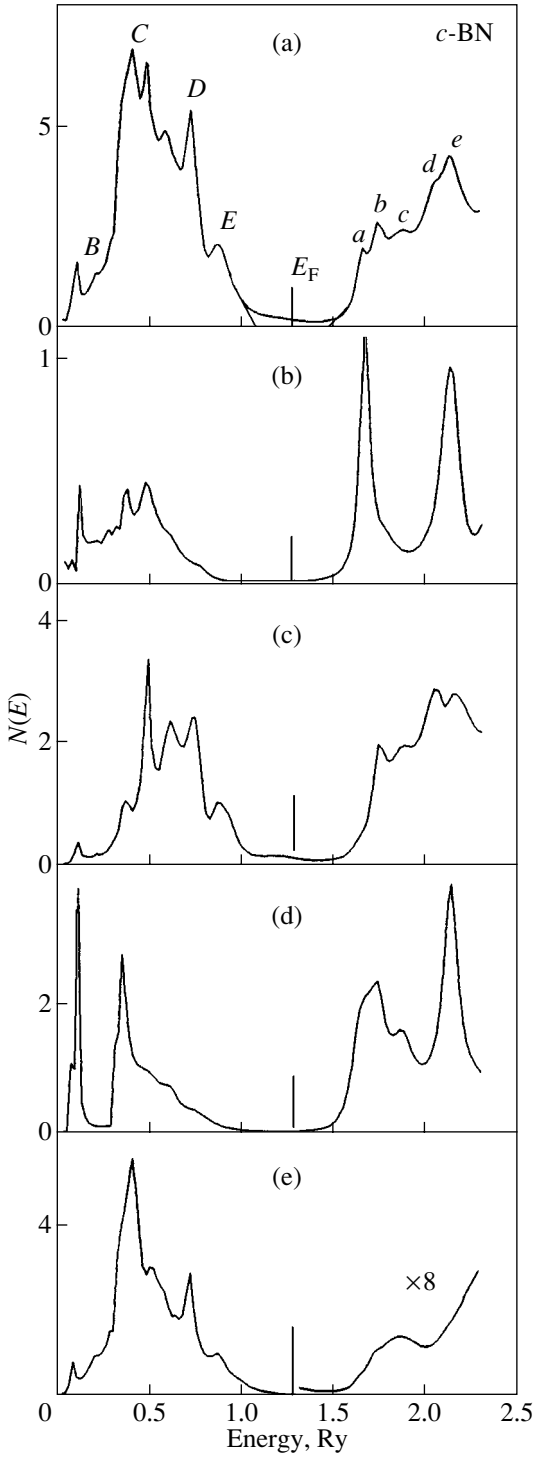

Fig. 4. (a) Total density of states and the local partial densities of (b) B 2*s*, (c) B 2*p*, (d) N 2*s*, and (e) N 2*p* states in sphalerite-type boron nitride.

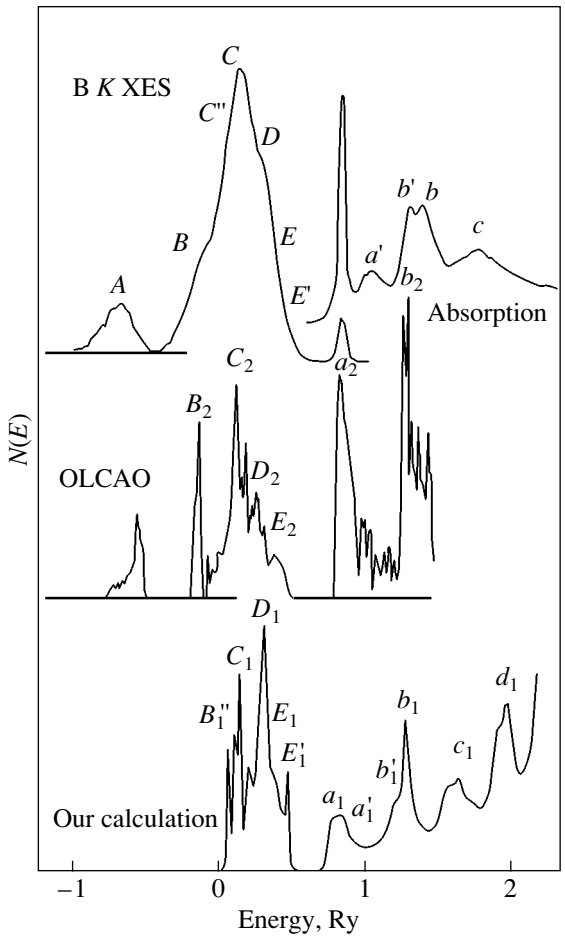

Fig. 5. Experimental boron *K* x-ray emission spectrum (B *K* XES) [32], the boron *K* x-ray absorption spectrum [6], and the local partial densities of boron 2*p* states according to the results of our calculation and the OLCAO method [19] for the *h*-BN modification.

in the high-energy range of the valence band top in the *h*-BN modification. The appearance of the *E* peak can be associated with the occurrence of the outer collective band formed by electrons of the metal and nonmetal ions, as is the case in the K_α emission bands of nitrogen [33]. The possibility of forming an outer collective band in the *c*-BN modification was discussed in our earlier work [34]. The calculations carried out in the present work demonstrate that the E_1 peak manifests itself not only for sphalerite-type (Fig. 4) and graphite-type (Fig. 2) crystals but also for wurtzite-type crystals (Fig. 3). A short-wavelength shoulder is observed in the experimental x-ray photoelectron spectra (shoulder *E*) [35] and in the nitrogen *K* emission photoelectron bands (peak *E*) [32]. Apparently, this fact was ignored by the authors of the aforementioned works. In our opinion, the concept of an outer collective band, which was originally proposed for transition metal nitrides [33], can be extended to binary nitrides.

The near-edge fine structure observed in the *K* x-ray absorption spectra of boron and nitrogen (the XANES region) can be interpreted using the results of the band-structure calculations. Actually, it is found that the *a*, *b*, and *c* peaks in the theoretical spectra coincide in energy location with those in the experimental spectra. The *c*

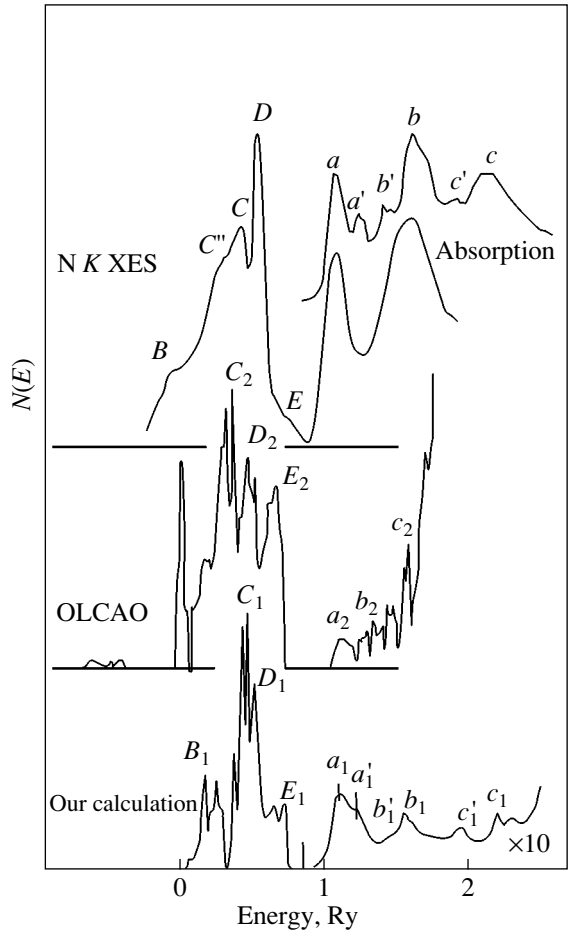

Fig. 6. Experimental nitrogen *K* x-ray emission spectrum (N *K* XES) [31], the nitrogen *K* x-ray absorption spectrum [6], and the local partial densities of nitrogen 2*p* states according to the results of our calculation and the OLCAO method [19] for the *h*-BN modification.

band in the nitrogen *K* x-ray emission spectrum (Fig. 6) can be attributed to localized 2*p* states with an energy of 2.2 Ry (peak c_1). Analysis of the data presented in Figs. 5 and 6 allows the assumption that the π interaction of boron and nitrogen atoms substantially affects the electronic band structure of the *h*-BN modification (as judged from the same energy location of the *a* peaks). It can be assumed that, in this case, the σ interaction of boron and nitrogen atoms also plays a significant role (see the energy location of the *b* and *c* peaks).

In boron nitride crystals, chemical bonding in planar layers exhibits mixed covalent–ionic nature and the interlayer interaction is associated with the electrostatic forces. For sphalerite-type crystals, the contribution from the ionic component of bonds does not exceed 20%. Judging from the partial charge distributions (Table 3), the valence electrons of nitrogen atoms adopt an sp^3 configuration, whereas the valence electrons of boron atoms, for the most part, are characterized by a mixture of sp^2 and sp^3 configurations.

4. CONCLUSIONS

Thus, it was demonstrated that, although the crystal structures of 2*H*, 4*H*, and 3*C* boron nitride polytypes differ significantly, the electronic band structures of *h*-BN, *w*-BN, and *c*-BN are characterized by a number of common features. Specifically, the TDOS curves exhibit features typical of boron nitride polytypes, namely, the *C* and *D* peaks associated with the ground states of nitrogen and boron atoms in the crystal. It was found that the experimental boron and nitrogen *K* x-ray emission spectra and theoretical spectra of 2*p* electrons in the boron nitride polytypes under investigation contain the short-wavelength shoulder *E*. This suggests that the high-energy features and, in particular, the so-called outer collective band have the same origin in transition metal nitrides [33] and in a larger family of binary nitrides, including boron nitride polytypes.

However, the width of the valence subband in the vicinity of the valence band top (subband **I**-VB) for the *h*-BN modification is considerably less than those for wurtzite and sphalerite modifications. This is caused by the decrease in the degree of overlap of the wave functions for boron and nitrogen atoms. The decrease observed in the band gap when changing over from wurtzite and sphalerite to hexagonal boron nitride is associated with the change in the coordination number of the components, which, in turn, leads to variations in the energy location of the conduction band bottom, specifically to a shift by approximately 7 eV toward the low-energy range. The role played by the coordination in the formation of subband **I**-VB was confirmed by the results of calculations of the total density of states. According to the calculations, the energy separation between the ground-state peaks *C* and *D* for the *h*-BN modification is equal to half the energy separation between these peaks for the *w*-BN and *c*-BN modifications.

REFERENCES

1. V. V. Bel'kov, Yu. V. Zhilyaev, G. N. Mosina, *et al.*, Fiz. Tverd. Tela (St. Petersburg) **42** (9), 1563 (2000) [Phys. Solid State **42**, 1606 (2000)].
2. S. N. Grinyaev and V. V. Lopatin, Zh. Strukt. Khim. **38** (1), 32 (1997).
3. R. Molnar, W. Goetz, L. T. Romano, and N. M. Johnson, J. Cryst. Growth **178**, 147 (1997).
4. V. G. Aleshin, A. N. Sokolov, and A. A. Shul'zhenko, Sverkhtverd. Mater. **38** (5), 12 (1985).
5. V. V. Nemoshkalenko, A. V. Bochko, and A. I. Senkevich, Dokl. Akad. Nauk Ukr. SSR **10**, 77 (1986).
6. V. A. Fomichev, Izv. Akad. Nauk SSSR, Ser. Fiz. **31** (6), 957 (1967); Fiz. Tverd. Tela (Leningrad) **9** (11), 3167 (1967) [Sov. Phys. Solid State **9**, 2496 (1967)]; Fiz. Tverd. Tela (Leningrad) **13**, 907 (1971) [Sov. Phys. Solid State **13**, 754 (1971)].
7. V. A. Fomichev and N. A. Rumsh, J. Phys. Chem. Solids **29**, 153 (1972).

8. V. A. Fomichev, T. M. Zimkina, and I. I. Lyakhovskaya, Fiz. Tverd. Tela (Leningrad) **12** (1), 156 (1970) [Sov. Phys. Solid State **12**, 123 (1970)].
9. A. Mansour and S. E. Schnatterly, Phys. Rev. B **36** (17), 9234 (1987).
10. Y. Muramatsu, H. Kounzuki, and M. Motoyama, Phys. Rev. Lett. **71**, 448 (1993).
11. A. Agui, S. Shin, M. Fujisawa, *et al.*, Phys. Rev. B **55** (4), 2073 (1997).
12. V. V. Ilyasov and I. Ya. Nikiforov, Fiz. Tverd. Tela (St. Petersburg) **43** (2), 233 (2001) [Phys. Solid State **43**, 242 (2001)].
13. F. Bassani and M. Yoshimine, Phys. Rev. **130**, 20 (1963).
14. M. S. Nakhmanson and V. P. Smirnov, Fiz. Tverd. Tela (Leningrad) **13**, 905 (1971) [Sov. Phys. Solid State **13**, 752 (1971)]; Fiz. Tverd. Tela (Leningrad) **13**, 3288 (1971) [Sov. Phys. Solid State **13**, 2763 (1971)].
15. V. G. Aleshin and V. P. Smirnov, Fiz. Tverd. Tela (Leningrad) **11**, 1920 (1969) [Sov. Phys. Solid State **11**, 1546 (1969)].
16. D. R. Wiff and R. Keown, J. Chem. Phys. **47**, 3113 (1967); K. T. Park, K. Terakura, and N. Namada, J. Phys. C **20**, 1241 (1987); Z. Catellani, M. Posternak, A. Balderreschi, and A. J. Freeman, Phys. Rev. B **36**, 6105 (1987).
17. A. Zunger and A. J. Freeman, Phys. Rev. B **17**, 2030 (1978).
18. Ming-Zhu Huang and W. Y. Ching, J. Phys. Chem. Solids **46** (8), 977 (1985).
19. Yong-Nian Xu and W. Y. Ching, Phys. Rev. B **44** (15), 7787 (1991).
20. W. R. L. Lambrecht and B. Segall, Phys. Rev. B **40** (14), 9909 (1989); Phys. Rev. B **47** (15), 9289 (1993).
21. O. V. Boev and S. E. Kul'kova, Fiz. Tverd. Tela (St. Petersburg) **34**, 2218 (1992) [Sov. Phys. Solid State **34**, 1184 (1992)].
22. J. C. Phillips, J. Chem. Phys. **48**, 5740 (1968); R. M. Wentzcovitch, K. J. Chang, and M. L. Cohen, Phys. Rev. B **34**, 1071 (1986); R. M. Wentzcovitch, M. L. Cohen, and P. K. Lam, Phys. Rev. B **36**, 6058 (1987); R. M. Wentzcovitch, S. Fahy, M. L. Cohen, and S. G. Louie, Phys. Rev. B **38**, 6191 (1988).
23. V. V. Ilyasov, N. Yu. Safontseva, and I. Ya. Nikiforov, Fiz. Tverd. Tela (St. Petersburg) **36** (2), 451 (1994) [Phys. Solid State **36**, 247 (1994)]; Phys. Status Solidi B **185**, 171 (1994); J. Phys. C **7**, 6035 (1995).
24. V. V. Ilyasov and I. Ya. Nikiforov, Fiz. Tverd. Tela (St. Petersburg) **39** (6), 1064 (1997) [Phys. Solid State **39**, 955 (1997)].
25. T. P. Zhdanova, V. V. Ilyasov, and I. Ya. Nikiforov, Fiz. Tverd. Tela (St. Petersburg) **43** (8), 1388 (2001) [Phys. Solid State **43**, 1445 (2001)]; Zh. Strukt. Khim. **39** (6), 1083 (1998); Zh. Strukt. Khim. **41** (6), 1149 (2000).
26. V. A. Pesin and L. I. Fel'dgun, Zh. Fiz. Khim. **52** (5), 1320 (1978).
27. A. V. Kurdyumov, N. F. Ostrovskaya, and A. N. Pilyankevich, Neorg. Mater. **13** (11), 2001 (1977).
28. V. B. Shipilo and L. M. Gameza, Sverkhtverd. Mater. **67** (4), 17 (1990).
29. L. B. Litinskiĭ, Available from VINITI, No. 7592-B88 (Moscow, 1988), pp. 1–20.
30. O. P. Bugaets, A. A. Smekhnov, and S. P. Kuzenkov, J. Electron Spectrosc. Relat. Phenom. **68**, 713 (1994).
31. A. S. Vinogradov, S. V. Nekipelov, and A. A. Pavlychev, Fiz. Tverd. Tela (Leningrad) **33** (3), 896 (1991) [Sov. Phys. Solid State **33**, 508 (1991)].
32. Y. Muramatsu, H. Kouzuki, M. Motoyama, *et al.*, in *Photon Factory Activity Report* (National Laboratory for High Energy Physics, Oho-machi, 1994–1995).
33. I. N. Frantsevich, E. A. Zhurakovskiĭ, and N. N. Vasilenko, Dokl. Akad. Nauk SSSR **198** (5), 1066 (1971) [Sov. Phys. Dokl. **16**, 481 (1971)].
34. V. V. Ilyasov and I. Ya. Nikiforov, Fiz. Tverd. Tela (St. Petersburg) **43** (4), 598 (2001) [Phys. Solid State **43**, 621 (2001)].
35. V. P. Elyutin, I. V. Blinov, I. I. Goryunova, *et al.*, Neorg. Mater. **26** (5), 978 (1990).

Translated by O. Borovik-Romanova

Physics of the Solid State, Vol. 45, No. 5, 2003, pp. 825–829. Translated from Fizika Tverdogo Tela, Vol. 45, No. 5, 2003, pp. 786–790.

SEMICONDUCTORS AND DIELECTRICS

Metastable-State Population in *n*-GaAs

V. V. Krivolapchuk, M. M. Mezdrogina, and N. K. Poletaev

Ioffe Physicotechnical Institute, Russian Academy of Sciences, Politekhnicheskaya ul. 26, St. Petersburg, 194021 Russia
e-mail: Vlad.krivol@pop.ioffe.rssi.ru

Received May 20, 2002; in final form, September 3, 2002

Abstract—The population of metastable states in *n*-GaAs is determined by investigating the low-temperature slow edge photoluminescence as a function of temperature, uniaxial compression, and magnetic-field strength. Analysis of the evolution of the integrated intensity of slow afterglow revealed that in the allowed band, there is a free-carrier trapping state located a few millielectronvolts above the band edge and not related to the direct (Γ) band. The filling of this trap occurs through carrier tunneling exchange between the free-carrier subsystem and the reservoir of metastable localized states and is resonant in character. © *2003 MAIK "Nauka/Interperiodica".*

1. INTRODUCTION

Studies of the photoluminescence (PL) decay of the (D^0, h) and (D^0, x) lines in *n*-GaAs epitaxial layers revealed the decay curve to contain a slow component with $\tau \approx 10^{-5}$ s [1]. Figure 1 presents [1, 2] a PL decay curve of the (D^0, h) line. The fast decay time τ_0 corresponds to a photoexcited carrier lifetime $\tau_0 \leq 10^{-8}$ s, which is characteristic of the optical transitions responsible for the above lines [2, 3]. Our experiments [4, 5] led to the conclusion that the slow PL intensity decay can be assigned to the existence of metastable states which capture holes. The long afterglow of the (D^0, h) emission line is due to nonactivated delocalization into the valence band of a hole from a metastable center, which subsequently recombines with the electron of a shallow donor. The main characteristics of the slow radiation decay are the intensity decay time τ_s and the time-integrated intensity bounded by the slow-decay curve, I_τ. The slow-decay time τ_s is determined by the time it takes the holes to escape from the metastable states; this time is constant for all samples studied and is practically independent of external factors. The integral I_τ is proportional to the number of holes released from the metastable states and naturally depends on the concentration of metastable centers and their population.

The population of metastable centers is effected during a pump pulse and is determined by its intensity (generation rate) and the efficiency of the mechanism of carrier transfer to these centers, which is connected with the capture cross section σ_{MS}. The total number of holes trapped in the metastable centers after the pulse termination is also proportional to the concentration of these centers, N_{MS}. The integrated intensity of the slow afterglow I_τ is determined by the concentration of the metastable centers populated during the pumping and, therefore, is different in different samples (Fig. 1b) because the values of N_{MS} are different. The number of holes captured can be experimentally estimated from the sum of light emitted by the sample after termination of the pump pulse. This light sum can be defined as the area bounded by the photoluminescence decay curve; this area is cross-hatched in Fig. 1a and is equal to the integral $I_\tau = \int I(t)dt$. The capture of carriers into metastable states and their release are not directly connected with radiative recombination (D^0, h; D^0, x); hence, when analyzing experimental data, the influence of external factors on radiative recombination must be separated from the processes responsible for metastable-center population. To correctly take into account the various factors affecting the (D^0, h) and (D^0, x) line intensities, we normalized this integral against the intensity of the (D^0, h) and (D^0, x) lines at the instant of excitation ($B_{MS} = I_\tau/I_{ex}$, where I_{ex} is the integrated luminescence intensity at the instant of pulse excitation). Thus, the determined value of B_{MS} should not depend on the variation of the (D^0, h) line emission process itself; therefore, B_{MS} can serve as a measure of the metastable-center population. To reveal specific features in the mechanisms of metastable center population, we studied the behavior of B_{MS} under various external conditions. The dependence of B_{MS} on excitation intensity was investigated earlier in [4]. An analysis of the experimental data, together with the results of a numerical model calculation conducted in the present work, made it possible to describe the behavior of B_{MS} throughout the pump light intensity range covered. This permitted us to estimate the metastable center concentration ($N_{MS} \approx 10^{13}$ cm^{-3}). The center population is governed, to a considerable extent, by the energy position of the trapping center, which can be in both a forbidden and an allowed band. In the latter case, such states will operate as sources of free-carrier resonant scattering [6].

1063-7834/03/4505-0825$24.00

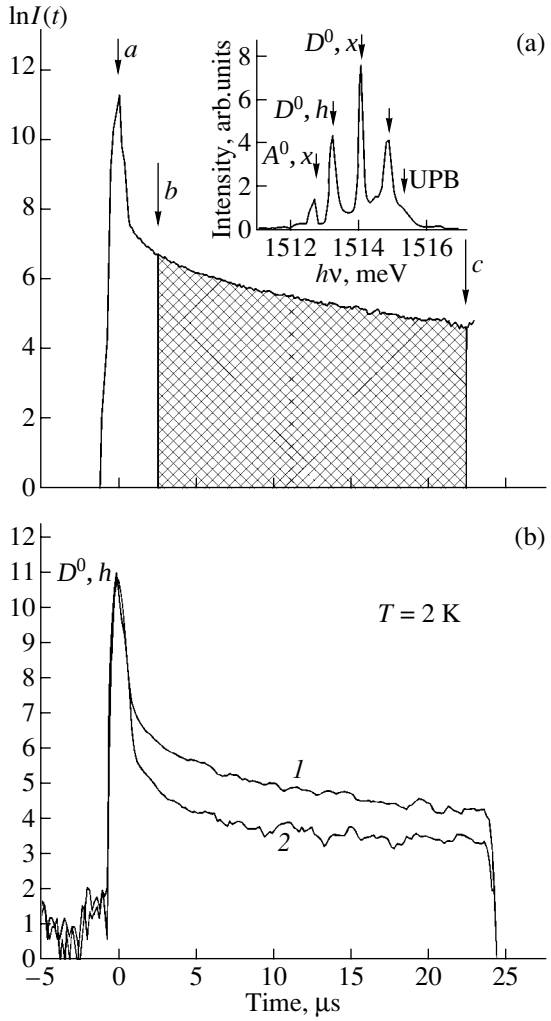

Fig. 1. (a) D^0, h emission line decay measured on an n-GaAs sample at $T = 2$ K. The cross-hatched region refers to the integral $I_\tau = \int I(t)dt$ corresponding to the slow afterglow. The inset shows a typical n-GaAs spectrum in the exciton region obtained at $T = 2$ K, where LPB and UPB are the lower and upper polariton branches, respectively; the A^0,x line is the emission of a neutral acceptor-bound exciton. (b) D^0,h emission line decay curves measured on two different n-GaAs samples at $T = 2$ K.

This study was aimed at establishing specific features of the process of population of metastable states. This was done by investigating the behavior of B_{MS} in slow decay (which reflects the population of metastable states in a given sample) as a function of temperature (T_b), uniaxial pressure (P_d), and magnetic field (B_f).

2. EXPERIMENT

We studied n-GaAs epitaxial samples with N_d–N_a = 10^{13}–10^{15} cm^{-3}. The layers were grown on ⟨100⟩-oriented substrates using different methods, namely, liquid-phase epitaxy (LPE), chloride vapor-phase epitaxy (HVPE), and MOCVD. All samples used in the experiments produced a sufficiently high photoluminescence intensity in the exciton spectral region. The luminescence was excited by a pulsed YAG laser (λ_{ex} = 530 nm, $\tau = 10^{-7}$ s) or a semiconductor laser (λ_{ex} = 759 nm, τ = 10^{-6}–10^{-7} s). The PL spectra and kinetics were measured with a DFS-52 double-grating spectrometer in the lock-in photon counting mode. The low-temperature measurements were conducted in an UTREX cryostat in the interval 2–25 K. The dependence of the PL decay spectra (D^0, x; D^0, h) on the external magnetic field was studied at 1.8 and 4.2 K, and that on uniaxial pressure, at 4.2 K only. Measurements of the spectra and kinetics in a magnetic field were performed in the Faraday geometry (with the magnetic field oriented perpendicular to the sample surface). The magnetic field strength was varied from 0 to 4 T.

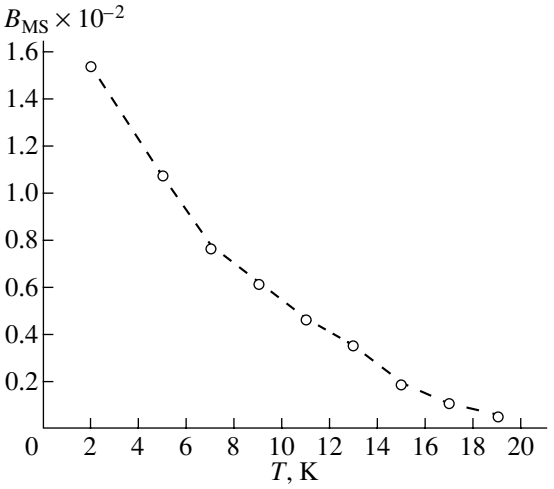

Fig. 2. Temperature dependence of B_{MS}.

3. EXPERIMENTAL RESULTS AND DISCUSSION

Figure 2 presents an experimental dependence of B_{MS} on temperature (T_b). One readily sees that B_{MS} decreases with increasing temperature by about an order of magnitude. Studies of the dependence of B_{MS} (at $T = 4.2$ K) on the magnitude of uniaxial pressure (P_d) and magnetic field strength (B_f) (Figs. 3a, 3b, respectively) showed that integral B_{MS} also decreases (by about one half) with increasing P_d and B_f. As follows from Figs. 2 and 3, while the dependences of B_{MS} on T_b, P_d, and B_f are functionally different, the overall behavior is qualitatively the same; namely, B_{MS} decreases monotonically. It is essential that the decrease in B_{MS} (which reflects the behavior of a deep local center) occurs at low values (and within a narrow range of variation) of T_b, P_d, and B_f.

Turning now to discussion, we note that the temperature dependence of the capture cross section for vari-

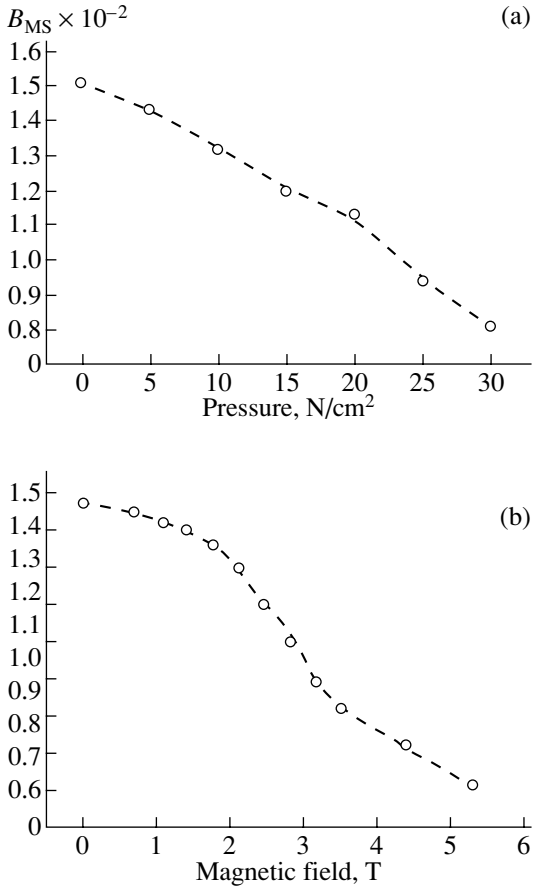

Fig. 3. Variation of B_{MS} at $T = 4.2$ K with (a) uniaxial pressure and (b) magnetic field.

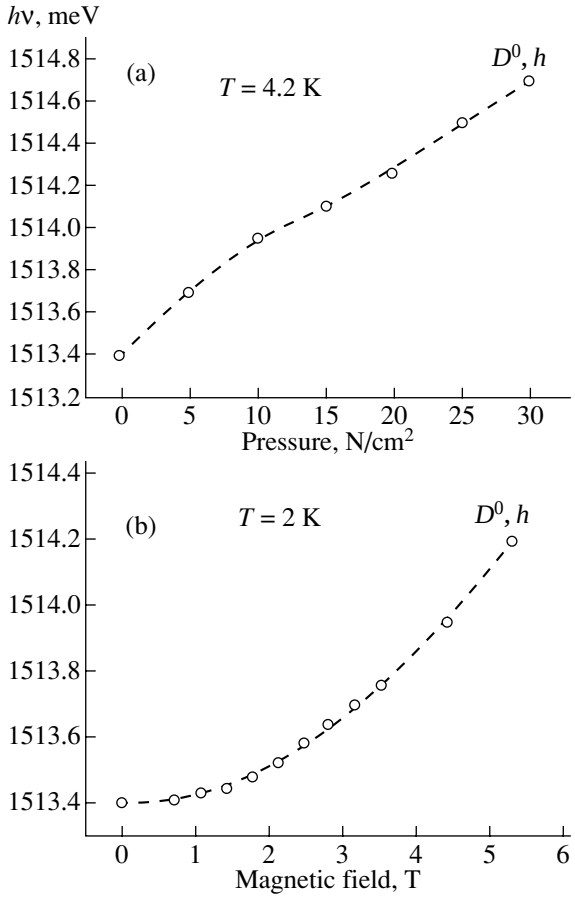

Fig. 4. Variation of the spectral position of the D^0,h line ($T = 4.2$ K) with increasing (a) uniaxial pressure and (b) magnetic field.

ous centers has been studied in considerable detail for a range of semiconductor compounds [7–9] and has been shown to be governed by many factors. It should be pointed out that the character of the temperature dependence of the cross section $\sigma_{MS} = F(T_b)$ is sensitive to the parameters of a given center and the carrier trapping mechanism operating in the given conditions. If the mechanism involves thermal activation, the trapping cross section (and, hence, $B_{MS} \sim \sigma_{MS}$) grows with increasing temperature [7], while in the case of cascade capture by an attracting center [8] it decreases with increasing temperature; this exactly was observed in our conditions. However, the applicability of the cascade capture mechanism to interpretation of the above experimental data may be questionable, because the detrapping time from metastable states is independent of temperature. Furthermore, studies of the nanosecond-range kinetics and of the bound-exciton ionization (the D^0, x line) as a function of temperature [10] revealed that the behavior of B_{MS} exhibits a noticeable feature in the 6- to 8-K interval.

In view of the above, as well as taking into account that the cross section in the cascade model is, from a formal standpoint, independent of pressure and magnetic field [8] (the density of energy levels is not likely to change with a small variation of P_d and B_f), we chose the tunneling mechanism [11, 12] as a model of deep-center population in the analysis of experimental data on the dependence of B_{MS} on T_b, P_d, and B_f (the nature of the potential barrier is not essential to the phenomenological consideration presented below and, hence, is not discussed here). Within this model, metastable centers are populated by tunneling transitions of carriers from the free state E_f in the band ($E = hk^2/2m^*$) to the trapping level E_{MS} of the metastable center. The tunneling probability is defined, in general, by the relation [13] $W_t \approx \exp(-\{(2m)^{1/2}/h\}\int[U(x) - E_{MS}]^{1/2}dx)$, where m is the particle mass, $U(x)$ is the barrier potential, and E_{MS} is the energy for which the tunneling transition probability is calculated. The number of free carriers tunneling from E_f to the metastable level will be determined by the population of the state (a metastable center can, in principle, be populated if the band state at $E_f = E_{MS}$ is occupied).

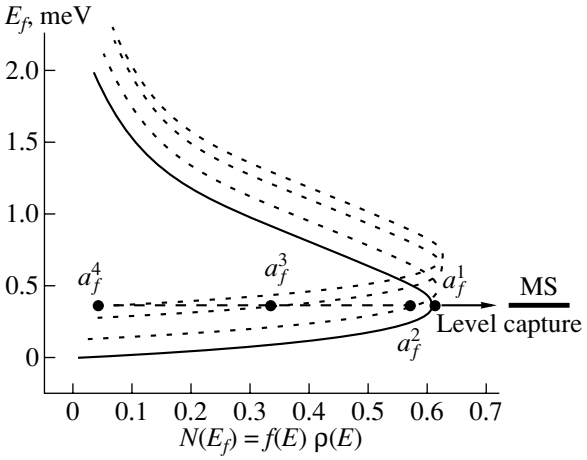

Fig. 5. Decrease in the population $N(E_f) = f(E)\rho(E)$ in the band at energy $E_f = E_{MS}$ measured at four values of uniaxial pressure P_d in ascending order ($a_f^1 < a_f^2 < a_f^3 < a_f^4$).

In this connection, we consider the reasons for the change in the population of metastable states (B_{MS}) under variation of the external factors (T_b, P_d, B_f), which are determined by the response of the free carriers to these external factors and, thus, depend on the carrier distribution function in the allowed band. It may be conjectured that the state of the local center remains practically unchanged under the comparatively low P_d and B_f used in the experiment; therefore, all the changes are related to the free-carrier distribution function. It should be pointed out that an increase in P_d and B_f leads (despite the different natures of these factors) to the same result, namely, to an effective increase in the band gap at the Γ point; the change in the gap width is indicated by the same shift of all spectral emission lines (*Fx*; D^0, *x*; D^0, *h*) toward higher energies (this shift is shown in Fig. 4 for the D^0, *h* line). The shift of the band edge affects the population at the energy $E_f = E_{MS}$. The population is given by the expression $N(E) = \rho(E)f(E)$, where $\rho(E)$ is the density of states and $f(E)$ is the carrier distribution function in the allowed band. To visualize this process qualitatively, $f(E)$ was chosen in the form of a Maxwellian distribution (T = 4.2 K). The maximum of the $f(E)$ function lies at E_f. The variation of the population function $N(E)$ thus found at the energy $E_f = E_{MS}$ is shown in Fig. 5 for four successively increasing values of P_d. This graph illustrates the decrease in population at the band level of energy $E_f = E_{MS}$ with increasing uniaxial pressure and magnetic field strength. Indeed, as is evident from Fig. 5, as P_d, B_f and, hence, the energy corresponding to the maximum in the $f(E)$ distribution function increase, the population $N(E_f)$ of the band level will fall off monotonically (points a_f^1, a_f^2, a_f^3, a_f^4 in Fig. 5). Note two aspects following immediately from the above tunneling transition model: (i) the centers can be populated if the tunneling transition energy E_{MS} (corresponding to the level of the metastable state) falls into an energy interval equal to the halfwidth of the carrier distribution function in the band (this condition provides resonance tunneling), and (ii) the value of B_{MS} (and, hence, the metastable-state population) will decrease with increasing P_d and B_f only if the energy corresponding to the maximum in the distribution function (E_F) at a fixed temperature T (2, 4.2 K), $P_d = 0$, and $B_f = 0$ is higher than that corresponding to the level of the metastable state (E_{MS}).

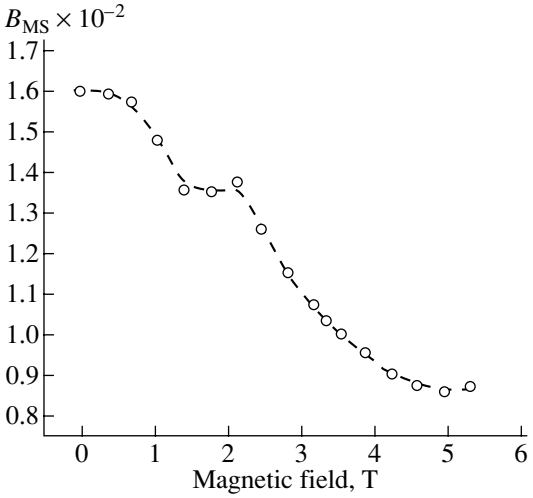

Fig. 6. B_{MS} vs. magnetic field measured at T = 2 K.

The resonance character of tunneling is corroborated by the dependence of the integral B_{MS} on the magnetic field strength at T = 2 K, which is represented graphically in Fig. 6. We readily see that, as the magnetic field is increased, a noticeable feature appears at H = 1.5 T against the background of a monotonic decay of the integral B_{MS}. The increase in the population (in the magnitude of the integral B_{MS}) at a given magnetic field strength can be assigned to the formation of Landau levels. Indeed, in this case, the expression for the carrier energy in the band, calculated without inclusion of the spin component, assumes the form $E = h^2k_z^2/2m + (n + 1/2)h\omega_c$, where $\omega_c = eH/m^*$ is the cyclotron frequency, e is the electronic charge, H is the magnetic field strength, and m^* is the effective carrier mass. This expression shows that an increase in the external magnetic field shifts the band edge toward higher energies; this is what accounts for the monotonic falloff of the MS-level population (pointed out above) at 4.2 K.

The appearance of a local maximum at B = 1.5 T against the background of monotonic decay is due to a modification of the density of states; more specifically, critical points defined by the condition $\partial E_n(k_z)/\partial k_z = 0$ appear in the Landau subbands. As a result, as the energy of the maximum (E_F) in the modified density of

states coincides with the energy E_{MS} of the metastable state, tunneling increases, thus increasing the population of this state (the integral B_{MS} grows). The magnitude of the local maximum in the integral B_{MS} (and even the existence of this maximum) depends on the relative magnitude of the halfwidth of the carrier energy distribution function, determined by the temperature (k_BT), and the energy separation ($\hbar\omega_B$ between the Landau levels. Indeed, the maximum is observed at $T = 2$ K and a magnetic field $B = 1.5$ T; at a temperature of 4.2 K, however, where kT exceeds $\hbar\omega_c$, there is no maximum and only monotonic decay is seen in the behavior of the MS-level population.

By analyzing the above experimental data on the dependence of B_{MS} on P_d, B_f, and T_b, one can estimate, to first approximation, the energy boundaries within which the trapping level E_{MS} of the metastable center is located. This estimate rests on the following considerations. For $E_f < E_{MS}$, as E_f approaches E_{MS}, the number of carriers tunneling to the state of energy E_{MS} will increase monotonically and, hence, B_{MS} will grow. Because the integral B_{MS} was observed to decrease monotonically with increasing P_d and B_f, the energy level E_{MS} which traps the carriers is lower than that corresponding to the maximum in the carrier distribution in the band ($E_{MS} < E_f$). Only in this case, as the carrier distribution function shifts toward higher energies (under application of pressure or magnetic field), will the number of carriers $N(E_f = E_{MS})$ with energy equal to that of the trapping level E_{MS} decrease (points a_f^1, a_f^2, a_f^3, a_f^4 in Fig. 5). B_{MS} reaches a maximum at a_f^1 and a minimum at a_f^4 (Fig. 3). Thus, the determination of the trapping level energy (E_{MS}) reduces to finding the energy interval within which the maximum in the distribution function varies and its position E_f relative to the band edge for $P_d = 0$, $B_f = 0$ and the temperatures at which the experiment was conducted, $T = 2$ and 4.2 K. The variation of the energy position (for T = const) of the maximum in the distribution function $f(E)$ (a_f) caused by the increase in E_g can be found from the emission line shift (Fig. 4) and is approximately 1 meV. Determination of the real value of E_f is complicated by the fact that the distribution function is nonequilibrium and the effective carrier temperature T^* differs markedly from the lattice temperature. Finding the explicit form of a nonequilibrium distribution function is a problem of staggering complexity. To make a rough estimate, we used the data from [14], which quotes the effective temperature for excitons as $T^* \approx 7$ K (0.6 meV). An estimate made on these grounds suggests that E_{MS} lies within a few millielectronvolts from the band edge.

Thus, the totality of experimental data on the evolution of B_{MS} with increasing P_d, T_b, and B_f suggests the existence of a trapping center in the allowed band which is spaced a few millielectronvolts from the band edge. It may be conjectured that this trap is populated by resonance tunneling exchange of carriers between the free-carrier subsystem and the reservoir of metastable localized states. The dependence of the integral B_{MS} on P_d and B_f permits qualitative determination of the low-energy tail of the nonequilibrium function.

REFERENCES

1. A. V. Akimov, A. A. Kaplyanskiĭ, V. V. Krivolapchuk, and E. S. Moskalenko, Pis'ma Zh. Éksp. Teor. Fiz. **46**, 35 (1987) [JETP Lett. **46**, 42 (1987)].
2. A. V. Akimov, V. V. Krivolapchuk, N. K. Poletaev, and V. G. Shofman, Fiz. Tekh. Poluprovodn. (St. Petersburg) **27**, 310 (1993) [Semiconductors **27**, 171 (1993)].
3. D. Bimberg, H. Munzel, A. Steckenborn, and J. Christen, Phys. Rev. B **31**, 7788 (1985).
4. A. V. Akimov, Yu. V. Zhilyaev, V. V. Krivolapchuk, *et al.*, Fiz. Tekh. Poluprovodn. (Leningrad) **25**, 713 (1991) [Sov. Phys. Semicond. **25**, 429 (1991)].
5. V. V. Krivolapchuk, N. K. Poletaev, and L. M. Fedorov, Fiz. Tekh. Poluprovodn. (St. Petersburg) **28**, 310 (1994) [Semiconductors **28**, 188 (1994)].
6. B. B. K. Ridley, *Quantum Processes in Semiconductors*, 2nd ed. (Mir, Moscow, 1986; Clarendon, Oxford, 1988).
7. C. H. Henry and D. V. Lang, Phys. Rev. B **15**, 989 (1977).
8. V. N. Abakumov, V. I. Perel', and I. N. Yassievich, Fiz. Tekh. Poluprovodn. (Leningrad) **12**, 3 (1978) [Sov. Phys. Semicond. **12**, 1 (1978)].
9. V. N. Abakumov, I. A. Merkulov, V. I. Perel', and I. N. Yassievich, Zh. Éksp. Teor. Fiz. **89**, 1472 (1985) [Sov. Phys. JETP **62**, 853 (1985)].
10. V. V. Krivolapchuk and N. K. Poletaev, Fiz. Tekh. Poluprovodn. (St. Petersburg) **32**, 307 (1998) [Semiconductors **32**, 277 (1998)].
11. R. Kubo, Phys. Rev. **86**, 929 (1952).
12. R. Kubo and Y. Toyozawa, Prog. Theor. Phys. **13**, 160 (1957).
13. L. D. Landau and E. M. Lifshitz, *Course of Theoretical Physics*, Vol. 3: *Quantum Mechanics: Non-Relativistic Theory*, 3rd ed. (Nauka, Moscow, 1974; Pergamon, New York, 1977).
14. V. M. Botnaryuk, Yu. V. Zhilyaev, V. V. Rossin, *et al.*, Fiz. Tverd. Tela (Leningrad) **28**, 201 (1986) [Sov. Phys. Solid State **28**, 109 (1986)].

Translated by G. Skrebtsov

Physics of the Solid State, Vol. 45, No. 5, 2003, pp. 830–837. Translated from Fizika Tverdogo Tela, Vol. 45, No. 5, 2003, pp. 791–797.

SEMICONDUCTORS AND DIELECTRICS

Relaxing Local Modes and the Theory of Low-Frequency Raman Scattering in Glasses

V. N. Bondarev and S. V. Zelenin

Research Institute of Physics, Odessa National University, ul. Pastera 27, Odessa, 65026 Ukraine

e-mail: akhmerov@niif.odessa.ua

Received February 27, 2002

Abstract—Raman scattering in glasses is investigated theoretically. The experimental Raman spectra of glasses exhibit a low-frequency peak (at ~10 cm^{-1}) that, as a rule, is attributed to vibrational modes of nanometer-sized structural units (nanocrystallites). It is established that the elastic moduli of nanocrystallites must necessarily be dependent on their sizes due to the Laplace pressure effect. A theory of the low-frequency peak is constructed using a realistic size distribution function of nanocrystallites with allowance made for the Laplace pressure effect and the dissipation of vibrational energy. Within this theory, the shape of the low-frequency peak and its evolution with temperature can be analyzed quantitatively. The proposed approach offers a physical interpretation of the experimental data and provides insight into the relation of the characteristic nanocrystallite sizes to the elastic moduli and surface tension coefficients of materials. © *2003 MAIK "Nauka/Interperiodica".*

1. INTRODUCTION

Experimental investigations of light scattering in random media provide valuable information on their structure and dynamic properties (see, for example, [1]). Of special interest are experiments on light scattering in disordered media, specifically in vitreous materials, which, at present, have been extensively studied in view of increasing industrial demands [2]. The disordered media are also of fundamental physical interest, because they exhibit features unusual for ordered (crystalline) systems (for example, the non-Debye Kohlrausch-type stretched exponential behavior of dynamic-response functions [3, 4]). In the present paper, we will discuss optical experiments on vitreous materials. In our opinion, the analysis of the experimental results within an adequate theoretical model should reveal clear evidence of the existence of a medium-range order (with a characteristic size of ~1 nm), which is a distinguishing feature of the glass structure [5, 6]. Note that, as a rule, information on the medium-range order can be obtained from experimental data on x-ray or neutron diffraction in these materials [7, 8].

For glasses, one of the indications of the medium-range order can be the so-called boson peak observed in the Raman spectra at a frequency of ~10 cm^{-1}, which is considerably less than the characteristic frequencies of optical phonons [2, 9–12]. Concepts regarding the origin of the boson peak have been developed by many authors (see, for example, [10–13]). According to these concepts, the frequency location of the boson peak at the maximum (ω_{max}) is associated with the characteristic frequency of vibrational modes of nanometer-sized structural units (nanocrystallites). At present, the structure and composition of nanocrystallites are not quite clear. However, the sufficiently large amount of experimental data accumulated to date indicates that glasses contain structural inhomogeneities with a crystalline order and a characteristic size of ~1 nm [14] (see also [15]). Champagnon *et al.* [10] considered the simplest model of a nanocrystallite as a free elastic sphere of radius r_c. For the frequency of the boson peak, they used the relationship $\omega_{max} = kc_L/r_c$ [16]. Here, c_L is the longitudinal velocity of sound in the material of the sphere and k is the proportionality coefficient (of the order of unity), which is determined as the ratio of the longitudinal velocity c_L to the transverse velocity c_T of sound (the vibration damping and the size distribution function of spheres were taken into account in [17, 18]).

A serious argument indicating that the above model should be improved was adduced by Börjesson *et al.* [19] in their comment on the paper by Sokolov *et al.* [13]. In [19] (see also [15]), the authors cast doubt on the results obtained in [13], because the coefficient k determined in [13] appeared to be underestimated compared to the coefficients following from the experimental data for lithium and silver borate glasses [19]. Börjesson *et al.* [19] asserted that the microcrystalline model proposed in [13] can be inadequate to the real situation in glasses. In their reply to this comment, Sokolov *et al.* [20] advanced arguments in favor of the nanostructural concept of the glasses under investigation and admitted that the problem regarding the correct interpretation of the Raman spectra of vitreous materials calls for further closer examination.

1063-7834/03/4505-0830$24.00

In the framework of the concept treating nanocrystallites as structural units of glasses, we should take into account the fact that the key role in nanoobjects is played by the effects associated with the curvature of their surface and, as a consequence, with the Laplace pressure $2\kappa/r_c$ [21]. Here, κ is the surface tension coefficient at the interface between the nanocrystallite and the matrix and r_c is the nanocrystallite radius. The Laplace pressure brings about a change in the elastic properties of the nanocrystallite. As a result, the effective value of c_L for the nanocrystallite turns out to be larger than that in the bulk material by the factor $\sqrt{1 + \frac{2\kappa}{r_c}\frac{1}{K_{L\infty}}\frac{\partial K_L}{\partial p}}$, where $K_{L\infty}$ is the bulk modulus responsible for the longitudinal velocity of sound in the nanocrystallite material and the derivative $(\partial K_L/\partial p) > 0$ is taken at the pressure $p = 0$. This factor can be estimated by setting $\kappa \approx 500$ dyn/cm (close values of κ are characteristic of solids [22]) and $\frac{1}{K_{L\infty}}\frac{\partial K_L}{\partial p} \approx 6 \times 10^{-11}$ cm^2/dyn (this value was obtained for the silver-containing compound $RbAg_4I_5$ [23]). As a consequence, the proportionality coefficient k in the above relationship should be replaced by the effective coefficient $k[1 + 0.35/r_c$ (nm)], which significantly exceeds the coefficient k at $r_c \sim 1$ nm (as will be shown below, the dependence of the coefficient k on r_c can be ignored). Therefore, it can be assumed that the inclusion of the Laplace pressure will provide a deeper insight into the nature and mechanism of local vibrations in glasses with a nanostructure and will bridge the gap between the viewpoints outlined in [19] and [20].

In this paper, we consider the main features of Raman scattering in glasses with nanocrystallites in the spectral range corresponding to their vibrational modes with due regard for damping and the effect of the Laplace pressure on the elastic properties of the nanocrystallite material (Section 2). It is shown that the theoretical results regarding the shape of the Raman spectrum and its temperature evolution can fit the experimental data fairly well. This makes it possible to estimate correctly the parameters of the size distribution function of nanocrystallites and the damping constant of their vibrational modes. Consequently, Raman scattering can be used to reveal qualitative transformations in the structure of the material from the dependence of the aforementioned parameters on the concentration of the glass components. This is illustrated with $(Ag_2O)_y(B_2O_3)_{1-y}$ glasses as an example in Section 3, in which we also discuss the relation of the mean nanocrystallite size to the elastic characteristics and surface tension coefficients of the materials.

2. THEORETICAL MODEL

The Raman spectra can be calculated from the general relationship for the scattering tensor [24]

$$I_{ijkl}(\omega) = \int_{-\infty}^{\infty} dt \int d\mathbf{R} \int d\mathbf{R}' \langle \alpha_{ij}(\mathbf{R}, t)\alpha^*_{kl}(\mathbf{R}', 0)\rangle e^{-i\omega t} \quad (1)$$

which is expressed through the statistical averages (indicated by the angle brackets) over the bilinear combinations of the fluctuation tensor $\alpha_{ij}(\mathbf{R}, t)$. In this case, the fluctuation tensor determines the scattering properties of the medium at the point $\mathbf{R}$ at the instant of time t. In relationship (1), spatial integration is performed over the entire scattering volume and ω is the change in the frequency of Raman scattering. It is assumed that the low-frequency Raman scattering in the glass is caused by the local modes corresponding to damped vibrations of nanocrystallites [10–13]. These local vibrations result in fluctuation changes in the tensor $\alpha_{ij}(\mathbf{R}, t)$. In what follows, we will assume that vibrations in different nanocrystallites are uncorrelated. This assumption and the fact that the characteristic sizes of nanocrystallites are considerably less than the light wavelength allow us to avoid the introduction of a phase factor (including the change in the light wave vector due to Raman scattering) into relationship (1).

On this basis, the tensor $\alpha_{ij}(\mathbf{R}, t)$ can be written in the form

$$\alpha_{ij}(\mathbf{R}, t) = \sum_n \alpha^{(n)}_{ij}(t)\delta(\mathbf{R} - \mathbf{R}^{(n)}), \quad (2)$$

where the superscript n indicates the nanocrystallite number, the δ function accounts for the "point" nature of nanocrystallites, and $\mathbf{R}^{(n)}$ is the radius vector of the center of the nth nanocrystallite. For simplicity, nanocrystallites are simulated by spheres in the calculations of the Raman scattering tensor. The function $\alpha^{(n)}_{ij}(t)$ can be represented as an integral of the local tensor $\alpha^{(n)}_{ij}(\mathbf{r}, t)$ over the volume of the nth crystallite; that is,

$$\alpha^{(n)}_{ij}(t) = \int d\mathbf{r}\alpha^{(n)}_{ij}(\mathbf{r}, t), \quad (3)$$

where the radius vector $\mathbf{r}$ is measured from the center of the sphere. Under the assumption that the crystallites have quasi-macroscopic sizes, we will describe their vibrations in the framework of the elastic-continuum theory. In this respect, we introduce the fluctuation strain tensor $u^{(n)}_{ij}(\mathbf{r}, t)$ at an arbitrary point $\mathbf{r}$ on the sphere. It is this tensor that determines the local tensor $\alpha^{(n)}_{ij}(\mathbf{r}, t)$. Within the isotropic-continuum model, the latter tensor can be defined as [24]

$$\alpha^{(n)}_{ij}(\mathbf{r}, t) = a_1 u^{(n)}_{ij}(\mathbf{r}, t) + a_2\delta_{ij}u^{(n)}_{ll}(\mathbf{r}, t), \quad (4)$$

where a_1 and a_2 are the elasto-optic constants.

As in [10], we will consider radial vibrations of spherical nanocrystallites. The Raman scattering by these vibrations is scalar in character. In order to determine the symmetric contribution to the Raman scattering, it is necessary to take into consideration the nonsphericity of the nanocrystallites (see the discussion given below). However, these vibrations of nanocrystallites in the glass-forming matrix must necessarily be damped (in [17], this circumstance was taken into account by introducing the Lorentzian with a width determined from the comparison of the model shape of the boson peak with the experimental low-frequency Raman spectra of glasses). The best way to account for the dynamic relation between the nanocrystallite and the matrix consists in introducing the effective dissipative force at their interface, which makes it possible to avoid explicit consideration of the microscopic model of the interface.

In the theory of elasticity, the dissipative effects, as a rule, are included by introducing a component dependent on the time derivatives of the strain tensor into the stress tensor [16]. It is reasonable to assume that the main contribution to the damping of vibrational modes of the nanocrystallite is determined by the aforementioned interface effects. Hence, the expression for the effective dissipative force per unit of interfacial area can be derived from the dissipative part of the stress tensor in the region where the strains associated with nanocrystallite vibrations decrease. There are grounds to believe that the nanocrystallite is rather weakly bound to the matrix [25]. Therefore, it can be expected that this region is characterized by a microthickness (hereafter, the region thickness will be designated as d). Consequently, the expression for the stress tensor in this region can be used only for qualitative evaluations.

The boundary condition at the surface of the vibrating sphere should be specified with due regard for the fact that, as was noted above (the estimates will be given below), when the sphere radius $r^{(n)}$ falls in the nanometer range, the surface tension forces appreciably affect the vibrational process. These forces are responsible for the Laplace pressure $2\kappa/r^{(n)}(t)$, where $r^{(n)}(t) = r^{(n)} + u_r^{(n)}(r, t)|_{r = r^{(n)}}$ is the instantaneous radius of the vibrating sphere, $u_r^{(n)}(r, t)$ is the radial component of the displacement tensor at the point $r = |\mathbf{r}|$ of the nanocrystallite, and κ is the surface tension coefficient at the interface between the nanocrystallite and the glass-forming matrix. Furthermore, similar forces also act in the static case and determine the corresponding static stresses through the Laplace pressure $2\kappa/r^{(n)}$. Therefore, under the assumption that $|u_r^{(n)}(r^{(n)}, t)| \ll r^{(n)}$, the dynamic boundary condition can be written in the following form:

$$\left[-\sigma_{rr}^{(n)}(r, t) - \frac{\eta}{d}\frac{\partial u_r^{(n)}(r, t)}{\partial t} + 2\kappa\frac{u_r^{(n)}(r, t)}{r^2}\right]\Bigg|_{r = r^{(n)}} = 0. \quad (5)$$

Here, the first term in square brackets determines the rrth component of the dynamic tensor of elastic stresses; the second term characterizes the corresponding component of the viscous stress tensor; and the third term describes the dynamic component of the Laplace pressure, which is reckoned from the static component. The parameter $\eta > 0$ has the meaning of the viscosity coefficient [16] and can be estimated in the same manner as for very viscous liquids [16]. By introducing the mass density ρ of the nanocrystallite material, we obtain the estimate $\eta/d \sim \gamma\rho c_L$, where the dimensionless coefficient γ actually determines the degree of connectivity of the nanocrystallite with the glass-forming matrix.

Next, we write $u_r^{(n)}(r, t) = \dfrac{\partial\psi^{(n)}(r, t)}{\partial r}$, where $\psi^{(n)}(r, t)$ is the "displacement" potential, and solve the equations of vibrations inside the sphere in much the same way as in Problem 3 in [16, Section 22]. As a result, we have

$$\psi^{(n)}(r, t) = A^{(n)}e^{i\omega^{(n)}t}\frac{\sin(\omega^{(n)}r/c_L)}{r}, \quad (6)$$

where $A^{(n)}$ is the vibration amplitude and $\omega^{(n)}$ is the vibration frequency. It should be noted that the imaginary part of this frequency should be positive in order to provide vibration damping at $t \longrightarrow \infty$. Substitution of expression (6) into boundary condition (5) gives the equation

$$\frac{\tan\Omega}{\Omega} = \frac{1 - i\left(\dfrac{c_L}{2\tilde{c}_T}\right)^2\gamma\Omega}{1 - \left(\dfrac{c_L}{2\tilde{c}_T}\Omega\right)^2 - i\left(\dfrac{c_L}{2\tilde{c}_T}\right)^2\gamma\Omega}. \quad (7)$$

The solutions of this equation $\Omega = \Omega' + i\Omega''$ determine the complex frequencies $\omega^{(n)} = \Omega c_L/r^{(n)}$ of natural vibrations of the sphere of radius $r^{(n)}$; in this case, $\Omega'' > 0$. It should be noted that Eq. (7) involves the renormalized transverse velocity of sound $\tilde{c}_T = \sqrt{c_T^2 + \kappa/(2\rho r^{(n)})}$ in the sphere material.

Now, we take into consideration that the quantities $c_T = \sqrt{\mu/\rho}$ and $c_L = \sqrt{(K + 4\mu/3)/\rho}$ should explicitly depend on the Laplace pressure through the corresponding dependences of the bulk modulus K, the shear modulus μ, and the mass density ρ:

$$K = K_\infty + \frac{\partial K}{\partial p}\frac{2\kappa}{r^{(n)}}, \quad \mu = \mu_\infty + \frac{\partial\mu}{\partial p}\frac{2\kappa}{r^{(n)}},$$
$$\rho = \rho_\infty + \frac{\partial\rho}{\partial p}\frac{2\kappa}{r^{(n)}} = \rho_\infty\left(1 + \frac{2\kappa}{K_\infty r^{(n)}}\right). \quad (8)$$

Here, the quantities with the subscript ∞ correspond to their bulk values (at $r^{(n)} \longrightarrow \infty$), the derivatives are taken at zero pressure p, and the compressibility is writ-

ten as $1/K_\infty$ [16]. Making allowance for the standard expression $\mu = 3K(1 - 2\sigma)/[2(1 + \sigma)]$, which relates the above quantities through the Poisson ratio σ [16], and disregarding the possible dependence of σ on p (i.e., on $r^{(n)}$), it is easy to show that the parameter $c_L^2/(4\tilde{c}_T^2)$ entering into Eq. (7) can be treated to be independent of the Laplace pressure when the following condition is satisfied:

$$\frac{\kappa(1+\sigma)}{3r^{(n)}K_\infty(1-2\sigma)\left(1+\dfrac{2\kappa}{r^{(n)}K_\infty}\dfrac{\partial K}{\partial p}\right)} \ll 1. \qquad (9)$$

Below, we will evaluate the term on the left-hand side of relationship (9) for $(Ag_2O)_y(B_2O_3)_{1-y}$ glasses and will then analyze the available experimental data on Raman scattering in these glasses [9]. With the use of the experimental values $K_\infty \approx 4.6 \times 10^{11}$ dyn/cm^2 and $\mu_\infty \approx 2 \times 10^{11}$ dyn/cm^2 taken from [25], we find $\sigma \approx 1/3$. Since the experimental value of the parameter $\dfrac{1}{K_{L\infty}}\dfrac{\partial K_L}{\partial p}$ for these glasses is unavailable, as before, we use its value for $RbAg_4I_5$. Moreover, we assume that $r^{(n)} \approx 0.7$ nm (a close value will be obtained below). Then, it can easily be demonstrated that the term on the left-hand side of relationship (9) is approximately equal to 4×10^{-2}. This circumstance allows us to calculate the roots of Eq. (7) with the use of the parameter $c_L^2/(4\tilde{c}_T^2)$ taken equal to $(K_\infty + 4\mu_\infty/3)/(4\mu_\infty)$. Note also that the relative change in ρ in formula (8) at the aforementioned parameters is approximately equal to 0.01. Hence, we assume that $\rho = \rho_\infty$.

Before proceeding to the calculation of the averages in relationship (1), we use expression (2) to rewrite relationship (1) in the following form:

$$I_{ijkl}(\omega) = \sum_n I_{ijkl}(\omega; r^{(n)}),$$
$$I_{ijkl}(\omega; r^{(n)}) = \int_{-\infty}^{\infty} dt e^{-i\omega t}\langle \alpha_{ij}^{(n)}(t)\alpha_{kl}^{(n)*}(0)\rangle. \qquad (10)$$

Here, we explicitly take into account that the dynamic fluctuations are correlated only within each nanocrystallite. Hereafter, the experimental data will be interpreted (as was done in [10–13]) with allowance made for only the first root of Eq. (7). The integral in formula (10) can be calculated using the procedure accepted in the fluctuation theory (see, for example, [26]). This implies that the solution decaying with time in the range $t > 0$ is extended to the range $t < 0$. In other words, we take solution (6) corresponding to Ω in the former range and solution (6) corresponding to Ω^* in the latter range. Next, with the use of solution (6) and relationship (4), we calculate integral (3). By substituting the obtained result into formula (10), it is easy to verify that the Raman scattering tensor has the form $I_{ijkl}(\omega; r^{(n)}) = \delta_{ij}\delta_{kl}I(\omega; r^{(n)})$; i.e., it corresponds to the scalar scattering by radial vibrations of the spherical nanocrystallite. We omit intermediate manipulations and write the expression for the intensity $I(\omega; r^{(n)})$ in the following form:

$$I(\omega; r^{(n)}) = 32\pi^2\left(\frac{a_1}{3} + a_2\right)^2$$
$$\times \langle (A^{(n)})^2\rangle \frac{r^{(n)}}{c_L\Omega'^2}|\Omega\cos\Omega - \sin\Omega|^2 \qquad (11)$$
$$\times \frac{\Omega''}{[\omega r^{(n)}/(c_L\Omega') - 1]^2 + (\Omega''/\Omega')^2}.$$

Here, the angle brackets indicate the thermodynamic average of the square of the amplitude of local vibrations of the spherical nanocrystallite with radius $r^{(n)}$. Note that, in the absence of damping [$\Omega'' \longrightarrow +0$ in relationship (11)], the frequency dependence of the intensity $I(\omega; r^{(n)})$ is reduced to the delta function $\delta(\omega - c_L\Omega'/r^{(n)})$.

Now, we should use the explicit dependence of c_L on $r^{(n)}$ (see above). As regards the constants a_1 and a_2, their possible dependence on $r^{(n)}$ could be included through the dependence of ρ on $r^{(n)}$, because, according to the experimental data [27], the elasto-optic constants are determined by the refractive index of glass, which, in turn, is governed by the density. However, the density can be considered to be equal to ρ_∞ when $r^{(n)}$ is of the order of several nanometers (see the above estimates). This allows us to ignore the dependences of a_1 and a_2 on $r^{(n)}$.

The average in relationship (11) is defined by the normalized functional integral

$$\langle (A^{(n)})^2\rangle = \frac{\int \mathcal{D}A^{(n)}(A^{(n)})^2\exp\left(-\dfrac{F\{A^{(n)}\}}{T}\right)}{\int \mathcal{D}A^{(n)}\exp\left(-\dfrac{F\{A^{(n)}\}}{T}\right)}, \qquad (12)$$

where the distribution probability $\exp(-F\{A^{(n)}\}/T)$ is expressed through the functional of the vibrational free energy $F\{A^{(n)}\}$ [corresponding to solution (6) at $t = 0$] and T is the temperature. This functional is the integral of the vibrational free energy density over the sphere volume. In terms of the linear theory of elasticity [16], the vibrational free energy is determined by the quadratic form of the strain tensor $u_{ij}^{(n)}(\mathbf{r}, 0)$. By determining this tensor with the use of expression (6) and calculating $F\{A^{(n)}\}$, we find that $\langle (A^{(n)})^2\rangle$ is represented by the relationship

$$\langle (A^{(n)})^2 \rangle = \frac{T(r^{(n)})^3}{4\pi K f(\Omega)}. \quad (13)$$

Relationship (13) involves the substantially positive quantity

$$f(\Omega) = \frac{3}{2(1+\sigma)}\int_0^1 \frac{du}{u^4}\{(1-2\sigma)g_1(\Omega u) + \sigma g_2(\Omega u)\}, \quad (14)$$

which is defined by the integral of the functions

$$g_1(\Omega u) = \{\mathrm{Re}[\sin(\Omega u)(2-\Omega^2 u^2) - 2\Omega u\cos(\Omega u)]\}^2 + 2\{\mathrm{Re}[\Omega u\cos(\Omega u) - \sin(\Omega u)]\}^2, \quad (15)$$

$$g_2(\Omega u) = \{\mathrm{Re}[\Omega^2 u^2 \sin(\Omega u)]\}^2. \quad (16)$$

The average squared (13) should be calculated with due regard for the dependences of K and (in principle) σ on $r^{(n)}$. However, the estimates obtained from the experimental data for $RbAg_4I_5$ [23] demonstrate that the dependence of the Poisson ratio σ on $r^{(n)}$ is almost three times weaker than the dependence of the modulus K on $r^{(n)}$. Therefore, in numerical calculations, we will assume that σ is constant (recall that, as was shown above, the dependence of Ω on $r^{(n)}$ can be ignored).

In order to use the obtained results for describing experimental data on the Raman scattering by local modes of glasses, it is necessary to specify the size distribution of the nanocrystallites. According to [18] (see also [28, 29] for porous silicon), this distribution can be represented by a lognormal function. By changing over from summation over n in expression (10) to integration over the normalized lognormal distribution in the space of radii $\tilde{r}$, we obtain the expression for the Raman scattering intensity in the following form:

$$I(\omega) = \sum_n I(\omega; r^{(n)}) \longrightarrow \frac{1}{\sqrt{2\pi}\Delta}\int_0^\infty \frac{d\tilde{r}}{\tilde{r}}\exp\left[-\frac{1}{2\Delta^2}\ln^2\left(\frac{\tilde{r}}{r_0}\right)\right] I(\omega; \tilde{r}), \quad (17)$$

where r_0 and Δ are the distribution parameters. In this case, the mean radius is determined to be $\bar{r} = r_0 e^{\Delta^2/2}$. The relationship for the Raman scattering by local vibrational modes of the glass can be derived by substituting expression (11) [with allowance made for formula (13)] into relationship (17) and changing over to a new integration variable in the last relationship. As a result, we have

$$I(\omega) = BT\Omega''\int_{-\infty}^{\infty} \frac{d\nu}{(1+\hat{\kappa}e^{-\nu})^{3/2}} e^{-\nu^2/(2\Delta^2)+4\nu} \times \frac{1}{[\omega(1+\hat{\kappa}e^{-\nu})^{-1/2}e^{\nu}/\omega_0 - 1]^2 + (\Omega''/\Omega')^2}. \quad (18)$$

Here, we introduced the following designations:

$$\omega_0 = \frac{\Omega'}{r_0}\sqrt{\frac{1}{\rho_\infty}\left(K_\infty + \frac{4}{3}\mu_\infty\right)}, \quad \hat{\kappa} = \frac{2\kappa}{K_\infty r_0}\frac{\partial K}{\partial p}. \quad (19)$$

Moreover, in expression (18), the frequency-independent factors, except for the quantities T and Ω'' (the latter quantity is retained in the explicit form with the aim of providing the correct passage to the limit $\Omega'' \longrightarrow +0$), are included in the constant B.

As follows from expression (18), the effective width of the spectrum depends on both the width Δ of the radius distribution of nanocrystallites and the imaginary part Ω'' of their local vibrational mode. At the same time, the parameter $\hat{\kappa}$ in expression (18) accounts for the effects associated with the surface tension of nanocrystallites.

Expression (18) was derived using the Boltzmann statistics. However, the quantization of vibrations can appear to be significant at low temperatures. Therefore, in order to describe the Stokes component of the Raman scattering, as is universally accepted (see, for example, [9]), T in expression (18) should be replaced by $\omega[n(\omega, T) + 1]$, where $n(\omega, T)$ is the Bose–Einstein distribution function [26].

3. COMPARISON OF THEORETICAL AND EXPERIMENTAL DATA AND DISCUSSION

Expression (18), which is the basic result of our work, can be used to describe quantitatively the experimental data on the low-frequency Raman scattering in glasses. This description can be conveniently performed in terms of the dimensionless frequency $\tilde{\omega} = \omega/\omega_{max}$. For this purpose, the frequency ω_{max} corresponding to the peak of the Raman scattering intensity should be chosen as the unit frequency. In this case, the frequency is plotted along the abscissa axis and the dimensionless intensity $I(\tilde{\omega})/I(1)$ is plotted along the ordinate axis. The results obtained will be illustrated using the experimental data taken from [9] for the $(Ag_2O)_y(B_2O_3)_{1-y}$ glasses. Figures 1a and 1b show the theoretical spectra (solid lines) obtained by fitting [with the use of expression (18)] to the experimental Raman spectra (points) of the $(Ag_2O)_y(B_2O_3)_{1-y}$ glasses with $y = 0.10$ and 0.15 at 293 K [9]. The parameters of the theory, which were determined by this fitting, are listed in the first two rows of the table.

First and foremost, we should note that the role played by the damping of local vibrational modes of nanocrystallites is enhanced (the ratio Ω''/Ω' increases, see table) with a decrease in the Ag_2O content in the $(Ag_2O)_y(B_2O_3)_{1-y}$ glasses. [Note also that Ω' weakly depends on γ at $\gamma < 1$; at $c_L/(2c_T) = 0.9$ in the absence of damping, $\Omega' = 2.62$ corresponds to the first root of Eq. (7).] According to our interpretation of the damping mechanism, this means that the role of the surface effects increases with a decrease in y, which indirectly supports the assumption that the mean nanocrystallite size $\bar{r}$ increases with an increase in the content y. As far as we know, the corresponding experimental data for $(Ag_2O)_y(B_2O_3)_{1-y}$ glasses are unavailable. Nonetheless, the increase in $\bar{r}$ with an increase in y for the related glasses $(Li_2O)_y(B_2O_3)_{1-y}$ was experimentally observed by Börjesson *et al.* [19].

The theoretical treatment of the experimental Raman spectra of $(Ag_2O)_y(B_2O_3)_{1-y}$ glasses at $y = 0.10$ and 0.15 (Fig. 1) also demonstrates that the parameters Δ coincide with each other (see table). The obtained parameter $\Delta = 0.59$ differs from the "universal" variance (≈ 0.48) reported in [14, 18], because the form of expression (18) differs from that of the simplest lognormal distribution, which was used in [14, 18] for simulating the shape of the Raman spectra of glasses in the frequency range of the boson peak.

For the glass with $y = 0.20$, expression (18) makes it possible to describe the experimental data [9] only at reduced frequencies $\tilde{\omega} < 1.4$ (the parameters of the theory are given in the third row of the table), whereas the data for the other two glasses can be described at frequencies as high as $\tilde{\omega} \approx 2.3$. Note that the parameter Δ at $y = 0.20$ differs considerably from this parameter at $y = 0.10$ and 0.15. A much better description of the experimental spectrum of the "anomalous" glass (at $y = 0.20$) can be achieved under the assumption that the Raman band shown in Fig. 1c has a complex structure; i.e., it is a superposition of two spectral bands. The decomposition into individual bands (despite a somewhat conventional character of this procedure) and their processing with the use of expression (18) give the parameters listed in the last two rows of the table (the superscripts {1} and {2} refer to the numbers of the individual bands). It should be noted that the parameters Δ for both individual bands of this anomalous glass differ noticeably from the value of 0.59 obtained for the glasses with $y = 0.10$ and 0.15.

The anomalous properties of the glass with $y = 0.20$ are confirmed by the data available in the literature. In particular, Carini *et al.* [30] directly measured the fraction N_4 of fourfold-coordinated boron atoms in the $(Ag_2O)_y(B_2O_3)_{1-y}$ glasses and found that the dependence of N_4 on y exhibits an anomalous behavior only at $y \approx 0.2$–0.3. This can imply that, in the glass with $y = 0.20$, there arise nanocrystallites formed with the participation of anomalously coordinated boron atoms in addition to the clusters observed in glasses with $y = 0.10$ and 0.15.

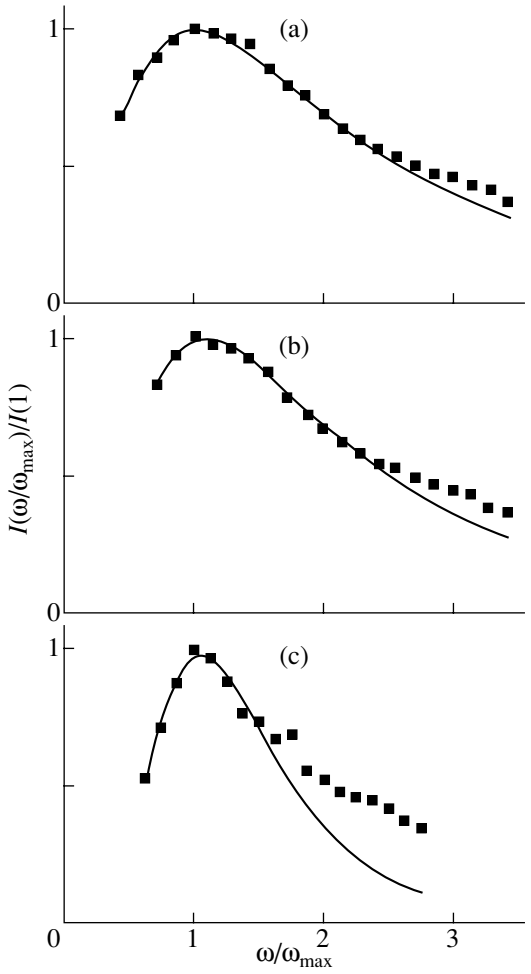

Fig. 1. Experimental Raman spectra of $(Ag_2O)_y(B_2O_3)_{1-y}$ glasses (points) at a temperature of 293 K in the frequency range of local vibrational modes for y = (a) 0.10, (b) 0.15, and (c) 0.20 [9]. Solid lines correspond to the results of calculations from formula (18) (the parameters involved in the formula are given in the table).

One more useful corollary of the proposed theory is as follows. During the processing of the experimental data (Fig. 1), we varied the parameters Δ, Ω''/Ω', and ω_0

Parameters of theoretical formula (18), determined by fitting to the experimental Raman spectra of $(Ag_2O)_y(B_2O_3)_{1-y}$ glasses [9]

y	Δ	Ω''/Ω'	$\hat{\kappa}$	ω_0, cm^{-1}
0.10	0.59	0.4	1	140
0.15	0.59	0.2	1	140
0.20	0.36	0.1	0.7	60
$0.20^{\{1\}}$	0.45	0.1	1	90
$0.20^{\{2\}}$	0.10	0.1	0.8	30

in theoretical expression (18). It was revealed that the smallest root-mean-square difference between the theoretical results and the experimental data [9] (with due regard for the experimental points at $\tilde{\omega} \le 2$) is achieved at $\hat{\kappa} \approx 1$ both for the glasses with $y = 0.10$ and 0.15 and for the anomalous glass ($y = 0.20$). This result can have a physical meaning. Indeed, from formula (19) at $\hat{\kappa} \approx 1$, we obtain the approximate relationship

$$r_0 \approx \frac{2\kappa}{K_\infty}\frac{\partial K}{\partial p}. \quad (20)$$

The dimensionless factor $2\partial K/\partial p$ in relationship (20) suggests that this formula not only gives size estimates but also can play a more important role. Furthermore, there are grounds to believe that this factor is not small: for example, $2\partial K/\partial p \approx 14$ for the $RbAg_4I_5$ crystal [23]. By setting, as before, $\frac{1}{K_{L\infty}}\frac{\partial K_L}{\partial p} \approx 6 \times 10^{-11}$ cm^2/dyn [23] and $\kappa \approx 500$ dyn/cm [22] (see above), from formula (20), we find $r_0 \approx 0.6$ nm. As a result, the mean nanocrystallite radius is estimated as $\bar{r} \approx 0.7$ nm, which agrees with the correlation length estimated in [9] for the $(Ag_2O)_y(B_2O_3)_{1-y}$ glasses.

So far, there has been no consistent concept regarding the formation of the structure of vitreous materials. Hence, formula (20) can be treated as an empirical relationship in which numerical values of the factors depend on the glass composition. Therefore, a consistent theory of glass formation should include an expression that would make it possible to give estimates similar to those provided by formula (20). According to this expression, the characteristic size of structural inhomogeneities should be determined by the competition between the bulk (logarithmic derivative of the elastic modulus with respect to pressure) and surface (the surface tension coefficient at the interface) parameters of glasses. In this case, the hypothesis of a universal inhomogeneity size (~1 nm) in glasses [14] would receive certain support if the relation between κ and $\partial \ln K/\partial p$ were to appear similar to an inverse proportionality with the coefficient weakly dependent on the material composition (qualitative considerations count in favor of the proportionality of κ and K_∞).

The aim of the present work was to demonstrate the role played by the relaxation processes and the surface effects that manifest themselves in Raman scattering by local vibrational modes of glasses. In this respect, we restricted our consideration to the simplest case of scalar scattering. The generalization of the model to other nanocrystallites (for example, nanocrystallites ellipsoidal in shape) would lead to the appearance of a symmetric contribution to the Raman scattering. However, this problem is beyond the scope of the present work.

4. CONCLUSIONS

Thus, the basic results obtained in this work can be summarized as follows. The theory of Raman scattering of glasses in the frequency range of the so-called boson peak was constructed using the concept of local modes associated with the damped vibrations of spherical nanocrystallites of randomly distributed radii with due regard for the curvature factors affecting their elastic properties. The theoretical relationships derived were used to described quantitatively the experimental Raman spectra of $(Ag_2O)_y(B_2O_3)_{1-y}$ glasses. It was demonstrated that the theoretical analysis of the experimental Raman spectra makes it possible to determine the parameters of the size distribution of nanocrystallites and their relaxation characteristics and also to reveal indications of an anomalous glass structure at large values of y, which were observed earlier in the experiments. A relationship was proposed for estimating the mean nanocrystallite size. This relationship includes not only the dimension factors associated with the bulk (elastic modulus) and surface (surface tension at interfaces) properties but also a large dimensionless factor (twice the derivative of the elastic modulus with respect to pressure). The results obtained can provide a way of resolving the controversy that has arisen in the literature [19, 20] as to the applicability of the nanocrystallite model to the description of the structure and optical properties of vitreous materials.

REFERENCES

1. *Light Scattering in Solids*, Ed. by M. Cardona and G. Guntherodt (Springer-Verlag, Berlin, 1975; Mir, Moscow, 1984), No. 2.
2. A. Fontana, G. Mariotto, E. Cazzanelli, *et al.*, Phys. Lett. A **93** (4), 209 (1983).
3. L. Börjesson, Phys. Rev. B **36** (9), 4600 (1987).
4. L. Börjesson, L. M. Torell, S. W. Martin, *et al.*, Phys. Lett. A **125** (6–7), 330 (1987).
5. L. Börjesson, L. M. Torell, U. Dahlborg, and W. S. Howells, Phys. Rev. B **39** (5), 3404 (1989).
6. D. L. Sidebottom, Phys. Rev. B **61** (21), 14507 (2000).
7. J. Swenson, R. L. McGreevy, L. Börjesson, *et al.*, J. Phys.: Condens. Matter **8**, 3545 (1996).
8. J. D. Wicks, L. Börjesson, G. Bushnell-Wye, *et al.*, Phys. Scr. T **57**, 127 (1995).
9. G. Carini, M. Cutroni, A. Fontana, *et al.*, Phys. Rev. B **29** (6), 3567 (1984).
10. A. Champagnon, B. Andrianasolo, A. Ramos, *et al.*, J. Appl. Phys. **73** (6), 2775 (1993).
11. E. P. Denisov, S. V. Karpov, E. V. Kolobkova, *et al.*, Fiz. Tverd. Tela (St. Petersburg) **41** (7), 1306 (1999) [Phys. Solid State **41**, 1194 (1999)].
12. A. Gaĭsin, S. V. Karpov, E. V. Kolobkova, *et al.*, Fiz. Tverd. Tela (St. Petersburg) **41** (8), 1505 (1999) [Phys. Solid State **41**, 1378 (1999)].
13. A. P. Sokolov, A. Kisliuk, M. Soltwisch, and D. Quitmann, Phys. Rev. Lett. **69**, 1540 (1992).

14. V. K. Malinovskiĭ, Fiz. Tverd. Tela (St. Petersburg) **41** (5), 805 (1999) [Phys. Solid State **41**, 725 (1999)].
15. L. Börjesson, A. K. Hassan, J. Swenson, *et al.*, Phys. Rev. Lett. **70** (9), 1275 (1993).
16. L. D. Landau and E. M. Lifshitz, *Course of Theoretical Physics*, Vol. 7: *Theory of Elasticity*, 4th ed. (Pergamon, New York, 1986; Nauka, Moscow, 1987).
17. V. K. Malinovsky, V. N. Novikov, A. P. Sokolov, and V. G. Dodonov, Solid State Commun. **67** (7), 725 (1988).
18. V. K. Malinovskiĭ, V. N. Novikov, and A. P. Sokolov, Usp. Fiz. Nauk **163** (5), 119 (1993) [Phys. Usp. **36**, 440 (1993)].
19. L. Börjesson, A. K. Hassan, J. Swenson, and L. M. Torell, Phys. Rev. Lett. **70** (25), 4027 (1993).
20. A. P. Sokolov, A. Kisliuk, M. Soltwisch, and D. Quitmann, Phys. Rev. Lett. **70** (25), 4028 (1993).
21. L. D. Landau and E. M. Lifshitz, *Course of Theoretical Physics*, Vol. 6: *Fluid Mechanics*, 3rd ed. (Nauka, Moscow, 1986; Pergamon, Oxford, 1987).
22. *Tables of Physical Data: A Reference Book*, Ed. by I. K. Kikoin (Atomizdat, Moscow, 1976).
23. L. J. Graham and R. Chang, J. Appl. Phys. **46** (6), 2775 (1975).
24. L. D. Landau and E. M. Lifshitz, *Course of Theoretical Physics*, Vol. 8: *Electrodynamics of Continuous Media*, 3rd ed. (Nauka, Moscow, 1982; Pergamon, New York, 1984).
25. G. Carini, M. Cutroni, M. Federico, and G. Tripodo, Phys. Rev. B **32** (12), 8264 (1985).
26. L. D. Landau and E. M. Lifshitz, *Statistical Physics*, 3rd ed. (Nauka, Moscow, 1976; Pergamon, Oxford, 1980), Part 1.
27. P. Benassi, V. Mazzacurati, G. Ruocco, and G. Signorelli, Phys. Rev. B **48** (9), 5987 (1993).
28. Y. Kanemitsu, T. Ogawa, K. Shiraishi, and K. Takeda, Phys. Rev. B **48** (7), 4883 (1993).
29. S. Guha, J. Appl. Phys. **84** (9), 5210 (1998).
30. G. Carini, M. Cutroni, M. Federico, and G. Tripodo, Philos. Mag. B **56** (2), 215 (1987).

Translated by O. Borovik-Romanova

Physics of the Solid State, Vol. 45, No. 5, 2003, pp. 838–844. Translated from Fizika Tverdogo Tela, Vol. 45, No. 5, 2003, pp. 798–803.

SEMICONDUCTORS AND DIELECTRICS

First-Principles Calculations of the Electronic and Spatial Structures of the $Ba_{1-x}La_xF_{2+x}$ System within the Supercell Model

A. Yu. Kuznetsov*, A. B. Sobolev*, A. N. Varaksin*, J. Andriessen, and C. W. E. van Eijk****

**Ural State Technical University, ul. Mira 19, Yekaterinburg, 620002 Russia*

e-mail: kay@dpt.ustu.ru

***Interfaculty Reactor Institute, Delft University of Technology, 2629 JB Delft, The Netherlands*

Received June 5, 2002

Abstract—The electronic and spatial structures of the La impurity in BaF_2 are investigated using the *ab initio* method of linear combinations of atomic orbitals based on the Hartree–Fock approximation in the supercell model. Calculations are performed using the CRYSTAL-98 software package. Possible models of defects are discussed. The MOLSTAT computer code is employed to estimate the energies of formation of defects and their parameters. The influence of defects on the BaF_2 band structure is analyzed. © *2003 MAIK "Nauka/Interperiodica".*

1. INTRODUCTION

The electronic structure of BaF_2 crystals differs from that of other alkaline-earth fluorides in that the former has an energy gap E_{g2} between the occupied states of the anion and cation; this gap is less than one-half the main band gap E_{g1}. Due to this energy gap and core–valence band transitions, or cross luminescence (CL), BaF_2 is the fastest scintillator among the currently available phosphors (its luminescence lifetime is shorter than 1 ns). However, luminescence from BaF_2 also contains an intense slow component (with a lifetime longer than 0.6 μs), which essentially restricts the efficiency of this fast scintillator. This slow-luminescence (SL) component is strongly quenched in crystals doped with rare-earth elements (*R*) [1–4]. In practice, solid solutions $Ba_{1-x}R_xF_{2+x}$ were fabricated with values of *x* reaching 0.3–0.4 (i.e., with 30–40 mol % RF_3), with their crystalline structure remaining that of fluorite. Of all the rare-earth elements, lanthanum most efficiently quenches SL in barium fluoride while improving the other characteristics (mechanical strength, radiation resistance, density) of multicomponent BaF_2-based scintillators [2]. Several SL-quenching mechanisms more or less consistent with the experimental data have been proposed [4]. For instance, it was pointed out in [1] that when BaF_2 is doped with *R*, the energy of exciton dissociation (nonradiative decay) decreases due to the STE relaxation in much the same way as in the case of thermal quenching of exciton luminescence in nominally pure BaF_2. The processes of CL and STE relaxation can depend essentially on the nonstoichiometry of $Ba_{1-x}La_xF_{2+x}$ solid solutions [2], because compensating interstitial fluorine ions are not located on the fluorite sublattice and the structure is distorted with the formation of fragments of LaF_3 tysonite structure. The incorporated lanthanum affects the valence band of barium fluoride; in particular, extra states can be created in this band [4]. Such effects can be thoroughly studied using computational methods of physics and quantum chemistry.

Defect crystals are currently investigated using the supercell model in combination with *ab initio* methods for calculating the electronic structure [5] or with molecular-static (MS) methods [6]. In this paper, we study the electronic and spatial structures of the La impurity in BaF_2 using the *ab initio* method of linear combinations of atomic orbitals within the Hartree–Fock (HF) approximation. Computer simulation is performed by employing the CRYSTAL-98 software package [5, 7]. The energies of formation of defects and their parameters are calculated using the MOLSTAT computer code [8, 9]. Particular attention is given to possible models of defects, the energies of formation of defects, and lattice distortions induced by them.

2. MODELS, METHODS, AND PARAMETERS USED

BaF_2 crystals have fluorite structure and belong to space group $Fm3m$. Their crystal lattice can be subdivided into two interpenetrating lattices, one of which is the simple cubic lattice of halogen ions and the other is the fcc lattice of alkaline-earth ions (the sites of this fcc lattice coincide with the interstitial sites of the simple cubic lattice of halogen ions). It has been shown experimentally [10] and theoretically [6] that as R^{3+} ions are

1063-7834/03/4505-0838$24.00 © 2003 MAIK "Nauka/Interperiodica"

incorporated into an alkaline-earth fluoride crystal, defects of two types can form involving a charge-compensating interstitial fluorine ion F_i. A defect of the first type has tetragonal symmetry of the (100) type, with the F_i ion located at a cubic interstitial site which is a nearest neighbor (NN) of the impurity ion. An ion F_i belonging to a defect of the second type is situated at a trigonal (111)-type interstitial site which is a next-to-nearest neighbor (NNN) of the impurity ion.

A detailed description of the methods used by us and of the CRYSTAL-98 software package can be found in [5, 7]. In solving the linearized HF equation for each type of atom, the Bloch functions were found using basic sets (BSs) of functions of the Gaussian type (GFTs). The electron subsystem of an atom was described by a linear combination of GFTs with the corresponding exponential functions and contraction factors [5]. For a fluorine atom, a BS consisting of twelve functions was used (7 + 3 + 1 + 1 GFTs for the 1*s*, 2*sp*, 3*sp*, and 4*sp* shells, respectively); this BS was tested earlier in calculations for CaF_2 [11]. For Ba and La atoms, we used the so-called effective core potentials (ECPs) [12] (the HAYWSC computer code) and valence BSs consisting of five functions for Ba (3 + 1 + 1 GFTs for the 5*sp*, 5*d*, and 6*sp* shells, respectively) [11] and of six functions for La (3 + 1 + 1 + 1 GFTs for the 5*sp*, 5*d*, 6*sp*, and 7*sp* shells, respectively) [13]. The parameters determining the thresholds for truncating the Coulomb and exchange series, as well as the parameters involved in the criterion for achieving self-consistency in calculating the total energy, were chosen in accordance with the recommendations in the CRYSTAL-98 user's manual [7]. The parameter IS (contraction factor) [7], determining the number of **k** points (at which the Fock matrix is diagonalized) in an irreducible part of the first Brillouin zone, was taken equal to eight.

The equilibrium lattice parameter was taken to be 6.35 Å (the experimental value is $a = 6.2$ Å); this value was calculated by us for a perfect BaF_2 crystal by minimizing the total energy. It is common knowledge that the HF method overestimates the lattice parameter with respect to its experimental value [5]. The total energy of barium fluoride (per unit cell, consisting of one barium atom and two fluorine atoms) for this value of the lattice parameter was calculated to be –224.080337 hartrees.

The translational symmetry of a perfect crystal is broken in the presence of a defect. In order to use a periodic model in simulating a defect crystal, the supercell (SC) method is commonly employed. The CRYSTAL-98 software package allows one to vary crystal unit cells within a wide range: to incorporate and remove atoms, create defects, produce local distortions of the crystal lattice, construct a supercell, etc. A supercell is constructed by translating an original unit cell through the corresponding lattice vectors (SC translation vectors), with a defect located at the center of the SC. In modeling a crystal with a defect by employing CRYSTAL-98, we investigated an SC with 24 ions (S24). The actual number of ions in S24 was 25, because substitution of an La^{3+} ion for a Ba^{2+} ion is accompanied by incorporation of a charge-compensating interstitial fluorine ion F_i into the SC. In most papers where the electronic and spatial structures of defect crystals have been calculated within periodic models, it is argued that the SC must contain a large number of ions (as many as 128 or more) in order for calculations to be adequate [14–16]. In actuality, this argument is conclusive in the case of a point defect. In our case, however, calculations for smaller SCs are also of interest; for example, in the supercell S24 with a defect, the impurity content is 12.5 mol % LaF_3, which lies in the range of practically important concentrations [2].

For the results obtained for defect SCs of various sizes to be adequate, it is necessary that the calculated bulk properties of the defect-free crystal be independent of the SC size. A parameter suitable to this criterion is the total SC energy per unit cell of the crystal [14]. In our case, this parameter for the defect-free supercell S24 is equal to –224.080335 hartrees; i.e., the criterion formulated above is satisfied with an accuracy of 10^{-5}.

To calculate the energy of defect formation E_{def} by means of CRYSTAL-98, we used the following values for the energy of isolated atoms: –99.37495 [11], –24.83430, and –30.77017 hartrees [12] for F, Ba, and La atoms, respectively. The values for Ba and La were calculated using ECP. The energy of defect formation was found from the formula $E_{def} = E_{La} - E_{perf} - E_F^{at} - E_{La}^{at} + E_{Ba}^{at}$, where E_{La} and E_{perf} are the total energies of the defect SC and the perfect SC, respectively, and E_F^{at}, E_{La}^{at}, and E_{Ba}^{at} are the total energies of the corresponding atoms.

The MS method is simple and allows one to investigate the spatial structure of defects in a crystal. In [17], we performed MS calculations for SrF_2 crystals doped with cerium. The MS method is based on pairwise ion–ion interaction potentials, which have a Coulomb and a short-range component. Given the ionic charges, the MS model is used to calculate the parameters of the short-range component of the pairwise potential, which is commonly represented in the form of a Born–Mayer–van der Waals potential. The parameters of the short-range component for the BaF_2 crystal were taken from [6]. The electronic (inertialess) polarization of fluorine ions was described in terms of the Dick–Overhauser shell model. With the parameters of the MS model of the crystal, we reproduced the structure of the perfect crystal, the zero pressure (i.e., the minimum total energy of the crystal) for the unit-cell dimensions used, and the experimental values of the bulk modulus and dielectric constants of the crystal.

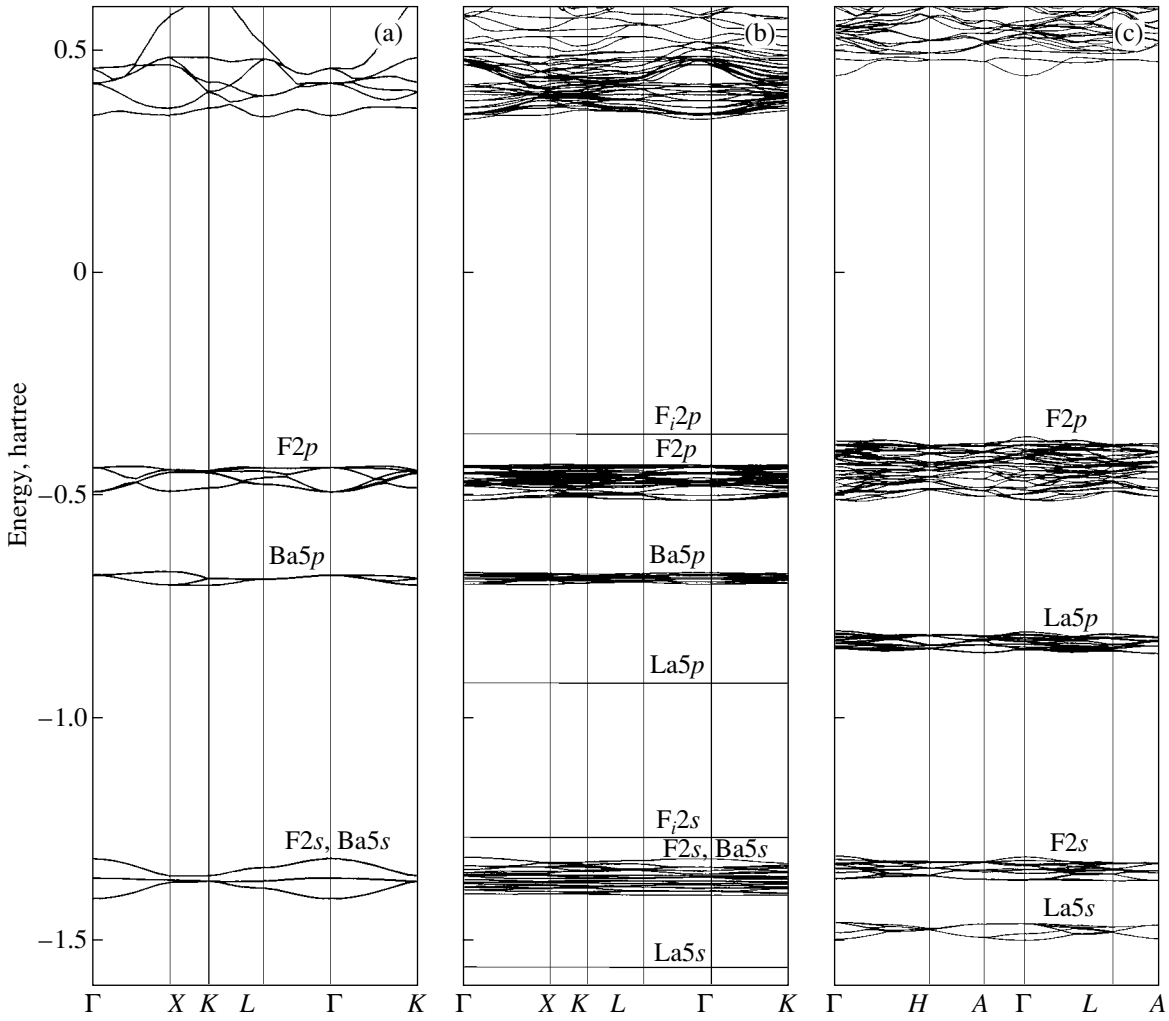

Fig. 1. Calculated band structures of crystals (a) BaF_2, (b) BaF_2 : La (supercell S24), and (c) LaF_3. The states with negative energies correspond to the valence and quasi-core bands, and the states with positive energies, to the conduction band.

3. RESULTS AND DISCUSSION

3.1. The Electronic Structure of BaF_2 and LaF_3 Crystals

At the initial stage, we calculated the electronic structure of perfect BaF_2 and LaF_3 crystals using CRYSTAL-98. Up to now, no consistent calculations of the electronic structure of LaF_3 crystals (trigonal tysonite structure, space group *P*–3*C1* [18]) had been carried out. It should be noted that the band gap width found by us for all systems considered (BaF_2, LaF_3, BaF_2 : La) was overestimated, which is characteristic of conventional HF approximations [5].

The calculated band structure of barium fluoride (Fig. 1a) agrees satisfactorily with the available experimental data and calculations [19, 20]. The calculations show that the valence band of the crystal is predominantly formed by the F2*p* states and that the lower levels of the conduction band correspond to the 6*s* and 5*d* states of barium. The valence band width ΔE_v is 1.9 eV, E_{g2} = 4.84 eV, and the width of the first core band (Ba5*p*) is 0.9 eV. The effective charges Q_{Ba} = +1.904 and $Q_F = -0.952|e|$, found from the charge-density distribution following Mulliken, indicate the purely ionic character of chemical bonding in this compound.

The band structure of LaF_3 is shown in Fig. 1c. It should be noted that ΔE_v for this crystal is 1.9 eV larger than that for BaF_2. This fact can be explained by the more complex crystal structure of LaF_3 (24 atoms in a unit cell, three nonequivalent positions of fluorine ions) in comparison to that of BaF_2. The calculated effective charges of fluorine ions in the nonequivalent positions are –0.898, –0.872, and $-0.866|e|$. Other parameters of the calculated band structure are as follows: E_{g2} = 8.16 eV, the La5*p* band width is 1.3 eV, and the energy gap between the F2*s* and La5*s* bands is 2.99 eV. The

adequacy of the model electronic structure of LaF_3 can be judged from the reasonable agreement between the relative positions of peaks in the total density of states (TDOS) and the experimental x-ray photoelectron spectroscopy (XPS) data [21] (Fig. 2). The evident structure of the F2*p* peak is, perhaps, due to weak Coulomb anisotropy of regular fluorine ions in the crystal.

3.2. Molecular-Static Modeling of the Spatial Structure of an La Defect in BaF_2

We calculated the energy of defect formation and the interaction energy between defects by using the MS method and the periodic-defect model. The dependence of the energy of formation of an $[La^{3+}–F_i^-]$ dipole in BaF_2 on the dipole concentration is presented in the table for SCs with 12, 24, 48, and 96 ions. According to our calculations, the formation of an NNN defect in BaF_2 is energetically favored over that of an NN defect. The energy of formation of an isolated (point) defect (0.16 eV) agrees satisfactorily with the published data (0.123 eV) [6]. Note that the opposite situation occurs with CaF_2 and CrF_2. The difference in the results of computer simulation of the defect structure for CaF_2 and BaF_2 is commonly explained by the difference in their lattice parameters [6]. We analyzed this situation in more detail by using various MS-calculated contributions to the energy of defect formation. The MS energies of dipole formation listed in the table were calculated from the formula $E_{def} = E_{La} - E_{perf}$, where E_{La} is the energy of the crystal with one Ba^{2+} ion substituted by an La^{3+} ion and with an F^- ion placed at an adjacent interstitial site; it is assumed that the Ba^{2+} ion is removed from the crystal to infinity and the La^{3+} and F ions that are incorporated into the crystal are transferred from infinity. Therefore, the MS and HF methods should give different values for the defect energies but approximately the same values for the difference between the energies E_{NN} and E_{NNN}.

From the table, it follows that, as the defect concentration increases, the NNN defect becomes progressively more advantageous than the NN defect. Let us discuss the formation of an NNN dipole in the case of the S24 supercell. The initial energy of the SC with an NN defect (without regard for relaxation) is $E_{La} = –215.35$ eV and consists of two parts: the Coulomb energy (–237.67 eV) and the short-range interaction energy (+22.32 eV). The initial energy of the SC with an NNN defect is equal to –214.55 eV and consists of the Coulomb energy (–236.85 eV) and the short-range interaction energy (+22.31 eV). Therefore, the short-range energies of defects of both types are equal if the lattice relaxation is ignored. The formation of the NN defect is more advantageous in this case. The situation is reversed if the lattice relaxation is included. The final energy of the NN dipole is –218.96 eV (with the Coulomb energy being –242.89 eV and the short-range energy being +23.93 eV), whereas the NNN-defect energy is –219.51 eV (with the Coulomb energy being –243.62 eV and the short-range energy being +24.11 eV). Therefore, the NNN dipole is more advantageous. The values of E_{def} listed in the table are obtained by subtracting the energy of the perfect crystal (equal to $E_{perf} = –194.22$ eV in the MS method) from the values of E_{La} presented above.

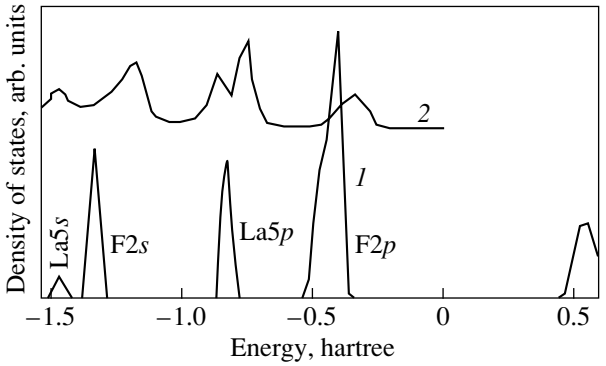

Fig. 2. (*1*) Calculated TDOS and (*2*) experimental XPS spectrum of an LaF_3 crystal. The states with negative energies correspond to the valence and quasi-core bands, and the states with positive energies, to the conduction band.

Thus, the formation of the NN and NNN defects depends on the lattice relaxation, which affects the Coulomb energy. In contrast to CaF_2, whose lattice parameter is smaller than that of BaF_2, relaxation of the BaF_2 crystal lattice favors the formation of the NNN defect.

Let us consider the relaxation of the BaF_2 crystal lattice in the vicinity of the $[La^{3+}–F_i^-]$ dipole in the case of the S24 supercell. Since the NNN dipole is symmetric, only the fluorine ions nearest to the La^{3+} ion are displaced noticeably; seven of these eight ions shift from their regular positions by 4.8% toward the lanthanum

Formation energy (in electronvolts) of the NN and NNN configurations of the $[La^{3+}–F_i^-]$ dipole calculated using the MS method with allowance for relaxation; $\Delta E = E_{NN} - E_{NNN}$; the S_∞ supercell corresponds to the case of an isolated (point) defect

Supercell	E_{NN}	E_{NNN}	ΔE
S12	–24.00	–25.30	1.30
S24	–24.76	–25.28	0.52
S48	–24.83	–25.12	0.29
S96	–24.86	–25.07	0.21
S_∞	–24.86	–25.02	0.16

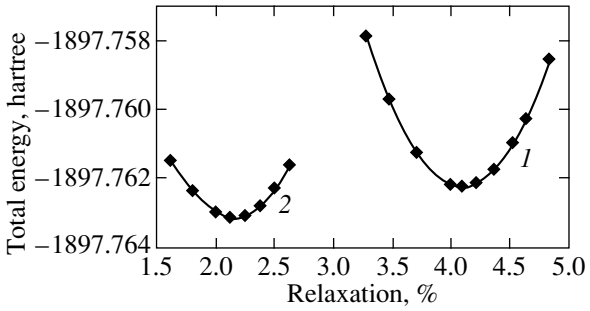

Fig. 3. Calculated total energy of the S24 supercell of the BaF_2 : La crystal as a function of relaxation of ions in the first coordination shell of the defect. The total energy was minimized first (*1*) with respect to the relaxation of the fluorine ions nearest to the lanthanum ion and then (*2*) with respect to the relaxation of the barium ions nearest to the F_i ion.

ion (here and henceforth, the displacements are expressed as a percentage of the lattice constant of the crystal), and the remaining fluorine ion [the most remote from the F_i ion along the (111) axis] shifts by 4.7%. The other fluorine ions are displaced only slightly; for example, the ions in the second coordination shell of the lanthanum ion shift by 1.0–1.4%. The nearest neighbors of the other component of the dipole (six barium ions) shift from their regular positions by 1.8% toward the interstitial fluorine ion. In the case of the NN dipole, the fluorine ions in the first coordination shell of the La^{3+} ion, as well as the fluorine ions situated between the lanthanum ion and the interstitial fluorine ion, are displaced by 3.8% toward the lanthanum ion; the other four nearest neighbor fluorine ions relax by 4.0–4.5% in the same direction. The La^{3+} ion shifts by 1.25% toward the interstitial fluorine ion, which relaxes by 2.8% in the same direction. The barium ions nearest to the charge-compensating fluorine ion are displaced by 1.9% toward F_i. It should be noted that the relaxation of the Ba^{2+} ions in the first coordination shell of F_i is of importance. Without this relaxation, the NN defect becomes more advantageous than the NNN defect.

3.3. Computer Simulation of BaF_2 : La within the Supercell Model Using CRYSTAL-98

In band-structure calculations, allowance for distortions arising in the vicinity of a defect makes the problem complicated, because both the local and spatial symmetries of the problem are changed. Only symmetric distortions of one or two coordination shells of the defect are frequently considered in this case. Experience in computing with the use of the CRYSTAL software package suggests that the electronic structure of a defect system can be adequately described even by taking into account only distortions in the first coordination shell of the defect. Inclusion of the second and more distant coordination shells brings about only an insignificant decrease in the energy of defect formation [14]. In our computer simulations of $Ba_{1-x}La_xF_{2+x}$ with the use of CRYSTAL-98, the initial relaxation parameters were taken to be those found by the MS method. Since, according to MS calculations, the relaxation in the second coordination shell is small, we took into account only relaxation of the nearest neighbors of the La impurity ion in BaF_2 in calculating the NN and NNN defects. CRYSTAL-98 calculations for the S24 supercell showed that the total energy of the NNN defect in barium fluoride is 0.65 eV lower than that of the NN defect, which is close to the value of this energy difference found using the MS method (0.52 eV). In band-structure calculations, the equilibrium configuration of a defect is found by minimizing the total energy of a supercell. For the S24 supercell, we minimized the total energy first with respect to the relaxation of the fluorine ions nearest to the lanthanum ion and then with respect to the relaxation of the barium ions nearest to F_i. The results are shown in Fig. 3. The F- and Ba-ion relaxations thus found are 0.7% smaller and 0.2% larger, respectively, than the corresponding values found using the MS method.

The band structure of the $Ba_{1-x}La_xF_{2+x}$ system with NNN defects calculated using the S24 supercell is shown in Fig. 1b, and the corresponding maps of the total and difference charge densities are presented in Fig. 4. It follows from Fig. 1b that the qualitative changes in the electronic structure of the barium fluoride crystal are associated not only with the substitutional defect (lanthanum) but also with the charge-compensating impurity F_i. A set of energy levels appears in the band gap; these levels correspond to the F_i2p states and lie ~1.7 eV above the top of the valence band. The valence-band width increases up to 2.2 eV. This increase in ΔE_v relative to its value in BaF_2 (1.9 eV) is due to the Coulombic interaction between the [La^{3+}–F_i^-] dipole and the surrounding ions, which causes the fluorine ions in various coordination shells of the defect to become anisotropic. An analysis of the charge-density distribution, determined according to Mulliken, reveals that in the S24 supercell with the defect, there are nonequivalent fluorine ions of four types, with charges –0.947, –0.938, –0.944, and $-0.958|e|$. From crystallographic data, it follows that the first two types of ions are relaxing fluorine ions in the first coordination shell of the defect (the La–F distance is 2.49 Å), the ions of the second type also being close to the interstitial fluorine ion F_i (3.01 Å). The fluorine ions of the third type are in the first coordination shell of F_i (the F_i–F distance is 2.75 Å), and the ions of the fourth type are separated from the components of the dipole by a distance larger than 5 Å. The existence of several types of fluorine ions in the S24 supercell with the defect is manifested in the map of the difference charge density of the system presented in Fig. 4.

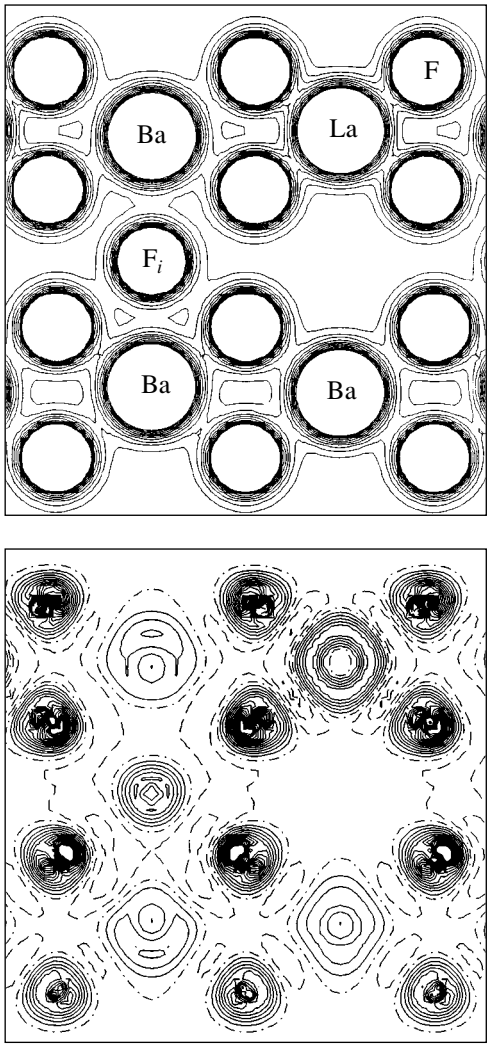

Fig. 4. Maps of the total (upper panel) and difference (lower panel) charge densities in the (110) plane of BaF_2 : La calculated for the S24 supercell. The spacing between consecutive contours is 0.01 and $0.001e/r_B^3$ (r_B is the Bohr radius) for the total and difference charge densities, respectively. Solid, dashed, and dot-and-dash curves correspond to positive, negative, and zero values of the charge density, respectively. The difference charge density was calculated relative to the superposition of isolated Ba^{2+}, F^-, and La^{3+} ions.

Now, we discuss the influence of relaxation of ions surrounding the defect on the macroscopic properties of the system in the case of the S24 supercell with the NNN defect. According to our calculations with the use of CRYSTAL-98, allowance for the relaxation of ions in the first coordination shell of the defect brings about the following changes: the energy of defect formation decreases from 8.368 to 5.303 eV, the F_i2p states shift downward by 1.6 eV relative to the valence-band top, the valence band narrows by 0.5 eV and becomes less dispersive, the La5*p* states shift upward by 3 eV, and the energy gap between the F2*p* and La5*p* bands becomes closer to its value for LaF_3.

4. CONCLUSIONS

Thus, we have investigated the effect of a lanthanum impurity on the band structure of BaF_2 and calculated the energy of defect formation within the HF approximation. The changes in the valence band of the crystal were shown to be due to the Coulomb interaction between the $[La^{3+}–F_i^-]$ dipole and the surrounding ions. The boundaries of the spatial region within which the electron subsystem of the crystal is affected by a defect were found for the case of an S24 supercell with a defect.

The results of our investigation of the spatial structure of the defect support the conclusion that the NNN defect in BaF_2 is energetically favored over the NN defect. Despite the fact that the ion–ion interaction is described using fundamentally different methods within the MS and HF approximations, the estimates of the difference between the energies of formation of the NN and NNN defects made in these approximations are close to each other.

REFERENCES

1. P. Schotanus, P. Dorenbos, C. W. E. van Eijk, and H. J. Lamfers, Nucl. Instrum. Methods Phys. Res. A **281**, 162 (1989).
2. B. P. Sobolev, E. A. Krivandina, S. E. Derenzo, *et al.*, Mater. Res. Soc. Symp. Proc. **348**, 277 (1994).
3. E. Radzhabov, A. Shalaev, and A. I. Nepomnyashikh, Radiat. Meas. **29** (3–4), 307 (1998).
4. A. I. Nepomnyashikh, E. A. Radzhabov, A. V. Egranov, and V. F. Ivashechkin, Radiat. Meas. **33** (5), 759 (2001).
5. R. Dovesi, R. Orlando, C. Roetti, *et al.*, Phys. Status Solidi B **217** (1), 63 (2000).
6. J. Corish, C. R. A. Catlow, P. W. M. Jacobs, and S. H. Ong, Phys. Rev. B **25** (10), 6425 (1982).
7. V. R. Saunders, R. Dovesi, C. Roetti, M. Causa, N. M. Harrison, R. Orlando, and C. M. Zicovich-Wilson, *CRYSTAL-98 User's Manual* (Univ. of Torino, Torino, 1998).
8. Yu. N. Kolmogorov and A. N. Varaksin, Zh. Strukt. Khim. **32** (4), 162 (1991).
9. J. L. Gavartin, C. R. A. Catlow, A. L. Shluger, *et al.*, Modell. Simul. Mater. Sci. Eng. **1** (1), 29 (1992).
10. *Crystals with the Fluorite Structure. Vibrational and Defect Properties*, Ed. W. Hayes (Clarendon, Oxford, 1974).
11. http://www.ch.unito.it/ifm/teorical/Basis_Sets.
12. P. J. Hay and W. R. Wadt, J. Chem. Phys. **82** (1), 270 (1985).
13. http://www.tcm.phy.cam.ac.uk/~mdt26/basis_sets.

14. A. Lichanot, C. Larrieu, R. Orlando, and R. Dovesi, J. Phys. Chem. Solids **59** (1), 7 (1998).
15. A. Lichanot, Ph. Baranek, M. Mérawa, *et al.*, Phys. Rev. B **62** (19), 12812 (2000).
16. G. Mallia, R. Orlando, C. Roetti, *et al.*, Phys. Rev. B **63**, 235102 (2001).
17. A. B. Sobolev, A. N. Varaksin, and A. Yu. Kuznetsov, Fiz. Tverd. Tela (St. Petersburg) **38** (9), 2729 (1996) [Phys. Solid State **38**, 1497 (1996)].
18. B. Maimov and H. Schulz, Acta Crystallogr. B **41** (2), 88 (1985).
19. P. A. Rodnyĭ, Fiz. Tverd. Tela (St. Petersburg) **34** (7), 1975 (1992) [Sov. Phys. Solid State **34**, 1053 (1992)].
20. L. K. Ermakov, P. A. Rodnyĭ, and N. V. Starostin, Fiz. Tverd. Tela (Leningrad) **33** (9), 2542 (1991) [Sov. Phys. Solid State **33**, 1435 (1991)].
21. K.-H. Park and S.-J. Oh, Phys. Rev. B **48** (20), 14833 (1993).

Translated by Yu. Epifanov

Physics of the Solid State, Vol. 45, No. 5, 2003, pp. 845–853. Translated from Fizika Tverdogo Tela, Vol. 45, No. 5, 2003, pp. 804–812.

SEMICONDUCTORS AND DIELECTRICS

Transient Optical Absorption and Luminescence of Lithium Triborate LiB_3O_5

I. N. Ogorodnikov*, V. Yu. Yakovlev, and L. I. Isaenko*****

**Ural State Technical University, ul. Mira 19, Yekaterinburg, 620002 Russia*

e-mail: ogo@dpt.ustu.ru

***Tomsk Polytechnical University, pr. Lenina 30, Tomsk, 634021 Russia*

****Technological Institute for Single Crystals, Siberian Division, Russian Academy of Sciences, Novosibirsk, 630058 Russia*

Received July 15, 2002

Abstract—The transient optical absorption and luminescence of LiB_3O_5 (LBO) nonlinear crystals in the visible and UV spectral ranges were studied. Measurements made using absorption optical spectroscopy with ns-scale time resolution revealed that the transient optical absorption (TOA) in LBO originates from optical transitions in hole centers and that the kinetics of optical density relaxation are rate-limited by interdefect nonradiative tunneling recombination involving these hole centers and the Li^0 electronic centers, which represent neutral lithium atoms. At 290 K, the Li^0 centers can migrate in a thermally stimulated, one-dimensional manner, a process which is not accompanied by carrier delocalization into the conduction or valence band. It is shown that the pulsed LBO cathodoluminescence kinetics is rate-limited by a recombination process involving two competing valence-band-mediated hole centers and shallow B^{2+} electronic centers. The radiative recombination accounts for the characteristic σ-polarized LBO luminescence in the 4.0-eV region. © *2003 MAIK "Nauka/Interperiodica".*

1. INTRODUCTION

LiB_3O_5 lithium triborate (LBO) belongs to space group $Pna2_1$ and contains four formula units in an orthorhombic unit cell with parameters $a = 8.4473$, $b = 7.3788$, and $c = 5.1395$ Å. Two of the three inequivalent boron atoms have a plane threefold coordinated bond structure similar to that of B_2O_3. The third boron atom is tetrahedrally fourfold coordinated. There are five inequivalent oxygen atoms. The structure of the crystal consists of a boron–oxygen cage with lithium ions located in connecting cage voids [1]. These voids form continuous channels along the *c* axis (2_1 axis), thus providing favorable conditions for the onset of ionic conduction. Experimental studies of the electrical conductivity of LBO crystals have revealed the existence of quasi-one-dimensional ionic conductivity caused by the motion of Li^+ cations along these channels [2]. The existence of an array of mobile cations should dramatically affect the electronic excitation dynamics and the specific features of radiation-induced defect formation. In our previous publications, this aspect was explored in the case of crystals with an array of mobile cations of lithium ($Li_2B_4O_7$ (LTB) [3]) and hydrogen ($NH_4H_2PO_4$ (ADP), KH_2PO_4 (KDP) [4]). The ac electrical conductivity of an LBO crystal measured at 290 K along the *c* axis is $\sigma = 7 \times 10^{-5}\ \Omega^{-1}\ cm^{-1}$ [2], which exceeds that for the LTB crystal in the same conditions by about 20 times. In this connection, investigation of LBO appears to be of fundamental importance from the standpoint not only of its individual characteristics but also of the evolution some general properties determined by the dynamics of the mobile cation sublattice undergo in the ADP–KDP–LTB–LBO series of nonlinear optical crystals.

The present communication reports on a study of LBO crystals by ns-scale time-resolved luminescence and optical spectroscopy under electron beam excitation.

2. EXPERIMENT

We used in the study undoped crystals of lithium triborate LiB_3O_5, whose growth technology was described in [5]. The samples measured $8 \times 8 \times 1$ mm and had laser-quality polished plane-parallel surfaces. The orientation of the crystallographic axes and the geometry of the experiment are sketched in Fig. 1.

The experimental setup and specific features of ns-scale time-resolved luminescence and absorption spectroscopy are described in considerable detail in [6]. The specifics of the experiment are outlined in our previous publication [3]. The pump pulse duration used in measurements of the dependence of transient optical absorption (TOA) and pulsed cathodoluminescence (PCL) on pump power were maintained constant. The pump power was varied by means of calibrated grid diaphragms.

The polarization measurements were performed with Rochon (TOA) and Frank–Richter (PCL) prisms.

1063-7834/03/4505-0845$24.00

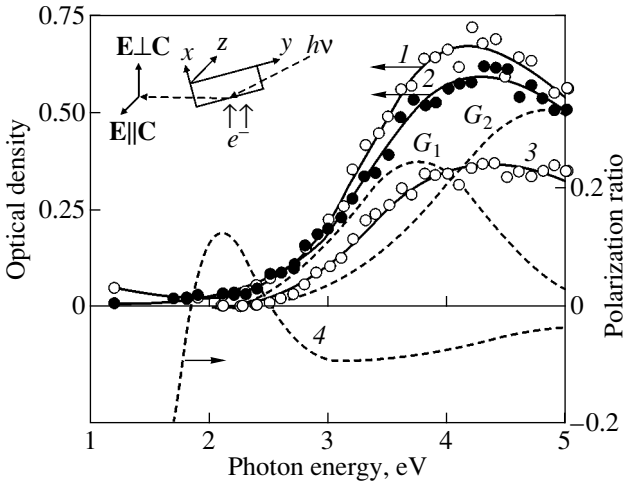

Fig. 1. Polarized TOA spectra of LBO crystal measured at 290 K (*1*, *3*) in the **E** ⊥ **C** configuration and (*2*) in the **E** ∥ **C** configuration (*1*, *2*) immediately after pump pulse termination and (*3*) with a 10-μs delay, and (*4*) the polarization ratio. $G_0 \ldots G_2$ are the resolved constituent bands.

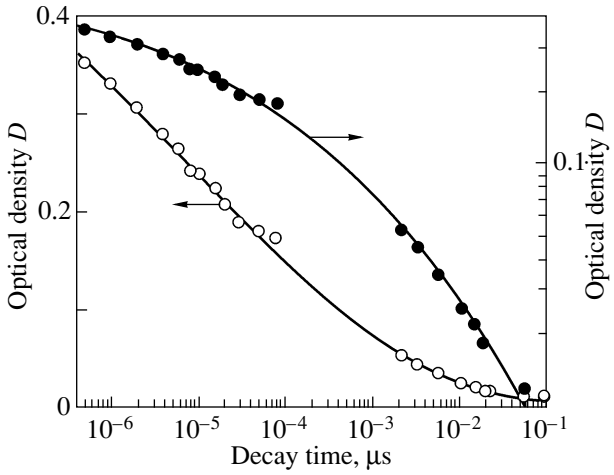

Fig. 2. LBO TOA kinetics in the 3.8-eV band measured at 290 K. Circles are experimental points and solid lines are fits.

The degree of polarization was estimated from the expression

$$P = (I_{\parallel} - I_{\perp})/(I_{\parallel} + I_{\perp}), \quad (1)$$

where indices ∥ and ⊥ label the electric vector orientation of the probe light parallel or perpendicular to the [001] direction (subsequently, the *C* axis) and *I* is the luminescence intensity for PCL or optical density for TOA.

Figure 1 displays time-resolved spectra of polarized TOA of the LBO crystal measured at 290 K in the **E** ⊥ **C** and **E** ∥ **C** configurations. The spectra consist of three partially overlapping Gaussian-shaped bands at 2.24, 3.75, and 4.82 eV (Table 1). The main band parameters basically agree with those of the electron-beam-excited unpolarized spectra of stable (80 K) and transient (295 K) optical absorption of LBO crystals studied by us earlier [7, 8]. The optical absorption dichroism is comparatively small. As follows from Table 1, the constituent TOA bands $G_0 \ldots G_2$ are polarized to +30, –13, and about –1%, respectively. The observed spectral response of the degree of polarization in the range 2–5 eV is caused by superposition of the fundamental $G_0 \ldots G_2$ bands, and that in the long-wavelength range, by the contribution of the TOA infrared band peaking below 1 eV (Fig. 1).

At 290 K, the LBO TOA decays fairly uniformly over the spectrum (Fig. 1), with the crystal completely regaining its optical transparency in a time shorter than 1 s. The main component of the TOA decay kinetics in the $G_0 \ldots G_2$ bands features a slow monotonic optical density decay observed on a time scale extending over

Table 1. Parameters of LBO polarized TOA spectra measured at 295 K immediately after pump pulse termination (D_{max}) and 10 μs later [D (10 μs)]

Band	**E** ∥ **C**		**E** ⊥ **C**	
	D_{max}	D (10 μs)	D_{max}	D (10 μs)
E_{m1}, eV	2.24	2.24	2.24	2.24
ΔE_1, eV	0.94	0.94	0.94	0.94
D_{01}	0.028	0.013	0.015	0
E_{m2}, eV	3.75	3.75	3.75	3.75
ΔE_2, eV	1.4	1.4	1.4	1.4
D_{02}	0.286	0.106	0.374	0.169
E_{m3}, eV	4.82	4.82	4.82	4.82
ΔE_3, eV	2.04	2.04	2.04	2.04
D_{03}	0.494	0.294	0.504	0.305

Note: E_m, ΔE, and D_0 are the positions of the maximum, FWHM, and band amplitude, respectively.

not less than six decades (Fig. 2). Within a limited region of decay time of about three to four decades, the optical density can be fitted by a log–linear function of time. On the other hand, the TOA kinetics can be well rectified within the same time interval in the log–log coordinates, thus making it possible make an approximation using a power-law function:

$$D(t) \propto t^{-p}, \tag{2}$$

where p is the exponent. The magnitude of p depends slightly on the decay time and lies within the interval 0.04–0.20. It is known that such properties are characteristic of the kinetics of interdefect tunneling recombination [9]. In the case where the concentration N of one of the recombination partners greatly exceeds that of defects of the other species, n, which accounts for the observed TOA, the following equation can be used:

$$n(t) = n_0 \exp\left(-\frac{4}{3}\pi a^3 N \ln^3(\nu_0 t)\right), \tag{3}$$

where ν_0 is the prefactor and a is one half the Bohr radius; these values determine the probability W of electron tunneling transfer,

$$W(r) = \nu_0 \exp\left(-\frac{r}{a}\right). \tag{4}$$

Figure 2 illustrates approximation of the LBO TOA kinetics in the band at 3.8 eV made using Eq. (3) over a decay time range covering about five decades.

Increasing the excitation pulse power brings about an increase in the initial concentration of the radiation defects produced by this pulse. This also entails a shortening of the TOA decay kinetics. Plotted on a log–log scale, the initial optical density D_0 proportional to the initial radiation defect concentration grows linearly with a unit slope throughout the spectral region studied (Fig. 3). This may imply an intrinsic nature of the LBO color centers and a common mechanism of destruction of the radiation defects responsible for the various LBO TOA bands.

Heating the crystal also brings about a shortening of the TOA decay kinetics (Fig. 4), but with the optical density retaining its initial value $D(t \longrightarrow 0)$. A comprehensive analysis of TOA at different temperatures revealed the existence of an additional fast exponential component in the TOA decay kinetics. At 315 K, its initial intensity constitutes about 30% of that for the main component (3), and the time constant $\tau = 3$ μs. A quantitative comparison of the TOA kinetics in different spectral intervals made for relatively short decay times provided indirect confirmation of the existence of this component. Indeed, the relative decay of the G_0 and G_2 bands during the first 2 μs reaches as high as 20% and that for the first 10 μs reaches 40%. The corresponding values for the G_1 band are 40 and 60%. This indicates clearly the presence in the TOA kinetics of an additional fast component with a μs-scale decay time,

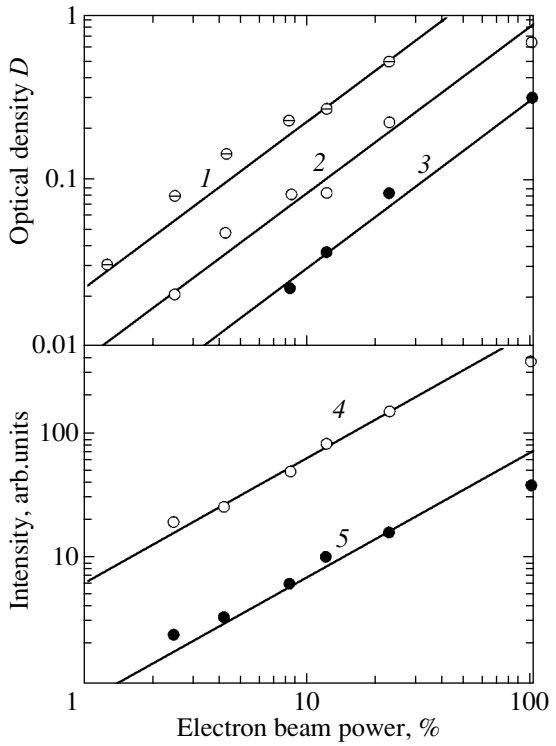

Fig. 3. Dependences of (*1–3*) optical density and (*4*, *5*) luminescence intensity in the LBO bands at (*1*) 3.8, (*2*) 2.8, (*3*) 2.1, and (*4*) 3.6 eV, measured at 290 K (*1–4*) immediately after pulse termination and (*5*) at the maximum of fast PCL rise, on electron beam power.

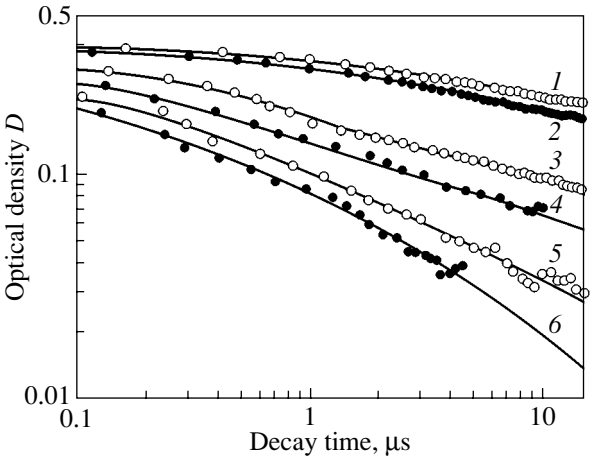

Fig. 4. LBO TOA kinetics in the 3.8-eV band measured at (*1*) 304, (*2*) 353, (*3*) 420, (*4*) 480, (*5*) 568, and (*6*) 618 K.

which manifests itself primarily in the G_1 band. Therefore, the TOA kinetics in the short decay time range at different temperatures was approximated by a sum of two components, namely, a fast exponential term and dependence (3). The temperature dependence of τ of the fast component obeys the Arrhenius law with an activation energy of about 215 meV. The temperature

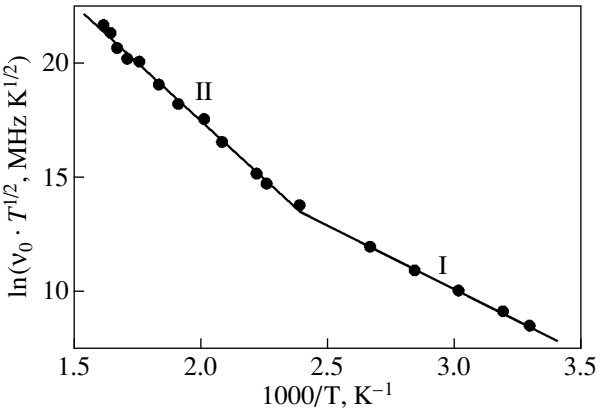

Fig. 5. Temperature dependence of the LBO TOA kinetics parameter ν_0 measured in the 3.8-eV band.

dependence of the slow component (3) is dominated by the prefactor $\nu_0(T)$. According to [10],

$$\nu_0(T) = \frac{C}{T^{1/2}}\exp\left(-\frac{E_a}{k_bT}\right), \quad (5)$$

where C is a constant and E_a is the tunneling activation energy. Fitting Eq. (3) to the slow component of the TOA kinetics for a fixed value $a^3N = 4.3 \times 10^{-4}$ yielded values of ν_0 for various temperatures. Plotted in the Arrhenius coordinates, the relation $\nu_0(T)T^{1/2}$ can be rectified in two temperature intervals (I, II in Fig. 5) with the activation energies E_a = 420 and 770 meV, respectively.

Besides the transient optical absorption, excitation by an electron beam produces, in the LBO crystal, a burst of cathodoluminescence featuring both fast and slow decay kinetics components. Figure 6 displays time-resolved PCL spectra. A PCL spectrum measured immediately after termination of the pump pulse consists of several Gaussian-shaped elemental bands (Table 2) and a broad-band pedestal with a height of about 7% of the observed maximum. The spectrum of the slow PCL measured with a 1- or 10-μs decay has one band at 3.94 eV (FWHM = 1.0 eV). A delay of 100 μs makes a long-wavelength shift of the band by 0.15 eV visible (E_m = 3.79 eV, FWHM = 0.51 eV).

Table 2. Parameters of the LBO fast PCL spectrum measured at 295 K

Band	G_1	G_2	G_3	G_4
E_m, eV	3.28	3.66	4.22	4.75
ΔE, eV	0.93	0.53	0.57	0.33
A, %	51.6	55.7	44.2	13.5

Note: E_m and ΔE are the position of the maximum and FWHM; A is the band amplitude in percentage of the observed PCL maximum.

The PCL decay kinetics is displayed in Fig. 7. It features a slow stage in the time interval 1–10 μs where the luminescence intensity exhibits a rise. The LBO PCL kinetics in the decay time range below 200 μs can be formally approximated by the relation

$$I(t) = A_0\exp(-t/\tau_1) + A_1\exp(-t/\tau_2) + I_0(1 - I_1\exp(-t/\tau_3))\exp(-t/\tau_4). \quad (6)$$

The parameters of the approximation depend on the actual experimental conditions (sample temperature, pump power, luminescence band). For instance, the parameters obtained for the PCL decay kinetics in the 3.8-eV band at 23% pump power and 295 K are as follows: A_0 = 35.66, A_1 = 0.14, I_0 = 3.62, I_1 = 0.62, τ_1 = 12 ns, τ_2 = 200 ns, τ_3 = 6.3 μs, and τ_4 = 40 μs. The local minimum in PCL intensity (I_{min}) lies in the decay time interval 100–200 ns. The maximum in the sharp rise is observed near 10 μs. Figure 3 presents the dependences of PCL intensity on pump power measured immediately after termination of the pump pulse, $I(0)$, and at the maximum of the sharp rise. The experimental points plotted on the log–log scale can be fitted, except the point corresponding to 100% pump power, by straight lines with a unit slope (Fig. 3). Note that if the pump power is varied, the parameter I_1 and the ratio $I(0)/I_{min}$, which in the 3.6-eV band is about 12, are retained.

Figure 6 presents the spectral responses of the kinetics parameters I_0 and I_1. We readily see that the spectral response of I_0 resembles the spectrum of the slow LBO PCL. This does not come as a surprise, because it is the I_0 parameter that determines the initial intensity of the slow PCL. Parameter I_1 grows linearly in the 3- to 5-eV spectral region from 0.40 to 0.74 (Fig. 6). This results in an increase in the difference in relative magnitude between the intensity minimum in the 0.1–1-μs interval and intensity maximum at 10 μs; in other words, the sharp intensity rise in slow PCL becomes more pronounced in the short-wavelength spectral region. In the spectral region below 3 eV, the intensity of the slow PCL decreases to a level comparable to that of fast PCL tails in the 100- to 200-ns decay time range. This behavior masks the intensity rise effect in the visible range.

Figure 8 plots the angular dependence of slow PCL polarization in the 3.8-eV band, which was measured at the maximum of the intensity rise with the analyzer rotated in the (010) plane. The angle ϑ is reckoned from the **E** || **C** direction. The experimental data were fitted by the relation

$$I(\vartheta) = A_0 + A_1\cos^2\vartheta, \quad (7)$$

where A_0 and A_1 are the fitting parameters. The degree of polarization estimated from the fitting (Fig. 8) is +56%.

Figure 9 illustrates the decay kinetics of polarized PCL measured with an SS-4 band color filter (2.7–3.3 eV) for the **E** || **C** and **E** ⊥ **C** orientations. Two main exponential components with time constants 150 ns and

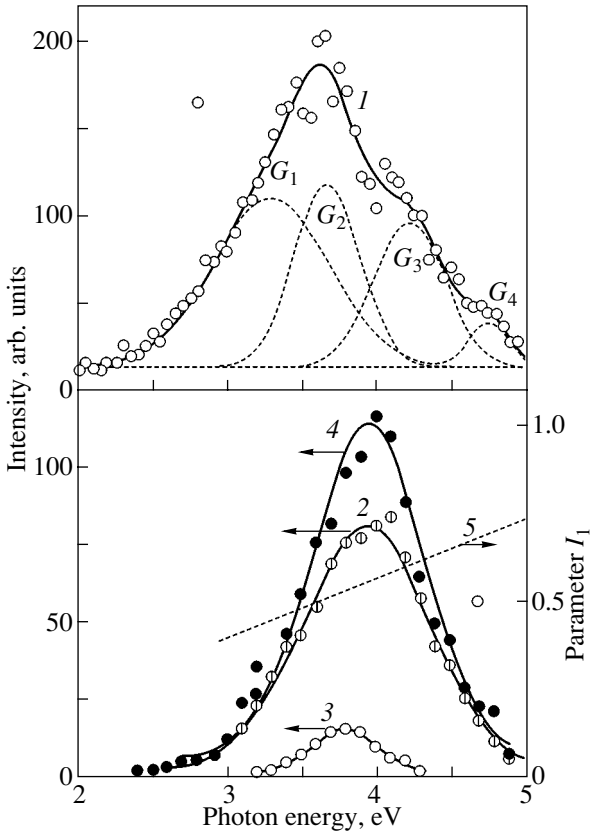

Fig. 6. LBO PCL spectra measured at 290 K (*1*) immediately after pump pulse termination and with a delay of (*2*) 10 and (*3*) 100 μs; spectral response of the kinetics parameters (*4*) I_0 and (*5*) I_1.

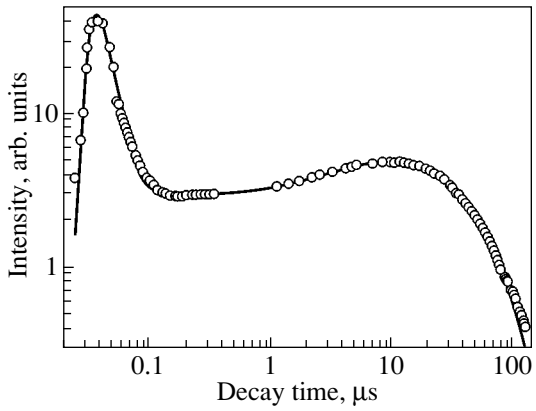

Fig. 7. LBO PCL decay kinetics in the 3.8-eV band measured at 300 K at 23% pump power.

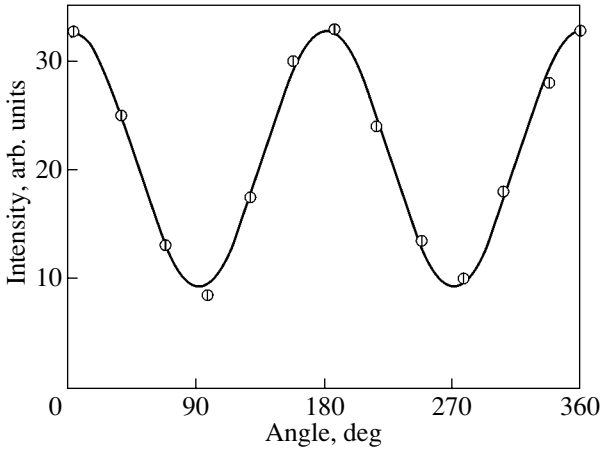

Fig. 8. LBO PCL polarization in the 3.8-eV band measured after a 10-μs delay with the analyzer rotated in the (010) plane. The angle is reckoned from the **E** || **C** direction.

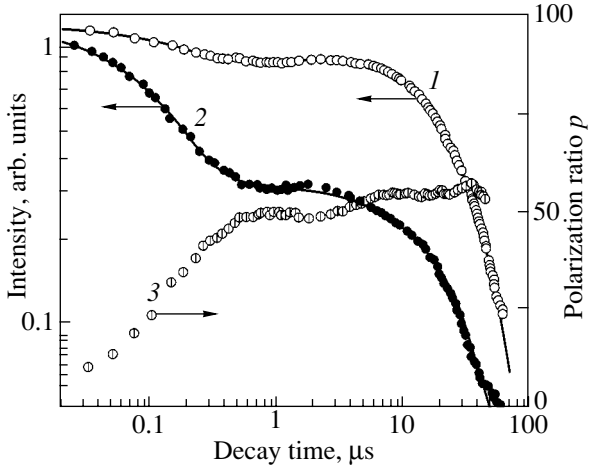

Fig. 9. Decay kinetics of polarized PCL measured with a SS-4 band color filter (2.7–3.3 eV) for (*1*) **E** || **C** and (*2*) **E** ⊥ **C** and (*3*) the polarization ratio.

26 μs, which differ in degree of polarization, were isolated in the decay kinetics of the polarized PCL. The degree of polarization of these components, as found using the fitting procedure, is –26 and +56%, respectively. It is the superposition of these two components with different degrees of polarization that accounts for the observed evolution of the polarization ratio p (Fig. 9); namely, in the region 200–500 ns the degree of PCL polarization increases from 10 to 48%, to rise smoothly thereafter to 56% in the μs-range of decay times.

3. DISCUSSION OF RESULTS

A detailed comparison of the main properties of transient optical absorption in LBO (Figs. 1–3) and LTB [3] crystals argues convincingly in favor of their being similar. According to the model proposed by us earlier, the optical absorption of undoped LTB [3] and LBO [7] in the visible and UV regions of the spectrum is produced by optical hole transitions from the local defect level to states in the valence band (VB) of the crystal. The TOA spectral profile is determined here to a considerable extent by the VB density of states. The energy threshold of the onset of optical absorption cor-

responds to the energy of the optical transition connecting the local level of the hole center with the valence band top, i.e., the optical activation energy E_O of the hole center. We can use the Lyddane–Sachs–Teller relation to estimate this energy from the known thermal activation energies E_T (0.25 eV for LTB, and 0.5 eV for LBO):

$$E_O \approx E_T \epsilon(0)/\epsilon_\infty, \tag{8}$$

where $\epsilon(0)$ and ϵ_∞ are the static and high-frequency dielectric permittivities of the crystal. Accepting as a rough estimate that $\epsilon(0)/\epsilon_\infty$ equals 8 for LTB and 4 for LBO, we obtain $E_O \approx 2$ eV for both crystals. This is in satisfactory agreement with the experimental TOA spectra of LTB [3] and LBO (Fig. 1).

The local level of the hole O^- center in the LBO crystal forms through the splitting of states from the VB top to the band gap near a negatively charged defect, namely, a lithium vacancy [11, 12]. The O^- center forms when the hole is localized at the oxygen atom bridging the three- and fourfold coordinated boron atoms, i.e., between the BO_4 and BO_3 fragments [13]. The VB top of LBO derives from nearly pure $2p\pi$ orbitals of oxygen atoms belonging primarily to the BO_4 structural fragments [14–16]. Therefore, we associate the optical absorption mechanism with photoinduced hole transfer between the $2p$ states of adjacent anions surrounding the lithium vacancy. The theory of small radius polarons considers this to be interpolaron absorption. At 290 K, the hole performs thermally activated and tunneling migration between the four almost equivalent anions surrounding the vacancy. This may be one of the reasons accounting for the low degree of TOA polarization (Fig. 1). Note that a similar, comparatively small optical dichroism of TOA was also found to exist by us in LTB [3], ADP, and KDP [4] crystals.

The optical absorption observed in LBO (Fig. 1) and LTB [3] in the 2- to 2.5-eV region is apparently of another nature. It differs in its sign of polarization and a comparatively small induced optical density and can originate, in our opinion, from intrapolaron absorption, i.e., from optical transitions between crystal-field split $2p$ orbitals of the same oxygen atom. From a purely formal standpoint, $p_z \longrightarrow p_x, p_y$ transitions are forbidden by Laporte's selection rule, however, in real conditions, the forbiddenness is partially lifted to allow transitions with a weak oscillator strength ($f < 10^{-5}$), which account for the weak OA band at relatively long wavelengths [17]. Using the data in Table 1 for the LBO TOA band at 2.25 eV, we can estimate the energy of the corresponding phonons from the relation [18]

$$\hbar\omega = \frac{(\Delta E)^2}{8E_m} = \frac{(0.94)^2}{8 \times 2.25} \approx 49 \text{ meV}. \tag{9}$$

It is worth mentioning that the LTB and LBO crystals have a 342-cm^{-1} (42 meV) phonon mode [19, 20]; in addition, various lithium compounds, including LTB and LBO, revealed a vibrational absorption band near 420 cm^{-1} (52 meV) originating from vibrations of lithium ions in an oxygen environment [21].

The hole color centers responsible for the TOA are native defects of the LBO lattice, whose concentration, if plotted on a log–log scale, grows linearly with increasing excitation pump pulse power by nearly two orders of magnitude (Fig. 3). Efficient formation of high concentrations of comparatively long-lived hole centers under irradiation requires the presence of the corresponding number of electronic trapping centers involving native lattice defects. Because the lithium vacancy is part of the hole center under consideration, it appears natural to assume that the electronic center is actually an interstitial lithium atom, i.e., an antimorphous defect. We observed earlier a similar mechanism of electronic center formation at 290 K in a study of transient optical absorption of LTB (Li^0 center) [3], ADP, and KDP (H^0 center) [4]. A common feature of these crystals is the existence of a sublattice of mobile cations (lithium in LTB and LBO, and hydrogen in ADP and KDP) where antimorphous metastable defects form and the tunneling mechanism of their nonradiative recharging, which accounts for the TOA decay kinetics according to Eq. (3), operates.

The specific features of mobile cation dynamics inherent to each of these crystals affect the TOA decay kinetics. For instance, the ADP and KDP crystals belong to systems with an order–disorder-type phase transition and have Curie temperatures T_c of 148 and 123 K, respectively. It is known [22] that the order–disorder-type ferro- and antiferroelectrics exhibit, in the paraelectric phase, many properties characteristic of superionic conductors. At 290 K, ADP and KDP are in the paraelectric phase and feature ionic conductivity involving hydrogen cations. This gives rise to the appearance in the TOA decay kinetics of ADP and KDP of additional slow, second-scale hyperbolic components, which derive from diffusion-limited annihilation of hydrogen vacancies with interstitial hydrogen ions [4]. In going from ADP to KDP, we observed a decrease in the time constant and an increase in the amplitude of the hyperbolic component, which is in quantitative agreement with available data on the diffusion and ionic electrical conductivity of these crystals.

The main properties of the slow TOA decay component in LBO (Figs. 2–4) are comparable, both qualitatively and quantitatively, with those of the LTB TOA decay kinetics [3], which should certainly be assigned to the mobile cation dynamics having common features. In both cases we did not, however, succeed in detecting the hyperbolic TOA decay component that originates from the diffusion-limited annihilation of lithium vacancies with mobile lithium ions. At the same time, it is known that the ac electrical conductivity measured at 290 K increases by nearly three orders of magnitude in going from KDP to LTB and that the conductivity of the LBO crystal along the c axis is 20 times that of the LTB crystal in the same conditions [2]. The

absence of a hyperbolic component in the TOA decay kinetics does not come as a surprise, because, as follows from NMR data, diffusive transport of lithium cations in LBO occurs only at temperatures above 500 K and has an activation energy of 760 meV [23, 24]. At lower temperatures, Li^+ ions move by the hopping mechanism with an activation energy of 430 meV [25–27]. Both values of the activation energy are in accord with our data obtained in analyzing the temperature dependence of the LBO TOA kinetics (Fig. 5). This gives us grounds to believe that the observed temperature dependence of the tunneling recharging probability for TOA centers in lithium borates is dominated by thermally stimulated migration of Li^+ cations.

It is known that tunneling recombination can be either nonradiative or radiative [28]. In the first case, the difference between the energies of the initial and final states of the system (the thermal tunneling effect J in Fig. 10) is donated to the lattice predominantly in the hole center region by exciting ion vibrations or displacement. In the second case, tunneling is accompanied by luminescence. In all the crystals with mobile cations studied by us, namely, ADP and KDP [4], LTB [3], and LBO (Figs. 1–7), the PCL decay kinetics cannot be represented as a derivative of the optical density decay relation with respect to time; this relation depends on the concentration of the color centers under consideration. This suggests that the character of tunneling recombination in the mobile cation–hole polaron pair is nonradiative. We believe that it is the mobility of the Li^0 center in LTB and LBO (or of the H^0 center in ADP and KDP), which is one of the tunneling partners, that accounts for the nonradiative tunneling recombination. We note for comparison that tunneling luminescence in alkali halide crystals can be efficiently suppressed by the interaction of a tunneling electron with local vibrational modes or by a change in the spatial orientation of the tunneling partners. At temperatures favoring the mobility of one of the partners at the ionic level, tunneling luminescence in alkali halide crystals is also not observed [28]. In LBO, the instability of the lithium sublattice becomes manifest at temperatures above 240 K [29]; this value can be accepted for the temperature at which Li^0 defects can already move.

Figure 10 shows the energy level schematic of the tunneling partners in configurational coordinates and specifies the energy parameters of the process. As follows from the theory of tunneling processes [10], the tunneling efficiency can increase with increasing temperature, decrease, or remain unchanged, depending on the relative magnitude of the thermal effect J and the energy of system reorganization E_r. Our data on LTB [3] and LBO (Fig. 5) suggest that in lithium borates the first case, which corresponds to $J < E_r$, occurs. This may indicate indirectly that the local level of the Li^0 electron center should lie deep in the crystal band gap.

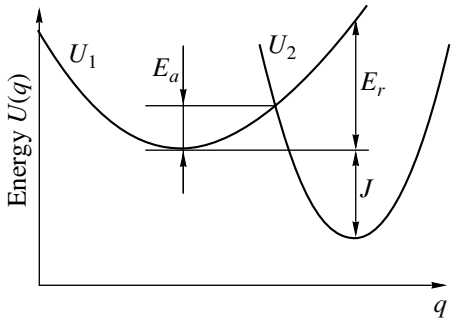

Fig. 10. Configurational curves of atomic motion potential energy calculated for the cases of the electron bound to (U_1) a donor and (U_2) an acceptor. q is the configuration coordinate, E_a is the activation energy, J is the thermal tunneling effect, and E_r is the reorganization energy of the system.

The nonradiative character of tunneling recombination in the mobile cation–hole polaron pair suggests that the PCL and TOA in lithium borates are determined by different relaxation processes. A detailed comparison of our results for the PCL of the borates shows that the situation with the PCL in LBO (Figs. 6–9) differs radically from that for LTB [3]. One observes, in particular, a sharp rise in the intensity of the slow luminescence component. The characteristic time of this intensity rise practically coincides with the time constant of the fast component of the TOA decay kinetics, whereas the time constant of the fast PCL component is close to the pump pulse duration. A similar PCL intensity rise was observed earlier in other complex crystalline systems, for instance, in the chlorates $(K,Na)ClO_3$ and nitrates $(K,Na)NO_3$ [30], as well as in Al_2O_3 [31]. Although no physical model was proposed in [30, 31] for this phenomenon, this observation argues, in our opinion, for the physical processes responsible for the PCL intensity rise in these systems and in the LBO crystal having much in common.

We put forward earlier a recombination model of the rise in PCL intensity in LBO based on a system of two competing hole color centers of the O^- type (denoted by *a* and *b*) mediated by the valence band [32, 33]. This model assumes that hole centers *a* and *b* differ in their properties, more specifically, that center *a* is luminescence active, while center *b* accounts for the TOA and, at the same, serves as a reservoir for the accumulation of an additional number of carriers, which cause a rise in PCL intensity at later stages. The model quantifies the relations between the formal parameters of the PCL and TOA kinetics, the color center parameters, and the concentration of localized carriers. The reasons for the difference between the *a* and *b* centers in LBO and for the absence of a system of such centers in the related LTB crystal were, however, not revealed [32, 33].

The analysis of the pump power dependence of PCL kinetics (Fig. 3) performed in this study indicates that

the competing hole centers responsible for the sharp rise in PCL intensity are native (intrinsic) lattice defects forming on the lithium sublattice under electron beam irradiation. In view of the lack of calculations on the mechanisms of radiation defect formation on the cation sublattice of lithium borate crystals, analysis of the structure of lithium borate glasses $xLi_2O–(1 – x)B_2O_3$, with $x = 0.2–0.5$, can shed some light on this problem. Note that the values of the x parameter corresponding to the formula composition of the lithium tetraborate (diborate) LTB and of the lithium triborate LBO are 1/3 and 1/4, respectively. Due to a lack of long-range order, glasses contain considerable amounts of structural fragments which cannot exist in crystals with an intact lattice. Irradiation may, however, form stable and metastable defects in crystals that are similar in structure to glass fragments [34]. In this connection, it appears reasonable to analyze the available calculations of the structure of the anion and lithium-cation environment in lithium borate glasses of various compositions.

The local environment of the lithium cation in these compounds depends both on temperature and on the relative lithium content. Theoretical calculations [35–37] indicate convincingly that the triborate composition ($x = 1/4$) is radically different from the other lithium borate compounds. Various kinds of motion of metal cations in alkali borate glasses were considered in [36]. It was shown, in particular, that in neutral systems the Me^+ cation is coordinated primarily with the edges of the BO_4^- tetrahedra, is localized on the outer side of the B–O–B fragment, and can easily change its position through rotation without a noticeable energy loss. Only in the triborate is one position more stable than the others. Molecular dynamics calculations [37] show that the lithium cation can have, in lithium borate glasses, a regular environment of two types, namely, (a) the $Li^{(a)}$ position formed by the not-bridging oxygen atoms of charged trigonal groups with involvement of bridging oxygens of the neutral trigonal groups and (b) the $Li^{(b)}$ position, whose environment includes only the bridging oxygen atoms of charged tetrahedral and neutral trigonal groups.

Because the hole center under consideration contains a lithium vacancy, it appears natural to assume the existence of O^- centers of two types, with the vacancy in the $Li^{(a)}$ and $Li^{(b)}$ positions. Our experimental data on thermally stimulated luminescence [38] and electron paramagnetic resonance [13] of LBO crystals also suggest the formation of O^- centers of two different configurations in them. Calculations show [37] that the relative population of the $Li^{(a)}$ positions in glasses grows with increasing relative lithium content x, for instance, in going from LBO ($x = 1/4$) to LTB ($x = 1/3$). This means that, with all other conditions being equal, the cation vacancy in the $Li^{(a)}$ position in LBO should have a higher stability with respect to annihilation with the cation than an analogous vacancy in LTB. In our opinion, this is one of the reasons for the formation of a system of two competing hole centers, *a* and *b*, in LBO and for the absence of noticeable manifestations of such a system in LTB.

Moreover, one should expect differences in the character of electron recombination on hole centers near cation vacancies in the $Li^{(a)}$ and $Li^{(b)}$ positions. Calculations made for lithium borate glasses [37] predict the presence of not-bridging oxygen atoms in the anion environment of the $Li^{(a)}$ position, whereas the $Li^{(b)}$ environment should not have them. The model of the hole core of the self-trapped exciton in the form of a not-bridging oxygen atom has been put forward for a number of oxide crystals (for instance, for SiO_2 [34]). We showed [13] that electron recombination at the O^- center in LBO is accompanied by the formation of a self-trapped exciton, whose radiative annihilation explains the broad-band luminescence at 4.0–4.2 eV. Since the conditions for the formation of a not-bridging anion in the vicinity of the $Li^{(a)}$ position are more favorable, the probability the self-trapped exciton being formed here is also higher. In our opinion, this accounts for the different activity of type *a* and *b* hole O^- centers with respect to radiative recombination and is fully in accord with the model of a rise in PCL intensity in LBO crystals proposed by us earlier [32, 33].

In summing up our series of studies on the formation and decay of native defects in nonlinear optical crystals with a sublattice of mobile cations of hydrogen (ADP, KDP) and lithium (LTB, LBO), which was started in [3, 4] and continued in the present paper, we note a number of common features. To begin with, the presence of a weakly bound mobile cation in these crystals favors spatial separation of radiation-induced pairs of vacancy–interstitial atom defects on the cation sublattice. This accounts for the efficient buildup of comparatively long-lived metastable electronic (interstitial H^0 or Li^0 atoms) and hole (small-radius polarons near cation vacancies) centers in high concentrations. Transient optical absorption of these crystals in the visible and near UV spectral regions derives from optical transitions from VB states of the crystal to the local level of the hole center. The optical absorption spectral profile is determined to a considerable extent by the VB density of states, and its decay kinetics are determined by nonradiative tunneling recharging in the mobile cation–hole polaron pair. All manifestations of radiative recombination observed in these crystals are accounted for by the involvement of additional electronic and hole centers of a different nature in the recombination process.

REFERENCES

1. H. König and R. Hoppe, Z. Anorg. Allg. Chem. **439**, 71 (1978).
2. S. F. Radaev, N. I. Sorokin, and V. I. Simonov, Fiz. Tverd. Tela (Leningrad) **33** (12), 3597 (1991) [Sov. Phys. Solid State **33**, 2024 (1991)].

3. I. N. Ogorodnikov, V. Yu. Yakovlev, A. V. Kruzhalov, and L. I. Isaenko, Fiz. Tverd. Tela (St. Petersburg) **44** (6), 1039 (2002) [Phys. Solid State **44**, 1085 (2002)].
4. I. N. Ogorodnikov, V. Yu. Yakovlev, B. V. Shul'gin, and M. K. Satybaldieva, Fiz. Tverd. Tela (St. Petersburg) **44** (5), 845 (2002) [Phys. Solid State **44**, 880 (2002)].
5. I. N. Ogorodnikov, E. A. Radzhabov, L. I. Isaenko, and A. V. Kruzhalov, Fiz. Tverd. Tela (St. Petersburg) **41** (2), 223 (1999) [Phys. Solid State **41**, 197 (1999)].
6. B. P. Gritsenko, V. Yu. Yakovlev, G. D. Lyakh, and Yu. N. Safonov, in *Modern State and Perspectives of Development of High-Speed Photography, Cinematography, and Metrology of High-Speed Processes* (VNIIOFI, Moscow, 1978), p. 61.
7. I. N. Ogorodnikov, A. V. Porotnikov, S. V. Kudyakov, *et al.*, Fiz. Tverd. Tela (St. Petersburg) **39** (9), 1535 (1997) [Phys. Solid State **39**, 1366 (1997)].
8. I. N. Ogorodnikov, A. V. Kruzhalov, A. V. Porotnikov, and V. Yu. Yakovlev, J. Lumin. **76–77**, 464 (1998).
9. V. N. Parmon, R. F. Khaĭrutdinov, and K. I. Zamaraev, Fiz. Tverd. Tela (Leningrad) **16** (9), 2572 (1974) [Sov. Phys. Solid State **16**, 1672 (1974)].
10. J. J. Hopfield, Proc. Natl. Acad. Sci. USA **71**, 3640 (1974).
11. A. F. Porotnikov, I. N. Ogorodnikov, S. V. Kudyakov, *et al.*, Fiz. Tverd. Tela (St. Petersburg) **39** (8), 1380 (1997) [Phys. Solid State **39**, 1224 (1997)].
12. I. N. Ogorodnikov, A. V. Porotnikov, S. V. Kudyakov, and A. V. Kruzhalov, Mater. Sci. Forum **239–241**, 239 (1997).
13. I. N. Ogorodnikov, L. I. Isaenko, A. V. Kruzhalov, and A. V. Porotnikov, Radiat. Meas. **33** (5), 577 (2001).
14. W. Y. Hsu and R. V. Kasowski, J. Appl. Phys. **73** (8), 4101 (1993).
15. A. B. Sobolev, A. Yu. Kuznetsov, I. N. Ogorodnikov, and A. V. Kruzhalov, Fiz. Tverd. Tela (St. Petersburg) **36** (5), 1517 (1994) [Phys. Solid State **36**, 829 (1994)].
16. A. Y. Kuznetsov, A. B. Sobolev, I. N. Ogorodnikov, and A. V. Kruzhalov, Radiat. Eff. Defects Solids **134** (1–4), 69 (1995).
17. O. F. Schirmer, J. Phys. C: Solid State Phys. **11** (2), L65 (1978).
18. O. F. Schirmer, K. W. Blazey, W. Berlinger, and R. Diehl, Phys. Rev. B **11** (11), 4201 (1975).
19. L. Kovács, K. Polgár, Á. Péter, and R. Capelletti, Mikrochim. Acta, Suppl. **14**, 523 (1997).
20. L. Kovács, E. Beregi, K. Polgár, and Á. Péter, Proc. SPIE **3724**, 256 (1999).
21. N. D. Zhigadlo, M. Zhang, and E. K. H. Salje, J. Phys.: Condens. Matter **13**, 6551 (2001).
22. G. A. Smolenskiĭ, V. A. Bokov, and V. A. Isupova, *Ferroelectrics and Antiferroelectrics* (Nauka, Leningrad, 1971).
23. T. Matsuo, M. Shibasaki, N. Saito, and T. Katsumata, J. Appl. Phys. **79** (4), 1903 (1996).
24. A. Schirmer, P. Heitjans, B. Bader, *et al.*, J. Phys.: Condens. Matter **3** (24), 4323 (1991).
25. R. Guo, S. A. Markgraf, Y. Furukawa, *et al.*, J. Appl. Phys. **78** (12), 7234 (1995).
26. J. W. Kim, C. S. Yoon, and H. G. Gallagher, Appl. Phys. Lett. **71** (22), 3212 (1997).
27. Y. Wang, Y. J. Jiang, Y. L. Liu, *et al.*, Appl. Phys. Lett. **67** (17), 2462 (1995).
28. Yu. R. Zakis, L. N. Kantorovich, E. A. Kotomin, V. N. Kuzovkov, I. A. Tale, and A. L. Shlyuger, *Model of Progress in Wide-Gap Solids with Defects* (Zinatne, Riga, 1991).
29. S. Matyyasik and Yu. V. Shaldin, Fiz. Tverd. Tela (St. Petersburg) **43** (8), 1405 (2001) [Phys. Solid State **43**, 1464 (2001)].
30. V. S. Dolganov and Yu. N. Safonov, in *High-Current Pulse Electron Beams and Technologies* (Sib. Otd. Akad. Nauk SSSR, Novosibirsk, 1983), p. 81.
31. V. V. Mürk, A. I. Kuznetsov, and B. R. Namozov, Phys. Status Solidi A **63** (1), K131 (1981).
32. I. N. Ogorodnikov, A. V. Porotnikov, A. V. Kruzhalov, and V. Ya. Yakovlev, Fiz. Tverd. Tela (St. Petersburg) **40** (11), 2008 (1998) [Phys. Solid State **40**, 1817 (1998)].
33. I. N. Ogorodnikov, A. V. Kruzhalov, A. V. Porotnikov, and V. Yu. Yakovlev, Radiat. Eff. Defects Solids **150** (1–4), 299 (1999).
34. A. R. Silin' and A. N. Trukhin, *Point Defects and Elementary Excitations in Crystalline and Vitreous SiO_2* (Zinatne, Riga, 1985).
35. H. Jain, J. Non-Cryst. Solids **131**, 961 (1991).
36. A. S. Zyubin, O. A. Kondakova, and S. A. Dembovskiĭ, Élektrokhimiya **35** (9), 1105 (1999).
37. C.-P. E. Varsamis, A. Vegiri, and E. I. Kamitsos, Phys. Rev. B **65** (10), 104203 (2002).
38. I. N. Ogorodnikov, A. Yu. Kuznetsov, and A. V. Porotnikov, Pis'ma Zh. Tekh. Fiz. **20** (13), 66 (1994) [Tech. Phys. Lett. **20**, 549 (1994)].

Translated by G. Skrebtsov

Physics of the Solid State, Vol. 45, No. 5, 2003, pp. 854–858. Translated from Fizika Tverdogo Tela, Vol. 45, No. 5, 2003, pp. 813–817.

SEMICONDUCTORS AND DIELECTRICS

First-Principles Calculations of the Hyperfine Fields on Ligands in Fluorides

O. A. Anikeenok

Kazan State University, Kremlevskaya ul. 18, Kazan, 420008 Tatarstan, Russia

e-mail: falin@kfti.knc.ru

Received August 12, 2002

Abstract—In solid-state physics, a crystal lattice is frequently approximated by an array of interacting ions. In this case, the wave functions of individual ions are assumed to be a fairly good zeroth approximation in calculating the matrix elements of the interaction Hamiltonian of electrons and nuclei of the lattice from first principles. Use of the second-quantization method is proposed for such calculations in the basis of these functions. As an example, the electron transition amplitude from a ligand to the central ion is estimated. The results agree well with the experimental data. *© 2003 MAIK "Nauka/Interperiodica".*

1. INTRODUCTION

Hyperfine ligand interactions in ionic crystals are intensively studied using the NMR and ENDOR methods, because the local fields acting on the ionic nuclei differ significantly from the dipole–dipole interaction fields and can provide a large amount of information on the electronic structure of a crystal (see, for example, [1, 2]). For iron-group ions, the nature of these fields has been well studied [3]. However, the straightforward extension of the mechanisms of generation of these fields to rare-earth ions yields results in conflict with the experimental data [4, 5].

Based on the available experimental data, a model of a rare-earth impurity center was proposed in [6]. This model takes into account not only the overlap and covalence effects of the 4*f* shell but also the virtual charge transfer from a ligand to the 5*d* shell and the processes that upset the compensation of the 5*s* and 5*p* shells. The covalent bonding, which is commonly treated using the method of molecular orbitals [3], is equivalent to charge transfer from a ligand to the central ion described by second-order perturbation theory in the configuration-interaction method [7, 8]. However, the so-called covalence parameters [3, 6] in these methods are fitting parameters [1, 2, 9], whose order of magnitude is determined by the corresponding overlap integral. First-principles calculation of these parameters presents difficulties when calculating the matrix elements of operators between Slater determinants of partly nonorthogonal orbitals.

In [10, 11], the relevant operators were represented in the second-quantized form, which made it possible to calculate the matrix elements between the Slater determinants to within terms quadratic in the overlap integrals. By using this technique, in combination with the second-quantization methods developed in atomic spectroscopy [12], virtual processes of charge transfer were taken into account to higher than second order in perturbation theory [6, 8]. However, expressions allowing one to estimate the covalence parameters within microscopic theory were not derived in those papers. It should be noted that, in certain problems treated within the approach in question, nonzero contributions arise only in fourth-order perturbation theory; therefore, in order for quantitative estimates to be correct, the matrix elements should be calculated to at least fourth order in the overlap integrals. Such a situation occurs, for example, in calculating the hyperfine fields acting on the ion nuclei in the second coordination shell of a selected ion [13, 14] and in calculating the superexchange constants [15, 16].

In this paper, by using the results obtained in [17], we construct a basis of multielectron orthonormal functions and represent one-particle and two-particle operators in a second-quantized form in this basis to any order in the overlap integrals. As an example, the electron transition amplitude from the 2*s* shell of the fluorine ion to the 4*f* shell of the rare-earth impurity ion Yb^{3+} in $KMgF_3$ is estimated.

2. THEORY

Let us consider a system consisting of an arbitrary number of ions. The positions and quantum numbers of the orbitals of ions will be specified by indices ξ, ξ', η, η', …; i.e., for example, $\xi = (\bar{\mathbf{R}}_i, nlm_lm_s)$. Then, each distribution of electrons in the system is represented by a determinant $\Phi_{\{\xi\}}$, where $\{\xi\} = \xi_1, \xi_2, \ldots, \xi_n$ is a set of quantum numbers characterizing the distribution. The

matrix element of an operator between functions $\Phi_{\{\xi\}}$ can be calculated from the formulas [17]

$$\langle\Phi_{\{\xi'\}}|H|\Phi_{\{\xi\}}\rangle = \left\langle 0\left|\prod_{\xi'} a_{\xi'} \times H_\Phi \times \prod_{\xi} a_\xi^+\right|0\right\rangle \equiv \langle\{\xi'\}|H_\Phi|\{\xi\}\rangle, \quad (1)$$

$$H_\Phi = N\left\{\exp\left[\sum_{\eta\neq\eta'} a_\eta^+ a_{\eta'}\langle\eta|\eta'\rangle\right]H\right\}, \quad (2)$$

$$H = \sum a_\xi^+ a_{\xi'}\langle\xi|h|\xi'\rangle + \frac{1}{2}\sum a_\xi^+ a_\eta^+ a_{\eta'} a_{\xi'}\langle\xi\eta|g|\xi'\eta'\rangle, \quad (3)$$

$$|\{\xi\}\rangle = \prod_\xi a_\xi^+|0\rangle, \quad (4)$$

where h and g are a one-particle and a two-particle operator, respectively; a_ξ^+ ($a_{\xi'}$) is the electron creation (annihilation) operator satisfying the commutation relations for fermions

$$a_\xi a_{\xi'} + a_{\xi'} a_\xi = a_\xi^+ a_{\xi'}^+ + a_{\xi'}^+ a_\xi^+ = 0, \quad a_{\xi'} a_\xi^+ + a_\xi^+ a_{\xi'} = \delta_{\xi\xi'}, \quad (5)$$

N is the normal-product sign; and $\langle\eta|\eta'\rangle$ is an overlap integral for orbitals. It should be noted that the expansion of Eq. (2) to second order in the overlap integrals contains all operators considered in [10, 11]. By putting $H = I$ in Eq. (1) (I is the identity operator), we obtain the overlap integral between the determinants $\Phi_{\{\xi\}}$ and Eq. (2) in this case takes the form [17]

$$I_\Phi = N\left\{\exp\left[\sum_{\eta\neq\eta'} a_\eta^+ a_{\eta'}\langle\eta|\eta'\rangle\right]\right\} = \exp(Q), \quad (6)$$

$$Q = \sum a_\eta^+ a_{\eta'} \sum_{n=1}^{\infty} \frac{(-1)^{n+1}}{n}\langle\eta|S^n|\eta'\rangle, \quad (7)$$

where $\langle\xi|S|\xi'\rangle \equiv \langle\xi|\xi'\rangle$ are the matrix elements of the overlap matrix S for one-electron orbitals. We introduce the following orthonormal set of many-electron functions $\Psi_{\{\eta\}}$:

$$\Psi_{\{\eta\}} = \sum_{\{\xi\}} \Phi_{\{\xi\}}\left\langle\{\xi\}\left|\exp\left(-\frac{1}{2}Q\right)\right|\{\eta\}\right\rangle, \quad (8)$$

or, in the matrix form,

$$\Psi = \Phi\exp\left(-\frac{1}{2}Q\right), \quad (9)$$

where Ψ and Φ are row matrices.

According to Eqs. (1) and (8), a matrix element of an arbitrary operator between functions $\Psi_{\{\eta\}}$ can be calculated from the formula

$$\langle\Psi_{\{\eta\}}|H|\Psi_{\{\eta'\}}\rangle = \left\langle\{\eta\}\left|\exp\left(-\frac{1}{2}Q\right)\times H_\Phi \times \exp\left(-\frac{1}{2}Q\right)\right|\{\eta'\}\right\rangle. \quad (10)$$

Using commutation relations (5), we represent Eq. (2) in the form

$$H_\Phi = N\left\{\exp\left[\sum_{\eta\neq\eta'} a_\eta^+ a_{\eta'}\langle\eta|\eta'\rangle\right]H\right\} = \exp(Q)\times\tilde{H}, \quad (11)$$

$$\tilde{H} = \sum a_\xi^+ a_{\xi'}\langle\xi|\tilde{h}|\xi'\rangle + \frac{1}{2}\sum a_\xi^+ a_\eta^+ a_{\eta'} a_{\xi'}\langle\xi\eta|\tilde{g}|\xi'\eta'\rangle, \quad (12)$$

$$\langle\xi|\tilde{h}|\xi'\rangle = \sum\langle\xi|(I+S)^{-1}|\theta\rangle\langle\theta|h|\xi'\rangle, \quad (13)$$

$$\langle\xi\eta|\tilde{g}|\xi'\eta'\rangle = \sum\langle\xi|(I+S)^{-1}|\theta\rangle \times\langle\eta|(I+S)^{-1}|\zeta\rangle\langle\theta\zeta|g|\xi'\eta'\rangle, \quad (14)$$

where $\langle\xi|(I+S)^{-1}|\theta\rangle$ is the matrix element of the matrix inverse of the matrix $(I+S)$.

Substituting Eq. (11) into Eq. (10) gives

$$\langle\Phi_{\{\eta\}}|H|\Psi_{\{\eta'\}}\rangle = \langle\{\eta\}|H_\Psi|\{\eta'\}\rangle, \quad (15)$$

$$H_\Psi = \exp\left(\frac{1}{2}Q\right)\times\tilde{H}\times\exp\left(-\frac{1}{2}Q\right). \quad (16)$$

It follows from Eq. (10) that the operator H_Ψ is Hermitian; therefore, Eq. (16) can be written as

$$H_\Psi = H_\Psi^+ = \exp\left(-\frac{1}{2}Q\right)\times\tilde{H}^+\times\exp\left(\frac{1}{2}Q\right). \quad (17)$$

By expanding Eqs. (16) and (17) in commutators and rearranging them, we obtain the following expression for an arbitrary operator H in the basis of the function $\Psi_{\{\eta\}}$:

$$H_\Psi = \sum_{n=0}^{\infty} c_n[Q, \tilde{H}+\tilde{H}^+]^{(2n)}, \quad (18)$$

where

$$[Q, \tilde{H}+\tilde{H}^+]^{(0)} = \tilde{H}+\tilde{H}^+,$$
$$[Q, \tilde{H}+\tilde{H}^+]^{(1)} = [Q, \tilde{H}+\tilde{H}^+],$$
$$[Q, \tilde{H}+\tilde{H}^+]^{(2)} = [Q, [Q, \tilde{H}+\tilde{H}^+]], \ldots.$$

The first five terms in Eq. (18) determine the expansion to the eighth order in the overlap integrals of one-electron orbitals. The corresponding coefficients are

$$c_0 = \frac{1}{2}, \quad c_1 = -\frac{1}{2^3 \times 2!} \approx -0.0625,$$

$$c_2 = \frac{5}{2^5 \times 4!} \approx 0.00651,$$

$$c_3 = -\frac{61}{2^7 \times 6!} \approx -0.000661,$$

$$c_4 = \frac{5 \times 277}{2^9 \times 8!} \approx 0.0000671.$$

In solving solid-state spectroscopy problems by using the configuration interaction method, the following orthonormal set of many-electron functions is commonly used [18]:

$$\begin{aligned}\Psi &= \Phi(I+P)^{-\frac{1}{2}} \\ &= \Phi\left(I - \frac{1}{2}P + \frac{3}{8}P^2 - \frac{5}{16}P^3 + \ldots\right),\end{aligned} \tag{19}$$

where the matrix elements of the matrix P, in the notation of this paper, have the form $P_{\{\xi\},\{\xi'\}} = \langle\Phi_{\{\xi\}}|\Phi_{\{\xi'\}}\rangle$; i.e., they are equal to the overlap integrals of many-electron functions $\Phi_{\{\xi\}}$. As mentioned above, these integrals are always calculated to second order in the overlap integrals of one-electron orbitals. In order to solve the problem of nonorthogonality in Eq. (18), one should calculate the matrix elements of functions whose argument is the overlap matrix of one-electron orbitals. Such functions can be calculated using currently available methods. In terms of the matrix elements of these functions, the convergence of the series in Eq. (18) is more rapid than that of the series calculated in the set of functions given by Eq. (19).

3. ESTIMATION OF THE TRANSITION AMPLITUDE

Virtual processes of charge transfer are usually treated in terms of the covalence parameters γ, which are defined as [3]

$$\gamma = -\frac{\langle\varphi|h|\chi\rangle - \langle\varphi|\chi\rangle\langle\chi|h|\chi\rangle}{|\Delta_{\varphi\chi}|}, \tag{20}$$

where $|\varphi\rangle$ is the central-ion orbital, $|\chi\rangle$ is a ligand orbital, and $|\Delta_{\varphi\chi}|$ is the difference in energy between the excited and ground states, which can be calculated from the ionization energies (see, for example, [19]). The quantity in the numerator of Eq. (20) is commonly treated as a model parameter. Let us introduce the quantity $\tilde{\gamma}$:

$$\tilde{\gamma} = -\frac{\langle\Psi_{\{\xi\}}|H|\Psi_{\{\xi'\}}\rangle}{|\Delta_{\{\xi\},\{\xi'\}}|}, \tag{21}$$

where $|\Psi_{\{\xi'\}}\rangle$ is the ground state of the system and $|\Psi_{\{\xi\}}\rangle$ is an excited state resulting from the ground state when an electron passes from a ligand to the central ion. If only one-particle terms proportional to the central-ion–ligand overlap are kept in the operator H in Eq. (21), then the following approximate relation can be derived between the parameters defined by Eqs. (20) and (21):

$$\tilde{\gamma} \approx \gamma + \frac{1}{2}s, \tag{22}$$

where s is the overlap integral between the one-electron orbitals involved in the electron transfer.

Let us calculate the electron transition amplitude from the ligand orbital $|2s\rangle$ to the Yb^{3+} ion orbital $|4f0\rangle$ in $KMgF_3$ to first order in the metal–ligand overlap. Using the approach developed in the previous section and Eq. (18), one can reduce the problem to calculation of the matrix elements of second-quantized one- and two-particle operators between states differing in the quantum number for one orbital. As a result, the transition amplitude $\langle\Psi_{\{\xi\}}|H|\Psi_{\{\xi'\}}\rangle$ is found to be (to the order of accuracy indicated above)

$$\begin{aligned}\langle\Psi_{\{\xi\}}|H|\Psi_{\{\xi'\}}\rangle &= \frac{1}{2}\Bigg\{\langle 4f0|(I+S)^{-1}|2s\rangle\Bigg[\varepsilon_{\mathrm{HF}}^{Yb^{2+}} + \varepsilon_{\mathrm{HF}}^{F^-} \\ &+ \langle 4f0|h_{\mathrm{M}}|4f0\rangle + \langle 2s|h_{\mathrm{M}}|2s\rangle - \left\langle 2s\left|\frac{1}{|\bar{\mathbf{R}}_a - \bar{\mathbf{r}}|}\right|2s\right\rangle\Bigg] \\ &+ [\langle 4f0|(I+S)^{-1}|4f0\rangle + \langle 2s|(I+S)^{-1}|2s\rangle] \\ &\times\Bigg[\langle 4f0|h_k|2s\rangle + \langle 4f0|h_{\mathrm{M}}|2s\rangle - \left\langle 4f0\left|\frac{Z_a' + 1}{|\bar{\mathbf{R}}_a - \bar{\mathbf{r}}|}\right|2s\right\rangle \\ &+ \sum_{\xi\in\{a\}}\langle 4f0,\xi|g|2s,\xi\rangle - \left\langle 4f0\left|\frac{Z_b'}{|\bar{\mathbf{R}}_b - \bar{\mathbf{r}}|}\right|2s\right\rangle \\ &+ \sum_{\xi\in\{b\}}\langle 4f0,\xi|g|2s,\xi\rangle - \sum_{\xi\in\{a,b\}}\langle 4f0,\xi|g|\xi,2s\rangle\Bigg]\Bigg\},\end{aligned} \tag{23}$$

where $\varepsilon_{\mathrm{HF}}^{Yb^{2+}}$ is the Hartree–Fock energy of the rare-earth ion orbital $|4f0\rangle$; $\varepsilon_{\mathrm{HF}}^{F^-}$ is the Hartree–Fock energy of the ligand orbital $|2s\rangle$; h_k is the kinetic-energy operator; h_{M} is the Madelung energy; Z_a' and Z_b' are the numbers of electrons of the rare-earth ion and the ligand in the ground state, respectively; g is the Cou-

lomb interaction operator between the electrons; $\{a\}$ and $\{b\}$ are the sets of orbitals of the rare-earth ion and ligand, respectively; and $\bar{\mathbf{R}}_a$ and $\bar{\mathbf{R}}_b$ are the position vectors of the nuclei of the central ion and ligand, respectively.

The numerical values of the quantities involved in Eq. (23) are (in atomic units)

$$\langle 4f0|(I+S)^{-1}|2s\rangle = -0.007891,$$

$$\varepsilon_{\mathrm{HF}}^{\mathrm{Yb}^{2+}} = -1.203\ [20],$$

$$\varepsilon_{\mathrm{HF}}^{\mathrm{F}^{-}} = -1.074\ [21],$$

$$\langle 4f0|h_{\mathrm{M}}|4f0\rangle = 0.7442,$$

$$\langle 2s|h_{\mathrm{M}}|2s\rangle = -0.3887,$$

$$\left\langle 2s\left|\frac{1}{|\bar{\mathbf{R}}_a-\bar{\mathbf{r}}|}\right|2s\right\rangle = 0.2405,$$

$$\left\langle 4f0\left|\frac{1}{|\bar{\mathbf{R}}_b-\bar{\mathbf{r}}|}\right|2s\right\rangle = 0.006175,$$

$$\langle 4f0, 2s|g|2s, 2s\rangle = 0.005696,$$

$$\langle 4f0|h_k|2s\rangle = -0.001151,$$

$$\langle 4f0|h_{\mathrm{M}}|2s\rangle = 0.00052,$$

$$\langle 4f0, 2p0|g|2s, 2p0\rangle = 0.0054398,$$

$$\langle 4f0, 2p1|g|2s, 2p1\rangle = 0.005182,$$

$$\left\langle 4f0\left|\frac{1}{|\bar{\mathbf{R}}_a-\bar{\mathbf{r}}|}\right|2s\right\rangle = 0.0037184,$$

$$\langle 4f0, 5s|g|2s, 5s\rangle = 0.003581,$$

$$\langle 4f0, 5p0|g|2s, 5p0\rangle = 0.0042672,$$

$$\langle 4f0, 5p1|g|2s, 5p1\rangle = 0.0031746,$$

$$\langle 4f0, 4f0|g|2s, 4f0\rangle = 0.004031,$$

$$\langle 4f0, 4f1|g|2s, 4f1\rangle = 0.0038957,$$

$$\langle 4f0, 4f2|g|2s, 4f2\rangle = 0.0036116,$$

$$\langle 4f0, 4f3|g|2s, 4f3\rangle = 0.0033773,$$

$$\langle 4f0, 4d0|g|2s, 4d0\rangle = 0.0039504,$$

$$\langle 4f0, 4d1|g|2s, 4d1\rangle = 0.0037733,$$

$$\langle 4f0, 4d2|g|2s, 4d2\rangle = 0.0034723,$$

$$\langle 4f0, 4p0|g|2s, 4p0\rangle = 0.0040373,$$

$$\langle 4f0, 4p1|g|2s, 4p1\rangle = 0.0035423,$$

$$\langle 4f0, 4s|g|2s, 4s\rangle = 0.0037081.$$

Calculations were performed for the wave functions presented in [21]. Using the numerical data presented above, it is easy to verify that the following condition is satisfied for all sums:

$$\sum_{m_l m_s}\left[\langle 4f0, nlm_lm_s|g|2s, nlm_lm_s\rangle - \left\langle 4f0\left|\frac{1}{|\bar{\mathbf{R}}_{nlm_lm_s}-\bar{\mathbf{r}}|}\right|2s\right\rangle\right]\le 0. \quad (24)$$

Here, $\bar{\mathbf{R}}_{nlm_lm_s}$ is the nucleus position vector of the ion corresponding to the orbital $|nlm_lm_s\rangle$. In Eq. (24), nearly complete compensation takes place starting from the 4*s* shell; therefore, deeper shells can be disregarded. The overlap–nucleus interaction is always stronger than the overlap–shell interaction. Substituting the above numerical data into Eq. (23), the transition amplitude is found to be (in atomic units)

$$\langle\{\ldots, 4f0, \ldots\}|H_\Psi|\{\ldots, 2s, \ldots\}\rangle = -0.01056. \quad (25)$$

Using the relation between $\tilde{\gamma}$ and γ given by Eq. (22) and the value of the electron transfer energy $|\Delta_{4f0,\,2s}| = 1$ au [6], we obtain $\gamma_s = 0.007$. When γ_s is treated as a fitting parameter in interpreting the experimental data, its value is usually found to be $\gamma_s \approx 0.01$, which agrees well with the value determined by Eq. (23) to the first-order approximation. In this paper, all calculations associated with the nonorthogonality of orbitals are related to a central-ion–ligand pair. In a future publication, we will consider a cluster consisting of a paramagnetic ion and its nearest neighbors, because the ligand–ligand overlap can be significant [22] and, hence, the matrix $\langle\xi|(I+S)^{-1}|\xi'\rangle$ should be found for the orbitals of the whole cluster. We will also perform first-principles calculations of the covalence parameters $\gamma_{4f\sigma}$, $\gamma_{4f\pi}$, γ_{5ds}, $\gamma_{5d\sigma}$, and $\gamma_{5d\pi}$, in order to test the validity of the model proposed in [6].

ACKNOWLEDGMENTS

This paper was supported by the Russian Foundation for Basic Research, project no. 02-02-16648.

REFERENCES

1. R. E. Walstedt and S. W. Cheong, Phys. Rev. B **64**, 014404 (2001).
2. M. L. Falin, V. A. Latypov, B. N. Kazakov, *et al.*, Phys. Rev. B **61** (14), 9441 (2000).
3. A. Abragam and B. Bleaney, *Electron Paramagnetic Resonance of Transition Ions* (Clarendon, Oxford, 1970; Mir, Moscow, 1972).
4. J. D. Axe and G. Burns, Phys. Rev. **152** (1), 331 (1966).
5. J. M. Baker, J. Phys. C **1** (6), 1670 (1968).
6. O. A. Anikeenok, M. V. Eremin, M. L. Falin, *et al.*, J. Phys. C **17** (15), 2813 (1984).
7. J. Hubbard, D. E. Rimmer, and F. R. A. Hopgood, Proc. Phys. Soc. London **88** (1), 13 (1966).

8. O. A. Anikeenok and M. V. Eremin, Fiz. Tverd. Tela (Leningrad) **23** (3), 706 (1981) [Sov. Phys. Solid State **23**, 401 (1981)].
9. B. Z. Malkin, A. M. Leushin, A. I. Iskhakova, *et al.*, Phys. Rev. B **62** (11), 7063 (2000).
10. M. V. Eremin and A. M. Leushin, Fiz. Tverd. Tela (Leningrad) **16** (7), 1917 (1974) [Sov. Phys. Solid State **16**, 1252 (1974)].
11. M. V. Eremin and A. A. Kornienko, Fiz. Tverd. Tela (Leningrad) **19** (10), 3024 (1977) [Sov. Phys. Solid State **19**, 1769 (1977)].
12. B. R. Judd, *Second Quantization and Atomic Spectroscopy* (The Johns Hopkins Press, Baltimore, 1967).
13. D. Monien, D. Pines, and M. Takigava, Phys. Rev. B **43** (1), 258 (1991).
14. J. M. Baker and L. M. Bluck, J. Phys. C **18** (32), 6051 (1985).
15. P. W. Anderson, Solid State Phys. **14**, 145 (1963).
16. M. V. Eremin, *Spectroscopy of Crystals* (Nauka, Leningrad, 1985), p. 150.
17. O. A. Anikeenok, Available from VINITI, No. 2442-B87 (1987).
18. P. O. Lowdin, Adv. Quantum Chem. **5** (1), 185 (1970).
19. D. S. McClure, *NATO Adv. Study Inst. Chem. Lab. and St. Johns College*, Oxford (1974), p. 113.
20. K. M. S. Saxena and C. Malli, *Numerical Hartree–Fock Results for Some Triply and Doubly Ionized Rare-Earths*, Technical Report TR-1970-01 (Department of Chemistry, Simon Fraser Univ., 1970).
21. E. Clementi and L. Roetti, At. Data Nucl. Data Tables **14**, 177 (1974).
22. A. P. Vala and R. S. Dagis, Litov. Fiz. Sb. **12** (2), 265 (1972).

Translated by Yu. Epifanov

Physics of the Solid State, Vol. 45, No. 5, 2003, pp. 859–863. Translated from Fizika Tverdogo Tela, Vol. 45, No. 5, 2003, pp. 818–822.

SEMICONDUCTORS AND DIELECTRICS

Electron Paramagnetic Resonance of Gd^{3+} Aqua Complexes in Vitrified Aqueous Solutions and Gd^{3+} Aqua Ions Adsorbed on the Capillary Surface

G. P. Vishnevskaya*, E. N. Frolova*, and A. M. Gataullin**

** Zavoĭskiĭ Physicotechnical Institute, Kazan Scientific Center, Russian Academy of Sciences, Sibirskiĭ trakt 10/7, Kazan, 420029 Tatarstan, Russia*

*** Kazan State University of Power Engineering, Kazan, Tatarstan, Russia*

Received May 22, 2002; in final form, August 20, 2002

Abstract—Electron paramagnetic resonance (EPR) spectra of Gd^{3+} aqua complexes are measured in dilute aqueous solutions of $Gd(NO_3)_3$ ($C < 0.2$ *M*) at room temperature. A partial resolution of the fine structure observed in the spectra is characteristic of solid disordered systems and results in an increase in the effective width of the EPR line with a decrease in the Gd^{3+} concentration. This phenomenon is explained in terms of adsorption of Gd^{3+} aqua ions on the surface of the measuring capillaries. The fine structure is revealed in the EPR spectra of $Gd(NO_3)_3$ aqueous solutions, namely, the $Gd(NO_3)_3$ solutions vitrified at a temperature of 77 K (with an addition of 10–15 vol % glycerol) and $Gd(NO_3)_3$ solutions quasi-vitrified at 298 K (with an addition of 70–90 vol % glycerol). Analysis of the EPR spectra demonstrates that these solutions contain two types of aqua complexes with fine structure parameters $D_1 = 180$ G and $D_2 = 580$ G. Reasoning from a comparison with x-ray diffraction data, the fine structure parameters D_1 and D_2 are assigned to higher symmetric eight-coordinate and lower symmetric nine-coordinate Gd^{3+} aqua complexes, respectively. © *2003 MAIK "Nauka/Interperiodica".*

1. INTRODUCTION

It is known that lanthanides exhibit different thermodynamic properties, including a hydration capacity. Extended x-ray absorption fine structure (EXAFS) investigations of rare-earth ions in aqueous solutions in liquid and vitreous states have demonstrated that, in aqua complexes of Sm^{3+}, Eu^{3+}, and Gd^{3+} lanthanides, the hydroxyl numbers vary from nine for light ions to eight for heavy ions [1].

Electron paramagnetic resonance (EPR) spectroscopy can also provide valuable information on the local symmetry associated with the nearest environment of a paramagnetic ion. The degree of distortion of local symmetry of a complex can be judged from the fine structure parameters, which, in turn, can be determined either from the positions of the resolved lines in the EPR spectra of vitrified solutions or from the temperature (and frequency) dependences of the EPR linewidth and the spin–lattice relaxation time for liquid solutions.

However, the results obtained in earlier studies concerning linewidths in the EPR spectra of Gd^{3+} ions in liquid aqueous solutions are rather contradictory. In particular, Powell *et al.* [2] explained the experimental EPR data in terms of eight-coordinate gadolinium aqua ions. Southwood-Jones *et al.* [3] assigned the specific features revealed in the EPR spectra to nine-coordinate gadolinium aqua complexes. Until presently, no satisfactory explanations have been offered for the observed increase in the effective width of the EPR line with a decrease in the Gd^{3+} concentration $C < 0.1$ *M* [4] and the occurrence of dipole–dipole interactions in aqueous solutions with unduly high concentrations of gadolinium ions ($C > 0.5$–0.8 *M*) as compared to those predicted for the spin $S = 7/2$. Moreover, in our recent study [5], we revealed an inhomogeneous broadening of the EPR lines in the spectra of liquid aqueous solutions of gadolinium nitrate.

The aim of the present work was to elucidate the origin of the inhomogeneous broadening of the EPR lines for dilute aqueous solutions of gadolinium nitrate at room temperature and to determine the types of Gd^{3+} aqua complexes with different degrees of distortion of local symmetries from analyzing the EPR spectra of vitrified aqueous solutions of $Gd(NO_3)_3$.

2. SAMPLE PREPARATION AND EXPERIMENTAL TECHNIQUE

The aqueous solutions used in the experiments were prepared from a salt of gadolinium nitrate (analytical grade). The concentration of Gd^{3+} ions in the aqueous solutions prepared varied in the range from 0.00065 to 3.6 *M*. The solutions obtained were slightly acidified to prevent hydrolysis. Particular care was taken in preparing dilute solutions in which dipole–dipole interactions either did not occur or were insignificant.

The EPR spectra were recorded at room temperature on a spectrometer operating in the *X* and *Q* bands,

1063-7834/03/4505-0859$24.00

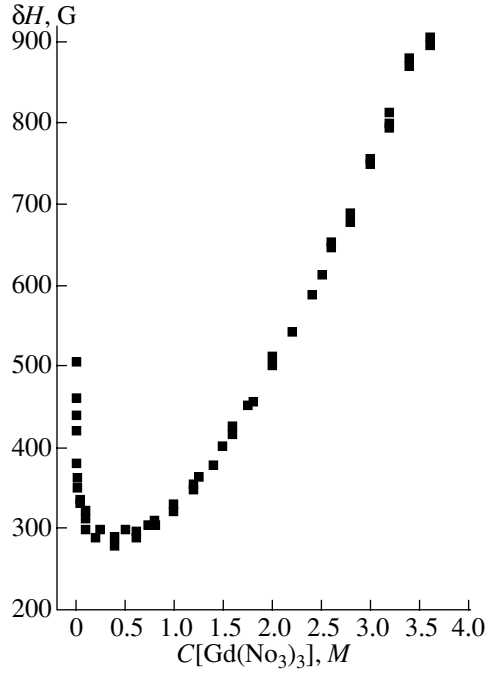

Fig. 1. Dependence of the EPR linewidth on the $Gd(NO_3)_3$ concentration in aqueous solutions at a temperature of 298 K.

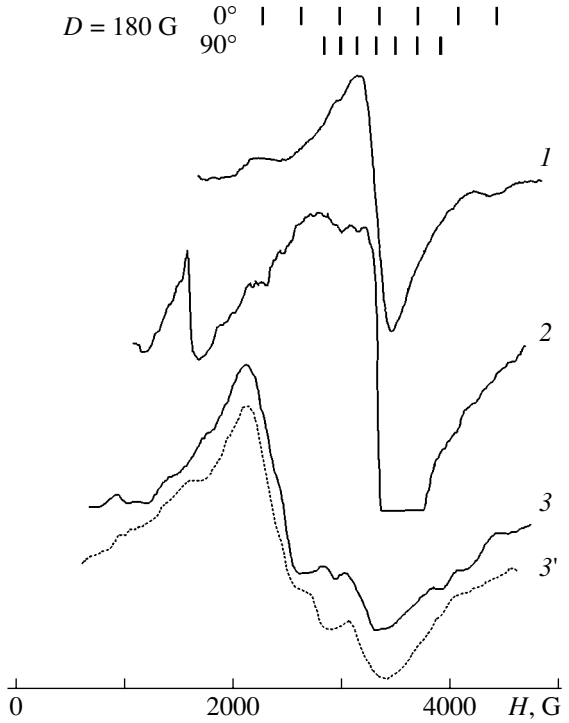

Fig. 2. EPR spectra of Gd^{3+} aqua ions adsorbed on the capillary surface: (*1*) 0.1 *M* aqueous solution of $Gd(NO_3)_3$ at a temperature of 298 K and the calculated position of the fine structure line at D = 180 G, (*2*) 0.0025 *M* aqueous solution of $Gd(NO_3)_3$ at temperatures of 298 and 100 K (in weak magnetic fields, the EPR signals are attributed to the Fe^{3+} ions involved in capillaries fabricated from conventional glass), (*3*) after removal of the major portion of the 0.0025 *M* aqueous solution of $Gd(NO_3)_3$ from the capillary at 298 and 100 K, and (*3*') the simulated spectrum at fine structure parameters D_1 = 838 G, δH = 250 G and D_2 = 1240 G, δH = 550 G. Spectra *1* and *3* are measured for samples in silica capillaries.

which correspond to Larmor frequencies $\omega_0 = 0.6 \times 10^{11}$ and 2.3×10^{11} rad/s, respectively. The low-temperature measurements were performed only in the *X* band. The samples to be studied were placed in thin capillaries ~1 mm in diameter.

The solutions prepared were vitrified at a temperature of 77 K. Glycerol (10–15 vol %) added to the aqueous solutions served as a glass-forming agent. The gadolinium nitrate solution quasi-vitrified at room temperature was obtained through the addition of 70–90 vol % glycerol. The signals observed in the EPR spectra of $Gd(NO_3)_3$ aqueous solutions with both low and high glycerol contents were attributed to gadolinium aqua complexes [5]. In our opinion, it is highly improbable that the noncomplexing anion NO_3^- can be involved in the nearest environment of the Gd^{3+} cation.

3. RESULTS AND DISCUSSION

3.1. Figure 1 shows the dependence of the EPR linewidth on the $Gd(NO_3)_3$ concentration in aqueous solutions at room temperature. Two interesting features are noteworthy: (i) a broadening of the EPR lines at low concentrations of Gd^{3+} ions ($C < 0.2$ *M*) and (ii) a manifestation of dipole–dipole broadening at higher concentrations of Gd^{3+} as compared to those predicted for the spin $S = 7/2$. It should be noted that, in Mn^{2+} salt solutions ($S = 5/2$), the dipole–dipole broadening of the EPR lines manifests itself even at concentrations C = 0.05 *M*.

Earlier, the line broadening observed in the EPR spectra with a decrease in the Gd^{3+} concentration below 0.2 *M* was explained by Sur and Bryant [4] in terms of the complex formation. Owing to the more appropriate choice of the conditions for recording the EPR spectra, we revealed that, at Gd^{3+} concentrations $C \le 0.1$ *M*, the EPR spectra measured in liquid aqueous solutions exhibit a partially resolved fine structure, which is typical of solid disordered systems (such as glasses and powders). In this case, the width of the EPR line recorded at frequencies in the *X* band corresponds to an envelope of signals associated with several transitions (curve *1* in Fig. 2). The EPR spectrum can be described by the spin Hamiltonian

$$\hat{H} = g\beta\mathbf{HS} + D[S_z^2 - 1/3S(S+1)] + E(S_x^2 - S_y^2) \quad (1)$$

with $D \ll h\nu$ and $D \gg E$. Here, D and E are the fine structure parameters characterizing the strength and symmetry of the local crystal field at the central ion.

The fine structure parameter $D = 180$ G, which was determined from the positions of the extreme components of the EPR spectrum (curve *1* in Fig. 2), agrees well with the parameter D obtained from the electron spin–lattice relaxation times T_1 measured using the technique of nonresonance paramagnetic absorption in parallel fields in 0.1–1 *M* aqueous solutions of gadolinium nitrate [5]. This indicates that the above value of D is characteristic of Gd^{3+} aqua complexes. However, it remains unclear why the conditions for averaging of the fine structure of the EPR spectrum are violated by motion of the aqua complexes in the solution.

In our opinion, this phenomenon can be explained by the adsorption of Gd^{3+} aqua ions on the surface of the capillaries used in the EPR measurements. The Gd^{3+} aqua complexes interact with the capillary walls and, thus, appear to be bound to the capillary surface. The mobility of the Gd^{3+} aqua complexes becomes close in magnitude to the mobility of solid molecules (physical adsorption) [6], which, in turn, results in a resolution of the fine structure of the EPR spectrum. This assumption is confirmed by a visual inspection. It can be seen that the solution spreads over the capillary walls with time. A decrease in the concentration of the solution under investigation leads to a change in the ratio of the number of free aqua complexes in the solution to the number of complexes adsorbed on the capillary surface. Consequently, as the concentration of the dissolved salt decreases, the EPR signals attributed to the adsorbed complexes manifest themselves more clearly in the spectra and exhibit a more complex shape. The inhomogeneous broadening observed in the EPR spectra of aqueous solutions masks a manifestation of dipole–dipole interactions between Gd^{3+} ions at low concentrations. It is worth noting that no adsorption is observed when the relaxation times are measured using the technique of nonresonance paramagnetic absorption in parallel fields, because, in this case, the aqueous solution is placed in ampules ~1 cm in diameter.

It is found that variations in the physical and (or) chemical properties of the aqueous solution affect the concentration dependence of the EPR linewidth as follows. Upon addition of an acid or glycerol to dilute solutions, the broadening of the EPR line shifts toward low concentrations of Gd^{3+} ions. Figure 3 depicts the dependence of the EPR linewidth on the $Gd(NO_3)_3$ concentration in water–glycerol (15 vol % glycerol) solutions. The absence of broadening of the EPR lines at low concentrations can be explained by the fact that the introduction of glycerol into the solution brings about a substantial enhancement of intermolecular interactions (the viscosity of the medium increases by a factor of 1.5) and, consequently, a decrease in the residence time of aqua complexes near the capillary walls. It should also be noted that the dipole–dipole broadening of the EPR lines in the spectra of water–glycerol solutions is observed beginning with concentrations of ~0.05 *M* instead of ~0.5 *M*, as is the case in aqueous solutions.

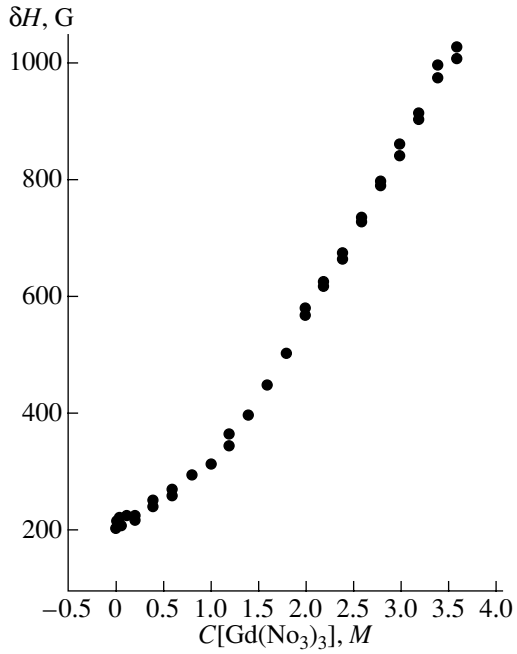

Fig. 3. Dependence of the EPR linewidth on the $Gd(NO_3)_3$ concentration in water–glycerol (15 vol % glycerol) solutions at a temperature of 298 K.

Thus, we demonstrated that the broadening of the EPR lines in the spectra of dilute solutions is associated with the inhomogeneity of these lines due to an incomplete resolution of the fine structure formed upon the interaction of aqua complexes with the capillary surface. The inhomogeneous broadening of the EPR lines also masks the manifestation of dipole–dipole interactions between Gd^{3+} ions in dilute solutions at concentrations up to 0.5–0.8 *M*.

The evolution of the EPR spectra of Gd^{3+} aqua ions adsorbed on the capillary surface occurs with a decrease in the Gd^{3+} concentration (curve *2* in Fig. 2) and the thickness of the surface liquid layer (curve *3* in Fig. 2). At the same time, it makes no difference for adsorption whether conventional or silica glass capillary is used in the experiments. As could be expected, a change in temperature (298 or 100 K) also does not significantly affect the EPR spectra, because, at room temperature, the gadolinium ions interacting with the glass surface exhibit an EPR spectrum typical of solid-state materials. After the major portion of the $Gd(NO_3)_3$ aqueous solution was removed from the capillary, the intensity of the EPR line centered at $g = 2$ (physical adsorption) decreased and there appeared a more intense line with $g_{eff} \sim 3$. The theoretical EPR spectrum (curve *3′* in Fig. 2) is closely similar to the experimental spectrum (Fig. 2c) for two types of aqua complexes with fine structure parameters $D_1 = (840 \pm 5)$ G and $D_2 = (1240 \pm 5)$ G. The lowering of symmetry of the aqua complexes can be caused by the fact that the gadolinium ions interact not only with oxygen ions of

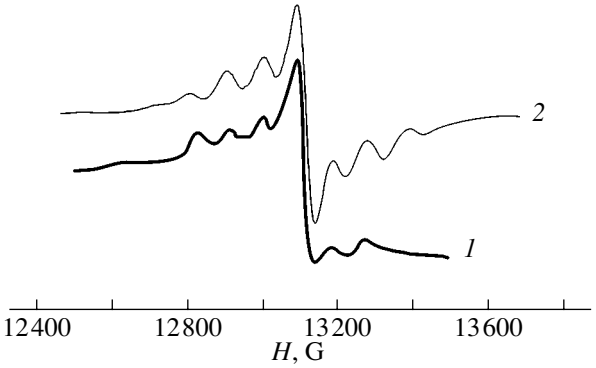

Fig. 4. (*1*) Experimental EPR spectrum of 0.1 *M* $Gd(NO_3)_3$ in water–glycerol (15 vol % water + 85 vol % glycerol) solutions measured at frequencies in the *Q* band at a temperature of 298 K and (*2*) the simulated spectrum at fine structure parameters $D = 110$ G and $\delta H = 50$ G (determined from the data on nonresonance paramagnetic absorption in parallel fields).

water molecules but also with the oxygen ions involved in the glass (chemical adsorption). After the capillary was washed with running water, both signals disappeared.

The phenomenon of adsorption of a dissolved substance on a surface is not uncommon. In the case under consideration, the surprising thing is the magnitude of the observed effect. The interaction of Gd^{3+} ions ($S = 7/2$) with the surface of the glass capillary manifests itself in the EPR spectra and, thus, significantly affects their shape at relatively high concentrations (~0.8 *M*). Earlier, the evolution of the EPR spectra of Cu^{2+} solutions ($S = 1/2$) due to interactions with the surface was observed by Filippov (Zavoĭskiĭ Physicotechnical Institute, Kazan). Unfortunately, the results of those investigations were not published.

3.2. Since the EPR lines are characterized by an inhomogeneous broadening and their analysis offers overly high values of the fine structure parameters, the quantities *D* for liquid solutions can be most correctly determined from measurements of the electron spin–lattice relaxation times T_1. In our recent work [5], these measurements were performed using nonresonance paramagnetic absorption in parallel fields [7, 8] at different frequencies and temperatures. It was demonstrated that, for 0.1–1 *M* aqueous solutions of $Gd(NO_3)_3$, the fine structure parameter $D = (187 \pm 5)$ G is constant and does not depend on temperature. This value is relatively small, which is characteristic of complexes with high symmetry. According to x-ray diffraction investigations [1], eight-coordinate aqua complexes of lanthanides in solutions have a higher symmetry than nine-coordinate aqua complexes. It turned out that, for nine-coordinate aqua ions, the Debye–Waller factors, which account for the specific features of the hydrated structure of the aqua complexes, exceed those for eight-coordinate aqua ions. These results are consistent with the fact that, in $Pr(OH)_9^{3+}$ crystals with a structure of a tricapped trigonal prism, the Pr–O equatorial bonds are 0.03–0.12 Å longer than the prismatic bonds [9], whereas the Ln–O bonds in eight-coordinate rare-earth ions (D_{2h} symmetry) are nearly equal to one another. A comparison of the x-ray diffraction data and the results of EPR measurements shows that the fine structure parameter $D = (187 \pm 5)$ G can be assigned to eight-coordinate aqua complexes.

However, we cannot rule out the possibility that the eight-coordinate ions, which constitute the major portion of the complexes in aqueous solutions, are in equilibrium with complexes of lower symmetry (i.e., nine-coordinate complexes) that play no part in relaxation processes. It is well known that, in the presence of complexes with different local symmetries in liquid solutions, contributions to relaxation processes can only be made by complexes with fine structure parameters that are averaged simultaneously due to their motion at a given temperature [10]. The presence of aqua complexes of one or more types in solutions can be judged from the results of EPR measurements of vitrified aqueous solutions.

An aqueous solution at room temperature can be considered a quasi-vitrified solution provided it contains no free water and motion of aqua complexes in this solution is retarded. Indeed, the experimental EPR spectrum measured in water–glycerol solutions of Gd^{3+} with a high glycerol content (70–90 vol %) at *Q*-band frequencies is similar to EPR spectra typical of vitreous materials (Fig. 4) and exhibits a well-resolved fine structure (in the *X* band, the spectrum is characterized by a partially resolved fine structure). The theoretical EPR spectrum was simulated with the use of the fine structure parameter $D = 110$ G and the linewidth of a single fine component $\delta H = 50$ G determined from the electron spin–lattice relaxation times T_1 and T_2, which, in turn, were obtained from nonresonance paramagnetic absorption measurements in parallel fields in aqueous solutions with a high glycerol content [5]. As can be seen from Fig. 4, the simulated and experimental spectra are in good agreement. It was noted earlier in [5] that, compared to pure aqueous solutions, the fine structure parameter *D* for water–glycerol solutions decreases as the glycerol content increases to 60 vol % and higher. These findings were explained by the fact that the structure of the solution can undergo ordering due to the formation of strong hydrogen bonds and the incorporation of Gd^{3+} aqua complexes into solvent "cells." It is also possible that the aqua complexes can have a higher symmetry, because glycerol molecules are capable of binding water from the unstable second hydrated shell of the gadolinium ion.

Therefore, Gd^{3+} aqua complexes with high symmetry are predominantly formed at room temperature. Aqua complexes with low symmetry do not manifest

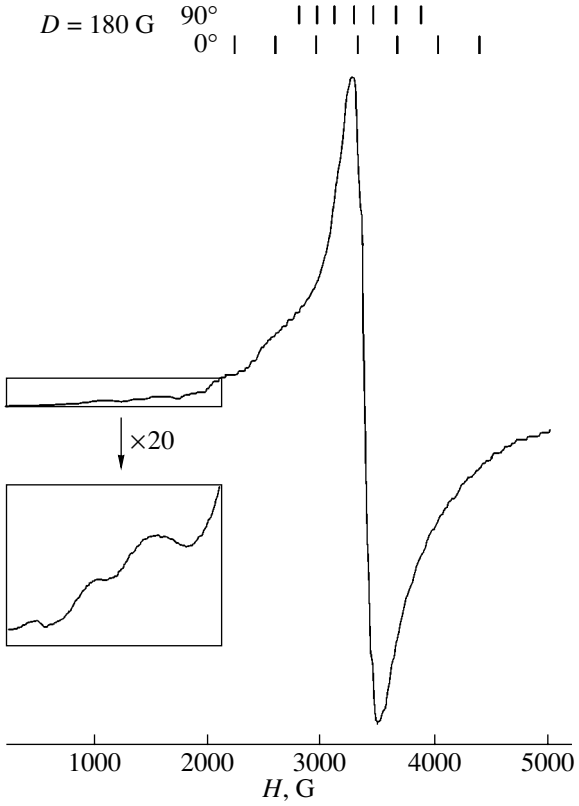

Fig. 5. EPR spectrum of a 0.1 *M* $Gd(NO_3)_3$ aqueous solution (with an addition of 15 vol % glycerol) vitrified at a temperature of 77 K and measured at frequencies in the *X* band. The central line is an envelope of signals attributed to Gd^{3+} centers with the fine structure parameter D_1 = 180 G, and the peaks observed in weak magnetic fields correspond to signals assigned to Gd^{3+} centers with the parameter D_2 = 580 G.

themselves in solutions quasi-vitrified at room temperature.

Figure 5 displays the EPR spectrum of a 0.1 *M* $Gd(NO_3)_3$ aqueous solution vitrified at a temperature of 77 K (with an addition of 15 vol % glycerol as a glass-forming agent). The number of fine structure lines observed in the experimental low-temperature spectrum indicates that the vitrified solution contains two types of aqua complexes with different local symmetries. The theoretical spectrum simulated with the use of parameters $D_1 = (180 \pm 5)$ G and $D_2 = (580 \pm 5)$ G agrees well with the experimental data. The fine structure parameters D_1 and D_2 can be assigned to higher symmetric eight-coordinate and lower symmetric nine-coordinate aqua complexes, respectively. Our results are consistent with the EXAFS data [1], according to which the number of nine-coordinate aqua complexes should increase with decreasing temperature.

ACKNOWLEDGMENTS

This work was supported by the Russian Foundation for Basic Research, project nos. 00-03-32915 and 01-03-06165.

REFERENCES

1. T. Yamaguchi, M. Nomura, H. Wakita, and H. Ohtaki, J. Chem. Phys. **89** (8), 5153 (1988).
2. D. H. Powell, A. E. Merbach, G. Gonzalles, *et al.*, Helv. Chim. Acta **76**, 2129 (1993).
3. R. V. Southwood-Jones, W. L. Earl, K. E. Newman, and A. E. Merbach, J. Chem. Phys. **73**, 5909 (1980).
4. S. K. Sur and R. G. Bryant, J. Magn. Reson. B **111**, 105 (1996).
5. G. P. Vishnevskaya, E. N. Frolova, and A. R. Fakhrutdinov, Zh. Fiz. Khim. **76** (5), 874 (2002).
6. *Adsorption from Solution at the Solid/Liquid Interface*, Ed. by G. Parfitt and C. R. Rochester (Academic, London, 1983; Mir, Moscow, 1986).
7. B. A. Volkov, G. P. Vishnevskaya, V. A. Gorozhanin, and R. T. Ramazanov, Prib. Tekh. Éksp., No. 4, 167 (1973).
8. G. P. Vishnevskaya, *Radio-Frequency Spectroscopy of Condensed Matter* (Nauka, Moscow, 1990).
9. J. Albertsson and I. Elding, Acta Crystallogr. B **33**, 1460 (1977).
10. L. Burlamacchi, G. Martini, M. F. Ottaviani, and M. Romanelli, Adv. Mol. Relax. Interact. Processes **12**, 145 (1978).

Translated by O. Borovik-Romanova

Physics of the Solid State, Vol. 45, No. 5, 2003, pp. 864–867. Translated from Fizika Tverdogo Tela, Vol. 45, No. 5, 2003, pp. 823–826.

SEMICONDUCTORS AND DIELECTRICS

The Structure of Mixed Fluorides $Ca_{1-x}Sr_xF_2$ and $Sr_{1-x}Ba_xF_2$ and the Luminescence of Eu^{2+} in These Crystals

A. E. Nikiforov, A. Yu. Zakharov, V. A. Chernyshev, M. Yu. Ugryumov, and S. V. Kotomanov

Ural State University, pr. Lenina 51, Yekaterinburg, 620083 Russia

Received May 22, 2002; in final form, September 9, 2002

Abstract—The structure of the mixed fluorites $Ca_{1-x}Sr_xF_2$ and $Sr_{1-x}Ba_xF_2$, as well as the structure of the Eu^{2+} impurity center in these crystals, is calculated within the framework of the virtual-crystal method realized in the shell model and pair-potential approximation. The phenomenological dependence of the position of the lower level of the $4f^65d$ configuration of the Eu^{2+} ion on distance to the Eu^{2+}–ligand is derived. The dependences of the Stokes shift and the Huang–Rhys factor on x are calculated for the yellow luminescence in $Sr_{1-x}Ba_xF_2$:Eu^{2+}. The value of x at which the lower level of the $4f^65d$ configuration of the Eu^{2+} ion in $Sr_{1-x}Ba_xF_2$:Eu^{2+} falls within the conduction band is found. © *2003 MAIK "Nauka/Interperiodica".*

1. INTRODUCTION

Alkaline-earth fluorides CaF_2, SrF_2, and BaF_2, as well as mixed crystals based on them, have already been attracting the attention of scientists for more than four decades [1–5]. The optical spectra of rare-earth ions in MeF_2 (Me = Ca, Sr, Ba) were investigated by Kaplyanskiĭ and Feofilov in [4, 5]. In recent years, the optical spectra of rare-earth ions in the mixed crystals $Me_{1-x}Me'_x$ Fe (Me, Me' = Ca, Sr, Ba) have been under investigation [2, 3]. The spectra of the Eu^{2+} ion in $Ca_{1-x}Sr_xF_2$:Eu^{2+} and $Sr_{1-x}Ba_xF_2$:Eu^{2+} are qualitatively different. In $Ca_{1-x}Sr_xF_2$:Eu^{2+}, the blue luminescence is observed whose spectrum contains the zero-phonon line associated with the transition between the lower level of the $4f^65d$ configuration and the $^8S(4f^7)$ ground state of the Eu^{2+} ion [2, 5]. In $Sr_{1-x}Ba_xF_2$:Eu^{2+}, yellow luminescence appears for $x > 0.2$ [3]. This luminescence corresponds to the transition between the excitonic state of Eu^{2+}, in which an electron is delocalized at the nearest metal ions, and the $^8S(4f^7)$ ground state. Replacement of Sr^{2+} cations by Ba^{2+} leads to a decrease in the crystal field and in the $t_{2g} - e_g$ splitting of the $5d$ level of the Eu^{2+} ion in the matrix crystal; as a result, the lower level of the $4f^75d$ configuration appears to be higher than the level of the impurity exciton (Fig. 1). For $0.2 < x < 0.5$, both types of luminescence are observed [3], which can be explained by the different cation surroundings of the Eu^{2+} ions. For $x > 0.5$, only yellow luminescence is detected [3].

In the first part of this paper, we study the influence of the crystal matrix on the position of the lower level

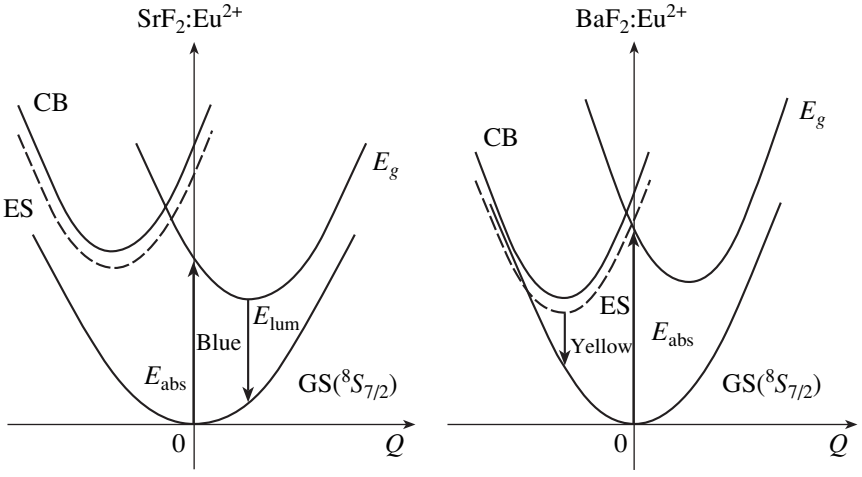

Fig. 1. Diagram of the configuration curves describing the mechanism of the blue and yellow luminescence in SrF_2:Eu^{2+} and BaF_2:Eu^{2+} [14].

1063-7834/03/4505-0864$24.00 © 2003 MAIK "Nauka/Interperiodica"

of the $4f^6 5d$ configuration of the Eu^{2+} ion in $Ca_{1-x}Sr_xF_2$:Eu^{2+} and $Sr_{1-x}Ba_xF_2$:Eu^{2+}. In the second part of this paper, the dependences of the Huang–Rhys factor and Stokes shift on x are calculated for the yellow luminescence in $Sr_{1-x}Ba_xF_2$:Eu^{2+}.

2. CALCULATION OF THE CRYSTAL ENERGY

According to experimental data [1], binary CaF_2–SrF_2 and SrF_2–BaF_2 systems form solid solutions at any ratio between the components. The lattice constants of these systems are experimentally determined with an accuracy of 0.001–0.002 Å and satisfy the additivity law [1]. The data of x-ray structure analysis suggest that the systems CaF_2–SrF_2 and SrF_2–BaF_2 are solid solutions of cubic symmetry with an unordered lattice [1]. Isovalent substitution of cations with similar electronic structure occurs in this case; the cations are separated by the anion sublattice. The presence of narrow zero-phonon lines in the Eu^{2+} luminescence spectra of the mixed crystals [2] is evidence of the equiprobable distribution of cations of different types in the lattice. These facts suggest that these systems can be described using the method of a virtual crystal, which has already been used in the framework of the shell model in the pair-potential approximation. A model expression for the energy of the crystal and application of the expression to pure fluorites were considered in previous studies [6–8]. The only difference between the mixed crystals $Ca_{1-x}Sr_xF_2$, $Sr_{1-x}Ba_xF_2$ and pure fluorites is the short-range interaction Me^{2+}–F^- (short-range interaction Me^{2+}–Me^{2+} is disregarded in our calculations because of the large distance between the cations). For the mixed crystal, the parameters of the potentials of the short-range interaction were determined in the following way. The sum of the corresponding short-range interactions Me_1^{2+}–F^- and Me_2^{2+}–F^- (here, Me_1 and Me_2 are different cations) were calculated for each type of short-range interaction for a given distance R, and each term in the sum was proportional to the concentration of the corresponding cation in the crystal:

$$V_{\text{sum}}(R) = (1-x)V_{Me_1}(R) + xV_{Me_2}(R), \qquad (1)$$

where $V_{Me_1}(R)$ is the short-range interaction at the distance R calculated with the parameters of the interaction for the cation, whose fraction is $1-x$, and $V_{Me_2}(R)$ is the short-range interaction at the distance R calculated with the parameters of the interaction for the cation, whose fraction is x. By varying R within the limits of the characteristic cation–anion distance (the distance was varied from 3 to 16 au in this case), we obtained a set of points $V_{\text{sum}}(R)$. This set of points was approximated by a dependence corresponding to the given type of short-range interaction. The parameters of all contributions of the short-range interaction were found in this way. The calculation of the structure of the impurity center was considered in [8].

3. CALCULATION OF THE CRYSTAL STRUCTURE OF $Ca_{1-x}Sr_xF_2$ AND $Sr_{1-x}Ba_xF_2$

The dependences of the lattice constants of $Ca_{1-x}Sr_xF_2$ and $Sr_{1-x}Ba_xF_2$ on x were found within the approximation of a virtual crystal. The experimental dependence of the lattice constant of $Sr_{1-x}Ba_xF_2$ on x was approximated by the linear function $a = kx + b$, where $k = 0.41$ Å, $b = 5.80$ Å, and $x \in [0, 1]$ (see [1]). The calculation yields $k = 0.44$ Å and $b = 5.81$ Å. The calculated dependence is in agreement with the Vegard law. We also found a similar dependence for $Ca_{1-x}Sr_xF_2$.

4. THE Eu^{2+} IMPURITY ION IN THE $Ca_{1-x}Sr_xF_2$ AND $Sr_{1-x}Ba_xF_2$ CRYSTALS

The absorption and luminescence spectra of Eu^{2+} ions in MeF_2 (Me = Ca, Sr, Ba) were studied by Kaplyanskiĭ and Feofilov in [5] and Kaplyanskiĭ and Przhevuskiĭ in [9]; the spectra of Eu^{2+} in $Ca_{1-x}Sr_xF_2$ and $Sr_{1-x}Ba_xF_2$ were investigated by Dujardin *et al.* in [10] and Kawano *et al.* in [2, 3]. The absorption and luminescence spectra of Eu^{2+} are associated with interconfiguration transitions between the $^8S(4f^7)$ ground state and the lower excited states of the $^8 4f^6 5d$ configuration [5, 9]. Two broad bands are observed in the absorption spectra. The Eu^{2+} ion is located at the center of a cube consisting of eight F^- ions. In the cubic crystal field, the splitting of the $^8S(4f^7)$ ground state is small and does not exceed 0.2 cm^{-1} [11]. In the excited $4f^6 5d$ configuration, the binding between the $5d$ electron and the $4f^6$ core is relatively weak [9]; as a result, the lower states of the $4f^6 5d$ configuration can be constructed from the lower state of the $4f^6$ core (level $^7F_0$ of the ^7F multiplet) and the sublevels of the $5d$ configuration. In the cubic crystal field, the level $5d$ splits into the sublevels t_{2g} and e_g. The magnitude $10Dq$ attains values of 12–16×10^3 cm^{-1} [5], which significantly exceed the spin–orbit interaction in the t_{2g} state (about 1000 cm^{-1} [12]) defining the structure of the short-wavelength absorption peak. The multiplet splitting of the $4f^6$ core (^{7}F term) is about 5000 cm^{-1} [12] and determines the width of the long-wavelength absorption peak.

The energy spectrum of the impurity ion depends heavily on the distance between the impurity ion and ligand. In the context of our model, we calculated the distance Eu^{2+}–F^- in our crystals and found a phenomenological dependence of the positions of the e_g and t_{2g} levels of the Eu^{2+} ion on this distance. The position of the zero-phonon line in $Ca_{1-x}Sr_xF_2$:Eu^{2+}, which corresponds to the interconfiguration transition from the e_g level to the $^8S(4f^7)$ ground state, is described by the dependence

$$v(r) = C + A/r^n - B/r^k, \qquad (2)$$

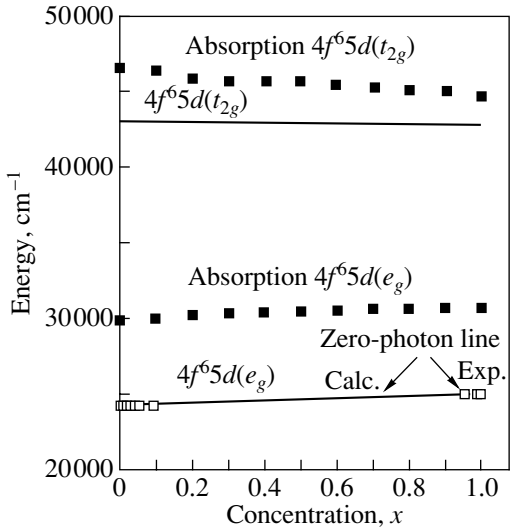

Fig. 2. Spectral position of the zero-phonon line and the level t_{2g} depending on Sr content x in the $Ca_{1-x}Sr_xF_2:Eu^{2+}$ crystal. The squares show experimental results taken from [2].

where $n = 12$ and $k = 5$. The first term determines the position of the degenerate 5*d* level in a free Eu^{2+} ion, the second term accounts for the shift of this level upon embedding the ion into the crystal, and the third term is associated with the influence of the crystal field on the t_{2g}–e_g splitting. The parameters *A*, *B*, and *C* are derived by fitting the formula to the positions of the zero-phonon line in CaF_2 and SrF_2 [2] and to the value of $10Dq$ in the crystals CaF_2, SrF_2, and BaF_2 [3, 5] (the distance Eu^{2+}–F^- was taken from our calculations). The values of the parameters are $A = 439.7 \times 10^6$ cm^{-1} Å^{12}, $B = 280 \times 10^5$ cm^{-1} Å^5, and $C = 36940$ cm^{-1}. The dependence of the position of the zero-phonon line on *x* (Fig. 2) can be found by calculating the distance Eu^{2+}–F^- in $Ca_{1-x}Sr_xF_2:Eu^{2+}$ at different values of *x*. The results of the calculation are in agreement with the experimental data. Thus, the position of the lower level of the $4f^65d$ configuration in the cubic crystal field of the fluorites can be described by formula (2) quite well. By using this formula, one can also estimate the position of the t_{2g} level taking into account that the first two terms in this formula determine the position of the degenerate 5*d* level in the crystal and the third term describes the position of the e_g level with respect to it. Our calculations are shown in Fig. 2. The difference between the calculated position of the t_{2g} level and the experimentally determined position of the short-wavelength absorption peak can be ascribed to the Stokes shift in the absorption spectrum.

The yellow luminescence of Eu^{2+} in $Sr_{1-x}Ba_xF_2:Eu^{2+}$ appears at $x > 0.2$ [3], and its spectra do not contain zero-phonon lines. For $0.2 < x < 0.5$, there are both types of luminescence in $Sr_{1-x}Ba_xF_2$: blue luminescence at 430–450 nm and yellow luminescence at 500–580 nm. For $x > 0.5$, only yellow luminescence is observed and its spectrum consists of a broad peak which linearly shifts to longer wavelengths as the concentration of Ba^{2+} grows and is located in the vicinity of 580 nm in $BaF_2:Eu^{2+}$ [3]. The yellow luminescence is associated with the interconfigurational transitions between the states of the impurity exciton, which forms upon transition of an electron to the nearest 12 cations, and the $^8S(4f^7)$ ground state [3, 10]. The diagram of the corresponding configuration curves is shown in Fig. 1. As the concentration of Ba^{2+} in the $Sr_{1-x}Ba_xF_2:Eu^{2+}$ crystal increases, the lower level of the $4f^65d$ configuration moves upward; its position can be calculated using formula (2). The top of the valence band in SrF_2 and BaF_2 is formed by the fluorine 2*p* states, and the bottom of the conduction band, by the cation *s* states; the band-gap width in these crystals has been measured experimentally [13]. Replacement of Sr^{2+} by Ba^{2+} in $Sr_{1-x}Ba_xF_2$ gives rise to a downward shift of the conduction band. The distance between the lower level of the $4f^65d$ configuration of Eu^{2+} and the bottom of the conduction band in $SrF_2:Eu^{2+}$ is taken from [14]. Assuming that the substitution of the Sr^{2+} cations by Ba^{2+} does not affect the position of the fluorine 2*p* states, one can calculate the change in the position of the bottom of the conduction band as a function of *x*, because the band-gap width in the series CaF_2, SrF_2, BaF_2 decreases virtually linearly with an increase in the lattice constant [13]; the dependence of the $Sr_{1-x}Ba_xF_2$ lattice constant on *x* was found as a result of our calculations. In this way, we can calculate the decrease in the distance between the bottom of the conduction band and the e_g level of the Eu^{2+} ion with increasing concentration of Ba^{2+} ions in $Sr_{1-x}Ba_xF_2:Eu^{2+}$. According to the calculations, the lower level of the $4f^65d$ configuration falls within the conduction band of $Sr_{1-x}Ba_xF_2:Eu^{2+}$ at $x = 0.2$. At the same concentration, yellow luminescence is observed in $Sr_{1-x}Ba_xF_2:Eu^{2+}$ [3].

Configuration curves with respect to the fully symmetrical coordinate can also be found in the framework of our model by calculating the dependence of the crystal energy *E* on the distance Eu^{2+}–F^-, which can be changed by compressing or expanding the cube formed by the eight fluorine ions surrounding Eu^{2+} with respect to its equilibrium dimension. The symmetrical coordinate *Q* is directly proportional to the change in the distance Eu^{2+}–F^- in this case. The $E(Q)$ dependences obtained for $Sr_{1-x}Ba_xF_2:Eu^{2+}$ are closely approximated by the parabolic function $1/2kQ^2$. By calculating for different values of *x*, we obtain the dependence of the coefficient *k* in the configuration curve on the concentration *x*. Next, we simulate the exciton state by increasing the charge of the Eu^{2+} ion by unity and decreasing the charge of each of the 12 nearest Me^{2+} ions by 1/12.

Then, the dependence of the coefficient k of the configuration curve of the exciton state on x is calculated in a similar way. The obtained dependences are linear: $k_{ES} = 33.95–5.26x$ and $k_{GS} = 21.18 – 4.61x$, where $x \in [0, 1]$ and all the coefficients are expressed in eV Å^{-2}. According to the calculations, the coefficient k of the configuration curve of the excitonic state is larger than that of the configuration curve of the ground state. As the concentration of Ba^{2+} ions increases, the coefficients k_{ES} and k_{GS} decrease, which is consistent with the fact that the elastic moduli of BaF_2 are smaller than those of SrF_2. Upon formation of the excitonic state, the cube composed of eight F^- ions undergoes compression, whose value changes from 0.14 Å in SrF_2:Eu^{2+} to 0.2 Å in BaF_2:Eu^{2+}. In the $Sr_{1-x}Ba_xF_2$:Eu^{2+} crystal, the dependence of the compression ΔR on x is described by the linear function $\Delta R = 0.143 + 0.036x$ (coefficients are expressed in Å). Knowing the coefficient k_{GA} of the configuration curve of the ground state and the change in the distance Eu^{2+}–F^- (ΔR) corresponding to the transition from the excitonic to the ground state, we find the Stokes shift for the yellow luminescence. By calculating for a number of different concentrations x, we obtain the dependence of the Stokes shift on x. According to the calculations, the Stokes shift in $Sr_{1-x}Ba_xF_2$:Eu^{2+} increases as x grows: $E_S = 1090x + 5011$ (the coefficients are expressed in cm^{-1}). The yellow luminescence in $Sr_{1-x}Ba_xF_2$:Eu^{2+} is observed for $0.2 < x < 1$, and its peak shifts to longer wavelengths as the concentration x grows [3]. According to the calculations, the Stokes shift increases by approximately 800 cm^{-1}. Further, let us estimate the frequency of the A_{1g} oscillations of the cube consisting of eight F^- ions:

$$\nu_{A_{1g}} = \frac{1}{2\pi}\sqrt{\frac{k_{GS}}{m_F}}, \qquad (3)$$

where m_F is the mass of the fluorine ions. The frequency changes from 547 cm^{-1} in SrF_2 to 484 cm^{-1} in BaF_2; the frequency change is well approximated by the dependence $\nu = 547 – 63x$, where ν is measured in cm^{-1}. Knowing the Stokes shift and the frequency of the cluster oscillations, we find the value of the Huang–Rhys factor for the yellow luminescence. According to the calculations, this factor in $Sr_{1-x}Ba_xF_2$:Eu^{2+} increases from 9 to 12 as x changes from 0 to 1 (obeying the law $3.38x + 9.133$).

Thus, the virtual-crystal method realized within the shell model in the pair-potential approximation makes it possible to describe the structure of the mixed fluorites $Ca_{1-x}Sr_xF_2$ and $Sr_{1-x}Ba_xF_2$ quite well and to obtain the lattice constant. In the doped mixed crystals $Ca_{1-x}Sr_xF_2$:Eu^{2+} and $Sr_{1-x}Ba_xF_2$:Eu^{2+}, the distance Eu^{2+}–F^- can also be found within this method. The position of the lower level of the excited $4f^65d$ configuration of the Eu^{2+} ion in these crystals is described by the phenomenological dependence on the distance Eu^{2+}–F^-.

For the yellow luminescence of the Eu^{2+} ion in $Sr_{1-x}Ba_xF_2$:Eu^{2+}, which is associated with the transitions from the exciton to the ground state, the dependence of the Stokes shift and the Huang–Rhys factor on the concentration x is calculated. According to the calculations, the Stokes shift increases by 1000 cm^{-1} as x grows from 0 to 1 and the Huang–Rhys factor increases from 9 to 12 in this case. This is in agreement with the experimental data from [3], which indicate that the peak in the yellow luminescence shifts to longer wavelengths with an increase in x. Our calculations indicate that the lower level of the $4f^65d$ configuration of the Eu^{2+} ion is in the conduction band if $x \geq 0.2$.

ACKNOWLEDGMENTS

This study was financially supported through grant REC 005 (CRDF).

REFERENCES

1. É. G. Chernavskaya and G. V. Anan'eva, Fiz. Tverd. Tela (Leningrad) **8** (1), 216 (1966) [Sov. Phys. Solid State **8**, 169 (1966)].
2. R. Nakata, H. Satoh, J. Tominaga, *et al.*, J. Phys. C **3**, 5903 (1991).
3. K. Kawano, K. Katoh, and R. Nakata, J. Phys. Soc. Jpn. **66** (6), 1803 (1997).
4. P. P. Feofilov, *Spectroscopy of Crystals* (Nauka, Moscow, 1966), p. 87.
5. A. A. Kaplyanskiĭ and P. P. Feofilov, Opt. Spektrosk. **13** (2), 235 (1962).
6. A. E. Nikiforov and S. Yu. Shashkin, *Spectroscopy of Crystals* (Nauka, Leningrad, 1989), p. 274.
7. V. A. Chernyshev, A. D. Gorlov, A. A. Mekhonoshin, *et al.*, Appl. Magn. Reson. **14** (1), 37 (1998).
8. A. D. Gorlov, V. B. Guseva, A. Yu. Zakharov, *et al.*, Fiz. Tverd. Tela (St. Petersburg) **40** (12), 2172 (1998) [Phys. Solid State **40**, 1969 (1998)].
9. A. A. Kaplyanskiĭ and A. K. Przhevuskiĭ, Opt. Spektrosk. **19** (4), 235 (1965).
10. D. Dujardin, B. Moine, and C. Pedrini, J. Lumin. **54**, 259 (1993).
11. C. Ryter, Helv. Phys. Acta **30**, 353 (1957).
12. S. Methfessel and D. C. Mattis, in *Handbuch der Physik*, Ed. by H. P. J. Wijn (Springer, Berlin, 1968; Mir, Moscow, 1972), Vol. 18, Part 1.
13. G. W. Rubloff, Phys. Rev. B **5** (2), 663 (1972).
14. D. S. McClure, Proc. SPIE **2706**, 315 (1996).

Translated by A. Poushnov

Physics of the Solid State, Vol. 45, No. 5, 2003, pp. 868–874. Translated from Fizika Tverdogo Tela, Vol. 45, No. 5, 2003, pp. 827–832.

SEMICONDUCTORS AND DIELECTRICS

Recrystallization and Ageing of Undoped and Strontium-Doped Potassium Chloride Crystals after Incomplete Polymorphic Transformation under Pressure

E. B. Borisenko and B. A. Gnesin

Institute of Solid-State Physics, Russian Academy of Sciences, Chernogolovka, Moscow oblast, 142432 Russia
e-mail: borisenk@issp.ac.ru

Received October 2, 2002

Abstract—This paper reports on the results of investigations into the room-temperature recrystallization and ageing of undoped and doped potassium chloride crystals after incomplete polymorphic transformation under high pressure. It is demonstrated that the recrystallization proceeds through several stages. The first stage involves nucleation and growth of grains with twin orientations with respect to the orientation of the initial single crystal. It is found that, after the transformation, the doped crystals undergo ageing at room temperature. This process is accompanied by the precipitation of orthorhombic strontium chloride and complex potassium strontium chloride (KSr_2Cl_5) phases. Depending on the strontium concentration in the initial crystal, particles of the precipitated phases can substantially impede the growth of recrystallized grains. The high-pressure phase is revealed under normal conditions. The diffusion coefficient of strontium in the materials after the polymorphic transformation is estimated. The kinetics and mechanisms of recrystallization and ageing in pure crystals and crystals with the same doping level after compression and treatment under high hydrostatic pressure are analyzed. © *2003 MAIK "Nauka/Interperiodica".*

1. INTRODUCTION

Nearly 25 years ago, it was found that a fourfold or fivefold hardening (with respect to the yield point) achieved through plastic deformation in alkali halide crystals completely disappears within one or two months due to recrystallization occurring even at room temperature [1]. The possibility of recrystallizing materials at relatively low temperatures ($T/T_m \sim 0/3$) is associated primarily with the high purity of the alkali halide crystals used in infrared optics. There are only a few bivalent cation dopants whose introduction is efficient from the hardening standpoint and does not lead to a noticeable decrease in the absorption coefficient. Among these dopants, for example, are Sr^{2+} (1.27 Å), Ca^{2+} (1.06 Å), and Mg^{2+} (0.78 Å) (the ionic radii are given in parentheses). However, it is known that their introduction even in small amounts (hundredths of a weight percent) results in the formation of second phases [2]. Therefore, the doping level of practical interest is limited by only several fractions of a weight percent. In this respect, strontium as a dopant for potassium chloride is of particular importance, because, among the above cations, the ionic radii of K^+ (1.33 Å) and Sr^{2+} are closest to each other. This circumstance allows us to assume that, compared to other elements, strontium is best matched to the KCl lattice.

In our recent works [2–5], we analyzed the specific features of recrystallization in alkali halide crystals at relatively low temperatures. The results obtained in these studies are not only of considerable scientific interest due to the unusual regularities revealed in recrystallization with the use of new techniques but also of great practical importance, because it was experimentally found that the time of retaining the strain-hardened state can be increased significantly (by a factor of five to ten).

The purpose of the present work was to investigate the recrystallization of Sr-doped KCl single crystals after their treatment under pressures higher than the onset but lower than the completion of the B1–B2 polymorphic transformation. Furthermore, we revealed and analyzed the effect of concurrent ageing processes on the recrystallization of these crystals at room temperature.

2. SAMPLE PREPARATION AND EXPERIMENTAL TECHNIQUE

Single crystals of KCl, KCl : 0.02 wt % Sr, and KCl : 0.06 wt % Sr served as the objects of investigation. According to the chemical analysis performed earlier in [2], these crystals are characterized by a sufficiently high purity. In our experiments, we used single-crystal samples cut along the {100} cleavage plane. The samples were treated under high pressures (up to 20–21 kbar) according to the procedure described in [4, 6]. X-ray diffractometry and texture analysis (Mo radiation, monochromator) were carried out using an incident beam [2–4]. For each sample, several x-ray dif-

fraction patterns were recorded for different sample orientations specified by the tilt and rotation angles. The necessity of using this technique stems from the fact that samples subjected to high-pressure treatment are neither powders nor single crystals. Different diffraction lines of a particular phase were recorded by varying orientations of the sample with respect to the diffraction vector (Table 1). Each phase was identified using several characteristic lines obtained for different orientations of the sample in the case when the difference between the experimental and reference diffraction angles for a given line did not exceed 0.4° (this value was of the order of the instrumental error associated with the sample tilt at an angle of no more than 35°). It should be noted that, in the phase analysis, we included only diffraction lines whose maximum intensity I_{max} with respect to the background intensity I_{back} satisfied the reliability criterion $I_{max} \geq 3(I_{back})^{1/2}$ [6].

Earlier [2, 4], we described a technique for evaluating the volume fraction of a material after a pressure-induced phase transformation with the use of optical microscopy (the random-section method). The volume fraction was estimated from the fraction occupied by planar defects formed upon the polymorphic transformation on a metallographic section parallel to the {100} plane. The grain diameter was determined as the maximum distance (measured on the metallographic section) between two points of a particular grain. The volume fraction of the optically anisotropic phases precipitated in the course of ageing was determined using the Glagolev method [7]. The diffuse scattering patterns and the pole figures were recorded under the same conditions, with the sole exception that, in the former case, the counter was rotated through 1° with respect to the exact position of the diffraction peak. This corresponds to the Huang scattering range, i.e., the range of diffuse scattering predominantly by point defects.

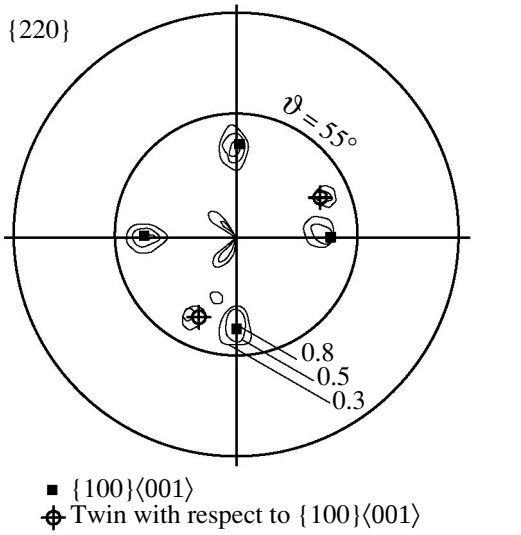

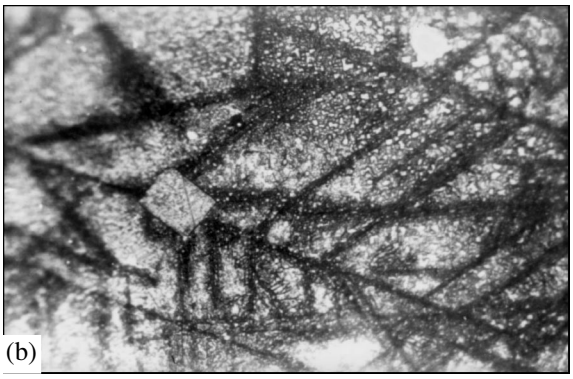

Fig. 1. Nucleation of recrystallized grains in a KCl : 0.06 wt % Sr sample after high-pressure treatment at P = 21 kbar and exposure to room temperature for two weeks: (a) {220} pole figure and (b) {100} section. Numbers near the curves indicate the relative intensities.

3. RESULTS AND DISCUSSION

To the best of our knowledge, there are two estimates of the pressure corresponding to the onset of the polymorphic transformation in pure KCl at room temperature: 19.1 ± 0.2 [8] and 20.9 ± 0.3 kbar [9]. According to Livshits *et al.* [9], the polymorphic transformation in KCl is completed at a pressure of 28.2 ± 1 kbar.

It can be seen from the data presented in Table 2 that, in pure KCl, the fractions of the material involved in the polymorphic transformation under pressures of 20 and 21 kbar are estimated at 40 and 70%, respectively. Our estimates made for the pressure of the onset of the B1–B2 phase transition with the use of optical microscopy and single-crystal x-ray diffractometry after pressure release are in better agreement with the results obtained in [8] than with the data reported in [9]. In our opinion, the x-ray diffraction techniques employed in the present work and in [8] are more sensitive and, consequently, provide more reliable data on the onset of the phase transition as compared to the results obtained from the measurements of the bulk effect of the polymorphic transformation in [9].

According to our observations, grains with twin orientations (with respect to the initial orientation {100}⟨001⟩) nucleate and grow in pure and strontium-doped potassium chloride samples subjected to high-pressure treatment at P = 20–21 kbar. As can be seen from Fig. 1a, the nucleation and growth of grains with {212} orientations of KCl manifest themselves in the {220} pole figure. Twinned grains nucleate in stripes of planar defects that arise from direct and reverse lattice transformations upon the polymorphic transition (Fig. 1b). For an undoped KCl crystal treated under a pressure of 21 kbar, this stage lasts nearly half a month. Then, the grains continue to grow through the migration of high-angle boundaries. After exposure to room

Table 1. X-ray diffractometric data for KCl samples doped with 0.06 wt % Sr* after high-pressure treatment and subsequent exposure to room temperature for six months

P	Phase	Line	Θ_t	Θ_{exp}	I_{max}/I_{back}	ϑ	φ
20	α-$SrCl_2$	(101)	10.54	10.66	75/50	25	180
20	α-$SrCl_2$	(101)	10.54	10.66	75/50	10	275
21	α-$SrCl_2$	(101)	10.54	10.52	82/50	5	330
21	α-$SrCl_2$	(200)	10.77	10.52	75/50	15	165
21	α-$SrCl_2$	(121)	14.08	14.03	75/50	10	275
21	α-$SrCl_2$	(211)	14.75	14.74	70/40	5	330
20	α-$SrCl_2$	(211)	14.75	14.75	65/40	10	275
21	α-$SrCl_2$	(222)	23.28	23.26	313/60	25	180

Note: P is the pressure used in high-pressure treatment (kbar), Θ_t is the angle corresponding to the reference interplanar distance (JCPDS) for the specified line of the phase (deg), Θ_{exp} is the experimental angle corresponding to the local intensity maximum in the x-ray diffraction pattern (deg), I_{max}/I_{back} is the experimental intensity ratio of the line to the background, and ϑ and φ are the tilt and rotation angles of the sample during recording, respectively (deg).

*The strontium concentration in the initial sample.

Table 2. Characteristics of the structure, phase composition, and recrystallization kinetics for samples after high-pressure treatment

Composition	P, kbar	T°_{an}, C	Phase			α, %	Microstructure				
			KCl(B2)	α-$SrCl_2$	KSr_2Cl_5		t_{TW}, h	t_{100}, h	D, μm	δ	Stability of the initial texture
KCl	20			Absent	Absent	40	130	400	1000	Absent	****
	21		Observed	Absent	Absent	70	400	1600	350	Absent	***
KCl : 0.02 wt % Sr	21		Observed	Observed	Observed	70	>4000	6000	100.350	Observed	***
	21	550	Observed		Observed	70	800	>6000	100.350	Observed	*
KCl : 0.06 wt % Sr	20		Observed	Observed	Observed	35	4000	>6000	100.350	Observed	****
	21		Absent	Observed	Observed	80	1000	4000	100	Absent	*

Note: Empty squares indicate an insufficient amount of experimental data, P is the applied pressure, T_{an} is the temperature of annealing prior to high-pressure treatment, α is the volume fraction of the material after the polymorphic transformation, t_{TW} is the duration of the stage of growing grains with twin orientations, t_{100} is the time required for the volume fraction of the recrystallized material to reach 100%, D is the diameter corresponding to a maximum in the size distribution of grains at the halt of the primary crystallization, and δ is the parameter indicating the presence or absence of the bimodal size distribution of grains. In the last column, the degree of relative stability of orientations with respect to the initial orientation $\{100\}\langle001\rangle$ are scored on a five-point scale from the maximum (*****) to minimum (*) stability.

Table 3. Microhardness of KCl crystals after high-pressure treatment

Sample	Microhardness, MPa					β, %	High-pressure treatment, kbar
	initial (averaged over the sample)	after pressure release (averaged over the sample)	after exposure to RT for 2 months (averaged over the sample)	after exposure to RT for 3 months (averaged over the sample)	after exposure to RT for 3 months (averaged over recrystallized grains)		
KCl	93	150	80	80	80	100	21
KCl : 0.02 wt % Sr	118	160	150	140	106		20
	118	250	195	195	136	60	21
	141	175	150	150	130	40	21*
KCl : 0.06 wt % Sr	153	210	120	120	108	60	20
	153	250	122	122	96	70	21

Note: RT is room temperature, and β is the fraction of the recrystallized material after high-pressure treatment and exposure to room temperature for three months.

*Annealing at 550°C prior to high-pressure treatment.

temperature for two months, the recrystallized grains occupy virtually the whole volume of the sample (Table 2). For undoped KCl crystals, the microhardness measured for the sample faces perpendicular to the crystal growth axis increases by more than 60% after high-pressure treatment at $P = 21$ kbar (Table 3). However, as follows from Table 3, the microhardness decreases with time and becomes even somewhat less than the initial value. The time it takes for primary recrystallization to be completed coincides with the time a mean microhardness of the KCl crystal subjected to high-pressure treatment takes to decrease to its initial value. In our case, the initial microhardness was measured for the metallographic section parallel to the {100} plane. The decrease in the microhardness below its initial value can be explained by the fact that the volume fraction of grains with other orientations increases with time and that the structure of recrystallized grains is more perfect than the structure of as-grown crystals.

In the course of the above experiments, we repeatedly observed that the samples studied contained a high-pressure phase of the CsCl type (the B2 structural type) for a long time (over a period no shorter than 12 months after the release of high pressure). The lines attributed to this phase can be seen in the x-ray diffraction patterns (Fig. 2). It should be noted that, after the pressure release, the x-ray patterns of single crystals involve the diffraction lines assigned to the {110}, {200}, and {211} planes of the B2 phase, which coincide with the lines observed for KCl powders directly under pressures higher than 19.3 kbar [8] and correspond to the standard set of the most intense lines for this structural type. As a rule, the lower the strontium content in the sample, the larger the number of lines attributed to the residual high-pressure phase and the higher their intensity.

The microhardness of KCl : 0.02 wt % Sr crystals increases by 112%. This is the maximum relative hardening achieved through high-pressure treatment of the crystals under investigation. As in the case of pure KCl crystals, the time of decreasing the microhardness to its initial value coincides with the time required for the primary recrystallization to be completed. The primary recrystallization lasted eight months; i.e., its rate was four times less than that of pure crystals. The recrystallization brought about the formation of structures characterized by a bimodal distribution of grains over their diameters (Table 2). In this case, the orientation of the samples remained similar to that of the initial single crystal (Table 2). Such a stability of the orientation can be ensured only in the case when the number of twinned grains is relatively small and the orientation of large-sized grains occupying approximately two-thirds of the sample volume is close to the initial orientation. This situation frequently occurs when large-sized grains slowly grow through the coalescence of subgrains [10].

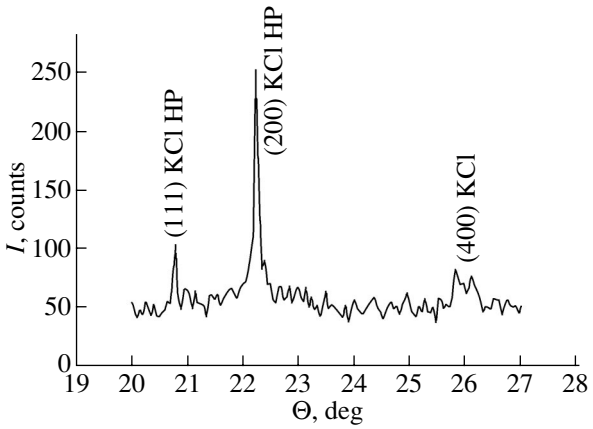

Fig. 2. X-ray diffraction pattern of the undoped KCl crystal after high-pressure treatment at $P = 21$ kbar and exposure to room temperature for five months.

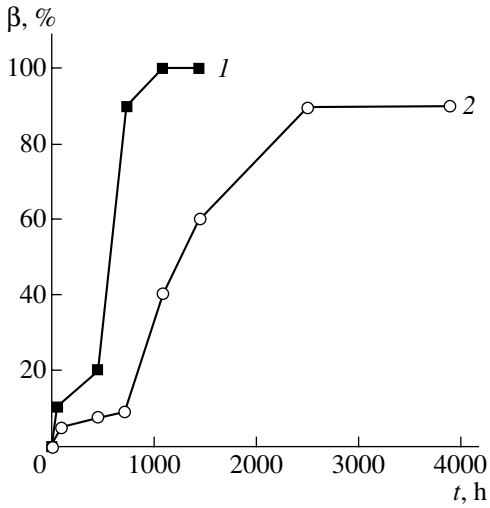

Fig. 3. Kinetic curves of recrystallization of (*1*) the undoped KCl crystal and (*2*) KCl : 0.06 wt % Sr at room temperature after high-pressure treatment at $P = 21$ kbar.

The kinetic curve of recrystallization of KCl : 0.06 wt % Sr crystals after treatment under a pressure of 21 kbar is similar to that of undoped samples. The only difference lies in the fact that the primary recrystallization in KCl : 0.06 wt % Sr crystals at both the growth stage of twinned grains and later stages proceeds more slowly than in pure crystals (Fig. 3) but more rapidly than in lighter doped crystals containing 0.02 wt % Sr (Table 2). After the primary recrystallization of KCl : 0.06 wt % Sr crystals is complete, the diameter distribution of grains exhibits one maximum at approximately 100 μm. From this standpoint, the recrystallization proceeding in KCl : 0.06 wt % Sr crystals more closely resembles the recrystallization observed in pure crystals than that in KCl : 0.02 wt % Sr crystals.

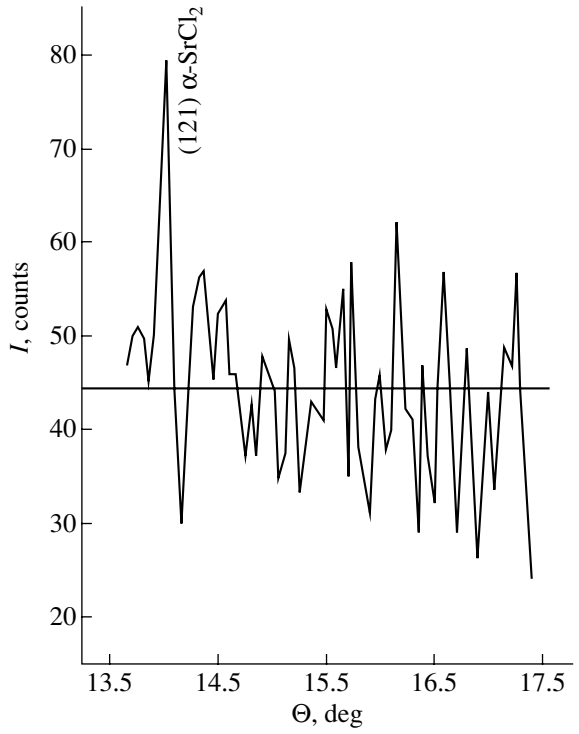

Fig. 4. X-ray diffraction pattern of a KCl : 0.06 wt % Sr crystal after high-pressure treatment at P = 21 kbar and exposure to room temperature for five months.

It is revealed that annealing prior to high-pressure treatment of KCl : 0.02 wt % Sr crystals at P = 21 kbar affects recrystallization at room temperature. In this case, the relative increase in the microhardness due to high-pressure treatment appears to be substantially less than that for unannealed crystals of the same composition and reaches only 25% (Table 3). The deviation of the orientation of recrystallized grains from the initial orientation and the decrease in the growth rate of grains at the stage of migration of high-angle boundaries of the general type turn out to be more pronounced than those for unannealed crystals.

As was shown earlier in [2], the initial single crystals containing 0.02 wt % Sr are similar in structure to a saturated solid solution, whereas the initial crystals with 0.06 wt % Sr are two-phase mixtures of KCl with cubic $SrCl_2$. The x-ray diffraction patterns of strontium-doped potassium chloride samples after treatment under high pressures contain not only the diffraction lines attributed to the high-pressure phase (KCl HP) typical of undoped KCl crystals but also the lines associated with the KSr_2Cl_5 phase and the α-$SrCl_2$ orthorhombic phase. These lines manifest themselves in the x-ray diffraction patterns only within six to eight months after the onset of exposure to room temperature. At the same time, examination under an optical microscope in polarized light revealed the appearance of particles of an optically anisotropic phase against the background of optically isotropic cubic KCl. The volume fractions of particles of this anisotropic phase in KCl samples containing 0.02 and 0.06 wt % Sr are determined to be $\gamma = 0.08 \pm 0.02\%$ and $0.20 \pm 0.02\%$, respectively. According to optical microscopic observations, the diameter of these particles is estimated as d = 2–3 μm. The particles are observed not only at the boundaries of new grains formed upon recrystallization but also in stripes of defects of the martensitic structural type [9]. Let us now assume that the strontium content c_{exp} in the particles observed does not exceed the strontium content in the sample, which was measured using inductively coupled plasma spectroscopy [4]. Then, we made an estimation from the following relationship:

$$c_{exp} = \gamma^*(\rho_p/\rho_s)M, \quad (1)$$

where M stands for wt % Sr, ρ_p is the density of the phase, ρ_s is the density of the solid solution (approximately equal to the density of KCl), and γ^* is the Sr content in the phase. The estimate obtained indicates that particles of complex strontium chloride predominantly precipitate in the course of ageing after high-pressure treatment. The x-ray diffraction patterns of heavier doped samples also exhibit lines assigned to the α-$SrCl_2$ phase, namely, the (101), (200), (121), and (211) lines (Fig. 4), which, according to JCPDS (32-1225), are the most intense lines of this phase.

The KSr_2Cl_5 phase with a monoclinic lattice is formed in the KCl–$SrCl_2$ equilibrium system in the presence of approximately 65 wt % $SrCl_2$ at a temperature close to 630°C under atmospheric pressure [11]. Orthorhombic α-$SrCl_2$ is a high-pressure phase. The α-$SrCl_2$ phase was observed in the study of the P–T diagram at temperatures higher than 800°C and at pressures no less than 2 kbar [12]. According to [12], this phase can be frozen to lower temperatures and pressures. None of the aforementioned phases is observed in the initial state and immediately after the pressure release.

The formation of new phases substantially impedes the recrystallization in the case when the growth stage of twinned grains is comparable in duration to the processes of ageing and precipitation of strontium-containing phases (Tables 2, 3).

For crystals treated under high pressures, the ageing rate is, on average, three or four times lower and the growth rate of grains is three or four times higher than those for crystals of the same composition after compression. Judging from the pole figures, the crystals subjected to high-pressure treatment are characterized by a higher degree of monocrystallinity as compared to the crystals subjected to compression. Most likely, the differences between the phase compositions of aged crystals after the polymorphic transformation and plastic deformation are associated with the differences in

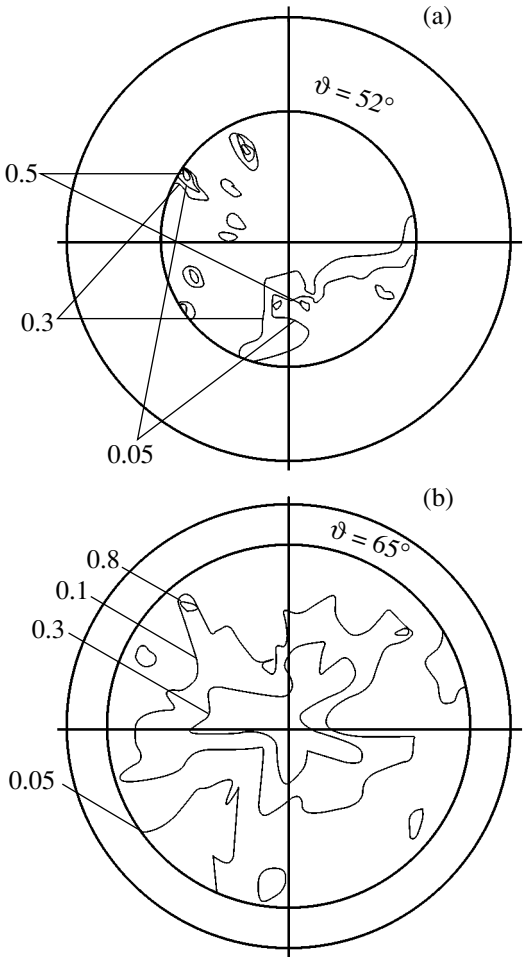

Fig. 5. Diffuse scattering patterns in the vicinity of the {220} Wulff–Bragg position at $2\Theta = 19.4°$ for a KCl : 0.02 wt % Sr crystal after exposure to room temperature for five months: (a) high-pressure treatment at $P = 21$ kbar and (b) 70% compression at $T = 250°C$. Numbers near the curves indicate the relative intensities.

the structure and density of defects and, primarily, with the smaller number of vacancies and other point defects in the crystals treated under high pressures. It should also be noted that, according to our experimental data, no pronounced anisotropy of diffuse x-ray scattering is observed in the vicinity of reciprocal lattice points in the case when the crystals subjected to high-pressure treatment are held at room temperature (Fig. 5a). In contrast, for the crystals subjected to plastic deformation, the threefold symmetry in the distribution of Huang scattering intensities clearly manifests itself in the diffuse scattering patterns with an increase in the exposure time (Fig. 5b) [2]. This indicates that impurities and lattice defects interact differently in the situations under consideration.

The diffusion coefficient of strontium in KCl after the phase transformation under pressure was estimated under the assumption that precipitated particles of the strontium-containing phases are spherical in shape. The radius R of the region in which strontium diffuses to form a particle was calculated under the condition that the mass of strontium in the particles did not exceed the mass of strontium in the sample at a given concentration. For α-$SrCl_2$ and KSr_2Cl_5 particles, the radii are found to be equal to 36 and 30 μm, respectively. Then, taking into account the possibility of precipitating particles of each type, we estimate the diffusion coefficients from the relationship $R = (Dt)^{1/2}$, where D is the diffusion coefficient and t is the diffusion time ranging from six to eight months. For α-$SrCl_2$ particles, the diffusion coefficient is determined to be $D = 0.9 \times 10^{-12}$ cm^2/s. In the case of KSr_2Cl_5 particles, the diffusion coefficient is half the above coefficient and is approximately two orders of magnitude less than that for plastically deformed crystals of the same chemical composition after exposure to room temperature.

It was found that the increase in the microhardness upon treatment under high pressures is 40% greater than that due to plastic deformation. However, the former effect persists for a considerably shorter time as compared to the latter effect. Most probably, this is associated with the higher degree of recrystallization, slower ageing, and different phase compositions of the ageing samples.

4. CONCLUSIONS

Thus, it was experimentally revealed that, upon treatment under high pressures of 20–21 kbar, the KCl crystals undoped and doped with 0.02–0.06 wt % Sr can undergo both incomplete and incompletely reversible polymorphic transformations. Subsequent exposure of these crystals to room temperature is accompanied by their ageing. This process involves the precipitation of strontium chloride and complex potassium strontium chloride particles that substantially affect the recrystallization kinetics at room temperature.

REFERENCES

1. E. B. Borisenko, Materialovedenie, No. 11, 23 (1999).
2. E. B. Borisenko and B. A. Gnesin, Fiz. Tverd. Tela (St. Petersburg) **42** (7), 1261 (2000) [Phys. Solid State **42**, 1299 (2000)].
3. E. B. Borisenko and B. A. Gnesin, Fiz. Tverd. Tela (St. Petersburg) **41** (2), 259 (1999) [Phys. Solid State **41**, 230 (1999)].
4. E. B. Borisenko and B. A. Gnesin, Textures Microstruct. **26–27**, 369 (1996).
5. E. B. Borisenko, B. A. Gnesin, O. O. Likhanova, and I. B. Savchenko, Fiz. Tverd. Tela (St. Petersburg) **37** (7), 2029 (1995) [Phys. Solid State **37**, 1105 (1995)].

6. V. M. Avdyukhina, D. Batrus', V. V. Zubenko, *et al.*, *X-ray Diffraction Analysis: A Special Practical Course*, Ed. by A. A. Katsnel'son (Mosk. Gos. Univ., Moscow, 1986).
7. S. A. Saltykov, *Stereometric Metallography* (Metallurgiya, Moscow, 1970).
8. Nozomu Hamaya and Suin-iti Akimoto, High Temp.–High Press. **13**, 347 (1981).
9. L. D. Livshits, Yu. N. Ryabinin, I. V. Larionov, and A. S. Zverev, Zh. Éksp. Teor. Fiz. **55** (4), 1173 (1968) [Sov. Phys. JETP **28**, 612 (1968)].
10. S. S. Gorelik, *Recrystallization of Metals and Alloys* (Metallurgiya, Moscow, 1967).
11. B. G. Korshunov and V. V. Safonov, *Halide Systems: A Handbook* (Metallurgiya, Moscow, 1984).
12. E. Yu. Tonkov, *Phase Diagrams of Materials at High Pressure* (Nauka, Moscow, 1983).

Translated by O. Borovik-Romanova

Physics of the Solid State, Vol. 45, No. 5, 2003, pp. 875–879. Translated from Fizika Tverdogo Tela, Vol. 45, No. 5, 2003, pp. 833–836.

SEMICONDUCTORS AND DIELECTRICS

Anomalous Dispersion of SH Acoustic Waves in a Piezoelectric Sandwich Structure

V. I. Alshits and V. N. Lyubimov

Shubnikov Institute of Crystallography, Russian Academy of Sciences, Leninskiĭ pr. 59, Moscow, 119333 Russia

e-mail: alshits@ns.crys.ras.ru

Received October 21, 2002

Abstract—A transformation of the dispersion spectrum of shear horizontal (SH) acoustic eigenwaves in a sandwich structure due to a piezoelectric effect is described. The structure consists of two plates separated by a gap whose thickness is considerably less than the wavelength. Under these conditions, acoustic fields induced in the plates interact through the piezoelectric effect. The piezoelectric effect brings about a distortion and divergence of the initially (in the zeroth approximation) independent dispersion curves; i.e., all points of intersection of the dispersion curves disappear. Each of the new dispersion branches is formed by a set of adjacent portions of initial branches. A change in the wave number (or in the frequency) results in a periodic gradual displacement of the localization zone of the acoustic field from one plate to the other. © *2003 MAIK "Nauka/Interperiodica".*

1. INTRODUCTION

The purpose of this paper is to elucidate the mechanism of both the radical transformation observed in the dispersion spectrum of shear horizontal (SH) acoustic eigenwaves in a sandwich structure and substantial changes in the wave fields due to relatively weak electromechanical coupling, namely, the piezoelectric effect. In this situation, new properties manifest themselves under the action of perturbations relieving the degeneracy. As a result, the points of intersection of the dispersion curves disappear. A similar mechanism was described, for example, in our previous works [1, 2], for Lamb waves propagating in isolated anisotropic plates under conditions when perturbations led to a deviation of the direction of wave propagation from symmetric orientations.

In this work, we will consider a sandwich structure consisting of two piezoelectric plates separated by a gap whose thickness is considerably less than the wavelength. Under these conditions, acoustic fields generated in the plates interact through the piezoelectric effect alone. The gap ensures that no dry friction occurs between the plates. The above comment regarding the gap refers equally to the sliding contact between the plates. The results obtained in our calculations are appropriate for two types of contacts, because, in both cases, we deal with SH acoustic waves for which the displacement fields are aligned parallel to the interface.

In the absence of a piezoelectric interaction, wave fields induced in the plates are independent of one another. Shear horizontal waves propagating the sandwich structure under investigation are characterized by a set of dispersion curves. It should be noted that each of the dispersion curves describes SH waves only in one of the two plates constituting the sandwich structure. In the absence of a piezoelectric effect, the intersection points of the dispersion curves belonging to two families correspond to noninteracting wave fields in the two plates simultaneously. The piezoelectric effect brings about the mutual penetration of the wave fields and, hence, interaction between SH waves propagating in the plates. As a consequence, at each point of intersection of the dispersion curves belonging to two families, there should occur divergence and, consequently, distortion of the dispersion branches. The dispersion branches of the spectrum transformed under the action of piezoelectric coupling are formed by a set of adjacent portions of the initial branches. Therefore, a gradual change in the wave number along one of the new dispersion curves should result a periodic displacement of the localization zone of the acoustic wave field from one piezoelectric plate to the other. This phenomenon will be thoroughly investigated below.

2. FORMULATION OF THE PROBLEM

Let us consider a sandwich structure consisting of two plates prepared from transversely isotropic piezoelectric materials (Fig. 1). The symmetry of the materials used can be described in any one of the following three groups: ∞mm, $6mm$, or $4mm$ [3]. In our treatment, we will use the tensor components of piezoelectric coefficients **e**, permittivities **ε**, and elastic moduli **c**:

$$e_{15} = e_{24} \equiv e, \quad \varepsilon_1 = \varepsilon_2 \equiv \varepsilon, \quad c_{44} = c_{55} \equiv c. \qquad (1)$$

These parameters characterize the lower plate with a thickness d and a density ρ, which occupies the region $0 \le y \le d$. The upper plate ($-\tilde{d} \le y \le 0$) is characterized

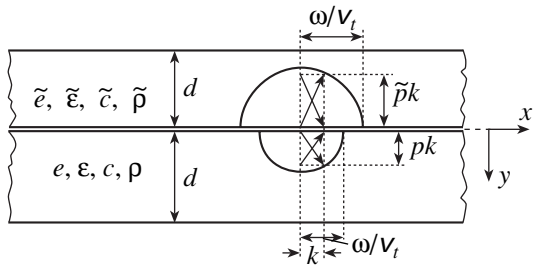

Fig. 1. Schematic drawing of the sandwich structure under investigation and its acoustic parameters. Semicircles are sections of the constant-frequency surfaces of bulk shear waves. Arrows indicate the wave vectors of the partial waves in a waveguide mode.

by the parameters $\tilde{e}$, $\tilde{\varepsilon}$, $\tilde{c}$, and $\tilde{\rho}$. The principal crystallographic axes of the lower plate are assumed to be parallel to those of the upper plate. The sagittal plane *xy* (the plane passing through all the wave vectors involved) is chosen to be perpendicular to the principal crystallographic axes of the plates.

It is assumed that the shear horizontal waves under consideration can be described by the displacement vectors **u** and $\tilde{\mathbf{u}}$, which are perpendicular to the sagittal plane. The displacement vector **u** has only one nonzero component, namely, $u_z = u(x, y, t)$. Similarly, the displacement vector $\tilde{\mathbf{u}} = (0, 0, \tilde{u}_z)$ has a nonzero component $\tilde{u}_z = \tilde{u}(x, y, t)$. The displacement vectors **u** and $\tilde{\mathbf{u}}$ are aligned parallel to the boundary between the plates. Under the given conditions, when the contact between the plates occurs through a gap (or when we are deal with sliding contact), any mechanical contact between the plates is absent. However, the piezoelectric effect induces an electromechanical coupling; hence, the acoustic fields generated in the plates interact with one another. By virtue of the piezoelectric effect, elastic waves of the displacements **u** give rise to quasi-static electric fields. These fields are characterized by the potential $\Phi_u = (e/\varepsilon)u(x, y, t)$. Moreover, the total wave field contains a contribution from Coulomb inhomogeneous waves of the electric field described by the potential Φ_c (see [4]). Therefore, the total potential $\Phi(x, y, t)$ should be equal to the sum $\Phi = \Phi_u + \Phi_c$. In this case, the wave field in the lower plate can be represented in the following form:

$$\begin{pmatrix} u(x, y, t) \\ \Phi(x, y, t) \end{pmatrix} = \begin{pmatrix} u(y) \\ (e/\varepsilon)u(y) + \Phi_c(y) \end{pmatrix} \exp[ik(x - vt)]. \quad (2)$$

Here, *k* is the wave number, $v = \omega/k$ is the phase velocity of propagation of the wave field along the *x* axis, ω is the frequency, and *t* is the time. In relationship (2), we introduced the functions $u(y)$ and $\Phi_c(y)$, which can be written in the form

$$u(y) = a^+ \exp[ipk(y - d/2)] + a^- \exp[-ipk(y - d/2)], \quad (3)$$

$$\Phi_c(y) = b^+ \exp[-k(y - d/2)] + b^- \exp[k(y - d/2)]. \quad (4)$$

The dimensionless parameter *p* involved in expressions (3) and (4) specifies the direction of propagation of two bulk partial waves (Fig. 1):

$$p \equiv p(v) = \sqrt{v^2/v_t^2 - 1}, \quad v_t^2 = (c + c^2/\varepsilon)/\rho. \quad (5)$$

Here, v_t is the velocity of propagation of an SH wave in the plate material. The wave field in the upper plate can be represented by the same relationships after the substitutions $u, \Phi, \Phi_c, e, \varepsilon, a^\pm, b^\pm, p, v_t, c$, and $\rho \longrightarrow \tilde{u}$, $\tilde{\Phi}$, $\tilde{\Phi}_c$, $\tilde{e}$, $\tilde{\varepsilon}$, $\tilde{a}^\pm$, $\tilde{b}^\pm$, $\tilde{p}$, $\tilde{v}_t$, $\tilde{c}$, and $\tilde{\rho}$, respectively.

The relationships between the amplitude factors $a^\pm$, $b^\pm$, $\tilde{a}^\pm$, and $\tilde{b}^\pm$ of the partial waves can be obtained from the boundary conditions. For the given contact between the plates, all the normal (with respect to the boundaries) components of the mechanical stresses should become zero at the outer boundaries ($y = d$ and $y = -\tilde{d}$) and at the inner boundary ($y = 0$): $\sigma_{yi} = 0$ and $\tilde{\sigma}_{yi} = 0$ (in the case under consideration, only the stress components $\sigma_{yz} = 0$ and $\tilde{\sigma}_{yz}$ do not identically reduce to zero). At the inner boundary, both the electric potentials and normal (with respect to this boundary) components of the electric induction should be continuous: $\Phi(x, 0, y) = \tilde{\Phi}(x, 0, y)$ and $D_y(x, 0, y) = \tilde{D}_y(x, 0, y)$, respectively. In order to simplify further calculations, the outer boundaries are assumed to be metallized (in this case, the long-range interaction of the electric fields is confined to the sandwich structure). Therefore, the electric potentials Φ and $\tilde{\Phi}$ must necessarily become zero at the outer boundaries. As a result, we obtain a system of eight algebraic homogeneous equations in which the amplitude factors $a^\pm$, $b^\pm$, $\tilde{a}^\pm$, and $\tilde{b}^\pm$ are unknown. To avoid cumbersome calculations, we do not present these equations in an explicit form. The solubility condition for this system (i.e., the situation where the determinant of the system reduces to zero) determines an infinite spectrum of dependences of the phase velocity v on the wave number: $v = v^{(n)}(k)$, where $n = 1, 2, \ldots$. This spectrum will be considered in further analysis.

3. DISPERSION CURVES IN THE ABSENCE OF A PIEZOELECTRIC EFFECT

In the absence of a piezoelectric effect, acoustic coupling between the plates is absent and wave fields of

the adjacent plates do not interact with one another. For the chosen orientation of the sagittal plane, the description of these fields in each of the two isolated plates is identical to that in plates prepared from an isotropic material (see [5, 6]). Our prime interest here is in both the structure of the spectrum obtained upon superposition of the dispersion curves associated with the aforementioned two plates and the points of intersection of the dispersion branches.

For each of the two plates under investigation, there are symmetric and antisymmetric eigenwaves. Upon reflection in the central plane of the plate, the vector wave field of elastic displacements remains unchanged for symmetric eigenwaves and reverses sign for antisymmetric eigenwaves. The dispersion relation that describes both types of eigenwaves in the lower plate simultaneously has the form

$$\sin(pkd) = 0. \tag{6}$$

Hence, it follows that

$$p(v^{(n)}) = \pi n/kd, \tag{7}$$

where $n = 0, 2, 4, \ldots$ for symmetric eigenwaves ($a^+ = a^-$) and $n = 1, 3, 5, \ldots$ for antisymmetric eigenwaves ($a^+ = -a^-$). For the upper plate, we can write similar relationships. As a result, we have

$$\tilde{p}(v^{(\tilde{n})}) = \pi\tilde{n}/k\tilde{d}. \tag{8}$$

Hereafter, the discrete parameters n and $\tilde{n}$ will denote the numbers of dispersion curves in the lower and upper plates, respectively.

By solving Eqs. (7) and (8) for the phase velocities [see relationship (5)], we can easily obtain the explicit formulas describing all the undistorted dispersion branches for the lower and upper plates; that is,

$$\begin{aligned} v^{(n)}(k) &= v_t\sqrt{(\pi n/kd)^2 + 1}, \\ v^{(\tilde{n})}(k) &= \tilde{v}_t\sqrt{(\pi\tilde{n}/k\tilde{d})^2 + 1}. \end{aligned} \tag{9}$$

Each of these two formulas describes a series of nonintersecting curves (Fig. 2). However, in the case when numerical values of the material characteristics of the lower and upper plates differ from each other ($v_t \neq \tilde{v}_t$, $d \neq \tilde{d}$), superposition of dispersion curves belonging to these families results in a large number of intersections (Fig. 3a). From formulas (9), we can obtain the coordinates of the complete set of intersection points of dispersion branches determined by the numbers n and $\tilde{n}$

$$\begin{aligned} k^{n\tilde{n}} &= \pi\sqrt{\frac{(nv_t/d)^2 - (\tilde{n}\tilde{v}_t/\tilde{d})^2}{\tilde{v}_t^2 - v_t^2}}, \\ v^{n\tilde{n}} &= v_t\tilde{v}_t\sqrt{\frac{(n/d)^2 - (\tilde{n}/\tilde{d})^2}{(nv_t/d)^2 - (\tilde{n}\tilde{v}_t/\tilde{d})^2}}. \end{aligned} \tag{10}$$

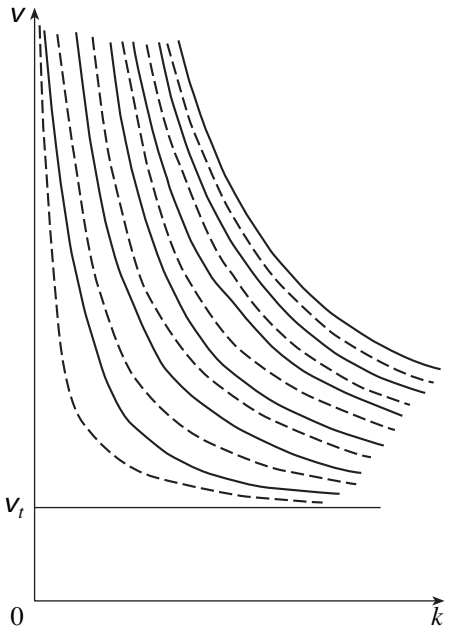

Fig. 2. Dispersion curves for eigenwaves in the lower plate in the absence of a piezoelectric effect. Solid and dashed lines are the dispersion curves in symmetric and antisymmetric wave fields, respectively.

The requirement imposed on the coordinates of intersection points is that they be real quantities. It is this requirement that determines the complete set of numbers n and $\tilde{n}$ for intersecting branches.

Knowing the phase velocities of propagation of acoustic waves, we can determine their group velocities with the use of the general relationship between velocities of these types: $v_g = v + k\partial v/\partial k$. As a result, from expressions (9), we have

$$v_g^{(n)}(k) = v_t^2/v^{(n)}(k), \quad \tilde{v}_g^{(\tilde{n})}(k) = \tilde{v}_t^2/v^{(\tilde{n})}(k). \tag{11}$$

Consequently, for the coordinates of points at which the branches attributed to group velocities intersect one another, we obtain the relationships

$$\begin{aligned} k_g^{n\tilde{n}} &= \pi v_t\tilde{v}_t\sqrt{\frac{(n/v_td)^2 - (\tilde{n}/\tilde{v}_t\tilde{d})^2}{v_t^2 - \tilde{v}_t^2}}, \\ v_g^{n\tilde{n}} &= v_t\tilde{v}_t\sqrt{\frac{(n/v_td)^2 - (\tilde{n}/\tilde{v}_t\tilde{d})^2}{(n/d)^2 - (\tilde{n}/\tilde{d})^2}}. \end{aligned} \tag{12}$$

It follows from relationships (10) and (12) that, at $v_t = \tilde{v}_t$, intersections of the branches in families of both phase and group velocities are absent.

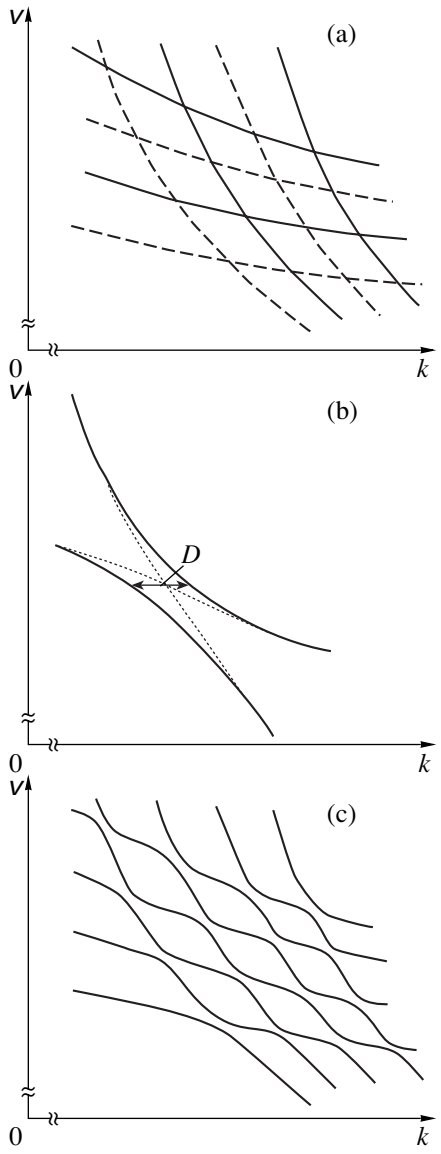

Fig. 3. Schematic drawings illustrating the evolution of the dispersion curves due to the piezoelectric effect: (a) intersections of the dispersion curves for eigenwaves in noninteracting fields in the absence of a piezoelectric interaction, (b) divergence of the dispersion curves at any point of their intersection (dotted lines are the dispersion curves in the absence of a piezoelectric interaction), and (c) changes in the dispersion curves shown in Fig. 3a due to the piezoelectric effect.

4. TRANSFORMATION OF THE DISPERSION SPECTRUM DUE TO THE PIEZOELECTRIC EFFECT

The piezoelectric effect induces an interaction between acoustic fields in the lower and upper plates; as a result, the wave fields lose their symmetry properties, because the plates have different material characteristics. At the same time, what is more important, the piezoelectric effect brings about a radical transformation of the entire set of dispersion curves. Let us now describe a transformation initiated by the piezoelectric effect for a family of dispersion branches associated with phase velocities. In this situation, the piezoelectric effect leads to divergence of the dispersion curves; i.e., all the points of intersection of the dispersion curves disappear (Figs. 3a–3c). Leaving out rather cumbersome algebraic manipulation and assuming that the piezoelectric effect is a weak perturbation, we write the parameter characterizing the divergence of the dispersion branches attributed to phase velocities with numbers n and $\tilde{n}$ in the following form:

$$D^{n\tilde{n}} = 2|\Delta k| = \frac{(k/\pi)^2}{|F_1|} \times \sqrt{(\kappa^2 G d/n^2 + \tilde{\kappa}^2 \tilde{G}\tilde{d}/\tilde{n}^2)^2 - 8(\kappa^2 F_1 d/n^2)(\tilde{\kappa}^2 F_2 \tilde{d}/\tilde{n}^2)}. \quad (13)$$

Here, $\kappa^2 = e^2/\varepsilon c$ and $\tilde{\kappa}^2 = \tilde{e}^2/\tilde{\varepsilon}\tilde{c}$ are the piezoelectric coupling coefficients for the lower and upper plates, respectively. In relationship (13), we introduced the functions

$$F_1 = \varepsilon g_c \tilde{g}_s + \tilde{\varepsilon} g_s \tilde{g}_c,$$
$$F_2 = \varepsilon g_s(\tilde{g}_c - 1) + \tilde{\varepsilon}\tilde{g}_s(g_c - 1), \quad (14)$$

$$G = \varepsilon g_s \tilde{g}_s + 2\tilde{\varepsilon}\tilde{g}_c(g_c - 1),$$
$$\tilde{G} = \tilde{\varepsilon} g_s \tilde{g}_s + 2\varepsilon g_c(\tilde{g}_c - 1), \quad (15)$$

$$g_s = (-1)^n \sinh(kd), \quad \tilde{g}_s = (-1)^{\tilde{n}} \sinh(k\tilde{d}),$$
$$g_c = (-1)^n \cosh(kd), \quad \tilde{g}_c = (-1)^{\tilde{n}} \cosh(k\tilde{d}). \quad (16)$$

In expressions (13) and (16), the quantity k is the coordinate of the intersection point of the branches, which is specified by relationships (10).

In the case when the lower and upper plates have identical material characteristics and the piezoelectric effect is absent, the dispersion curves for these plates completely coincide with each other. In the presence of a piezoelectric effect (identical for both plates), the dispersion branches begin to diverge. The separation between the divergent branches with numbers $n = \tilde{n}$ is also determined from relationship (13). Note that, in this case, the quantity k should be treated as a continuous parameter (argument). Finally, let us consider a situation where either of these two plates is not piezoelectric. Under these conditions, the piezoelectric effect is induced only in one of the plates and does not eliminate the intersections of dispersion branches but only slightly displaces the intersection points. The degree of displacement is characterized by the parameter $D^{n\tilde{n}}$ in relationship (13).

It is revealed that the divergence of the dispersion branches associated with group velocities is also observed but has a higher order of smallness ($\sim\kappa^2\tilde{\kappa}^2$) as compared to the divergence of the branches attrib-

uted to phase velocities. The appropriate expressions are rather cumbersome, and their derivation does not enter into the scope of the present paper.

The approximate analysis performed demonstrates that the piezoelectric coupling coefficients should be sufficiently small. As a rule, this assumption works very well in practice. However, although the piezoelectric effect is relatively weak, its influence on the geometry of the dispersion curves proves to be significant. Under the electromechanical action, the points of intersection of the dispersion curves disappear and the separation between the curves becomes proportional to the piezoelectric coupling coefficients $\kappa^2 \sim \tilde{\kappa}^2$ [see relationship (13)]. The piezoelectric effect brings about a distortion of the initially independent dispersion branches. Each of the new dispersion branches is formed by a set of adjacent portions of the initial branches, which correspond to wave fields both in one plate and in the other. As a result, the dependence of the localization of the wave field on the wave number (or on the frequency) changes radically. A gradual change in the wave number should result in a periodic displacement of the localization zones of the wave field from one plate to the other. In both plates, the localization zones become commensurate as the points of discontinuity are approached. In the vicinity of these points, the derivative $\partial v/\partial k$ changes drastically; i.e., an insignificant change in the wave number implies a substantial change in the group velocity of propagation of the wave field. It is quite reasonable that the piezoelectric effect also leads to divergence of the dispersion branches associated with group velocities; however, in this case, the separation between the dispersion branches is considerably less than that for phase velocities (for group velocities, the separation is proportional to $\kappa^2\tilde{\kappa}^2$).

In conclusion, we should note that sandwich structures in which the outer surfaces are not metallized exhibit similar dispersion anomalies.

ACKNOWLEDGMENTS

This work was supported by the Russian Foundation for Basic Research, project no. 01-02-16228.

REFERENCES

1. V. N. Lyubimov and V. I. Alshits, Kristallografiya **33** (2), 279 (1988) [Sov. Phys. Crystallogr. **33**, 163 (1988)].
2. V. I. Alshits, M. Deschamp, and G. A. Maugin, Wave Motion **37** (2003) (in press).
3. Yu. I. Sirotin and M. P. Shaskolskaya, *Fundamentals of Crystal Physics* (Nauka, Moscow, 1975; Mir, Moscow, 1982).
4. M. K. Balakirev and I. A. Gilinskiĭ, *Waves in Piezoelectric Crystals* (Nauka, Novosibirsk, 1982).
5. I. A. Viktorov, *Rayleigh and Lamb Waves: Physical Theory and Applications* (Nauka, Moscow, 1966; Plenum, New York, 1967).
6. I. A. Viktorov, *Sonic Surface Waves in Solids* (Nauka, Moscow, 1981).

Translated by O. Borovik-Romanova

Physics of the Solid State, Vol. 45, No. 5, 2003, pp. 880–885. Translated from Fizika Tverdogo Tela, Vol. 45, No. 5, 2003, pp. 837–842.

DEFECTS, DISLOCATIONS, AND PHYSICS OF STRENGTH

The Cross Slip of a Dislocation in an Ultrasound Field and Its Dependence on the Ultrasound Amplitude and Frequency, Sample Orientation, and Dynamic Viscosity

N. A. Tyapunina, G. V. Bushueva, M. I. Silis, D. S. Podsoblyaev, Yu. B. Likhushin, and V. Yu. Bogunenko

Moscow State University, Vorob'evy gory, Moscow, 119899 Russia

Received July 16, 2002

Abstract—The motion of a screw dislocation under the action of ultrasound is simulated with account taken of its cross slip in a spatially nonuniform stress field created by a fixed dislocation of the same sense. Only dislocations started from certain regions in the space are shown to undergo cross slip. The variations in the sizes and shapes of these regions with the ultrasound parameters, crystallographic orientation of the sample, and coefficient of dynamic viscosity are given. © *2003 MAIK "Nauka/Interperiodica".*

1. INTRODUCTION

Dislocation cross slip is known to play an important role in the development of plastic deformation. Cross slip comes into play when a crystal is subjected to an alternating load, including ultrasound (US). Tyapunina *et al.* [1] convincingly showed that an experimentally detected increase in the dislocation density by three or four orders of magnitude cannot be explained without taking into account cross slip.

From the physical standpoint, the most strongly grounded cause for cross slip is a stress field having a shear component in the plane of cross slip in front of a moving dislocation. The sources of such stress fields in real crystals are dislocations and their ensembles.

The purpose of this work is to simulate the cross slip of a dislocation under the action of US in the presence of an elastic-field component that is constant in time but spatially nonuniform and to find its dependence on the ultrasound amplitude and frequency, sample orientation, and coefficient of dynamic viscosity. To this end, we analyzed the motion of a probe screw dislocation under the action of US in the field of a fixed like master screw dislocation of the same sense.

2. MODEL AND ALGORITHM

We considered the motion of a screw dislocation with allowance for its cross slip in NaCl crystals. The (011) plane was the plane of easy slip, and (100) was the plane of cross slip (Fig. 1a).

Dislocations were taken to be linear, infinite, and parallel to the $[01\bar{1}]$ axis. It is convenient to observe the mutual arrangement of the dislocations in the projection onto the $(0\bar{1}1)$ plane (*xy* plane in Fig. 1b). The location of each dislocation is characterized by a point with coordinates *x*, *y*. The master dislocation *1* runs along the *z* axis. The probe dislocation *2* of the same sense is parallel to the *z* axis and can move in the *xz* planes of easy slip and in the *yz* planes of cross slip (their traces are shown as dashed lines in Fig. 1b) that are normal to them. A crystal was subjected to US tension–compression deformation along the *d*–*d* axis lying in the (001) plane at an angle θ to the [010] fourfold axis (Fig. 1a).

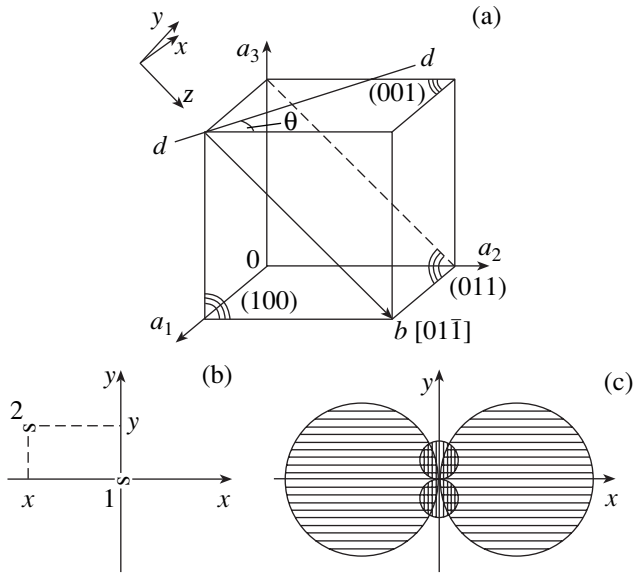

Fig. 1. (a) Planes of easy slip (011) and cross slip (100) in an NaCl crystal, (b) arrangement of the points of emergence of dislocations onto the $(0\bar{1}1)$ plane, and (c) regions in which a probe dislocation cannot be present in the absence of US.

1063-7834/03/4505-0880$24.00 © 2003 MAIK "Nauka/Interperiodica"

The trajectory of dislocation *2* is determined from the equation of viscous motion:

$$B\mathbf{V} = \mathbf{F}_1 + \mathbf{F}_2 + \mathbf{F}_3, \quad (1)$$

where $\mathbf{V}$ is the dislocation velocity, B is the coefficient of dynamic viscosity, $F_1 = m\sigma b$ is the force acting on the dislocation and induced by the applied load (b is the modulus of the Burgers vector, σ is the stress changing harmonically with time, and m is the corresponding Schmid factor), $F_2 = b\tau^{st}$ is the force analogous to the maximum dry friction force (τ^{st} is the threshold stress for the dislocation to start), and $F_3 = b\tau$ is the force caused by the spatially nonuniform field of internal stresses τ induced by the interaction between the dislocations [2].

In the chosen coordinate system (Fig. 1b), Eq. (1) of the motion of the probe dislocation in the basic slip plane *xz* and in the cross slip plane *yz* (normal to it) can be rewritten in the form

$$V_x = dx/dt = (b/B)\tau_1^{eff}, \quad V_y = dy/dt = (b/B)\tau_2^{eff}. \quad (2)$$

Here, τ_i^{eff} are the effective resolved shear stresses operating in the basic ($i = 1$) and normal ($i = 2$) slip planes, which are written as $\tau_i^{eff} = (m_i\sigma + \tau_i) - \tau_i^{st}\,\mathrm{sgn}(m_i\sigma + \tau_i)$, where $\tau_1 = kx/(x^2 + y^2)$, $\tau_2 = ky/(x^2 + y^2)$, $m_1 = (\cos^2\theta)/2$, $m_2 = -(\sin 2\theta)/(2\sqrt{2})$, and $k = Gb/2\pi$. Here, G is the shear modulus; $\sigma = \sigma^0 \sin 2\pi ft$; σ^0 and f are the US amplitude and frequency, respectively; and t is the time.

The passage of a straight-line screw dislocation from an easy-slip plane to a cross-slip plane and vice versa is determined by the ratio of the components of the effective resolved shear stresses operating in these planes [3].

The passage condition is determined by the following set of inequalities:

$$|m_1\sigma + \tau_1| - \tau_1^{st} > 0, \quad (3)$$

$$|m_2\sigma + \tau_2| - \tau_2^{st} > 0, \quad (4)$$

$$|\tau_1^{eff}| > |\tau_2^{eff}|, \quad (5)$$

$$|\tau_2^{eff}| > |\tau_1^{eff}|. \quad (6)$$

When condition (3) or (4) is satisfied, the dislocation can start moving on the corresponding slip plane, since the force acting on the dislocation exceeds the dry-friction-type force. When both conditions are satisfied, the dislocation should move in the easy-slip plane if inequality (5) is valid and in the cross-slip plane if inequality (6) is valid.

As the dislocation moves in the easy-slip plane in a spatially nonuniform stress field or under the effect of an applied load changing in time, it can pass to the cross-slip plane and then again come back to an easy-slip plane parallel to the initial one. We will call the distance between the initial and final easy-slip planes the height of ejection.

Repulsive forces act between the master and probe dislocations. In the absence of an external field, the probe dislocation remains motionless in the field of the master dislocation because of friction forces if it is located in the region

$$|\tau_1| \le \tau_1^{st} \quad \text{and} \quad |\tau_2| \le \tau_2^{st}, \quad (7)$$

that is, beyond circles of radii $r_1 = k/2\tau_1^{st}$ and $r_2 = k/2\tau_2^{st}$, which are marked in Fig. 1c by horizontal and vertical hatching, respectively. In these regions, the dislocation can reside in a stationary state in a real crystal in the absence of an applied load.

For simulation, we used the following algorithm. Let, at the instant t, the probe dislocation be at a point with coordinates (x, y) with effective shear stresses τ_1^{eff} and τ_2^{eff} operating in the easy-slip and cross-slip planes, respectively. By comparing the magnitudes of $|\tau_1^{eff}|$ and $|\tau_2^{eff}|$, we find the largest magnitude and, thus, determine the plane in which dislocations will move. The displacements Δx or Δy within the time interval Δt are obtained from the equations of viscous motion (2). Then, at the instant $t + \Delta t$, the probe dislocation will be at a point with coordinates $(x + \Delta x, y)$ or $(x, y + \Delta y)$. This procedure is repeated at each time step. As a result, we obtain the trajectory of the probe dislocation.

Since the dislocation displacement Δx (or Δy) and, hence, the dislocation trajectory depend on the time interval Δt, we choose the time step Δt^* such that the trajectory remains unchanged at $\Delta t < \Delta t^*$. This condition is fulfilled if Δx or Δy in each time step does not exceed 2×10^{-8} m.

The joint action of the applied load and the internal stress is identical for the dislocation starting to move from the left to the right during a positive US half-cycle and for the dislocation starting to move from the right to the left during a negative US half-cycle. Therefore, it is sufficient to solve the problem for one of these conditions.

We consider the case where the dislocation starts during a positive US half-cycle from any point in space satisfying conditions (7).

For calculations, we used the values $G = 1.8 \times 10^{10}$ Pa, $b = 3.99 \times 10^{-10}$ m, $\tau_1^{st} = 0.3$ MPa, and $\tau_2^{st} = 1.5$ MPa characteristic of an NaCl crystal [4].

Simulation showed that the dislocation motion depends on the US amplitude and frequency, the crystallographic orientation of the sample, and the coeffi-

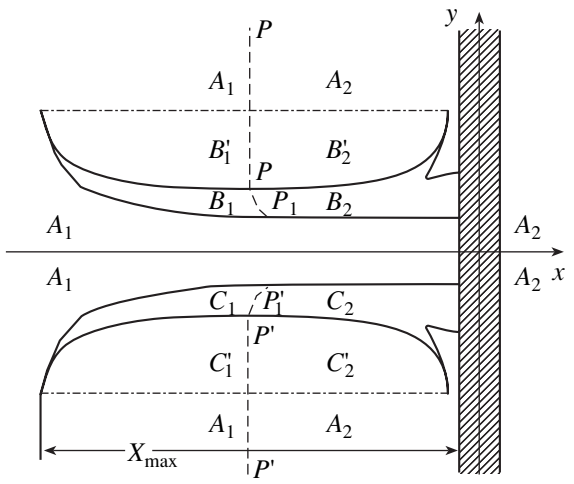

Fig. 2. Schematic representation of the possible arrangement of starting regions.

cient of dynamic viscosity. Therefore, we varied the parameters σ^0, f, θ, and B in the course of simulation.

Owing to the symmetry of the problem, it was sufficient to consider the angular range $0 \le \theta \le 90°$. Following experiments, we varied the US frequency in the range 40–100 kHz and chose the upper US amplitude ($\sigma^0 = 12.5$ MPa) to be lower than the stress required for dislocation multiplication [5]. The coefficient of dynamic viscosity was varied from 0.021 to 0.1 mPa s following the experimental data from [6]. The variation of this coefficient is of particular interest, since B is the only parameter that changes with temperature in the given crystal.

3. RESULTS AND DISCUSSION

In the case of an alternating load, time becomes an important parameter. Which of the pairs of inequalities (3)–(6) will be satisfied at a given instant depends on both the coordinates of the gliding dislocation and the US oscillation phase. Figuratively, for cross slip to be realized, the moving dislocation must be at the appropriate point in the field of the master dislocation at the correct time.

Starting from an arbitrary point of the space on an easy-slip plane, the dislocation may not fall into the place where passage into a cross-slip plane is possible in the correct time. In other words, when starting from certain regions of the crystal space, the dislocation may undergo cross slip, whereas starting from another region it does not undergo cross slip. The trajectory of the probe dislocation in this case depends on the coordinates of the start of dislocation (x_0, y_0). Therefore, the whole space is divided into a number of regions depending on the trajectory type. Hereafter, we will call these regions starting regions.

The possible arrangement of starting regions is schematically shown in Fig. 2. The dislocation cannot be in the shaded area at the initial instant (when $\sigma = 0$), since conditions (7) are not fulfilled for it. Therefore, we exclude this area from consideration. If the dislocation is in a starting region at the end of an US period (nT, where $n = 1, 2, ...$), its further motion will occur as if it started from this region. Hence, it is sufficient to consider only the first US period to completely describe the trajectory of motion.

If the dislocation starts from regions A_i (Fig. 2), it will not undergo cross slip and will always remain in the initial easy-slip plane. Its motion can be described by the superposition of an oscillating motion and drift, i.e., by a relatively slow directed displacement caused by the field of the master dislocation superimposed on its oscillating motion. Because of the existence of dry-friction-type forces, the dislocation is immobile in certain time intervals.

Starting from the region A_1, the dislocation drifts toward lower x with time; we could say that the dislocation is "rejected" by the field of the master dislocation. Starting from the region A_2, it drifts toward higher x with time. The region A_2 can be divided into two parts. When starting from the part with an initial coordinate $x_0 < 0$, the dislocation overcomes the field of the master dislocation, whereas when starting from the region with an initial coordinate $x_0 \ge 0$, it is forced out by this field.

The dislocation initially located in the regions B_i, C_i, B_i', or C_i', where $i = 1$ or 2, undergoes cross slip during its motion. If it starts from the regions B_i or B_i', cross slip is directed toward higher y values, whereas upon starting from the regions C_i or C_i', it is directed toward lower y.

If the probe dislocation is in the regions B_1 or B_2 at $t = 0$, it undergoes cross slip even in the first US period. Starting from the region B_1, the dislocation can fall into either the region B_1 or B_1' at the end of the US period as a result of cross slip, whereas starting from the region B_2, it can find itself either in A_2 or B_2'. If the dislocation is in the regions A_1 or A_2 at the end of the period as a result of cross slip, it will move only on the basic slip plane and will gradually drift toward lower or higher x, respectively.

Since the dislocation is in the region B_1' or B_2' at the end of the US period, it drifts during one or more periods on the basic slip plane until it reaches the region B_1 or B_2 at the end of any US period. Then, the dislocation again undergoes cross slip. This process is repeated until the dislocation reaches the region A_1 or A_2 by the end of any US period because of multiple cross slip.

When starting from the region B_1' or B_2', the dislocation drifts on easy-slip planes toward lower or higher x, respectively, until it reaches the region B_1 or B_2 by the end of a certain period.

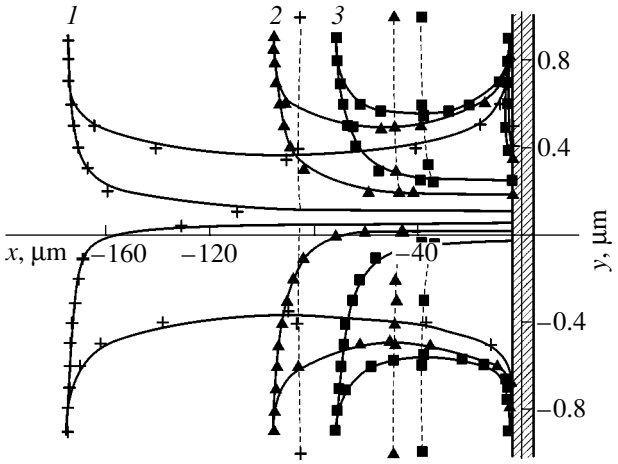

Fig. 3. Starting regions for a probe dislocation at θ = 20°, f = 60 kHz, B = 0.06 mPa s, and various US amplitudes σ^0: (*1*) 12.5, (*2*) 7.5, and (*3*) 6.0 MPa.

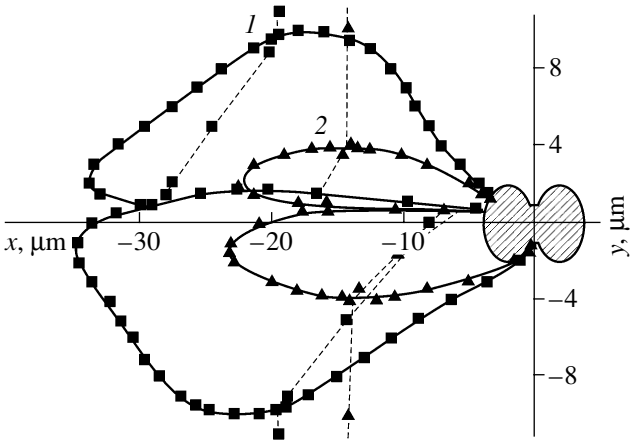

Fig. 4. Starting regions for a probe dislocation at θ = 50°, f = 60 kHz, B = 0.06 mPa s, and various US amplitudes σ^0: (*1*) 7.5 and (*2*) 6.0 MPa.

When starting from the region C_i or C_i', the dislocation behaves similar to the case where it starts from the region B_i or B_i', but cross slip is directed toward lower y values.

The dashed line that separates starting regions *1* from starting regions *2* in Fig. 2 is the projection of a certain surface onto the plane of Fig. 2. Starting from its sections P–P or P'–P', the dislocation comes back to its initial position at the end of every period; that is, it moves periodically without drifting. Starting from the sections P–P_1 or P'–P_1' of the surface, the dislocation moves to the P–P or P'–P' section, respectively, at the end of the first US period because of cross slip. Then, it moves periodically as was described above. We will call this surface the "entrapment surface."

The shape and size of the starting regions that provide cross slip for the dislocation depend on the US parameters, the coefficient of dynamic viscosity, and the crystallographic orientation of the sample.

For given f and B, the shape and size of these regions depend on σ^0 and θ.

Examples of the starting regions for various θ and σ^0 at f = 60 kHz and B = 0.06 mPa s are given in Figs. 3 and 4. As is seen, the shapes of the regions are substantially different at θ < 35.3° (Fig. 3) and θ > 35.3° (Fig. 4) (the angle θ = 35.3° corresponds the case $|m_1| = |m_2|$). As σ^0 increases, the starting regions grow. At θ < 35.3°, they grow predominantly along the x axis and at θ > 35.3°, along both the x and y axes. As σ^0 increases, the distance between the B_i and C_i regions decreases and the entrapment surface shifts toward lower x. If the angle θ increases under a constant US amplitude, the entrapment surface shifts toward higher x values.

We established that the variation of the shape and size of the starting regions with f and B are similar at various σ^0 and θ.

To illustrate the effect of f and B on the shape and size of the starting regions, we take two angles θ (20° and 50°), one of which is lower than 35.3° and the other is greater, at σ^0 = 7.5 MPa (Figs. 5, 6).

The starting regions at θ = 20° and B = 0.06 mPa s and various f values are given in Fig. 5 (curves *1–3*). It is seen that only the extent of these regions along the x axis (X_{max} in Fig. 2) changes, whereas the maximum size of these regions along the y axis remains unchanged. Similar starting regions for θ = 50° are shown in Fig. 6. The shapes of these regions are seen to

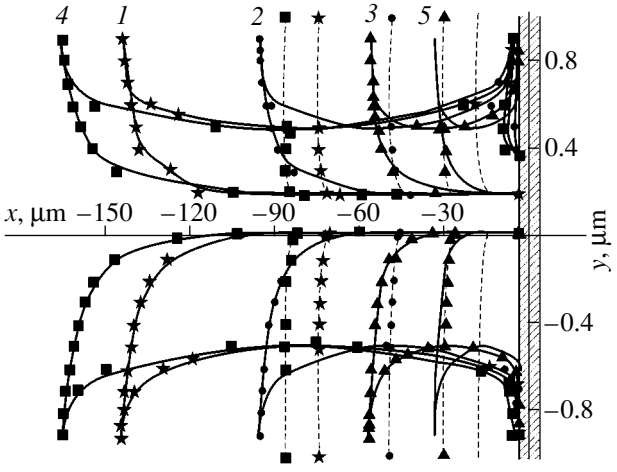

Fig. 5. Shapes and sizes of the starting regions for σ^0 = 7.5 MPa and θ = 20° at various f and B: (*1*) f = 40 kHz and B = 0.06 mPa s, (*2*) f = 60 kHz and B = 0.06 mPa s, (*3*) f = 100 kHz and B = 0.06 mPa s, (*4*) f = 100 kHz and B = 0.021 mPa s, and (*5*) f = 100 kHz and B = 0.1 mPa s.

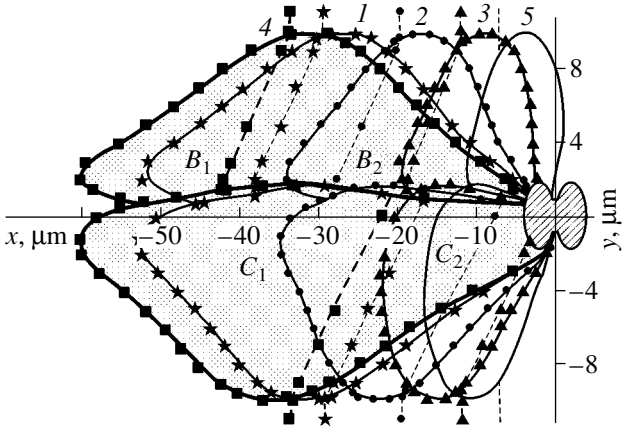

Fig. 6. Shapes and sizes of the starting regions for σ^0 = 7.5 MPa and θ = 50° at the *f* and *B* values given in Fig. 5.

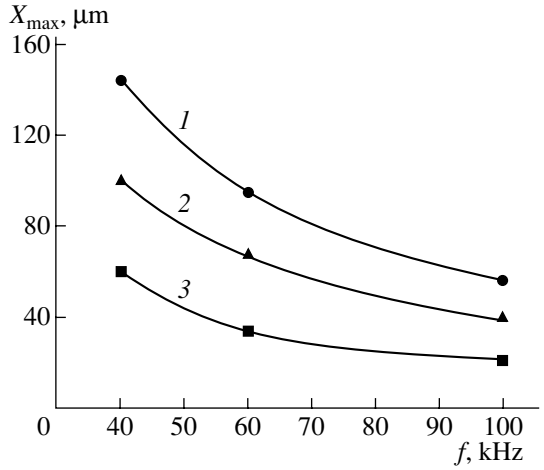

Fig. 7. Variations in the lengths X_{max} of the starting regions with the US frequency *f* at *B* = 0.06 mPa s, σ^0 = 7.5 MPa, and (*1*) θ = 20°, (*2*) 35.3°, and (*3*) 50°.

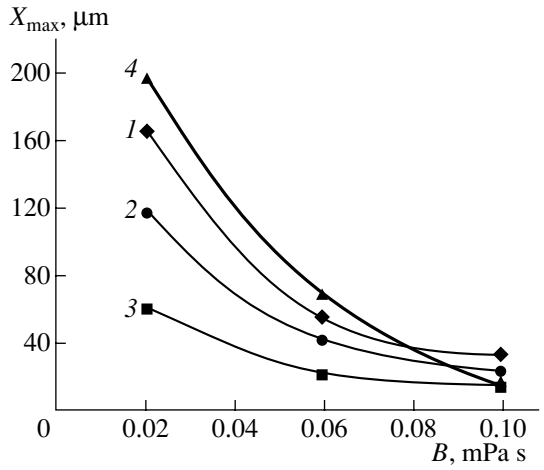

Fig. 8. Variations in the lengths X_{max} of the starting regions with the coefficient of dynamic viscosity *B* at σ^0 = 7.5 MPa and (*1*) *f* = 100 kHz and θ = 20°, (*2*) *f* = 100 kHz and θ = 35.3°, (*3*) *f* = 100 kHz and θ = 50°, and (*4*) *f* = 60 kHz and θ = 35.3°.

be different from those given above, and their variation with *f* is similar to that given above for θ = 20°. In both cases, the sizes of the regions decrease with increasing *f* due to a decrease in the length along the *x* axis.

The dependence of X_{max} on the US frequency at various angles θ (at *B* = 0.06 mPa s) is given in Fig. 7. As is seen, X_{max} and, hence, the size of the regions vary nonlinearly.

The starting regions at θ = 20° and 50°, *f* = 100 kHz, and various *B* are given in Figs. 5 and 6 (curves *3–5*). Similarly, only the length of regions along the *x* axis varies for both angles. The region size decreases with increasing *B*.

The dependences of X_{max} on *B* at *f* = 100 kHz and θ = 20°, 35.3°, and 50° are shown in Fig. 8 (curves *1–3*, respectively). Figure 8 also shows the dependence of X_{max} on *B* at θ = 35.3° and *f* = 60 kHz (curve *4*). The variation of the region sizes with *B*, like with *f* (Fig. 7), is also nonlinear. By comparing curves *2* and *4* in Fig. 8, we may conclude that the dependence of X_{max} on *B* becomes more pronounced as *f* decreases.

As *f* or *B* decreases, the entrapment surface shifts toward lower *x* values. At θ < 35.3° (Fig. 5) and various *f* and *B*, the ratios of the region pairs B_1 and B_2, B_1' and B_2', C_1 and C_2, and C_1' and C_2' remain approximately the same. At θ > 35.3° (Fig. 6), the ratios of the region pairs B_1 and B_2 and C_1 and C_2 change in favor of the regions B_1 and C_2 with increasing *f* and *B* up to virtually complete disappearance of the regions B_2 and C_1 (curve *5*, Fig. 6). Moreover, the regions B_1' and C_2' slightly increase as *f* or *B* increases. The regions B_1 and C_1 in Fig. 6 are shown only for *f* = 100 kHz and *B* = 0.021 mPa s (shaded area).

Simulation allowed us not only to determine the trajectory types of the probe dislocation starting from various regions of the space but also to gain insight into the time characteristics of cross slip and the heights of ejection. We found that the dislocation in an US field can undergo both single and multiple cross slip.

Calculations showed that the height and direction of ejections depend on σ^0, *f*, θ, *B*, and the initial coordinates of the probe dislocation. We will consider the dependences of the height of ejection on σ^0, *f*, θ, *B*, and the initial coordinates of the probe dislocation in detail in our next paper.

4. CONCLUSIONS

Thus, the algorithm proposed in this work and the software package developed allow us to comprehensively characterize the process of cross slip.

The model used makes it possible to determine regions such that a dislocation, starting from them, undergoes cross slip, as well as regions such that, starting from them, the dislocation will move only on an

easy-slip plane. We found the dependences of the shape and size of these regions on the US parameters, the crystallographic orientation of the sample, and the coefficient of dynamic viscosity. The dislocation in an US field was established to undergo both single and multiple cross slip.

REFERENCES

1. N. A. Tyapunina, V. V. Blagoveshchenskiĭ, G. M. Zinenkova, and Yu. A. Ivashkin, Izv. Vyssh. Uchebn. Zaved., Fiz., No. 6, 118 (1982).
2. J. P. Hirth and J. Lothe, *Theory of Dislocations* (McGraw-Hill, New York, 1967; Atomizdat, Moscow, 1972).
3. S. I. Igonin and A. A. Predvoditelev, Vestn. Mosk. Univ., Ser. 3: Fiz., Astron., No. 5, 588 (1975).
4. G. I. Nichugovskiĭ, V. I. Veselov, and G. V. Bushueva, Izv. Vyssh. Uchebn. Zaved., Fiz., No. 12, 68 (1988).
5. N. A. Tyapunina, E. K. Naimi, and G. M. Zinenkova, *Ultrasound Action on Crystals with Defects* (Mosk. Gos. Univ., Moscow, 1999).
6. V. I. Al'shits and V. L. Indenbom, Usp. Fiz. Nauk **115** (1), 3 (1975) [Sov. Phys. Usp. **18**, 1 (1975)].

Translated by K. Shakhlevich

Physics of the Solid State, Vol. 45, No. 5, 2003, pp. 886–889. Translated from Fizika Tverdogo Tela, Vol. 45, No. 5, 2003, pp. 843–846.

DEFECTS, DISLOCATIONS, AND PHYSICS OF STRENGTH

The Fracture Energy of Materials under Pulse Microsecond-Scale Loading

A. A. Gruzdkov, S. I. Krivosheev, and Yu. V. Petrov

Dinamika Research Center, St. Petersburg State University, Petrodvorets, 198504 Russia

e-mail: dyn@unicorn.math.spbu.ru

Received May 14, 2002; in final form, October 22, 2002

Abstract—Based on the results of fracture in polymethyl methacrylate and a spheroplastic using a magnetic-pulse setup, the specific work of the formation of a new surface is estimated, which is similar to Griffith's surface energy for quasi-static tests. The value obtained is greater than the corresponding value determined from the quasi-static tests by an order of magnitude and tends to increase as the loading time decreases. © *2003 MAIK "Nauka/Interperiodica".*

1. ENERGY APPROACH TO FRACTURE

A classical approach to fracture mechanics is the Griffith theory, which is based on the statement that a crack propagates if the total energy of a system $\mathscr{E}$ decreases [1–3]. The condition for crack growth in a slab of unit thickness is expressed as

$$\frac{d\mathscr{E}}{dL} = 2\gamma. \quad (1)$$

The quantity 2γ was initially interpreted by Griffith as the surface energy, since it represents the specific (per unit surface) work of the formation of a new surface. Irwin and Orowan [2, 3] showed that this quantity should be treated as the total work (including plastic work) in the fracture zone. It can be considered the resistance to a certain dissipative process that proceeds in a small region near the crack tip. Further study of this quantity is divided into ascertaining its physical nature, which is different for different classes of materials, and its experimental determination.

2. QUASI-STATIC AND DYNAMIC TESTS

For brittle fracture, in the case of the crack loading mode I, criterion (1) becomes equivalent to the critical stress-intensity factor [1]:

$$K_\mathrm{I} = K_\mathrm{Ic}.$$

For a linearly elastic body, Griffith's surface energy γ is

$$\gamma = \frac{K_\mathrm{Ic}^2}{2E}, \quad (2)$$

where E is Young's modulus. Thus, it is possible in this case to indirectly determine γ based on conventional K_Ic tests. One of the direct methods is the R-curve method [2]. Forces and displacements measured experimentally allow one to determine the work of applied forces for crack opening, which, in combination with the measurement of the crack length, gives the specific fracture energy. We should also mention the generalized Irwin–Griffith method [2], which is based on the simulation of crack extension via stress relaxation ahead of it.

Fracture under short-term loading was studied in many works attempting to use models with the specific fracture energy as a key parameter. However, the values determined in quasi-static tests, as a rule, did not provide satisfactory agreement with experimental data. The fact that the energy consumed per unit of surface area fracture substantially depends on time has been universally accepted [1]. The other parameters of dynamic fracture (the critical stress-intensity factor or the applied load amplitude) are also functions of time. These factors make the problem of determining the Griffith specific surface energy upon rapid fracture challenging.

Conventional methods for creating short-term loading do not allow us to adequately study energy balance, since it is rather difficult to precisely estimate the portion of energy transferred to a specimen. For example, impact loading provides only rough estimations of the parameters of loading. In general, complex energy transfer process occur between a specimen and a loading setup [4], which does not allow unambiguous determination of the moment of fracture. This is also true for widely used pendulum and hammer impact tests (e.g., for Charpy impact tests).

3. TESTS ON A MAGNETIC-PULSE SETUP

A technique using a magnetic-pulse setup is not complicated by the disadvantage described above. A load was formed by a magnetic-pulse method in which the mechanical pressure was specified by the spatial configuration of the current-carrying elements. Given a

current distribution, the parameters of the current pulse and the magnetic pressure are interrelated in a unique manner. The magnetic pressure for a set of planar busbars of width l with a uniform current distribution and $h/l \ll 1$, where h is the gap between the busbars, is determined as follows:

$$P_m(t) = \frac{\mu}{2}\left(\frac{I(t)}{l}\right)^2,$$

where $I(t)$ is the current and $\mu = 4\pi \times 10^{-7}$ H/m is the magnetic constant. The setup [5] used in experiments provides microsecond loading pulses with an amplitude of up to 1000 MPa.

The complex problem of determining the parameters of a mechanical pressure pulse is reduced in this case to a simple problem of measuring the parameters of an electric current pulse. Moreover, the energy state of a specimen at the instant of fracture can be determined exactly in many cases.

This is performed as follows. First, the pressure applied to the crack faces is monitored during the whole pulse duration (1–10 μs). Second, high-speed photography of the fracture process allows one to determine the instant when the crack starts propagating exactly, which can occur after unloading in some cases. Third, there is no interaction between the specimen and the setup after the completion of a loading pulse, which means that the system becomes energetically closed.

These principles have been actualized for testing specimens with a cutout imitating a macrocrack. Specimens were made of a spheroplastic material $120 \times 120 \times 10$ mm in size with a 60×2.2-mm cutout [6] and polymethyl methacrylate (PMMA) $200 \times 200 \times 10$ mm in size with a 100×3-mm cutout [7]. At the cutout corners, we made a thin notch 3 mm long and 0.2 mm wide. Uniform pressure created on the cutout faces was approximated by the relationship

$$P(t) = A\sin^2\frac{\pi t}{T}, \quad 0 \le t \le T. \tag{3}$$

We studied the dependence of the crack length L on the amplitude A of an applied load for each pulse duration T. We aimed at determining the threshold amplitude value. The dependences obtained were well approximated by straight lines (Fig. 1)

$$\Delta L = k(A - A_0), \quad \text{at} \quad A > A_0. \tag{4}$$

The quantity A_0 has the meaning of a threshold amplitude above which the crack starts growing. Its magnitude was found by extrapolating the experimental data to $\Delta L = 0$.

The minimum (threshold) fracture amplitudes obtained allow us to determine the incubation period of fracture [1]. For the materials studied, it was found to be 32 μs for PMMA [5] and 5.3 μs for spheroplastic [6].

The high-speed photography of the fracture process revealed that the crack propagation was delayed with respect to the maximum of the stress-intensity factor [8]. Fracture at threshold loads was shown to proceed with a delay close to the incubation period of fracture. The time it takes the crack to start propagating proved to be significantly longer than the time of the applied pressure pulse.

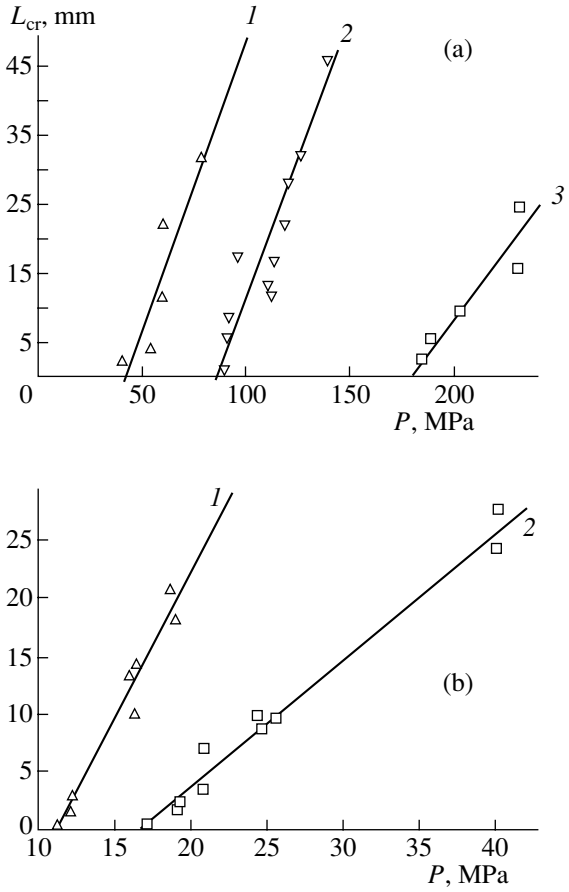

Fig. 1. Experimental data for determining the fracture threshold of specimens of PMMA and spheroplastic. (a) The length L_{cr} of a crack growing from the corner of a cutout in PMMA specimens as a function of the amplitude P of the breaking pulse at various times t of reaching the load peak: (*1*) $t = 4.6$, (*2*) 2, and (*3*) 1 μs. (b) The length L_{cr} of a crack growing from the corner of a cutout in spheroplastic specimens as a function of the amplitude P of the breaking pulse at various times t of reaching the load peak: (*1*) $t = 4.4$ and (*2*) 2.76 μs.

This experimental finding indicates that the whole energy of the applied load transforms into elastic and kinetic energy of the material upon loading specimens with pulses shorter than the incubation period of fracture; the process of crack propagation is then specified by this internal energy. Since the potential of the applied forces at the instant of fracture is equal to zero at the crack tip, we may assume that the function $\mathscr{E}$ in Eq. (1) coincides with the internal energy of the specimen.

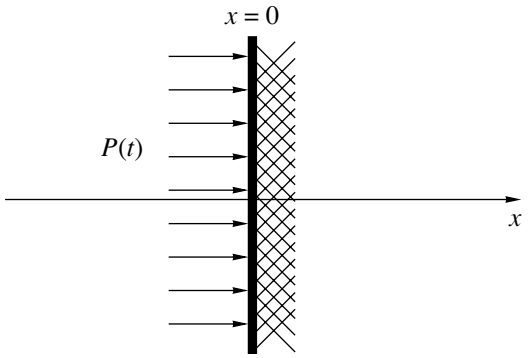

Fig. 2. Idealized schematic diagram for the calculation of the energy transferred to a specimen.

4. ENERGY BALANCE

We make an analytical estimation of the energy transferred to a specimen during its interaction with the setup. In the time of loading, a wave has no time to pass along the cutout faces edges; therefore, as a first approximation, we may consider the problem of a plane wave in half-space (Fig. 2):

$$U_{tt} - c^2 U_{xx} = 0,$$

$$U_x(0, t) = -\frac{P(t)}{c^2 \rho}, \quad U(x, 0) = 0, \quad U_t(x, 0) = 0.$$

Here, x and U are the coordinate and the displacement in the longitudinal direction, respectively; c is the velocity of the longitudinal wave; t is the time; and ρ is the density. The problem can easily be solved by d'Alembert's method. The solution has the form

$$U(x, t) = \begin{cases} 0, & x > ct \\ \dfrac{1}{c\rho} \displaystyle\int_0^{t - x/c} P(\xi) d\xi, & x < ct. \end{cases} \quad (5)$$

The energy transferred to the specimen (per unit area of the contact surface) is

$$\mathscr{E}_{\text{spec}} = \int_0^T P(t) dU(0, t). \quad (6)$$

Using Eq. (5), we find the velocity of the contact interface $U_t(0, t)$. Substituting it into (6), we finally find that

$$\mathscr{E}_{\text{spec}} = \frac{1}{c\rho} \int_0^T P^2(t) dt. \quad (7)$$

Equation (7) is valid for any pulse shape. Obviously, the contact area is HD, where D is the cutout length and H is the slab thickness. Taking (3) into account, we have

$$\mathscr{E} = \frac{HDA^2}{c\rho} \int_0^T \sin^4 \frac{\pi t}{T} dt = \frac{3DHA^2 T}{8c\rho}. \quad (8)$$

The relationship obtained allows us to estimate the energy transferred to the specimen. A similar estimation has also been performed using the finite-element method [9]. To this end, it was sufficient to carry out calculations for only the early stage of the process without allowance for fracture. The results of calculations using the finite-element method agree well with the estimation of the energy by Eq. (8).

Taking into account that the crack grows at $A > A_0$, we find the threshold energy $\mathscr{E}_0$. This is the critical energy that can be absorbed by the specimen without failure. We assume that the crack propagates due to an excess energy localized in the zone of radius $D_* = ct_*$, where t_* is the time from the instant of applying the load to the instant of fracture at the crack tip. In other words, the excess energy should be taken into account in the area where the signal is attained from the crack tip within the time t_*. Based on this assumption, we estimate the energy per unit length of the crack extension during its start.

It follows from Eq. (4) that the crack length increment is connected with the increment of the amplitude of the applied pressure pulse by the relation

$$dL = kdA.$$

As follows from (8), the energy increment is expressed by the formula

$$d\mathscr{E} = \frac{3DHAT}{4c\rho} dA.$$

Taking into account that the surface area formed due to crack growth is expressed as $dS = HdL$, we obtain the specific (per unit area) energy of fracture at the moment the crack starts

$$\left.\frac{d\mathscr{E}}{dS}\right|_{\Delta L = 0} = \frac{3TA_0 D}{4kc\rho}. \quad (9)$$

Substituting $D_* = ct_*$ for D in (9), where t_* is the time it takes for the crack to start and taking into account the second face of the cutout, we have

$$\frac{3TA_0 t_*}{2k\rho} = 2\gamma_d. \quad (10)$$

The quantity γ_d is an analog of the quantity γ in Eq. (1). Since c and ρ are the known parameters of the material and the magnitudes of A_0, k, and t_* have been experimentally determined for pulses of various duration T, Eq. (10) allows us to plot this quantity as a function of the loading time.

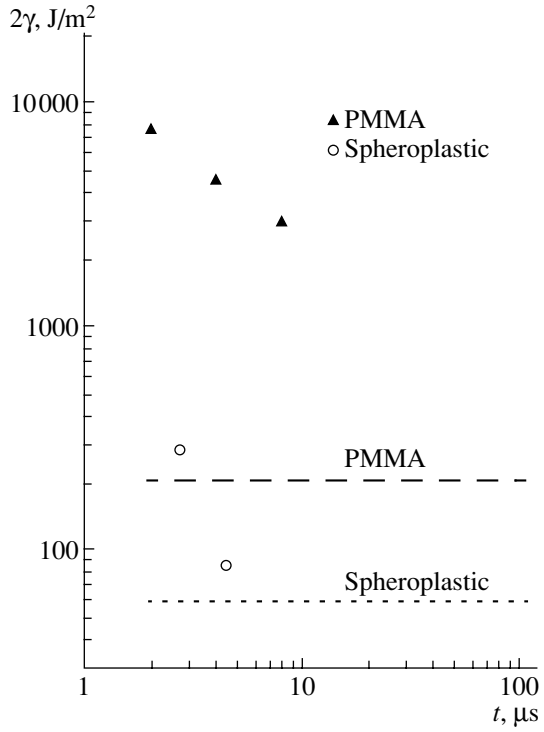

Fig. 3. Dependence of the fracture energy on the duration of a loading pulse (dashed line correspond to the quasi-static values).

5. DISCUSSION OF THE RESULTS

Figure 3 shows that the γ_d values for both materials studied are greater than the corresponding value calculated using Eq. (2) and based on quasi-static tests by more than an order of magnitude. However, as the loading time increases, its magnitude significantly decreases. For PMMA, the values calculated using Eq. (9) fall on a straight line in the logarithmic coordinates:

$$\log\gamma_d + \alpha\log T = \text{const},$$

which means that for microsecond-scale loading the following relationship holds:

$$\gamma_d T^{\alpha} = \text{const}. \qquad (11)$$

ACKNOWLEDGMENTS

This work was supported in part by the St. Petersburg State University Grant Center (project no. E00-4.0-174), the Russian Foundation for Basic Research (project nos. 02-01-01035 and 00-01-05020), the FTsP of the Ministry of Industry and Science (project no. 40.010.11.1195), and the federal program "Integratsiya."

REFERENCES

1. N. F. Morozov and Yu. V. Petrov, *Problems of the Dynamics of Solid Fracture* (S.-Peterb. Gos. Univ., St. Petersburg, 1997).
2. A. Carlson, in *Theoretical and Applied Mechanics*, Ed. by W. Koiter (North-Holland, Amsterdam, 1977; Mir, Moscow, 1979).
3. V. Weiss and S. Yukawa, in *Proceedings of Symposium on Fracture Toughness Testing and Its Applications, Chicago, 1964* (Am. Soc. for Testing and Material, Philadelphia, 1965; Mir, Moscow, 1968), pp. 1–29.
4. Yu. V. Petrov and V. I. Smirnov, *Nonstationary Oscillations and Behavior of the Internal Energy of One-Dimensional Bodies* (IPMASh Ross. Akad. Nauk, St. Petersburg, 2002).
5. S. I. Krivosheev, N. F. Morozov, Yu. V. Petrov, and G. A. Shneerson, Izv. Ross. Akad. Nauk, Mekh. Tverd. Tela **165** (5), 78 (1999).
6. S. A. Atroshenko, S. I. Krivosheev, Yu. V. Petrov, *et al.*, in *Proceedings of the 3rd Khariton Topical Scientific Readings on Extremal State of Substance, Detonation, and Shock Waves* (Vseross. Nauchno-Issled. Inst. Éksp. Fiz., Sarov, 2001), p. 131.
7. S. I. Krivosheev and G. I. Shneerson, in *Strength and Fracture of Materials and Constructions* (St.-Petersb. Gos. Univ., St. Petersburg, 1999), No. 18, p. 116.
8. A. N. Berezkin, S. I. Krivosheev, Yu. V. Petrov, and A. A. Utkin, Dokl. Akad. Nauk **375** (3), 328 (2000) [Dokl. Phys. **45**, 617 (2000)].
9. V. A. Bratov and A. A. Gruzdkov, in *Abstracts of International Youth Scientific Conference: XVII Gagarin Readings* (Mosk. Aviats.–Tekhnol. Inst., Moscow, 2001), p. 119.

Translated by K. Shakhlevich

Physics of the Solid State, Vol. 45, No. 5, 2003, pp. 890–894. Translated from Fizika Tverdogo Tela, Vol. 45, No. 5, 2003, pp. 847–852.

MAGNETISM AND FERROELECTRICITY

Ferromagnetic and Spin-Wave Resonance in Co/Pd/CoNi Multilayer Films

R. S. Iskhakov*, Zh. M. Moroz, L. A. Chekanova*, E. E. Shalygina***, and N. A. Shepeta******

** Kirenskii Institute of Physics, Siberian Division, Russian Academy of Sciences, Akademgorodok, Krasnoyarsk, 660036 Russia*

*** Siberian State University of Transport, Krasnoyarsk, Russia*

**** Moscow State University, Vorob'evy gory, Moscow, 119899 Russia*

***** Siberian Aerospace University, Krasnoyarsk, Russia*

e-mail: rauf@iph.krasn.ru

Received July 5, 2002

Abstract—It has been found that the magnitude and sign of exchange interaction between Co(5 nm) and CoNi(5 nm) ferromagnetic layers through Pd depend on magnetization orientation of ferromagnetic layers. If magnetization is oriented in a layer plane, exchange interaction can be both ferromagnetic and antiferromagnetic. If magnetization orientation is orthogonal to a layer plane, the exchange constant is always positive at $d_{Pd} < d_c$ and equals zero at $d_{Pd} > d_c$ (d_c is the characteristic length). *© 2003 MAIK "Nauka/Interperiodica".*

1. INTRODUCTION

A great number of experimental and theoretical papers [1, 2] are devoted to investigation of the magnetic properties of multilayer systems with alternative layers of ferromagnet/ferromagnet, ferromagnet/paramagnet, ferromagnet/diamagnet types. The interest in these systems is explained by the possibility of creating film materials with a set of necessary magnetic properties by selecting the thickness and chemical composition of individual layers. It is well known that ferromagnetic layers formed of Fe, Co, Ni, and their alloys and separated by nonferromagnetic layers of Ag, Pt, Cr, Cu, etc., can be exchange-coupled either ferromagnetically or antiferromagnetically depending on the nonferromagnetic layer thickness. This exchange interaction between ferromagnetic layers separated by a metal interlayer leads to the formation of a magnetically unified system in a multilayer film. As a result, the integral electrical and magnetic characteristics (remagnetization curve, perpendicular anisotropy, etc.) of these multilayer structures are mostly governed by some effective exchange interaction. At the same time, traditional methods (low-temperature run of saturation magnetization, neutron diffraction analysis, etc.) used to evaluate the exchange integral describing the interaction of a local magnetic moment with its nearest surroundings in ferromagnets turn out to be poorly informative for the study of effective exchange in multilayer structures. Resonance methods of investigation, i.e., ferromagnetic resonance (FMR) and spin-wave resonance (SWR), seem to be the only methods which allow both the detection of signals caused by this exchange-coupling effective constant and measurement of the value of this constant in such composite materials as ferromagnetic multilayer films.

In this paper, we report the results of an experimental study on the FMR and SWR spectra in a complex composition system, Co/Pd/CoNi multilayer films, with the aim of determining the effective exchange-coupling constant and of finding the dependence of this constant on the thickness of individual layers.

2. EXPERIMENTAL

The main attention in the work was paid to the study of the resonance characteristics of Co/Pd, Co/CoNi, and Co/Pd/CoNi multilayer films in two different orientations (external field parallel or perpendicular to the film plane). Experimental results allowed us to determine the exchange-coupling effective constants of these composite materials and to calculate partial values of the exchange-coupling constant in individual layers of a multilayer film.

SWR is known to be a very sensitive and specific method of investigation with certain requirements on the quality of the film (absence of macroscopic heterophase zones in the layer plane, narrow resonance-absorption line, etc.). We used a chemical precipitation method which allowed us to synthesize high-quality multilayer structures suitable for resonance investigation.

Let us consider FMR and SWR spectra of Co/Pd and Co/Pd/CoNi multilayer films. SWR spectra of these films were studied using a standard x-band spectrometer with a frequency of the resonator pumping $f = 9.2$ GHz at room temperature. For ferromagnetic films 200 nm thick, SWR is usually realized in the range of wavenumbers of standing spin waves from 10^5 to 10^6 cm^{-1}.

Multilayer films for the investigation were obtained through chemical precipitation from a water solution of

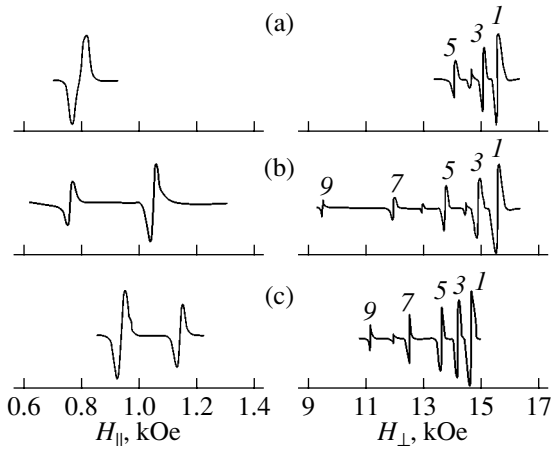

Fig. 1. Typical resonance spectra of three series of samples measured in two orientations: magnetic field ($H_{\parallel}$) parallel and ($H_{\perp}$) perpendicular to the film plane. (a) Co/Pd series; (b) Co/Pd/CoNi series; and (c) Co/CoNi series.

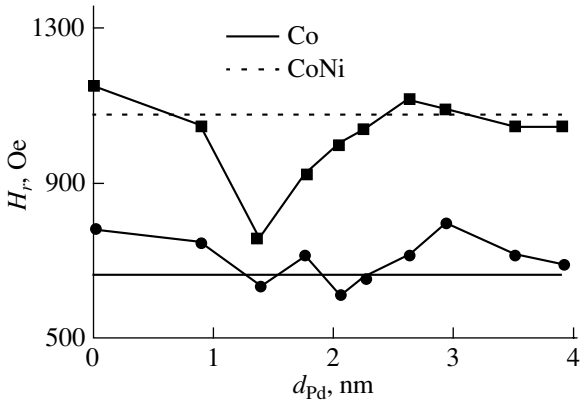

Fig. 2. The dependence of the ferromagnetic resonance fields of individual ferromagnetic layers on Pd-interlayer thickness in Co/Pd/CoNi films for samples oriented parallel to an external magnetic field.

the appropriate metal salts onto a glass substrate. The first series of samples consisted of three pairs of Co/Pd layers. The Co layer thickness d_1 = 5 nm was constant, and the Pd-layer thickness d_2 varied from 0.5 to 4 nm; the total thickness of the film did not exceed 30 nm. Previous x-ray study of Co–P thin films showed that, if 5–9 at. % P is introduced into a Co solution, the precipitate has the structure characteristic of a face-centered cubic (fcc) packing of atoms. Thus, the introduction of 7 at. % phosphorus provided fcc-structure in the Co layers in CoPd multilayer films and undistorted fcc-structure in the Pd layers precipitated on Co layers. The second series of samples under investigation differed from the first one in the introduction of an additional CoNi layer to the Co/Pd multilayer structure. The presence of 20 at. % Ni in the Co solution allowed us to form ferromagnetic layers with different magnetization in [Co/Pd/CoNi] $*$ 7 multilayer films. As in the first series of samples, the Co and CoNi ferromagnetic layer thicknesses were constant, d_1 = 5 nm, while the Pd-layer thickness d_2 varied from 0.5 to 4 nm; the total thickness of the [Co(5 nm)/Pd(x)/CoNi(5 nm)] $*$ 7 film varied from 70 to 130 nm. The third series of multilayer films was produced as [Co(X nm)/CoNi(X nm)] $*$ 10 type. The thicknesses of the Co and CoNi ferromagnetic layers were selected equal and varied from 2 to 10 nm, so that the total thickness of these films varied from 40 to 200 nm.

The resonance characteristics of these three series of samples, measured in two orientations (magnetic field parallel or perpendicular to the film surface), are shown in Fig. 1. As is evident from the experimental curves, the FMR spectrum in parallel geometry in Co/Pd samples is represented by a single resonance line, the coordinate (resonance field H_r value) and width ΔH_r of which weakly depend on Pd-layer thickness. This resonance field magnitude can be determined from a standard expression:

$$\frac{\omega}{\gamma} = [H(4\pi M_{\text{eff}} + H)]^{1/2}, \qquad (1)$$

where γ is the gyromagnetic ratio.

The films of the second and third series featured a specific FMR spectrum; at parallel orientation of both [Co(5 nm)/Pd(x)/CoNi(5 nm)] $*$ 7 and [Co/CoNi] $*$ 10 films to the external field, there were two distinct resonance peaks in the FMR spectrum, i.e., low-field (caused by Co layers) and high-field peaks (caused by CoNi layers). The dependences of resonance fields of individual ferromagnetic layers on Pd-layer thickness in Co/Pd/CoNi films are shown in Fig. 2. These results cannot be described using formula (1); therefore, it requires modification. When the film is oriented perpendicular to a magnetic field, the SWR spectrum is observed in all three series. SWR spectra in Co/Pd/CoNi and Co/CoNi films have as many as nine peaks and in Co/Pd films up to five peaks. The analysis of the spectra allows us to conclude that surface spin pinning similar to Kittel pinning takes place here; the intensities of odd peaks exceed those of even peaks by more than an order of magnitude. The angular dependence, peak-intensity behavior and the arrangement of the peaks indicate that spin-wave modes are observed in these films. Resonance fields of these modes are described by a standard Kittel expression:

$$\frac{\omega}{\gamma} = H - 4\pi M_{\text{eff}} + \frac{2A_{\text{eff}}}{M}\left(\frac{n\pi}{d}\right)^2, \qquad (2)$$

where n is a peak number, d is the total film thickness, and M_{eff} and A_{eff} are the basic parameters of the composite system requiring determination. By plotting H_r vs. the square of n, we can measure the value of A_{eff} experimentally. Dependences of the resonance field H_r

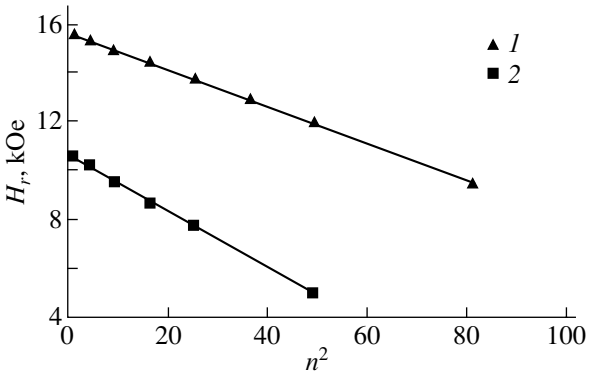

Fig. 3. Typical dependences of resonance field H_r on the square of the spin-wave mode index n of SWR spectra for Co/Pd/CoNi films. (*1*) [Co(5 nm)/Pd(0.9 nm)/CoNi(5 nm)] ∗ 7; and (*2*) [Co(5 nm)/Pd(2.7 nm)/CoNi(5 nm)] ∗ 7.

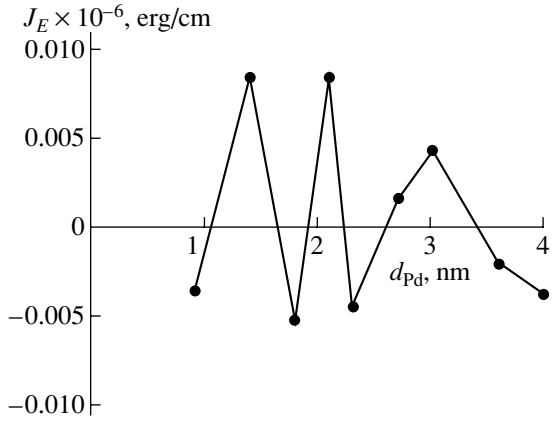

Fig. 4. The dependence of the constant of interlayer exchange interaction in Co/Pd/CoNi films on Pd-layer thickness as calculated from FMR spectra obtained at parallel orientation of the films in an external field.

on the square of the spin-wave mode n^2 of the SWR spectra in the [Co(5 nm)/Pd(x)/CoNi(5 nm)] ∗ 7 multilayer film series are shown in Fig. 3 (the SWR spectrum shape is shown in Fig. 1).

3. ANALYSIS OF EXPERIMENTAL RESULTS

Let us assume that the shift in the CoNi- and Co-layer resonance peaks in Co/Pd/CoNi multilayer films from the H_r values for reference films (Co and CoNi single-layer films were characterized by a single resonance peak corresponding to the conventional FMR) results from exchange modification of the value of the internal field in individual layers [3]. An expression for this exchange modification can be obtained using a model of a connected two-layer film system consisting of two ferromagnetic layers interacting through an intermediate nonmagnetic layer with interaction energy per unit area $E_{AB} = -J_E\mathbf{M}_A\mathbf{M}_B$, where J_E is the exchange-interaction constant and the vectors $\mathbf{M}_A$ and $\mathbf{M}_B$ denote magnetization in layers A and B, respectively [4]. If $d_A = d_B = d$ and the anisotropy field can be ignored ($H_{KeffA} = H_{KeffB} = 0$), we assume that it is possible to express the total energy for a two-layer system of interaction in the following form:

$$\begin{aligned} E &= [-(\mathbf{H}\mathbf{M}_A) + 2\pi M_A^2\cos^2\Theta_A]d \\ &+ [-(\mathbf{H}\mathbf{M}_B) + 2\pi M_B^2\cos^2\Theta_B]d - J_E\mathbf{M}_A\mathbf{M}_B. \end{aligned} \quad (3)$$

The dispersion relation for this system is defined by the solution to the Landau–Lifshitz equation and can be written as

$$\begin{aligned} &(\omega/\gamma)^4 - (\omega/\gamma)^2[H4\pi(M_A + M_B) \\ &+ 8\pi J_E M_A M_B + J_E^2(M_A + M_B)^2] + H^2 16\pi^2 M_A M_B \\ &+ H16\pi^2 M_A M_B J_E(M_A + M_B) \\ &+ H4\pi J_E^2(M_A + M_B)(M_A^2 + M_B^2) = 0. \end{aligned} \quad (4)$$

At large values of J_E, this relation has roots corresponding to acoustical and optical oscillations of magnetization vectors in the A and B ferromagnetic layers. If $J_E \longrightarrow 0$, there are also two roots which describe two resonance curves for zones with different magnetization values (M_A, M_B):

$$\begin{aligned} \left(\frac{\omega^2}{\gamma^2}\right)_1 &= 4\pi M_A H + J_E M_B M_A, \\ \left(\frac{\omega^2}{\gamma^2}\right)_2 &= 4\pi M_B H + J_E M_A M_B. \end{aligned} \quad (5)$$

Plotting the experimental values of the resonance field for the two modes obtained from FMR spectra for the Co/Pd/CoNi multilayer film and fitting the curves calculated from equation (5) allows us to determine the dependence $J_E(d_{Pd})$ (see Fig. 4). The calculated $J_E(d_{Pd})$ magnitudes vary in the range from 0.005 to 0.01 erg/cm depending on the Pd-layer thickness. The oscillation period $J_E(d_{Pd})$ is equal to 0.7 nm. It can be seen that the $J_E(d_{Pd})$ dependence is described by the product of an oscillating function and some function f, which decreases with increasing d_{Pd}.

Our previous systematic investigation of the magnetooptical properties (Faraday effect, equatorial Kerr effect) of Co/Pd and Co/Pd/CoNi multilayer films [5, 6] revealed corresponding oscillations, which allows us to conclude that the electronic structure of these composite materials is different from that of Co single-layer films. Thus, analysis of the specific features in the FMR spectrum for Co/Pd/CoNi films, as well as of the specific features of magnetization curves for Co/Pd films, shows that individual ferromagnetic layers in these films are linked to each other through an interlayer exchange interaction J_E, the magnitude and sign of which change as the Pd-layer thickness varies.

We now consider the SWR spectra. Plotting the linear dependence $H_r(n^2)$ allowed us to calculate the exchange-coupling effective constant A_{eff} for the composite material formed by combinations of Co/Pd, Co/Pd/CoNi, and Co/CoNi multilayer films. For example, it can be seen from dependence $A_{\text{eff}}(d_{\text{Pd}})$ for Co/Pd/CoNi films in Fig. 5 that, while d_{Pd} changes from 1 to 3 nm, the value of A_{eff} increases monotonically; at $d_{\text{Pd}} > 3$ nm, it is evidently equal to zero. The latter fact means that there are no standing spin waves which propagate through the entire sample thickness in Co/Pd/CoNi multilayer films with Pd-layer thicknesses exceeding 3 nm; i.e., $A_{\text{eff}}(d_{\text{Pd}} > d_c) = 0$. An important point is that the experimental $A_{\text{eff}}(d_{\text{Pd}})$ values for the Co/Pd/CoNi system are considerably smaller than the reference A_{eff} values calculated for Co and CoNi ferromagnetic films. Co and CoNi single-layer 200-nm-thick films were chosen as reference samples. The SWR spectra were measured, the $H_r(n^2)$ dependences were constructed, and then the A values were measured for reference films at perpendicular film orientation in an external magnetic field. The obtained reference values $A_{\text{Co}} = 1.2 \times 10^{-6}$ erg/cm and $A_{\text{CoNi}} = 0.5 \times 10^{-6}$ erg/cm coincide with the known tabulated values for similar film samples.

It should be noted that, according to the basic theory on employing the SWR method for multilayer structures, the exchange effective constant determined from SWR spectra for the multilayer structure under investigation (Co/Pd/CoNi) depends on both the partial exchange-coupling constant A_i, characteristic of Co and CoNi layers and the partial exchange between ferromagnetic layers that takes place through Pd layers. The following expression for determining exchange-coupling effective constant of a multilayer film in terms of partial exchanges in individual ferromagnetic metal layers, which form the multilayer system, was suggested in [7]:

$$\frac{d}{A_{\text{eff}}} = \frac{d_1}{A_1} + \frac{d_2}{A_2} + \ldots. \qquad (6)$$

Here, d_1 and d_2 are the thickness of different-composition individual layers in the multilayer films with A_1 and A_2 exchange constants, respectively, and $d = d_1 + d_2$ is the multilayer-film period. It is easy to show that, if the condition $d_1 = d_2$ is satisfied, expression (6) for A_{eff} is equivalent [8] to

$$A_{\text{eff}} = \langle A \rangle [1 - (\Delta A / \langle A \rangle)^2], \qquad (7)$$

where $\langle A \rangle = (A_1 + A_2)/2$, $\Delta A = A_1 - \langle A \rangle = \langle A \rangle - A_2 \equiv (A_1 - A_2)/2$.

Thus, expression (7) can be used to calculate partial exchanges for Co/CoNi films produced with equal thickness of the ferromagnetic layers.

The presence of up to nine peaks described by expression (2) in SWR spectra for these films and the linear dependence $H_r(n^2)$ allowed us to calculate the exchange-coupling effective constant A_{eff} for this [Co(x)/CoNi(x)] $*$ 10 system (curve *1*, Fig. 6). Taking into account that the thickness of the ferromagnetic layers for these multilayer films are equal, we used (6) and (7) to derive the following expression for the partial-exchange constant for CoNi:

$$A_{\text{CoNi}} = \frac{A_{\text{eff}}(\alpha + 1)}{2}. \qquad (8)$$

Here, the exchange-constant ratio $\alpha = A^c_{\text{CoNi}}/A^c_{\text{Co}}$ can be replaced by the reference-constant ratio obtained from SWR spectra for CoNi and Co reference single-layer films 200-nm thick. The obtained dependence $A_{\text{CoNi}}(d_{\text{Co, CoNi}})$ is shown in Fig. 6 (curve *2*).

It can be seen from the dependences shown in Fig. 6 that the effective- and partial-exchange constants in Co/CoNi films decrease drastically as the ferromag-

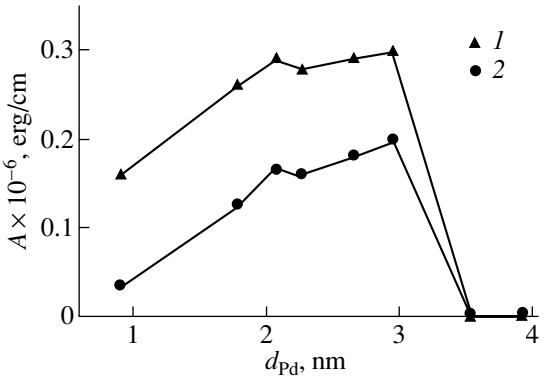

Fig. 5. (*1*) The dependence of the exchange constant obtained from SWR spectra at perpendicular orientation of Co/Pd/CoNi film samples in an external magnetic field on Pd-layer thickness, and (*2*) calculated dependence for the constant of exchange interaction through Pd layers A_{Pd}.

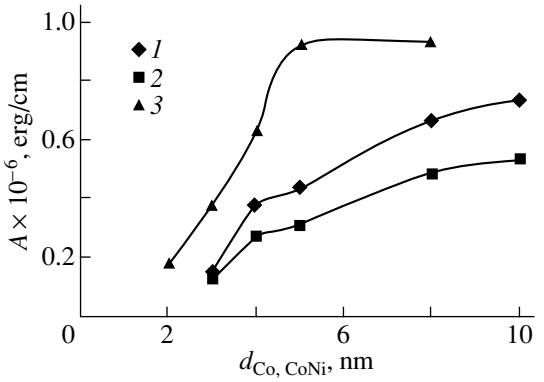

Fig. 6. The dependence of the exchange-coupling constant on Co and CoNi ferromagnetic-layer thickness: (*1*) results obtained from SWR spectra for Co/CoNi films; (*2*) magnitude of the exchange constant in CoNi layers of Co/CoNi films calculated using (8); and (*3*) the exchange constant obtained from the Bloch law ($T^{3/2}$) for [Co(x)/Pd(1.4 nm)] $*$ 25 samples.

netic-layer thickness decreases. For the samples with a ferromagnetic-layer thickness smaller than 5 nm, this value is smaller than the reference values obtained for Co and CoNi single-layer films. Therefore, for Co and CoNi layers each 5-nm thick, each partial-exchange constant should be assumed to be equal to 0.63×10^{-6} and 0.31×10^{-6} erg/cm, respectively. It should be noted that the exchange constants calculated from thermomagnetic curves (Bloch law) for Co/Pd films are consistent with the analogous values of A_{Co} and A_{CoNi} calculated from SWR spectra (curve *3*, Fig. 6).

Thus, having determined the partial-exchange constants in 5-nm-thick Co and CoNi layers and having rewritten expression (6) for the case Co/Pd/CoNi as

$$\frac{d_{Co} + d_{Pd} + d_{CoNi}}{A_{eff}} = \frac{d_{Co}}{A_{Co}} + \frac{d_{Pd}}{A_{Pd}} + \frac{d_{CoNi}}{A_{CoNi}}, \quad (9)$$

we can use experimental values of A_{eff} to calculate A_{Pd}, the constant of exchange coupling through Pd layers in [Co(5 nm)/Pd(x)/CoNi(5 nm)] $*$ 7 multilayer films. The calculations of A_{Pd} were carried out using the formula

$$A_{Pd} = \frac{A_{eff} d_{Pd}}{(2d_{Co,\,CoNi} + d_{Pd}) - A_{eff} d_{Co,\,CoNi}(1/A_{Co} + 1/A_{CoNi})}, \quad (10)$$

where $d_{Co,\,CoNi}$ and d_{Pd} are the ferromagnetic and palladium layer thickness, respectively, and A_{Co} and A_{CoNi} are the partial-exchange-coupling constants in the Co and CoNi layers.

The results of calculating, in this manner, the partial constant of exchange interaction through a Pd layer in relation to interlayer thickness for Co/Pd/CoNi multilayer films are also shown in Fig. 5. It can be seen that the calculated $A_{Pd}(d_{Pd})$ values are two to three times smaller than the A_{eff} values. However, the functional dependence $A_{Pd}(d_{Pd})$ turned out to be similar to the $A_{eff}(d_{Pd})$ dependence. The data shown in Fig. 5 suggest that $A_{Pd}(d_{Pd})$ is always positive and increases gradually as the palladium interlayer thickness increases up to a critical thickness d_c.

The results of our experiments show that the model usually used to describe ferromagnetic-layer interaction through a nonmagnetic metal layer and to define this interaction in terms of a quasi-Heisenberg isotropic Hamiltonian $J_{12}(d_y)\mathbf{M}_1 \cdot \mathbf{M}_2$ needs to be modified. The simplest modification consists in the following. It is known that an anisotropic Heisenberg Hamiltonian can be written as

$$H = -2\sum_{j>i}\sum [J_z S_i^z S_j^z + J_\perp (S_i^x S_j^x + S_i^y S_j^y)], \quad (11)$$

where S_i and S_j are the spins of neighboring atoms (the superscripts denote the spin-function components along the corresponding axes of the Cartesian system), J_z is the component of exchange-coupling constant along the z axis, and $J_\perp$ is the analogous component in the xy plane. Therefore, if the plane of the multilayer film under investigation coincides with the xy plane of a chosen coordinate system, only the $J_\perp$ component of the exchange-coupling constant can be determined from measuring FMR spectra at parallel orientation of the sample relative to an external magnetic field. In this case, it is reasonable to assume that SWR investigation yields information on the z component of the aforementioned quantity.

Thus, according to the above assumptions, it follows from our experiments that, in Co/Pd/CoNi multilayer films, the exchange constant component in the film plane (xy) features oscillating behavior with increasing palladium-layer thickness (FMR measurements), while the z component of the exchange constant (calculated from SWR spectra) gradually increases with increasing palladium-interlayer thickness up to a critical value and is always positive ($d < d_c$) or equal to zero ($d > d_c$). Therefore, the experimental results of our study indicate that there is an anisotropic exchange interaction in Co/Pd/CoNi multilayer films; these results can be described by introducing an anisotropic quasi-Heisenberg Hamiltonian

$$H = J_{12}^z(d_y) M_{1z} M_{2z} + J_{12}^\perp(d_y)(M_{1x} M_{2x} + M_{1y} M_{2y}). \quad (12)$$

Here, the FMR method is used to determine the value and form of the function $J_{12}^\perp(d_y)$ and the SWR method is used to determine the value and form of the function $J_{12}^z(d_y)$; the J components (as seen from the curves in Figs. 4, 5) may be characterized by completely different functional dependences.

ACKNOWLEDGMENTS

This work was supported by the Russian Foundation for Basic Research, grant Yeniseĭ-2002 no. 02-02-97717.

REFERENCES

1. Z. J. Wang, S. Mitsudo, and K. Watanable, J. Magn. Magn. Mater. **176**, 127 (1997).
2. P. Grunberg, J. Phys.: Condens. Matter **13**, 7691 (2001).
3. R. S. Iskhakov, Zh. M. Moroz, E. E. Shalygina, *et al.*, Pis'ma Zh. Éksp. Teor. Fiz. **66** (7), 487 (1997) [JETP Lett. **66**, 517 (1997)].
4. A. Layadi, J. Magn. Magn. Mater. **92**, 143 (1990).
5. R. S. Iskhakov, Zh. M. Moroz, I. S. Édel'man, and L. A. Chekanova, Pis'ma Zh. Éksp. Teor. Fiz. **63** (9), 735 (1996) [JETP Lett. **63**, 770 (1996)].
6. E. E. Shalyguina, N. I. Tsidaeva, R. S. Iskhakov, and J. M. Moroz, J. Magn. Soc. Jpn. **21** (S2), 181 (1997).
7. R. P. van Stapele, F. J. A. M. Greidanus, and J. W. Smits, J. Appl. Phys. **57** (4), 1282 (1985).
8. R. S. Iskhakov, Fiz. Tverd. Tela (Leningrad) **19**, 3 (1977) [Sov. Phys. Solid State **19**, 1 (1977)].

Translated by A. Titov

Physics of the Solid State, Vol. 45, No. 5, 2003, pp. 895–898. Translated from Fizika Tverdogo Tela, Vol. 45, No. 5, 2003, pp. 853–856.

MAGNETISM AND FERROELECTRICITY

Geometric Resonance in the Optical Properties of Microinhomogeneous $PdMn_xFe_{1-x}$ Alloys

N. I. Kourov*, Yu. V. Knyazev*, E. V. Zenkov, and A. S. Moskvin****

**Institute of Metal Physics, Ural Division, Russian Academy of Sciences, ul. S. Kovalevskoĭ 18, Yekaterinburg, 620219 Russia*
e-mail: kourov@imp.uran.ru
***Ural State University, pr. Lenina 51, Yekaterinburg, 620083 Russia*
Received July 8, 2002

Abstract—The optical properties of $PdMn_xFe_{1-x}$ ternary alloys in the homogeneous ferromagnetic (F_1, for $x \sim 0$) and antiferromagnetic (A, for $x \sim 1$) states, as well as in the microinhomogeneous state (at $x = 0.7$), are discussed. In the $x = 0.7$ alloy, the presence of nuclei of the low-resistivity, PdFe-type F_1 phase in the high-resistivity, PdMn-type A matrix was shown to produce a narrow maximum on the optical-conductivity $\sigma(\omega)$ curve at $E \sim 0.1$ eV, which is due to a geometric resonance associated with light scattering from phase inhomogeneities of the sample. The behavior of $\sigma(\omega)$ in the interband transition region is dominated by parameters of the electronic spectrum of both the A and F_1 phases. © *2003 MAIK "Nauka/Interperiodica".*

The $PdMn_xFe_{1-x}$ ternary alloy system is known to undergo, under variation of x, a transition from the antiferromagnetic state in PdMn ($T_N = 815$ K) to the ferromagnetic state in PdFe ($T_C = 730$ K) [1]. In the intermediate concentration range ($0.2 \le x \le 0.8$), alloys pass through a microinhomogeneous state, which as represented as a mixture of magnetical F_1 and A regions. Along the lines separating these regions, within which the moments are collinearly ordered, layers with a noncollinear magnetic order (F_2 phase) form. Considered from the structural standpoint, alloys of the intermediate concentration range consist of two $L1_0$-type phases which have different lattice parameters and degrees of tetragonality close to those observed in binary alloys of the boundary compositions.

Electronic band structure LMTO calculations show [2, 3] that the magnetic-cell doubling induced by A ordering of PdMn gives rise to a pseudogap of an unusually large width, $\Delta \sim 1$ eV, and depth (the density of states at the Fermi level $n(E_F)$ decreases almost by a factor of 20). At the same time, the relative shift of the spin subbands oriented along and counter to the spontaneous magnetization direction, which arises due to the F_1 ordering, does not entail anywhere near significant changes in the electronic-spectrum parameters in the vicinity of E_F.

As a result of these features in the band structure of the magnets under study, the electrical resistivity of PdMn grows strongly under A ordering to become $\rho_0 \sim 110$ μΩ cm at $T \sim 0$ K. Furthermore, the antiferromagnet PdMn exhibits, above 500 K, a "semiconducting" pattern (with a negative temperature coefficient of resistivity, TCR < 0) of the $\rho(T)$ relation [3, 4]. At the same time, experiments showed the ferromagnet PdFe to have $\rho_0 \sim 8$ μΩ cm, with the resistivity $\rho(T)$ following a typical "metallic" behavior (TCR > 0) over the entire temperature range studied. Alloys with intermediate concentrations reveal a still stronger growth of the residual resistivity and a fairly unusual temperature dependence of ρ [4]. When the metallic F_1 phase nucleates (in the form of platelets of various sizes [1, 5]) in the weakly conducting A matrix of $x \sim 0.8$ alloys, ρ_0 becomes greater than 200 μΩ cm.

Our optical studies of samples with $x = 0$ and 1 lend support to the electronic band structure calculations of these two magnets and agree with the measurements of their electrical resistivity.[1] The question of the optical properties of the microinhomogeneous $PdMn_xFe_{1-x}$ alloys is, however, left unanswered. The dispersion of the complex dielectric constant of such objects should be determined not only by the contributions due to band-to-band transitions and electron acceleration at E_F, which are common for homogeneous metals, but also by the contribution associated with light scattering from the phase inhomogeneities of the sample. Interference occurring in a microinhomogeneous material along specific directions and at specific wavelengths [depending on the actual dimensions and shape of the microinhomogeneities (clusters)] should bring about attenuation of reflected light, the so-called geometric resonance (see, e.g., [6]). For the alloy system under study, inclusion of the latter contribution is particularly important in samples with $x \sim 0.8$, whose weakly conducting PdMn-type matrix contains nuclei of the PdFe-type metallic phase with a dielectric constant dif-

[1] A more comprehensive discussion of the optical studies of PdFe (F phase) and PdMn (A phase) compound is published in journal *The Physics of Metals and Metallography.*

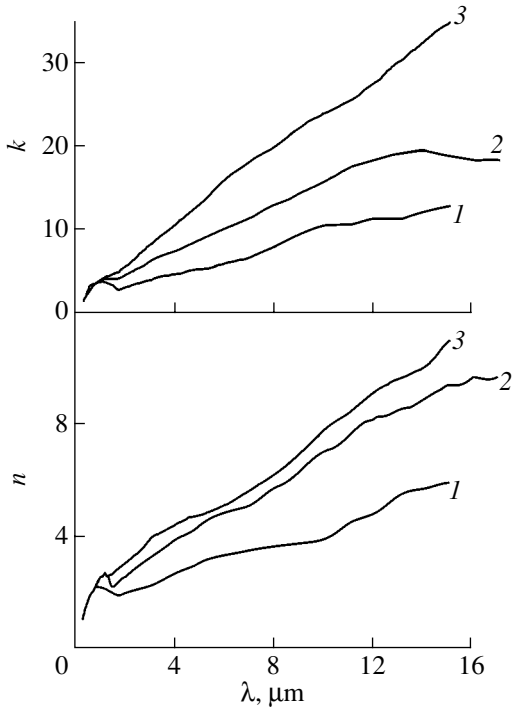

Fig. 1. Optical constants n and k plotted vs. wavelength of reflected light λ for alloys (*1*) PdMn, (*2*) $PdMn_{0.7}Fe_{0.3}$, and (*3*) PdFe.

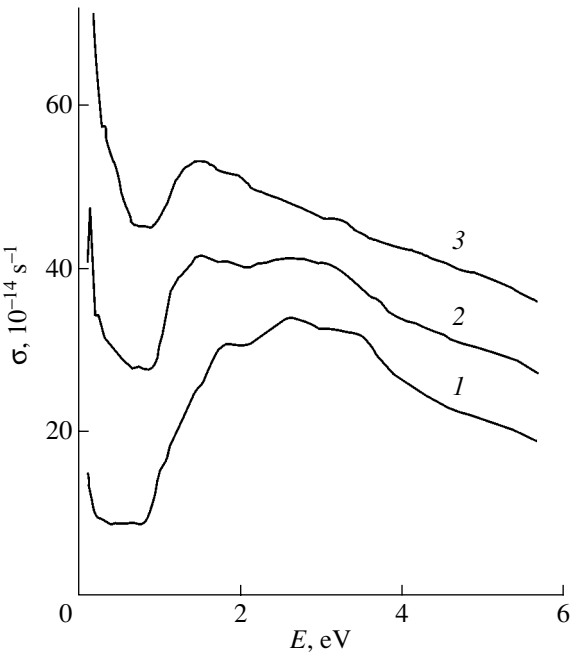

Fig. 2. Dispersion of the optical conductivity σ(ω) for (*1*) PdMn, (*2*) $PdMn_{0.7}Fe_{0.3}$, and (*3*) PdFe.

fering in magnitude from its value in the remainder of the sample.

We carried out a room-temperature study (T is much smaller than T_N and T_C) of the optical properties of the $PdMn_xFe_{1-x}$ system in the microinhomogeneous state for an $x = 0.7$ alloy. The measurements were performed in the photon energy range 0.083–5.64 eV or wavelength interval 15–0.22 μm. The optical refraction index n and the absorption coefficient k were determined polarimetrically with one reflection in the visible and UV regions and two reflections in the infrared range. In the preliminary stage of preparation, the reflecting surfaces of the samples were ground with abrasives of various grades, and in the final stage, polished by a diamond-based paste.

Figure 1 plots the optical constants n and k as functions of the wavelength λ of reflected light for a microinhomogeneous sample with $x = 0.7$. Also shown are the results of measurements of the optical constants for the homogeneous F-alloy PdFe and the A-compound PdMn. The $n(\lambda)$ and $k(\lambda)$ dispersion is seen to be characterized for $\lambda \geq 2$ μm by a monotonic growth. Significantly, as one goes from the homogeneous F-alloy PdFe to the $x = 0.7$ microinhomogeneous alloy and, particularly, to the A-compound PdMn, the values of n and k increase fairly strongly, thus showing that A ordering degrades the metallic properties of $PdMn_xFe_{1-x}$ alloys.

Figure 2 displays, in graphical form, the dispersion of optical conductivity $\sigma(\omega) = nk\omega/2\pi$ of the alloys under study. The $\sigma(\omega)$ relation for the microinhomogeneous sample with $x = 0.7$ measured in the photon energy range $1 \leq E \leq 6$ eV features a broad absorption band with two weakly pronounced maxima. A comparison of the $\sigma(\omega)$ curves in Fig. 2 suggests that these maxima for the $x = 0.7$ microinhomogeneous multiphase sample practically coincide in position with those observed for single-phase binary alloys with $x = 0$ and 1. An earlier analysis of the nature of optical absorption in the single-phase ferromagnet PdFe and the single-phase antiferromagnet PdMn revealed that the spectral profile of $\sigma(\omega)$ in this energy region derives from band-to-band electron transitions and depends on the structure of the energy spectrum of these compounds. We did not find any additional anomalies in the $\sigma(\omega)$ curve of the $x = 0.7$ microinhomogeneous sample which would be unaccountable for within the frame of band-to-band transitions with inclusion of the electronic spectra available for single-phase PdFe and PdMn alloys. Hence, the specific features of the microinhomogeneous state in $PdMn_xFe_{1-x}$ alloys manifest themselves in optical conductivity in the spectral region corresponding to the interband transitions, $E \geq 1$ eV, only in that the spectral profile of $\sigma(\omega)$ is determined here by the parameters of the electronic spectra of the PdFe- and PdMn-type phases making up this state.

More significant differences in the behavior of the $\sigma(\omega)$ curves between homogeneous samples of extreme composition and the $x = 0.7$ microinhomogeneous alloy are observed in the low-energy part of the spectrum, where the Drude approximation holds, as a rule, for metals. As seen from Fig. 2, for the homogeneous F-

alloy PdFe, this approximation does indeed hold. For the homogeneous *A*-compound PdMn, however, the Drude growth of $\rho(\omega)$ for $\omega \longrightarrow 0$ is seen to occur only in the region of extremely small values of ω. In the broad Drude interval $0.3 < E < 1$ eV, the $\sigma(\omega)$ curve of the PdMn antiferromagnet passes through a deep minimum. This behavior of $\sigma(\omega)$ in PdMn is accounted for by the existence of a deep pseudogap in its electronic spectrum near E_F.

The specific behavior of $\sigma(\omega)$ for the $x = 0.7$ microinhomogeneous alloy in the low-energy part of the spectrum can be described in the following way (Figs. 2, 3). First, as the photon energy decreases in this energy range, $\sigma(\omega)$ exhibits, as it were, a conventional Drude rise, which stops at $E \sim 0.1$ eV to form a narrow peak. A similar behavior of $\sigma(\omega)$ at low energies was observed earlier to occur in other inhomogeneous and even homogeneous metals. When seen in high-resistivity (inhomogeneous) alloys, such features in the optical properties found in the low-energy part of the spectrum were usually assigned to the existence of a narrow pseudogap at E_F [7], Anderson carrier localization induced by strong disorder in an alloy [8], formation at E_F of a narrow impurity band weakly hybridized with the electronic states of the matrix [9], many-particle correlation effects [10], etc. The low-frequency anomalies in $\sigma(\omega)$ observed in homogeneous metals were explained as being due to absorption in a near-surface layer of the sample where surface electronic states are present [11]. We do not exclude all these possible reasons for the appearance of the low-frequency anomaly in $\sigma(\omega)$, but suggest that geometric resonance plays here the major role, at least for the microinhomogeneous alloys under consideration.

Note that one should always expect geometric resonances to appear in the spectra of systems with inhomogeneities whose size is comparable in scale to the wavelength. It is known (see, e.g., [6]) that taking into account effects related to the presence of an interface separating two media with different values of the dielectric constant ε results in new solutions to equations describing physical phenomena (various surface modes). The various aspects of the physical behavior typical of composites derive from the significant part being played by the surface in these systems, which abound in interfaces. The appearance of geometric resonances in their optical spectra is connected with the singular behavior of local-field corrections to the polarizability of an inhomogeneous medium, of which one usually takes into account only the dipole terms described by relations of the type of the Clausius–Mossotti law [12]. For instance, the coupling of the internal field in an ellipsoidal particle with the external field is expressed through a tensor with the principal values $\frac{\varepsilon_m}{\varepsilon_m + L_i(\varepsilon - \varepsilon_m)}$, where ε and ε_m are the (scalar) dielectric constants of the external medium and of the particle and L_i are its depolarization factors, with $i = 1, 2, 3$. It follows that the polarizability should resonantly increase at the frequencies ω_i, which are roots of the equations $\mathrm{Re}(\varepsilon + L_i(\varepsilon - \varepsilon_m)) = 0$. A simple solution can be obtained by assuming ε to be a real constant and describing ε_m using the Drude expression. In this case, we have $\omega_i = \omega_p \sqrt{\frac{L_i}{\varepsilon - L_i(\varepsilon - 1)}}$, where ω_p is the plasma frequency. It follows, in particular, that the position of a geometric resonance depends, through the depolarization factors, on particle shape (which accounts for the corresponding resonance being called geometric).

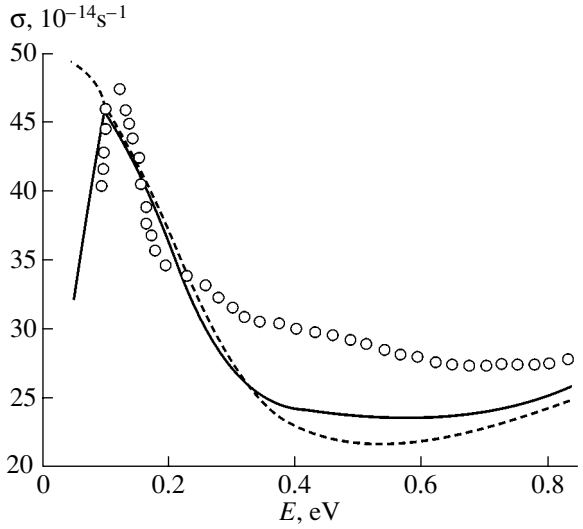

Fig. 3. Dispersion of the optical conductivity $\sigma(\omega)$ for $PdMn_{0.7}Fe_{0.3}$ in the IR region. The solid line is the conductivity $\sigma(\omega)$ calculated from Eq. (3) for metallic particles coated by an envelope, and the dashed line is that for particles without an envelope.

To verify the hypothesis of the resonance at $E = 0.1$ eV being of geometric origin, we calculated the optical conductivity of the $PdMn_{0.7}Fe_{0.3}$ inhomogeneous alloy in the effective-medium approximation. The complex dielectric constants of both alloy components were derived from the experimental data on the optical conductivity of boundary compositions, namely, of the antiferromagnet PdMn and the ferromagnet PdFe. The free-carrier contribution was taken into account with the Drude relation

$$\varepsilon = 1 - \frac{\omega_p^2}{\omega(\omega + i\gamma)}, \qquad (1)$$

and the contribution due to the band-to-band transitions was described by Lorentzians

$$\varepsilon = 1 + \frac{1}{\pi}\sum_k \frac{I_k}{\omega_k^2 - \omega^2 - i\omega\gamma_k} \qquad (2)$$

(their parameters are given in the table). In accordance with [1, 5], PdMn and PdFe particles were assumed to be disk-shaped. Furthermore, because a transition F_2

Parameters of the curves used to fit the contributions to the experimental spectra

Alloy	Parameters of Drude relation (1)		Parameters of Lorentzians (2)					
	Ω_p, eV	γ, eV	ω_1, eV	I_1	γ_1, eV	ω_2, eV	I_2	γ_2, eV
PdFe	5.56	0.3	1.4	250.07	2.4	3.7	364.43	4.95
PdMn	1.63	0.2	2.4	344.32	3.9			

phase with noncollinear magnetic order forms on the PdFe grain boundaries, the dielectric constant of grains was described by the well-known expression for an ellipsoid coated by an envelope. The transition phase F_2 differs in physical properties from the F_1 and A phases of the boundary compositions. The dielectric constant of the envelope was simulated by taking the experimental values of ε_{PdFe} and subtracting the free-carrier contribution from them. This can be justified by the fact that, while the carrier mobility in the F_2 transition phase is suppressed, the contributions due to interband transitions are related to intraatomic processes and, as such, are modified to a lesser extent by structural and magnetic fluctuations.

The effective dielectric constant of the alloy, ε_{eff}, was found from the equation

$$f\sum_i \frac{\varepsilon_1 - \varepsilon_{eff}}{\varepsilon_{eff} + L_i^{\langle PdFe\rangle}(\varepsilon_1 - \varepsilon_{eff})} + (1-f)\sum_i \frac{\varepsilon_{PdMn} - \varepsilon_{eff}}{\varepsilon_{eff} + L_i^{\langle PdMn\rangle}(\varepsilon_{PdMn} - \varepsilon_{eff})} = 0, \quad (3)$$

where

$$\varepsilon_1 = \frac{1}{3}\sum_i \hat{\varepsilon}\frac{(\hat{\varepsilon} - \varepsilon_{PdFe})(p(\hat{L}_1 - 1) - L_i^{\langle PdFe\rangle})}{(\hat{\varepsilon} - \varepsilon_{PdFe})(p\hat{L}_i - L_1^{\langle PdFe\rangle})}. \quad (4)$$

Here, $f = 0.45$ is the PdFe-particle concentration and L_i ($i = 1, 2, 3$) are the depolarization factors of particles of the two phases. In Eq. (4), $p = 0.5$ is the volume fraction of a PdFe particle occupied by an envelope and symbols with hats relate to the envelopes.

The calculated optical conductivities of the alloy are shown graphically in Fig. 3. The theoretical curve is seen to reproduce well the main features of the low-frequency experimental spectrum. The narrow peak at 0.1 eV appears in the calculated spectrum as geometric resonance. As follows from a comparison of a similar calculation made for metallic particles without envelopes (dashed line), taking into account the microscopic structure of alloy particles results in a nontrivial complication of the spectrum of a microinhomogeneous alloy already for the simplest version of the model.

Thus, our studies have shown that the predictions of band theory relating to alloys in which martensitic transformations and phase segregation can take place should be approached with caution. Indeed, nanoscopic inhomogeneities in such systems determine the scale size on which the ideal-crystal approximation is certain to be invalid and the physical properties suggest the possible appearance of new specific features. Their description becomes actually possible in terms of the classical theory of light propagation in inhomogeneous media. This approach makes it possible to address interpretation of the optical and magnetooptical properties of a broad class of systems with violated stoichiometry, such as doped cuprates ($La_{2-x}Sr_xCuO_4$, $YBa_2Cu_3O_{7-y}$) and manganites ($La_{1-x}M_xMnO_3$, La_xMnO_3), in a new way. We may add that the specific features of the optical conductivity of $La_{2-x}Sr_xCuO_4$ and $La_{1-x}Sr_xMnO_3$ observed in the infrared region can be related to geometric resonances [13, 14].

REFERENCES

1. N. V. Volkova, Yu. A. Dorofeev, V. A. Kazantsev, *et al.*, Phys. Status Solidi A **188** (3), 1115 (2001).
2. V. I. Anisimov and M. A. Korotin, Fiz. Met. Metalloved. **68** (3), 474 (1989).
3. N. I. Kourov, M. A. Korotin, and N. V. Volkova, Fiz. Tverd. Tela (St. Petersburg) **44** (2), 193 (2002) [Phys. Solid State **44**, 199 (2002)].
4. N. I. Kourov, Yu. G. Karpov, N. V. Volkova, and L. N. Tyulenev, Fiz. Met. Metalloved. **84** (6), 86 (1997).
5. A. V. Korolyov, N. V. Volkova, N. I. Kourov, and L. N. Tulenev, *Abstract Book EAST-MAG-2001, Yekaterinburg, Russia* (2001), p. 19.
6. H. C. van de Hulst, *Light Scattering by Small Particles* (Wiley, New York, 1957; Inostrannaya Literatura, Moscow, 1961).
7. A. S. Shcherbakov, A. F. Prekul, and N. V. Vol'kenshteĭn, Pis'ma Zh. Éksp. Teor. Fiz. **26**, 703 (1977) [JETP Lett. **26**, 540 (1977)].
8. Imry Yoseph, Phys. Rev. Lett. **44**, 469 (1980).
9. M. I. Katsnelson and A. S. Shcherbakov, Philos. Mag. B **46**, 357 (1982).
10. M. I. Katsnel'son and A. V. Trefilov, Pis'ma Zh. Éksp. Teor. Fiz. **40**, 303 (1984) [JETP Lett. **40**, 1092 (1984)].
11. V. P. Shirokovskiĭ, M. M. Kirillova, and N. A. Shilkova, Zh. Éksp. Teor. Fiz. **82** (3), 784 (1982) [Sov. Phys. JETP **55**, 464 (1982)].
12. J. A. A. J. Perenboom, P. Wyder, and F. Meier, Phys. Rep. **78** (2), 173 (1981).
13. A. S. Moskvin, E. V. Zenkov, and Yu. D. Panov, Fiz. Tverd. Tela (St. Petersburg) **44** (8), 1455 (2002) [Phys. Solid State **44**, 1522 (2002)].
14. A. S. Moskvin, E. V. Zenkov, and Yu. D. Panov, J. Lumin. **94–95**, 163 (2001).

Translated by G. Skrebtsov

Physics of the Solid State, Vol. 45, No. 5, 2003, pp. 899–902. Translated from Fizika Tverdogo Tela, Vol. 45, No. 5, 2003, pp. 857–860.

MAGNETISM AND FERROELECTRICITY

Entropy Contribution to Thermal Expansion of Rare-Earth Compounds

N. P. Kolmakova, L. V. Takunov, and O. A. Shishkina

Bryansk State Technical University, Bryansk, 241035 Russia

e-mail: npk@bitmcnit.bryansk.su

Received June 4, 2002; in final form, August 16, 2002

Abstract—The magnetoelastic contribution to the thermal expansion of orthorhombic rare-earth compounds is calculated to second order in perturbation theory. The entropy contribution to the free energy is found and analyzed. The case of higher, tetragonal symmetry is exemplified. © *2003 MAIK "Nauka/Interperiodica".*

1. Thermal expansion of rare-earth (RE) compounds at low temperatures is well known to be determined by the magnetoelastic contribution, which comes from the variation of the asphericity of the 4*f* shell of the RE ion with temperature. The corresponding anomalies in thermal expansion (i.e., the temperature dependences of the lattice parameters) vary widely in character depending on the RE ion and on the symmetry of its crystalline environment. Such anomalies have been observed experimentally in many RE compounds: RE intermetallides [1, 2], RE-paramagnetic garnets [3], RE zircons [4, 5], etc. As far as we know, the experimental data have been interpreted only in terms of the magnetoelastic contribution calculated to first order in perturbation theory. In this case, for crystals which have symmetry lower than cubic, the contribution from the magnetoelastic interaction to thermal expansion is proportional to the quadrupole moment of the RE ion, which is equal to the thermal average (over the eigenstates of the crystal-field Hamiltonian) of the corresponding second-order operator, e.g., the Stevens operator $O_2^0 = 3J_z^2 - J(J+1)$. Within this approach, the theory agrees qualitatively and even semiquantitatively with the experimental data. However, it is instructive to calculate the second-order corrections, which include, in particular, the entropy term in the free energy. In this connection, it should be noted that the theory developed in [6] in terms of generalized susceptibilities is not self-consistent, because the magnetoelastic contribution to the spontaneous strain is calculated to first order in perturbation theory while the other quantities (anomalous elastic constants, magnetostriction, etc.) are calculated to second order in perturbation theory.

In this paper, thermal expansion (fully symmetric spontaneous strain) is investigated theoretically and calculations are performed to second order in the magnetoelastic interaction Hamiltonian for orthorhombic RE-compound crystals. Expressions are derived for the entropy term in the free energy and for the magnetoelastic contribution to thermal expansion. The simpler case of tetragonal crystals is also considered. The results are compared with those obtained within the other approach mentioned above.

2. The Hamiltonian of the problem includes the crystal-field Hamiltonian $H_{\rm CF}$, the one-particle magnetoelastic interaction $H_{\rm ME}$, and the pairwise quadrupole interaction $H_{\rm Q}$:

$$H = H_{\rm CF} + H_{\rm ME} + H_{\rm Q} + E_{\rm Q} + E_{\rm el}. \qquad (1)$$

It is known that $H_{\rm CF}$ consists of nine invariants (i.e., it contains nine crystal-field parameters) in the case of the environment of the RE ion being orthorhombic and five invariants in the case of the environment being tetragonal. In the linear (harmonic) approximation in the strain-tensor components ε^μ and with allowance for only invariants consisting of second-rank operators, the Hamiltonian $H_{\rm ME}$ in the symmetric notation [7] has the form

$$H_{\rm ME} = -\alpha_J \sum_{m=0,\,2k=1}^{3} B_m^{\alpha k} \varepsilon^{\alpha k} O_2^m \qquad (2)$$

[the shear components of the strain tensor are dropped in Eq. (2)]. Here, α_J is the Stevens coefficient, $B_m^{\alpha k}$ are the magnetoelastic coefficients,

$$\varepsilon^{\alpha 1} = \frac{1}{\sqrt{3}}(\varepsilon_{xx} + \varepsilon_{yy} + \varepsilon_{zz}),$$

$$\varepsilon^{\alpha 2} = \sqrt{\frac{2}{3}}\left(\varepsilon_{zz} - \frac{\varepsilon_{xx} + \varepsilon_{yy}}{2}\right), \quad \varepsilon^{\alpha 3} = \frac{1}{\sqrt{2}}(\varepsilon_{xx} - \varepsilon_{yy}), \qquad (3)$$

$$O_2^0 = 3J_z^2 - J(J+1), \quad O_2^2 = J_x^2 - J_y^2.$$

The pairwise quadrupole interaction Hamiltonian $H_{\rm Q}$ in the molecular-field approximation can be written

1063-7834/03/4505-0899$24.00

(without regard for the shear components of the strain tensor) as

$$H_Q = -\alpha_J \sum_{m=0,2} K_{2m} Q_{2m} O_2^m. \quad (4)$$

The quadrupole moments Q_{2m} of the RE ion are

$$Q_{2m} = \alpha_J \frac{1}{Z} \sum_i e^{-W_i/T} \langle i|O_2^m|i\rangle. \quad (5)$$

In Eq. (1), E_Q is a correction commonly introduced in molecular-field theory:

$$E_Q = \frac{1}{2} \sum_{m=0,2} K_{2m} Q_{2m}^2. \quad (6)$$

The elastic energy (without the shear components ε^μ) is

$$E_{el} = \frac{1}{2} \sum_{i,k=1}^{3} C_0^{\alpha ik} \varepsilon^{\alpha i} \varepsilon^{\alpha k}, \quad (7)$$

where $C_0^{\alpha ik}$ are the symmetrized elastic constants in the absence of magnetic interactions [7].

We calculate the free energy $F = -T \ln Z$ (where Z is the partition function) to second order in one-ion magnetoelastic and pairwise quadrupole interactions $H_{ME} + H_Q$:

$$F = F_0 - \sum_{m=0,2} \left(\sum_{k=1}^{3} B_m^{\alpha k} \varepsilon^{\alpha k} + K_{2m} Q_{2m} \right) Q_{2m}^{(0)} - \frac{1}{2} \sum_{n,m=0,2} \chi_2^{nm} \left(\sum_{k=1}^{3} B_m^{\alpha k} \varepsilon^{\alpha k} + K_{2m} Q_{2m} \right) \times \left(\sum_{k=1}^{3} B_n^{\alpha k} \varepsilon^{\alpha k} + K_{2n} Q_{2n} \right) + E_{el} + E_Q. \quad (8)$$

The generalized strain susceptibility χ_2^{nm} is given by

$$\chi_2^{nm} = \alpha_J^2 \frac{1}{Z} \sum_j e^{-W_j/T} \left[\frac{\langle j|O_2^n|j\rangle \langle j|O_2^m|j\rangle}{T} - \sum_{r \neq j} \frac{\langle j|O_2^n|r\rangle \langle j|O_2^m|r\rangle^* + \langle j|O_2^n|r\rangle^* \langle j|O_2^m|r\rangle}{W_j - W_r} \right] - \frac{Q_{2n}^{(0)} Q_{2m}^{(0)}}{T} \quad (9)$$

and, as well as $Q_{2m}^{(0)}$, involves the eigenvalues and eigenfunctions of the unperturbed Hamiltonian H_{CF}. For tetragonal crystals, χ_2^{nm} vanishes for $n \neq m$; therefore, the nonzero strain susceptibilities are $\chi_\alpha \equiv \chi_2^{00}$ and $\chi_\gamma \equiv \chi_2^{22}$, which were considered in [6] within the generalized-susceptibility formalism. The physical interpretation of the strain susceptibilities is that they determine the relation between the quadrupole moments of the RE ion and the corresponding components of the strain tensor.

The free energy F in Eq. (8) contains the entropy contribution from the spontaneous strain and quadrupole moments. We write this contribution in the explicit form using the relation $F = U - TS$, where U is the internal energy:

$$F = U - TS = U - T[S_0 + S(\varepsilon^\mu, Q_{2m})],$$

$$S(\varepsilon^\mu, Q_{2m}) = \frac{1}{2T} \sum_{n,m=0,2} (\chi_2^{nm})' \left(\sum_{k=1}^{3} B_n^{\alpha k} \varepsilon^{\alpha k} + K_{2n} Q_{2n} \right) \times \left(\sum_{k=1}^{3} B_m^{\alpha k} \varepsilon^{\alpha k} + K_{2m} Q_{2m} \right). \quad (10)$$

The quantity $(\chi_2^{nm})'$ differs from χ_2^{nm} in Eq. (9) in that it does not contain the Van Vleck term responsible for the mixing of different states of the RE ion:

$$(\chi_2^{nm})' = \alpha_J^2 \frac{1}{Z} \sum_j e^{-W_j/T} \frac{\langle j|O_2^n|j\rangle \langle j|O_2^m|j\rangle}{T} - \frac{Q_{2n}^{(0)} Q_{2m}^{(0)}}{T}. \quad (11)$$

It follows from Eqs. (10) and (11) that the entropy contribution from the spontaneous strain and quadrupole moments to the free energy arises in second order in perturbation theory. Our calculations of the term $-TS(\varepsilon^\mu, Q_{2m})$ for equilibrium values of the strain and quadrupole moments for a large number of RE compounds for which the crystal field and quadrupole constants are known showed that this term is important; it exhibits a strong temperature dependence (nonmonotonic for many compounds studied) below 100 K, and its magnitude is not small even at liquid-helium temperature, 4.2 K. The entropy contribution decreases significantly at liquid-helium temperatures for certain compounds and vanishes as $T \longrightarrow 0$ K.

3. The fully symmetric spontaneous eigenstrains $\varepsilon^{\alpha i}$ ($i = 1, 2, 3$) can be found by minimizing the free energy F given by Eq. (8) and, for orthorhombic crystals, are rather cumbersome linear combinations of the quadrupole moments calculated for the eigenstates of the unperturbed Hamiltonian H_{CF}:

$$\varepsilon^{\alpha i} = \frac{1}{\Delta_C \Delta} \sum_{m=0,2} Q_{2m}^{(0)} \sum_{n=0,2} \omega_{nm} \sum_{k=1}^{3} B_n^{\alpha k} q_{ki}^{(C)}. \quad (12)$$

Using Eqs. (12) and (3), the magnetoelastic contributions to the parameters a, b, and c of the orthorhombic unit cell can be calculated in the ordinary way. In Eq. (12), Δ_C and $q_{ki}^{(C)}$ are the determinant and the cor-

responding algebraic adjunct, respectively, of the symmetrized [7] matrix of the elastic constants $C^{\alpha jl}$ [for example, $C^{\alpha 11} = \frac{1}{3}(2C_{11} + 2C_{12} + 2C_{13} + 2C_{23} + C_{33})$, etc.] and Δ is the determinant of the matrix ω_{nm}

$$\omega_{nm} = \begin{pmatrix} 1 - K_{22}\chi_2^{22} & K_{20}\chi_2^{02} \\ K_{22}\chi_2^{02} & 1 - K_{20}\chi_2^{00} \end{pmatrix}. \quad (13)$$

The elastic constants $C^{\alpha jl}$ renormalized by the one-ion magnetoelastic and pairwise quadrupole interactions are given by

$$C^{\alpha jl} = C_0^{\alpha jl} - \sum_{m,n=0,2} B_m^{\alpha j} B_n^{\alpha l} \frac{1}{K_{2m}} \left(\frac{\omega_{mn}}{\Delta} - \delta_{mn} \right). \quad (14)$$

For tetragonal crystals, there are only two nonzero spontaneous strain components and the expressions for them become much simpler:

$$\varepsilon^{\alpha 1} = \frac{B_0^{\alpha 1} C_0^{\alpha 22} - B_0^{\alpha 2} C_0^{\alpha 12}}{C_0^{\alpha 11} C_0^{\alpha 22} - (C_0^{\alpha 12})^2} \frac{Q_{20}^{(0)}}{1 - \chi_2^{00} G_{20}},$$
$$\varepsilon^{\alpha 2} = \frac{B_0^{\alpha 2} C_0^{\alpha 11} - B_0^{\alpha 1} C_0^{\alpha 12}}{C_0^{\alpha 11} C_0^{\alpha 22} - (C_0^{\alpha 12})^2} \frac{Q_{20}^{(0)}}{1 - \chi_2^{00} G_{20}}, \quad (15)$$

where

$$G_{20} = \frac{(B_0^{\alpha 1})^2 C_0^{\alpha 22} + (B_0^{\alpha 2})^2 C_0^{\alpha 11} - 2B_0^{\alpha 1} B_0^{\alpha 2} C_0^{\alpha 12}}{C_0^{\alpha 11} C_0^{\alpha 22} - (C_0^{\alpha 12})^2} + K_{20}.$$

Thus, in the simpler case of tetragonal crystals, one can see how the magnetoelastic interaction affects the temperature dependence of the fully symmetric spontaneous strains calculated to second order in this interaction. The quantity $(1 - \chi_2^{00} G_{20})$ in the denominator of Eq. (15) makes the temperature dependence of $\varepsilon^{\alpha 1, 2}$ stronger in comparison with that of the quadrupole moment $Q_{20}^{(0)}$.

4. It is obvious that the magnitude of this renormalization depends on the magnitude of the strain susceptibility $\chi_2^{00} \equiv \chi_\alpha$ and its temperature dependence, which, in turn, varies widely depending on the RE ion and its crystalline environment. For instance, from the temperature dependences of the quadrupole moment $Q_{20}^{(0)}$ and "enhanced" quadrupole moment $Q_{20}^{(0)}/(1 - \chi_2^{00} G_{20})$ presented in the figure for the tetragonal paramagnetic $TbPO_4$ with zircon structure, it is seen that the effect is noticeable at low temperatures. At the same time, for the analogous compound $TmPO_4$, the effect under study is insignificant (figure). Such a difference is due to the different relative positions of the lowest energy levels of the Tb^{3+} and Tm^{3+} ions in the phosphate structure: in Tb^{3+}, the lowest excited levels (singlets) are ~4 and ~10 cm^{-1} above the ground level (doublet), whereas in Tm^{3+}, the first excited level (doublet) is ~30 cm^{-1} above the ground singlet. Our calculations show that, in tetragonal compounds with a similar splitting of the RE ion levels (the ground orbital doublet and the low-lying first excited level), e.g., in intermetallic compounds $HoAg_2$ and $TmAg_2$, the effect under study is also significant (the values of the crystal-field parameters and G_{20} are taken from [8]).

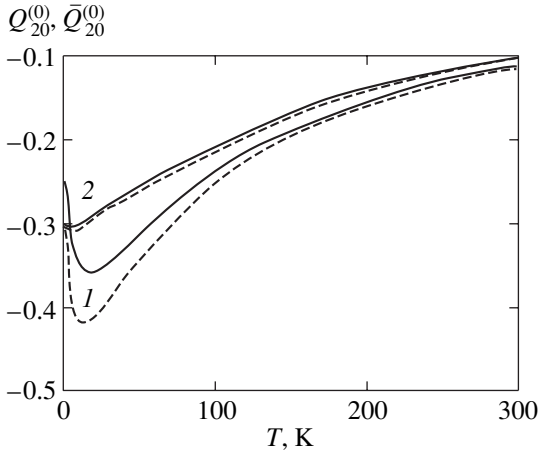

Temperature dependences of the quadrupole moment $Q_{20}^{(0)}$ (solid curves) and "enhanced" quadrupole moment $\bar{Q}_{20}^{(0)} = Q_{20}^{(0)}/(1 - \chi_2^{00} G_{20})$ (dashed curves) for (*1*) $TbPO_4$ and (*2*) $TmPO_4$.

Using the relations derived in this paper [Eq. (12) for orthorhombic crystals and Eq. (15) for tetragonal crystals] and the experimental data, it is found that, for compounds (such as $TbPO_4$, considered above) in which the second-order effect is significant, the calculated magnetoelastic constants $B_m^{\alpha i}$ are slightly smaller than their values obtained from the formulas in which the second-order corrections are ignored. However, one should take into account the restrictions on the accuracy with which these constants are determined, e.g., the restriction imposed by the quadrupole approximation used in the theory of magnetoelasticity; this approximation for RE zircons was analyzed in [5] (for RVO_4) and [9] (for RPO_4) with allowance for the variation in the phonon contribution depending on the RE ion. It should also be noted that the quadrupole constants G_{20} used to construct the figure were calculated in [10] from experimental data on the magnetic and magnetoelastic properties of RE phosphates RPO_4 within the approximation described in [6]; in that approximation, the spontaneous strain is calculated to first order in the magnetoelastic interaction and then the

basic Hamiltonian is constructed on the basis of the expressions obtained, while the effects caused by a magnetic field (such as magnetostriction) are calculated to second order in perturbation theory.

Thus, our calculations showed that second-order corrections should be taken into account in calculating fully symmetric magnetoelastic constants from experimental data on thermal expansion. Such a determination of $B_m^{\alpha i}$ is presently more realistic than their theoretical calculation, which requires knowledge of a large number of microscopic parameters of the compound under study.

ACKNOWLEDGMENTS

This study was supported by the Russian Foundation for Basic Research, project no. 00-02-17756.

REFERENCES

1. B. Lüthi and H. R. Ott, Solid State Commun. **33**, 717 (1980).
2. B. Lüthi, M. Niksch, R. Takke, *et al.*, in *Crystalline Electric Field Effects in f-Electron Magnetism*, Ed. by R. P. Guertin, W. Suski, and Z. Zolnierek (Plenum, New York, 1982), p. 233.
3. N. P. Kolmakova, R. Z. Levitin, V. N. Orlov, and N. F. Vedernikov, Phys. Status Solidi A **115**, K87 (1987); J. Magn. Magn. Mater. **87** (1), 218 (1990).
4. V. I. Sokolov, Z. A. Kazeĭ, N. P. Kolmakova, and T. V. Solov'yanova, Zh. Éksp. Teor. Fiz. **99** (3), 945 (1991) [Sov. Phys. JETP **72**, 524 (1991)].
5. Z. A. Kazeĭ and N. P. Kolmakova, Zh. Éksp. Teor. Fiz. **109** (5), 1687 (1996) [JETP **82**, 909 (1996)].
6. P. Morin, J. Rouchy, and D. Schmitt, Phys. Rev. B **37** (10), 5401 (1988).
7. E. de Lacheisserie, Ann. Phys. (Paris) **5**, 267 (1970).
8. P. Morin and J. Rouchy, Phys. Rev. B **48** (1), 256 (1993).
9. Z. A. Kazeĭ, N. P. Kolmakova, and O. A. Shishkina, Fiz. Tverd. Tela (St. Petersburg) **39** (1), 106 (1997) [Phys. Solid State **39**, 91 (1997)].
10. P. Morin and Z. Kazei, J. Phys.: Condens. Matter **11**, 1289 (1999).

Translated by Yu. Epifanov

Physics of the Solid State, Vol. 45, No. 5, 2003, pp. 903–906. Translated from Fizika Tverdogo Tela, Vol. 45, No. 5, 2003, pp. 861–863.

MAGNETISM AND FERROELECTRICITY

Exchange Constants for a V_{15} Magnetic Molecular Nanocluster

V. V. Kostyuchenko* and A. K. Zvezdin**

** Institute of Microelectronics and Informatics, Russian Academy of Sciences, Universitetskaya ul. 21, Yaroslavl, 150007 Russia*

*** Institute of General Physics, Russian Academy of Sciences, ul. Vavilova 38, Moscow, 119991 Russia*

Received September 17, 2002

Abstract—The spin structure and ground-state energies of a V_{15} magnetic molecular nanocluster are calculated using a modified Lanczos method. The exchange interaction constants for the V_{15} magnetic nanocluster (J = 290 K, J' = 60 K, J_1 = 30 K, J'' = 200 K, and J_2 = 68 K) are determined from the comparison of the calculated and experimental data. The exchange constants obtained differ significantly from those predicated earlier and permit one to describe quantitatively the magnetization of the V_{15} nanocluster in weak and strong magnetic fields. *© 2003 MAIK "Nauka/Interperiodica".*

1. INTRODUCTION

Macroscopic quantum phenomena (such as macroscopic quantum coherency and macroscopic quantum tunneling) have been intensively studied in magnetic molecular nanoclusters (see, for example, [1–3] and references therein). It should be noted that, for the most part, recent investigations have been concerned with macroscopic quantum phenomena occurring in magnetic molecular nanoclusters with a total integer spin. This is associated in part with the synthesis of Mn_{12} and Fe_8 magnetic molecular nanoclusters, which are convenient objects of investigation (see, for example, [3]). For magnetic nanoclusters with a large total integer spin, the steps arising in the hysteresis loop due to spin tunneling can be explained within the multiplet approximation without regard for the transition between the states with different total spins. The constant of exchange interaction between magnetic ions inside the molecule (~10^2 K) substantially exceeds the constant of interaction between the spins in neighboring molecules (~10^{-3} K). Therefore, the transitions between the states with different total spins require high energies (more than 10^2 K [4]).

A radically different situation is observed for a V_{15} magnetic molecular nanocluster of the chemical formula $K_6[V_{15}^{IV}As_6O_{42}H_2O] \cdot 8H_2O$. Polyoxovanadate V_{15} is of considerable interest for the study of molecular magnetism, because this compound is involved in very interesting phenomena (slow magnetization relaxation at low temperatures and quantum coherent effects [5, 6]), even though the V_{15} nanocluster has an odd total spin and, therefore, according to the theory [7, 8], macroscopic quantum tunneling is forbidden in it. An important property of the V_{15} polyoxovanadate is that direct exchange interaction between the spins of the central triangle in the polyoxovanadate molecule (see figure) is virtually absent. This stems from the fact that exchange coupling between these spins is very long-range (~10 Å): V–O–As–O–As–O–V. According to estimates [9], the exchange integral for this coupling should be considerably less than 0.7 meV (~8 K). Consequently, the interaction between the spins of the cen-

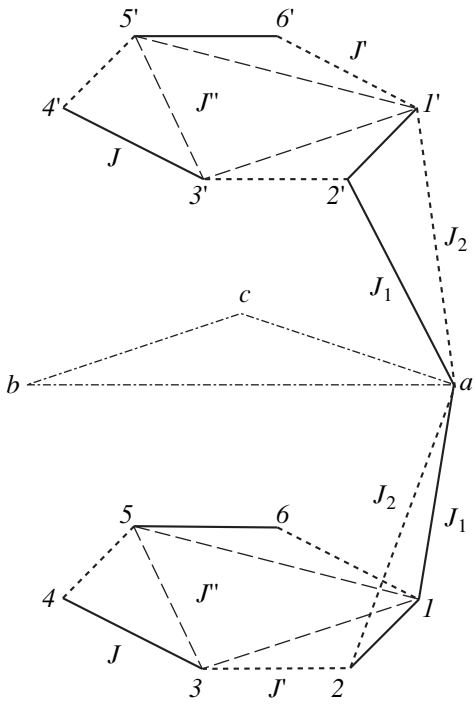

Structure of exchange interactions in the V_{15} magnetic molecular nanocluster.

1063-7834/03/4505-0903$24.00 © 2003 MAIK "Nauka/Interperiodica"

tral triangle is governed by their exchange interactions with spins of the upper and lower hexagons. This means that the energy spectrum in the vicinity of the ground state on an energy scale of the order of 1 K and the properties of the V_{15} nanocluster in weak magnetic fields are determined by the exchange interactions on a scale of the order of 10^2 K (for greater detail, see [10]). Owing to this property, the V_{15} nanocluster differs noticeably from the aforementioned nanoclusters with a large spin (Mn_{12}, etc.).

In the case when the Zeeman energy sequentially exceeds the energy gaps separating multiplets with different total spins, an increase in the external magnetic field brings about jumpwise changes in the total spin of the cluster. In turn, these variations lead to magnetization jumps and give rise to peaks in the dependence of the magnetic susceptibility on the external magnetic field $\chi(H)$. The exchange constants can be determined by comparing the calculated and experimental peaks of the magnetic susceptibility. In fact, this is a direct method for determining the exchange constants. Barbara *et al.* [6] demonstrated that the transition $S_\Sigma = 1/2 \longrightarrow S_\Sigma = 3/2$ occurs in an external magnetic field $H = 2.8$ T. This transition was theoretically investigated by Raghu *et al.* [11] and Rudra *et al.* [12], who used a numerical method for calculating the energy of excited states. Platonov *et al.* [4] experimentally studied further transformation of the spin structure from $S_\Sigma = 3/2$ to $S_\Sigma = 15/2$ in megagauss fields. A theoretical interpretation of these results in terms of the perturbation theory was proposed in [13]. However, since the magnetization reversal in strong and weak magnetic fields has not been examined in the framework of a single model, none of the sets of exchange constants proposed thus far can be used for adequate quantitative description of magnetization reversal in both strong and weak magnetic fields.

In this work, from analyzing the available experimental data, we proposed a set of exchange constants that made it possible for the first time to achieve reasonable agreement between the theoretical and experimental data over the entire range of magnetic fields.

2. COMPUTATIONAL TECHNIQUE

A V_{15} magnetic molecular cluster consists of 15 V^{4+} ions, each having a spin of 1/2. The V^{4+} ions occupy vertices of two plane hexagons and one triangle between them. The scheme of exchange interactions between the ions of the cluster is given in the figure. Since all the exchange interactions are ferromagnetic, the total spin of the cluster in the ground state is equal to 1/2. The spin Hamiltonian of the V_{15} molecular cluster has the form

$$\begin{aligned}\mathcal{H} = &\sum_i g\mu H S_i^z + J(\mathbf{S}_1\mathbf{S}_2 + \mathbf{S}_3\mathbf{S}_4 + \mathbf{S}_5\mathbf{S}_6 + (\,)') \\ &+ J'(\mathbf{S}_2\mathbf{S}_3 + \mathbf{S}_4\mathbf{S}_5 + \mathbf{S}_6\mathbf{S}_1 + (\,)') \\ &+ J''(\mathbf{S}_2\mathbf{S}_4 + \mathbf{S}_4\mathbf{S}_6 + \mathbf{S}_6\mathbf{S}_2 + \mathbf{S}_1\mathbf{S}_3 + \mathbf{S}_3\mathbf{S}_5 + \mathbf{S}_5\mathbf{S}_1 + (\,)') \\ &+ J_1(\mathbf{S}_a\mathbf{S}_1 + \mathbf{S}_b\mathbf{S}_3 + \mathbf{S}_c\mathbf{S}_5 + \mathbf{S}_a\mathbf{S}_{2'} + \mathbf{S}_b\mathbf{S}_{4'} + \mathbf{S}_c\mathbf{S}_{6'}) \\ &+ J_2(\mathbf{S}_a\mathbf{S}_2 + \mathbf{S}_b\mathbf{S}_4 + \mathbf{S}_c\mathbf{S}_6 + \mathbf{S}_a\mathbf{S}_{1'} + \mathbf{S}_b\mathbf{S}_{3'} + \mathbf{S}_c\mathbf{S}_{5'}).\end{aligned} \quad (1)$$

As was shown by Chiorescu *et al.* [5], the spin structure of the V_{15} molecular cluster undergoes a transformation at $H = 2.8$ T. Specifically, the projections of spins of the ions located at the vertices of the triangle in the polyoxovanadate molecule take the following values: $S_a^z = S_b^z = S_c^z = 1/2$; as a result, the total spin of the molecular cluster becomes equal to 3/2 [5]. According to [13], further transformation of the spin structure from a ferrimagnetic state ($S_\Sigma = 3/2$) to a ferromagnetic state ($S_\Sigma = 15/2$) occurs in strong magnetic fields through three jumps with the same amplitude $\Delta S = 2$. Experimental investigations in magnetic fields as high as 450 T revealed that the dependence of the magnetic susceptibility on the external magnetic field exhibits peaks at 200 and 350 T [4].

In this work, the exchange interaction constants were calculated using a numerical method. The computational algorithm is as follows. Initially, the minimum energy is calculated for a fixed projection of the total spin in a zero external field. Then, the external magnetic field required to compensate for the increase in the exchange energy is determined from the difference in the energies for states with different total spins. The magnetic fields thus obtained correspond to peaks in the magnetic susceptibility. After comparison of the calculated peaks with the experimental data, the exchange constants should be properly corrected with the aim of achieving better agreement with the experiment. The energy spectrum and its structure in the ground state were calculated using a modified Lanczos method [14, 15]. By virtue of its rapid convergence and the small size of the program code, this method is most suitable for solving the above problem.

In [13], the expression for magnetic fields corresponding to peaks in the magnetic susceptibility was obtained in the second order of the perturbation theory (it was assumed that $J' = J_1$ and $J'' = J_2$). Gatteschi *et al.* [10] also used the perturbation theory for calculating the effective exchange interaction between the spins of the triangle in the molecular nanocluster [10]. The magnitude of this interaction determines the position of the first peak, i.e., the transition $S_\Sigma = 1/2 \longrightarrow S_\Sigma = 3/2$.

3. RESULTS AND DISCUSSION

A comparison of the results of numerical calculations and the analytical expressions, which were derived in terms of the perturbation theory [10, 13], shows that the numerical calculations are in rather poor agreement with the perturbation theory. Although the critical fields determined in numerical calculations are close to those calculated from the perturbation theory, the difference between the results obtained using both methods is substantially larger than that predicted from the error in the numerical calculation and the infinitesimal parameters of the perturbation theory. The difference is significant even in the case when the infinitesimal parameters of the perturbation theory are equal to 0.01 ($J'/J \sim J''/J \sim J_1/J \sim J_2/J \sim 0.01$) and the results of the numerical calculation should virtually coincide with the results obtained in terms of the perturbation theory.

In order to elucidate the cause of this difference, exact energy levels were calculated analytically for $S_\Sigma^z = 13/2$. To simplify the calculations, it was assumed that $J' = J_1$ and $J'' = J_2$. These analytical expressions are in complete agreement with the numerical calculations. It turned out that the relationships for energy levels involve expressions of the type

$$\sqrt{16J_1^2 + 32J_1J_2 + 25J_2^2}.$$

The presence of such radicals in the relationships obtained indicates that expressions for energy levels cannot be represented as a power series in terms of J'/J, J''/J, J_1/J, and J_2/J. Therefore, the methods of the perturbation theory are inapplicable for analyzing the energy spectrum of the spin subsystem of the V_{15} magnetic molecular nanocluster.

Another characteristic difference between the results of the numerical calculation and the results obtained in terms of the perturbation theory lies in the fact that, in strong magnetic fields, the transition from the state $S_\Sigma = 3/2$ to the state $S_\Sigma = 15/2$ occurs through six jumps with $\Delta S = 1$ rather than through three jumps with $\Delta S = 2$. However, these six jumps can be divided into three pairs: $S_\Sigma = 3/2 \longrightarrow S_\Sigma = 5/2$ and $S_\Sigma = 5/2 \longrightarrow S_\Sigma = 7/2$, $S_\Sigma = 7/2 \longrightarrow S_\Sigma = 9/2$ and $S_\Sigma = 9/2 \longrightarrow S_\Sigma = 11/2$, and $S_\Sigma = 11/2 \longrightarrow S_\Sigma = 13/2$ and $S_\Sigma = 13/2 \longrightarrow S_\Sigma = 15/2$. For each pair, the peaks are separated by a distance of approximately 1 T. Consequently, when the experiments were performed in megagauss fields, two peaks attributed to a particular pair were superposed one onto the other; therefore, it was very difficult, if not impossible, to separate these peaks experimentally.

The table presents the results of calculations of peaks corresponding to different sets of exchange constants. As follows from analyzing the tabulated data, none of the sets of exchange constants proposed earlier offers reasonable agreement with the experimental data. Using the set of exchange constants proposed in this work, we succeeded in achieving satisfactory agreement. Unfortunately, there are no experimental data on the critical fields corresponding to the transitions $S_\Sigma = 11/2 \longrightarrow S_\Sigma = 13/2$ and $S_\Sigma = 13/2 \longrightarrow S_\Sigma = 15/2$. These data could make it possible to refine the numerical values of the exchange constants.

Experimental and theoretical peaks of the magnetic susceptibility (T) of the V_{15} magnetic molecular nanocluster at different exchange constants

H_{exp} [4, 6]	H^*_{theor}	H^{**}_{theor}	H^{***}_{theor}
2.8	2.8	14.5	5.7
200	224.4	631.8	382.2
	225.9	645.4	387.9
350	342.6	829.2	489.3
	344.0	843.4	495.8
–	470.7	1048.1	606.9
–	471.4	1054.0	609.9

* $J = 290$ K, $J' = 60$ K, $J_1 = 30$ K, $J'' = 200$ K, $J_2 = 68$ K.
** $J = 800$ K, $J' = J_1 = 150$ K, $J'' = J_2 = 300$ K [10].
*** $J = 490$ K, $J' = J_1 = 80$ K, $J'' = J_2 = 161$ K [4].

It follows from the table that there is a substantial difference between the results of numerical calculations performed in this work and the results of calculations in terms of the perturbation theory [13]. This can be caused by two factors. First, according to the data presented in the table, the available set of exchange parameters is inappropriate for finding the parameter small enough to satisfy the requirements of the standard perturbation theory. Second, the applicability of the standard perturbation theory to the problem under consideration is most likely restricted by the aforementioned complex structure of the energy spectrum in the vicinity of the ground state.

So far, the use of the perturbation theory has remained the only way to derive analytical expressions for the ground-state energy and the wave function of the magnetic molecular nanocluster and can serve as the starting point for further investigations into the other properties of the nanocluster. In this respect, it is important to make serious efforts toward improving the perturbation theory for V_{15}.

4. CONCLUSIONS

Thus, the exchange constants of the Heisenberg interaction in the V_{15} magnetic molecular nanocluster were calculated using the available experimental data [4, 6] on the dependence of the magnetic susceptibility on the external magnetic field. In this work, we proposed a set of exchange constants that made it possible for the first time to describe adequately the magnetization in weak (no more than 5 T) [6] and strong (100–400 T) [4] magnetic fields.

ACKNOWLEDGMENTS

This work was supported by the International Association of Assistance for the promotion of cooperation with scientists from the New Independent States of the former Soviet Union (project INTAS no. 99-01839).

REFERENCES

1. E. M. Chudnovsky and J. Tejada, *Macroscopic Quantum Tunneling of the Magnetic Moment* (Cambridge Univ. Press, Cambridge, 1998).
2. B. Barbara and L. Gunther, Phys. Today **12** (3), 35 (1999).
3. I. Tupitsyn and B. Barbara, *Quantum Tunneling of Magnetization in Molecular Complexes with Large Spins: Effect of the Environment*, Preprint (2000); cond-mat/0002180.
4. V. V. Platonov, O. M. Tatsenko, V. I. Plis, *et al.*, Fiz. Tverd. Tela (St. Petersburg) **44** (11), 2010 (2002) [Phys. Solid State **44**, 2104 (2002)].
5. I. Chiorescu, W. Wernsdorfer, A. Müller, *et al.*, Phys. Rev. Lett. **84** (15), 3454 (2000).
6. B. Barbara, A. Müller, H. Bogge, *et al.*, J. Magn. Magn. Mater. **221** (1–2), 103 (2000).
7. D. Loss, D. P. DiVinchenzo, and G. Grinstein, Phys. Rev. Lett. **69** (22), 3232 (1992).
8. J. von Delft and J. L. Henley, Phys. Rev. Lett. **69** (22), 3236 (1992).
9. G. Chaboussant, R. Basler, A. Sieber, *et al.*, Europhys. Lett. **59** (2), 291 (2002).
10. D. Gatteschi, L. Pardi, A. Barra, *et al.*, Nature **354**, 463 (1991).
11. C. Raghu, I. Rudra, D. Sen, and S. Ramasesha, Phys. Rev. B **64** (6), 64419 (2001).
12. I. Rudra, S. Ramasesha, and D. Sen, J. Phys.: Condens. Matter **13** (50), 11717 (2001).
13. A. K. Zvezdin, V. I. Plis, A. I. Popov, and B. Barbara, Fiz. Tverd. Tela (St. Petersburg) **43** (1), 177 (2001) [Phys. Solid State **43**, 185 (2001)].
14. E. R. Gagliano, E. Dagotto, A. Moreo, and F. C. Alcaraz, Phys. Rev. B **34** (3), 1677 (1986).
15. E. Dagotto, Rev. Mod. Phys. **66** (3), 763 (1994).

Translated by N. Korovin

Physics of the Solid State, Vol. 45, No. 5, 2003, pp. 907–910. Translated from Fizika Tverdogo Tela, Vol. 45, No. 5, 2003, pp. 864–867.

MAGNETISM AND FERROELECTRICITY

Effect of the Crystal Structure and Interlayer Exchange Coupling on the Coercive Force in Co/Cu/Co Films

L. A. Chebotkevich, Yu. D. Vorob'ev, A. S. Samardak, and A. V. Ognev

Far East State University, ul. Sukhanova 8, Vladivostok, 690950 Russia

Received September 20, 2002

Abstract—Co/Cu/Co/Si(111) trilayer films prepared by magnetron sputtering with different thicknesses of the Cu buffer were studied. The magnitude of the coercive force was shown to oscillate with variation of the nonmagnetic-buffer thickness. A good correlation between the saturation field and the coercive force was established. It was experimentally revealed that modification of the film structure by annealing within a broad temperature range affects the indirect exchange coupling between the Co layers. A qualitative analysis of the coercive-force behavior under variation of the strength and type of the ferromagnetic-layer coupling was performed. *© 2003 MAIK "Nauka/Interperiodica".*

1. INTRODUCTION

The increasing interest centered presently on multilayer metal nanostructures is connected with the discovery of the giant magnetoresistance effect in them, which makes multilayer magnetic structures attractive for use in practice [1, 2]. One of the specific features of magnetic nanostructures is that the exchange coupling between the ferromagnetic layers oscillates between ferromagnetic and antiferromagnetic (AFM), depending on the thickness of the nonmagnetic buffer. A number of models have been put forward to explain the oscillating character of the coupling, among them the RKKY [3, 4], free-electron [5, 6], quantum-well [7], and *sd*-mixing [8] models. Oscillations of the indirect exchange coupling give rise to oscillations in the magnetic and magnetoresistance properties of multilayer structures.

This study deals with the effect of crystal structure and indirect exchange coupling between Co ferromagnetic layers on the coercive force of Co/Cu/Co films.

2. SAMPLE PREPARATION

Co/Cu/Co samples were prepared by dc magnetron sputtering in an argon environment at $P_{Ar} = 5 \times 10^{-3}$ Torr. Films were deposited on (111)Si single crystals at room temperature. The film thickness was monitored from the deposition time. The Co and Cu deposition rate was 0.1 and 0.08 nm/s, respectively. We studied Co/Cu/Co films with a Co layer thickness d_{Co} = 6 nm and a copper buffer thickness d_{Cu} varied from 0 to 2.6 nm. The film structure was studied using electron microscopy and electron diffraction. The magnetization and coercive force H_C were measured on an automated vibrating-sample magnetometer, with the saturation field derived from magnetoresistance loops.

3. EXPERIMENTAL RESULTS AND DISCUSSION

All films were prepared in one operation (at the same substrate temperature and gas pressure) and deposited on identical substrates. One might thus expect the films to have the same crystal structure. Electron microdiffraction and micrographs showed all the films to be polycrystalline with a grain size on the order of 5–6 nm.

Figure 1 shows the $H_C = f(d_{Cu})$ dependence for the polycrystalline Co/Cu/Co trilayers. The coercive force was determined from the magnetic hysteresis loop. H_C is seen to oscillate with variation of the Cu buffer thick-

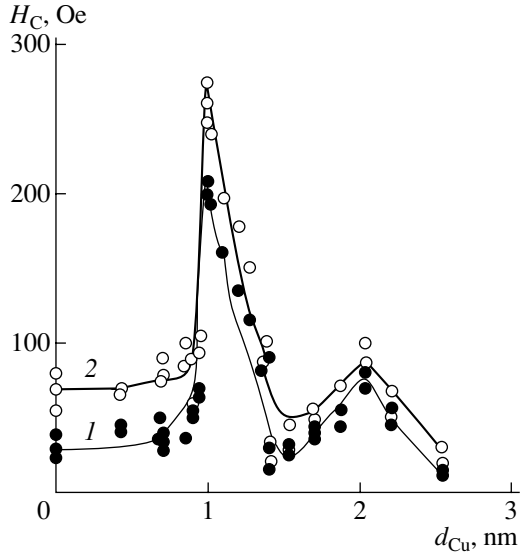

Fig. 1. Coercive force plotted vs. thickness of the copper buffer layer in Co/Cu/Co films (*1*) as-prepared and (*2*) annealed at 250°C.

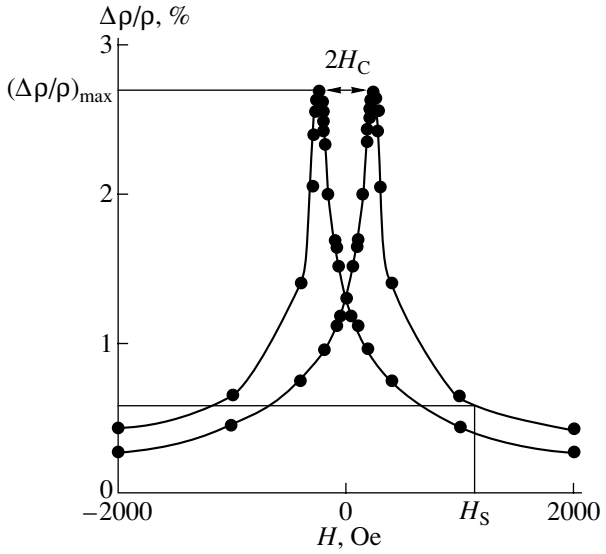

Fig. 2. Typical magnetoresistance hysteresis curve. Saturation field measured at $0.2(\Delta\rho/\rho)_{max}$.

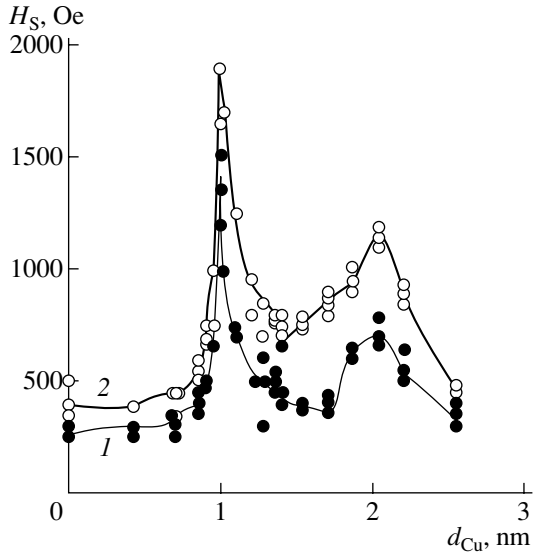

Fig. 3. Saturation field plotted vs. thickness of the copper buffer layer in Co/Cu/Co films (*1*) as-prepared and (*2*) annealed at 250°C.

ness, which originates from oscillations in the indirect exchange coupling J_{ie} between the Co layers. The strength of the indirect exchange coupling binding the Co ferromagnetic layers can be judged from the magnitude of the saturation field H_S (the field in which the magnetic moments in the top and bottom Co layers align parallel to each other): $|J_{ie}| = \frac{H_S M_S d}{2}$ [9], where M_S is the saturation magnetization and d is the ferromagnetic-layer thickness. The stronger the indirect exchange coupling between the Co layers, the higher the field applied to the sample has to be to achieve parallel magnetization in the Co layers. The magnitude of H_S may be considered an indicator of AFM coupling between the magnetic layers. The saturation field was derived from the magnetoresistance loop $\frac{\Delta\rho}{\rho} = \frac{\rho(H) - \rho(H_{max})}{\rho(H_{max})} = f(H)$ (ρ is the electrical resistivity); $\rho(H_{max})$ was measured in the field H_{max} = 1.13 T. Because the magnetoresistance loop tails off to high fields, H_S was taken to be a field at a height of $0.2(\Delta\rho/\rho)_{max}$ on the curve $\Delta\rho/\rho = f(H)$ [10] (Fig. 2).

The maxima of the coercive force in the $H_C = f(d_{Cu})$ curve are reached at the thicknesses $d_{Cu} \simeq 1$ and 2 nm, at which the saturation field is maximum, i.e., where the ferromagnetic Co layers are antiferromagnetically coupled (Fig. 3). The lowest value of H_C ($d_{Cu} \simeq 1.4$ nm) is attained at the lowest saturation fields (with the Co layers coupled ferromagnetically). The coercive force and the saturation field in the Co/Cu/Co trilayers are seen to correlate well. The correlation coefficient is 0.94. Thus, the experimental data show that the coercive force due to exchange coupling between the ferromagnetic layers is $H_C^* \sim H_S$. The nature of this coupling remains unclear.

The coercive force in trilayers is determined not only by the component H_C^* originating from the exchange coupling between the ferromagnetic layers but also by the component H_C^0 due to domain wall (DW) pinning by structural defects:

$$H_C = H_C^0 + H_C^*. \quad (1)$$

Structural defects in a polycrystalline film are grain boundaries, dispersion between the crystallographic anisotropy axes, and surface roughness. These are defects whose dimensions and separation are less than the domain wall width. A grain boundary can be visualized as a planar layer of width a. The structure of the material in a grain boundary layer is different from that in the grain bulk. The grain boundary magnetization M_{gb} is less than the grain saturation magnetization M_S by ΔM_S. Inside such a grain boundary, there is a demagnetizing field. A moving DW interacts with grain boundaries magnetostatically.

We assume the easy magnetization axes (EMA) to lie in the film plane and to be randomly oriented. As a DW translates, the angle between the magnetization and the EMA direction in the grain varies, as does the anisotropy energy, and it is this that determines the force with which a DW interacts with a grain.

Film surface roughness can be visualized as an array of pits on the surface. As a DW moves across such a pit, the DW magnetostatic energy varies.

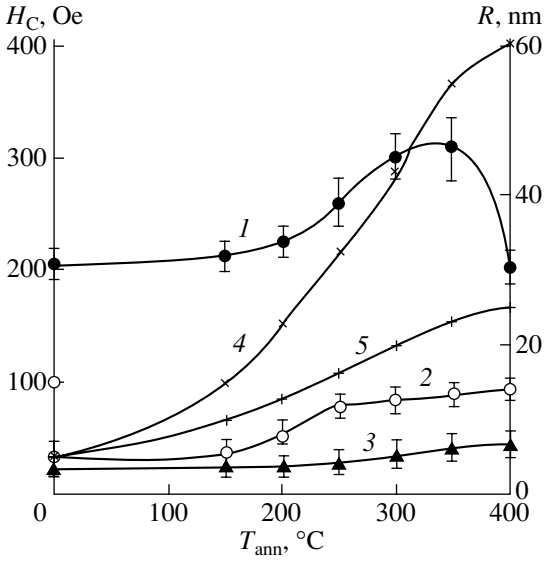

Fig. 4. Dependence of (*1–3*) coercive force and (*4*, *5*) grain size R on annealing temperature for (*2*, *4*) Co, (*1*, *5*) Co/(1.0 nm)Cu/Co, and (*3*) Co/(1.4 nm)Cu/Co.

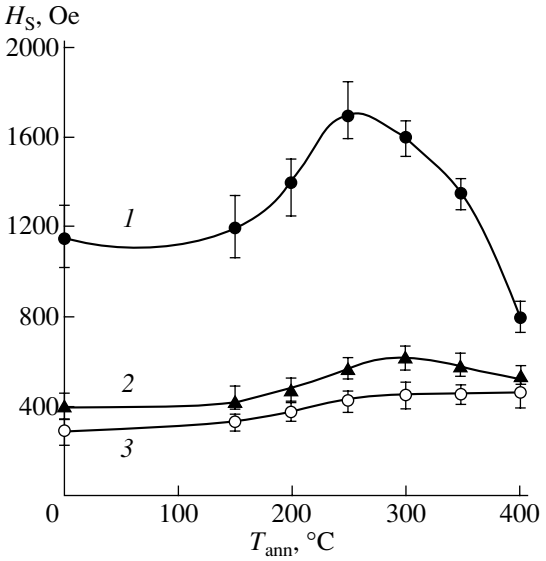

Fig. 5. Saturation field plotted vs. annealing temperature for (*1*) Co/(1.0 nm)Cu/Co, (*2*) Co/(1.4 nm)Cu/Co, and (*3*) Co.

The coercive force component due to structural defects can be represented in the form [11]

$$H_C^0 = C\frac{\sum_i (\langle F_i^2 \rangle)^{2/3}}{M_S D^{4/3} \gamma^{1/3} \delta}, \quad (2)$$

where D is the film thickness, γ is the DW surface energy density, δ is the DW width, C is a coefficient of proportionality, and F_i is the force of DW interaction with defects of species i. The component of the coercive force due to structural defects is $H_C^0 \approx 30$ Oe, which is in accord with the value of H_C of the Co films, where the coercive force originates from DW pinning by structural defects.

The oscillations of exchange coupling between the cobalt layers from ferromagnetic to antiferromagnetic observed to occur in trilayers under variation of the copper buffer thickness are accompanied by variation in the coercive-force component H_C^*. Estimates of the H_C^* component made for $H_S \approx 200$ and 1200 Oe for ferromagnetically and antiferromagnetically coupled Co layers, respectively, revealed that H_C^* for films with AFM coupling is six times that for films with ferromagnetically coupled Co layers.

To investigate the effect of crystal structure and indirect exchange coupling on the magnitude of the coercive force H_C as a function of annealing temperature T_{ann}, we studied the $H_C = f(T_{ann})$ relation within the temperature interval 150–550°C. Figure 4 plots the $H_C = f(T_{ann})$ relation obtained for three films, namely, pure Co, Co/(1 nm)Cu/Co, and Co/(1.4 nm)Cu/Co. The Co film thickness was $2d_{Co}$. Increasing the anneal temperature increased the grain size in all films. It should, however, be pointed out that, in films of pure cobalt annealed at $T_{ann} = 350$°C, grains grow in size nearly tenfold to ~60 nm, whereas in Co/Cu/Co films annealed at the same temperature, grains increase in size by four to five times only, reaching 25 nm (Fig. 4).

The coercive force of single-layer Co films annealed at $T_{ann} = 250$°C increases by a factor 2.5, and of those annealed at 350°C, by 3.5–4 times. The increase in H_C of Co films observed to occur under annealing is caused by the increase in grain size and redistribution of point defects (vacancies, residual-gas atoms) over grain boundaries [12].

Low-temperature annealing (200–250°C) of Co/Cu/Co films with $d_{Cu} = 1.4$ nm results in a slight increase in grain size to ~10 nm and a partial relaxation of internal stresses. The former factor should somewhat increase H_C, and the latter, decrease H_C. These effects may cancel; indeed, H_C of films with $d_{Cu} = 1.4$ nm (Fig. 4) annealed at 200–250°C practically did not change. Further increase in the annealing temperature ($T_{ann} \geq 350$°C) brings about an increase in H_C. As in the Co films, the increase in the coercive force of these films is due to the increase in the grain size and in the defect concentration at grain boundaries.

The situation is different with films with $d_{Cu} = 1$ nm annealed at $T_{ann} = 250$°C. The relaxation of internal stresses and the leveling off of the buffer layer in thickness are accompanied by strengthening of the AFM coupling between the Co layers (Fig. 5), and it is this

that accounts for the growth of the coercive force component H_C^* by a factor of about 1.2–1.3.

The growth of the grains in films with d_{Cu} = 1 nm which were annealed at T_{ann} = 350°C also favors an increase in the coercive force component originating from DW interaction with structural defects. At the same time, an increase in grain size implies an increase in interface roughness, which weakens AFM coupling between the Co layers (Fig. 5). While H_S in films annealed at T_{ann} = 350°C decreases, its value is still fairly large; therefore, H_C changes insignificantly. The correlation between H_C and H_S of films annealed at 350°C is 0.83.

The coercive force of the Co/(1 nm)Cu/Co films annealed at $T_{ann} \geq 400$°C decreases by about 40%, whereas in the Co and Co/(1.4 nm)Cu/Co films, H_C continues to grow. This can be assigned to the fact that the increase in grain size (by more than a factor of 6–7) and interface degradation, which is caused by mutual diffusion of Co and Cu atoms in Co/(1 nm)Cu/Co films, bring about a strong weakening of the AFM coupling between the Co layers (Fig. 5); this effect is accompanied by a decrease in the coercive force component H_C^*.

The decrease in the correlation coefficient between H_C and H_S in annealed films can be accounted for in the following way. The strong increase in grain size and interface degradation are accompanied by a weakening of AFM coupling between the Co layers and, hence, by a decrease in the coercive force component H_C^*. On the other hand, an increase in grain size entails an increase in the coercive force component H_C^0. Therefore, the change in the magnitude of H_C of the films subjected to high-temperature annealing somewhat lags behind the decrease in H_S. The observation that the correlation coefficient between H_C and H_S after annealing remains large suggests that the coercive force of multilayered films is determined primarily by the actual type of exchange coupling between the Co ferromagnetic layers.

CONCLUSION

Thus, we have studied the coercive force and indirect exchange coupling between Co layers in Co/Cu/Co films. It has been shown that exchange coupling between the Co layers in a trilayer depends on the film structure and that the coercive force in multilayer films consists of two components, namely, H_C^0, which is due to DW interaction with structural defects in the Co layers, and H_C^*, which originates from exchange coupling between the ferromagnetic layers. The AFM coupling that binds the cobalt layers accounts for the larger coercive force. The increase in H_C in films with d_{Cu} = 1.0 nm (maximum AFM coupling), which is initiated by low-temperature annealing, is associated with an increase in AFM coupling between the Co layers. After high-temperature annealing, the AFM coupling between the Co layers is destroyed because of interface degradation; this brings about a decrease in H_C. The increase in coercive force in trilayers in which the Cu buffer layer thickness corresponds to ferromagnetic coupling between the Co layers is caused primarily by the increase in grain size and point defect redistribution over grain boundaries.

ACKNOWLEDGMENTS

This study was supported by the Ministry of Industry, Science, and Technologies of the Russian Federation (contract no. 3-02/DVGU).

REFERENCES

1. F. J. Himpsel, J. E. Ortega, G. J. Mankey, and R. F. Willis, Adv. Phys. **47** (4), 511 (1998).
2. P. M. Levy, Solid State Phys. **47**, 367 (1994).
3. P. Bruno and C. Chappert, Phys. Rev. Lett. **67** (12), 602 (1991).
4. Zhu-Pei Shi and P. M. Levy, Phys. Rev. B **49** (21), 15159 (1991).
5. J. C. Slonczewski, J. Magn. Magn. Mater. **150**, 13 (1995).
6. J. Barnas, J. Magn. Magn. Mater. **128**, 171 (1994).
7. J. Mathon, D. M. Edvards, R. B. Muniz, and M. S. Phan, Phys. Rev. Lett. **67**, 493 (1991).
8. P. Bruno, J. Magn. Magn. Mater. **116**, L13 (1992).
9. S. S. P. Parkin, in *Ultra Magnetic Structures II* (Springer, Berlin, 1994), p. 148.
10. K. Ratzke, M. J. Hall, D. B. Jardine, *et al.*, J. Magn. Magn. Mater. **204**, 61 (1999).
11. A. A. Ivanov, I. V. Lobov, and Yu. D. Vorob'ev, Fiz. Met. Metalloved. **58** (1), 11 (1984).
12. V. É. Osukhovskiĭ, Yu. D. Vorob'ev, L. A. Chebotkevich, *et al.*, Fiz. Met. Metalloved. **57** (2), 254 (1984).

Translated by G. Skrebtsov

Physics of the Solid State, Vol. 45, No. 5, 2003, pp. 911–913. Translated from Fizika Tverdogo Tela, Vol. 45, No. 5, 2003, pp. 868–870.

MAGNETISM AND FERROELECTRICITY

Giant Magnetorefractive Effect in Magnetic Granular CoFe–MgF Alloys

A. Granovskiĭ[1], V. Gushchin[1], I. Bykov[1], A. Kozlov[1], N. Kobayashi[2], S. Ohnuma[2], T. Masumoto[2], and M. Inoue[3, 4]

[1] *Moscow State University, Vorob'evy gory, Moscow, 119992 Russia*
e-mail: granov@magn.ru
[2] *Research Institute for Electric and Magnetic Materials, 2-1-1, Yagiymaminami, Taihakaku, Sendai, 982-0807 Japan*
[3] *Toyohashi University of Technology, Toyohashi, 441-8580 Japan*
[4] *CREST, Japan Science and Technology Corporation, Kawaguchi, 332-0012 Japan*
Received September 26, 2002

Abstract—This paper reports on an IR study (5–20 μm) of the dispersion and field dependences of the magnetorefractive effect in granular CoFe–MgF (metal–insulator) systems, which exhibit, in compositions close to the percolation threshold, a tunneling magnetoresistance of 7.5% in a field of 1700 Oe. The change in the reflectivity of *p*-polarized light under magnetization in the IR spectral region 5–7 μm is of the order of 0.1%, while in the 10- to 12-μm region, this change, reaches record-high values of 1.2–1.5%, which exceed the usual odd and even magnetooptic reflectivities in the IR range by two orders of magnitude. The magnetorefractive effect in magnetic systems with tunneling conduction originates from spin-dependent high-frequency tunneling.

The magnetorefractive effect (MRE) consists essentially in a change in the coefficients of reflection *R*, transmission *T*, and absorption *A* of light induced by the application of a magnetic field to a sample. The MRE is negligible in magnetic and nonmagnetic materials not possessing a large magnetoresistance. In magnetic materials with giant, tunneling, or colossal magnetoresistance, the conductivity changes considerably under magnetization; therefore, the dielectric permittivity $\varepsilon(\omega)$ in the IR range, which is linearly related to the conductivity $\sigma(\omega)$, also becomes a function of the applied magnetic field. Because the refraction indices and all optical coefficients (*R*, *T*, *A*) are governed by the permittivity, the MRE can obviously be considered a frequency analog of giant magnetoresistance and is an even function of magnetization. Note that the usual magnetooptic effects, both even and odd in magnetization, observed in IR light reflection from metals and composites do not exceed 0.01%, which confers considerable practical importance to the search for materials exhibiting a large MRE.

The MRE was first studied theoretically and observed experimentally on Fe/Cr multilayers [1]. MRE theory for metal multilayers was also developed in [2–4]. Although there is certain disagreement between the results of those studies (see, e.g., the discussion in [4]) on the frequency dependence of the MRE and its magnitude, the effect is well pronounced in the near IR region and reaches 0.1–0.5% in reflection [1, 4]. The theory of the MRE in granular metal–metal alloys was developed in [5] and recently modified in [6]. The magnitude of the MRE measured experimentally on Co–Ag granular systems [6, 7] in fairly strong magnetic fields did not exceed 1%. The simplest relation for the MRE in metal systems, derived in [5] for the Hagen–Rubens spectral region ($\omega\tau \ll 1$, where τ is the electron relaxation time), can be written as

$$\xi = \frac{\Delta R}{R} = \frac{R_{H=0} - R_{H_{\max}}}{R_{H=0}} = -\frac{1}{2}(1-R)\frac{\rho_{H=0} - \rho_{H_{\max}}}{\rho_{H=0}} = -\frac{1}{2}(1-R)\frac{\Delta\rho}{\rho}, \quad (1)$$

where $\Delta\rho/\rho$ is the magnetoresistance. As follows from this relation, large values of the MRE should be observed in systems with a large magnetoresistance and a small reflectivity rather than in metallic systems. We undertook, therefore, to study the MRE in granular metal–insulator systems Co–Al–O [8], Fe–SiO_n, and CoFeZr–SiO_n [9] and found that the largest MRE in reflection (amplified by interference to 0.8% [8]) occurred in the Co–Al–O system. A recent publication [10] also reported on the MRE observed in the Co–Al–O system; however, this effect was not in excess of 0.35% in magnitude and was seen only within a narrow spectral interval near 9 μm.

This communication reports on experimental data on the MRE obtained by us on granular CoFe–MgF alloys, which exhibit tunneling conduction and a large room-temperature magnetoresistance of 13% in relatively weak fields [11]. Investigation of the MRE in sys-

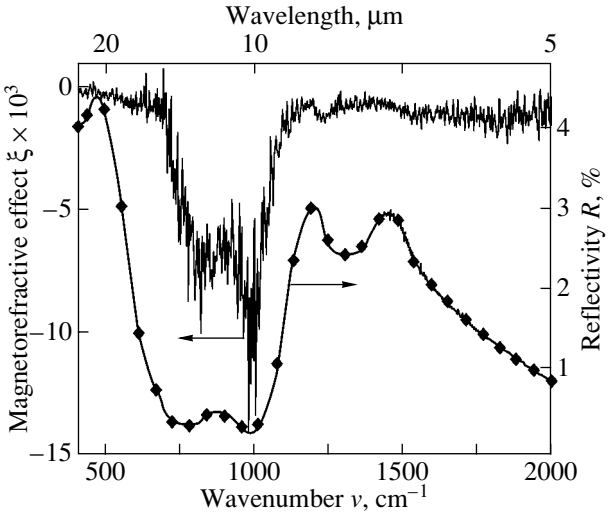

Fig. 1. Spectra of MRE ξ measured in a field H = 1700 Oe and of the reflectivity $R_{H=0}$ for a $(Co_{0.4}Fe_{0.6})_{48}$–(MgF_{52}) granular alloy film. Averaging was performed over 300 scans.

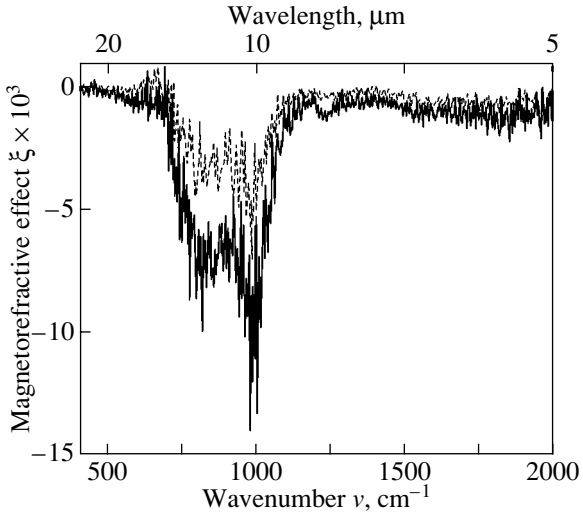

Fig. 2. Frequency response of MRE measured at H = 1700 Oe with a resolution of 2 cm^{-1} (solid line) and at H = 1400 Oe with a resolution of 4 cm^{-1} (dashed line) on a $(Co_{0.4}Fe_{0.6})_{48}$–(MgF_{52}) film.

tems with tunneling conduction is of particular interest, because, in this case, this effect originates from spin-dependent high-frequency tunneling. At low frequencies, the tunneling probability does not depend on frequency. At high frequencies, however, one can expect both a decrease in tunneling transparency, when the period of the electromagnetic wave becomes less than the characteristic tunneling time, and an increase in the tunneling probability due to photon absorption by the tunneling electron.

Thin-film samples of the $(Co_{0.4}Fe_{0.6})_{48}$–(MgF_{52}) composition close to the percolation threshold were prepared by rf magnetron cosputtering [11]. Corning-7059 glass was used as the substrate. The film thickness was 2 μm, and the CoFe grain size was 2–3 nm. The technology of preparation, structural and magnetic properties, and experimental data on the magnetoresistance can be found in [11, 12]. The reflectivity and MRE were measured with a FTIR PU9800 Fourier spectrometer [8] with a magnetooptical attachment allowing both ac demagnetization of the sample and the application of an in-plane dc field. The MRE measurements were conducted at room temperature in magnetic fields of up to 1700 Oe, with *p*-polarized light impinging at an angle 8°–10° and measured with a spectral resolution of 2 cm^{-1}. Figure 1 shows an MRE spectrum obtained for a $(Co_{0.4}Fe_{0.6})_{48}$–$(MgF)_{52}$ sample by averaging over 300 scans in a magnetic field of 1700 Oe. The magnetoresistance measured in the same field is 7.5%. In the spectral interval 10–12 μm, where the reflectivity R reaches a minimum (below 5%) (Fig. 1), the MRE exhibits the largest fluctuations. Figure 2 displays MRE plots obtained for two values of the magnetic field. The strong increase in the effect observed to occur with a small change in the field from 1400 to 1700 Oe indicates a nonlinear dependence of the MRE on the magnetic field, a feature similar to the field dependence of magnetoresistance.

As follows from the inset to Fig. 1, in the intervals 5–7 and 15–20 μm in the IR region, the MRE is about 0.1%. Thus, the MRE persists over a broad spectral region, including the near IR region. It should be stressed that, as follows from straightforward estimates of the characteristic tunneling time t (which for a tunneling barrier width a = 1 nm and a Fermi velocity ϑ = 10^8 cm/s is $t = a/\vartheta = 10^{-15}$ s), the characteristic tunneling time and the electromagnetic-wave period in the near IR region are of the same order of magnitude.

At frequencies of 10–12 μm, the MRE increases considerably to reach high and even giant (at clearly pronounced resonances) values, 1.5%, which exceeds the magnetooptic effects usually observed in the IR range by two orders of magnitude. Moreover, the MRE measured at resonances exceeds that observed in all metallic and nonmetallic systems studied thus far. This is due primarily to the decrease in the reflectivity, which is qualitatively described by Eq. (1). On the other hand, the nature of the resonance character of the MRE spectrum near 10 μm remains unclear.

The observed giant MRE opens up new possibilities both for investigating spin-dependent high-frequency tunneling and for practical application of infrared magnetooptics.

ACKNOWLEDGMENTS

This study was supported by the Russian Foundation for Basic Research, project no. 00-02-17797, and the “Universities of Russia” program.

REFERENCES

1. J. C. Jacquet and T. Valet, MRS Symp. Proc. **384**, 477 (1995).
2. N. F. Kubrakov, A. K. Zvezdin, K. A. Zvezdin, and V. A. Kotov, Zh. Éksp. Teor. Fiz. **114** (3), 1101 (1998) [JETP **87**, 600 (1998)].
3. G. M. Genkin, Phys. Lett. A **241** (4), 293 (1998).
4. S. Uran, M. Grimsditch, E. Fullerton, and S. D. Bader, Phys. Rev. B **57** (5), 2705 (1998).
5. A. Granovskiĭ, M. Kuzmichev, and Zh. P. Klerk, Zh. Éksp. Teor. Fiz. **116** (5), 1762 (1999) [JETP **89**, 955 (1999)].
6. V. G. Kravets, D. Bozec, J. A. D. Matthew, *et al.*, Phys. Rev. B **65** (5), 054415 (2002).
7. J. P. Camplin, S. M. Thompson, D. R. Loraine, *et al.*, J. Appl. Phys. **87** (9), 4846 (2000).
8. I. V. Bykov, E. A. Gan'shina, A. B. Granovskiĭ, and V. S. Gushchin, Fiz. Tverd. Tela (St. Petersburg) **42** (3), 487 (2000) [Phys. Solid State **42**, 498 (2000)].
9. I. Bykov, E. Ganshina, V. Guschin, *et al.*, in *Book of Abstracts of Moscow International Symposium on Magnetism* (Moscow, 2002), p. 68.
10. D. Bozec, V. G. Kravets, J. A. D. Matthew, and S. M. Thompson, J. Appl. Phys. **91** (10), 8795 (2002).
11. N. Kobayashi, S. Ohnuma, T. Masumoto, and H. Fujimori, J. Appl. Phys. **90** (8), 4159 (2001).
12. N. Kobayashi, S. Ohnuma, T. Masumoto, and H. Fujimori, J. Magn. Soc. Jpn. **23** (1), 76 (1999).

Translated by G. Skrebtsov

Physics of the Solid State, Vol. 45, No. 5, 2003, pp. 914–921. Translated from Fizika Tverdogo Tela, Vol. 45, No. 5, 2003, pp. 871–877.

MAGNETISM AND FERROELECTRICITY

Specific Features of Magnetic and Transport Properties of $La_{1-x}Mn_{1+x}O_3$ Manganites

V. P. D'yakonov[1, 2], V. P. Pashchenko[1], É. E. Zubov[1], V. I. Mikhaĭlov[1], Yu. Bukhantsev[2], I. M. Fita[1], V. A. Turchenko[1], N. A. Doroshenko[1], A. Szevczik[2], R. Zuberek[2], and G. Szymczak[2]

[1] *Donetsk Physicotechnical Institute, National Academy of Sciences of Ukraine, Donetsk, 83114 Ukraine*

[2] *Institute of Physics, Polish Academy of Sciences, Warsaw, 02-668 Poland*

e-mail: dyakon@dyakon.fti.ac.donetsk.ua

Received October 1, 2002

Abstract—The magnetic and transport properties of $La_{1-x}Mn_{1+x}O_3$ manganites with excess manganese are studied. It is shown that magnetic and charge ordering heavily depends on the superstoichiometric manganese content, magnetic field, and pressure. The magnetoresistive effect (MRE) is enhanced as the manganese concentration increases. In addition to the paramagnet–ferromagnet transition, the temperature dependences of the magnetization exhibit anomalies at low temperatures in samples with $x = 0.1$–0.4. The magnetization decreases at $T < 45$ K in fields $H < 0.2$ kOe and increases as H changes from 0.2 to 10 kOe. An analysis shows that the features observed at low temperatures are most probably related to the transition from the ferromagnetic state to the canted spin structure in clusters of mixed-valence manganese ions. The temperature dependences of the magnetization and resistivity remain unchanged as the pressure increases. It is demonstrated that the Curie and metal–dielectric transition temperatures shift to higher values as the manganese concentration increases under pressure. The temperature of the MRE peak increases under pressure, while the MRE decreases. © *2003 MAIK "Nauka/Interperiodica".*

1. INTRODUCTION

Doped manganites have been actively studied owing to their unique magnetic and electrical properties [1, 2]. The colossal magnetoresistance (CMR) effect makes them promising for use as functional materials in microelectronics.

The magnetism of doped manganites is associated with the indirect and double exchange mechanisms [3]. Substitution of lower valence cations for lanthanum gives rise to mixed Mn^{3+}/Mn^{4+} ionic states. This leads to a metal–dielectric transition related to the ferromagnetic (FM) order. Moreover, the replacement of manganese at B sites by other transition metals causes modification of their magnetic and transport properties [4, 5].

To understand the correlation of the FM phase transition and the metal–dielectric transition with the CMR effect, new magnetic materials should be searched for and studied. Oxides with excess manganese and deficient lanthanum, being self-doped systems, are of particular interest. These systems contain both mixed-valence manganese ions and vacancies. Moreover, clusters with a mixture of Mn^{3+} and Mn^{4+} ions can be formed near vacancies or incorporated manganese ions. A canted magnetic structure can arise in clusters and low-doped manganites at a certain carrier concentration.

Physical properties of $LaMnO_3$ [6–10] and manganites with deficient lanthanum [11–16] are well understood. However, the magnetism and transport in compounds with excess manganese and deficient lanthanum were not actively studied. Only the resonance studies of manganites with superstoichiometric manganese concentration are available in the literature [5, 17, 18].

One of the purposes of this study is to elucidate how the superstoichiometric manganese concentration affects the transport properties and the feature of the magnetic state of $La_{1-x}Mn_{1+x}O_3$ compounds.

The pressure can influence the exchange interactions in doped manganites, control the number of carriers at a fixed chemical composition, and, thus, control both the Curie temperature and the metal–dielectric transition.

The second objective of this study is to show the influence of the pressure on the phase transitions in compounds with excess manganese.

2. SAMPLES AND EXPERIMENTAL TECHNIQUE

The $LaMnO_3$ system was taken as a basic structure in which the manganese concentration increased at the expense of lanthanum to produce mixed-valence manganese ions.

Table 1. Molar formulas of manganite–lanthanum perovskites $La_{1-x}Mn_{1+x}O_3$

Composition x (sample)	Molar formulas of the real structure
0.1	(1) $La^{3+}_{0.86}Mn^{3+}_{1.05}V^{(c)}_{0.09}O^{2-}_{2.86}V^{(a)}_{0.14}$,
(LM1O)	(2) $\{La^{3+}_{0.86}V^{(c)}_{0.09}\}_A[Mn^{3+}_{0.90}Mn^{4+}_{0.05}]_B(Mn^{2+}_{0.05}Mn^{3+}_{0.05})_{cl}O^{2-}_{2.86}V^{(a)}_{0.14}$
0.2	(1) $La^{3+}_{0.76}Mn^{3+}_{1.14}V^{(c)}_{0.10}O^{2-}_{2.85}V^{(a)}_{0.15}$,
(LM2O)	(2) $\{La^{3+}_{0.76}V^{(c)}_{0.10}\}_A[Mn^{3+}_{0.80}Mn^{4+}_{0.14}]_B(Mn^{2+}_{0.14}Mn^{3+}_{0.06})_{cl}O^{2-}_{2.85}V^{(a)}_{0.15}$
0.3	(1) $La^{3+}_{0.66}Mn^{3+}_{1.23}V^{(c)}_{0.11}O^{2-}_{2.84}V^{(a)}_{0.16}$,
(LM3O)	(2) $\{La^{3+}_{0.66}V^{(c)}_{0.11}\}_A[Mn^{3+}_{0.70}Mn^{4+}_{0.23}]_B(Mn^{2+}_{0.23}Mn^{3+}_{0.07})_{cl}O^{2-}_{2.84}V^{(a)}_{0.16}$
0.4	(1) $La^{3+}_{0.57}Mn^{3+}_{1.32}V^{(c)}_{0.11}O^{2-}_{2.83}V^{(a)}_{0.17}$,
(LM4O)	(2) $\{La^{3+}_{0.56}V^{(c)}_{0.12}\}_A[Mn^{3+}_{0.60}Mn^{4+}_{0.32}]_B(Mn^{2+}_{0.32}Mn^{3+}_{0.08})_{cl}O^{2-}_{2.82}V^{(a)}_{0.18}$

Note: (1) The defect structure without regard for the ion distributions over sites, and (2) the real defect clustered structure.

Table 2. Lattice parameters, Curie temperature T_C, metal–dielectric transition temperature T_{MD}, magnetoresistance $\Delta R/R$, experimental M_{FC}, and calculated magnetic moment m

x	Unit cell parameters			T_C, K	T_{MD}, K	$\Delta R/R$, %	M_{FC}, μ_B/atom Mn	m, μ_B
	a, Å	b, Å	c, Å					
0.1	5.506	5.552	7.796	239.6	234.6	21.5	1.13	2.1
0.2	5.497	5.527	7.736	240.0	238.2	25.6	1.17	2.3
0.3	5.464	5.515	7.728	240.4	239.1	27.8	1.18	2.4
0.4	5.471	5.513	7.719	240.9	239.5	28.5	1.16	2.6

As is known, the manganite properties are very sensitive to synthesis conditions. For this reason, the samples to be studied were prepared according to the same technology, which allowed comparison of their properties. The ceramic $La_{1-x}Mn_{1+x}O_3$ (x = 0.1–0.4) samples were synthesized through two-stage (at 900 and 950°C) 20-h annealing followed by sintering at 1150°C in air (P = 0.5 MPa). The redox processes during synthesis, annealing, and cooling bring about the formation of both cation $V^{(c)}$ and anion $V^{(a)}$ vacancies in the real structure of oxides. The synthesis procedure and the characterization of the crystal structure of manganites with an excess manganese concentration were described in detail in [19, 20].

Table 1 lists the molar formulas of the manganites under study, which were obtained using x-ray structure analysis with due regard for the electroneutrality, crystal chemistry, and superposition mixed-valence manganese ions.

The temperature dependence of the magnetization $M(T, H)$ (in zero and applied magnetic fields) was measured using a vibrating-coil magnetometer in magnetic fields from 2 Oe to 12 kOe in the temperature range 4.2–300 K.

The dependence of the resistivity on the temperature and magnetic field was measured using a conventional dc four-point probe method. The magnetoresistive effect (MRE) was measured at temperatures of 77–300 K and magnetic fields up to 8 kOe. The temperature was determined from the resistivity of a bifilarly reeled copper coil.

The magnetic measurements under a pressure up to 1 GPa were carried out in a beryllium bronze microcontainer 60 mm long with inner and outer diameters of 1.4 and 4 mm, respectively. The transport properties under a pressure up to 1.8 GPa were studied using a high-pressure chamber 120 mm long with inner and outer diameters of 6 and 30 mm, respectively. A mixture of mineral oil and kerosene was used as the pressure-transferring medium. The pressure at low and high temperatures was measured using the dependence of the superconducting transition temperature of tin on pressure and the pressure dependence of the resistivity of a manganin pressure gage.

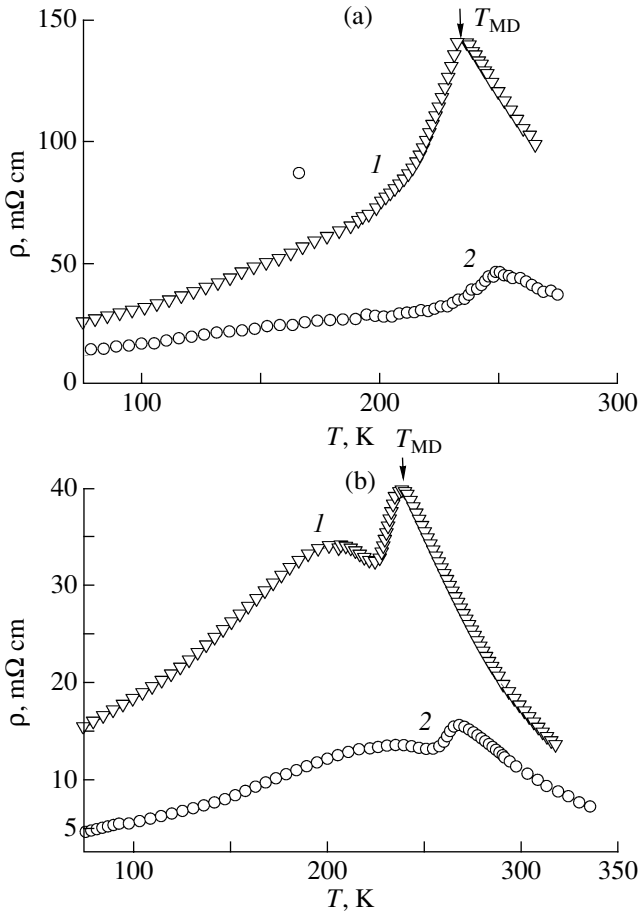

Fig. 1. Dependence ρ(*T*) of (a) $La_{0.9}Mn_{1.1}O_3$ and (b) $La_{0.7}Mn_{1.3}O_3$ at $H = 0$ and P = (*1*) 0 and (*2*) 1.8 GPa.

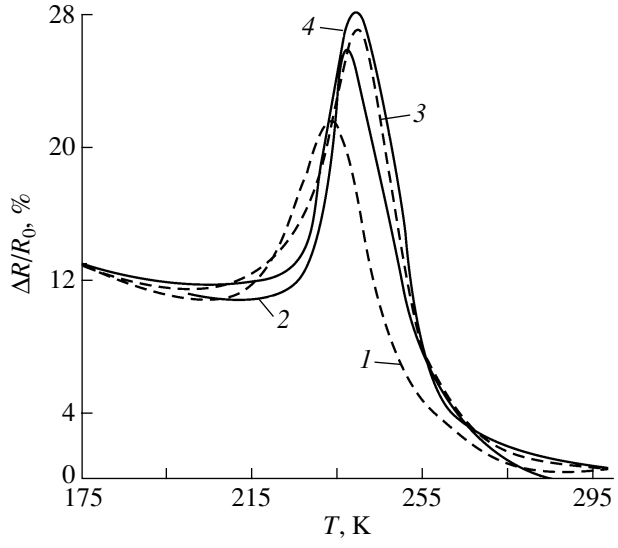

Fig. 2. Temperature dependence of the MRE of $La_{1-x}Mn_{1+x}O_3$ samples with x = (*1*) 0.1, (*2*) 0.2, (*3*) 0.3, and (*4*) 0.4 in the magnetic field H = 8 kOe.

3. RESULTS

3.1. Influence of Superstoichiometric Manganese on the Structural, Transport, and Magnetic Properties of $La_{1-x}Mn_{1+x}O_3$

A structural analysis of the ceramic samples under consideration was carried out at room temperature on a DRON-3 x-ray diffractometer (CuK_α radiation). The phase composition, lattice type, and lattice parameters were determined. According to the x-ray diffraction data, the samples had a single-phase composition with an orthorhombically (*Pnma*) distorted perovskite structure. The orthorhombic structure was determined from analyzing all the lines with emphasis on the splitting of the (0.40) and (400) reflections. The lattice parameters are listed in Table 2. The structural symmetry remains unchanged as the manganese concentration increases. An increase in the manganese concentration (from x = 0.1 to 0.4) results in a decrease in the lattice parameters and the Curie temperature T_C. This suggests complete dissolution of excess manganese in the host structure of the perovskites under study. No secondary phases were detected in the samples.

The x-ray diffraction analysis with due regard for the diffuse halo showed that manganese ions in combination with vacancies form clusters in $La_{1-x}Mn_{1+x}O_3$. It was found that both the cation and anion vacancy concentrations and the degree of clusterization increase with increasing x [21, 22]. As will be show below, some features in the low-temperature magnetic behavior of the samples are related to the magnetism of these clusters.

Figure 1 shows the temperature dependences of the resistivity ρ for ceramics with x = 0.1 and 0.3 in a zero magnetic field. All the studied samples were characterized by the resistivity peak caused by the metal–dielectric transition. The resistivity decreases as the manganese concentration increases due to an increase in the carrier concentration. We note that another broad peak is observed in ρ(*T*) in addition to the major maximum for ceramics with $x > 0.1$. The two resistive transitions are most likely associated with mesoscopic structural and magnetic inhomogeneities [23–25]. As the magnetic field increases, the resistivity peak shifts to higher temperatures. An increase in the lanthanum deficiency causes an insignificant increase in the temperature T_{MD} of the metal–dielectric transition, which is close to the FM transition (see Table 2).

Figure 2 displays the temperature dependences of the magnetoresistance $\Delta R/R_0 = [1 - R(H)/R(0)]$ of the ceramics under study ($R(H)$ and $R(0)$ correspond to the magnetoresistance in external and zero magnetic fields). The MRE value and the temperature of the magnetoresistance T_{MR} peak increase with an increase in the manganese concentration. The temperature T_{MR} is virtually independent of the magnetic field, while the MRE value increases by a factor of approximately 4.5

in a magnetic field of 8 kOe for this series of ceramic samples.

The magnetization was measured in different fields in the samples cooled in zero (ZFC) and applied (FC) magnetic fields. Figure 3 shows the temperature dependences of the ZFC magnetization of the LM2O sample at 2 and 10 Oe. Figure 4 displays the temperature dependences of the magnetization $M(T, H)$ in the sample with $x = 0.2$ in magnetic fields $H = 0.1$–10 kOe. Similar dependences $M(T, H)$ were observed for the other samples under study. Figure 5 shows the dependences $M(T)$ for the LM1O, LM2O, and LM4O samples in the magnetic field $H = 0.5$ kOe. All the samples exhibit ferromagnetic behavior below the paramagnet–ferromagnet transition temperature. The Curie temperature T_C, which is determined as the inflection point of the curves $M(T)$ and corresponds to the averaged transition temperature, correlates with the metal–dielectric transition temperature (Table 2). It can be seen from Figs. 3–5 that the magnetization remains almost unchanged in the temperature range $50 < T < 220$ K.

The FC magnetization in weak fields (Fig. 3) exceeds the ZFC magnetization below the characteristic temperature of freezing, which is insignificantly lower than T_C. As the magnetic field increases, the difference between M_{FC} and M_{ZFC} almost disappears (Figs. 4, 5). This indicates low anisotropy in the manganites under consideration.

The magnetization decreases in fields $H < 100$ Oe at low temperatures (Fig. 3) and remains unchanged in fields $100 < H < 200$ Oe as the temperature decreases. In magnetic fields $H > 200$ Oe, the dependences $M_{FC}(T)$ and $M_{ZFC}(T)$ exhibit an upward jump at $T < 45$ K (Figs. 4, 5). It is assumed that the decrease and increase in the magnetization at low temperatures are caused by changes in the spin configurations in clusters of mixed-valence Mn ions.

Figure 6 shows the field dependences of the magnetization $M(H)$ measured at 4.2 and 100 K in the field range $H = 0$–12 kOe. The saturation magnetization (increasing with an increase in the manganese concentration) is reached even in fields of approximately 4 kOe at $T < 150$ K. It can be seen from Fig. 6 that the dependences $M(H)$ are typical of ferromagnets. The experimental and calculated saturation magnetizations at 12 kOe and 4.2 K are listed in Table 2. The average magnetic moments for completely ordered spins were calculated as $m(\mu_B) = A3\mu_B + B4\mu_B$ (magnetic moments equal to $3\mu_B$ and $4\mu_B$ were used; the concentrations A and B were taken from Table 1 for Mn^{3+} and Mn^{4+}, respectively; only the spin magnetism was assumed). It is seen that the calculated total magnetic moments exceed the experimental values. This is due to the fact that some spins do not participate in long-range magnetic ordering. The disagreements between the measured and calculated saturation magnetizations are also caused by the neglect of the effect of vacancies in the course of long-range ordering, as well as of additional

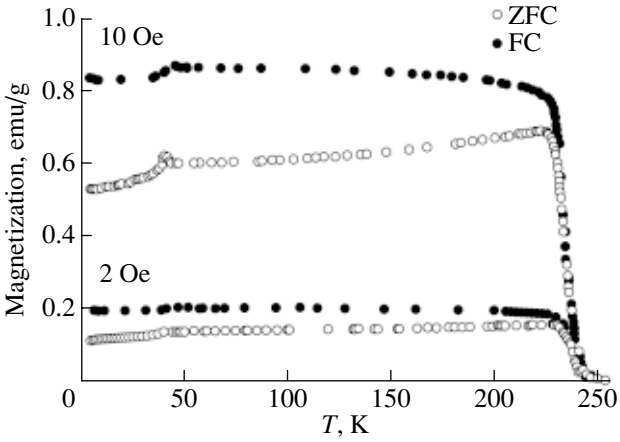

Fig. 3. Temperature dependences of FC and ZFC magnetizations of $La_{0.8}Mn_{1.2}O_3$ in magnetic fields $H = 2$ and 10 Oe.

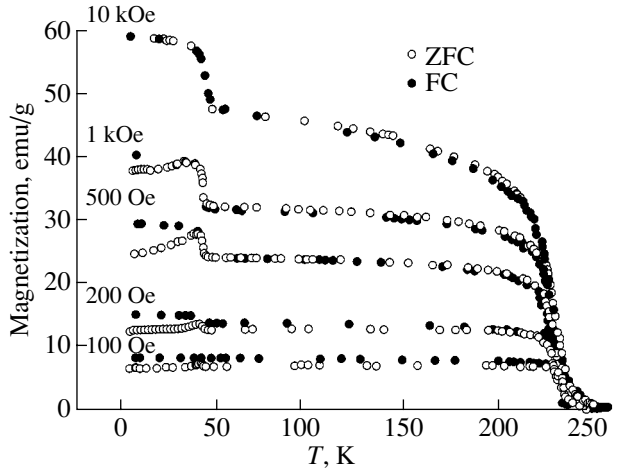

Fig. 4. Temperature dependences of FC and ZFC magnetizations of $La_{0.8}Mn_{1.2}O_3$ in magnetic fields $H = 0.1$–10 kOe.

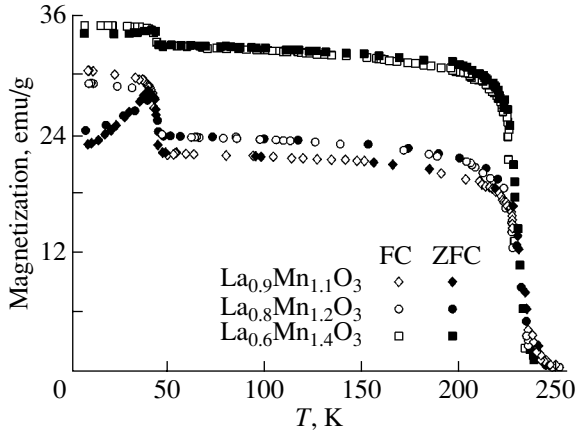

Fig. 5. Comparison of the dependences $M(T)$ for $La_{1-x}Mn_{1+x}O_3$ ($x = 0.1$, 0.2, 0.4) in the magnetic field $H = 0.5$ kOe.

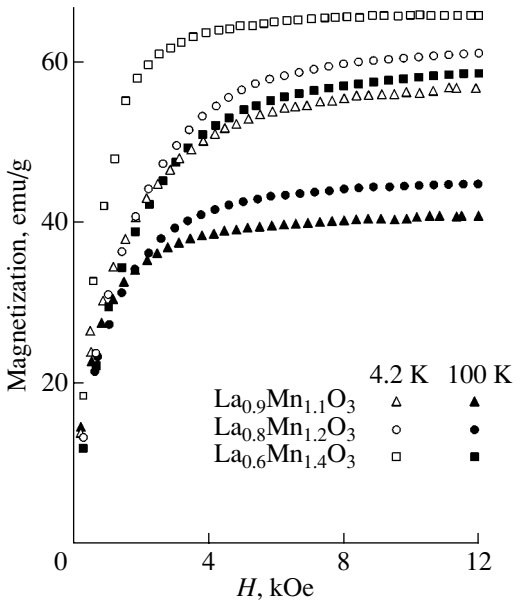

Fig. 6. Field dependences of the magnetization of $La_{1-x}Mn_{1+x}O_3$ (x = 0.1, 0.2, 0.4) at 4.2 and 100 K.

inhomogeneities in clusters and the host perovskite structure [26]. According to [20], clusters can also contain a set of different valence and magnetic states of manganese ions.

3.2. Effect of Pressure on the Magnetic and Transport Properties

Figures 7 and 8 displays the temperature dependences of the FC magnetization of $La_{0.9}Mn_{1.1}O_3$ and $La_{0.6}Mn_{1.4}O_3$, which were measured in a field of 5 Oe under pressure. As could be expected, the Curie temperature increases under pressure; i.e., the pressure increases the volume of the FM phase. At pressures up to 1.0 GPa, the temperature T_C increases almost linearly. In this case, the pressure coefficient dT_C/dP decreases from +21 to +15 K/GPa as the concentration x increases from 0.1 to 0.4. Manganites $La_{1-x}(Sr,Ca)_xMnO_3$ are characterized by similar values (15–30 K/GPa) [27, 28]. The temperature of the transition from the FM phases to the canted state insignificantly changes under pressure ($dT_{cant}/dP \approx +4$ K/GPa).

As can be seen from Fig. 1, the resistivity decreases under pressure (e.g., by factors of 3 and 2.4 in LM1O and LM3O samples, respectively, at P = 1.8 GPa). The resistivity of the samples under pressure exhibits a reversible anhysteretic behavior in the phase transition region. The effect of the pressure on the resistivity decreases with an increase in the manganese concentration, while this effect on the metal–dielectric transition temperature, on the contrary, decreases. In the pressure range under study, the temperature T_{MD} increases almost linearly by 15 K in LM1O and 30 K in LM3O under a pressure of 1.8 GPa. The pressure coefficients dT_{MD}/dP are very sensitive to the manganese concentration and change from 8 to 17 K/GPa as x changes from 0.1 to 0.3.

The MRE value decreases under pressure, while the temperature T_{MR} of the MRE peak increases. For example, the MRE in LM1O decreases by approximately 4% and the T_{MR} increases by 14 K at P = 1.8 kbar in a field H = 8 kOe. The T_{MR} temperature increases almost linearly with pressure with the same pressure coefficient as for T_{MD}.

4. DISCUSSION

It was established that the magnetization drastically increases near the Curie temperature and then remains almost unchanged as temperature decreases in different magnetic fields. Taking also into account that the magnetic phase transitions are very narrow, we assume that they are first-order transitions. This is also confirmed

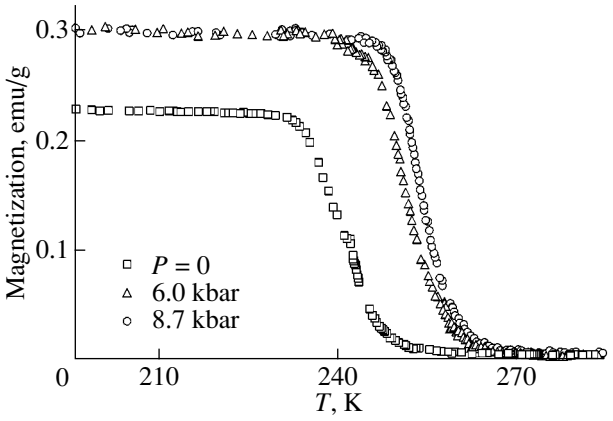

Fig. 7. Temperature dependence of the magnetization of $La_{0.9}Mn_{1.1}O_3$ in the field H = 5 Oe at different pressures.

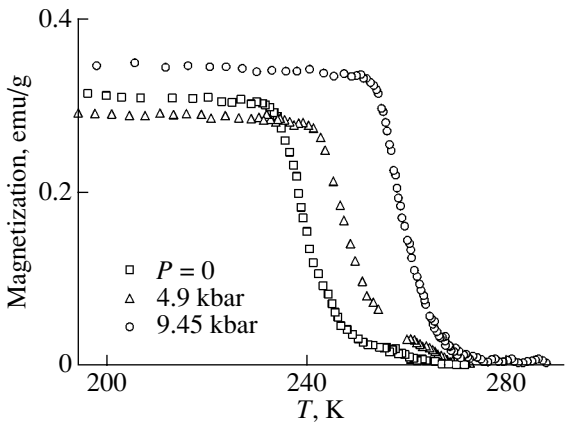

Fig. 8. Temperature dependence of the magnetization of $La_{0.6}Mn_{1.4}O_3$ in the field H = 5 Oe at different pressures.

by the fact that the dependences $M(T)$ cannot be described by the Brillouin function.

The large values of dT_C/dP in the FM materials containing charge carriers are caused by the fact that the pressure increases the electron hopping energy and the carrier mobility. This is also associated with the decrease in the average inclination angle of the MnO_6 octahedron under pressure and, hence, with decreasing the Mn–O distance and opening the Mn–O–Mn angles [27, 28].

The absence of the frequency dependence of the susceptibility and the ZFC magnetization peak near T_C indicates that the difference between the FC and ZFC magnetizations is not related to the spin-glass state [29]. According to Figs. 3 and 4, the ZFC magnetization remains almost unchanged between 50 and 230 K. This is probably caused by the suppression of the magnetic moment below T_C, when the sample is cooled in a zero or very weak magnetic field. This complicates domain-wall motion during magnetization and favors a manifestation of relaxation effects. The magnetic field promotes the overcoming of freezing for domains and properly orients them by increasing the magnetization. As a result, there is in fact no difference between the ZFC and FC magnetizations in strong magnetic fields (see Fig. 4).

The M_{ZFC} and M_{FC} magnetization sign reversal with an increase in the field (Figs. 3, 4) at $T < 45$ K cannot be explained within the model of phase separation into antiferromagnetic (AFM) and FM regions in manganites [30].

The presence of secondary magnetic phases (manganese oxides Mn_3O_4 and Mn_2O_3) can have an effect on the low-temperature behavior of the magnetization, because their temperatures of magnetic phase transitions are approximately 42 K. Under the condition of the ceramic technology employed, superstoichiometric manganese is completely dissolved in the solid solution and no other crystallographic phases are formed. This is confirmed by the changes in the lattice parameters and the Curie temperature as the manganese concentration increases. Mixed-valence Mn ions, together with vacancies, form planar clusters that manifest themselves as a diffuse halo in the x-ray diffraction patterns [21, 22]. The results of nuclear magnetic resonance [31, 32] and Mössbauer [33] investigations also confirm the existence of clusters incorporating Mn^{4+}, Mn^{3+}, and Mn^{2+} ions. The distorted planes of these clusters can be structurally close to separate planes of manganese oxides (Mn_2O_3, Mn_3O_4) [20, 22].

We also note that, in the case when the secondary phase exists in the manganites under study, magnetic ordering of Mn_2O_3 and Mn_3O_4 oxides should always be accompanied by an increase in the magnetization during a phase transition, which disagrees with the experimental results.

The experimental dependences $M(T, H)$ suggest the existence of regions with different magnetic orders at low temperatures: the major portion of the sample is in the FM-ordered state, and the rest is a canted spin (CS) structure with the FM interaction between the magnetic moments in clusters of mixed-valence manganese ions.

In order to determine the conditions of existence of the magnetic CS structure, we considered the experimental data under the assumption that the existing clusters contain Mn^{4+} and Mn^{3+} charge states. In this case, the concentration of Mn^{4+} ions is substantially lower than that of Mn^{3+} ions. Thus, the clusters are characterized by a composition similar to that of self-doped $LaMnO_3$, whose interaction energies of double and indirect exchanges can be comparable in magnitude. In this analysis, we used the following expression for the free energy of superexchange interactions:

$$F_{\text{exch}} = -T\ln\left\{\sum_{m=-S}^{S}\exp(\tilde{H}m/T)\right\} + H_0^{\text{const}}, \qquad (1)$$

where $\tilde{H} = 2\sqrt{J^2(0)\cos^2\alpha + J^2(\mathbf{k}_0)\sin^2\alpha}\langle S\rangle$ is the effective field of indirect exchange, α is the canting angle of the collinear AFM structure, $J(\mathbf{k})$ is the Fourier components of the indirect exchange for the FM ($\mathbf{k} = 0$) and AFM [$\mathbf{k} = \mathbf{k}_0 = (0, 0, \pi/a)$] ($A$-type structure) ordering types, a is the lattice constant, $J_1 > 0$ and $J_2 < 0$ are the parameters of the FM-intraplanar and AFM-interplanar pair superexchange interactions, and $\langle S\rangle$ is the average spin. The operator constant H_0^{const} is given by

$$H_0^{\text{const}} = N\langle S\rangle^2\{J(\mathbf{k}_0)\sin^2\alpha + J(0)\cos^2\alpha\}.$$

The double exchange energy can be written as

$$E_{\text{el}} = -\frac{W}{2}n(1-n), \qquad (2)$$

where $W = 4t(2 + \cos\gamma)$ is the width of the mobile electron band in the case of the CS structure [34]; t and n are the hopping integral and the concentration of mobile electrons, respectively; $\cos\gamma = (1 + d)\cos\alpha/\sqrt{(1-d)^2 + 4d\cos^2\alpha}$, $d = J_2(2J_1) < 0$.

Minimizing the total free energy $E = E_{\text{exch}} + E_{\text{el}}$ with respect to the parameter $\langle S\rangle$, we come to the conclusion that the existence of AFM, FM, and CS structures depends on the relation between the parameters $b = tn(1-n)/(4|J_2|S^2)$ and d. The calculations demonstrate that a domain of CS and FM phase coexistence arises at $d < -1/7$ in a certain range of the parameter b. There is a potential barrier between the FM and CS states in this domain. This potential barrier (approximately equal to 0.5 K) can explain the low-temperature magnetization behavior related to the emergence of the canted phase. Indeed, the FC magnetization in fields below the potential barrier always decreases during the FM–CS phase

transition. The external magnetic field can change the volume ratio of FM and CS phases by transferring a portion of the magnetic ions through the potential barrier. If the magnetic field is higher than the potential barrier, a stable FM state arises in the clusters and a positive M_{FC} jump will take place at 45 K, which is observed in the experiment.

Using the exchange parameters $J_1 = 9.6$ and $J_2 = -6.7$ K [35], we obtain the ratio $d = -0.35$. A numerical calculation by formulas (1) and (2) at $T = 0$ yields the value $b = 0.6$, at which the energies of the FM and CS phases coincide. Then, the parameter $n(1 - n)$ is approximately equal to 0.05 at $b = 0.6$, which characterizes the low hole concentration in clusters. For $b = 0.6$ and $d = -0.35$, the FM–CS transition temperature calculated using the relation $T_{cant}/4J_1 = 0.7$ is $T_{cant} \approx 30$ K, which agrees with the experimental value.

Thus, the above discussion of the experimental data makes it possible to explain the experimentally observed features of the magnetic behavior of manganites with excess manganese. Since the free carrier concentration in clusters is very low (~0.05) in comparison with n of the host matrix and since the clusters compose a component of the manganite structure, the clusters should be ordered ferromagnetically as the host matrix in the FC process. The magnetization decrement at 45 K is approximately 15% of the total magnetization and is virtually independent of the external magnetic field, which evidently indicates the formation of the CS structure. This is due to the fact that the superexchange interactions in the clusters are comparable to the double exchange in magnitude, which is considerably less than that in the host matrix because of the low hole concentration. Due to the competition of these interactions, the canted state arises at low temperatures. In strong magnetic fields, a stable FM state will arise in clusters and the positive magnetization jump will always take place at low temperatures.

In summary, we note that the metal–dielectric transition takes place in manganite–lanthanum perovskites with excess manganese. Moreover, the MRE manifests itself and increases with an increase in the Mn concentration. For samples with $x > 0.1$, the magnetization decreases in fields $H < 100$ Oe at $T < 45$ K and increases at $H > 200$ Oe. The theoretical consideration showed that this behavior is caused by the FM–CS phase transition in clusters of mixed-valence Mn ions in which the carrier concentration is substantially lower than in the host matrix and the superexchange interactions are comparable to the double exchange in magnitude. The competition of the double and indirect exchanges in the clusters promotes the formation of the state with a canted magnetic sublattice in the low-temperature region. Under pressure, the Curie, metal–dielectric transition, and MRE peak temperatures increase, while the MRE value decreases.

ACKNOWLEDGMENTS

This study was supported in part by the Basic Research Committee (Komitet Badan Naukowych, KBN), Poland (project no. 2P03B 139 18).

REFERENCES

1. A. P. Ramirez, J. Phys.: Condens. Matter **9** (1), 8171 (1997).
2. J. M. D. Coey, M. Viret, and S. von Molnar, Adv. Phys. **48** (2), 167 (1999).
3. P.-G. de Gennes, Phys. Rev. **118** (1), 141 (1960).
4. A. Maignan, F. Damay, C. Martin, and B. Raveau, Mater. Res. Bull. **32** (8), 965 (1997).
5. V. P. Pashchenko, A. A. Shemyakov, V. K. Prokopenko, *et al.*, J. Magn. Magn. Mater. **220** (2), 52 (2000).
6. J. E. O. Wollan and W. C. Koehler, Phys. Rev. **100** (2), 545 (1955).
7. B. A. A. Elemans, B. van Laar, K. R. van der Veen, and B. O. Loopstra, J. Solid State Chem. **3** (3), 238 (1971).
8. V. C. Tofield and W. R. Scott, J. Solid State Chem. **10** (2), 183 (1974).
9. J. A. M. van Roosmalen, E. H. P. Cordfunke, R. B. Helmholdt, and H. W. Zandbergen, J. Solid State Chem. **10** (1), 109 (1974).
10. Q. Huang, A. Santoro, J. W. Lynn, *et al.*, Phys. Rev. B **55** (22), 14987 (1997).
11. R. de Renzi, G. Allodi, G. Amoretti, *et al.*, Physica B (Amsterdam) **289–290**, 85 (2000).
12. R. Mahendiran, S. K. Tiwary, A. K. Raychaudhuri, *et al.*, Phys. Rev. B **53** (6), 3348 (1996).
13. R. Mahendiran, S. K. Tiwary, A. K. Raychaudhuri, *et al.*, Phys. Rev. B **54** (14), R9604 (1996).
14. J. A. Alonso, M. J. Martinez-Lope, M. T. Casias, and A. Minoz, Solid State Commun. **102** (1), 7 (1997).
15. K. N. Mikhalev, S. A. Lekomtsev, A. P. Gerashchenko, *et al.*, Pis'ma Zh. Éksp. Teor. Fiz. **72** (2), 867 (2000) [JETP Lett. **72**, 599 (2000)].
16. G. J. Chen, Y. H. Chang, and H. W. Hsu, J. Magn. Magn. Mater. **219** (2), 317 (2000).
17. V. N. Krivoruchko, S. I. Khartsev, A. D. Prokhorov, *et al.*, J. Magn. Magn. Mater. **207** (1–3), 168 (1999).
18. V. Dyakonov, A. Prokhorov, V. Shapovalov, *et al.*, J. Phys.: Condens. Matter **13** (18), 4049 (2001).
19. V. P. Pashchenko, A. A. Adreev, A. A. Shemyakov, *et al.*, Neorg. Mater. **34**, 62 (1998).
20. V. S. Abramov, V. P. Pashchenko, and O. P. Cherenkov, Funkts. Mater. **6**, 64 (1999).
21. V. P. Pashchenko, S. I. Khartsev, O. P. Cherenkov, *et al.*, Neorg. Mater. **35**, 1509 (1999).
22. V. P. Pashchenko, V. K. Prokopenko, A. A. Shemyakov, *et al.*, Metallofiz. Noveishie Tekhnol. **22** (1), 18 (2000).
23. V. P. Pashchenko, E. G. Darovskikh, V. S. Abramov, *et al.*, Neorg. Mater. **30**, 939 (1994).
24. V. V. Runov, D. Yu. Chernyshev, A. I. Kurbakov, *et al.*, Zh. Éksp. Teor. Fiz. **118** (5), 1174 (2000) [JETP **91**, 1017 (2000)].
25. M. Itoh, K. Hishi, J. D. Yu, and Y. Inaguma, Phys. Rev. B **55** (21), 14408 (1997).

26. M. Uehara, S. Mori, C. H. Chen, and S.-W. Cheong, Nature **399**, 560 (1999).
27. J. J. Neumeier, M. F. Hundley, J. D. Thompson, and R. H. Heffner, Phys. Rev. B **52** (11), R7006 (1995).
28. K. Kamenev, G. Balakrishnam, M. R. Lees, *et al.*, Phys. Rev. B **56** (5), 2285 (1997).
29. J. A. Maydosh, *Spin Glass: An Experimental Introduction* (Taylor and Francis, London, 1993).
30. É. L. Nagaev, Usp. Fiz. Nauk **166** (8), 833 (1996) [Phys. Usp. **39**, 781 (1996)].
31. G. J. Tomka, P. C. Riedi, Cz. Kapusta, *et al.*, J. Appl. Phys. **83** (11), 7151 (1998).
32. J. Dho, I. Kim, S. Lee, *et al.*, Phys. Rev. B **59**, 492 (1999).
33. V. Chechersky, A. Nath, I. Isaak, *et al.*, Phys. Rev. B **59** (1), 497 (1999).
34. P. W. Anderson and H. Hasegawa, Phys. Rev. **100** (2), 675 (1955).
35. F. Moussa, M. Hennion, and J. Rodriguez-Carvajal, Phys. Rev. B **54** (21), 15149 (1996).

Translated by A. Kazantsev

Physics of the Solid State, Vol. 45, No. 5, 2003, pp. 922–926. Translated from Fizika Tverdogo Tela, Vol. 45, No. 5, 2003, pp. 878–882.

MAGNETISM AND FERROELECTRICITY

High-Amplitude Precession and Dynamic Unsusceptibility of Magnetic Moments of a Two-Layer Film

D. I. Sementsov and A. M. Shutyĭ

Ulyanovsk State University, ul. Tolstogo 42, Ulyanovsk, 432700 Russia

e-mail: shuty@mail.ru

Received June 26, 2002; in final form, October 14, 2002

Abstract—The precession motion of magnetization in a longitudinal alternating magnetic field for a system of two antiferromagnetically coupled magnetoactive layers is studied. New dynamic modes characterized by large precession amplitudes and doubling of the period are found. The modes can be efficiently controlled using an external magnetic bias field. A new effect consisting in the unsusceptibility of a magnetic subsystem to excitation by an alternating field has been revealed. *© 2003 MAIK "Nauka/Interperiodica".*

Considerable study has been given over many years to static and dynamic properties of various magnetically coupled structures [1–6]. Among such structures, one can single out structures with weak interlayer coupling of magnetostatic nature [1, 2] and structures with strong coupling due to indirect exchange interaction [3–5]. The interlayer coupling plays a very important part in the static and dynamic behavior of magnetization in such structures. Dynamic modes associated with an abrupt jump in the angle of magnetization precession [6–9] are of particular interest among the various effects caused by the interaction of an rf field with both one-layer and multilayer structures. The resonance excitation of precession of a spin subsystem in one-layer and multilayer thin-film structures by a weak alternating field (i.e., in the range of linear ferromagnetic resonance) is usually achieved in an rf field directed normally to a static bias field [2, 10]. However, with increasing amplitude of the rf field (i.e., in the range of nonlinear resonance), the excitation of the spin system by the longitudinal rf field becomes more and more efficient [11]. In two-layer structures with antiferromagnetic interaction ensuring antiparallel orientation of the magnetic moments of layers in the absence of a bias field, it is possible to excite a magnetic subsystem more efficiently in a wide frequency range.

In this article, new high-amplitude dynamic modes of magnetization precession excited by a longitudinal microwave field are studied in the layers of a similar magnetically coupled system. The analysis of dynamic behavior is restricted to the structures with magnetostatic interlayer coupling. The magnetic layers in such structures are, as a rule, polycrystalline with uniaxial magnetic anisotropy. Typical representatives of such structures are the permalloy-based films with nonmagnetic SiO_2 interlayers [2]. Such structures are widely used in various microwave devices.

1. Let us consider a structure with two ferromagnetic layers separated by a nonmagnetic interlayer. Each magnetic layer is characterized by a width d_i, magnetization $\mathbf{M}_i$, and a planar uniaxial magnetic anisotropy characterized by the constant K_i. The external magnetic bias field $\mathbf{H}$ and rf field $\mathbf{h}(t)$ are applied along the coinciding easy magnetization axes of both layers. The magnetic subsystem energy per unit area of the film has the form

$$\begin{aligned} E = \sum_{i=1,2} d_i\{K_i\sin^2\varphi_i - (H+h)M_i\cos\varphi_i\cos\psi_i \\ - 2\pi M_i^2\cos^2\psi_i\} + AM_1M_2d_{12} \\ \times[\cos\psi_1\cos\psi_2\cos(\varphi_1-\varphi_2) + \sin\psi_1\sin\psi_2], \end{aligned} \quad (1)$$

where $d_{12} = d_1d_2(d_1 + d_2)^{-1}$ is the reduced width of two magnetic layers, $A > 0$ is the negative coupling constant of magnetic layers determined mainly by the demagnetization fields and dependent generally on the interlayer width, material, and structural characteristics [1]; the azimuth angle φ_i (measured from the y axis) and the angle ψ_i of inclination to the film plane define the orientation of vector $\mathbf{M}_i$ in the horizontal and vertical planes, respectively. The adopted sign of the coupling constant provides antiparallel orientation of the magnetic moments of layers in the equilibrium state at $H = 0$.

The equation of motion for the magnetization vectors of each layer $\mathbf{M}_i$ is chosen in the Landau–Lifshitz form. In a spherical coordinate system, this equation cam be written as

$$\begin{aligned} \dot\varphi_iM_id_i\sin\psi_i &= \gamma\frac{\partial E}{\partial\psi_i} + \frac{\lambda_i}{M_i}\frac{1}{\sin\psi_i}\frac{\partial E}{\partial\varphi_i}, \\ \dot\psi_iM_id_i &= \frac{\lambda_i}{M_i}\frac{\partial E}{\partial\psi_i} - \gamma\frac{1}{\sin\psi_i}\frac{\partial E}{\partial\varphi_i}, \end{aligned} \quad (2)$$

1063-7834/03/4505-0922$24.00 © 2003 MAIK "Nauka/Interperiodica"

where γ is the gyromagnetic ratio and λ_i is the damping parameter in the corresponding layer [10]. The calculations will be performed for the following values of parameters chosen close to those existing in real permalloy-type films [2]: $\lambda_1 = \lambda_2 = 5 \times 10^7$ s^{-1}; $H_{k1} = 10$ Oe and $4\pi M_1 = 1.1 \times 10^4$ G are the anisotropy field and the magnetization of the first film; $H_{k2} = 5$ Oe and $4\pi M_2 = 8 \times 10^3$ G (the same for the second film); $\gamma = 1.76 \times 10^7$ (Oe s)$^{-1}$; and the film thicknesses are equal, $d_1 = d_2 = 0.1$ μm. Because of the large values of the demagnetization fields for such films ($4\pi M_i \gg H_{ki}, AM_i$), the amplitude of the magnetization precession over the polar angle is much smaller than the amplitude of variation of the azimuth angle. Thus, in the absence of a static field, $\psi_i \sim h/4\pi M_i$, while $\varphi_i \sim h/H_{ki}$. Taking into account that $\psi_i \ll \varphi_i$, the inclination angles of magnetic moments with respect to the film planes can be considered equal to zero.

2. Equilibrium azimuth angles φ_{0i} can be determined from the conditions of equilibrium: $\partial E/\partial\varphi_i = 0$ and $\partial^2 E/\partial\varphi_i^2 > 0$. In view of Eq. (1), this gives the following system of equations:

$$\begin{aligned} &K_i \sin 2\varphi_{0i} + HM_i \sin\varphi_{0i} - Ad_{3-i}(d_1 + d_2)^{-1} \\ &\quad \times M_1 M_2 \sin(\varphi_{0i} - \varphi_{03-i}) = 0, \\ &H_{ki}\cos 2\varphi_{0i} + H\cos\varphi_{0i} - Ad_{3-i}(d_1 + d_2)^{-1} \\ &\quad \times M_{3-i}\cos(\varphi_{0i} - \varphi_{03-i}) > 0, \\ &\quad i = 1, 2. \end{aligned} \tag{3}$$

Analytical solution of these equations is possible only for small values of equilibrium angles $\varphi_{0i} \ll 1$, which takes place for $H \gg H_{ki}$ [12]. In the general case, these angles at the values of parameters in Eqs. (3) are no longer small; therefore, system (3) can be solved only by numerical methods. Figure 1 shows the equilibrium azimuth angles of magnetization in both layers, φ_{01} (dashed lines) and φ_{02} (solid lines), as functions of the magnetic bias H (initially oriented along vector $\mathbf{M}_1$). The angles were calculated for the constants $A = (1, 3, 5) \times 10^{-2}$ (curves *1–3*) corresponding to magnetostatic coupling. When the bias field is increased to reach H_c, an orientational phase transition occurs in the system of coupled magnetic moments. At small values of the coupling constant, $A \le A_c$ (curves *1*), the magnetization in the second film at the point of phase transition changes to the opposite direction and vector $\mathbf{M}_2$ becomes parallel to vector $\mathbf{M}_1$. If $A > A_c$ (curves *2*, *3*), the magnetization of the second film rotates by an angle different from 180° because of repulsion of the magnetic moments of the films; the direction of vector $\mathbf{M}_1$ also deviates from the initial direction. If $H = H_c$, the state of the system with $\varphi_{02} = \pi$ becomes unstable and the magnetization of the second film can be equiprobably oriented in both the $\varphi_{02} < \pi$ and $\varphi_{02} > \pi$ directions.

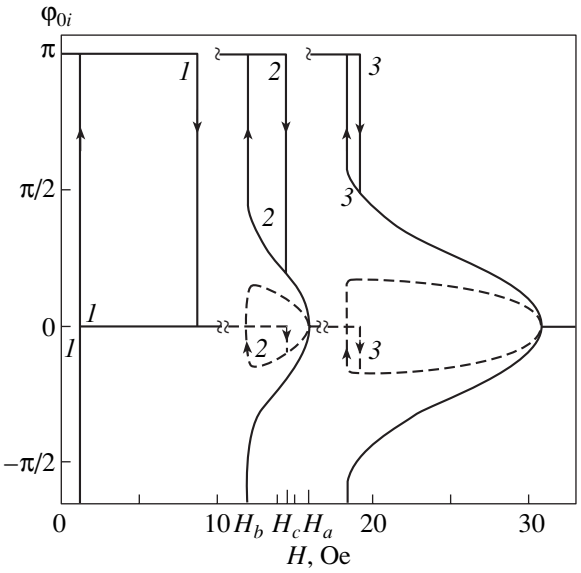

Fig. 1. Field dependences of equilibrium orientations of magnetic moments in each of the layers at different values of coupling constant A = 0.01 (*1*), 0.03 (*2*), and 0.05 (*3*). Other details are explained in the text.

Accordingly, the magnetization of the first film will be rotated either to the $\varphi_{01} < 0$ or $\varphi_{01} > 0$ direction. As a result, one of the two possible equilibrium states that are symmetrical with respect to the applied field direction is realized. Further increase of the field results in a decrease in the angle between $\mathbf{M}_1$ and $\mathbf{M}_2$. If $H = H_a$, this angle becomes equal to zero; i.e., for $H \ge H_a$, the equilibrium corresponds to unidirectional orientation of the magnetization vectors.

On decreasing the bias field, the state with unidirectional orientation of the magnetic moments transforms into one of two symmetrically noncollinear states upon reaching a bifurcation field $H = H_a$. Noncollinear states of magnetic moments of the films exist within the range of the bias field $H_b < H < H_a$. This range widens with an increase in the coupling constant. For $H = H_b$, the orientational transition occurs, resulting in the state with opposite directions of the magnetic moments of the films. At small values of the coupling constant (curve *1*), $H_b \cong H_a$; therefore, noncollinear equilibrium states are virtually absent. Depending on the magnitude of A, the value of H_a might be larger or smaller than H_c. For a chosen direction of the bias field and $H_c > H_b$, variation of H causes orientational hysteresis. It can be seen that the values H_c and H_b approach each other with increasing coupling constant and the hysteresis loop narrows. The width of the hysteresis loop can be as small as a fraction of an oersted, which is very important for the realization of the dynamic modes considered below. The exact magnitude of the field H_c at which the state

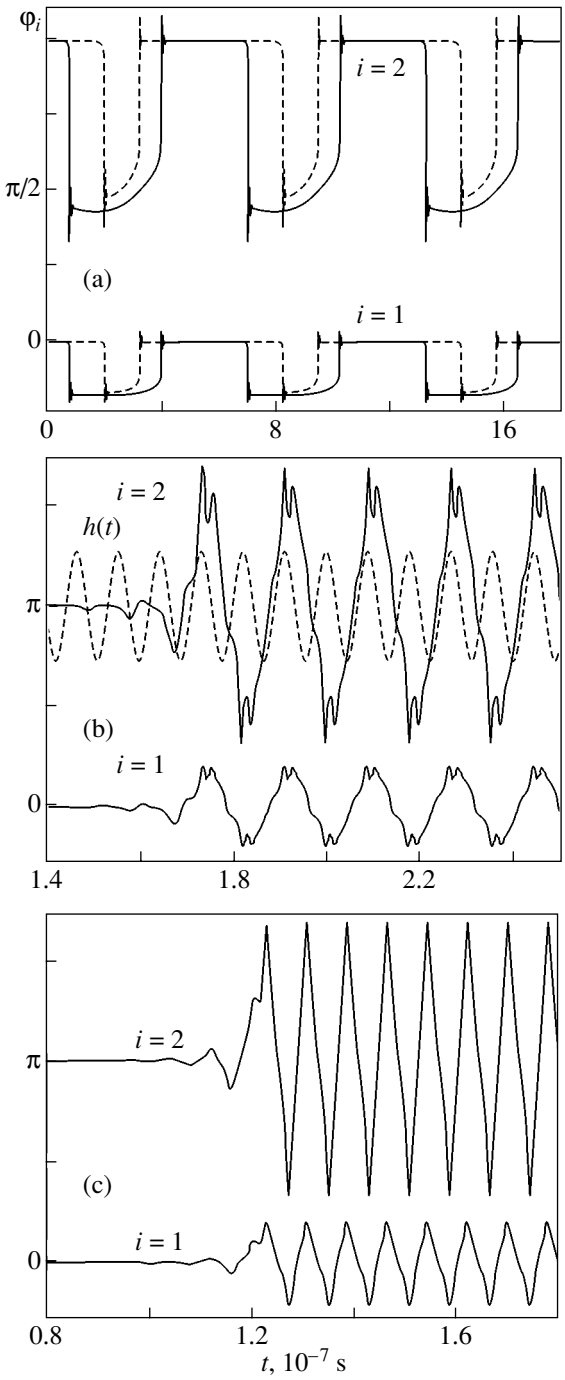

Fig. 2. Time variation of the azimuth angles of magnetic moments in layers at the frequencies $\omega \times 10^{-8} = 0.1$ (a), 7 (b), and 16 s^{-1} (c) of the longitudinal excitation field and corresponding to high-amplitude precession modes.

with the angles $\varphi_{01} = 0$ and $\varphi_{02} = \pi$ becomes unstable is determined by

$$H_c = 1/4(G_1 + \sqrt{G_1^2 + 8G_2}), \qquad (4)$$

where $G_1 = A(M_1 - M_2) + 2(H_{k2} - H_{k1})$ and $G_2 = A(M_1H_{k1} + M_2H_{k2}) + 2H_{k1}H_{k2}$. The magnitude of the field H_a can be determined using expression (4) upon changing the signs of M_2 and H_{k2}. The coupling constant A can be found by assuming that $H_c = H_a$.

3. The above analysis of the conditions for equilibrium of the magnetic moments of the two layers shows that, at certain magnitudes of the bias field, the system under consideration can exhibit orientational phase transitions at which the orientation of the magnetization in layers changes abruptly. In the vicinity of such critical fields, very favorable conditions are created for the excitation by a weak rf field **h** of various dynamic modes sensitive to small changes in the system parameters and the field magnitudes. Most suitable for the effective excitation of magnetic oscillations in the longitudinal alternating field are the systems with narrow ($\Delta H \le 1$ Oe) hysteresis loops. The magnitude of the magnetic bias field should be either inside the loop or close to its critical fields.

Figure 2 shows the time variation of the azimuth angles of the magnetic moments of layers (the coupling constant $A = 0.05$) in a microwave field with amplitude $h = 1$ Oe at the frequencies $\omega = 0.1 \times 10^8$ (Fig. 2a), 7×10^8 (Fig. 2b), and 16×10^8 s^{-1} (Fig. 2c) in the bias field $H = 19$ Oe. It can be seen from Fig. 2a that at low frequencies a "pulsed" mode occurs with short transition intervals and a period equal to the period T_h of the alternating field. The amplitude of this mode is determined by the difference of the angles of the equilibrium steady-state positions at the chosen values of H and A ($\varphi_{01} \approx 0, \mp 30°$; $\varphi_{02} \approx 180°, \pm 89°$) and weakly depends on the amplitude of the alternating field h. Oscillations of the magnetic moments in each of the layers occur between two potential wells, while the microwave field drives the system from equilibrium and compensates the energy losses of the precession motion. At $A = 0.05$, the minimum amplitude of the alternating field required for the realization of this oscillation mode is $h_{min} \approx 0.7$ Oe. An increase in h to 1 Oe and even higher does not change significantly the parameters of the mode. Because of the narrowing of the orientational hysteresis loop, the threshold value of the alternating field lowers with increasing coupling parameter A; e.g., at $A = 0.06$, $h_{min} \approx 0.4$ Oe. The mode under discussion allows the "dead time" to be controlled by varying the bias field. For example, when H shifts to the left side of the hysteresis loop ($H = 18.3$ Oe), the pulse duration shortens, as shown by the dashed line in Fig. 2a. Apart from the equilibrium antiparallel orientation of magnetic moments, in our case there exist two noncollinear equilibrium orientations [13]; therefore, two equally probable modes of remagnetization along the directions $0 < \varphi_2 < \pi$ and $-\pi < \varphi_2 < 0$ are possible as a result of the corresponding magnetization reversal in the first film. However, if the pulse mode is active, only one of the two above-mentioned reversals is possible.

In the frequency range $\omega \sim (7–17) \times 10^8$ s^{-1}, there exists a steady-state high-amplitude oscillation mode (Figs. 2b, 2c) with a doubled period $2T_h$ (the dependence $h(t)$ in relative units is shown in Fig. 2b by a dashed line) and an amplitude almost twice as large as that of the pulsed mode (Fig. 2). In this range, there exist some intervals with random oscillation of magnetic moments and also frequency intervals $\omega_n \sim (7.5–8.0) \times 10^8$ s^{-1} where the system becomes insensitive to the effect of an alternating field. At the frequencies preceding the dynamic unsusceptibility (DU), the period of steady-state high-amplitude oscillations contains several maxima and minima (Fig. 2b); at frequencies above the DU, the oscillation period also becomes twice as large as the period of the microwave field but contains only one maximum and one minimum (Fig. 2c). Note that in a transverse field of the same amplitude and frequency, the maximum attained angles of magnetization precession do not exceed 10°.

Between the frequency ranges of the precession modes (Figs. 2a, 2b), there exists a range of alternating fields featuring a sequence of arbitrary periods including periods with one of two oscillations symmetrical with respect to the direction $\varphi = 0$ and resulting in the appearance of random oscillation modes. The random oscillations occurring at the frequencies $\omega = (2.9; 3) \times 10^8$ s^{-1} are shown in Figs. 2a and 2b, respectively. It can be seen that these modes are very sensitive to the frequency of the alternating field.

The $\varphi_i(t)$ dependence at the frequencies $\omega = (7.15; 7.4; 7.5) \times 10^8$ s^{-1} for the indicated values of the fields and the coupling constant is shown in Fig. 4 (curves *1–3*). The curves demonstrate the behavior of magnetic moments near the DU interval, i.e., the transparency window of the spin system with respect to the longitudinal microwave field. From Fig. 4 it can be seen that the interval of random oscillation (curves *1*) precedes the DU interval. With increasing frequency, the random oscillations transform into regular oscillations with small amplitudes and the period equal to a period of the rf field (curves *2*). As the frequency approaches the DU interval, the amplitude of regular oscillations decreases and finally vanishes (curve *3*). Variation of the amplitude of the rf field shifts the frequency interval of DU; e.g., at $h = 0.8$ Oe, the DU interval falls in the frequency range $\omega_n \sim (6.8–7.5) \times 10^8$ s^{-1}.

The analysis made in this study shows that the use of a longitudinal microwave field for the excitation of layer magnetic structures with antiferromagnetic coupling makes it possible to considerably widen the frequency range of the high-amplitude precession mode towards lower frequencies. It is found that there exists a frequency interval in which the magnetically coupled system becomes insensitive to the action of an alternating field. Similar effects should also be observed in single-crystal two-layer films with strong exchange coupling and cubic anisotropy (Fe/Cr type). However, elu-

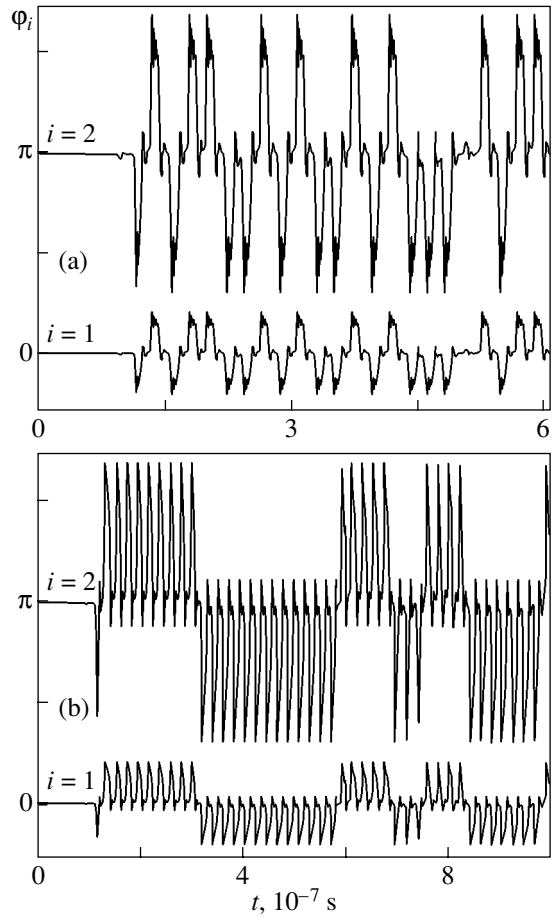

Fig. 3. Random oscillations of magnetic moments in the films at the frequencies between intervals of high-amplitude modes: $\omega \times 10^{-8} = 2.9$ (a), 3.0 s^{-1} (b).

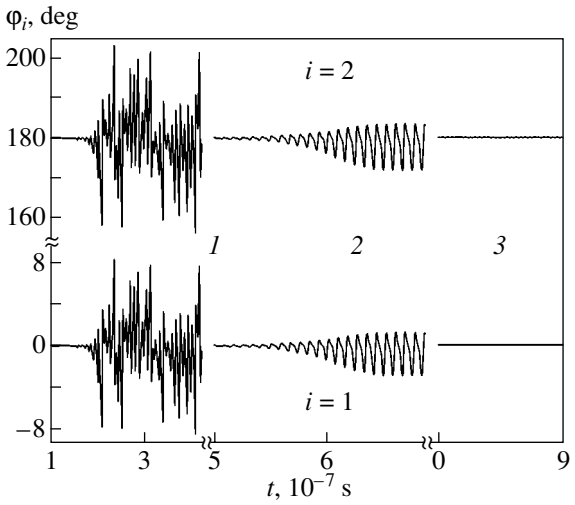

Fig. 4. Dynamic modes of magnetic moments in layers at the frequencies close to the interval of DU and the time dependence of azimuth angles within the DU interval: $\omega \times 10^{-8} = 7.15$ (*1*), 7.4 (*2*), and 7.5 s^{-1} (*3*).

cidation of their specific features requires separate analysis.

ACKNOWLEDGMENTS

This study was supported by the Ministry of Education of the Russian Federation, project no. PD02-1.2-72.

REFERENCES

1. A. Yelon, in *Physics of Thin Films: Advances in Research and Development*, Ed. by M. H. Francombe and R. W. Hoffman (Academic, New York, 1971; Mir, Moscow, 1973), Vol. 6.
2. N. M. Salanskiĭ and M. Sh. Erukhimov, *Physical Properties and Application of Magnetic Films* (Nauka, Novosibirsk, 1975).
3. V. V. Ustinov, M. M. Kirilova, I. V. Lobov, *et al.*, Zh. Éksp. Teor. Fiz. **109** (2), 477 (1996) [JETP **82**, 253 (1996)].
4. N. G. Bebenin, A. V. Kobelev, A. P. Tankeev, and V. V. Ustinov, Fiz. Met. Metalloved. **82** (4), 348 (1996).
5. A. K. Zvezdin and V. V. Kostyuchenko, Fiz. Tverd. Tela (St. Petersburg) **41** (3), 461 (1999) [Phys. Solid State **41**, 413 (1999)].
6. A. K. Kazansky and V. M. Uzdin, Phys. Rev. B **52** (9), 9477 (1995).
7. B. Neite and H. Doetsch, J. Appl. Phys. **62** (2), 648 (1987).
8. A. G. Temiryazev, M. P. Tikhomirova, and A. V. Maryakhin, *Abstracts of International Workshop–Seminar on New Magnetic Materials in Microelectronics, NMMM-XVI, Moscow* (1998), Part 1, p. 270.
9. A. M. Shutyĭ and D. I. Sementsov, Zh. Éksp. Teor. Fiz. **118** (3), 110 (2000) [JETP **91** (3), 531 (2000)].
10. A. G. Gurevich and G. A. Melkov, *Magnetic Oscillations and Waves* (Nauka, Moscow, 1994).
11. S. M. Rezende and F. M. de Aguiar, Proc. IEEE **78** (6), 893 (1990).
12. R. N. Nosov and D. I. Sementsov, Fiz. Tverd. Tela (St. Petersburg) **42** (8), 1430 (2000) [Phys. Solid State **42** (8), 1471 (2000)].
13. D. S. Sementsov and A. M. Shutyĭ, Pis'ma Zh. Éksp. Teor. Fiz. **74** (6), 339 (2001) [JETP Lett. **74** (6), 306 (2001)].

Translated by A. Zalesskiĭ

Physics of the Solid State, Vol. 45, No. 5, 2003, pp. 927–931. Translated from Fizika Tverdogo Tela, Vol. 45, No. 5, 2003, pp. 883–887.

MAGNETISM AND FERROELECTRICITY

Unidirectional Anisotropy in (*RE–TM*)/NiFe Film Systems

V. A. Seredkin*, R. S. Iskhakov*, V. Yu. Yakovchuk*, S. V. Stolyar, and V. G. Myagkov***

** Kirensky Institute of Physics, Siberian Division, Russian Academy of Sciences, Akademgorodok, Krasnoyarsk, 660036 Russia*

*** Krasnoyarsk State University, Krasnoyarsk, 660041 Russia*

e-mail: sva@iph.krasn.ru

Received August 12, 2002; in final form, October 14, 2002

Abstract—The quasi-static magnetic parameters of TbFe/NiFe and DyCo/NiFe bilayer exchange-biased films characterized by unidirectional anisotropy are studied. The characteristic temperatures are determined at which the unidirectional anisotropy disappears due to processes in the magnetically hard layer. The mechanisms responsible for the appearance of unidirectional anisotropy associated with the heterophase property of the magnetically hard layer are analyzed. © *2003 MAIK "Nauka/Interperiodica".*

1. INTRODUCTION

The phenomenon of unidirectional anisotropy in ferromagnets, which manifests itself in a shift of the magnetic hysteresis loop along the axis of the fields, was discovered by Meiklejohn and Bean in oxidized cobalt powders [1]. The physical cause of this phenomenon was ascertained at the same time. The cause of the unidirectional anisotropy was shown to be an exchange interaction at the ferromagnet–antiferromagnet interface under the condition of the collinear orientation of magnetizations of the ferrimagnet and one of the antiferromagnet sublattices. This effect was thoroughly studied in NiFe/NiFeMn and NiFe/FeMn film systems in [2–4]. In [5, 6], the (*RE–TM*)/NiFe bilayer systems were produced for the first time. Here, (*RE–TM*) is DyCo or TbFe, i.e., a ferrimagnet with perpendicular magnetic anisotropy (PMA), and NiFe is a ferromagnet (permalloy) with uniaxial anisotropy and magnetization in the sample plane. These systems, immediately after evaporation (without annealing), are also characterized by unidirectional anisotropy, and the shift in the hysteresis loop of NiFe (ΔH) along the axis of the fields considerably exceeds the values observed in [1–4] (see Fig. 1a).

The following circumstance was surprising. According to the current concepts of the magnetic structure of ferrimagnetic alloys of *RE–TM* compensation compositions, the orientations of the effective magnetization vectors in separate layers of (*RE–TM*)/NiFe bilayer films we studied are mutually orthogonal and, hence, are exchange-unbiased. Therefore, the features observed in the magnetization reversal curves for the NiFe layer in these bilayer systems cannot be interpreted within the conventional concepts.

In this work, we investigated the static magnetic properties and the temperature dependences of the static magnetic characteristics in DyCo/NiFe and TbFe/NiFe bilayer exchange-biased films with unidirectional anisotropy. The study was undertaken with the aim of elucidating the real magnetic microstructure of the films of *RE–TM* ferrimagnetic alloys with compensation compositions. Note that thin ferrimagnetic films of *RE–TM* alloys produced in the form of solid solutions over a wide concentration range are characterized

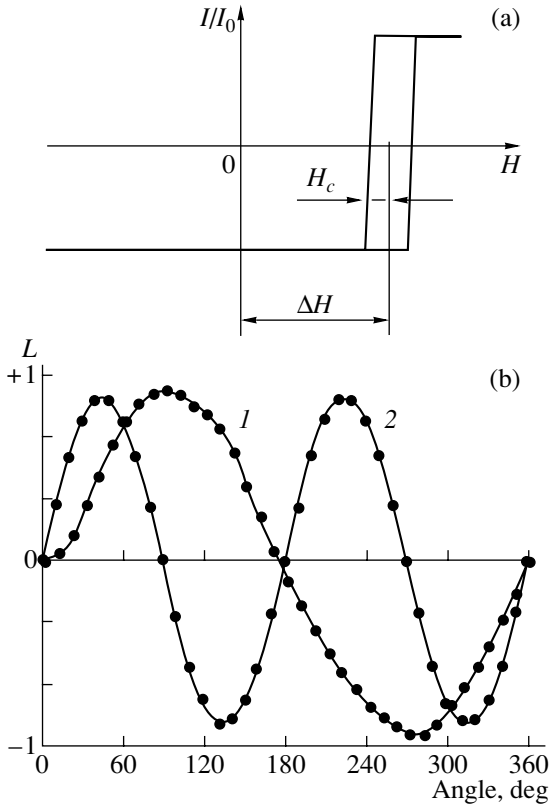

Fig. 1. (a) Typical magnetization reversal curve and (b) the angular momentum curves of the (*1*) *RE–TM*/NiFe and (*2*) NiFe film systems.

Numerical values of the coercive force and the bias field of DyCo/NiFe bilayer films at different thicknesses of NiFe

Thickness, nm	H_c, Oe	ΔH, Oe
50	4	60
100	2.5	26
150	1.5	14
300	0.7	6
400	0.4	4
700	0.3	2

by the magnetic compensation represented in the concentration–temperature plane by the curve $x_c(T_{comp})$, near which these materials become most magnetically hard. In the vicinity of the compensation temperature T_{comp}, these films in general exhibit anomalies: step magnetization curves, anomalous magnetooptic curves, anomalous Hall dependences, etc., which have not yet been properly explained. The necessity of interpreting experimental data requires a search for novel approaches to the study of thin films of *RE–TM* ferrimagnetic alloys. In our opinion, the second layer with known magnetic properties can be used for this purpose. Therefore, the study of the magnetic phenomena in (*RE–TM*)/NiFe bilayer films of (*RE–TM*) compensation compositions is of general physical interest.

2. SAMPLES AND EXPERIMENTAL TECHNIQUE

The (*RE–TM*)/NiFe bilayer exchange-biased films were produced through thermal evaporation under a vacuum of $\sim 3 \times 10^{-6}$ Torr. Cover glasses were used as substrates. The *RE–TM* and NiFe layers were sequentially deposited from three independent evaporators with ring-shaped cathodes. A ferrimagnet (TbFe or DyCo) was represented as a film with a perpendicular magnetic anisotropy of $\sim 3–5 \times 10^5$ erg/cm^3 and a coercive force of ~5–7 kOe. According to electron microscopy [7, 8], the ferrimagnetic layer is an amorphous or nanocrystalline alloy with a grain size of ~5 nm and the ferromagnetic layer is an NiFe film with uniaxial anisotropy in the sample plane. In order to obtain uniaxial anisotropy in NiFe during evaporation, a dc magnetic field of 20 Oe was applied in the sample plane. The ferrimagnet thickness was h = 70 nm, and the NiFe thickness was varied from 50 to 700 nm. The bilayer samples were produced in the following sequences. (i) The ferrimagnetic layer of precompensation or postcompensation composition was evaporated immediately onto the substrate, and then the NiFe layer was evaporated. (ii) The NiFe layer was evaporated immediately onto the substrate, and then the ferrimagnetic layer was evaporated onto it. We should note that, in case (i), the crystallite size in the NiFe layer is ~10–15 nm, because the amorphism (nanocrystallinity) of a ferrimagnet (TbFe, DyCo) layer has a significant effect on the formation of the crystal structure of the permalloy layer.

The static magnetic parameters of the magnetization reversal curves and their temperature dependences were measured using a loop scope in fields up to 250 Oe at a frequency of 50 Hz. The angular mechanical momenta were measured at room temperature using a torsional magnetometer in fields up to 12 kOe. In these techniques, a field that reverses the magnetism was applied in the sample plane in the course of the measurements and the ferrimagnetic *RE–TM* layer was always in a saturated state (at room temperature).

An extensive technological search was preliminarily carried out to optimize the growth of the film structures with exchange unidirectional anisotropy. From the application viewpoint, the most acceptable values of the parameters under study were obtained for ferromagnetic films with a nickel content of 80–83%, i.e., for conventional permalloys with zero magnetostriction.

The table lists the magnetic parameters of the DyCo/NiFe bilayer films with exchange unidirectional anisotropy versus the ferromagnetic layer thickness.

3. EXPERIMENTAL RESULTS

The dependences of mechanical momenta L on the angle φ for the DyCo/NiFe bilayer system with unidirectional anisotropy and the NiFe films with uniaxial anisotropy (Fig. 1b) were measured at room temperature using a torsional magnetometer. Similar dependences were also measured for systems with ferrimagnetic TbFe.

The dependence $L(\varphi)$measured in the angle range from 0 to 360° can be used to calculate the constants of uniaxial and unidirectional anisotropy (K_u and K_o, respectively) by a simple method using the following equations:

$$\frac{L(\varphi) + L(\varphi + \pi)}{2} = K_u \sin 2\varphi, \quad (1)$$

$$\frac{L(\varphi) - L(\varphi + \pi)}{2} = K_o \sin 2(\varphi - \gamma_o), \quad (2)$$

where γ_o is the angle between the easy magnetization axis (EMA) and the direction of unidirectional anisotropy.

The numerical values of K_u and K_o, as well as their dependences on the NiFe layer thickness, for the DyCo/NiFe and TbFe/NiFe exchange-biased systems with unidirectional anisotropy are given in Fig. 2.

It can be seen from Fig. 2 that the constants of uniaxial and unidirectional anisotropy of TbFe/NiFe and DyCo/NiFe film systems are characterized by similar dependences on the NiFe film thickness.

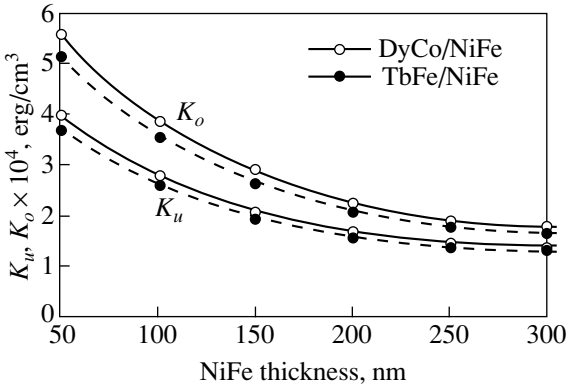

Fig. 2. Dependence of the constants of uniaxial (K_u) and unidirectional (K_o) anisotropies of the (*RE–TM*)/NiFe film system on the NiFe thickness.

As was noted above, in contrast to [2–4], the bilayer exchange-biased films are characterized by a sharp interface between layers; hence, the specific energy E_S of the surface interaction should be identical for all the samples and independent of the NiFe layer thickness (while the magnitude of unidirectional anisotropy is inversely proportional to the NiFe layer thickness [9]). We also note that the effective magnetic thickness Δh_{eff} of the surface exchange interaction between layers (we calculated in [10]) is ~50 nm.

The temperature dependences of the coercive force H_c and the bias fields ΔH for (*RE–TM*)/NiFe bilayer films with unidirectional anisotropy upon magnetization reversal in an ac field were measured at temperatures from +20 to +140°C. The magnetic field was applied along both the EMA and hard magnetization axes (HMA) of the NiFe layer (Figs. 3, 4). It is worth noting that the static magnetic parameters H_c and ΔH change insignificantly in the temperature range from –50 to +60°C, which is important from the application viewpoint.

An analysis of the curves shown in Figs. 3 and 4 demonstrates that there exists a certain temperature (~60 and ~90°C for TbFe/NiFe and DyCo/NiFe, respectively) at which H_c and ΔH change drastically and the unidirectional anisotropy almost disappears; i.e., the hysteresis loop becomes nearly symmetric with respect to zero field.

Upon magnetization reversal along the HMA, the hysteresis loop of the TbFe/NiFe bilayer film system is not open and is almost symmetric with respect to the zero applied field H. As the film system is heated from room temperature to 90°C, the magnetic system does not exhibit any changes. In the range of ~90°C, the hysteresis loop is sharply opened, which is characterized by the coercive force H_c^*. In [11], a similar change in the coercive force of DyCo films was observed in the course of their heating and magnetization reversal along the HMA. As compared to the TbFe system, the

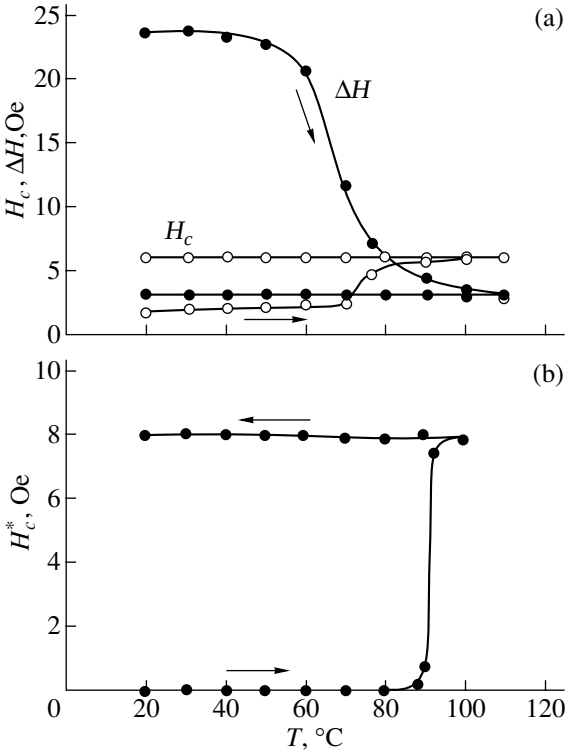

Fig. 3. Heating–cooling cycle of the TbFe/NiFe film system along the (a) EMA and (b) HMA.

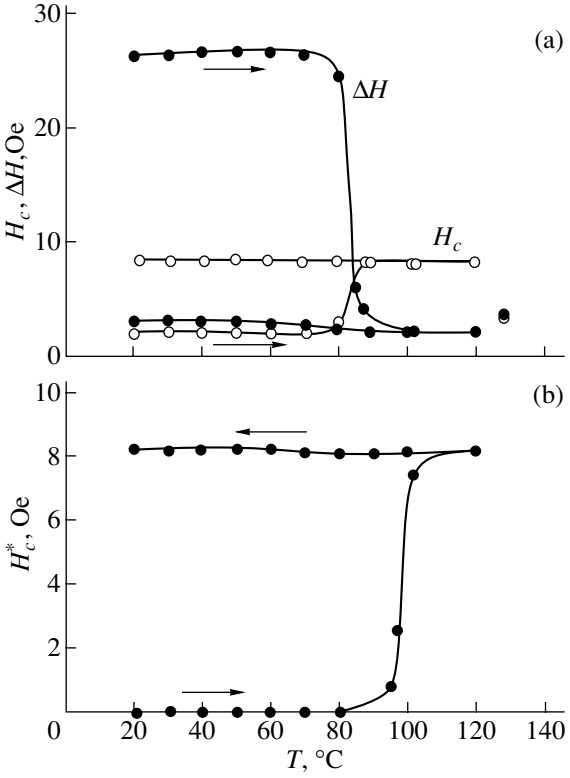

Fig. 4. Same as in Fig. 3 for DyCo/NiFe: (a) along the EMA and (b) along the HMA.

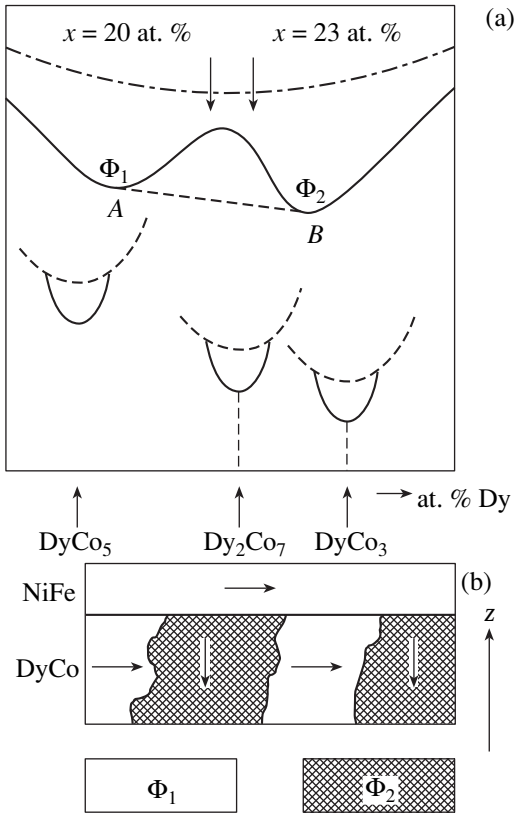

Fig. 5. Schematic drawings of (a) a portion of the phase diagram and (b) the hypothetical configuration of the magnetization vectors of the phases in the DyCo/NiFe system.

same transition in DyCo/NiFe is observed at a higher temperature (~100°C).

4. DISCUSSION

The $Dy_{22}Co_{78}/Ni_{81}Fe_{19}$ bilayer films produced are exchange-biased systems. The hysteresis loops measured for the NiFe layer in the EMA direction are characterized by the bias field ΔH, whose numerical values depend on the thicknesses of individual layers (table). At the same time, the significant perpendicular magnetic anisotropy in the DyCo magnetically hard ferrimagnetic layer, as well as the identical magnetooptical characteristics measured at different surfaces of the DyCo uniaxial film, indicate the following circumstance. In order to induce the required exchange field in the NiFe ferromagnetic film, the DyCo layer must contain percolation regions that emerge to its outer surfaces. In these regions, the magnetization vector of the sublattice of Co atoms should be aligned with the film plane. In our opinion, the exchange interaction of these regions with permalloy causes unidirectional exchange anisotropy. Thus, the static magnetic characteristics of the NiFe alloy layer can serve as an indicator of the magnetic microstructure of the DyCo alloy layer.

We believe that the magnetic inhomogeneity of DyCo (the regions comprising the major portion of the alloy in which the magnetization vector of the sublattice of Co atoms is perpendicular to the film plane and the regions in which the magnetization vector of the sublattice of Co atoms is parallel to the film plane) is associated with the heterophase composition of these alloys. Indeed, according to the results of electron microscopy (micrographs), the DyCo thin films [7, 8] are either amorphous or nanocrystalline heterophase alloys. To answer the question what is the local phase composition of the heterophase DyCo alloy films under study, one should consider a thermodynamically stable phase diagram of the DyCo crystalline alloys. We note that the melting diagrams of the *RE–TM* (Ho, Tb, Dy, Er, Gd, etc.)–(Fe, Co) alloys are similar to one another and that they present a number of stoichiometric compounds: RE_2TM_{17}, $RETM_5$, RE_2TM_7, $RETM_3$, $RETM_2$, and RE_4TM_3 [12]. The only difference lies in the temperature range of stability of these stoichiometric compounds.

Figure 5a shows a schematic drawing of the portion of the room-temperature phase diagram on the coordinates (G, C), where G is the Gibbs thermodynamic potential and C is the concentration in the range of compositions close to that of the films studied. Thermodynamic potentials G_i in the form of parabolas corresponding to the stoichiometric compounds $DyCo_5$, Dy_2Co_7, and $DyCo_3$ are also shown in Fig. 5a. The Gibbs potential of the melt (liquid phase) is plotted by the dash-dotted curve. The crystalline-to-amorphous or crystalline-to-nanocrystalline phase transition is accompanied, first, by an increase in the absolute values of the potentials and, second, by broadening of the parabolas describing the potentials G_i of the individual phases. The superposition of the G_i curves for alloys in the nanocrystalline state is shown in Fig. 5a by the heavy curve. The compositions of the DyCo alloy films we studied are indicated by arrows. Line AB corresponds to the possible phase composition of the mechanical mixture of the phases Φ_1 and Φ_2. Since the stoichiometric compounds $DyCo_5$, Dy_2Co_7, and $DyCo_3$ are characterized by similar closely packed structures [12], the crystal structures of the phases Φ_1 and Φ_2 are also similar to each other. However, in contrast to the crystal structures of the stoichiometric compounds $DyCo_5$, Dy_2Co_7, and $DyCo_3$, their room-temperature magnetic characteristics differ significantly [12, 13]. At room temperature, the magnetization of the Co sublattice in the DyCo crystal is stronger than that of the Dy sublattice: $M_{Co} > M_{Dy}$. In the case of the $DyCo_3$ crystal, the situation is reversed.

Thus, we assume that the dominant phase in the DyCo film is the Φ_2 phase with $M_{Co} < M_{Dy}$ at room temperature. The total magnetization M_s of this phase is orthogonal to the film plane. In our opinion, it is this phase that is responsible for the integral magnetic char-

acteristics of the $Dy_{22}Co_{78}$ alloy film. For the Φ_1 phase, which is an impurity phase, we have $M_s = M_{Co} - M_{Dy}$. It is probable that the short-range order of the Φ_1 phase is close to the stoichiometric compound $DyCo_5$. The small grain size (~5 nm) of the nanocrystalline heterophase alloy and the exchange interaction between the Co sublattices of the Φ_1 and Φ_2 phases cause M_{Co} of the Φ_1 phase to be parallel to the film plane. The assumed configuration of the magnetization vectors of 3*d* metals in the $Dy_{22}Co_{78}/Ni_{81}Fe_{19}$ bilayer films is shown in Fig. 5b. The exchange interaction between the magnetization of the $Ni_{81}Fe_{19}$ layer and M_{Co} of the Φ_1 phase causes the unidirectional exchange anisotropy in the $Dy_{22}Co_{78}/Ni_{81}Fe_{19}$ bilayer films.

We now discuss the temperature dependences $\Delta H(T)$ of the bias field. The curves $\Delta H(T)$ shown in Fig. 4 convincingly exhibit a singularity at $T \sim 90°C$. It is necessary to pay attention to the fact that no singularities are observed in the dependences $\Delta H(T)$ at the compensation temperature of the $Dy_{22}Co_{78}$ ferrimagnetic magnetically hard layer ($T_{comp} \sim 27°C$). This indirectly indicates once again the fact that the compensation temperature is controlled by the Φ_2 phase, whose M_{Co} is orthogonal to the film plane and, hence, does not participate in the exchange interaction with the magnetization of the permalloy layer.

The disappearance of the hysteresis loop shift for the $Ni_{81}Fe_{19}$ layer at $T > 90°C$ indicates that the plane projection of the magnetization M_{Co} of the Φ_1 phase significantly decreases above this temperature. We reason that this is caused by the magnetic phase transition in the Φ_1 phase. In our opinion, a number of magnetic transformations are possible at this temperature: (i) the transition of the Φ_1 phase to the paramagnetic state (Curie temperature); (ii) $T \sim 90°C$ is a compensation point of the Φ_1 phase; and (iii) at $T \sim 90°C$, an orientational phase transition takes place, at which the magnetization of the Φ_1 phase emerges from the film plane and becomes parallel to the *Z* axis. Similar phase transitions are characteristic of the stoichiometric RE_xTM_y compounds [14]. To identify the features of the magnetic transformation in the $Dy_{22}Co_{78}$ alloy films at $T \sim 90°C$, additional experimental techniques need to be invoked.

5. CONCLUSIONS

The static magnetic characteristics of DyCo/NiFe and TbFe/NiFe bilayer exchange-biased films characterized by unidirectional anisotropy have been studied. The NiFe layer represents a magnetically soft ferromagnetic alloy whose easy magnetization axis is in the film plane. The ferrimagnetic DyCo layer with integral perpendicular anisotropy represents a heterophase nanocrystalline system consisting of at least two phases. The magnetization vector of the 3*d* metal sublattice of one of the components of the heterophase ferrimagnetic alloy is parallel to the film plane. In our opinion, the exchange interaction between the magnetization of the permalloy layer and the planar component of the magnetization vector of the heterophase magnetically hard alloy causes the unidirectional anisotropy in the films under study. The magnetic transition observed at $T \sim 90°C$ (where the unidirectional anisotropy disappears in the bilayer films under consideration) takes place in one of the components of the nanocrystalline heterophase alloy $Dy_{22}Co_{78}$. This magnetic transformation in the DyCo alloy films is revealed for the first time. To ascertain its character, additional methods need to be invoked.

ACKNOWLEDGMENTS

This study was supported by the Krasnoyarsky Kraĭ Science Foundation–Russian Foundation for Basic Research, project no. 02-02-97717.

REFERENCES

1. W. H. Meiklejohn and C. P. Bean, Phys. Rev. **105** (3), 904 (1957).
2. A. A. Glazer, R. I. Tagirov, A. P. Potapov, and Ya. S. Shur, Fiz. Tverd. Tela (Leningrad) **8** (10), 3022 (1966) [Sov. Phys. Solid State **8**, 2413 (1966)].
3. A. Yelon, in *Physics of Thin Films: Advances in Research and Development*, Ed. by M. H. Francombe and R. W. Hoffman (Academic, New York, 1971; Mir, Moscow, 1973), Vol. 6.
4. V. S. Gornakov, V. I. Nikitenko, A. I. Shapiro, *et al.*, in *Proceedings of XVII International School–Seminar on New Magnetic Materials in Microelectronics* (Mosk. Gos. Univ., Moscow, 2000).
5. V. A. Seredkin, G. I. Frolov, and V. Yu. Yakovchuk, Pis'ma Zh. Tekh. Fiz. **9** (23), 1446 (1983) [Sov. Tech. Phys. Lett. **9**, 621 (1983)].
6. V. V. Polyakov, G. I. Frolov, A. G. Vladimirov, and V. Yu. Yakovchuk, in *Abstracts of VII All-Union Conference on Problems of Magnetic Measurements and Magnetic Instrumentation, Leningrad* (1990), p. 97.
7. L. I. Vershinina, N. D. Zakharov, S. Z. Sklyuev, *et al.*, Fiz. Met. Metalloved. **66** (2), 278 (1988).
8. E. M. Artem'ev, L. I. Vershinina, V. G. Myagkov, *et al.*, Fiz. Met. Metalloved., No. 2, 77 (1990).
9. V. A. Seredkin, G. I. Frolov, and V. Yu. Yakovchuk, Fiz. Met. Metalloved. **63** (3), 457 (1987).
10. R. S. Iskhakov, V. Yu. Yakovchuk, S. V. Stolyar, *et al.*, Fiz. Tverd. Tela (St. Petersburg) **43** (8), 1462 (2001) [Phys. Solid State **43**, 1522 (2001)].
11. G. V. Popov, V. A. Seredkin, G. I. Frolov, and V. Yu. Yakovchuk, Fiz. Met. Metalloved., No. 2, 61 (1990).
12. E. M. Savitskiĭ and V. F. Terekhova, *Physical Metallurgy of Rare-Earth Metals* (Nauka, Moscow, 1975).
13. E. V. Shcherbakova and A. S. Ermolenko, Fiz. Met. Metalloved. **59** (2), 344 (1985).
14. A. S. Ermolenko, E. V. Rozenfel'd, Yu. P. Irkhin, *et al.*, Zh. Éksp. Teor. Fiz. **69**, 1743 (1975) [Sov. Phys. JETP **42**, 885 (1975)].

Translated by A. Kazantsev

Physics of the Solid State, Vol. 45, No. 5, 2003, pp. 932–937. Translated from Fizika Tverdogo Tela, Vol. 45, No. 5, 2003, pp. 888–892.

MAGNETISM AND FERROELECTRICITY

UV Absorption Spectra of Thin Films of Cs_2CdI_4 and Rb_2CdI_4 Ferroelectrics

O. N. Yunakova*, V. K. Miloslavskiĭ*, and E. N. Kovalenko**

**Kharkov National University, pl. Svobody 4, Kharkov, 61077 Ukraine*

***Physics and Technology Research Center, Ministry of Education and NAS of Ukraine, ul. Novgorodskaya 1, Kharkov, 61145 Ukraine*

Received June 20, 2002

Abstract—Thin films of M_2CdI_4 ferroelectrics (M = Cs, Rb) of orthorhombic structure were synthesized, and their electronic optical spectrum was studied. It was established that both compounds belong to direct-gap dielectrics and that their low-frequency excitons are localized on a sublattice made up of $(CdI_4)^{2-}$ tetrahedra. The temperature dependence of the exciton band parameters was studied for Cs_2CdI_4 within the temperature interval 90–420 K. The phase transitions occurring in this interval manifest themselves as breaks in the temperature behavior of the band spectral positions and weak peaks in the halfwidth and oscillator strength. © *2003 MAIK "Nauka/Interperiodica".*

1. INTRODUCTION

Cs_2CdI_4 is a ferroelectric compound. Depending on the method used to prepare the crystals (from melt or water solution), Cs_2CdI_4 crystallizes either in the orthorhombic (space group *Pnma*, a = 10.74 Å, b = 8.458 Å, c = 14.85 Å [1, 2]) or monoclinic (space group $P12_1/m$, a = 7.827 Å, b = 8.397 Å, c = 11.05 Å [3]) phase. The second phase can be transformed to orthorhombic through annealing at $T \geq 120$°C As the temperature is lowered, the compound undergoes a number of phase transitions, more specifically, from the commensurate orthorhombic to incommensurate phase at 332 K, to the monoclinic phase at 260 K, and to the triclinic ferroelectric phase at 180 K [1]. The monoclinic phase produced in the phase transition differs in its lattice parameters from that grown from water solution and approaches the orthorhombic phase. Thus, the two low-temperature phases may be considered as a distorted orthorhombic lattice [1]. The existence of phase transitions in Cs_2CdI_4 has been ascertained by various methods, namely, by x-ray diffraction and from the temperature dependences of the heat capacity, dielectric permittivity, and birefringence [1, 4]. Rb_2CdI_4 has been studied to a lesser extent. The temperature behavior of the dielectric permittivity [5] and luminescence spectrum of the Mn^{2+} impurity ions [6, 7] have also been studied.

The electronic spectrum of these compounds remains practically unstudied. A band structure calculation of Cs_2CdI_4 yielded the width of the band gap corresponding to indirect band-to-band transitions (E_g = 3.56 eV) [8]. We are not aware of any experimental investigations on the fundamental bands in Cs_2CdI_4 and Rb_2CdI_4. We present here a study of the UV absorption spectra of thin films of Cs_2CdI_4 and Rb_2CdI_4, which is of interest for reconstructing the electronic bands of these compounds, and of the temperature dependence of exciton band parameters in Cs_2CdI_4 in the 90- to 420-K interval, which includes the temperatures of the above phase transitions.

2. EXPERIMENT

Thin films of Cs_2CdI_4 were prepared using thermal evaporation of a stoichiometric mixture of CsI and CdI_2 in vacuum. The deposition was made on quartz substrates warmed to 80°C. We encountered the following difficulties. The phase composition of the films was monitored primarily directly from the low-temperature absorption spectra. It was found that the absorption spectrum consists of several exciton bands (Fig. 1), with the strongest short-wavelength bands A_0 and C occupying stable positions and the weaker long-wavelength A' band varying markedly, both its position in the 3.9- to 4.3-eV interval and in intensity, for identically prepared samples. To reveal the nature of this band, the films were annealed at $T > 120$°C. Annealing resulted in complete disappearance of the A' band and, simultaneously, in strengthening and sharpening of the A_0 band. It was also found that the strongest A' band forms in the first stages of evaporation of the melt. If the first portions of the melt are deposited on a shutter placed between the evaporator and the substrate, a crystalline residue is left on the bottom of the evaporator (a tantalum boat), which can be evaporated on the substrate by slightly increasing the evaporator temperature. The spectrum of the Cs_2CdI_4 films prepared by this procedure coincides with that of annealed films. These observations suggest the following conclusion. The films

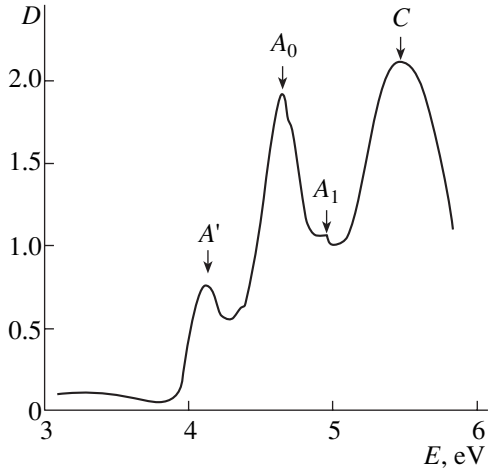

Fig. 1. Absorption spectrum of a thin Cs_2CdI_4 film with an admixture of the monoclinic phase obtained at T = 90 K. Film thickness t = 130 nm.

produced on the substrate under conventional evaporation consist apparently of a mixture of two phases, orthorhombic and monoclinic, and annealing at $T \geq$ 120°C transfers the monoclinic to the orthorhombic phase, which is in accord with the data on phase transformations of monoclinic phase crystals under heating [1, 2]. The monoclinic phase forms apparently at lower average kinetic energies of the molecular beam, which permits one to use the above procedure to prepare spectrally stable films of the orthorhombic phases of Cs_2CdI_4 and Rb_2CdI_4 (Figs. 2, 3). Thin films of Rb_2CdI_4 were produced in the same way.

The absorption spectrum of thin Cs_2CdI_4 films was measured on an SF-46 spectrophotometer within an energy interval of 2.5–6 eV and at temperatures ranging from 90 to 420 K. The spectra of Rb_2CdI_4 were obtained at 90 and 293 K. The film thickness was determined by the Tolanski method. The exciton band parameters (position E_{ex}, halfwidth Γ, oscillator strength f) were found following the technique described in [9].

3. UV SPECTRA OF Cs_2CdI_4 AND Rb_2CdI_4

The absorption spectrum of thin Cs_2CdI_4 films (Fig. 2) exhibits strong A_0 and A_1 bands at 4.65 and 4.89 eV (90 K) in the long-wavelength wing of the fundamental absorption edge and C_1 and C_2 bands at 5.25 and 5.6 eV, respectively, in the short-wavelength region. In Rb_2CdI_4, the A_0 and A_1 bands lie at 4.608 and 4.87 eV (90 K) and the C_1 and C_2 bands lie at 5.35 and 5.6 eV, respectively (Fig. 3). The A bands shift with increasing temperature to longer wavelengths, broaden, and weaken because of the exciton–phonon coupling, which indicates their relation to excitonic excitations. The C bands are less sensitive to temperature and are apparently related to interband absorption.

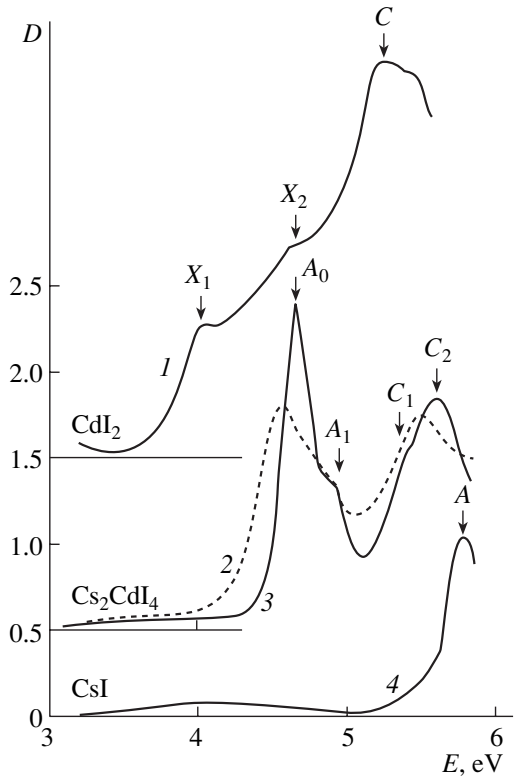

Fig. 2. Absorption spectra of thin films: (*1*) CdI_2 (T = 90 K, t = 60 nm); (*2*) Cs_2CdI_4 (T = 290 K, t = 125 nm) and (*3*) the orthorhombic phase (T = 90 K); and (*4*) CsI (T = 90 K, t = 90 nm).

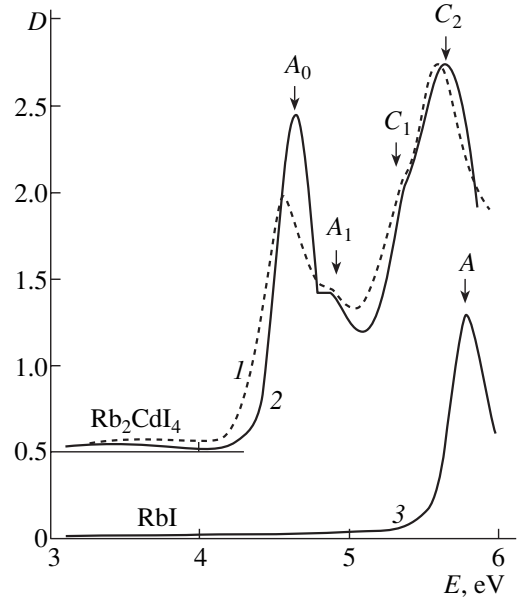

Fig. 3. Absorption spectra of thin films: (*1*) Rb_2CdI_4 (T = 290 K, t = 135 nm), (*2*) the orthorhombic phase (T = 90 K), and (*3*) RbI (t = 110 nm).

The absorption spectra of thin Cs_2CdI_4 and Rb_2CdI_4 films are similar both in the spectral structure and in position of their main bands. The only difference is in the intensity of the *C* bands. To assign the absorption spectrum of thin M_2CdI_4 films (*M* = Cs, Rb) correctly, it is compared with the spectra of the starting components, namely, CdI_2, CsI, and RbI (Figs. 2, 3). The absorption edge in CdI_2 derives from indirect transitions with a band gap E_g = 3.473 eV, and the long-wavelength X_1 band peaking at 4.03 eV is formed in direct transitions between the valence band deriving from the 5*p* states of I and the conduction band due to the 4*s* states of Cd [10, 11]. Our measurements place the long-wavelength exciton band of CsI at 5.8 eV (Fig. 2) and that of RbI at 5.7 eV, which is in agreement with [12]. The high intensity of the *C* bands in the absorption spectrum of Rb_2CdI_4 compared with those of Cs_2CdI_4 results apparently from superposition of excitonic absorption on the RbI sublattice of the compound on the *C* bands.

As seen from Figs. 2 and 3, the strongest long-wavelength A_0 band occupies an intermediate position in the spectrum with respect to the X_1 band in CdI_2 and the exciton bands in CsI and RbI. The high intensity of the A_0 band implies its association with $n = 1$ excitons and its relation to the direct allowed interband transitions in M_2CdI_4. The corresponding X_1 band in CdI_2 is substantially weaker because of its being autoionized in coupling with the interband transition continuum. In contrast to the assignment made in [8], we attribute the M_2CdI_4 compounds to direct-gap dielectrics. The A_0 band lies closer to the X_1 band in CdI_2 than to the excitonic bands in *M*I ($\Delta E = E_{A_0} - E_{x_1} \cong 0.6$ eV, $\Delta E = E_{MI} - E_{A_0} \cong 1.1$ eV), despite the *M*I : CdI_2 ratio being 2 : 1 in the compounds. This suggests exciton state localization in the structural elements CdI_4^{2-} of the compounds. This is corroborated by the smaller A_0 frequency interval between Cs_2CdI_4 and Rb_2CdI_4 (ΔE = 0.04 eV) compared to the interval between the band positions in CsI and RbI (ΔE = 0.1 eV). The structural elements in M_2CdI_4 are slightly distorted tetrahedra arranged in a periodic chain along the short axis **b** in the crystals [1, 2].

The tetrahedral bonding attests to the Cd–I interatomic bond becoming partially covalent, which is a factor that reduces d_{Cd-I} in Cs_2CdI_4 (d_{Cd-I} = 2.76–2.91 Å in the orthorhombic phase [2], 2.74–2.8 Å in the monoclinic phase [3]) compared to CdI_2 (d_{Cd-I} = 2.99 Å), where the Cd^{2+} ions are surrounded by an octahedron of I^- ions. On the other hand, tetrahedral bonding favors mixing of the 4*d* states of the Cd^+ ion with the 5*p* states of the I^- ion, as in silver and copper halides [13, 14]. This is apparently what distinguishes the electronic valence bands in M_2CdI_4 from those in CdI_2, where the upper 5*p* valence band of I is separated from the Cd 4*d* band by a gap [15, 16].

A weaker A_1 band is superposed on the short-wavelength wing of the A_0 band (Figs. 2, 3). To determine the parameters of these two bands (spectral position E_{ex}, halfwidth Γ, imaginary part of the dielectric permittivity at the maximum ε_{2m}), we fitted a symmetric profile constructed from a linear combination of a Lorentzian and a Gaussian to the bands following the technique described in [9]. The band parameters were derived from the best fit of the measured $D(E)$ spectrum to calculations in the 4- to 5-eV interval. The band maxima found for 90 K are E_{A_0} = 4.65 eV and E_{A_1} = 4.89 eV for Cs_2CdI_4 and E_{A_0} = 4.608 eV and E_{A_1} = 4.87 eV for Rb_2CdI_4. Separation of the bands made it possible to reveal the interband absorption edge at E_{g_1} = 5.2 and 5.15 eV for the two compounds, respectively. The existence of two bands comparatively strong in oscillator strength (see below) implies the existence of two subbands in the valence band. The interband absorption edge thus found corresponds to the optical transition from the lower valence subband to the conduction band of the compounds. The band-gap width of M_2CdI_4 can be estimated from the relation $E_{g_0} = E_{g_1} - (E_{A_1} - E_{A_0})$. We then obtain E_{g_0} = 4.96 eV for Cs_2CdI_4 and 4.89 eV for Rb_2CdI_4. These values of E_{g_0} yield an approximate estimate for the exciton binding energy $R_{ex} = E_{g_0} - E_{A_0}$, namely, R_{ex} = 0.31 eV for Cs_2CdI_4 and 0.28 eV for Rb_2CdI_4. The values of E_{ex}, Γ, and ε_{2m} were used to obtain the oscillator strength

$$f = \frac{mv}{4\pi e^2\hbar^2}\varepsilon_{2m}E_m\Gamma[1-\alpha(1-(\pi\ln 2)^{-1/2})], \quad (1)$$

where α is the fraction of the Gaussian constituent in the mixed band profile and v is the volume per molecule in a compound. Equation (1) yields f_{A_0} = 0.59 and f_{A_1} = 0.36 for Cs_2CdI_4 and f_{A_0} = 0.34 and f_{A_1} = 0.22 for Rb_2CdI_4. Despite the error in determination of the absolute magnitude of f for the two bands being large because of the error involved in determining α and v for the two compounds, the oscillator strength ratio for them is $f_{A_0}/f_{A_1} \cong 1.6$. The oscillator strength of the A_1 band is somewhat overevaluated as a result of its being superposed on the continuum for $E > E_{g_0}$. The above estimates of f_{A_0} and f_{A_1} suggest the conclusion that the I 5*p* electronic states contribute more to the upper than the lower valence subband of the compounds. The lower conduction subband in these compounds, as in CdI_2, derives from the 5*s* electronic states of Cd.

4. TEMPERATURE DEPENDENCE OF THE 1*s* EXCITON BAND PARAMETERS IN Cs_2CdI_4

The temperature dependences $E_m(T)$, $\Gamma(T)$, and $f(T)$ for the A_0 and A_1 bands in Cs_2CdI_4 were studied in the range 90–420 K, which includes the temperatures of the possible phase transitions. The measurements were carried out in heating runs. Spectral measurements at intermediate temperatures were conducted in a more narrow frequency interval, including the A_0 and A_1 bands. The method employed in determining the parameter was the same as that used at 90 K [9]. The fraction of the Gaussian constituent α in the composite profile was found to increase with temperature from 0.25 (90 K) to 1 (420 K).

Within the interval 90–183 K, the A_0 and A_1 bands (Fig. 4) shift linearly toward low frequencies with $dE_m/dT = -9.1 \times 10^{-4}$ and -10×10^{-4} eV/K, respectively. As the triclinic phase transforms into the monoclinic phase (183- to 260-K interval), dE_m/dT decreases noticeably down to -4.6×10^{-4} eV/K for the A_0 band and -2.1×10^{-4} eV/K for the A_1 band. The transition to the incommensurate orthorhombic phase (260–332 K) is not accompanied, within the experimental error, by a change in dE_m/dT; in the paraelectric phase (332–420 K), $dE_m/dT = -2.3 \times 10^{-4}$ eV/K for the A_0 band and -1.9×10^{-5} eV/K for the A_1 band. The interval $\Delta E = E_{A_0} - E_{A_1}$ was observed to increase from 0.24 to 0.31 deV with temperature.

The temperature-induced shift dE_m/dT of the exciton bands toward lower frequencies is characteristic, in order of magnitude, of many related compounds and is determined primarily by the exciton–phonon coupling. The large value of dE_m/dT in the interval 90–183 K is apparently associated with the noticeable thermal lattice expansion in the region of the triclinic phase, which occurs mostly because of the temperature-induced growth of the *c* parameter [1]. In the interval 183–260 K, the lattice thermal expansion coefficient decreases markedly, which accounts for the smaller value of dE_m/dT in the monoclinic and incommensurate phases. We did not observe a jump in $E_m(T)$ at 260 K for the two bands under discussion, although the transformation from the monoclinic to orthorhombic phase has been reported [1, 4] to be a first-order transition. The clearly detectable decrease in dE_m/dT in the paraelectric phase also remains unexplained.

The exciton–phonon coupling also brings about an increase in the band halfwidth (Fig. 4b). $\Gamma(T)$ increases from 0.18 eV (90 K) to 0.41 eV (420 K) for the A_0 band and from 0.35 eV (90 K) to 0.74 eV (420 K) for the A_1 band. Because Cs_2CdI_4, as CsI and CdI_2, belongs to ionic crystals with a small admixture of covalent bonding, the band broadening arises primarily from excitons coupling with longitudinal optical (LO) phonons. The value of $\hbar\omega_{LO}$ for Cs_2CdI_4 is unknown and was derived by us through linear extrapolation of the $(CsI)_{1-x}(CdI_2)_x$ system to $x = 0.33$ using the known values of 11 meV for CsI [12] and 21.7 meV for CdI_2 [17]; the value obtained is $\hbar\omega_{LO} = 14.6$ meV. A value close to this, $\hbar\omega_{LO} = 14.5$ meV, can be extracted from known frequencies of asymmetric stretch vibrations of the Cs_2I_2 and CdI_2 molecules [18]. The equality $\hbar\omega_{LO} = k_BT$ corresponds to $T = 170$ K. For $k_BT \gg \hbar\omega_{LO}$, the behavior of $\Gamma(T)$ depends on the dimension of the excitonic excitations. For three-dimensional excitons in cubic crystals, $\Gamma(T) \approx T^2$; for one- and two-dimensional excitons, $\Gamma(T) \approx T^{2/3}$ and *T*, respectively [19]. The behavior of $\Gamma(T)$ in the interval 90–420 K is generally close to linear for the A_0 band and to sublinear for the A_1 band. This suggests a low dimension of excitons in Cs_2CdI_4 (1D or 2D), which finds support in the conjecture that they are localized on the sublattice of CdI_4^{2-} tetrahedra.

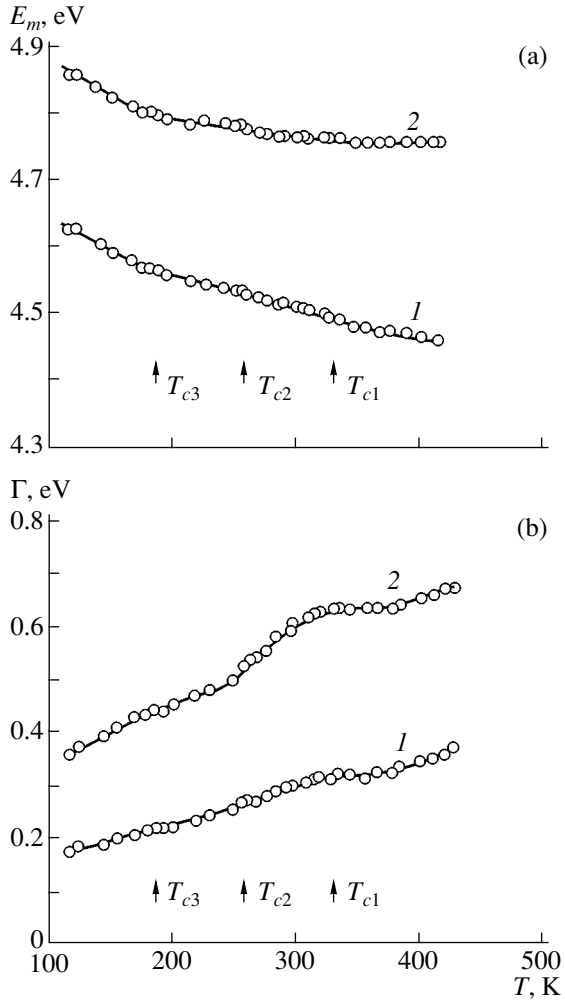

Fig. 4. Temperature dependences of (a) spectral position $E_m(T)$ and (b) halfwidth $\Gamma(T)$ of the exciton bands (*1*) A_0 and (*2*) A_1.

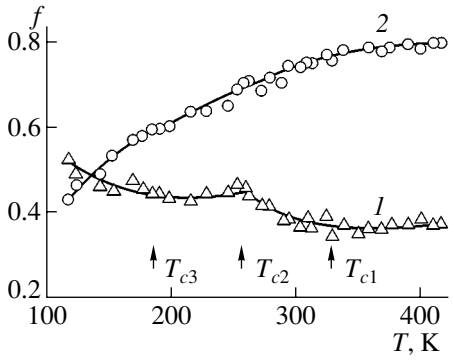

Fig. 5. Temperature dependence of the oscillator strength $f(T)$ of the exciton bands (*1*) A_0 and (*2*) A_1.

The derivative $d\Gamma/dT$ averaged over the total temperature range is 0.605×10^{-3} and 1.06×10^{-3} eV/K for the A_0 and A_1 bands. The steep growth in $d\Gamma/dT$ for the A_1 band is possibly due to the A_1 exciton autoionization growing in intensity as E_{g_0} decreases with increasing temperature; while at 90 K, $E_{g_0} > E_{A_1}$, at 420 K, $E_{g_0} = E_{A_1} + R_{ex} = 4.77$ eV and $E_{A_1} = 4.76$ eV, i.e., $E_{g_0} \approx E_{A_1}$. This is what accounts for the larger superposition of the E_{A_1} band on the interband transition edge and the associated additional broadening induced by autoionization. Phase transitions disrupt the monotonic course of $\Gamma(T)$ somewhat; at T_1, T_2, and T_3, one observes peaks in the halfwidth that are particularly pronounced at T_1. The peaks are temperature broadened, which is possibly associated with the diffuseness of phase transition temperatures in polycrystalline Cs_2CdI_4 films.

The oscillator strength of the A_0 and A_1 bands was calculated from Eq. (1) using the temperature dependence of the α parameter within the temperature interval studied. The value of $f(T)$ for the A_0 band was found to decrease from 0.59 at 90 K to 0.38 at 420 K (Fig. 5). The decrease f with increasing T is a sign of a zero-phonon band, whose value of f decreases because of the Debye–Waller factor. The behavior of $f_{A_0}(T)$ is, however, nonmonotonic; at the transition from the monoclinic to incommensurate orthorhombic phase (T_2 = 260 K) f_{A_0} passes through a peak, which is possibly caused by crystallite disordering at the first-order phase transition. The course of $f(T)$ for the A_1 band appears unusual; whereas at 90 K, $f_{A_1} = 0.36$ and $f_{A_1} < f_{A_0}$, which, as already mentioned, is related to the larger admixture of the Cd 4*d* states in the lower valence subband, at $T > 120$ K, we have $f_{A_1} > f_{A_0}$, with f_{A_1} increasing to 0.79 at 420 K. The method used for band deconvolution and separation of the bands from the *C* band is responsible for the strong growth in f_{A_1} due to several factors. First, the weakening of the A_0 band is accompanied by the appearance of a short-wavelength side phonon band which contributes to f_{A_1}. The value of this contribution in the interval 90–420 K is 0.21. Second, as T increases, interband transitions shift the absorption edge until it becomes superposed on the A_1 band, thus producing an additional contribution to f_{A_1} that is difficult to take account of. Finally, the admixture of Cd 4*d* states in the lower valence subband makes optical transition to the conduction band partially forbidden, thus resulting in the corresponding weakening of the A_1 band at low temperatures. As T increases, electron–phonon coupling makes this transition allowed. A similar lifting of forbiddenness and a temperature-induced growth in the oscillator strength of impurity bands have been observed for impurity ions with nd^{10} shells in alkali halide crystals [20].

A method of preparing thin Cs_2CdI_4 and Rb_2CdI_4 films in the orthorhombic phase was developed, and their UV absorption spectrum was measured at 90 and 293 K. The spectrum was found to have intense A_0 and A_1 exciton bands lying between the bands in CdI_2 and MI (M = Cs, Rb). Analysis of the spectra permits the conclusion that two subbands deriving from the I 5*p* and Cd 4*d* electronic states in the upper valence band of M_2CdI_4, that the compounds under study belong to direct-gap dielectrics, and that exciton localization occurs on the sublattice made up of CdI_4^{2-} tetrahedra. Study of the temperature dependence of the A_0 and A_1 band parameters of Cs_2CdI_4 in the interval 90–420 K indicates a low dimension of excitons (one- or two-dimensional) in this compound. The phase transitions occurring in this temperature interval comparatively weakly affect the temperature behavior of the band parameters and become manifest as breaks in the $E_m(T)$ dependences and as weak peaks in the temperature dependence of the band halfwidth and oscillator strength.

REFERENCES

1. K. S. Aleksandrov, S. V. Melnikova, I. N. Flerov, *et al.*, Phys. Status Solidi A **105**, 441 (1988).
2. V. Teuchard, M. Louer, J. P. Auffredic, and D. Louer, Rev. Chim. Miner. **24** (4), 414 (1987).
3. By Rune Sjovall, Acta Crystallogr. C **45**, 667 (1989).
4. K. S. Aleksandrov, S. V. Mel'nikova, and I. T. Kokov, Fiz. Tverd. Tela (Leningrad) **29** (8), 2487 (1987) [Sov. Phys. Solid State **29**, 1431 (1987)].
5. I. N. Flerov, M. V. Gorev, L. A. Kot, and V. A. Grankina, Fiz. Tverd. Tela (Leningrad) **30** (7), 1948 (1988) [Sov. Phys. Solid State **30**, 1125 (1988)].
6. I. M. Bolesta and Yu. M. Furgala, Ukr. Fiz. Zh. **36** (11), 1654 (1991).
7. I. Bolesta and Yu. Furgala, Ferroelectrics **130**, 309 (1992).

8. I. M. Bolesta, Doctoral Dissertation (Lviv, 1996).
9. V. K. Miloslavskiĭ, O. N. Yunakova, and Sun Tsya-Lin, Opt. Spektrosk. **78** (3), 436 (1995) [Opt. Spectrosc. **78**, 391 (1995)].
10. M. K. Tubbs, J. Phys. Chem. Solids **29** (7), 1191 (1968).
11. I. Pollini, J. Tomas, R. Coehoorn, and C. Haas, Phys. Rev. B **33**, 5747 (1986).
12. F. Beerwerth, D. Frohlich, and V. Leinweber, Phys. Status Solidi B **145** (1), 195 (1988).
13. A. Blacha, S. Ves, and M. Cardona, Phys. Rev. B **27** (10), 6346 (1983).
14. A. Goldmann, Phys. Status Solidi B **81** (1), 9 (1977).
15. Ya. O. Dovgiĭ and I. V. Kityk, Ukr. Fiz. Zh. **29** (6), 884 (1984).
16. I. Robertson, J. Phys. C: Solid State Phys. **12** (22), 4753 (1979).
17. A. B. Lyskovich, *Wide-Band Layered Crystals and Their Physical Properties* (Vishcha Shkola, Lvov, 1982).
18. *Molecular Constants of Inorganic Compounds: Handbook*, Ed. by K. S. Krasnov (Khimiya, Leningrad, 1979).
19. M. Schreiber and Y. Toyozawa, J. Phys. Soc. Jpn. **51** (5), 1528 (1982).
20. K. Fussgaenger, W. Martienssen, and H. Bilz, Phys. Status Solidi **12**, 383 (1965).

Translated by G. Skrebtsov

Physics of the Solid State, Vol. 45, No. 5, 2003, pp. 938–941. Translated from Fizika Tverdogo Tela, Vol. 45, No. 5, 2003, pp. 893–896.

MAGNETISM AND FERROELECTRICITY

Thermally Stimulated Electron Emission from Chromium-Doped Triglycine Sulfate in the Paraelectric Phase

A. A. Sidorkin, A. S. Sidorkin, O. V. Rogazinskaya, and S. D. Milovidova

Voronezh State University, Universitetskaya pl. 1, Voronezh, 394006 Russia

Received June 27, 2002

Abstract—Thermally stimulated electron emission from a ferroelectric chromium-doped triglycine sulfate (TGS) crystal was experimentally observed to occur in a temperature range 6 K above the Curie point from samples heated at a relatively high rate. Increasing the heating rate q was shown to cause the emission current density to increase throughout the temperature range studied. The emission onset temperature in chromium-doped TGS depends only weakly on the rate q and is close to that for pure TGS, and the emission cutoff temperature grows monotonically with q at comparatively low heating rates and stabilizes at high q. At the same time, the interval of emission extension into the paraelectric phase here is about one half that for pure TGS heated at the same rate. The specific features of emission observed for this crystal can be assigned to relaxation of the charges screening the spontaneous polarization. The lower emission cutoff temperature for the chromium-doped TGS compared to that for pure TGS is accounted for by the shorter Maxwellian relaxation time in the doped crystal.

1. INTRODUCTION

Electron emission is one of the phenomena accompanying the variation of macroscopic polarization in ferroelectrics. Investigation of the emission kinetics makes it possible to shed light on the nature of the electron emission observed experimentally. Our earlier study [1] dealt with the emission kinetics from pure triglycine sulfate (TGS), and it was shown that the temperature interval within which the emission occurs can vary depending on the heating rate. In particular, the temperature at which the emission is observed to cut off can substantially exceed the Curie point; i.e., emission can occur in the nonpolar phase of the ferroelectric material. This emission was assigned in [1] to the fact that the charges screening the spontaneous polarization are drawn into the nonpolar phase, and it is the field generated by these charges that accounts, in our opinion, for the experimentally observed emission.

Obviously enough, if this conjecture is right, one could vary the emission temperature range in ferroelectrics by properly acting on the screening- charge kinetics. It is known that the emission relaxation time in doped TGS-class ferroelectrics can vary depending on the dopant type [2], and as a result these materials offer a good chance of verifying the conjecture put forward in [1] on the nature of the emission observed in ferroelectrics.

2. EXPERIMENTAL TECHNIQUES AND RESULTS

As in [1], the electron emission current density j_{em} was measured following the standard technique [3, 4] in a vacuum of 6.5×10^{-3} Pa. The samples used in the measurements were polar Y cuts (20 mm^2 in area and 1 mm thick) of a chromium-doped (1 mol % in solution) TGS crystal. The sample linear heating rate $q = dT/dt$ was varied from 0.1 to 4 K/min. The sample temperature measurement performed using a copper–constantan thermocouple was paralleled by simultaneously measuring the capacitance of another TGS crystal sample with the same chromium dopant concentration. The sample temperature was varied in different experiments from +20 to +60°C. The temperature was measured accurate to within 5%.

The experiments showed that, as in the case of pure TGS, thermally stimulated electron emission from chromium-doped TGS occurs within a certain temperature interval, whose limits depend on the sample heating rate $q = dT/dt$. As in pure TGS, the low-temperature limit of this interval is practically independent of the rate q (Fig. 1). At low heating rates, the higher temperature limit of the interval within which electron emission occurs grows, as seen from Figs. 1 and 2, approximately proportionally to the sample heating rate q, as in pure TGS, and saturates at fairly high q. Depending on the magnitude of q, the emission cutoff temperature may be both higher and lower than T_C. In particular, at $q = 0.5$ K/min, the emission cutoff temperature in chromium-doped TGS, as in pure TGS, is 45–46°C, which is below the Curie temperature. For $q = 3.0$–4.5 K/min, it reaches approximately 55°C; i.e., the electron emission occurs at a temperature 6 K above the Curie point. Throughout the temperature interval where the emission is detected, the emission signal grows monotonically with q, following a close-to-linear course (Fig. 3).

1063-7834/03/4505-0938$24.00 © 2003 MAIK "Nauka/Interperiodica"

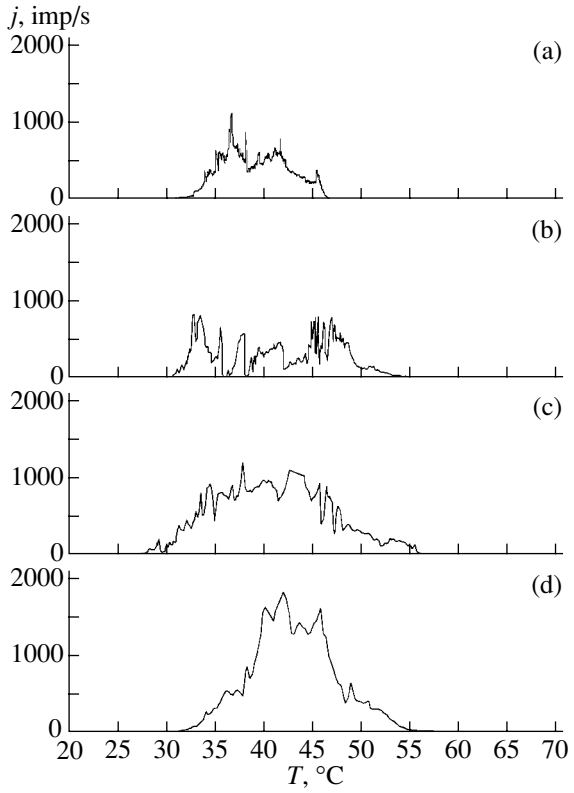

Fig. 1. Emission current density plotted vs. temperature for different heating rates q of a chromium-doped TGS single crystal: (a) 0.5, (b) 1.5, (c) 2.0, and (d) 4.0 K min^{-1}.

At the same time, one observes a decrease in the total number of emitted electrons with increasing sample heating rate (Fig. 4).

Comparison of the temperature dependences of the emission current density for pure and chromium-doped TGS plotted in Fig. 5 shows that, for the same sample heating rates, the temperature interval within which emission occurs from the chromium-doped crystal in the paraelectric phase is approximately one half that in the case of pure TGS. For a heating rate of about 4 K/min, the temperature of emission cutoff in chromium-doped TGS is 55°C, whereas in pure TGS, it is 65°C for the same q.

The growth rate of the maximum emission current with increasing q, which is characterized by the slope of the curves in Fig. 3, in chromium-doped TGS (curve *1*) is also lower than that in pure TGS (curve *2*). The net charge escaping from the surface of the chromium-doped sample and that escaping from surface of the pure TGS samples follow qualitatively similar dependences on the sample heating rate.

As pointed out in [1], the observed thermal emission activity of the ferroelectrics studied can be accounted for by the field emission of electrons from surface electronic states, which is driven by the total field generated by the charges screening the spontaneous polarization and the balancing charges. The disruption of this field balance, caused by a decrease in spontaneous polarization occurring as the Curie point is approached, gives rise to the generation of a nonzero net field, and it is this field that ejects electrons trapped in surface electronic states [3–5].

In general, emission kinetics is determined not only by domain structure relaxation but also by the depletion of electronic traps and by the competing process of Maxwellian relaxation of the charges screening the spontaneous polarization [3]. To estimate the relevant characteristic quantities in the limiting cases, the action of these factors can be considered separately. In particular, if the time in which the emission-active temperature interval is passed, $(T_l - T_{end})/q$, is considerably shorter than the Maxwellian screening-charge relaxation time τ, the emission kinetics can be treated as rate-limited by ionization of the surface defect centers. In this case, the emission current density can be written as [3–5]

$$j_{em}(T) = en(T)W(T), \quad (1)$$

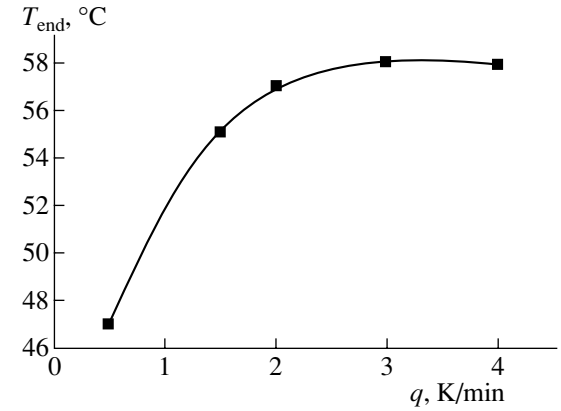

Fig. 2. Emission cutoff temperature plotted vs. heating rate for a chromium-doped TGS single crystal.

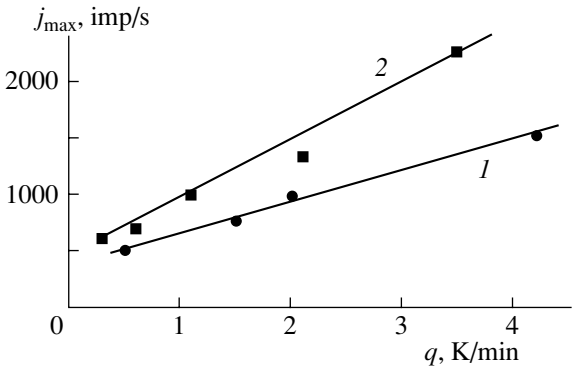

Fig. 3. Maximum emission current density plotted vs. heating rate for (*1*) chromium-doped and (*2*) pure TGS.

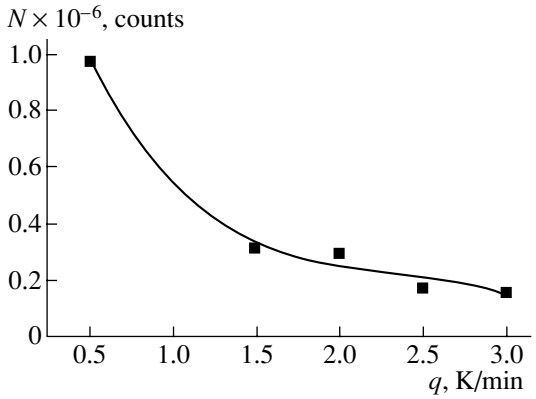

Fig. 4. Total number of emission pulses plotted vs. heating rate for chromium-doped TGS single crystal.

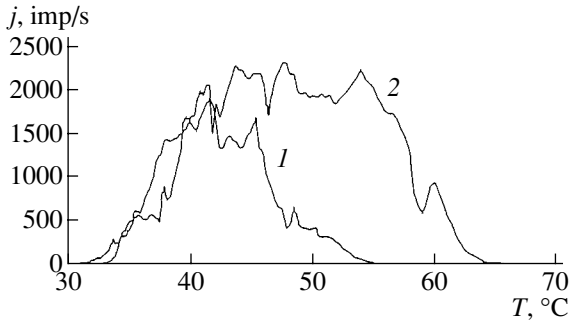

Fig. 5. Emission current density vs. temperature relation for (*1*) chromium-doped and (*2*) pure TGS plotted for the same sample heating rate, q = 4 K/min.

where $n(T)$ is the surface density of occupied surface electronic states at a given temperature,

$$W(T) = \frac{2\sqrt{2mA}\zeta}{mS}\exp\left(-\frac{4\sqrt{2m}A^{3/2}}{\hbar eE}\right) \qquad (2)$$

is the ionization probability, per unit time, of a surface center of depth A in a field E; ζ is the width of the potential well of the corresponding electronic trap; and S is the emission-active ferroelectric surface area.

The $n(T)$ relation is given by the equation

$$dn = -nWdt. \qquad (3)$$

Taking $dt = dT/q$ and the initial condition $n(T = T_l) = n_0$, where T_l is the starting heating temperature, for which $E(T = T_l) = 0$, we obtain from Eq. (3) for q = const

$$n = n_0\exp\left\{-\frac{1}{q}\int_{T_l}^{T} W dT\right\}. \qquad (4)$$

The temperature of the maximum of emission current is given by the condition $\partial j_{em}/\partial T = 0$, which, in view of Eqs. (1)–(4), yields

$$W(T_m) = q\frac{E^*}{E^2(T_m)}\frac{\partial E}{\partial T}\bigg|_{T = T_m}, \qquad (5)$$

where T_m is the temperature of the emission current maximum;

$$E(T) = \frac{2\pi}{\varepsilon_S}(P_l - \sqrt{\alpha_0(T_C - T)/\beta}) \qquad (6)$$

is the temperature-dependent net field of the spontaneous polarization and balancing charges, which causes autoionization of the impurity centers (P_l is the saturation polarization, ε_S is the permittivity of the surface nonferroelectric layer), and

$$E^* = \frac{4}{3}\frac{\sqrt{2m}A^{3/2}}{\hbar e}. \qquad (7)$$

For the emitted charge, we obtain

$$Q = \int_{T_l}^{T_{end}} j(T)dt/q. \qquad (8)$$

As seen from Eq. (5), the probability $W(T_m)$ is proportional to q. Assuming W in Eq. (4) to be constant and equal to $W(T_m)$ for the sake of simplicity of integration, we eliminate the dependence of n on q. Thus, the dependence of the maximum emission current on sample heating rate q acquires the form

$$j_{max}^{em} = en(T_m)\frac{E^*}{E^2(T_m)}\frac{\partial E}{\partial T}\bigg|_{T = T_m} q. \qquad (9)$$

The temperature interval within which the electron emission occurs can be limited on the high temperature side by either total depletion of the occupied electronic states or disappearance of the emission-inducing net field of the spontaneous polarization and balancing charges.

If the emission cuts off before the Curie point is reached, the cutoff is obviously due to realization of the first situation, because the balancing charge field can disappear only after the spontaneous polarization at the Curie point has completely disappeared. The conjecture of complete detrapping in the case illustrated by Fig. 1a is also argued for by the decrease in the charge emitted at high heating rates, i.e., the effect seen in Fig. 3.

The persistence of emission above T_C lends support to the conjecture that the emission-active charge is the balancing rather than spontaneous-polarization charge. As shown in [1], emission in the nonpolar phase can be due to the balancing charge persisting at these temperatures because of their Maxwellian relaxation time τ being sufficiently long. This conjecture is also corroborated by numerical estimates. Indeed, at the phase tran-

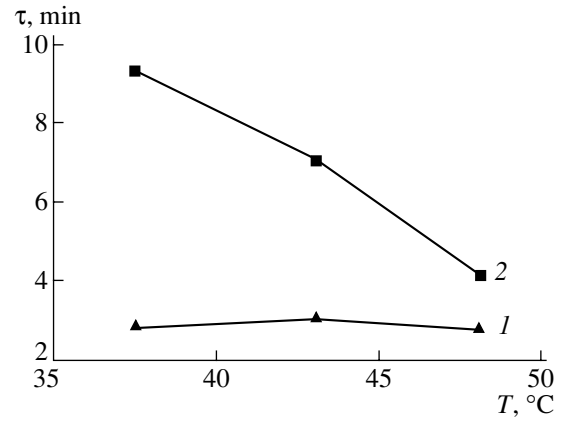

Fig. 6. Temperature dependence of electron emission relaxation time plotted for (*1*) chromium-doped and (*2*) pure TGS.

sition, the electrical resistivity of a nominally pure TGS crystal is 10^{12} Ω cm [6] and the permittivity ε is of the order of 10^3; therefore, the Maxwellian relaxation time of the balancing charge $\tau = \varepsilon/4\pi\sigma$ is of the order of 10^3 s, or a few minutes [2]. Multiplying the heating rate of 3.5 K/min by this time τ yields, for the temperature interval of persistence of these charges, about 10 K, which is in accord with the emission extension interval into the paraelectric phase of 10 K in nominally pure TGS (Fig. 5).

The decrease in the emission extension interval into the paraelectric phase observed in a chromium-doped TGS crystal can be explained within this model by a shortening of the Maxwellian relaxation time of the balancing charge in this material compared to that in pure TGS, which results from the experimentally observed increase in the conductivity of defective triglycine sulfate [6].

The experimentally revealed shortening of the emission relaxation time in doped TGS compared to that in pure TGS is also seen from Fig. 6. We readily see that, in the doped crystal, the emission relaxation time is much shorter, 2–3 min. The shorter relaxation time observed in the doped compared to pure TGS suggests that, if the sample heating rate is the same, the emission extension into the paraelectric phase in the doped material should be proportionally shorter.

In accordance with Fig. 6, the emission relaxation time in the ferroelectric phase of pure TGS decreases as one approaches the Curie point, which can be assigned, in the field model, to an increase in the net field responsible for the emission. The absence of a temperature dependence of the emission relaxation time in doped TGS is apparently due to the screening processes, which weaken the emission-active field and are felt already in the ferroelectric phase.

3. CONCLUSIONS

To sum up, our results show that the temperature at which electron emission from ferroelectrics stops does not necessarily coincide with the Curie point T_C. This temperature can be both lower and higher than T_C. The extent to which the emission tails off into the paraelectric phase depends on the Maxwellian relaxation time of the spontaneous-polarization screening charge and can be varied, in particular, through proper doping of the ferroelectric material.

ACKNOWLEDGMENTS

This study was supported by the Russian Foundation for Basic Research (project no. 01-02-16828) and CRDF (grant no. VZ-010).

REFERENCES

1. A. A. Sidorkin, A. S. Sidorkin, O. V. Rogazinskaya, and S. D. Milovidova, Fiz. Tverd. Tela (St. Petersburg) **44** (2), 344 (2002) [Phys. Solid State **44**, 358 (2002)].
2. A. S. Sidorkin, O. V. Rogazinskaya, S. D. Milovidova, *et al.*, Izv. Ross. Akad. Nauk, Ser. Fiz. **64** (9), 1763 (2000).
3. A. S. Sidorkin, A. M. Kostsov, and V. S. Zal'tsberg, Fiz. Tverd. Tela (Leningrad) **27** (7), 2200 (1985) [Sov. Phys. Solid State **27**, 1320 (1985)].
4. A. M. Kostsov, A. S. Sidorkin, V. S. Zal'tsberg, and S. P. Gribkov, Fiz. Tverd. Tela (Leningrad) **24**, 3436 (1982) [Sov. Phys. Solid State **24**, 1952 (1982)].
5. A. A. Sidorkin, S. D. Milovidova, O. V. Rogazinskaya, and A. S. Sidorkin, Fiz. Tverd. Tela (St. Petersburg) **42** (4), 725 (2000) [Phys. Solid State **42**, 743 (2000)].
6. M. V. Tsedrik, *Physical Properties of Crystals of the Triglycine-Sulfate Family* (Nauka i Tekhnika, Minsk, 1986).

Translated by G. Skrebtsov

Physics of the Solid State, Vol. 45, No. 5, 2003, pp. 942–945. Translated from Fizika Tverdogo Tela, Vol. 45, No. 5, 2003, pp. 897–900.

MAGNETISM AND FERROELECTRICITY

Time Delay in the Low-Temperature Phase of Relaxors

R. F. Mamin[1, 2] and R. Blinc[2]

[1] *Kazan Physicotechnical Institute, Russian Academy of Sciences, Sibirskiĭ Trakt 10/7, Kazan, 420029 Russia*
[2] *Jozef Stefan Institute, Ljubljana, 1000 Slovenia*

Received July 1, 2002

Abstract—A theoretical approach to the description of phase transition kinetics in the low-temperature phase of relaxors is put forward. The idea underlying the approach consists in the local direction of spontaneous polarization in relaxors being pinned by bound charge carriers. Strong electric fields gradually activate the localized carriers, with subsequent alignment of the local polarization with the field. This initiates a phase transition to a state with uniform spontaneous polarization, which occurs with a certain time delay. The dependence of the phase transition delay time on temperature and external electric field is described. © *2003 MAIK "Nauka/Interperiodica".*

Ferroelectrics with diffuse phase transitions, also called relaxors, belong to a class of ferroelectric materials that has been extensively studied [1–10]. A specific feature of these compounds is the presence of a strongly broadened maximum in the temperature behavior of dielectric permittivity, as well as the shift of this maximum toward higher temperatures with increasing measuring field frequency. Such dispersion in the behavior of dielectric permittivity becomes manifest at relatively low frequencies, $\omega = 1–10^6$ Hz, which are not typical of conventional ferroelectrics. The most well known in the family of these materials are the perovskites $Pb(Mg_{1/3}Nb_{2/3})O_3$ (PMN) [1–4] and $Pb_{1-y}La_y(Zr_{1-x}Ti_x)O_3$ (PLZT) [5]. Despite the fairly long history of investigation of these compounds, a clear enough understanding of the physical mechanisms responsible for the processes involved and unambiguous interpretation of the observed phenomena are still lacking [4, 10]. Several directions are being pursued in relaxor theory; some of them consider relaxors as objects with a glass-like behavior [5, 6], while others develop phenomenological approaches assuming the system to be broken down into nanosized regions by random fields [4, 9]. To reveal the main forces driving the relaxor behavior and to construct an adequate model, one has to compare the results of the theory with the totality of accumulated experimental data. The most perplexing phenomena occur in the low-temperature phase of relaxors. This was found in recent studies of the formation of a uniformly polarized phase in the low-temperature PMN phase under a strong electric field applied after zero-field cooling [6, 7]. These studies revealed slow relaxation of the dielectric permittivity and a subsequent abrupt change in it manifested as a delayed phase transition. The explanation of this relaxor behavior proposed in this communication is based on the assumption that the main properties of relaxors are connected with charge localization dynamics [11].

Note that the application of a dc electric field to a relaxor always greatly complicates the pattern of the observed phenomena. When cooled in fields above a certain threshold level ($E_{thr} \sim 1.5$ kV/cm), the temperature dependence of dielectric permittivity changes its course radically. When cooled in a zero field, relaxors have been shown [2, 8] to transfer, at a temperature T_f lying below the temperature T_m of the dielectric permittivity maximum, to a state of local spontaneous polarization extending over microregions with a characteristic size $\Delta l \approx 3–10$ nm. Uniform spontaneous polarization appears only under application of a dc field $E > E_{thr}$. Application of an electric field to a zero-field-cooled low-temperature phase initiates a phase transition to a state with uniform polarization (the ferroelectric phase). It was found in [6, 7] that the transition to the ferroelectric phase occurs a fairly long time after the field has been applied. The dependences of the phase transition delay time t_0 on external electric field E and temperature T are fitted well by relations of the type $t_0(E) = \tau_E \exp(E_0/E)$ and $t_0(T) = \tau_T \exp(T_0/T)$. The fitting constants T_0 and τ_T appeared so unusual to the authors of [7] that they stated that "the numerical values of τ_T and T_0 ($\tau_T = 8.3 \times 10^{-16}$ s, $T_0 \sim 7000$ K) have no physical meaning." Therefore, revealing the physical meaning of the observed relationships is important to gain a proper understanding of the totality of phenomena occurring in relaxors.

We start with the assumption that the low-temperature phase is a state in which the whole of the sample is broken down into microregions with differently oriented spontaneous polarizations. To explain the specific features of the time-delayed phase transition, we assume the direction of polarization in these microregions to be fixed by localized charges, which also deter-

mine the separation of the sample volume into microregions. Practically all the charges in the low-temperature phase are localized. Thermal activation is inefficient at these temperatures, and therefore charged centers can be ionized only by applying a sufficiently strong external electric field.

Application of an electric field affects both the thermal activation of localized charges and the direction of polarization in the microregions. In weak fields, bound charges cannot become delocalized and, therefore, efficiently maintain a nonuniform polarization distribution. Strong fields delocalize the carriers, and as a result the local direction of polarization becomes no longer fixed, and polarization reorients along the field. Thus, phase transition to a state with uniform polarization after application an electric field is dominated by ionization of the local centers, with subsequent redistribution of the polarization direction in local microregions. Local polarization around the newly trapped carriers is now reoriented primarily along the field (see Fig. 1). After most of the centers have passed through the ionization process, local polarization is predominantly directed along the external field. Spontaneous polarization in one direction throughout the sample is now energetically favorable, thus initiating phase transition to the ferroelectric state. This becomes manifest in a jumplike change in the dielectric permittivity. Even after this, however, there will remain some regions in which the local polarization has not yet aligned with the external field and spontaneous polarization in most of the crystal volume. This results in a gradual relaxation of dielectric permittivity, which is associated with the processes of ionization and subsequent carrier localization in these regions. Thus, the slow processes before and after the phase transition are connected with ionization of the charged centers and with partial polarization rotation in microregions. The phase transition itself, in turn, is related to the formation of uniform spontaneous polarization in most of the sample volume.

The above suggests that the delay time t_0 is determined by the processes involved in the ionization of the local centers. This time can be estimated as the interval required for most of the charges bound to traps to delocalize at least once:

$$t_0 = \frac{M}{p(E, T)}, \quad E > E_{\text{thr}}. \tag{1}$$

Here, $p(E, T)$ is the ionization probability per unit volume and the constant M is the local center concentration, $M \approx 10^{18}$–10^{19} cm^{-3}, which correlates well both with the characteristic concentration of native defects and with known microregion dimensions [2] ($\Delta l \approx M^{-1/3}$, $\Delta l \approx 3$–10 nm). We assume for definiteness that only defects of one type play a significant role in polarization switching and that its energy levels lie U_i below the conduction band bottom.

Let us discuss first the case of impact ionization (Fig. 1) [12, 13]. We have to bear in mind that in our case ($E \approx 1$–10 kV/cm) impact ionization does not entail a sharp rise in conductivity, because the released carriers become bound again very fast. However, if impact ionization events repeat for a sufficiently long time, any defect will become ionized for a certain interval at least once during this time. The impact ionization probability $p_i(E, T)$ is proportional to the conduction electron concentration $n(T)$ and can be written as

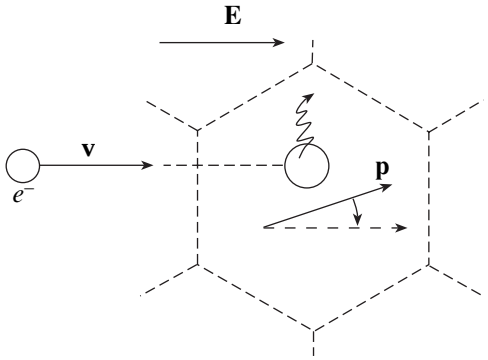

Fig. 1. Schematic representation of the polarization switching in nanoregions resulting from impact ionization of impurities.

$$p_i(E, T) = \int_{\text{cond}} W_i(E, \tilde{\varepsilon}) f(\tilde{\varepsilon}) N(\tilde{\varepsilon}) d\tilde{\varepsilon}. \tag{2}$$

Here, $W(E, \tilde{\varepsilon})$ is the ionization probability in the interaction of one free carrier with a localized charge calculated, in general, quantum mechanically; $N(\tilde{\varepsilon})$ is the density of states in the conduction band; and $f(\tilde{\varepsilon})$ is the Fermi–Dirac distribution function. The integral is taken over the conduction band. The dependence $W(E, \tilde{\varepsilon})$ on field E is dominated by the probability of an electron attaining an energy sufficient to ionize a local center. This is found in standard fashion [12] and, in our conditions ($U_i \gg kT$), can be presented in the form

$$W_i(E, \tilde{\varepsilon}) = A_0 E \exp\left(-\frac{\sqrt{2(U_i + \tilde{\varepsilon})m^*}}{e\tau\varepsilon E}\right), \qquad A_0 \approx \frac{e\varepsilon}{\sqrt{2U_i m^*}}. \tag{3}$$

Thus, the ionization probability depends on the electric field in the sample E, the separation of the local levels from the conduction band bottom U_i, and the electron effective mass m^*; ε is the dielectric permittivity. Finally, we obtain from Eqs. (1)–(3) the expression for the delay time:

$$t_0 \approx \frac{M}{\tilde{n}_0 A_0 (kT)^2 E} \exp\left(\frac{U_a}{kT}\right) \exp\left(\frac{E_0}{E}\right), \qquad E_0 = \frac{\sqrt{2U_i m^*}}{e\varepsilon\tau}, \tag{4}$$

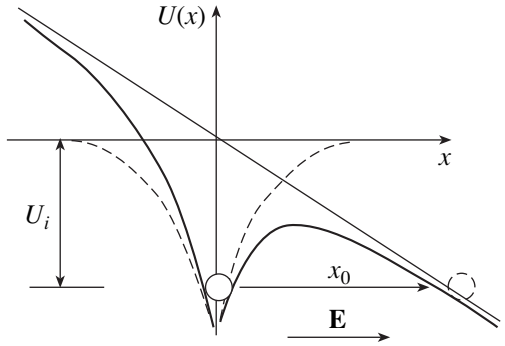

Fig. 2. Impurity ionization in tunneling through a potential barrier.

where τ is the conduction electron relaxation time and the thermally activated character of the conduction electrons was included through the relation $n(T) = \tilde{n}_0 \exp(-U_a/kT)$.

We should consider now the probability of local center ionization by tunneling through a sloped potential barrier created between a local state and the conduction band in the presence of an external field (Fig. 2)—a kind of internal field emission from a defect. This probability has the well-known form

$$p_{vl}(E) = MD_{vl}\exp\left(-\frac{E_0}{E}\right), \quad E_0 = \frac{4\sqrt{2m^*}}{3h\varepsilon_d e}U_i^{3/2}. \quad (5)$$

It follows the same dependence on the field E as the impact ionization. This process can contribute considerably in fields $\varepsilon_d E \approx 10^5$–$10^7$ kV/cm and can also play an important part in relaxors where the dielectric permittivity is high ($\varepsilon \approx 10^3$). Note also that ε_d is the dielectric permittivity felt by a charged defect upon screening. Being independent of the free electron concentration, this process is characterized by a temperature-independent probability. We believe therefore that the major contribution to the activation of localized charges is due to impact ionization, while tunneling processes may produce a certain additional effect.

The delay time t_0 can be related to the electrical conductivity of the material under study through the following estimates. Perovskites are known to have a strongly increased conductivity in electric fields $E \approx$ 10 kV/cm [14], which is assigned to ionization of the local centers: $\sigma_i(T, E) \approx \sigma_0(T)\exp(-E_0/E)$. This observation allows for description of the dependences of the phase transition delay time t_0 on temperature and external electric field observed in [6, 7] on a phenomenological level through the corresponding dependences of the conductivity:

$$t_0 = \frac{eM^{2/3}}{\sigma_i(T, E)E} \approx \frac{M^{2/3}}{\mu\tilde{n}_0 D_0 E}\exp\left(\frac{T_0}{T}\right)\exp\left(\frac{E_0}{E}\right). \quad (6)$$

Here, the thermal activation character of the conductivity, $\sigma_0(T) = e\mu\tilde{n}_0 \exp(-T_0/T)$, is included; note that one may assume the temperature dependence of the conductivity to be determined by the same levels with the characteristic energy U_i, i.e., $T_0 = U_i/2k$ (k is the Boltzmann constant); D_0 is the ionization constant.

We accept as an estimate $U_i \approx 1.2$ eV, which is in accord with the characteristic activation energies derived from conductivity experiments, $U_a \sim 0.6$–1 eV ($U_i \approx 2U_a$) [15, 16]. We obtain $T_0 \approx 7000$ K, and Eq. (4) yields $E_0 \approx 30$ kV/cm for $\varepsilon \approx 10^3$, $\tau \approx 10^{-15}$ s. The delay time can be estimated directly from experimental values of the conductivity $\sigma \approx 10^{10}$–10^{12} Ω^{-1} cm^{-1}, accepting that $M \approx 10^{18}$–10^{19} cm^{-3}, $E \approx$ 2–5 kV/cm, and we obtain $t_0 \approx 10^3$–10^5 s. As follows from the above estimates, Eq. (6) correctly describes the dependences of the delay time on temperature T and applied field E observed experimentally in [6, 7] and the parameters T_0 and E_0 coincide in magnitude with the experimental data. The specific features observed in the behavior of t_0 are associated with the strong exponential dependence of the probability $p(E)$ on field E and with the thermally activated behavior of the conductivity: $p(E) \sim \exp(-E_0/E)$, and $\sigma(T) \sim \exp(-T_0/T)$.

In some perovskites with hole conduction, local acceptor-type states form when an oxygen vacancy comes close to a lead vacancy [17]. The activation energy of such a level should be of the order of 0.6–0.7 eV [17], which is in good agreement with the above theoretical analysis. Moreover, studies of the conductivity in PLZT [15], which also exhibits relaxor properties, revealed, as already mentioned, an activation energy of 0.6–1 eV depending on the composition. Unfortunately, information on the conducting properties of relaxors are very scarce because their conductivity is very low.

It is known that the onset of relaxor behavior is connected intimately with atomic disorder [1, 2]. As seen from the specific example of PMN and PLZT, however, only disorder associated with disordered charge distribution initiates relaxor behavior. This is characteristic of all known relaxors. In addition, it has been shown that, in describing the behavior of relaxors, one should not disregard charge localization on defects and their detrapping [11].

The nature of the low-temperature phase and the specific features of the phase transition in this temperature region occurring after application of a field remain unclear [2]. Numerous experimental data [5–11] show the properties of the low-temperature phase to depend strongly on the sample prehistory, more specifically, on the sequence of cooling and heating cycles and on the application of an external electric field. Thus, relaxors exhibit nonergodic behavior in the low-temperature phase.

The above consideration shows that the characteristic behavior of relaxors in the low-temperature phase observed in [6, 7] can be described in terms of a model that treats this phase as a state with microregions of local polarization in which the polarization direction is pinned by local charged centers. Phase transition to a state with uniform polarization involves carrier detrapping in strong electric fields, followed by reorientation of the local polarization along the field. Besides being corroborated by available experimental data on the size of the observed microregions, the magnitude and field behavior of the conductivity, and the energy position of the local levels, this approach allows adequate description of the temperature and field dependences of the delay time measured in [6, 7]. This gives one grounds to believe that the other properties of relaxors can also be related to the pinning of local states by localized carriers in these microregions [11].

We have described phase transitions in the low-temperature phase of relaxors occurring in the presence of strong electric fields after zero-field cooling. Localized charges produce local strains and maintain in this way the given direction of polarization. When subjected to a strong electric field, the localized charges are detrapped from the local levels either by impact ionization or by tunneling through a potential barrier. As a result, spontaneous polarization in strong enough electric fields aligns with the external field throughout the sample after a certain time. This may be considered to be a structural phase transition extended in time manifesting itself in a jump in the dielectric permittivity. The dependence of the phase transition delay time on temperature and external field in strong enough electric fields is related to carrier detrapping processes and follows a characteristic behavior $t_0(E, T) \sim \exp(E_0/E)\exp(T_0/T)$.

ACKNOWLEDGMENTS

One of the authors (R.F.M.) is indebted to B.Z. Malkin and G.B. Teĭtel'baum for valuable discussions.

This study was supported by the Russian Foundation for Basic Research, project no. 01-02-16350.

REFERENCES

1. G. A. Smolenskiĭ, V. A. Isupov, A. I. Agranovskaya, and S. N. Popov, Fiz. Tverd. Tela (Leningrad) **2**, 2906 (1960) [Sov. Phys. Solid State **2**, 2584 (1960)].
2. L. E. Cross, Ferroelectrics **76**, 241 (1987).
3. R. Blinc, J. Dolinsek, A. Grigorovic, *et al.*, Phys. Rev. Lett. **83**, 424 (1999).
4. A. E. Glazounov and A. K. Tagantsev, Phys. Rev. Lett. **85**, 2192 (2000).
5. Z. Kutnjak, C. Filipic, R. Pirc, and A. Levstik, Phys. Rev. B **59**, 294 (1999).
6. E. V. Colla, E. Yu. Koroleva, N. M. Okuneva, and S. B. Vakhrushev, Phys. Rev. Lett. **74**, 1681 (1995).
7. E. V. Colla, E. Yu. Koroleva, N. M. Okuneva, and S. B. Vakhrushev, Ferroelectrics **184**, 209 (1996).
8. N. Setter and L. E. Cross, J. Appl. Phys. **68**, 2916 (1990).
9. W. Kleemann, Int. J. Mod. Phys. B **7**, 2469 (1993).
10. V. V. Gladkiĭ, V. A. Kirikov, S. V. Nekhlyudov, *et al.*, Pis'ma Zh. Éksp. Teor. Fiz. **71** (1), 38 (2000) [JETP Lett. **71**, 24 (2000)].
11. R. F. Mamin, Fiz. Tverd. Tela (St. Petersburg) **43**, 1262 (2001) [Phys. Solid State **43**, 1314 (2001)].
12. G. I. Skanavi, *Physics of Dielectrics (Strong Field Region)* (Fizmatgiz, Moscow, 1958).
13. W. Franz, *Dielektrischer Durchschlag* (Springer, Berlin, 1956; Inostrannaya Literatura, Moscow, 1961).
14. J. F. Scott and T. Chen, Integr. Ferroelectr. **1**, 71 (1992).
15. A. E. Krumins, U. I. Ilyin, and V. I. Dimza, Ferroelectrics **22**, 695 (1978).
16. V. A. Trepakov, N. N. Kraĭnik, and A. V. Olifir, Fiz. Tverd. Tela (Leningrad) **18**, 1751 (1976) [Sov. Phys. Solid State **18**, 1019 (1976)].
17. V. V. Prisedskiĭ and Yu. D. Tret'yakov, Neorg. Mater. **21**, 1389 (1982).

Translated by G. Skrebtsov

Physics of the Solid State, Vol. 45, No. 5, 2003, pp. 946–947. Translated from Fizika Tverdogo Tela, Vol. 45, No. 5, 2003, pp. 901–902.

LATTICE DYNAMICS AND PHASE TRANSITIONS

Specific Heat of the $[NH_2(CH_3)_2]_2ZnCl_4$ Crystal in the Temperature Region 80–300 K

A. U. Sheleg, T. I. Dekola, and N. P. Tekhanovich

Institute of Solid-State and Semiconductor Physics, National Academy of Sciences of Belarus, Minsk, ul. Brovki 17, 220072 Belarus

e-mail: sheleg@ifttp.bas-net.by

Received July 23, 2002

Abstract—The specific heat of $[NH_2(CH_3)_2]_2ZnCl_4$ was measured calorimetrically in the temperature region 80–300 K. As the temperature T decreases, the $C_p(T)$ dependence indicates a phase transition sequence, with the phase transition at $T_6 = 151$ K observed for the first time. The thermodynamic characteristics of the crystal were refined. The transformation occurring at $T_2 = 298.3$ K is shown to be an incommensurate–commensurate phase transition. *© 2003 MAIK "Nauka/Interperiodica".*

1. Dimethylammonium zincochloride $[NH_2(CH_3)_2]_2ZnCl_4$ [or $(DMA)_2ZnCl_4$] is a member of the $[NH_2(CH_3)_2]_2MeCl_4$ family (*Me* = Cu, Zn, Mn, Cd, Co), which belongs to a large group of crystals of the type A_2BX_4. The interest in this family is spurred by the fact that many of them exhibit a complex sequence of phase transitions (PTs) at various temperatures, which results from these crystals having diverse phases, namely, ferroelectric, ferroelastic, incommensurate, etc. The PTs in the $(DMA)_2ZnCl_4$ crystal were studied earlier by measuring the temperature dependence of the physical properties of the crystal [1, 2]. Heat capacity measurements showed $(DMA)_2ZnCl_4$ to undergo PTs at $T_1 = 310$ K, $T_2 = 272$ K, $T_3 = 250$ K, and $T_4 = 201$ K [1]. A study of optical birefringence and piezoelectric coefficients as a function of temperature revealed PTs in $(DMA)_2ZnCl_4$ occurring at $T_1 = 310$ K, $T_2 = 295$ K, $T_3 = 272$ K, $T_4 = 250$ K, $T_5 = 238$ K, and $T_6 = 217$ K [2]. It is thus seen that not all the PT temperatures quoted by different authors coincide. It appeared of interest to conduct precision measurements of the specific heat of $(DMA)_2ZnCl_4$ to refine the PT temperatures for this crystal.

2. The heat capacity was studied in the region 80–300 K with a vacuum adiabatic calorimeter under stepped heat supply to the sample ($m = 6.0102$ g). The sample heating rate was 0.02–0.08 K/min. The heat capacity measurements were conducted in steps of 0.4–1.5 K to within 0.3%. The sample temperature was monitored with a platinum resistance thermometer.

Figure 1 shows the temperature dependence of the specific heat of $(DMA)_2ZnCl_4$. The $C_p(T)$ curve is seen to have a number of anomalies, at PT temperatures $T_1 = 309.1$ K, $T_2 = 298.3$ K, $T_3 = 272.2$ K, $T_4 = 253.9$ K, $T_5 = 240.0$ K, and $T_6 = 151.0$ K. It should be noted that the PT temperatures found by us differ somewhat from those quoted in the literature. However, the 2- to 3-K difference of is not fundamental in nature and is, most probably, due to the state of the sample used, i.e., the extent to which its crystal structure is defected. It is significant that we detected a new, heretofore unknown PT at $T_6 = 151$ K, which is clearly pronounced in the $C_p(T)$ curve (Fig. 1). The entropies (in units of J/(K mol)) and enthalpies (in J/mol) of the transitions indicated above (found by numerical integration) are 0.02 and 6.89, 0.08 and 29.1, 0.05 and 12.8, 0.06 and 15.1, 0.04 and 9.59, and 0.32 and 48.8, respectively. Smoothed values of the specific heat and the changes in thermodynamic functions (entropy S, enthalpy H, Gibbs free energy Φ) calculated with their use are given in the table.

As found in the experiment, the system, after being heated, reaches equilibrium very slowly (in 30 min or longer) in the interval 135–155 K. This temperature interval includes a low-temperature anomaly at T_6 =

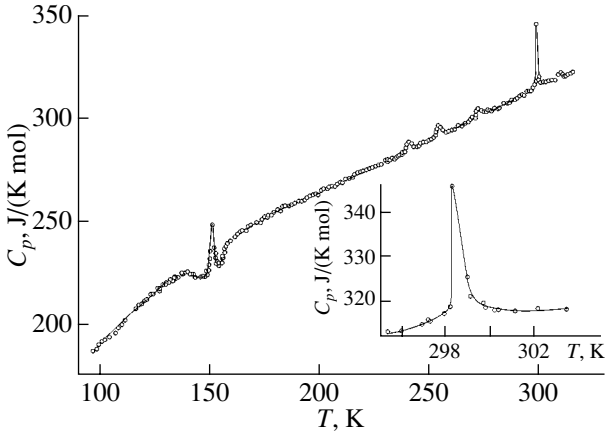

Fig. 1. Temperature dependence of the specific heat of the $(DMA)_2ZnCl_4$ crystal.

1063-7834/03/4505-0946$24.00 © 2003 MAIK "Nauka/Interperiodica"

Smoothed values of the specific heat and of the changes in thermodynamic functions of $(DMA)_2ZnCl_4$

T, K	$C_p(T)$	$S(T) - S(80\ K)$	$\Phi(T) - \Phi(80\ K)$	$H(T) - H(80\ K)$, J/mol
	J/(K mol)			
80	169.00	0.000	0.000	0.0
100	191.66	40.29	9.242	3607
120	211.11	77.05	22.18	7634
140	227.80	110.9	36.66	12 023
160	242.20	142.3	51.73	16 723
180	254.76	171.6	66.90	21 693
200	265.95	199.1	81.92	26 900
220	276.23	224.9	96.68	32 322
240	286.66	249.4	111.1	37 945
260	295.89	272.7	125.2	43 764
280	306.20	295.0	138.9	49 785
300	317.44	316.5	152.3	56 022

151.0 K. Note that $[N(CH_3)_4]_2ZnCl_4$ [3] and $[N(CH_3)_4]_2FeCl_4$ [4] also revealed a similar relaxation of the heat capacity.

The specific-heat anomaly at $T_2 = 298.3$ K exhibits a clearly asymmetric shape (inset to Fig. 1). On the high-temperature side, the specific heat is seen to fall off more smoothly. According to [5], the specific heat in an incommensurate phase should increase as $\Delta C_p \sim \{(T - T_c)[\ln(T - T_c)]^{-2}\}^{-1}$ because of the soliton structure. Figure 2 plots $(\Delta C_p)^{-1}$ vs. $T - T_2$ for $(DMA)_2ZnCl_4$ in the region of the PT at $T_2 = 298.3$ K. One readily sees that this relation is linear in the interval $T_2 + 0.7 < T < T_2 + 2.1$ K, which is in accord with the theoretical predictions. Hence, one may assume that, for temperatures $T > T_2$, the phase of the $(DMA)_2ZnCl_4$ crystal is incommensurate and the transformation at $T_2 = 298.3$ K is a transition from the incommensurate to a commensurate phase.

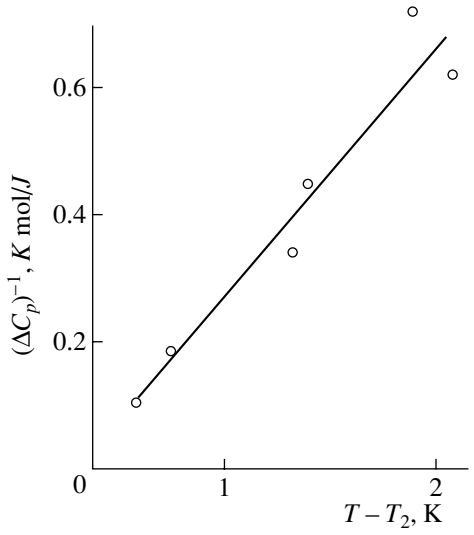

Fig. 2. $(\Delta C_p)^{-1}$ vs. $T - T_2$ relation for the $(DMA)_2ZnCl_4$ crystal in the vicinity of the phase transition at $T_2 = 298.3$ K.

This conjecture is also argued for by the magnitude of the entropy of the transition occurring at T_2, $\Delta S = 0.08$ J/(K mol). The entropy of the incommensurate–commensurate phase transition for A_2BX_4 compounds is, as a rule, by far less than that of displacive transitions, which is of the order of 0.1 R. The small value of ΔS for the lock-in transitions is due to the formation of a soliton structure in the incommensurate phase of most crystals near the phase transition temperature [6]. Other crystals of the A_2BX_4 family, with both an atomic and organic cation, exhibit a ΔS value of the incommensurate–commensurate transition that is of the same order of magnitude.

REFERENCES

1. V. E. Vasil'ev, V. M. Rudyak, Z. A. Bobrova, and V. M. Varikash, Fiz. Tverd. Tela (Leningrad) **29** (5), 1539 (1987) [Sov. Phys. Solid State **29**, 882 (1987)].
2. O. G. Vlokh, V. B. Kapustyanyk, and I. I. Polovinko, Zh. Prikl. Spektrosk., No. 5, 785 (1990).
3. B. A. Strukov, S. A. Taraskin, U. Uesu, *et al.*, Izv. Akad. Nauk SSSR, Ser. Fiz. **54** (4), 710 (1990).
4. J. Ruiz-Larrea, A. Lopez-Echarri, and M. J. Tello, Solid State Commun. **64** (8), 1099 (1987).
5. V. A. Golovko, Zh. Éksp. Teor. Fiz. **94** (2), 182 (1988) [Sov. Phys. JETP **67**, 316 (1988)].
6. *Incommensurate Phases in Dielectrics*, Ed. by R. Blinc and A. Levanyuk (North-Holland, Amsterdam, 1986), Vols. 1, 2.

Translated by G. Skrebtsov

Physics of the Solid State, Vol. 45, No. 5, 2003, pp. 948–952. Translated from Fizika Tverdogo Tela, Vol. 45, No. 5, 2003, pp. 903–907.

LOW-DIMENSIONAL SYSTEMS AND SURFACE PHYSICS

Mechanism of Primary Self-Organization in Porous Silicon with a Regular Structure

M. E. Kompan

Ioffe Physicotechnical Institute, Russian Academy of Sciences, Politekhnicheskaya ul. 26, St. Petersburg, 194021 Russia
e-mail: kompan@solid.ioffe.rssi.ru

Received July 1, 2002

Abstract—A mechanism for self-organization of a regular system of pores in porous silicon is proposed. According to this mechanism, the self-organization obeys the general kinetic laws for a system of charge carriers. The mean interpore spacing in porous silicon prepared from *p*-Si and the anodizing current density required for synthesizing porous silicon through anodic etching are evaluated in terms of the proposed mechanism. The results obtained are in good agreement with the available experimental data. The dependence of the mean interpore spacing on the carrier concentration in the initial silicon is predicted to be similar to the function $L(n) \sim n^{-1/2}$. The validity of the proposed mechanism is confirmed by computer simulation. © *2003 MAIK "Nauka/Interperiodica".*

1. INTRODUCTION

A new direction in the physics of condensed matter dealing with the development of techniques for producing nanoobjects and the study of their properties has emerged over the last decade. The particular interest expressed by researchers in these objects is motivated by a number of factors, such as the necessity of designing new materials for use in information technology and the possibility of revealing new useful properties of already existing materials. It should be noted that nanoobjects, as a rule, are not fabricated directly using special techniques but are spontaneously formed under appropriate macroscopic conditions. Suenaga *et al.* [1] and Gudiksen *et al.* [2] described nearly fantastic examples illustrating the possibility of self-organizing complex elements. However, despite the considerable progress achieved in the physics and technology of nanoelements, no techniques have been proposed for combining nanoelements into structures. This situation has aroused great interest in research into natural aggregates of nanoelements.

In the early 1990s, Canham [3] newly discovered porous silicon, which appeared to be a natural aggregate of nanoelements consisting of silicon, a known semiconductor material. Owing to the original attraction in silicon optoelectronics, porous silicon was intensively studied in the 1990s. This has made it possible to obtain numerous results of fundamental and practical importance (see, for example, the special collection of papers [4]). However, in spite of extensive investigations, many problems in this field have remained unsolved.

One of the problems unsolved thus far concerns the mechanism of self-organization of porous silicon, although its importance was perceived even in 1990 after the publication of Canham's work [3]. At present, there exist quite different procedures for preparing porous silicon, from the simplest, widely known, electrochemical method [5] to the technique of producing luminescent silicon with the use of high-power laser irradiation [6]. Probably, that is why a universal theory of self-organization, in principle, cannot be formulated for the structure of porous silicon. However, even the known electrochemical method (anodizing) first described by Terner [5] has not been properly explained yet.

In the course of anodizing, silicon is etched in hydrofluoric acid solutions when a positive electrical bias with respect to the solution is applied to the crystal. Over a wide range of parameters of the process, this method provides a way of forming a closely packed system of pores (including nanopores) with a small spread in pore sizes.

A large number of concepts and models have been proposed by different authors with due regard for the specific features and conditions of anodizing. In particular, Beale *et al.* [7] thoroughly argued for the necessity of applying a positive electrical bias (with respect to the etching solution) to the initial silicon crystal in order to ensure current pinching and narrowing of the etching channels. In the authors' opinion [7], this should be the governing factor for the formation of a porous structure. However, this mechanism in actual fact cannot provide the formation of a pore system, because it is well known that the current pinching results in an *S*-shaped current instability and a decrease in the voltage. In turn, this prevents the formation of subsequent current channels and pore etching at other sites on the surface.

Moreover, Terner [5] revealed that a positive bias is not necessary for producing porous silicon even in HF

1063-7834/03/4505-0948$24.00

solutions in H_2O. Earlier [8], we used a zero bias voltage (according to [5]) for preparing porous silicon in large amounts. Our estimates demonstrated that the formation rate for anodizing with zero voltage is virtually identical to that for the standard anode process. Therefore, the inference can be made that the positive bias is of no importance for this process. In our recent work [9], the anodizing with zero bias was qualitatively explained within the proposed concept of an electric field induced at the boundary between bulk silicon and a distributed system of pores (similar to the concept of an electrochemical double layer). One of the main principles underlying this concept is the assumption about the transfer of charge carriers (holes) from bulk silicon to ions in a solution and again to bulk silicon along quantum wires (walls between pores). In general, the anodizing with zero bias voltage is a nontrivial process in which the porous silicon structure formed at early stages should provide the reproduction of an identical or similar structure at subsequent stages. We believe that this is the main factor responsible for the structure of porous silicon at the later etching stages. The above principles of self-organization of the porous silicon structure were formulated in our previous work [9]. Consequently, we thus assumed that the porous structure of silicon is governed only by the structure formation at the initial stage involving the etching of the planar surface. One more inference drawn in [9] is also very essential for the present work: the initial event of removal of a silicon atom in etching even at zero anode bias should involve the localization of a hole on the silicon surface.

There have been only a few attempts to interpret the early stage of the pore formation. In particular, Valance [10] proposed a model based on the assumption that the planar surface profile is unstable in the course of anodic etching. This model includes a number of factors (such as the surface tension energy, the transport of holes in silicon, and the diffusion of ions in an electrolyte) affecting the silicon surface profile. However, the inference drawn in [10] is erroneous: this model cannot explain the self-organization of the closely packed system of nanopores in *p*-Si.

The mechanism proposed by Gorjachev *et al.* [11] for the initial stage of the formation of porous silicon is based on the existing chemical concepts [5] regarding the possibility of depositing silicon atoms according to the disproportionation reaction

$$2Si^{2+} \longrightarrow Si^{0}\downarrow + Si^{4+}. \quad (1)$$

In the framework of the model developed in [11], it is assumed that neutral silicon atoms can be incorporated into the silicon surface, which leads to the formation of branched structures. However, Unagami and Seki [12] found that the structure of porous silicon, for the most part, is similar to that of the initial crystal. Therefore, the verification of the validity of the mechanism proposed in [11] needs to include a new model of recrystallization.

Other approaches have also been proposed. Smith and Collins [13] assumed that the structure of porous silicon reflects the formation of hydrogen bubbles during the electrochemical reaction, even though it is known that porous silicon can be produced using reactions without hydrogen release. It was also assumed that defects on the silicon surface play the role of pore nuclei. However, Allongue *et al.* [14] demonstrated that pores are formed irrespective of defect locations. Thus, no reasonable model that would explain the mechanism of formation of a porous silicon structure has been proposed to date.

2. THE MECHANISM OF PORE SEPARATION

In this work, we propose a mechanism that can be responsible for the formation of a system of pores with an interpore spacing of several nanometers. A number of predictions that can be verified are made on the basis of the proposed mechanism. This mechanism accounts for the formation of porous silicon from *p*-Si. However, the original ideas are sufficiently general in character and the model can also prove useful in other cases.

The model of the above mechanism is related to our model used for explaining another unclear phenomenon, namely, the dependence of the quantum wire size in porous silicon on the carrier concentration in initial bulk *p*-Si. The latter model was published in electronic form in [15]. Now, we understand that both these models describe two aspects of the same phenomenon associated with the fundamental properties of a subsystem of mobile charge carriers.

Essentially, the mechanism is as follows. It is well known (for example, from the original model of the etching mechanism [5]) that the localization of a hole on a surface atom is the initial etching stage. (Note that *p*-Si has intrinsic holes and an external positive bias is necessary predominantly for overcoming the potential barrier in a depletion region in the vicinity of the surface.) In the case when the surface is initially smooth, the hole can be localized on any surface atom with equal probability. This initiates a chain of reactions that eventually result in the removal of one atom from the surface. The appearance of a vacant site renders the remaining sites on the surface nonequivalent. The atoms closest to the vacated site have one less bond in the lattice, so that the probability of etching away the atoms from these adjacent sites increases. This can lead to the known regime of etching with steps running along the surface.

However, it should also be taken into account that the escape of the atom from the surface brings about a change in the electronic subsystem of silicon. Actually, the escape of the atom from the surface should be accompanied by the escape of the hole (initially localized at the atom) from the electronic subsystem of the crystal. Since holes are required for initiating the etching, the escape of the hole leads to a decrease in the

probability of etching away the atoms occupying the sites in the vicinity of the vacated site. As a consequence, the probability that the atoms in the neighborhood of the site just vacated will be etched away becomes lower for a time.

To put it differently, the etch removal of the atom is attended by the escape of the localized hole, which disturbs the subsystem of mobile charge carriers. The spatial and temporal scales of the existence of this temporary region free of hole carriers are determined by the same laws that govern the behavior of any disturbance in a system of mobile charges. The size and the lifetime of the hole-free region are equal to the well-known Debye length R_D and the Maxwell time τ_M, respectively. In turn, these quantities can be expressed through the material parameters in the following form [16]:

$$(R_D)^2 = \varepsilon kT(e^2 n)^{-1}, \quad (2)$$

$$\tau_M = \varepsilon\rho, \quad (3)$$

where n is the concentration of mobile carriers; kT is the temperature in energy units; e is the elementary charge; and ε and ρ are the permittivity and the resistivity of the material, respectively. It should be emphasized that the exact values of parameters for the surface regions can differ from those for bulk silicon. As applied to the etching, this implies that the etch removal of the silicon atom disturbs the subsystem of mobile carriers and the hole in the region with a size of the order of R_D will be absent for a time. The local memory about the hole removal will be responsible for the decreased probability of etching away atoms in the neighborhood of the atom just etched away until a new hole diffuses into this region.

It is essential that the etching is stochastic in nature. The next etching event can occur at any site of the surface and only has a lower probability in the region with a size of the order of R_D in the vicinity of the atom just etched away. It is of importance that the proposed mechanism cannot provide a perfect periodicity in the arrangement of pores and only ensures their tendency to separation.

Let us estimate the mean interpore spacing with the use of the parameters for bulk silicon. In the framework of the proposed mechanism, the distance between pores is of the order of the Debye length ($L \approx R_D$) and, according to relationship (2), should vary with the carrier concentration as $n^{-1/2}$. For a hole concentration of 10^{18} cm^{-3} in initial silicon, relationship (2) gives $L \cong 4$ nm, which is in excellent agreement with the available empirical data. The dependence $L(n) \sim n^{-1/2}$ following from relationship (2) also agrees qualitatively with the experimental data. However, it should be taken into consideration that the depletion layer can cause a deviation from this dependence.

One more important feature of the aforementioned pore separation mechanism is its validity only for short times. Indeed, the local region characterized by a decreased probability of etching exists only for a limited time after escape of the atom. For example, when the etching current is small and the etching is not intensive, the time interval between subsequent etching events in the region under consideration can be sufficiently large and appear to be longer than the characteristic time τ_M. In this case, the correlation between etching events disappears and the studied mechanism ceases to be efficient. Furthermore, the etching rate can increase, because surface inhomogeneities can lead to a local increase in the electric field.

Now, we will estimate the minimum anodizing current required to realize the proposed mechanism. It should be noted once again that such an estimate has meaning only at the earliest etching stages. At later stages, according to Terner's observations [5], our model, and the data obtained in practical preparation of the material [8, 9], the current does not directly determine the etching rate. However, at the initial stage, we can assume that the number of etched atoms is equal to the number of holes injected into silicon from a positive electrode. Under this assumption, the anodizing current density j_a at which the mechanism of spatial pore separation becomes valid can be written in the following form:

$$j_a \approx e/\pi(R_D)^2\tau_M. \quad (4)$$

Formula (4) gives the estimate of the current density at which, on the average, one hole for the Maxwell time passes through a surface region with a linear size of the order of the Debye length. As follows from expression (4), it is this current density that provides the correlation between etching events.

Under the assumption that the Maxwell time is estimated as $\tau_M \approx 10^{-11}$ s, we find the current density j_a to be equal to 3×10^{-4} a/cm^{-2}, which is in agreement with the data obtained in many works. Note once again that the proposed mechanism is stochastic in nature and the estimated current density most likely should not correspond to a sharp threshold. We can only state that, at lower current densities, the correlation between the events of etch removal of atoms becomes weaker and our mechanism should be invalid.

Therefore, the formation of the closely packed, regular system of pores in porous silicon prepared from bulk p-Si can be clearly and naturally explained in terms of the most general properties of the charge subsystem. The proposed model makes it possible to estimate the spatial separation of pores and the required anodizing current density from the parameters of initial crystalline silicon. The obtained estimates agree well with the experimental data available in the literature.

3. MODELING OF THE PORE FORMATION

In order to verify the aforementioned qualitative concepts, we developed a computer model of the formation of porous silicon.

The etching was simulated on a square lattice. Empty and occupied sites in the lattice were initially separated by boundaries. The edge effects were eliminated by cycling the side boundaries. In this case, although we used a two-dimensional model, atoms inside the bulk (unetched region), as in the crystal lattice of silicon, had four neighbors. When the surface was initially specified as planar, the surface (boundary) atoms each had three bonds. At each step, the probability of etching away was calculated for each atom, followed by the removal of one atom, which was chosen by a random number generator with due regard for the calculated probability. The sequence of etchings (removals of individual atoms) resulted in the formation of a model surface relief representing a relief of the porous structure.

The probability of etching away particular atoms was calculated using the effective etching activation energy dependent on the position and environment of each atom. The main contribution to the activation energy for each atom was determined by the number of valence bonds of this atom with the existing neighbors, i.e., by the number of occupied sites in the nearest coordination sphere. The model also made it possible to include other factors affecting the etching, namely, the surface tension, the quantum confinement effect, and the external electrical bias. For simplicity, the analyzed mechanism of memory about the local disappearance of the hole was simulated in the model as follows: atoms in a region around a site just vacated were directly barred from etching away for a fixed time after the etching event.

There exists one more mechanism that can be responsible for pore separation. This mechanism is associated with the electrostatic repulsion of pore tips (see our previous work [9]). However, it is evident that this mechanism cannot play an important role when either the system of pores is not formed or their depth is less than the Debye length. Since we were interested in the primary mechanism responsible for the formation of the system of pores beginning with the planar surface, the mechanism of electrostatic repulsion of pore tips was not included in the model.

The typical profiles obtained by computer simulation are displayed in Figs. 1a–1d. In all four cases, the atoms to be etched away were chosen using the same random number generator. Figure 1a shows the typical profile in the case when the activation energy is directly proportional to the number of occupied sites. The profile simulated with inclusion of the contributions from all the above four mechanisms to the etching is represented in Fig. 1b. The profiles depicted in these figures were obtained for the same mean number of etching events (approximately 3.5 removed atoms per surface site). It is obvious that the profiles differ drastically and the joint action of the mechanisms under consideration can ensure the formation of a developed porous structure (analogs of pores).

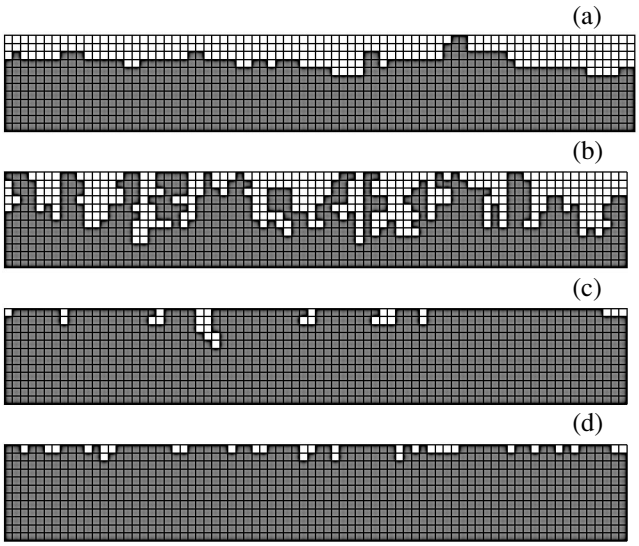

Fig. 1. Surface profiles obtained using a computer simulation under different conditions: (a) the activation energy for etch removal of an atom is directly proportional to the number of nearest neighbors; (b) the contributions of the surface tension, the quantum confinement effect, and the proposed mechanism of pore separation are included in the simulation in addition to the mechanism used in the preceding case; (c) only the dependence of the activation energy on the number of neighbors and the surface tension are taken into account; and (d) the mechanisms used in the preceding case are included in addition to the proposed mechanism of pore separation. The mean number of etching events per surface site: (a, b) 3.5 and (c, d) 0.35.

Figures 1c and 1d illustrate the governing role of the proposed mechanism at the initial stage of the pore formation (approximately 0.35 removed atoms per surface site). The surface profile displayed in Fig. 1c was simulated with allowance made for the chemical activation and the surface tension. The profile shown in Fig. 1d was obtained with due regard for the proposed mechanism of pore separation in addition to the mechanisms used for simulating the profile in Fig. 1c. It is easy to see that, instead of the tendency to aggregation observed in Fig. 1c, the profile represented in Fig. 1d is characterized by a distribution of free empty over the surface.

A detailed analysis of the results obtained in computer simulation and the role of particular mechanisms are of considerable interest and will be discussed in a separate work. However, regardless of details, the computer simulation clearly demonstrates the tendency to pore separation due to the proposed mechanism.

Thus, we proposed a new mechanism for self-organization of porous silicon with a closely packed regular structure. The mechanism is based on the general

kinetic laws for a subsystem of mobile charges. This generality suggests that the mechanism under consideration is applicable to a number of other processes, for example, to the self-organization of colloidal structures on the silicon surface, where the electric interaction forces between particles and the surface can play an important role.

It was demonstrated that, in terms of the proposed mechanism, the concentration dependence of the interpore spacing should have the form $L(n) \sim n^{-1/2}$. The interpore spacing and the anodizing current density were estimated for typical parameters of the initial material. The validity of the proposed mechanism was confirmed by computer simulation.

In conclusion, we note one nontrivial analogy. The proposed mechanism rests on the simple assumption that, in a small local crystal region, one hole exists at each instant of time and its escape from this region cannot be instantaneously compensated. This statement is virtually identical to the formulation of Pauli's exclusion principle. However, unlike the quantum nature of Pauli's principle, the proposed mechanism is purely classic in nature, which manifests itself particularly in the absence of spin parameters. Nonetheless, these approaches closely resemble each other.

ACKNOWLEDGMENTS

The author would like to thank I.Yu. Senichenkov and I.B. Volkovets for developing the simulation program used in this study.

REFERENCES

1. K. Suenaga, Y. Zang, and S. Iijima, Appl. Phys. Lett. **76**, 1564 (2000).
2. M. S. Gudiksen, L. J. Lauhon, J. Wang, *et al.*, Nature **415**, 617 (2002).
3. L. T. Canham, Appl. Phys. Lett. **57**, 1046 (1990).
4. Collection of papers from *First International Conference on Porous Semiconductors*, J. Porous Mater. **7** (1–3) (2000).
5. D. R. Terner, J. Electrochem. Soc. **105**, 402 (1958).
6. K. M. A. El-Kader, J. Ocwald, J. Kocka, and V. Chab, Appl. Phys. Lett. **64**, 2555 (1994).
7. M. I. J. Beale, J. D. Benjamin, M. J. Uren, *et al.*, J. Cryst. Growth **73**, 622 (1985).
8. M. E. Kompan and I. Yu. Shabanov, Fiz. Tverd. Tela (St. Petersburg) **36**, 125 (1994) [Phys. Solid State **36**, 68 (1994)].
9. M. E. Kompan and I. Yu. Shabanov, Fiz. Tekh. Poluprovodn. (St. Petersburg) **29**, 1859 (1995) [Semiconductors **29**, 971 (1995)].
10. A. Valance, Phys. Rev. B **52**, 8323 (1995).
11. D. N. Gorjachev, L. V. Beljakov, and O. M. Sreseli, Fiz. Tekh. Poluprovodn. (St. Petersburg) **34**, 1130 (1995) [Semiconductors **34**, 1090 (2000)].
12. T. Unagami and M. Seki, J. Electrochem. Soc. **125**, 1339 (1978).
13. R. L. Smith and S. D. Collins, J. Appl. Phys. **71**, R1 (1992).
14. P. Allongue, V. Costa-Keilling, and H. Gerischer, J. Electrochem. Soc. **140**, 1009 (1993).
15. M. E. Kompan, I. Yu. Senichenkov, I. Yu. Shabanov, and J. Salonen, http://zhurnal.are.relarn.ru/articles/1999/001.pdf.
16. L. D. Landau and E. M. Livshitz, *The Classical Theory of Fields*, 5th ed. (Nauka, Moscow, 1967; Pergamon, Oxford, 1975).

Translated by O. Borovik-Romanova

Physics of the Solid State, Vol. 45, No. 5, 2003, pp. 953–956. Translated from Fizika Tverdogo Tela, Vol. 45, No. 5, 2003, pp. 908–910.

LOW-DIMENSIONAL SYSTEMS AND SURFACE PHYSICS

On the Baric Fragmentation of a Crystal

M. N. Magomedov

Institute of Geothermal Problems, Dagestan Scientific Center, Russian Academy of Sciences, pr. Kalinina 39a, Makhachkala, 367003 Russia

e-mail: musa@dinet.ru

Received September 10, 2002

Abstract—An expression for the binding energy E_b of N atoms located in a parallelepiped with an arbitrary shape of the surface and an arbitrary microstructure is derived. The length ratio f of the lateral edge to the base edge determines the shape of the system. It is shown that the binding function $E_b(f)$ for any number N has an extremum at the shape parameter $f = 1$, which corresponds to a system in the form of a cube. The binding function $E_b(f)$ has a minimum when the external pressure P is less than the boundary pressure P_0, i.e., at $P < P_0$, and reaches a maximum at $P > P_0$ and $f = 1$. An analysis demonstrates that, under pressure $P > P_0$, the crystal should undergo exothermal fragmentation and the larger the difference $P - P_0$, the smaller the size of crystal fragments should be. The crystal fragments formed in the process tend to have the maximum possible surface area. Experimental works supporting the occurrence of exothermal fragmentation of a crystal under pressure are cited. © *2003 MAIK "Nauka/Interperiodica".*

1. INTRODUCTION

It is known that the first coordination number k_n for an atom on the surface is considerably less than that for an atom in the bulk of the material [1–8]. Consequently, the averaged (over all N atoms) coordination number $\langle k_n \rangle$ depends not only on the size but also on the shape of the nanocrystal [7, 8]. Since it is this dependence $\langle k_n \rangle(N)$ that is responsible for the binding energy E_b of atoms in the nanocrystal [1–6], the difference between the functional forms of $\langle k_n \rangle(N)$ for nanocrystals with different shapes of the surface leads to the fact that the formation of a nanocrystal with a minimum surface area can be energetically favorable under some conditions and of that with a maximum surface area, under other conditions. The question arises as to which conditions can provide the formation of a nanocrystal with the maximum possible surface area (i.e., dendritization) at the minimum binding energy $E_b(N)$. In the present work, in order to answer this question, a relationship was derived for describing the binding energy $E_b(N)$ as a function of the size and the shape of a nanocrystal with an arbitrary number of atoms.

2. THEORETICAL BACKGROUND

Let us consider a one-dimensional chain consisting of N atoms in which the distance between the centers of the nearest neighbor atoms is equal to c. Let B be some (linear) property of an atom that is located inside the chain and has two nearest neighbors and A be an analogous property of a terminal atom with only one neighbor. In this case, the averaged (over all N atoms of the chain) property $\langle B_1 \rangle$ can be represented as

$$\langle B_1 \rangle = B - (2/N)(B - A). \quad (1)$$

Next, we consider a two-dimensional rectangular system composed of N atoms, of which N_{po} atoms are located in the base and $N_{ps} = fN_{po}$ atoms occupy the lateral edge of the rectangle. The total number of atoms in this system can be defined by the expression $N = fN_{po}^2/\alpha_2$, where $f = N_{ps}/N_{po}$ is the shape parameter and α_2 is the microstructure parameter, which depends on the packing type of the regular two-dimensional atomic lattice. Hence, for the property $\langle B_2 \rangle$, we obtain $2N\langle B_2 \rangle = [N - 2(N_{fo} + N_{fs}) - 4]2B + 2(N_{fo} + N_{fs})(B + A) + 8A$, where $N_{fo} = N_{po} - 2$ and $N_{fs} = N_{ps} - 2$ are the numbers of atoms located in the base and along the lateral edge (without regard for the terminal atoms) of the rectangle, respectively. Then, for a two-dimensional rectangle, it is a simple matter to deduce the following relationship:

$$\langle B_2 \rangle = B - (\alpha_2/f)^{1/2}[(1 + f)/N^{1/2}](B - A). \quad (2)$$

By applying a similar procedure to a three-dimensional rectangular parallelepiped with a square base [$N = (f/\alpha_3)N_{po}^3$], we obtain the expression

$$\langle B_3 \rangle = B - (\alpha_3/f)^{2/3}[(2f + 1)/3N^{1/3}]2(B - A). \quad (3)$$

From comparing relationships (1)–(3), we can assume that, in the n-dimensional case,

$$\langle B_n \rangle = B - (\alpha_n/f)^{(n-1)/n} \times \{[(n-1)f + 1]/nN^{1/n}\}2(B - A). \quad (4)$$

1063-7834/03/4505-0953$24.00 © 2003 MAIK "Nauka/Interperiodica"

For the microstructure parameters α_n, we easily found that $\alpha_1 \equiv 1$, $\alpha_2 = \pi/4k_y(2)$, and $\alpha_3 = \pi/6k_y(3)$. Here, $k_y(n)$ is the packing coefficient of the atomic lattice: $0 < k_y(n) < 1$.

With the use of expression (4), we can determine the mean coordination number for an n-dimensional nanocrystal. An atom has B nearest neighbors in the bulk (on average, $B = k_n/n$ in a linear direction) and A nearest neighbors at the boundary ($A = k_n/2n$). As a result, the expression for the relative value of the mean coordination number takes the form

$$k_n^* = \langle k_n \rangle / k_n = 1 - [F_n(f)\alpha_n^{n-1}/N]^{1/n}, \quad F_n(f) = [(n-1)f + 1]^n / n^n f^{n-1}. \tag{5}$$

The shape function $F_n(f)$ reaches a minimum when the system has an n-dimensional cubic form: $F_n(f = 1) = 1$. For platelike ($f < 1$) or rodlike ($f > 1$) nanocrystals, the shape function is larger than unity; i.e., $F_n(f \neq 1) > 1$.

A comparison of the results obtained from relationship (5) with direct calculations of the mean coordination numbers $\langle k_n \rangle$ for nanocrystals with square ($n = 2$) and cubic ($n = 3$) lattices demonstrated exact coincidence for all possible forms of the surface. Relationship (5) is more accurate than the expression used in my earlier work [7] and, as will be shown below, agrees well with the results obtained in [1–6].

Now, we assume that the interaction of atoms in a crystal is described by the Mie–Lennard-Jones interatomic potential (another form of the interaction can also be chosen):

$$\varphi(r) = [D/(b-a)][a(r_0/r)^b - b(r_0/r)^a]. \tag{6}$$

Here, D is the depth of the potential well, r_0 is the coordinate of the minimum of the potential well, b is the stiffness parameter of the potential, and a is the parameter characterizing the long-range interaction. Then, by assuming that only the nearest neighbor atoms interact with one another [1, 2] and taking into account expression (5), the binding energy of atoms in a nanocrystal (at an arbitrary pressure P) can be represented in the following form:

$$E_b(N) = (\langle k_n \rangle/2) N\varphi(r = c) = (k_n/2)[1 - (C_n/N^{1/n})] N\varphi(r = c), \tag{7}$$

where $C_n = [\alpha_n^{n-1} F_n(f)]^{1/n}$.

As a result, for a three-dimensional nanocrystal with a cubic shape of the surface (i.e., when $n = 3$ and $f = 1$), we obtain

$$C_{n=3} = \alpha_3^{2/3} = \begin{cases} 0.7937 \text{ at } k_3 = 12 \text{ and } k_y = 0.7405 \ (\alpha_3 = 0.707) \\ 0.8255 \text{ at } k_3 = 10 \text{ and } k_y = 0.6981 \ (\alpha_3 = 0.750) \\ 0.8399 \text{ at } k_3 = 8 \text{ and } k_y = 0.6802 \ (\alpha_3 = 0.770) \\ 1.0000 \text{ at } k_3 = 6 \text{ and } k_y = 0.5236 \ (\alpha_3 = 1.000) \\ 1.3333 \text{ at } k_3 = 4 \text{ and } k_y = 0.6802 \ (\alpha_3 = 1.540). \end{cases}$$

These values agree well with the estimates made for C_n in the framework of different numerical models: $C_{n=1} = 0.571$–1.221 [4] for $k_1 = 2$;

$$C_{n=3} = \begin{cases} 0.530\text{–}0.790 \text{ [4] for } k_3 = 6 \\ 1.33 \pm 0.05 \text{ [1]; } 0.735\text{–}1.712 \text{ [4] for } k_3 = 8 \\ 1.33 \pm 0.07 \text{ [1]; } 0.739 \text{ [4]; } 1.452 \text{ [5]} \\ 1.698\text{–}1.864 \text{ [6] for } k_3 = 12. \end{cases}$$

Thus, we can assert that relationship (7) holds true for arbitrary values of $N \geq 2^n$.

Judging from the condition of minimization (for the structure under investigation and the given interatomic distance) of the specific binding energy ($\varepsilon(N, f) = E_b(N, f)/N$), the function $\varepsilon(f)$ has an extremum at the shape parameter $f = 1$. For a cubic shape of the surface of a nanocrystal, the specific binding energy $\varepsilon(f)$ of atoms forming the nanocrystal reaches a minimum at $\varphi(c) < 0$ and a maximum at $\varphi(c) > 0$.

Let us now define the boundary pressure P_0 as the pressure at which the interatomic potential described by relationship (6) becomes zero; i.e., $\varphi(\sigma) = 0$. The distance between the centers of the nearest neighbor atoms σ at which the above condition is satisfied can be determined from the form of the interatomic potential. For potential (6), we have the interatomic distance $\sigma = r_0(a/b)^{1/(b-a)}$. (It should be noted that the inclusion of the interaction of all the neighbors leads to the appearance of structure sums [1, 2] in the expression for the potential $\varphi(r = c)$ and to an appropriate renormalization of the interatomic distance σ but does not change the essence of the phenomenon.)

3. RESULTS AND DISCUSSION

It can be seen from relationship (7) that, at low pressures (i.e., under the conditions $P < P_0$, $c > \sigma$, and $\varphi(c) < 0$), the minimization of the specific binding energy $\varepsilon(f, N)$ of a nanocrystal should lead to a manifestation of the following effects: (i) an increase in the

number N of atoms, i.e., an increase in the size of the nanocrystal; (ii) a decrease in the magnitude of the shape function $F_n(f)$, i.e., the surface area of the nanocrystal should tend to a minimum and the nanocrystal itself should tend to take on the form of an n-dimensional cube ($f = 1$); and (iii) an increase in the coordination number k_n and a decrease in the microstructure parameter α_n, i.e., compaction of the nanocrystal microstructure. These effects clearly manifest themselves in experiments on nanocrystals with free surface (see reviews [1–3]).

At high pressures ($P > P_0$, $c < \sigma$), the interatomic potential changes sign ($\varphi(c) > 0$). Under these conditions, the minimization of the specific binding energy $\varepsilon(f, N)$ of a nanocrystal should result in a manifestation of the following effects: (i) a decrease in the number N of atoms in the nanocrystal, i.e., there should occur fragmentation of the crystal and the larger the difference $P - P_0$, the smaller the size of the crystal fragments should be; (ii) an increase in the magnitude of the shape function $F_n(f)$, i.e., the maximum possible deviation of the shape parameter f from unity when the surface area of the nanocrystals formed upon fragmentation tends to a maximum; and (iii) a decrease in the coordination number k_n and an increase in the value of α_n i.e., loosening of the nanocrystal microstructure.

The above effects of baric fragmentation, dendritization, and loosening of the crystal microstructure should be accompanied by energy release. The larger the difference $P - P_0$, the higher the energy released. In this case, the higher the rate of compression of the crystal to $P > P_0$, the higher the rate of release of the fragmentation energy; i.e., when the crystal is subjected to dynamic compression under a pressure higher than P_0, there should occur explosive phenomena accompanied by fragmentation of the material into nanocrystals with a rodlike or platelike habit. The energy released under these conditions is caused only by the fragmentation of the crystal at $P > P_0$. Although similar explosive effects were observed experimentally by P. Bridgman as early as in 1946 [9], they have hitherto defied theoretical explanation [10–12], because it has remained unclear why the formation of a surface with a large area (upon baric fragmentation of the crystal) is accompanied by energy release rather than by energy absorption.

Note that the nature of fragmentation of solids upon rapid removal of uniform compression has also remained unclear [13]. In [13], it was found that, after compression under a pressure higher than a critical value (specific to each material), followed by rapid (2 GPa/ms) unloading, not only metals and inorganic materials but also Teflon, rubber, and paraffin underwent fragmentation. An increase in the pressure of compression brought about an increase of the degree of fragmentation of the material. The size distribution of fragments, in general, had a bimodal functional form, which the authors of [13] failed to explain.

However, this phenomenon can be easily explained in terms of the effect of exothermal fragmentation of the crystal under pressure. In the case when the static load is rapidly removed from the compressed material, the dendritic crystals formed under compression (at $P > P_0$) do not manage to intergrow together. For this intergrowth, it is necessary that the fragmented material relieved from the load be supplied with the energy released from it into the environment during the fragmentation. Therefore, when the crystal is relieved from the load sufficiently slowly (so that the energy necessary for the intergrowth has time to transfer from the thermostat to the crystal), no fragmentation occurs. This is also confirmed by the fact that the fragments obtained in [13] had not cubic but exactly fragmented (dendritic) forms of the surface. The bimodal size distribution of fragments can be explained by the fact that, in this case, the three-dimensional nanocrystal exhibits a U-shaped dependence of the shape function on the shape parameter f [see relationship (5)] with a minimum at $f = 1$ (which corresponds to a cubic form). It is this U-shaped dependence of the function $F_3(f)$ that is responsible for the fact that, during baric fragmentation of the crystal, nanocrystals with different shapes of the surface (but with the same number of atoms) are formed with an equal probability: platelike nanocrystals at $f < 1$ and rodlike nanocrystals at $f > 1$. It is evident that the size (diameter) determined using a microscope for a platelike nanocrystal should be less than that for a rodlike nanocrystal (with the same number of atoms in the bulk and the same microstructure). This accounts for the bimodal size distribution of nanocrystals formed in the course of baric fragmentation.

From the aforesaid, it can be assumed that the fragmentation observed for a Cu_2O crystal in [4] under a hydrostatic pressure $P > 50$ kbar is also caused by the effect of baric fragmentation of the crystal. It seems likely that, upon baric fragmentation, nanocrystals undergo dendritization and exhibit a bimodal size distribution. Moreover, the baric fragmentation can be attended by a manifestation of exothermal effects, i.e., a release of energy.

ACKNOWLEDGMENTS

The author would like to thank K.N. Magomedov and Z.M. Surkhaeva for their assistance in performing this study.

This work was supported by the Russian Foundation for Basic Research, project no. 02-03-33301.

REFERENCES

1. B. M. Smirnov, Usp. Fiz. Nauk **162**, 119 (1992) [Sov. Phys. Usp. **35**, 37 (1992)].
2. B. M. Smirnov, Usp. Fiz. Nauk **171**, 1291 (2001) [Phys. Usp. **44**, 1229 (2001)].
3. Yu. I. Petrov, *Physics of Small Particles* (Nauka, Moscow, 1982).

4. L. Skala, Phys. Status Solidi B **110**, 299 (1982).
5. G. Matanson, F. Amar, and R. S. Berry, J. Chem. Phys. **78**, 399 (1983).
6. J. Xie, J. A. Northby, D. L. Freeman, *et al.*, J. Chem. Phys. **91**, 612 (1989).
7. M. N. Magomedov, Zh. Fiz. Khim. **73**, 2211 (1999).
8. M. N. Magomedov, Zh. Fiz. Khim. **76**, 752 (2002).
9. P. W. Bridgman, Rev. Mod. Phys. **18**, 1 (1946).
10. M. Ya. Yaroslavskiĭ, *Reological Explosion* (Nauka, Moscow, 1982).
11. N. S. Enikopolyan, A. A. Khzardzhyan, S. M. Khzardzhan, *et al.*, Dokl. Akad. Nauk SSSR **296**, 887 (1987).
12. V. P. Khan and E. G. Fateev, Pis'ma Zh. Tekh. Fiz. **16** (4), 81 (1990) [Sov. Tech. Phys. Lett. **16**, 317 (1990)].
13. V. T. Fedorov and Kh. B. Khokonov, Dokl. Akad. Nauk SSSR **300**, 1126 (1988) [Sov. Phys. Dokl. **33**, 463 (1988)].
14. E. G. Ponyatovskiĭ, G. E. Abrosimova, A. S. Aronin, *et al.*, Fiz. Tverd. Tela (St. Petersburg) **44** (5), 820 (2002) [Phys. Solid State **44**, 852 (2002)].

Translated by O. Moskalev

Physics of the Solid State, Vol. 45, No. 5, 2003, pp. 957–960. Translated from Fizika Tverdogo Tela, Vol. 45, No. 5, 2003, pp. 911–914.

LOW-DIMENSIONAL SYSTEMS AND SURFACE PHYSICS

Thermal Conductivity of the Opal–Epoxy Resin Nanocomposite

V. N. Bogomolov*, N. F. Kartenko*, D. A. Kurdyukov*, L. S. Parfen'eva*, I. A. Smirnov*, N. V. Sharenkova*, H. Misiorek, and A. Jezowski****

**Ioffe Physicotechnical Institute, Russian Academy of Sciences, Politekhnicheskaya ul. 26, St. Petersburg, 194021 Russia*

e-mail: Igor.Smirnov@pop.ioffe.rssi.ru

***Institute of Low-Temperature and Structural Research, Polish Academy of Sciences, Wroclaw, 50-950 Poland*

Received September 23, 2002

Abstract—The effective thermal conductivity κ_{eff} of seven opal + epoxy resin nanocomposite samples with 100% filling of first-order pores by epoxy resin was measured in the 100- to 300-K temperature interval. In the nanocomposite studied, the thermal conductivity of the matrix (amorphous SiO_2 spheres) is larger than that of the filler material (epoxy resin). $\kappa_{eff}(T)$ of the opal + epoxy resin nanocomposite at intermediate temperatures (100–300 K) is shown to behave similar to pure opal. An explanation of the observed effect is proposed. © *2003 MAIK "Nauka/Interperiodica".*

1. INTRODUCTION

This study deals with the thermal conductivity of the opal + epoxy resin nanocomposite and is a continuation of the research started by the present authors in 1995 and devoted to the thermal conductivity of single-crystal synthetic opals and related nanocomposites.[1]

Opals possess a highly unusual crystal structure [2, 3]. This structure consists of closely packed amorphous SiO_2 spheres, with diameters ranging mostly in the interval ~2000–2500 Å (first-order spheres), which are made up of smaller amorphous spheres ~300–400 Å in diameter (second-order spheres) which are, in turn, formed of amorphous particles with diameters of the order of 100 Å (third-order spheres).

An array of closely packed spheres has octahedral and tetrahedral pores which are interconnected by horn-shaped channels. Depending on the amorphous-sphere order, the pores are also divided into first, second, and third types. The octahedral and tetrahedral pores are commonly visualized as spheres interconnected by cylindrical (rather than horn-shaped) channels [2]. In this model, the diameters of the octahedral and tetrahedral pores and first-order channels in opals (for amorphous SiO_2 spheres ~2000 Å in diameter) are 800, 400, and 300 Å, respectively.

The total theoretical opal porosity is 59%. Actually, the porosity of the opal single crystals grown by us was ~46–50% (because of partial sintering of the second- and third-order amorphous spheres) [4]. However, the volume of the first-order spheres remained ~26%.

The amorphous SiO_2 spheres and first-order pores make up regular fcc lattices with a parameter a ~ 3000–4000 Å.

The first-order opal pores can be filled, following various techniques (chemical, melt injection, or impregnation of the sample by a filler material), with metals, semiconductors, or insulators. The nanocomposites thus produced are of three types.

In the first case, all opal pores are filled to 100% to form a regular cubic lattice of the filler material with the parameter a ~ 3000–4000 Å; as a result, this type of nanocomposite can be considered a system with two different sublattices, one of the matrix and one of the filler.

In the second case, the filling of the opal pores, while being partial rather than 100%, is still large, with the formation of regularly filled regions separated by the filler-free opal matrix.

In the third case (of a low filler concentration in the opal) "bubbles" of the filler material can form on the surface of the amorphous spheres.

Thus, correct interpretation of experimental data obtained on opal-based nanocomposites requires knowledge of the true pattern of opal pore filling.

In the case of 100% opal pore filling, three versions can be anticipated for the nanocomposite.

Version one: the thermal conductivity of the matrix κ_{mat} (amorphous SiO_2 sphere opal lattice) is much lower than that of the filler κ_{fill} ($\kappa_{mat} \ll \kappa_{fill}$);

Version two: the thermal conductivity of the matrix is much higher than that of the filler ($\kappa_{mat} \gg \kappa_{fill}$);

Version three: the thermal conductivity of the matrix is comparable to that of the filler ($\kappa_{mat} \simeq \kappa_{fill}$).

Our previous studies [5] revealed that, within a broad temperature range (5–300 K), the thermal conductivity of single crystals of synthetic opals is determined primarily by the quality of the contacts between

[1] The relevant publications are listed in [1].

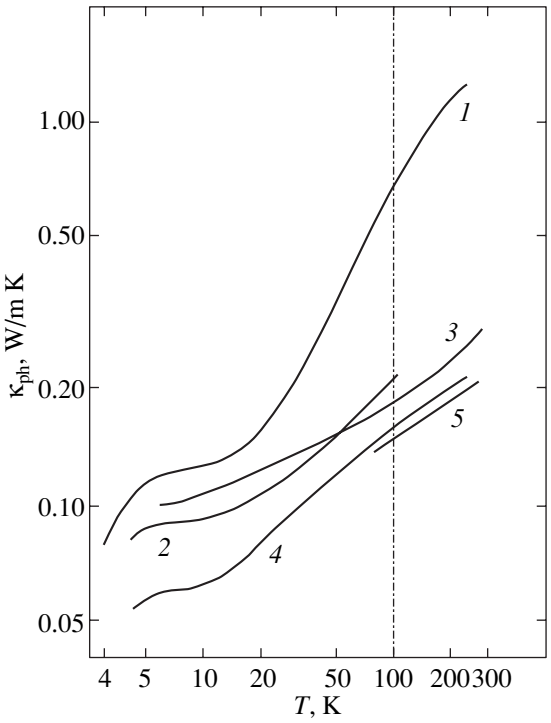

Fig. 1. Thermal conductivity of (*1*) fused quartz and (*2–5*) epoxy resin. (*1*) Data from [6], (*2*, *5*) our data, (*4*) data from [7], and (*3*) data from [8].

the amorphous SiO_2 spheres; i.e., it is dominated by the contact heat resistance between these spheres.

Most of our studies of the thermal conductivity of opal-based nanocomposites were conducted on samples with 100% filling of first-order opal pores, in which κ_{mat} was substantially lower than that of the filler κ_{fill} (see [1] and references therein to all our previous publications). In this case, the lattice component of thermal conductivity of the filler loaded in the opal, κ_{ph}^0, behaved differently at low and high temperatures [1]. In the low-temperature domain ($T \lesssim 20$–30 K), this component was dominated by boundary phonon scattering in the bottlenecks of the horn-shaped channels connecting the filler-loaded octahedral (and tetrahedral) opal pores. At high temperatures ($T \gtrsim 20$–30 K), κ_{ph}^0 decreased strongly in comparison with the thermal conductivity lattice of the bulk filler material; this phenomenon can be accounted for by phonon scattering from specific defects forming in the filler material loaded in the opal pores (vacancies and chain rupture in the filler lattice in the opal, surface defects, defects associated with stresses in the filler material, etc. [1]).

The goal of this study was to measure the thermal conductivity of the nanocomposite whose first-order pores would be loaded likewise to 100% by a filler with κ_{fill} substantially lower than κ_{mat}, the condition corresponding to version two. We chose epoxy resin as a filler satisfying this condition.

Figure 1 presents data on the thermal conductivity of fused quartz [6] and epoxy resin, obtained in part by us and from data taken from [7, 8]. We readily see that the values of the thermal conductivity of epoxy resin κ_{epox} quoted by various authors differ only slightly. The magnitude of κ_{epox} depends primarily on the amount of the curing agent introduced into the epoxy resin. Within the temperature region of most interest to us, 100–300 K, κ_{epox} is smaller by approximately five times than the thermal conductivity of fused quartz, which is in full accord with the condition $\kappa_{mat} \gg \kappa_{fill}$.[2]

2. PREPARATION OF SAMPLES AND EXPERIMENTAL TECHNIQUE

The opal samples used as matrices in the preparation of the opal + epoxy resin nanocomposites were cut from (111)-oriented single-crystal opal plates grown by us. The crystallographic orientation of all samples was arbitrary. While the opal single crystals were grown following the same technique, some samples cut from the plates could differ somewhat in structural perfection because of slight inhomogeneities which could arise in the opal plates in the course of their growth and thermal annealing. The porosities of these samples differed insignificantly.

The opal + epoxy resin nanocomposites were prepared by the technique described in [9]. A sample of single-crystal opal was placed in an ampoule evacuated to 10^{-2} mm Hg. In this stage, the water adsorbed in the opal pores was removed. Next, epoxy resin of a liquid enough consistency was poured into the ampoule and the enveloped the sample completely. The sample was taken out of the still liquid epoxy resin, and, after it had hardened, a layer of resin was removed from the sample down to the opal body. The percentage of opal filling by the epoxy resin was estimated from sample density measurements performed before and after the loading. It was found that our nanocomposite samples were loaded by the epoxy resin to 90–100%. Altogether, seven nanocomposite samples were prepared.

The samples intended for κ_{epox} measurements were cut from the hardened mass of the epoxy resin used to load the opal pores.

Samples of the epoxy resin and of the opal + epoxy resin nanocomposite were subjected to x-ray diffraction characterization made on a DRON-2 setup with CuK_α radiation (Ni filter). Figure 2 shows the diffraction pattern of an opal + epoxy resin nanocomposite sample. The diffractogram of the epoxy resin in opal is seen to have a weak diffusive maximum, which is apparently a superposition of two reflections, namely, one from the pure opal and one from the epoxy resin itself.

[2] The thermal conductivity κ_{eff} of one sample of the opal + epoxy resin nanocomposite was measured by us in [9]. We did not, however, carry out a detailed analysis of the results on κ_{eff} obtained in that experiment.

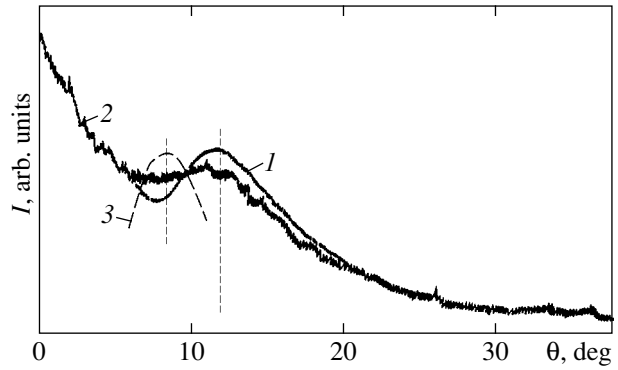

Fig. 2. Diffractograms of (*1*) opal and (*2*) an opal + epoxy resin nanocomposite. Dashed curve *3* specifies the position of the diffraction maximum of epoxy resin in the glassy state.

The thermal conductivity of epoxy resin was measured in the range 4.2–300 K, and κ_{eff} of the opal + epoxy resin nanocomposites, in the region 100–300 K, on a setup similar to the one employed in [10].

3. EXPERIMENTAL RESULTS AND DISCUSSION

Opals, epoxy resin, and the opal + epoxy resin nanocomposite are insulators; therefore, their thermal conductivity is that of the crystal lattice, $\kappa_{eff}(T) = \kappa_{ph}(T)$.

Figure 3a displays the results of thermal-conductivity measurements performed on seven opal + epoxy resin nanocomposite samples, with the opal pore filling varying from 90 to 100%. Also shown for comparison are the literature data on the thermal conductivity of fused quartz taken from [6].

Figure 3b presents the data on $\kappa_{ph}(T)$ of synthetic opal single crystals taken from one of our earlier publications [5]. As seen from Fig. 3, the $\kappa_{eff}(T)$ relation obtained for the opal + epoxy resin nanocomposite samples behaves similarly to $\kappa_{ph}(T)$ of the pure-opal samples.

Let us try to find an explanation for this observation. The opal-based nanocomposite with 100% filling of its pores can be considered a complex system consisting of two nested regular lattices with giant parameters and "atomic" masses (the opal and the filler lattices). Individual properties of these unusual lattices can become manifest in the behavior of $\kappa_{ph}(T)$ only at ultralow temperatures. At the fairly high temperatures ($T > 100$ K) at which the measurements of κ_{ph} of the nanocomposite were conducted, one can assume, as a first approximation, that both lattices behave independently and do not influence each other in any way (at these temperatures, for instance, the Kapitsa thermal resistance does not appear). In this case, the heat flux injected in measurements of the thermal conductivity of opal-based nano-

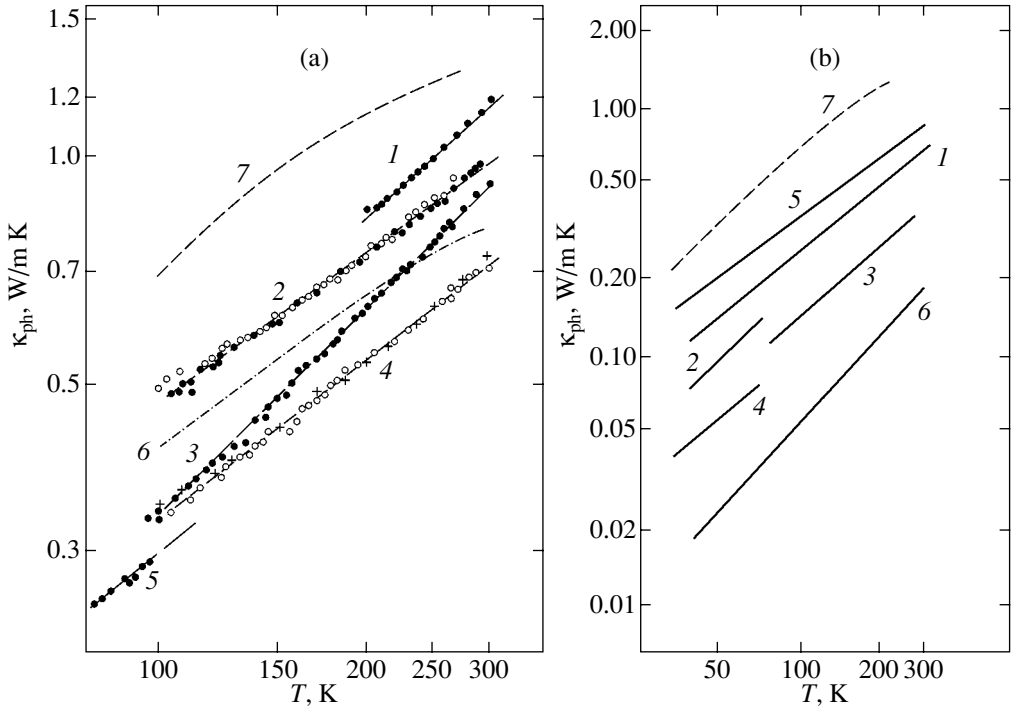

Fig. 3. (a) Temperature dependences of (*1–5*) opal + epoxy resin nanocomposites with different filling *x* of the opal pores by epoxy resin and (*7*) amorphous quartz [6]; *x* (%): (*1*, *3*) 90, (*2*) 95, and (*4*, *5*) 100. Measurements *2* and *4* relate to two different samples each; (*6*) calculation of $\kappa_{eff} = \kappa_{ph}$ made using relations for standard composites from [11] for the opal + 100% epoxy resin nanocomposite. (b) Temperature dependences of κ_{ph} for (*1–6*) single crystals of synthetic opals and (*7*) amorphous quartz [6]. (*1–4*) Data from [5] and (*5*, *6*) our new data.

composites will propagate in two parallel channels, more specifically, over the amorphous SiO_2 spheres making up the opal and over the filler lattice along the filler-material chains: tetrahedral (octahedral) filled pore–filled horn-shaped channel–tetrahedral (octahedral) filled pore–filled horn-shaped channel and, so on (see [1] and the opal structure diagram in [2]). For $\kappa_{fill} \gg \kappa_{mat}$, the heat flow will propagate primarily over the filler-material chains, and for $\kappa_{fill} \ll \kappa_{mat}$, over the amorphous SiO_2 opal spheres.

The above reasoning provides an explanation for the specific behavior of $\kappa_{ph}(T)$ of the opal + epoxy resin nanocomposites observed by us.

As already mentioned, $\kappa_{mat} \gg \kappa_{fill}$ in these nanocomposites in the 100- to 300-K region; therefore, the injected heat flow propagates here predominantly over the amorphous SiO_2 spheres. The heat flowing over the epoxy resin chains is insignificant, and the corresponding contribution to $\kappa_{eff}(T) = \kappa_{ph}(T)$ is small.

We shall assume, as a first approximation, that the heat in the opal + epoxy resin nanocomposite flows only over the SiO_2 spheres. In this case, the nanocomposite will follow the pattern typical of single-crystal opal samples [5, Fig. 2] and it becomes clear why the $\kappa_{fill}(T) = \kappa_{ph}(T)$ relation for the nanocomposites (Fig. 3a) behaves exactly as $\kappa_{ph}(T)$ for pure opal single crystals (Fig. 3b). The spread in the data (straight lines *1–5* in Fig. 3a) for $\kappa_{ph}(T)$ of the nanocomposites (as was the case with $\kappa_{ph}(T)$ of pure opal [5], Fig. 3b) is associated primarily with the nature of the opal samples used as matrices for the preparation of the nanocomposites. Opal samples, according to [5], may have different values of κ_{ph} because of small differences in the radius of contact r between amorphous SiO_2 spheres in the case of small r (in the limit as $r \longrightarrow 0$, the thermal conductivity should tend to zero).

Curve *6* in Fig. 3a plots calculated data for $\kappa_{eff}(T) = \kappa_{ph}(T)$ of the opal + 100% epoxy resin nanocomposite. The calculation was made using relations from [11] which are commonly employed to derive $\kappa_{eff}(T)$ for standard composites.[3] It turned out that using such a calculation for the nanocomposites studied by us is senseless, because their $\kappa_{eff}(T) = \kappa_{ph}(T)$, as pointed out more than once above, is dominated by the contact resistances forming between the amorphous SiO_2 opal spheres.

4. CONCLUSIONS

Thus, the main conclusion reached in this study can be formulated as follows. For opal-based nanocomposites whose first-order opal pores are filled to 100% and $\kappa_{mat}(T) \gg \kappa_{fill}(T)$ at medium temperatures, the thermal conductivity $\kappa_{ph}(T)$ behaves similarly to $\kappa_{ph}(T)$ for samples of pure opal, because under the above conditions the heat flow in the nanocomposite propagates predominantly over the amorphous SiO_2 spheres.

Studies of the thermal conductivity of opals and related nanocomposites reveal a specific feature: as new experimental material is amassed, we are forced to reconsider, and sometimes even abandon, our earlier conclusions and patterns, which then have to be replaced, in light of the refined concepts, by new interpretations; this approach appears to be natural for investigating nonstandard, complex objects. We hope, however, that we will gradually come closer to a deeper and more adequate understanding of the behavior of thermal conductivity of this unique material.

[3] The technique used to determine $\kappa_{mat}(T)$ of opals with due account of their porosity and to calculate $\kappa_{eff}(T)$ of nanocomposites from the relations given in [11] is described in considerable detail in [1].

ACKNOWLEDGMENTS

This study was supported by the Russian Foundation for Basic Research (project no. 00-02-16883) and carried out within bilateral agreements between the Russian and Polish Academies of Sciences.

REFERENCES

1. V. N. Bogomolov, N. F. Kartenko, D. A. Kurdyukov, *et al.*, Fiz. Tverd. Tela (St. Petersburg) **45** (3), 535 (2003) [Phys. Solid State **45**, 566 (2003)].
2. V. N. Bogomolov and T. M. Pavlova, Fiz. Tekh. Poluprovodn. (St. Petersburg) **29** (5/6), 826 (1995) [Semiconductors **29**, 428 (1995)].
3. V. G. Balakirev, V. N. Bogomolov, V. V. Zhuravlev, *et al.*, Kristallografiya **38** (3), 111 (1993) [Crystallogr. Rep. **38**, 348 (1993)].
4. V. V. Ratnikov, Fiz. Tverd. Tela (St. Petersburg) **39** (5), 956 (1997) [Phys. Solid State **39**, 856 (1997)].
5. V. N. Bogomolov, L. S. Parfen'eva, I. A. Smirnov, *et al.*, Fiz. Tverd. Tela (St. Petersburg) **44** (1), 170 (2002) [Phys. Solid State **44**, 176 (2002)].
6. *Handbook on the Thermal Conductivity of Solids*, Ed. by A. S. Okhotin (Énergoizdat, Moscow, 1984).
7. K. W. Garret and H. M. Rosenberg, J. Phys. D: Appl. Phys. **7**, 1247 (1974).
8. W. Scheibner and M. Jäckel, Phys. Status Solidi A **87**, 543 (1985).
9. V. N. Bogomolov, L. S. Parfen'eva, L. M. Sorokin, *et al.*, Fiz. Tverd. Tela (St. Petersburg) **44** (6), 1017 (2002) [Phys. Solid State **44**, 1061 (2002)].
10. A. Jezowski, J. Mucha, and G. Pompe, J. Phys. D: Appl. Phys. **20**, 1500 (1987).
11. E. Ya. Litovskiĭ, Izv. Akad. Nauk SSSR, Neorg. Mater. **16** (3), 559 (1980).

Translated by G. Skrebtsov

Physics of the Solid State, Vol. 45, No. 5, 2003, pp. 961–968. Translated from Fizika Tverdogo Tela, Vol. 45, No. 5, 2003, pp. 915–922.

LOW-DIMENSIONAL SYSTEMS AND SURFACE PHYSICS

Luminescence of Cr^{3+} Impurity Ions in $Li_2Ge_7O_{15}$ Nanocrystals and Clusters Embedded in Lithium Germanate Glasses

T. N. Vasilevskaya, A. A. Kaplyanskiĭ, A. B. Kulinkin, and S. P. Feofilov

Ioffe Physicotechnical Institute, Russian Academy of Sciences, Politekhnicheskaya ul. 26, St. Petersburg, 194021 Russia

Received September 26, 2002

Abstract—The properties of Cr^{3+}-doped $Li_2Ge_7O_{15}$ (LGO) lithium germanate nanocrystals produced in lithium germanate glasses under isothermal heating were studied. The samples were characterized by x-ray diffraction and small-angle scattering, as well as by transmission electron microscopy. The luminescence spectra of the impurity chromium measured in lithium germanate glasses containing LGO crystals revealed transitions in Cr^{3+} ions residing in the glass phase and in LGO crystallites starting from extremely small clusters. This provided the possibility of following the process of crystallization of the lithium germanate glass from Cr^{3+} luminescence spectra. The effects observed in the Cr^{3+} luminescence spectrum revealed a ferroelectric phase transition in LGO nanocrystals embedded in the glass.© *2003 MAIK "Nauka/Interperiodica".*

1. INTRODUCTION

The general trend currently being observed in solid-state physics, with predominant interest focused on the properties of nanoscale objects, is shown in the publication of numerous papers dealing with the investigation of nanocrystalline dielectrics. Considered from the standpoint of optical properties, dielectric nanocrystals containing impurity ions of rare earth and transition metals arouse particular interest (see, e.g., review [1] and references therein). The presence of a narrow-line structure in the well-known spectra of such ions also permits their use as highly sensitive spectroscopic probes in studying a number of phenomena connected with spatial confinement in nanocrystals. Among these phenomena are the modification of the phonon spectrum in nanocrystals [2, 3], the interaction of electronic excitations in nanocrystals with the environment [4, 5], and the enhanced role of the surface [6]. The optical properties of nanocrystalline dielectrics doped by 4*f* and 3*d* ions also have promising application potential.

Precipitation of crystals in glasses of specific chemical composition under heat treatment [7] occupies a prominent place among the known methods for preparing nanocrystalline dielectrics. This communication reports on the first study of the properties of Cr^{3+}-doped nanocrystals of $Li_2Ge_7O_{15}$ lithium germanate (LGO), which form under isothermal heating of lithium germanate glasses. The choice of the object for study was motivated, first, by the lithium germanate glasses being known to crystallize with the formation of LGO crystals [8] and, second, by the fact that the spectroscopic characteristics of bulk LGO : Cr^{3+} single crystals are well known [9–13]. It was shown in [9, 10] that Cr^{3+} ions substitute in the LGO lattice for Ge ions in the GeO_6 octahedral coordination and have optical spectra typical of the case of a strong crystal field. The interest in the properties of the LGO : Cr^{3+} crystals, as in the spectroscopic characteristics of LGO doped by other elements, was then initiated by the fact that at temperatures below T_c = 10°C LGO crystals are ferroelectrics [14, 15], thus permitting, in principle, the development of solid-state lasers with frequency self-doubling on the basis of doped off-centrosymmetric crystals.

This paper reports on the synthesis of lithium germanate oxide glasses with the addition of chromium oxide and on the path of subsequent isothermal heating of glass samples containing LGO : Cr^{3+} crystals. The samples were independently characterized by x-ray techniques and transmission electron microscopy, thus enabling identification of the LGO crystalline phase in the glass and estimation of the crystal dimensions. It was shown that the luminescence spectra of the impurity chromium in lithium germanate glass with LGO crystals can be identified with the known radiative transitions in the Cr^{3+} ions residing in the octahedral environment of six oxygen ions. We succeeded in separating the contribution to the luminescence spectrum of the Cr^{3+} ions in the glass phase from that of the Cr^{3+} ions in LGO crystals, starting from extremely small clusters. This permitted us to follow the crystallization of lithium germanate glass as a function of its composition, temperature, and annealing time according to the luminescence spectra. From the effects in the luminescence spectrum, a ferroelectric phase transition was also detected in LGO crystals embedded in the glass.

2. SAMPLE PREPARATION AND CHARACTERIZATION

Melts of chemical composition Li_2O–$11.5GeO_2$ and Li_2O–$7GeO_2$ (the latter corresponds to the $Li_2Ge_7O_{15}$ stoichiometry) were prepared by melting a mixture of

1063-7834/03/4505-0961$24.00

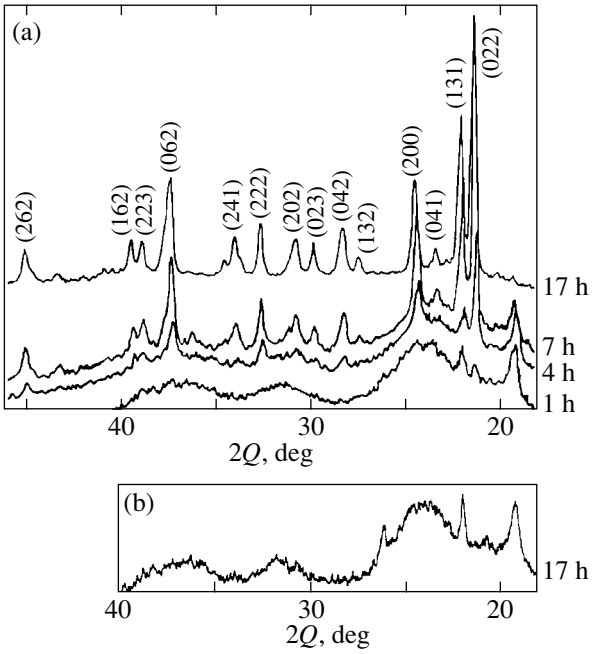

Fig. 1. X-ray scattering spectra (XPA) of Li_2O–$11.5GeO_2$ samples annealed isothermally for different times at T_{ann} = (a) 535 and (b) 523°C.

KhCh-grade Li_2CO_3 and GeO_2 reagents in platinum crucibles at 1000–1350°C for 1 h. Glasses of this composition were obtained by fast quenching of a melt drop from 1350°C between cold metal surfaces at a rate of 10^6 C/s. The glass samples thus produced were obtained as thin transparent plates 0.1–0.3 mm thick. Introducing 0.05 or 0.5% (in excess of 100%) chromium oxide into the melt conferred green color to the glasses. To form $Li_2Ge_7O_{15}$ (Li_2O–$7GeO_2$ = LGO) nanocrystals in the original homogeneous glass matrix, the glass plates were isothermally annealed in a muffle furnace for various times at temperatures ranging from 480 to 540°C. The heterogeneous samples thus produced were characterized by x-ray phase analysis (XPA), small-angle x-ray scattering (SAS), and transmission electron microscopy (TEM). These methods were employed to check the homogeneity of the original, unannealed glasses as well.

These methods permitted reliable identification of the crystalline LGO phase precipitating under isothermal glass annealing (by XPA), estimation of the average size of LGO particles and their size distribution and shape, and study of the properties of the glass with embedded LGO nanocrystals as a function of the anneal temperature and time of the initial homogeneous glass. We note immediately the extremely strong dependence of the phase segregation kinetics in lithium germanate glasses on the annealing temperature, which becomes manifest already within the comparatively narrow temperature interval of 480–540°C used by us. As a result, we succeeded in preparing extremely small LGO particles (clusters) by annealing the samples at slightly lower temperatures; under these conditions, the LGO crystallites formed at a strongly slowed rate.

XPA was performed on a Rigaku diffractometer with CuK_α radiation (λ = 1.54 Å) at scattering angles 2θ ranging from 10° to 90°. Figure 1a presents a series of x-ray spectra of Li_2O–$11.5GeO_2$ glass samples prepared with different anneal times t at a comparatively high temperature T_{ann} = 535°C. Figure 1 reflects the kinetics of formation of the crystalline LGO phase in the glass in the course of annealing. For t = 1 h, one can see single, weakly pronounced features corresponding to the strongest LGO lattice reflections, which are superposed on diffuse diffraction haloes typical of the glassy state. The number and intensity of the LGO crystal reflections increase with increasing glass anneal time, while their relative contribution to the spectrum associated with the glass phase decreases. For anneal times t = 17 h and longer, the observed spectrum differs very slightly from the well-known spectrum of powder samples of monolithic LGO prepared using standard technology. The halfwidth of the diffraction reflections is used to derive the average LGO crystallite size (45 nm) at the last anneal stage, which corresponds to the maximum possible precipitation of the LGO crystalline phase in the Li_2O–$11.5GeO_2$ glass.

The small-angle x-ray scattering method (SAS) was employed with CuK_α radiation (λ = 1.54 Å) on a setup with slit collimation following Kratky; this setup was equipped with a high-temperature chamber, which allowed investigation of the formation of inhomogeneities in samples directly at the anneal temperature. We measured the scattered intensity of the beam passing through a thin sample within an angular interval 0.1°–10°. In this angular interval, the modulus of the scattering wave vector $s = 4\pi\sin\theta/\lambda$ varies in the region $0.008 < s < 0.59$ Å^{-1}, thus making it possible to detect inhomogeneities with linear dimensions $L \sim 2\pi/s$ within the range 1–100 nm. The SAS method was found most efficient for studies of LGO crystallites forming in early stages of glass crystallization. Such studies were performed on glasses of the Li_2O–$11.5GeO_2$ composition at a relatively low anneal temperature of 523°C, which provided crystallization kinetics slow enough to allow comprehensive investigation of the structural changes occurring in glasses in the course of annealing.

Figure 2 illustrates small-angle scattering intensity measurements made on a sample of Li_2O–$11.5GeO_2$–0.05% Cr_2O_3 glass (density 3.87 g/cm^3), annealed at T_{ann} = 523°C for various times. These results are presented in the form of a dependence of the quantity $s^2I(s)$ on the modulus of the scattering wave vector s (a so-called Kratky graph). These graphs can be used to extract important parameters characterizing the inhomogeneities in a system that account for small-angle scattering. The quantity s_{max} representing the position of the maximum in $s^2I(s)$ is a characteristic of the aver-

age size L of the scattering particles ($L \sim s_{max}^{-1}$). The area Q under the curve is proportional to the rms fluctuation of the phase of density ρ_1 relative to the solvent of density ρ_2 present in relative volumes w_1 and w_2, taken over the total scattering volume V:

$$Q = \int s^2 I(s) ds = 2\pi^2 w_1 w_2 (\rho_1 - \rho_2)^2 V. \qquad (1)$$

The dependences of the quantities L and Q on the time of anneal at T_{ann} = 523°C of the Li_2O–11.5GeO_2–0.05% Cr_2O_3 glass are represented graphically in Fig. 3.

As seen from the inset to Fig. 2, the initial Li_2O–11.5GeO_2 glass contains only small inhomogeneities having an average size L = 2 nm, which can partially account for the local deviations of the glass composition from the Li_2O–11.5GeO_2 formula. Heating the glass at T_{ann} = 523°C for 1 h results in a considerable increase in the size of the observed inhomogeneities (to ~10 nm), whereas the integrated scattering intensity Q changes only slightly (Fig. 3a). In this initial stage (up to ~1.5 h), fairly large regions of higher density, 4.054 g/cm^3, and a composition Li_2O–7GeO_2 corresponding to the LGO crystal stoichiometry form in the glass. In the next stage (1.5- to 7-h long), LGO crystallization nuclei form in these Li_2O-enriched regions, which is accompanied by a decrease in the average size of the scatterers (Fig. 3b) and by an increase in their density (to 4.232 g/cm^3). Figure 2 clearly reveals an increase in this anneal stage of the $s^2I(s)$ function in the domain of intermediate and large s (from 0.05 to 0.25 Å^{-1}) corresponding to small particles. The particle size distribution is fairly broad, 2–10 nm (see Fig. 2). The average particle size of ~4 nm and the integrated scattering intensity Q reached in a 6- to 7-h anneal at T_{ann} = 523°C practically do not change thereafter with increasing the anneal time to over 7 h (Fig. 3).

It should be pointed out that prolonged heating at low temperature, T_{ann} = 523°C, gives rise only to the initial stage of crystallization involving the formation of LGO nuclei a few nm in size. The Li_2O–11.5GeO_2 glass annealed for 17 h at T_{ann} = 523°C exhibits an XPA spectrum (Fig. 1b) close to that of the sample subjected to 1-h heating at a higher temperature, T_{ann} = 535°C, at which large LGO particles (45 nm) crystallized only after many hours of annealing (Fig. 1a).

Large LGO particles forming in late crystallization stages were also observed using electron microscopy. The study was performed with an ÉM-100 microscope on Pt-carbon replicas through extraction from as-cleaved surfaces. The unannealed samples are single phase; indeed, their TEM micrographs are structureless. Study of the samples heated at T_{ann} = 535°C allows us to follow the growth of dendritic crystalline inclusions. After a 1-h anneal, phase segregation with small inclusions of rounded and needle-shaped crystalline formations is observed to occur. A similar micrograph was obtained on a sample studied using SAS and annealed at T_{ann} = 523°C for 17 h and proved to be in good agreement with the XPA data. After a 2- to 4-h anneal, the phases merge to produce aggregates of dendritic shape measuring up to 220 nm. In 7–21 h of heating, the aggregates grow still larger in size to form large blocks with cracks.

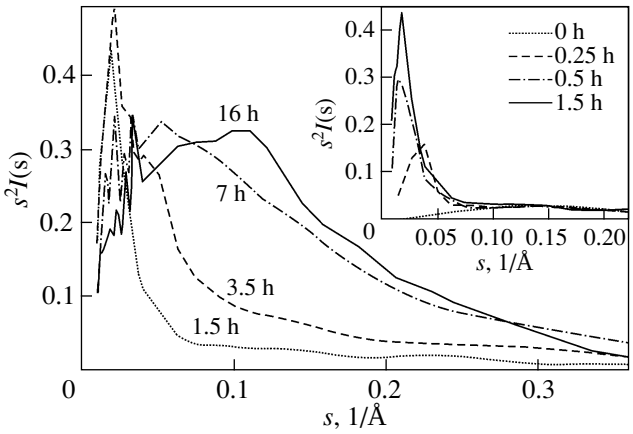

Fig. 2. Angular dependences of small-angle scattering (SAS) intensity $I(s)$ from Li_2O–11.5GeO_2–0.05% Cr_2O_3 glass samples annealed for different times at T_{ann} = 523°C.

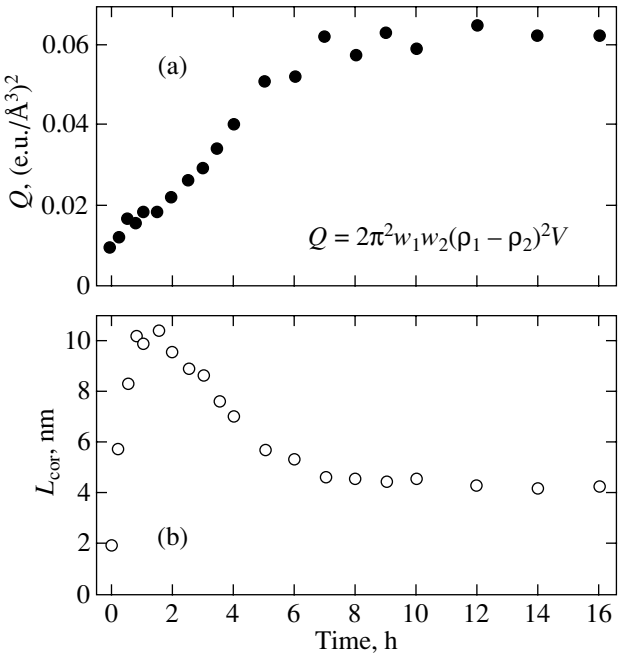

Fig. 3. (a) Dependence of integrated small-angle x-ray scattering (SAS) intensity on annealing time, and (b) dependence of average size (correlation length) of LGO crystallites on annealing time. Li_2O–11.5GeO_2: 0.05% Cr_2O_3 samples; T_{ann} = 523°C.

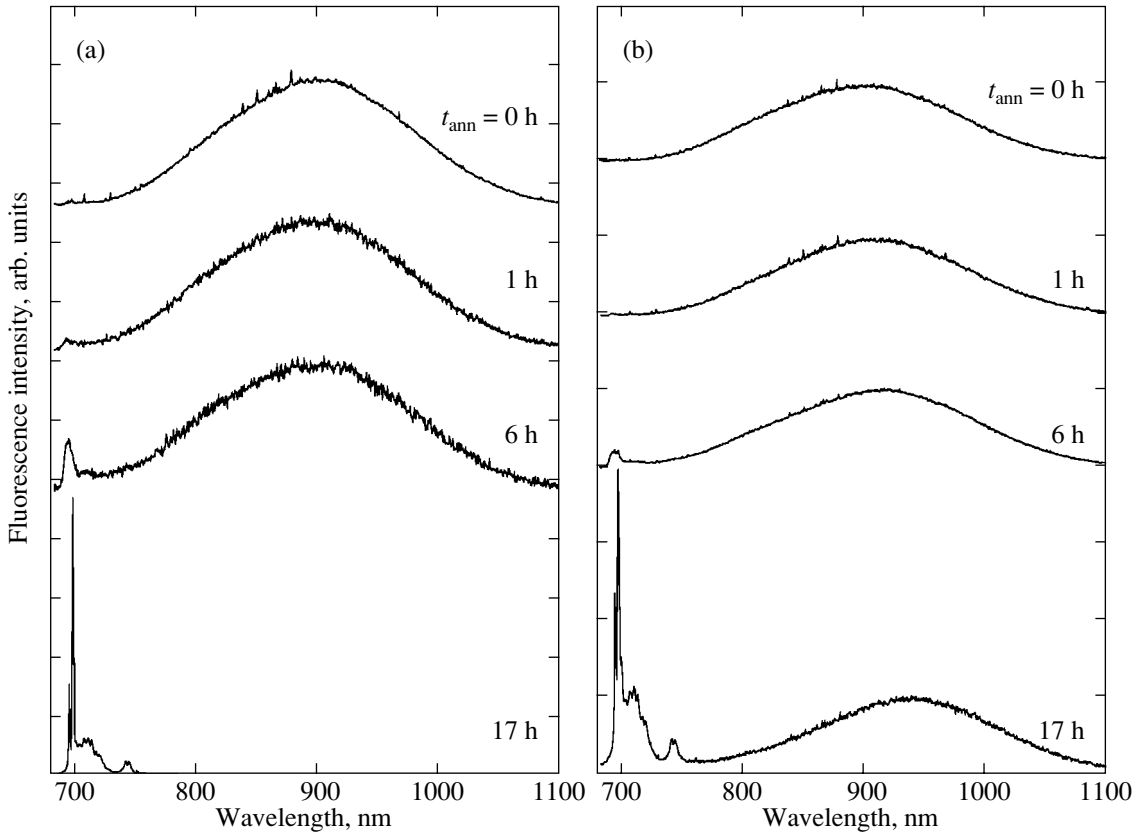

Fig. 4. 77-K luminescence spectra of Cr^{3+} in (a) Li_2O–$7GeO_2$ and (b) Li_2O–$11.5GeO_2$ glasses unannealed (t_{ann} = 0) and annealed at T_{ann} = 535°C.

3. LUMINESCENCE SPECTRA OF Cr^{3+} IN LITHIUM–GERMANATE GLASSES WITH EMBEDDED $Li_2Ge_7O_{15}$ CRYSTALLITES: RESULTS AND DISCUSSION

We studied luminescence of the samples at T = 77 K excited by Ar laser (514.5, 488.0 nm) and He–Ne laser (632.8 nm) lines. The luminescence spectrum was measured with a DFS-24 spectrometer and an MDR-23 monochromator.

Figure 4 presents a luminescence spectrum of chromium-doped homogeneous lithium germanate glasses prepared by rapid melt quenching and not subjected to isothermal annealing (t_{ann} = 0). The broad vibronic emission band produced by Cr^{3+} ions in glass exhibits a typical signature of the $^4T_2$–$^4A_2$ emission band of Cr^{3+} ions residing in a weak octahedral field. The lowest radiative excited level of Cr^{3+} in such a field corresponds to the $^4T_2$ (t^2e) state, and the radiative electronic transition connecting it with the $^4A_2$ (t^3) ground state and involving a change in the orbital state is coupled strongly with ligand vibrations. The assignment of the $^4T_2$–$^4A_2$ band to transitions in the Cr^{3+} ion is supported by the microsecond-scale kinetics of its decay (~100 μs), which is typical of such a transition. The possibility of the Cr^{3+} ions residing in an octahedral oxygen environment stems from the structure of the lithium germanate glasses, in which GeO_6 octahedra make up a sizeable fraction of the structure [8].

Figure 4 also shows Cr^{3+} luminescence spectra of glasses with Li_2O–$7GeO_2$ and Li_2O–$11.5GeO_2$ compositions subjected to annealing at 535°C (t_{ann} = 1, 6, 17 h). As the anneal time is increased, a 685- to 700-nm narrow emission band, similar in glasses of different compositions, appears in these luminescence spectra in addition to the broad $^4T_2$–$^4A_2$ band of Cr^{3+} ions in the glass phase. It is in this spectral region that the R emission lines of bulk LGO : Cr^{3+} crystals at T = 77 K are located and these lines belong to the ^2E–$^4A_2$ transitions in the Cr^{3+} ions substituting for Ge^{4+} in the octahedral GeO_6 complexes making up, side by side with the GeO_4 tetrahedra, the LGO crystal lattice. Observation of the narrow R luminescence lines connecting the $^2E(t^3)$ excited state with the $^4A_2(t^3)$ ground state corresponds to the case of a strong octahedral field in the oxygen environment, in which the ^2E level of Cr^{3+} is the lowest radiative excited state. The correctness of the assignment of the 685- to 700-nm luminescence to the ^2E–$^4A_2$

transitions is also confirmed by the observation of the slow millisecond-scale kinetics of their decay.

As the anneal time of the samples increases, their luminescence spectra exhibit a redistribution of the Cr^{3+} emission intensity in the region of the ^2E–$^4A_2$ and $^4T_2$–$^4A_2$ transitions. The luminescence spectrum of samples annealed for a long time (17 h) depends on the actual chemical composition of the glass. In the luminescence spectrum of Li_2O–$7GeO_2$ samples, only the short-wavelength emission in the region of the ^2E–$^4A_2$ transition is left (see Fig. 4a) whereas the luminescence spectra of the Li_2O–$11.5GeO_2$ glass exhibit, in addition to this emission, the broad $^4T_2$–$^4A_2$ band belonging to Cr^{3+} ions in the glass phase (Fig. 4b).

Now, we consider in greater detail the Cr^{3+} spectrum in the ^2E–$^4A_2$ transition region characteristic of luminescence spectra produced by chromium-doped glasses under heating. Figure 5 shows in expanded scale the *R*-line luminescence spectra of glass samples subjected to isothermal annealing for different times and at different temperatures. We readily see that a broad (~100 cm^{-1}) line is the first to appear in the *R*-line region of the spectra of samples annealed for short times. As the anneal time increases, characteristic narrow lines become superimposed on this broad line. This narrow-line spectrum becomes increasingly dominant with increasing anneal time, until practically nothing remains in the region of the ^2E–$^4A_2$ transitions in the spectra of the samples subjected to the longest annealing.

Figure 5 also shows the uminescence spectrum of bulk LGO : Cr^{3+} crystals at T = 77 K; at this temperature, the LGO lattice is in a ferroelectric phase of orthorhombic symmetry C_{2v}. The two pairs of lines, R_1–R_2 and R_1'–R_2', observed in the spectrum are due to radiative transitions to $^4A_2$ from the excited doublet state $\bar{E}$, $2\bar{A}$ (^2E) of the Cr^{3+} ions substituting for the Ge^{4+} lattice ions in the GeO_6 octahedra [9, 10]. The excess negative charge, $Cr^{3+}(Ge^{4+})$, in these centers is locally compensated by an interstitial Li^+ ion in the nearest octahedral void; due to this, the two Cr^{3+}–Li^+ centers responsible for the R_1–R_2 and R_1'–R_2' line pairs differ in the sign of projection of the Cr^{3+} dipole moment on the polar ferroelectric axis *c* of the ferroelectric phase [11]. As seen from Fig. 5, the narrow luminescence line spectrum in the ^2E–$^4A_2$ region produced at T = 77 K by glass annealed for a long period of time (17 h) is practically identical to the inhomogeneously broadened *R* spectrum of the bulk LGO : Cr^{3+} ferroelectric phase. This gives grounds to assign the observed luminescence line spectrum to LGO : Cr^{3+} crystallites forming in the glass during heating.

Thus, spectroscopic measurements, in full agreement with XPA studies, provide direct evidence of the formation of LGO crystals in glasses under heating. As

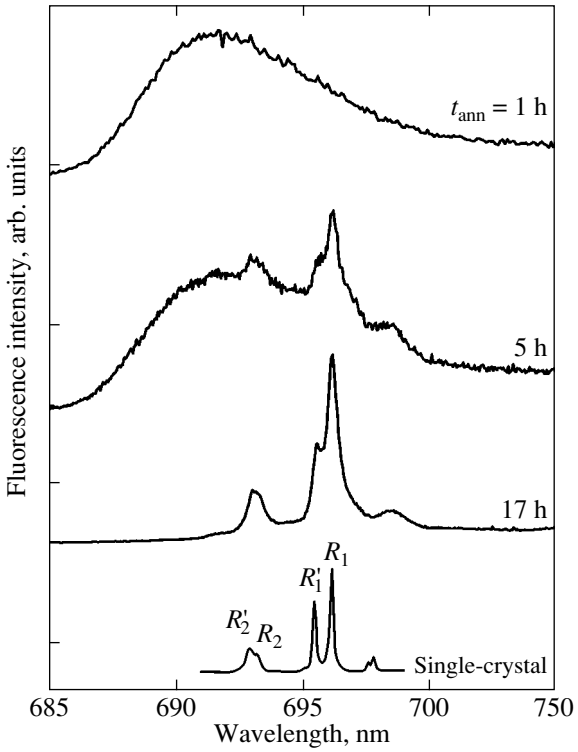

Fig. 5. 77-K Cr^{3+} luminescence spectra in the region of the ^2E–$^4A_2$ transitions (expanded scale) obtained on Li_2O–$11.5GeO_2$ glasses annealed at 535°C for t_{ann} = 1, 5, and 17 h. Bottom: luminescence spectrum of Cr^{3+} in the LGO single crystal.

the glass heating time increases, the intensity in the Cr^{3+} spectrum transfers from the broad-band $^4T_2$–$^4A_2$ luminescence of the Cr^{3+} ions in the glass phase to the narrow-line ^2E–$^4A_2$ luminescence of the Cr^{3+} ions in the LGO crystals. This transfer of intensity reflects the kinetics of LGO crystal precipitation. As seen from Fig. 4a, prolonged annealing, which, according to the XPA data, brings about saturation of the crystallization process, results in a complete disappearance, in the Cr^{3+} luminescence spectrum, of Li_2O–$7GeO_2$ glasses of the broad $^4T_2$–$^4A_2$ luminescence band produced by the Cr^{3+} ions in the glass phase, which implies complete crystallization of a glass whose chemical composition corresponds to the LGO crystal stoichiometry. At the same time, the luminescence spectrum of the Li_2O–$11.5GeO_2$ glasses obtained at the stage of crystallization saturation still contains, in addition to the LGO : Cr^{3+} luminescence (Fig. 4b), the $^4T_2$–$^4A_2$ emission band of Cr^{3+} in the glass phase. This obviously indicates the presence in the samples, in addition to LGO crystals, of remains of the glass (predominantly germanium) phase, which cannot transform into LGO crystals because of a lack of lithium in the starting material.

Now, we consider the possible origin of the broad (~100 cm^{-1}) line in the spectral region of the narrow-line *R* luminescence of the LGO : Cr^{3+} crystals (Fig. 5), which appears in the spectrum at the early stages of annealing as a precursor of the narrow *R* lines and practically disappears in the glass spectrum at the final stage of crystallization. Such inhomogeneously broadened lines produced in the $\bar{E}\,(^2E)$, $2\bar{A}\,(^2E)$–$^4A_2$ transitions are characteristic of the luminescence spectra of Cr^{3+} ions residing in an octahedral environment in structurally disordered oxide crystals, as well as in glasses. These matrices are characterized by an extremely large spread in the local crystal fields acting on the Cr^{3+} ions, and this accounts for both the large relative shifts of the centers of gravity of the R_1, R_2 doublets corresponding to the ^2E–$^4A_2$ transitions in single ions and the difference in the R_1, R_2 doublet width. As a result, the doublet character of the ^2E–$^4A_2$ transition in Cr^{3+} ions turns out to be completely masked by the inhomogeneously broadened profile of a single line and to reveal it, special techniques have to be applied (for instance, selective excitation in experiments with nonresonant fluorescence line narrowing [16–18]).

We believe that the inhomogeneously broadened *R* line in the luminescence spectrum of annealed glasses can be attributed to Cr^{3+} ions occupying octahedral positions in extremely small LGO crystals (clusters) containing only a few LGO lattice unit cells. In such aggregates, the oxygen octahedra enclosing the Cr^{3+} ions are in direct contact with the surrounding irregular glass phase, with the result that the Cr^{3+} environment may exert considerable perturbations of various magnitude. We note in this connection that, in the spectra of bulk LGO : Cr^{3+} crystals codoped by Mg, in addition to the main Cr^{3+}–Li^+ centers considered here, satellite Cr^{3+} centers differing in the type and position of the defect compensating for the $Cr^{3+}(Ge^{4+})$ charge in the nearest environment of the oxygen octahedra confining the Cr^{3+} ion have been identified [11]. Note also that the *R* lines of all observed Cr^{3+} centers lie within the energy interval 14 330–14 460 cm^{-1}, whose width ~100 cm^{-1} coincides with the inhomogeneous width of the above *R* line of Cr^{3+} in the lithium germanate glasses. It follows that, for such large (on the order of a few tens of cm^{-1}) transition frequency shifts to appear within the inhomogeneous profile of this *R* line, the lattice must undergo distortions already in the nearest environment of the oxygen octahedra enclosing the Cr^{3+} ions. These distortions arise in a natural way for Cr^{3+} ions in small LGO clusters as a result of their contacting the irregular structure of the surrounding glass. Note that the possibility of Cr^{3+} ions being located at the crystal–glass interface contributing to the inhomogeneous *R*-luminescence-line profile was mentioned in [7], which reported on a study of the *R* spectra of Cr^{3+} in glasses with embedded $MgAl_2O_4$ nanocrystals. This interpretation is close to the model of Cr^{3+} ions in small clusters discussed here, which is based on x-ray measurements (SAS, Section 2) indicating the formation, in the early stages of glass annealing, of extremely small (<4 nm) crystallites whose relative fraction decreases in the later stages of crystallization.

4. SPECTROSCOPIC MANIFESTATION OF A PHASE TRANSITION IN LGO NANOCRYSTALS

Let us discuss the manifestation of the D_{2h}–C_{2v} ferroelectric phase transition, which is known to occur in bulk LGO crystals (T_c = 10°C) [14, 15], in the spectra of lithium germanate glasses containing LGO : Cr^{3+} nanocrystals. Observation, in the Cr^{3+} spectra of LGO : Cr^{3+} glasses with nanocrystals at T = 77 K (Fig. 5), of two pairs of fluorescence lines, R_1–R_2 and R_1'–R_2', which are similar to those seen in spectra of the ferroelectric phase of bulk LGO : Cr^{3+} crystals [11, 13], unambiguously implies that the LGO nanocrystals embedded in glass at T = 77 K also belong to the C_{2v} ferroelectric phase of LGO. It is interesting, however, to determine whether the ferroelectric transition temperature in nanoparticles shifts from T_c = 10°C for free bulk LGO single crystals. As shown earlier [13], the Cr^{3+}–Li centers responsible for the appearance of two pairs of *R* lines in the ferroelectric phase become completely identical after the transition to the LGO paraphase; as a result, instead of two pairs of *R* lines one observes above T_c one pair, R_1–R_2. Because of the strong temperature-induced broadening, at close to room temperature, the merging of two lines of the ferroelectric phase, R_1–R_1', for $T \longrightarrow T_c^-$ into one R_1 line was detected from the clear break in the temperature dependence of the R_1 line halfwidth at T_c (Fig. 6). This break originated from the fact that the temperature-induced narrowing of the profile of the only R_1 line of the paraphase occurring for $T \longrightarrow T_c^+$ started to compete with the profile broadening at T_c, which was initiated by the appearance of a line splitting into R_1 and R_1' components below T_c that subsequently increases with decreasing temperature. Figure 6 presents the temperature dependence of the profile halfwidth in the region of the R_1 line of Cr^{3+} in nanocrystalline LGO in the Li_2O–$11.5GeO_2$–0.05% Cr_2O_3 glass. It is seen that this dependence exhibits a smoother break in the region of T_c and that the width of the total $R_1 + R_1'$ profile passes, for $T < T_c \sim 5$ cm^{-1}, above the similar profile plotted for bulk LGO : Cr^{3+}. It is in this difference that the contribution of the strong inhomogeneous broadening Γ_{inh} of the R_1 and R_1' lines in nanocrystals manifests itself (an estimate made for T = 10 K, where the R_1 and R_1' lines are resolved spec-

trally, yields $\Gamma_{inh} \sim 10$ cm^{-1}). At the same time, as evident from Fig. 6, for $T > T_c$, the halfwidths of the R_1 line for bulk LGO : Cr^{3+} and LGO : Cr^{3+} nanoparticles in glass become similar at high enough temperatures, where the contribution of the temperature-induced broadening of the R_1 and R_1' lines, which is the same in both cases, is dominant. The observed absence of a noticeable shift of the phase transition temperature in nanocrystalline LGO in glass relative to that in bulk LGO may be due to the nanocrystal size (~40 nm) being large enough for the size quantization effects [19, 20] to no longer be significant. Another factor of possible significance is that, in contrast to [19, 20], where free nanocrystals were studied, the present investigation dealt with ferroelectric nanocrystals embedded in a glass matrix. It would be of interest to study the phase transition in the smallest LGO crystallites (clusters) in glass; however, the large (~100 cm^{-1}) inhomogeneous *R*-line broadening (Fig. 5) would complicate this study if Cr^{3+} luminescence were to be used as a probe, thus necessitating a search for other, more adequate methods.

This study is one more demonstration of the broad potential of Cr^{3+} ions as spectroscopic probes in investigating heterophase oxide dielectrics (glass ceramics) [7]. It was shown that the luminescence spectra of Cr^{3+} in thermally annealed lithium germanate glasses make it possible to successively study the various stages of glass crystallization, starting from nucleation in glass of clusters of nanocrystalline LGO. The spectroscopic data thus obtained agree, on the whole, with independent x-ray (XPA, SAS) measurements. It proved possible to isolate reliably in lithium germanate glasses the contributions to the observed luminescence spectrum of annealed glass provided by Cr^{3+} ions residing in spatially separated regions of the glass ceramic with different structure. The isolation of the partial Cr^{3+} spectra was favored by both the absence of structural disorder in the LGO lattice, due to which the LGO : Cr^{3+} spectra contain characteristic narrow *R* lines, and the strongly pronounced difference between the spectra and kinetics of Cr^{3+} luminescence observed in the glass ($^4T_2$–$^4A_2$ transitions) and crystalline phase (^2E–$^4A_2$ transitions). As a result, three partial spectra were observed: (i) broad-band $^4T_2$–$^4A_2$ luminescence of Cr^{3+} ions in the glass, (ii) clearly resolved luminescence lines corresponding to the R_1 and R_2 transitions from the doublet ^2E state of the Cr^{3+} ions in LGO nanocrystals, and (iii) a single broad, inhomogeneously broadened *R* line originating from ^2E–$^4A_2$ transitions in very small (<4 nm) LGO nuclei (clusters).

Observation of a single broad (~100 cm^{-1}) *R* line similar to the inhomogeneously broadened *R* lines in Cr^{3+} spectra of bulk, structurally disordered oxide crystals is a manifestation of a new mechanism of strong inhomogeneous line broadening in the spectra of impurity centers. This broadening arises from the small size of the LGO crystallites (clusters) containing Cr^{3+} ions and the ensuing strong perturbation the structurally irregular glass-like matrix exerts on the crystallites with Cr^{3+} ions it surrounds. This interaction of Cr^{3+} ions in LGO crystallites with the matrix they are embedded in bears not only the static character responsible for the inhomogeneous broadening of spectral lines but also a dynamic character. Experiments on spectral hole burning in the inhomogeneously broadened *R* lines of Cr^{3+} in LGO clusters and nanocrystals present in lithium germanate glass have revealed that the homogeneous *R* line width has a linear temperature dependence characteristic of a Cr^{3+} ion in glass [21]. This observation is a direct indication that the homogeneous *R*-line width of Cr^{3+} in clusters and nanocrystals is determined by the dynamic properties of the surrounding glass matrix and is intimately connected with the long-range coupling of Cr^{3+} electronic levels with so-called two-level systems in glass.

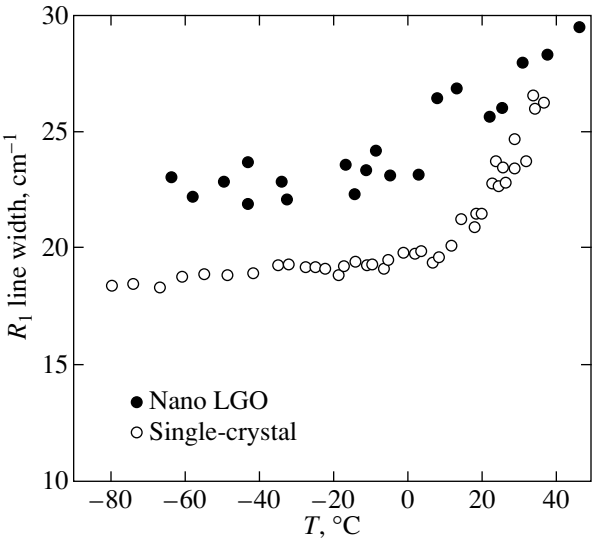

Fig. 6. Temperature dependence of the profile halfwidth in the region of the Cr^{3+} *R* line obtained for bulk LGO and nanocrystalline LGO embedded in Li_2O–11.5GeO_2–0.05% Cr_2O_3 glass.

ACKNOWLEDGMENTS

The authors are indebted to D. K. Nel'son for performing the spectral measurements in the IR range and to I.A. Drozdova for the TEM studies.

This study was supported by the Russian Foundation for Basic Research, project no. 02-02-17662.

REFERENCES

1. S. P. Feofilov, Fiz. Tverd. Tela (St. Petersburg) **44**, 1348 (2002) [Phys. Solid State **44**, 1407 (2002)].

2. S. P. Feofilov, A. A. Kaplyanskii, and R. I. Zakharchenya, J. Lumin. **66/67**, 349 (1996).
3. S. P. Feofilov, A. A. Kaplyanskii, R. I. Zakcharchenya, *et al.*, Phys. Rev. B **54**, 3690 (1996).
4. R. S. Meltzer, S. P. Feofilov, B. Tissue, and H. B. Yuan, Phys. Rev. B **60**, 14012 (1999).
5. R. S. Meltzer, W. M. Yen, Hairong Zheng, *et al.*, Phys. Rev. B **64**, 100201 (2001).
6. J. K. Krebs, S. P. Feofilov, A. A. Kaplyanskii, *et al.*, J. Lumin. **83/84**, 209 (1999).
7. F. Rossi, G. Pucker, M. Montagna, *et al.*, Opt. Mater. **13**, 373 (2000).
8. A. Marotta, P. Pernice, A. Aronne, and M. Catauro, J. Therm. Anal. **40**, 181 (1993).
9. R. C. Powell, J. Appl. Phys. **39**, 4517 (1968).
10. R. C. Powell, Phys. Rev. **173**, 358 (1968).
11. S. A. Basun, A. A. Kaplyanskiĭ, and S. P. Feofilov, Fiz. Tverd. Tela (St. Petersburg) **36**, 3429 (1994) [Phys. Solid State **36**, 1821 (1994)].
12. S. A. Basun, S. P. Feofilov, A. A. Kaplyanskii, *et al.*, J. Lumin. **53**, 24 (1992).
13. S. A. Basun, A. A. Kaplyanskiĭ, and S. P. Feofilov, Fiz. Tverd. Tela (St. Petersburg) **34**, 3377 (1992) [Sov. Phys. Solid State **34**, 1807 (1992)].
14. M. Wada and Y. Ishibashi, J. Phys. Soc. Jpn. **52**, 193 (1983).
15. Y. Iwata, I. Shibuya, M. Wada, *et al.*, J. Phys. Soc. Jpn. **56**, 2420 (1987).
16. F. J. Bergin, J. F. Donegan, T. J. Glynn, and G. F. Imbush, J. Lumin. **34**, 307 (1986).
17. S. A. Basun, P. Deren, S. P. Feofilov, *et al.*, J. Lumin. **45**, 115 (1990); S. A. Basun, P. Deren', A. A. Kaplyanskiĭ, *et al.*, Fiz. Tverd. Tela (Leningrad) **31** (3), 199 (1989) [Sov. Phys. Solid State **31**, 460 (1989)].
18. S. P. Feofilov, A. A. Kaplyanskii, and R. I. Zakharchenya, J. Lumin. **66/67**, 349 (1996); A. A. Kaplyanskiĭ, S. P. Feofilov, and R. I. Zakharchenya, Opt. Spektrosk. **79**, 709 (1995) [Opt. Spectrosc. **79**, 653 (1995)].
19. K. Ishikawa, K. Yoshikawa, and N. Okada, Phys. Rev. B **37**, 5852 (1988).
20. X. Wang, Z. Wang, M. Zhao, *et al.*, J. Alloys Compd. **224**, 130 (1995).
21. S. P. Feofilov, A. A. Kaplyanskii, A. B. Kulinkin, *et al.*, J. Lumin. **100**, 155 (2002).

Translated by G. Skrebtsov

Physics of the Solid State, Vol. 45, No. 5, 2003, pp. 969–971. Translated from Fizika Tverdogo Tela, Vol. 45, No. 5, 2003, pp. 923–925.

LOW-DIMENSIONAL SYSTEMS AND SURFACE PHYSICS

Excitation of Coherent Acoustic Phonons by a Femtosecond Pulse

Yu. E. Lozovik and V. A. Sharapov

Institute of Spectroscopy, Russian Academy of Sciences, Troitsk, Moscow oblast, 142092 Russia

e-mail: lozovik@isan.troitsk.ru

Received October 14, 2002

Abstract—Excitation of coherent acoustic phonons in superlattices or layered materials by a femtosecond pulse is considered. In superlattices, coherent acoustic phonons with a wave vector $Q = 2\pi/a$ can be excited, where a is the superlattice period. The number and statistical properties of coherent phonons are estimated. *© 2003 MAIK "Nauka/Interperiodica".*

The possibility of exciting coherent optical phonons in solids by ultrashort laser pulses was demonstrated experimentally in [1–5]. Coherent optical phonons were excited, in particular, in semiconductors GaAs [1], Ge [2], GaP and ZnSe [3], porous silicon [4], superconductor $YBa_2Cu_3O_{6+x}$ [5], and in semimetals (bismuth and antimony) [2]. The coherent phonons that can be excited in these materials have a wave vector $q = 0$ [6]; i.e., one can expect excitation of optical phonons only. This statement is valid, however, only for systems with a uniform electron density. We show that in layered systems, for instance, in superlattices, one can also excite coherent acoustic phonons with a nonzero wave vector q.

Consider the Hamiltonian of a system of electrons and phonons in a two-band layered semiconductor or in a superlattice:

$$\hat{H} = \sum_{\alpha, k} \varepsilon_{\alpha, k} c^{+}_{\alpha, k} c_{\alpha, k} + \sum_{q} \hbar\omega_q b^{+}_q b_q + V_{\text{int}}, \qquad (1)$$

where $c^{+}_k (b^{+}_q)$ and $c_k (b_q)$ are the operators of creation and annihilation of an electron with momentum k (phonon with wave vector q), respectively; $\alpha = 1, 2$ is the band index (subscript 1 refers to the valence band, and 2, to the conduction band), and V_{int} denotes the electron–phonon interaction, with

$$V_{\text{int}} = V_0 = \sum_{\alpha, k, q} g^{\alpha}_0 (b_q + b^{+}_{-q}) c^{+}_{\alpha k+q} c_{\alpha k} \qquad (2)$$

for the case of electrons interacting with optical phonons and

$$V_{\text{int}} = V_a = \sum_{\alpha, k, q} g^{\alpha}_a (b_q - b^{+}_{-q}) c^{+}_{\alpha k+q} c_{\alpha k} \qquad (3)$$

for electrons coupling with acoustic phonons. The deformation potential U_d is related differently to lattice displacement $u(r)$ for optical and acoustic phonons. In the case of optical phonons, U_d is proportional to the lattice displacement $u(r)$, whereas for acoustic phonons, $U_d \sim \nabla u(r)$ The electron–phonon coupling constant g_0 is practically independent of k and q, while g_a depends on q only:

$$g_a = -i\sigma \sqrt{\frac{\hbar}{2\rho V \omega_q}} |q|, \qquad (4)$$

where ρ and V are the density and volume of the solid, respectively, and σ is a constant.

A high-power femtosecond pulse with a characteristic photon energy $\hbar\omega$ greater than the band gap and with an instantaneous power of $\sim 10^{12}$ W/cm^2 excites a large number of electrons ($\sim 10^{20}$ cm^{-3}) from the valence to the conduction band, as well as (in the case of metals) from the conduction band to higher lying energy states near the surface of a solid within the extinction depth; this process radically changes the electron–phonon coupling. The electron–phonon coupling in the form of Eq. (2) or (3) can be considered an external force acting on the oscillator corresponding to the normal mode with wave vector q. Substituting

$$\begin{aligned} b_q &= \sqrt{\frac{\omega_q}{2\hbar}} x_q + i \frac{p_q}{\sqrt{2\hbar\omega_q}}, \\ b^{+}_q &= \sqrt{\frac{\omega_q}{2\hbar}} x_q - i \frac{p_q}{\sqrt{2\hbar\omega_q}}, \end{aligned} \qquad (5)$$

for b_q and b^{+}_q in Eq. (3), we obtain (setting $V = 1$)

$$V_a = g_a \sqrt{\frac{\omega_q}{2\hbar}} (\rho_q - \rho^{+}_q) x_g - g_a \sqrt{\frac{1}{2\hbar\omega_q}} (\rho_q + \rho^{+}_q) p_q, \qquad (6)$$

where $\rho_q = \sum_k c^+_{k+q} c_k$ is the Fourier component of the electron density function. The major contribution to electron–phonon interaction is provided by the conduction-band electrons; therefore, we understand by ρ_q the Fourier component of the electron density function in the conduction band (i.e., of the density function of the electrons excited by the femtosecond pulse). The electron density function in a superlattice can be approximated by the relation

$$\rho(x) = \rho_0 + \rho_1 \sin(Qx), \tag{7}$$

where $Q = 2\pi/a$ and a is the superlattice period. In this case, $\rho_Q = -\frac{i}{2}\rho_1$, i.e., $\mathrm{Re}(\rho_Q) = 0$, and the Hamiltonian of the oscillator corresponding to the mode with a wave vector $q = Q$ can be written as

$$H_q = \frac{p_q^2}{2} + \frac{\omega_q^2 x_q^2}{2} + f_q x_q, \tag{8}$$

where

$$f_q = i\rho_1 g_a \sqrt{\frac{\omega_Q}{2\hbar}}. \tag{9}$$

A similar situation occurs for the $q = 0$ mode. Because for the other modes we have $f_q = 0$ [as follows from Eq. (7)], the subscript q will be taken to be $q = 0$ or Q in what follows.

The excitation occurs on a time scale of the order of the femtosecond laser pulse duration (for instance, a few tens of femtoseconds). Electronic excitations relax usually in times shorter than the periods of optical and, even more so, acoustic phonons (for instance, in times of the order of hundreds of femtoseconds for metals and semiconductors). After electron relaxation in complete, the interaction $V_a(V_0)$ (i.e., the corresponding force f_q) is restored to its equilibrium value. Considered within the Hamiltonian formalism, this process is identical to the appearance of an effective force f_q at the instant of time $t = 0$ (the instant when the laser pulse strikes the sample) and the disappearance of this force at the time $t = t_0$, where t_0 is the electron relaxation time. It should be pointed out that ρ_Q in Eq. (9) for f_q is the Fourier component of the density function of excited electrons. As already mentioned, the electron excitation time is substantially shorter than $1/\omega_q$; hence, one may consider the electrons to be excited practically instantaneously. In this approximation, for analyzing the case of $q = Q$, the oscillator Hamiltonian can be written as

$$\begin{aligned} H_q(t) &= \frac{p_q^2}{2} + \frac{\omega_q^2 x_q^2}{2} + f_q(t) x_q, \\ f_q(t) &= f_q[\theta(t) - \theta(t - t_0)], \end{aligned} \tag{10}$$

where f_q is given by Eq. (9). Hence, we have reduced the problem to the consideration of a quantum system with a time-dependent quadratic Hamiltonian. Such systems can be studied in terms of the integrals of motion [7]. Using this method, one can find the evolution of the nth stationary state $\psi_n(x)$ of a system with Hamiltonian (10) after the application of a force f_q:

$$\begin{aligned} \psi_n(x, t) = \frac{1}{\sqrt{2^n n!}} \frac{1}{\sqrt{x_0\sqrt{\pi}}} \exp\Bigg(&-\frac{x^2}{2x_0^2} + \delta_0(t) x \\ &- \frac{y_0^2(t) x_0^2}{2} + i\varphi(t) \Bigg) H_n\left(\frac{x + y_0(t)}{x_0}\right). \end{aligned} \tag{11}$$

Here, the following notation was introduced:

$$\begin{aligned} \delta_0(t) &= \mathrm{Re}(\delta_0(t)) + i\,\mathrm{Im}(\delta_0(t)) \\ &= \begin{cases} -\frac{f_q}{\hbar\omega_q}(1 - \exp(-i\omega_q t)), & 0 \le t \le t_0 \\ -\frac{f_q}{\hbar\omega_q}(\exp(i\omega_q t_0) - 1)\exp(-i\omega_q t), & t \ge t_0, \end{cases} \end{aligned} \tag{12}$$

$$y_0(t) = -x_0^2 \mathrm{Re}(\delta_0(t)), \quad x_0 = \sqrt{\frac{\hbar}{\omega_q}}. \tag{13}$$

Knowing the function $\psi_n(x, t)$, one can readily calculate such characteristics as the displacement of the equilibrium lattice atom position caused by coherent phonons and the number of elementary excitations created by the impinging femtosecond pulse, as well as the statistical parameters of these excitations. The phonon creation and annihilation operators are related to the lattice displacement operator through the standard expression

$$\hat{u}(r) = \sum_q \sqrt{\frac{\hbar}{2\rho V \omega_q}} (b_q e^{iqr} + b_q^+ e^{-iqr}). \tag{14}$$

Hence,

$$\langle \hat{u}(r) \rangle = \sum_q \sqrt{\frac{\hbar}{2\rho V \omega_q}} (\langle b_q \rangle e^{iqr} + \langle b_q^+ \rangle e^{-iqr}). \tag{15}$$

The means $\langle b_q \rangle$ and $\langle b_q^+ \rangle$ can be easily found using Eq. (5) for the $\hat{b}_q$ and $\hat{b}_q^+$ operators and Eq. (11) for $\psi_n(x, t)$

$$\begin{aligned} \alpha_q &= \langle b_q \rangle \\ &= \int \psi_n^*(x, t) \left(\sqrt{\frac{\omega_q}{2\hbar}} x + \sqrt{\frac{\hbar}{2\omega_q}} \frac{\partial}{\partial x} \right) \psi_n(x, t)\, dx. \end{aligned} \tag{16}$$

The integral in Eq. (16) can be calculated with the use of the relation [8]

$$\int_{-\infty}^{\infty} H_m(x)H_n(\Lambda x + d)\exp(-Mx^2 + cx)dx = \sqrt{\frac{\pi}{M}}\exp\left(\frac{c^2}{4M}\right)H_{mn}^R(y_1, y_2), \quad (17)$$

where

$$R = 2\begin{pmatrix} 1-\frac{1}{M} & -\frac{\Lambda}{M} \\ -\frac{\Lambda}{M} & 1-\frac{\Lambda^2}{M} \end{pmatrix}, \quad (18)$$

$$\begin{pmatrix} y_1 \\ y_2 \end{pmatrix} = \frac{1}{2\left(1-\frac{(1+\Lambda^2)}{M}\right)}\begin{pmatrix} \frac{c}{M}+\frac{2\Lambda d}{M} \\ \frac{\Lambda c}{M}-\frac{2}{d}\left(1-\frac{1}{M}\right) \end{pmatrix}. \quad (19)$$

We finally obtain

$$\alpha_q = \frac{1}{\sqrt{2}}x_0\delta_0(t) \quad (20)$$

for any n and

$$\langle\hat{u}(r)\rangle = \frac{f_0x_0}{\sqrt{\rho V}\omega_0^2}\mathrm{Re}(\delta_0(t)) + \frac{f_Qx_0}{\sqrt{\rho V}\omega_Q^2}\mathrm{Re}(\delta_0(t))\cos(Qr) - \frac{f_Qx_0}{\sqrt{\rho V}\omega_Q^2}\mathrm{Im}(\delta_0(t))\sin(Qr). \quad (21)$$

The number of elementary excitations in modes with wave vectors $q = 0$ and $q = Q$ after the application of a femtosecond pulse can be found by calculating the mean of the phonon number operator $N_q = b_q^+b_q$:

$$\langle N_q\rangle = \langle b_q^+b_q\rangle = \int\psi_n^*(x,t)\left(\frac{\omega_q}{2\hbar}x^2 - \frac{\hbar}{2\omega_q}\frac{\partial^2}{\partial x^2} - \frac{1}{2}\right)\psi_n(x,t)dx. \quad (22)$$

On calculating integral (22), we obtain

$$\langle N_q\rangle = |\alpha_q|^2 + n. \quad (23)$$

The number of phonons excited by a femtosecond pulse is

$$n_{\mathrm{ph}} = \langle N_q\rangle - n = |\alpha_q|^2 = \frac{1}{2}x_0^2|\delta_0(t)|^2. \quad (24)$$

Substituting Eq. (12) for $\delta_0(t)$ in Eq. (24) for $t \geq t_0$, we obtain the final expression for the number of excited coherent phonons:

$$n_{\mathrm{ph}} = \frac{f_q^2}{2\hbar\omega_q}[1 - \cos(\omega_q t_0)]. \quad (25)$$

Let us determine now statistical parameters of the system of coherent phonons. Calculating the variances $\sigma_{pp} = \langle p^2\rangle - \langle p\rangle^2$, $\sigma_{xx} = \langle x^2\rangle - \langle x\rangle^2$, and $\sigma_{xp} = (1/2)\langle xp + px\rangle - \langle x\rangle\langle p\rangle$ yields

$$\sigma_{pp} = \hbar\omega_q(n + 1/2), \quad \sigma_{xx} = \frac{\hbar}{\omega_q}(n + 1/2), \quad \sigma_{xp} = 0, \quad \sigma_{pp}\sigma_{xx} = (n + 1/2)^2\hbar^2. \quad (26)$$

As seen from Eq. (26), purely coherent phonons, i.e., phonons corresponding to the minimum uncertainty, can be excited only from the $n = 0$ state, i.e., at $T = 0$, where T is the temperature of the solid. Let us make some estimates. Assuming $\rho = 5$ g/cm^3, $V = 1$ cm^3, $\omega_0 = 10$ THz, $\omega_Q = 20$ THz, $g_0 = 2 \times 10^{-12}$ eV, $\rho_0 = 10^{20}$ cm^{-3}, $\rho_Q = 10^{18}$ cm^{-3}, $a = 10^{-6}$ cm, and $g_a = 10^{-13}$ eV, we obtain $u_0 \simeq 10^{-3}$ nm for the maximum atom displacement. Setting $t_0 \approx 6 \times 10^{-13}$ s, we obtain $n_{\mathrm{ph}} \sim 10^{21}$ for the number of excited optical coherent phonons and $n_{\mathrm{ph}} \sim 10^{17}$ for the number of coherent acoustic phonons.

In this qualitative description of acoustic phonon generation, we have limited our consideration to one mechanism, according to which a laser pulse induces an instantaneous force acting on the corresponding lattice oscillator. The other possible mechanisms will be dealt with in a separate publication.

ACKNOWLEDGMENTS

This study was supported by the Russian Foundation for Basic Research and the Ministry of Industry, Science, and Technologies of the Russian Federation.

REFERENCES

1. G. C. Cho, W. Kutt, and H. Kurz, Phys. Rev. Lett. **65** (6), 764 (1990).
2. T. Pfeifer, W. Kutt, H. Kurz, and H. Scholz, Phys. Rev. Lett. **69** (22), 3248 (1992).
3. W. E. Bron, J. Kuhl, and B. K. Rhee, Phys. Rev. B **34** (10), 6961 (1986).
4. A. L. Dobryakov, V. A. Karavanskiĭ, S. A. Kovalenko, *et al.*, Pis'ma Zh. Éksp. Teor. Fiz. **71** (7), 430 (2000) [JETP Lett. **71**, 298 (2000)].
5. J. M. Chwalek, C. Uher, J. F. Withaker, and G. A. Mourou, Appl. Phys. Lett. **58** (9), 980 (1991).
6. A. V. Kuznetsov and C. J. Stanton, Phys. Rev. Lett. **73** (24), 3243 (1994).
7. V. V. Dodonov and V. I. Man'ko, *Invariants and Evolution of Nonstationary Quantum Systems* (Nova Science, New York, 1989), Proc. Lebedev Phys. Inst., Vol. 183.
8. V. I. Man'ko and A. Wunsche, Quantum Semiclassic. Opt. **9** (3), 381 (1997).

Translated by G. Skrebtsov

Physics of the Solid State, Vol. 45, No. 5, 2003, pp. 972–975. Translated from Fizika Tverdogo Tela, Vol. 45, No. 5, 2003, pp. 926–929.

LOW-DIMENSIONAL SYSTEMS AND SURFACE PHYSICS

Calculation of the Temperature Dependence of the Work Function of an Adsorption System

S. Yu. Davydov

Ioffe Physicotechnical Institute, Russian Academy of Sciences, Politekhnicheskaya ul. 26, St. Petersburg, 194021 Russia

Received July 2, 2002

Abstract—The effect of temperature on an adsorption system was considered in terms of the Anderson–Newns Hamiltonian. Both static effects associated with thermal expansion and the increase of the substrate and adsorbate atomic vibration amplitude with temperature were taken into account. Analytic expressions for the variation of the work function of the system with temperature were derived for the case of low coverages in the linear-in-temperature approximation. The results obtained are compared with experimental data on the adsorption of europium atoms on the (100) surface of tungsten. *© 2003 MAIK "Nauka/Interperiodica".*

1. INTRODUCTION

Despite the long history of this problem [1, 2], the effect of temperature T on the work function ϕ of an adsorption system remains poorly studied, which is indicated, for instance, by the lack of data anywhere near systematic in reference books [3]. Investigation of the $\phi(T)$ dependence is complicated by the fact that temperature influences both the electronic and phonon subsystems to produce frequent structural phase transitions in the substrate and/or adsorbed film. Similar transitions are also initiated by an increase in the surface concentration of adatoms (coverage) Θ. Thus, the $\phi(\Theta, T)$ dependence may vary strongly in character for various values of Θ.

To understand the nature of the experimentally observed $\phi(\Theta, T)$ relation, a corresponding theory has to be developed. The effect of temperature on the adatom dipole moment was considered in [4] in terms of a microscopic approach. Estimates made for atoms of Ni, Pd, Cu, Au, and Ag adsorbed on W(110) and W(211) showed the adatom dipole moment to increase with T, which is in accord with experimental data [5]. The present study analyzes the $\phi(\Theta, T)$ relation within the model proposed in [4].

2. BASIC RELATIONS

The work function of an adsorption system $\phi(\Theta, T)$ can be cast in the form [6, 7]

$$\begin{aligned}\phi(\Theta, T) &= \phi_s(T) + \Delta\phi_a(\Theta, T),\\ \Delta\phi_a(\Theta, T) &= -\Phi(T)Z(\Theta, T)\Theta,\\ \Phi(T) &= 4\pi e^2 N_{\mathrm{ML}} l(T),\end{aligned} \tag{1}$$

where ϕ_s is the work function of clean substrate, $\Delta\phi_a$ is the change in the work function caused by adsorption, N_{ML} is the adatom concentration in a monolayer corresponding to a coverage $\Theta = 1$, $2l$ is the arm of the surface dipole formed by the adsorbed ion and its image in the substrate, and e is the positron charge.

In the case of electropositive adsorption, the adatom transfers part of its electrons to the substrate and only one outer, one-electron adatom orbital $|a\rangle$ with occupation number n is involved in the electron exchange; charge $Z = 1 - n$. Conversely, if adsorption initiates electron transition from the substrate to the adatom (to an electron affinity level), then $Z = -n$ [8, 9] (electronegative adsorption).

We use in the subsequent analysis a modified Anderson–Newns Hamiltonian H_0 (disregarding correlations) [10, 11] describing the adsorption of a single atom:

$$H_0 = \sum_k \varepsilon_k c_k^+ c_k + \varepsilon_a c_a^+ c_a + V\sum_k (c_k^+ c_a + \text{h.c.}), \tag{2}$$

where ε_k is the dispersion relation for the substrate electrons, ε_a is the energy of the adatom orbital $|a\rangle$ involved in adsorption, V is the matrix element connecting the adatom state $|a\rangle$ with the substrate electron state $|k\rangle$ (considered constant for the sake of simplicity), c_k^+ (c_k) are the creation (annihilation) operators of the electron in state $|k\rangle$, and c_a^+ (c_a) is the same for state $|a\rangle$. Now, we take into account the dipole–dipole interaction of adsorbed ions by introducing a self-consistent electric field (for more details, see [6, 7]). The expression for the adatom charge can now be written as

$$\begin{aligned}n(\Theta, T) &= \frac{1}{\pi}\arctan\frac{\Omega_0 - \xi(T)\Theta^{3/2}Z(\Theta, T)}{\Gamma(T)},\\ Z(\Theta, T) &= 1 - n(\Theta, T),\\ \xi(T) &= 2e^2 l(T)^2 N_{\mathrm{ML}}^{3/2} A_0,\\ \Omega_0 &= -I_a + \phi_s(0),\end{aligned} \tag{3}$$

1063-7834/03/4505-0972$24.00

where Ω_0 is the position of the adatom level with respect to the substrate Fermi level in the case of electropositive adsorption [I_a is the ionization energy of the adsorbing atom, $\phi_s(0)$ is the substrate work function at the initial ("zero") temperature], ξ is the dipole–dipole coupling constant, $\Gamma = \pi V^2 \rho_s$ is the halfwidth of the adatom quasi-level (ρ_s is the substrate density of states, which is assumed constant for the sake of simplicity), $A_0 \approx 10$ is a coefficient that is only weakly dependent on the adlayer geometry [6, 12], and the factor π^{-1} accounts for only one electron being involved in adsorption. We neglect in Eqs. (2) and (3) the dependence of l and Γ on Θ while including their dependence on T. Note that $\Gamma \propto \exp(-2\gamma l)$, where γ is the characteristic inverse decay length of the matrix element V with increasing adatom–substrate distance [13].

3. TEMPERATURE DEPENDENCE OF THE WORK FUNCTION

We introduce a temperature coefficient of the work function of an adsorption system $\kappa \equiv d\phi(\Theta, T)/dT$. We then have

$$\begin{aligned} \kappa &= \kappa_s + \kappa_a, \quad \kappa_s = d\phi_s(T)/dT, \\ \kappa_a &= d\Delta\phi_a(\Theta, T)/dT, \\ \kappa_a &= -\Theta\left[Z(\Theta, T)\frac{d\Phi(T)}{dT} + \Phi(T)\frac{dZ(\Theta, T)}{dT}\right]. \end{aligned} \tag{4}$$

In a first approximation in Θ, which corresponds to an ensemble of noninteracting adatoms, we obtain

$$(\kappa_a)_{\Theta \to 0} = -\Theta\left[Z(0, T)\frac{d\Phi(T)}{dT} + \Phi(T)\frac{dZ(0, T)}{dT}\right]. \tag{5}$$

Note that in deriving Eqs. (4) and (5) we assumed that there is no thermal desorption of adatoms, i.e., that Θ does not change with increasing T.

Following the approach developed in [4], we separate the temperature effect contributions to κ into a static contribution, caused by thermal expansion of the components of the adsystem (the substrate lattice constant and the adsorption bond length), and a dynamic contribution, originating from atomic vibrations in the substrate and the adlayer. The first can be written as $\alpha(\partial\phi/\partial a)_T$ and the second as $(\partial\phi/\partial T)_a$, where α is the corresponding thermal expansion coefficient and a is the characteristic bond length.

The static contribution can be found by setting the lattice constant equal to

$$a = a_0(1 + \alpha_s T), \tag{6}$$

where $\alpha_s = a_0^{-1}(da/dT)$ is the coefficient of linear thermal expansion of the substrate and a_0 is the distance between nearest neighbors in the bulk of the substrate at zero temperature. (Here and in what follows, the subscript "0" indicates correspondence of the parameter to the initial temperature.) A similar expression can be written for the adsorption bond length:

$$l = l_0(1 + \alpha_a T), \tag{7}$$

where l_0 is the adsorption bond length (i.e., half the length of the surface dipole, or the distance from the adatom center to the image plane) at zero temperature and $\alpha_a = l_0^{-1}(dl/dT)$ is the linear expansion coefficient of the adsorption bond.

The second, dynamic, contribution can be presented in the form

$$\tilde{a}(t) = a + A_s \cos\omega_s t, \quad \tilde{l}(t) = l + A_a \cos\omega_a t, \tag{8}$$

where $A_s(A_a)$ is the vibration amplitude of the substrate atoms (adatoms) relative to the new equilibrium position and $\omega_s(\omega_a)$ is the characteristic vibration frequency of the substrate atoms (adatoms). Only vibrations normal to the substrate surface are considered for the adsorbate.

It should be stressed that such an additive response of a system to a change in temperature corresponds to the so-called quasi-harmonic approximation in lattice theory (see, e.g., [14]).

3.1. Substrate

We start by calculating the coefficient κ_s. The work function of a metal can be represented in the form [15]

$$\begin{aligned} \phi_s &= I_s - \Sigma, \quad \Sigma = C + K, \\ C &= D\frac{e^2}{a}, \quad K = B\frac{\hbar^2}{ma^2}. \end{aligned} \tag{9}$$

Here, I_s is the ionization energy of the substrate atoms; Σ is the transition energy; which is actually the sum of the Coulomb C and kinetic K components; $\hbar$ is Planck's constant; m is the electron mass; and D and B are dimensionless coefficients.

It can be easily verified that the static contribution to κ_s is

$$\kappa_s^{st} = (C + 2K)\alpha_s. \tag{10}$$

To find the dynamic contribution, we expand, following [4], the expressions for C and K to second order in parameter A_s/a, average the results of the expansion over the substrate atomic vibration period $T_s = 2\pi/\omega_s$, and equate A_s^2 to the rms displacement in the Debye approximation for high temperatures [14]:

$$\langle \delta_s^2 \rangle = (9\hbar^2 T/M_s T_D^2 k_B), \tag{11}$$

where M_s is the mass of the substrate atom (the substrate is assumed to be monatomic), T_D is the Debye

temperature, and k_B is Boltzmann's constant we thereby obtain

$$\kappa_s^{\rm dyn} = \frac{9}{2}(C+3K)\alpha^*, \quad \alpha^* = \hbar^2/a_0^2 M_s T_D^2 k_B. \quad (12)$$

Note that both the static and the dynamic components of the temperature coefficient of the substrate work function κ_s are positive. Hence, the work function of the substrate increases with temperature.

3.2. Adsorbate

Let us turn to the estimation of κ_a. As follows immediately from Eqs. (7) and (8), the variation of the Φ parameter with temperature is caused by the thermal expansion of the adsorption bond alone, because the average value $\langle l\rangle$ over the vibration period $T_a = 2\pi/\omega_a$ is l, whereas linear thermal expansion yields

$$(d\Phi/dT)^{\rm st} = \Phi_0\alpha_a. \quad (13)$$

As shown in [4], the coefficient α_a can be estimated as

$$\alpha_a = \frac{3}{4}(k_B/E_{\rm ads}), \quad (14)$$

where $E_{\rm ads}$ is the adatom adsorption energy.

Turning now to estimation of the temperature dependence of the charge of a single adatom, we use Eqs. (3), (5), and (7) and obtain

$$(dZ/dT)^{\rm st} = 2\rho_0\Omega_0\gamma l_0\alpha_a,$$
$$\rho_0 = \frac{1}{\pi}\frac{\Gamma_0}{\Omega_0^2+\Gamma_0^2}. \quad (15)$$

Here, ρ_0 is the density of states of a single adatom at the Fermi level. Therefore, the static contribution can be written as

$$\kappa_a^{\rm st} - \Theta\Phi_0\alpha_a(Z_0 + 2\rho_0\Omega_0\gamma l_0). \quad (16)$$

Because the energy Ω_0 can be both positive and negative, the coefficient $\kappa_a^{\rm st}$ can be greater or smaller than zero.

To find the dynamic contribution, we calculate the adatom charge to second order in parameter A_a/l average over the period, and equate A_a/l to the mean rms adatom displacement $\langle\delta_a^2\rangle$. As in [4] (see also [16]), we estimate $\langle\delta_a^2\rangle$ from the adatom adsorption energy $E_{\rm ads}$ assuming that

$$\langle\delta_a^2\rangle = (9k_BT/E_{\rm ads})l_0^2. \quad (17)$$

This yields the expression for the dynamic contribution:

$$\kappa_a^{\rm dyn} = -\frac{3}{2}\Theta\Phi_0\rho_0\Omega_0(2\gamma l_0)^2(k_B/E_{\rm ads})\left(\frac{\Gamma_0^2-\Omega_0^2}{\Gamma_0^2+\Omega_0^2}\right). \quad (18)$$

We readily see that, because Eq. (18) can be both positive and negative, estimates should be made for the parameters of a specific adsorption system.

Note one more point. As the temperature increases, the adatom occupation number $n = 1 - Z$ grows because of the temperature-induced broadening of the Fermi–Dirac distribution. The variation $n(T)$ can be estimated from the expression [17]

$$n(T) = n_0 + \Delta n(T),$$
$$\Delta n(T) = \frac{\pi^2}{3}(k_BT)^2\rho_0\frac{\Omega_0}{\Omega_0^2+\Gamma_0^2}. \quad (19)$$

Because the broadening of the Fermi–Dirac step is proportional to T^2, we neglect it here.

4. ADSORPTION OF Eu ATOMS ON W(100)

To test the results obtained, we consider experimental data on the Eu/W(100) system from [18], in which the temperature dependences of the work functions of the clean tungsten substrate, $\phi_s(T)$, and of the adsorption system as a whole, $\phi(\Theta, T)$, were measured for a range of europium adatom concentrations. The experiment revealed that $\phi_s(T)$ grows by approximately 0.03 eV as the temperature increases from room temperature to $T = 1000$ K, whereas $\phi(\Theta, T)$ remains practically unchanged.

Let us estimate the model parameters and calculate the variation with temperature of the work function of the clean substrate and of the adsystem.

4.1. Substrate

For tungsten, $K = 0.06$ eV and $C = 3.38$ eV [15]; therefore, $\kappa_s^{\rm st} = (C + 2K)\alpha_s = 3.5\ {\rm eV}\alpha_s$ [see Eq. (10)]. As reported in [2], the temperature coefficient α_s varies from 4.6×10^{-6} K^{-1} at $T = 300$ K to 4.9×10^{-6} K^{-1} at $T = 1000$ K. Thus, for $T = 1000$ K we have $\kappa_s^{\rm st} = 1.72\times10^{-5}$ eV K^{-1}.

In accordance with Eq. (12) and [15], we obtain $\kappa_s^{\rm dyn} = 16\ {\rm eV}\alpha^*$. To calculate α^*, we set $a_0 = 2.74$ Å and $T_D = 400$ K [19]. We then obtain $\alpha^* = 0.22\times10^{-6}$ K^{-1}, which yields $\kappa_s^{\rm dyn} = 0.35\times10^{-5}$ eV K^{-1}. Hence, $\kappa_s = 2.07\times10^{-5}$ eV K^{-1}. Experiment [20] suggests the value $\Delta\phi_s/\Delta T \approx 3\times10^{-5}$ eV K^{-1} for $T = 1000$ K. In view of the straightforward character of these estimates, the agreement between the calculation and experiment should be considered satisfactory. Moreover, linear approximation of the experimental value of $\phi_s(T)$ from room temperature to 1000 K yields $\Delta\phi_s/\Delta T \approx 2\times10^{-5}$ eV K^{-1}, which practically coincides with our figure.

4.2. Adsorbate

Using the values of the europium ionization energy I_a = 5.67 eV, (100)W work function ϕ_s = 4.63 eV [2], and adsorption bond length $l_0 = r_a$ = 2.04 Å (where r_a is the atomic radius of Eu [2]), we obtain Ω_0 = –1.04 eV. The Γ_0 parameter will be set equal to $|\Omega_0|$, whence it follows immediately that $\kappa_a^{\text{dyn}} = 0$. Then, Z_0 = 0.24 and ρ_0 = 0.15 eV^{-1}. We assume also that γ = 1 Å^{-1} [13].

Estimates made in [18] suggest that $N_{\text{ML}} = 10^{15}$ cm^{-2} and therefore Φ_0 = 36.9 eV. We consider both these values to be overestimated. Indeed, the separation between nearest neighbors in the bulk of tungsten d(W) = 2.74 Å is substantially smaller than that in the bulk of europium, d(Eu) = 3.96 Å [21]. It thus seems that the coverage in a europium monolayer cannot greatly exceed d^{-2}(Eu) = 6.6×10^{14} cm^{-2}. Accepting the latter figure for the monolayer, we obtain Φ_0 = 23.6 eV.

Using E_{ads} = 3 eV for the europium adsorption energy on tungsten [18], we obtain $\alpha_a = 2.15 \times 10^{-5}$ K^{-1}. Note that the averaged temperature coefficient of expansion of a bulk europium crystal at T = 500 K is 2.02×10^{-5} K^{-1} [19], which practically coincides, as in [4], with our value of α_a. Note also the coincidence between the values of α_a and α^*.

Thus, we have $\kappa_a^{\text{st}} = \kappa_a = 2.0\Theta \times 10^{-4}$ eV K^{-1} which yields $\kappa \approx 2(1 + 10\Theta) \times 10^{-5}$ eV K^{-1} for the temperature coefficient of the work function of the Eu/W(100) adsystem in the limit of low coverages. It follows that, as the temperature increases from room temperature to 1000 K at Θ = 0.1, the work function grows by approximately $\Delta\phi$ = 0.03 eV, whereas it practically does not change in the experiment. The necessary and sufficient condition for obtaining $\Delta\phi$ = 0 for Θ = 0.1 is

$$\kappa_s + \kappa_a = 0, \tag{20}$$

which implies that the temperature effects for the substrate and the adsorption layer cancel each other. Because the Γ_0 parameter is the hardest to determine in the Anderson–Newns model, it appears natural to derive its value from condition (20). We obtain $\Gamma_0 \approx$ 1.30 eV, which appears quite reasonable.

Thus, we have succeeded in adequately describing the temperature dependence of the work function of the metal/metal adsorption system at low coverages in terms of the Anderson–Newns Hamiltonian. To transfer to higher coverages, one should use Eqs. (4) instead of simplified relation (5). The main difficulty here will be connected with the term $dZ(\Theta, T)/dT$. It can be shown that

$$\begin{aligned}&\frac{dZ}{dT}[1 + \Theta^{3/2}\tilde{\rho}\xi] \\ &= \tilde{\rho}\xi\left[\Theta^{3/2}Z\left(\frac{d\ln\Gamma}{dT} - \frac{d\ln\xi}{dT}\right) - \frac{\Omega_0}{\xi}\frac{d\ln\Gamma}{dT}\right],\end{aligned} \tag{21}$$

where

$$\tilde{\rho} \equiv \tilde{\rho}(\Theta, T) = \frac{1}{\pi}\frac{\Gamma(T)}{\tilde{\Omega}(\Theta, T)^2 + \Gamma(T)^2},$$

$$\tilde{\Omega}(\Theta, T) = \Omega_0 - \Theta^{3/2}\xi(T)Z(\Theta, T).$$

In addition to the equations becoming too bulky, one has, in accordance with Eq. (1), to carry out a self-consistent calculation of the adatom charge. Therefore, in general, numerical calculation will be needed. The same conclusion can be made regarding the inclusion of effects which are nonlinear in temperature.

REFERENCES

1. C. Herring and M. Nichols, Rev. Mod. Phys. **21**, 185 (1949).
2. L. N. Dobretsov and M. V. Gomoyunova, *Emission Electronics* (Nauka, Moscow, 1966; Israel Program for Sci. Transl., Jerusalem, 1971).
3. V. S. Fomenko, *The Emission Properties of Materials: Handbook*, 4th ed. (Naukova Dumka, Kiev, 1981).
4. S. Yu. Davydov, Surf. Sci. **364**, 477 (1996).
5. J. Kolaczkiewicz and E. Bauer, Surf. Sci. **160**, 1 (1985).
6. J. P. Muscat and D. M. Newns, J. Phys. C **7**, 2630 (1974).
7. S. Yu. Davydov, Fiz. Tverd. Tela (Leningrad) **19**, 3376 (1977) [Sov. Phys. Solid State **19**, 1971 (1977)].
8. L. A. Bol'shov, A. P. Napartovich, A. G. Naumovets, and A. G. Fedorus, Usp. Fiz. Nauk **122**, 125 (1977) [Sov. Phys. Usp. **20**, 432 (1977)].
9. O. M. Braun, Ukr. Fiz. Zh. **23**, 1233 (1978).
10. P. W. Anderson, Phys. Rev. **124**, 41 (1961).
11. D. M. Newns, Phys. Rev. **178**, 1123 (1969).
12. C. E. Carrol and J. W. May, Surf. Sci. **29**, 60 (1972).
13. R. Brako and D. M. Newns, Rep. Prog. Phys. **52**, 655 (1989).
14. H. Böttger, *Principles of the Theory of Lattice Dynamics* (Physik, Weinheim, 1983; Mir, Moscow, 1986).
15. S. Yu. Davydov, Zh. Tekh. Fiz. **72** (1), 96 (2002) [Tech. Phys. **47**, 92 (2002)].
16. S. Yu. Davydov, Zh. Tekh. Fiz. **67** (5), 109 (1997) [Tech. Phys. **42**, 555 (1997)].
17. R. Kubo, *Statistical Mechanics: An Advanced Course with Problems and Solutions* (North-Holland, Amsterdam, 1965; Mir, Moscow, 1967).
18. M. V. Kuz'min and M. A. Mittsev, Pis'ma Zh. Tekh. Fiz. **27** (10), 86 (2001) [Tech. Phys. Lett. **27**, 437 (2001)].
19. *Physical Quantities. Handbook*, Ed. by I. S. Grigor'ev and E. Z. Meĭlikhov (Énergoatomizdat, Moscow, 1991).
20. B. K. Medvedev, N. I. Ionov, and Yu. I. Belyakov, Fiz. Tverd. Tela (Leningrad) **15**, 2620 (1973) [Sov. Phys. Solid State **15**, 1743 (1973)].
21. C. Kittel, *Introduction to Solid State Physics*, 5th ed. (Wiley, New York, 1976; Nauka, Moscow, 1978).

Translated by G. Skrebtsov

Physics of the Solid State, Vol. 45, No. 5, 2003, pp. 976–982. Translated from Fizika Tverdogo Tela, Vol. 45, No. 5, 2003, pp. 930–936.

LOW-DIMENSIONAL SYSTEMS AND SURFACE PHYSICS

Samarium Atom Yield under Electron-Stimulated Desorption from Oxidized Tungsten Surface

V. N. Ageev, Yu. A. Kuznetsov, and N. D. Potekhina

Ioffe Physicotechnical Institute, Russian Academy of Sciences, Politekhnicheskaya ul. 26, St. Petersburg, 194021 Russia

e-mail: kuznets@ms.ioffe.rssi.ru

Received September 23, 2002

Abstract—The yield of samarium (Sm) atoms under electron stimulated desorption from Sm layers adsorbed on the surface of oxidized tungsten was studied as a function of incident electron energy, surface coverage by samarium, degree of tungsten oxidation, and substrate temperature. The measurements were conducted by the time-of-flight technique with a surface ionization detector in the substrate temperature interval from 140 to 600 K. The yield vs. incident electron energy function has a resonance character. Overlapping resonance peaks of Sm atoms are observed at electron energies of 34 and 46 eV, which may be related to excitation of the Sm 5*p* and 5*s* levels. The Sm yield is a complex function of samarium coverage and substrate temperature. Sm atom peaks occur only in the Sm coverage range from 0 to 0.2 monolayers (ML), in which the yield passes through a maximum. The shape of the yield temperature dependence is a function of Sm coverage. For low Sm coverages (<0.07 ML), the yield decreases slowly with the temperature increasing to 270 K, after which it drops to zero at temperatures above 360 K. At higher coverages, the Sm yield passes through a maximum with increasing temperature and additional peaks appear at electron energies of 42, 54, and 84 eV, which can be assigned to excitation of the tungsten 5*p* and 5*s* levels. These peaks are most likely associated with desorption of SmO molecules, whose yield reaches a maximum at an Sm coverage of about 1 ML. *© 2003 MAIK "Nauka/Interperiodica".*

1. INTRODUCTION

Bombardment of the surface of a solid by electrons can give rise to desorption of charged or neutral particles. When desorption occurs as a result of a direct transformation of the potential energy of electronic excitation of an adsorption bond into the kinetic energy of desorbing particles, this phenomenon is commonly termed electron-stimulated desorption (ESD) [1]. ESD is used widely in the analysis and modification of adsorbed layers [2]. A wealth of information has been amassed to date on the ESD of positive and negative ions [3]. At the same time, the number of reliable measurements of neutral particle fluxes remains limited, which hinders the development of detailed models of this phenomenon.

The most extensive information on the ESD of neutrals has been gained for alkali metal atoms. The yield and energy distributions of alkali metal atoms have been measured in ESD from layers adsorbed on the surface of oxidized tungsten [4], molybdenum [5], and silicon oxide [6]. Data on the yield and energy distributions of barium atoms [7] and the yield of europium (Eu) atoms [8] in ESD from oxidized tungsten are also available. As shown by these measurements, the neutral ESD mechanism depends very strongly on the electron structure of adsorbed atoms and of the substrate. In particular, the yield of barium and alkali metal atoms varies monotonically with increasing electron energy [4, 7], while the yield of Eu atoms from oxidized tungsten has a resonance character [8, 9].

Rare-earth metals (REMs) enjoy broad application in electronics, electrical engineering, oil refinery, and in the automotive industry, as well as in space technology in the production of permanent magnets, construction materials, and HTSC ceramics [10]. Moreover, REMs stimulate considerable interest from a purely scientific standpoint; the 4*f* electron occupation number varies smoothly along the REM series, thus permitting elucidation of the influence this factor exerts on the ESD characteristics of REM atoms. We studied the yield of Eu atoms from Eu layers adsorbed on oxidized tungsten in [8, 9]. This communication reports on measurements of the Sm atom yield from Sm layers adsorbed on the surface of oxidized tungsten. These data will be compared with the corresponding measurements made earlier for Eu atoms. Samarium has a relatively low ionization potential (5.63 eV) [11] and a low activation energy of thermal desorption from tungsten as compared to other REMs [12]; therefore, the Sm atom flux can be readily measured with a surface ionization-based detector.

2. EXPERIMENTAL

The experimental setup and the procedures employed in sample preparation were described in considerable detail in [13]. Therefore, we restrict ourselves

here to description of only the main parts of the setup and improvements introduced in the course of its service. The measurements were conducted in a bakeable stainless-steel chamber at a base pressure below 5×10^{-10} Torr. The samples were textured tungsten ribbons that were predominantly (100)-oriented and measured $70 \times 2 \times 0.01$ mm. The samples were purified of carbon through annealing in an oxygen environment [$p(O_2) = 1 \times 10^{-6}$ Torr] for 3 h at temperature $T = 1800$ K. The impurity content in the samples was checked by Auger electron and thermal desorption spectroscopy. The oxygen monolayer on the sample surface was produced by exposing the sample to oxygen under a pressure of 1×10^{-6} Torr at sample temperature $T = 1600$ K for 300 s, and the oxide layer was grown under the same oxygen pressure at $T = 1100$ K for 600 s [14].

Samarium was deposited on the oxidized tungsten surface at $T = 300$ K from a directly heated evaporator in the form of a tantalum tube with samarium metal placed inside it. Several holes were drilled in the tube to allow uniform distribution of the samarium deposition rate along the sample. The concentration of deposited samarium was determined using thermal desorption spectroscopy [15] and was verified against the maximum of the samarium ESD yield. This maximum, which is associated with excitation of the tungsten 5*p* and 5*s* core levels, corresponds to one-monolayer samarium coverage. The adsorbed samarium concentration corresponding to an oxygen monolayer deposited on the W(100) surface was measured as 8.7×10^{14} atom/cm^2, and that on the oxide-coated W(100), as 1×10^{15} atom/cm^2 [15].

A sample could be cooled by passing gaseous nitrogen, precooled in a copper tube immersed in liquid nitrogen, through hollow current leads. The sample temperature was varied from 160 to 300 K by properly varying the flow rate of the cooled nitrogen. The sample temperature in the low-temperature region was derived from the temperature dependence of the electrical resistivity of the sample placed in a thermostat with a known temperature. The sample could be heated to $T = 2500$ K by passing an electric current through it. In the high-temperature region, the temperature was determined with an optical micropyrometer, and in the region between 300 K and the pyrometric temperatures, by linear extrapolation of the temperature dependence of the heater current to room temperature.

A polycrystalline tungsten filament, 100 μm in diameter and drawn parallel to the sample, served as the electron emitter. The electron energy includes a correction to the emitter work function [16]. The emission current density did not exceed 5×10^{-6} A/cm^2 in the electron energy range from 0 to 300 eV and did not produce noticeable sample heating under electron bombardment. A surface-ionization-based detector containing a textured tungsten ribbon heated to $T = 2000$ K was used to measure the Sm atom flux. The ion signal was amplified by a secondary electron multiplier, and the S/N ratio was improved through operation in the lock-in mode.

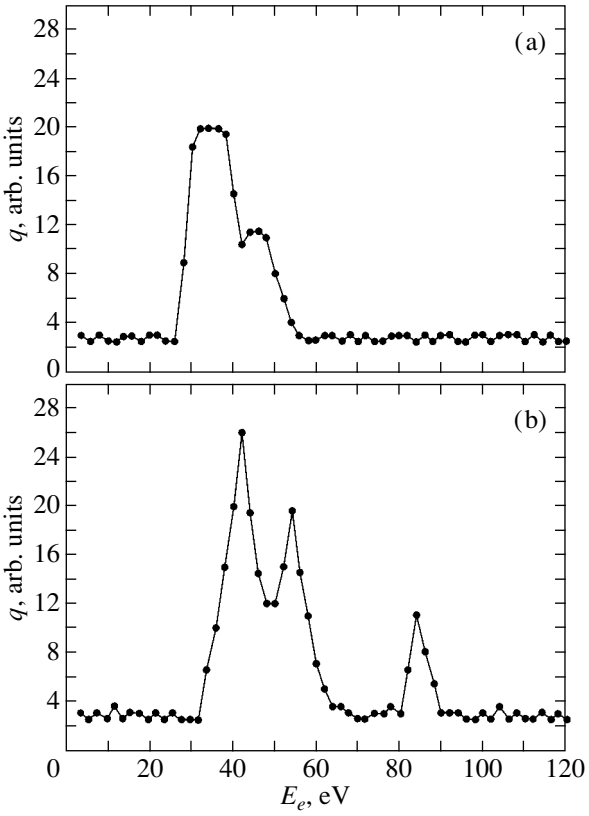

Fig. 1. Sm ESD yield from an Sm layer adsorbed on an oxygen-monolayer-covered tungsten surface, measured at $T = 300$ K as a function of incident electron energy for samarium coverages Θ (a) 0.10 and (b) 0.70.

3. RESULTS

Figure 1 plots the yield q of Sm atoms from an Sm layer adsorbed on an oxygen-monolayer-coated tungsten surface vs. incident electron energy E_e for two samarium coverages, Θ = 0.10 and 0.70. The Sm atom yield is seen to depend on electron energy in a resonant manner. The Sm atom ESD appearance threshold is close to the electron energy $E_e = 26$ eV (Fig. 1a) and passes through a maximum at $E_e = 34$ eV. One more feature is seen at the wing of this peak at $E_e = 46$ eV. The positions of these features correlate with the Sm 5*p* and 5*s* core level ionization energies [17]. As the Sm coverage increases, the intensity of the peaks at 34 and 46 eV decreases without changing the peak shape and additional peaks appear at electron energies of 42, 54, and 84 eV (Fig. 1b), which can be associated with the W 5*p* and 5*s* core level ionization [17].

Figure 2 presents the dependence of peak intensity on samarium coverage Θ of a tungsten surface covered by an oxygen monolayer. At low coverages, the peaks at $E_e = 34$ and 46 eV grow in intensity practically lin-

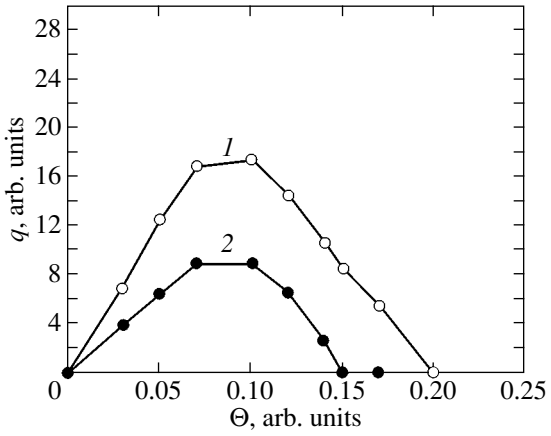

Fig. 2. Sm atom ESD yield from an Sm layer adsorbed on an oxygen-monolayer-covered tungsten surface, measured at $T = 300$ K as a function of samarium coverage Θ for electron energies E_e equal to (*1*) 34 and (*2*) 46 eV.

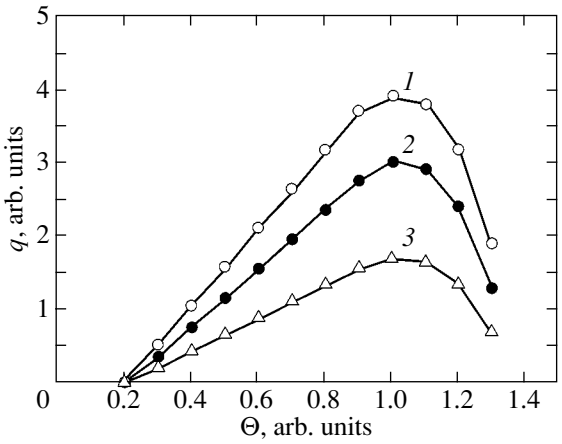

Fig. 3. SmO molecule ESD yield from an Sm layer adsorbed on an oxygen-monolayer-covered tungsten surface, measured at $T = 300$ K as a function of samarium coverage Θ for electron energies E_e equal to (*1*) 42, (*2*) 54, and (*3*) 84 eV.

early with increasing coverage, after which they pass through a maximum at about the same value $\Theta = 0.08$. The intensity of the 46-eV peak is lower than that of the peak at 34 eV over the whole coverage range, with the peak at 46 eV disappearing already at a coverage $\Theta = 0.15$ but that at 34 eV, only for $\Theta > 0.20$. The peaks corresponding to the tungsten core level ionization (42, 54, 84 eV) become visible at Sm coverages of about 0.2 ML. Their intensity grows close to linearly with increasing coverage, to pass afterwards through a maximum at $\Theta = 1$ (Fig. 3). These peaks decrease in intensity with increasing excitation energy for fixed Sm coverage.

While the ESD yield of Sm atoms from a Sm layer adsorbed on a tungsten oxide surface retains its resonance character of dependence on the incident electron energy, the dependence of its amplitude on the coverage Θ changes qualitatively (Fig. 4). The Sm atom yield grows strongly at very low Sm coverages ($\Theta < 0.025$), to fall off subsequently in a close-to-linear pattern with increasing coverage Θ. This pattern of the $q(\Theta)$ dependence resembles the Eu atom yield relation for the peaks associated with excitation of the Eu core levels in ESD from a Eu layer adsorbed on oxygen-monolayer-coated tungsten [8, 9].

The Sm atom peak intensity at $E_e = 34$ and 46 eV decreases with increasing extent of tungsten oxidation, and that of the peaks associated with excitation of the tungsten core levels (42, 54, 84 eV) is almost independent of the degree of substrate oxidation.

The Sm atom ESD yield is a complex function of the substrate temperature and of the substrate coverage by samarium. Figure 5 plots the dependence of the Sm atom ESD yield from a Sm layer adsorbed on an oxygen-monolayer-coated tungsten surface vs. substrate temperature for the electron energy $E_e = 34$ eV. We readily see that for $\Theta < 0.10$ the yield decreases slightly with the temperature increasing from 160 to 280 K, to fall off rapidly afterwards for $T > 350$ K. As the Sm coverage increases from 0.03 to 0.10, the yield grows smoothly with increasing coverage at a fixed temperature down to $T < 350$ K. For $\Theta > 0.10$, the Sm atom yield passes with increasing T through a smooth maximum, which shifts with increasing coverage toward higher temperatures. Note that its intensity and spread in temperature decrease. The temperature threshold of Sm atom ESD appearance increases and that of the yield disappearance decreases with increasing Sm coverage. A similar temperature dependence is observed to hold for the Sm atom yield at an excitation energy $E_e = 46$ eV. In contrast to the Sm case, the Eu atom yield associated with europium core level excitation always

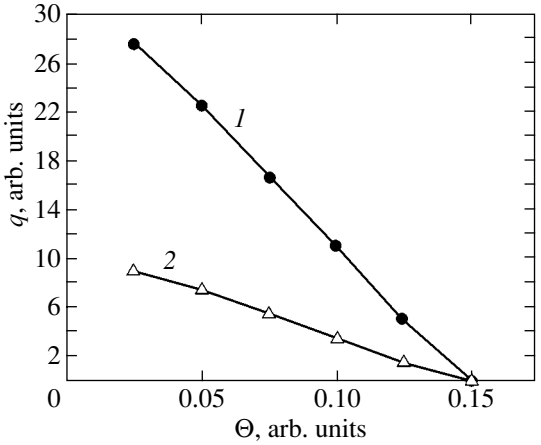

Fig. 4. Sm atom ESD yield from an Sm layer adsorbed on tungsten oxide and measured at $T = 300$ K vs. samarium coverage Θ for electron energies E_e equal to (*1*) 34 and (*2*) 46 eV.

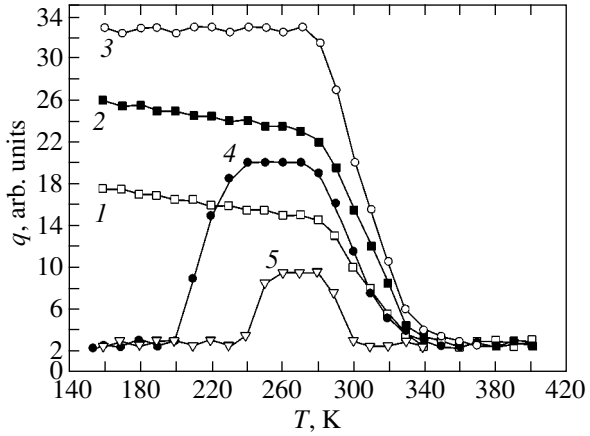

Fig. 5. Sm atom ESD yield from an Sm layer adsorbed on an oxygen-monolayer-covered tungsten surface, measured as a function of substrate temperature at the electron energy E_e = 34 eV and samarium coverages Θ = (*1*) 0.03, (*2*) 0.05, (*3*) 0.10, (*4*) 0.15, and (*5*) 0.20.

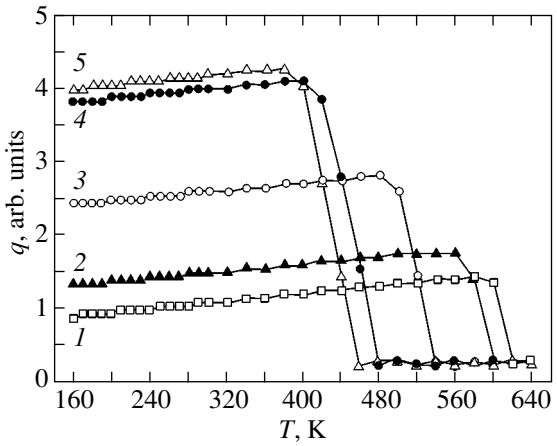

Fig. 6. SmO molecule ESD yield from an Sm layer adsorbed on an oxygen-monolayer-covered tungsten surface, measured as a function of substrate temperature at the electron energy E_e = 42 eV and samarium coverages Θ = (*1*) 0.40, (*2*) 0.50, (*3*) 0.70, (*4*) 0.90, and (*5*) 1.0.

passes through a maximum with increasing temperature for all europium coverages Θ ≤ 0.25 of oxidized tungsten. In this case, the appearance temperature of Eu atoms, as that of Sm atoms, grows with Θ, whereas the yield disappearance temperature of Eu atoms, unlike that of Sm atoms, does not depend on coverage [18].

Figure 6 shows the temperature dependence of the Sm atom ESD yield for E_e = 42 eV and for a range of Sm coverages of the tungsten surface coated by an oxygen monolayer. For low *T*, the yield grows first very slowly with *T* and subsequently drops to zero at a temperature which decreases with increasing Sm coverage. The other Sm yield peaks (at 54, 84 eV) associated with tungsten core level excitation exhibit a similar behavior. Throughout the temperature range covered, the yield behaves in a reversible manner with variation of the substrate temperature, which suggests that thermal desorption of samarium may be neglected.

Estimates show that the dissociation rate of SmO molecules on the heated tungsten detector ribbon, just as that of EuO molecules, is higher than the rate of thermal desorption of the Sm and Eu atoms, respectively; therefore, the surface ionization-based detector cannot discriminate between the desorption of SmO molecules and Sm atoms [19].

Hence, one can assume with reasonable confidence that tungsten core level excitation is followed by SmO molecule desorption.

4. DISCUSSION OF RESULTS

An Sm monolayer adsorbed on tungsten at *T* = 300 K reduces the work function [20]. Unfortunately, we are not aware of any measurements of the work function for the case of Sm adsorption on oxidized tungsten; therefore, we assume (in analogy with the alkali and alkaline-earth metals) that Sm adsorbs on oxidized tungsten in ionic form, is distributed over the surface in a random manner at below monolayer coverages, and forms clusters at coverages above one monolayer. Europium behaves in a similar way when adsorbing on oxidized tungsten [9].

The threshold of Sm atom ESD appearance from the surface of oxidized tungsten is ~26 eV, which is very close to the oxygen 2*s* level ionization energy, ~23 eV [17]. We believe, however, that the main channel of adsorption bond excitation for the ESD of alkali metals, which is associated with excitation of the O 2*s* level [4, 5], as in the Eu atom ESD [8, 9], does not operate in the ESD of Sm atoms. The alkali metal atom yield increases monotonically with electron energy within the interval 20–30 eV above the threshold, remains practically constant up to 100–200 eV, and falls off slowly thereafter. On the other hand, the yield of Sm and Eu atoms has a resonance character, with the peak positions correlating well with the Sm and Eu 5*p* and 5*s* core level energies. In addition, the existence of two valence electrons in Sm and Eu does not result in a noticeable increase in the size of these atoms after neutralization of the corresponding ions, which was essential for the onset of ESD of alkali metal atoms [4, 5]. Therefore, we assume that REMs desorb by another ESD mechanism and that the Sm atom ESD appearance threshold is connected with excitation of the Sm 5*p* electron to the 5*d* state, which descends in the field of the 5*p* hole below the Fermi level to form a core exciton.

As reported in a number of publications [21–23], only the formation of a core-bound exciton (excitation of a core electron to a local bound state), rather than ionization of a core electron followed by its transfer to the conduction band and higher, can produce a strong resonance peak in the absorption spectrum. This is equally relevant for to absorption spectra of the *F* cen-

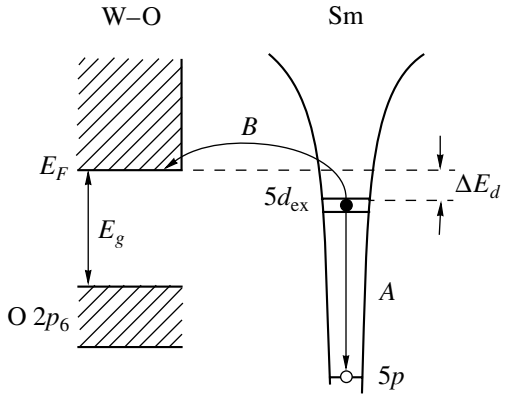

Fig. 7. Schematic of relaxation of the Sm adatom $5d_{ex}$ excited state with a hole in the 5*p* level. E_F is the Fermi level, and E_g is the band gap of oxidized tungsten.

ters in ionic crystals; resonance absorption near the *F* band is substantially stronger than the band due to transition to the continuum. The reasons for this large difference remain unclear [24]. Calculation of the absorption spectrum of lanthanum oxide in the region of the $2p \longrightarrow 5d$ transition showed, however, that the absorption does feature a clearly pronounced resonance character in the vicinity of the $2p$–$5d_{ex}$ exciton formation energy [23]. The $5d_{ex}$state is localized and forced below the Fermi level in the field of the 2*p* hole. At higher excitation energies, where the 2*p* electron transfers to the free state (6*sp*), the absorption probability is ~50 times lower than that in the exciton absorption region. The width of the calculated and observed resonance peak is 10–15 eV and is connected with the finite lifetime of this state, which decays as the $5d_{ex}$ electron transfers to the conduction band or the 5*p* state.

One can draw an analogy in electronic structure between Eu and Sm chemisorbed on an oxygen-monolayer-coated W and the compound La_2O_3. They form unoccupied 5*d* and 4*f* states above the Fermi level, which can descend in the field of the 5*d* hole into the valence electron band, thus exhibiting quasi-atomic behavior with intense resonances observed at the $5p \longrightarrow 5d$ transitions [21]. The fact that Eu and Sm, unlike La, in addition to unoccupied $4f^0$ states, also have occupied $4f^n$ states does not play a significant role, because they lie somewhere at the valence band level or lower, are strongly localized, and, lying closer to the nucleus than the 5*p* and 5*d* electrons (the radii of the 4*f*, 5*p*, and 5*d* electronic shells are ~0.3, ~0.75, and ~1.0 Å, respectively), do not change when the 5*p* hole forms [25].

Therefore, we assign the 34- and 46-eV resonance peaks in the Sm atom ESD yield to excitation of the Sm 5*p* and 5*s* states to the $5d_{ex}$ state lowered by the hole field under the Fermi level by ΔE_d and to its decay to the conduction band. In the final count, we obtain an adsorbed doubly-charged ion with a core hole.

While the result is the same as that for direct core level ionization, the probability of the two-stage process may turn out to be considerably higher if the probability *B* of transition to the conduction band is higher than the probability Å of hole recombination $5d_{ex} \longrightarrow 5p$ (Fig. 7). The ratio of these quantities for the allowed transition *A* can be estimated as $B/A \approx 1.5 \times 10^3 \exp(-\Delta E_d/kT)$ [24]. It thus follows that $B/A \geq 1$ for $\Delta E_d \leq 7.3kT$.

The quantity ΔE_d also depends on the local adatom environment, i.e., on the coverage, and, possibly, on *T*. The Sm^{2+} ion formed in the two-stage process moves toward the surface under the action of the image forces because of the increased charge and reduced repulsion between the outer shells of the Sm^{2+} ion and of the substrate atoms [26]. Electron excitation in more shallow levels does not bring about ESD of Sm atoms, because the lifetime of these excitations is short compared to the atom displacement time.

After neutralization, which occurs under simultaneous filling of the 5*p* hole and of the valence shell, Sm atoms are reflected from the surface and traverse the adsorbed Sm layer. The decrease in the Sm atom yield observed to occur at low coverages with increasing Θ (Fig. 2) can be accounted for by resonance reionization of the Sm atoms as they cross the Sm ion adlayer, as well as by a lowering of the $5d_{ex}$ level with respect to the Fermi level, ΔE_d, occurring in the field of positive adatom ions. The growth of $\Delta E_d(\Theta)$ reduces the probability of exciton decay to the conduction band and, hence, that of Sm^{2+} ion formation. The increase in resonance reionization with Θ is in agreement with experiments [27] and calculations [28] of the scattering of Li^+ ions of energy 1.2 keV from an Al(100) face partially covered by alkali metals. The Li^+ ion neutralization probability does not have a threshold and increases approximately linearly with increasing alkali metal coverage. The above calculations were made for 1.2-keV Li^+ ions, and the kinetic energy of the Sm atoms, if we use the data obtained on alkali-metal atoms [4] in the estimation, should not exceed a few tenths of an electronvolt. Since the Li^+ charge exchange probability grows nearly linearly with decreasing kinetic energy [29], it does not come as a surprise that the yield of very slow Sm atoms reaches a maximum value at coverages less than 0.1. Comparison of Figs. 2 and 4 suggests that neutralization of the Sm^{2+} ions proceeds much more efficiently on the surface of tungsten oxide than on that of tungsten covered by an oxygen monolayer. On the other hand, Eu^{2+} neutralization is practically independent of the degree of tungsten surface oxidation [19]. Because Sm and Eu are neighbors in the Periodic Table, such a qualitative difference in the neutralization indicates that it is very sensitive to the specific features of ion–surface interaction.

The above relates not only to the mechanism of formation of the Sm atom yield peak at E_e = 34 eV but in

equal measure to that located at E_e = 46 eV and associated with excitation of the Sm 5*s* level. The lower intensity of the 46-eV peak compared to that of the peak at 34 eV should apparently be attributed to the lower probability of excitation by electrons of deeper levels belonging to the same shell with a given quantum number [30], as well as to the *s–d* dipole transition being forbidden and the 6*p* state being strongly delocalized.

Thus, the yield of Sm (or Eu) atoms in this ESD channel is, in addition to being proportional to the coverage Θ, proportional to the probabilities of core exciton formation $Q_{ex}(E_e)$, $5d_{ex}$ transition to the conduction band $B(\Theta, T)$, hole filling in the interatomic transition $w_{5p}(\Theta, T)$, neutralization through substrate electron transition to an adatom valence level $w_n(\Theta, T)$, and reionization $w_r(\Theta)$ in the passage of the as-formed neutral atom through the Sm^+ adlayer:

$$q(E_e, \Theta, T) = Q_{ex}(E_e)B(\Theta, T)w_{5p}(\Theta, T)w_n(\Theta, T)w_r(\Theta)\Theta.$$

This quantity is seen to be a very complex function of coverage and temperature, because they act on the distance between the adatom and substrate, the conduction band filling, and the mutual positions of the $5d_{ex}$, 6*sp*, 5*p* adatom levels and the Fermi level. In particular, while a temperature increase enhances the conduction band population, thus reducing the probability $B(\Theta, T)$ of an exciton electron $5d_{ex}$ transferring to it, a rise in the vibration amplitude may increase the same quantity $B(\Theta, T)$ through decreasing ΔE_d.

The temperature dependence of the Sm atom yield can be associated with the exciton level rising above the substrate conduction band bottom (Fig. 7). For low Sm coverages ($\Theta < 0.1$), the exciton level is above the conduction band bottom and transition of the exciton electron into the substrate occurs without activation; i.e., the exciton breaks down with the formation of the Sm^{2+} ion. For high coverages ($\Theta > 0.1$), lateral interactions force the adsorbed Sm ions farther away from the surface, with the exciton level lowering under the conduction band bottom, so that exciton electron transfer to the substrate now requires an activation energy. The exciton level for adsorbed Eu ions lies below the conduction band bottom irrespective of the degree of substrate oxidation and of the surface coverage by europium, and exciton decay involving the formation of an Eu^{2+} ion can take place at elevated temperatures only. Therefore, Eu features a $q(T)$ relation of the type shown in curves *4* and *5* in Fig. 5.

As the Sm^{2+} ion moves away from the surface, its valence level drops below the valence band top, which results in neutralization of the receding ions. For $T >$ 280 K, one may expect either decay of the exciton through electron–hole recombination or a decrease in its localization time, with a corresponding decrease in the Sm adatom yield to zero. The Sm atom disappearance temperature decreases slightly with increasing surface coverage, apparently because the reionization cross section increases with growing coverage and temperature as Sm atoms traverse the adsorbed Sm ion film.

As already mentioned, the resonance peaks at E_e = 42, 54, and 84 eV correlate well with excitation of the $5p_{3/2}$, $5p_{1/2}$, and 5*s* tungsten core levels [17] and, hence, can be assigned to ESD of SmO molecules, which occurs as a result of rupture of the adsorption bond between tungsten and oxygen initiated by the formation of W core excitons. The decrease in the peak intensity observed in going from the peak corresponding to excitation of the W $5p_{3/2}$ level to that due to the W $5p_{1/2}$-level excitation correlates with the lower probability of excitation of a deeper level by electrons [30].

The fact that the critical coverage for SmO molecule ESD is the same, Θ = 0.20 (Fig. 3), irrespective of the W core-level excitation energy is apparently accounted for by the adsorbed layer undergoing rearrangement with increasing coverage; this process provides detection of SmO molecules within a narrow solid angle subtended by a surface ionization detector. The decrease in SmO molecule yield after the maximum occurring at the coverage Θ = 1 can be assigned to the formation of Sm islands, which reduces the lifetime of repulsive excited states.

The yield of SmO molecules grows smoothly with increasing temperature, apparently due to increasing molecular vibration amplitudes (Fig. 6). The abrupt drop in the SmO molecule yield is accounted for by exciton destruction, with the tungsten exciton decay rate being temperature independent in the interval T = 280–460 K (Fig. 6), even though the SmO molecule disappearance falls off close to linearly with increasing surface coverage by samarium. The excitons apparently decay through tunneling processes, whose probability is determined by the samarium coverage of the surface.

We have shown that Sm ESD yield from Sm layers adsorbed on oxidized tungsten behaves in a resonant manner as a function of incident electron energy. The Sm atom yield is related to excitation of the Sm 5*p* and 5*s* core levels, whose resonance excitation is explained as being due to a high density of free 5*d* states in the core hole field. Sm atoms form as a result of reverse motion, which is determined by the reionization of atoms as they pass through the adsorbed Sm ion layer. The temperature dependence of the Sm atom yield can be accounted for by the position of the Sm exciton level relative to the conduction band bottom, which depends on the adsorbed samarium concentration. The resonant yield of SmO molecules finds explanation in the core exciton formation following excitation of the tungsten 5*p* and 5*s* levels, with the exciton lifetime depending both on temperature and on the concentration of adsorbed samarium.

ACKNOWLEDGMENTS

The authors are indebted to I.P. Ipatova, O.V. Konstantinov, and R.A. Suris for useful discussions and valuable criticisms.

This study was supported by the Russian State program "Surface Atomic Structures."

REFERENCES

1. V. N. Ageev, Prog. Surf. Sci. **47**, 55 (1994).
2. T. E. Madey, Surf. Sci. **299/300**, 824 (1994).
3. *Proceedings of the Eighth International Workshop on Desorption Induced by Electronic Transitions, DIET-8*, Ed. by T. E. Madey, F. M. Zimmerman, and R. A. Bartynski (San Alfonso, USA, 1999); Surf. Sci. **451** (2000); *Proceedings of the Seventh International Workshop on Desorption Induced by Electronic Transitions, DIET-7*, Ed. by E. M. Williams and R. E. Palmer (Ambleside, England, 1997); Surf. Sci. **390** (1997).
4. V. N. Ageev, Yu. A. Kuznetsov, and N. D. Potekhina, Fiz. Tverd. Tela (St. Petersburg) **39** (8), 1491 (1997) [Phys. Solid State **39**, 1324 (1997)].
5. V. N. Ageev and Yu. A. Kuznetsov, Phys. Low-Dimens. Semicond. Struct., No. 1/2, 113 (1999).
6. B. V. Yakshinskiy and T. E. Madey, Nature **400**, 643 (1999).
7. V. N. Ageev, Yu. A. Kuznetsov, and N. D. Potekhina, Fiz. Tverd. Tela (St. Petersburg) **36** (5), 1444 (1994) [Phys. Solid State **36**, 790 (1994)].
8. V. N. Ageev and Yu. A. Kuznetsov, Pis'ma Zh. Tekh. Fiz. **26** (13), 86 (2000) [Tech. Phys. Lett. **26**, 579 (2000)].
9. V. N. Ageev, Yu. A. Kuznetsov, and T. E. Madey, J. Vac. Sci. Technol. A **19** (4), 1481 (2001).
10. G. V. Tsyganova, N. Yu. Pasechnik, and N. N. Smirnova, Vysokochist. Veshchestva, No. 2, 43 (1991).
11. *CRC Handbook of Chemistry and Physics* (CRC, Boca Ration, FL, 1992), pp. 10–12.
12. V. K. Medvedev, Candidate's Dissertation (Leningrad State Univ., Leningrad, 1974).
13. V. N. Ageev, O. P. Burmistrova, and Yu. A. Kuznetsov, Fiz. Tverd. Tela (Leningrad) **29** (6), 1740 (1987) [Sov. Phys. Solid State **29**, 1000 (1987)].
14. V. N. Ageev and N. I. Ionov, Fiz. Tverd. Tela (Leningrad) **11** (11), 3200 (1969) [Sov. Phys. Solid State **11**, 2593 (1969)].
15. V. N. Ageev and E. Yu. Afanas'eva, Fiz. Tverd. Tela (St. Petersburg) (in press).
16. M. L. Knotek, Springer Ser. Chem. Phys. **24**, 139 (1983).
17. *Practical Surface Analysis by Auger and X-ray Photoelectron Spectroscopy*, Ed. by D. Briggs and M. Seah (Wiley, New York, 1983; Mir, Moscow, 1987).
18. V. N. Ageev and Yu. A. Kuznetsov, Fiz. Tverd. Tela (St. Petersburg) **44** (6), 1121 (2002) [Phys. Solid State **44**, 1171 (2002)].
19. V. N. Ageev, Yu. A. Kuznetsov, and N. D. Potekhina, Fiz. Tverd. Tela (St. Petersburg) **43** (10), 1894 (2001) [Phys. Solid State **43**, 1972 (2001)].
20. M. V. Loginov and M. A. Mittsev, Fiz. Tverd. Tela (Leningrad) **20**, 2781 (1978) [Sov. Phys. Solid State **20**, 1603 (1978)]; A. Lohani and V. Bhattacharyya, J. Electron Spectrosc. Relat. Phenom. **122**, 79 (2002).
21. F. P. Netzer, G. Strasser, G. Rosina, and J. A. D. Matthew, J. Phys. F **15**, 753 (1985).
22. D. H. Tracy, Proc. R. Soc. London, Ser. A **357**, 485 (1977).
23. A. Mori, Y. Kayanuma, and A. Kotani, Prog. Theor. Phys. Suppl. **106**, 75 (1991).
24. N. F. Mott and R. W. Gurney, *Electronic Processes in Ionic Crystals*, 2nd ed. (Clarendon, Oxford, 1948; Inostrannaya Literatura, Moscow, 1950).
25. J. T. Waber and D. T. Grower, J. Chem. Phys. **42**, 4116 (1965).
26. P. R. Antoniewicz, Phys. Rev. B **21** (9), 3811 (1980).
27. C. B. Weare and J. A. Yarmoff, Surf. Sci. **348**, 369 (1996).
28. D. G. Goryunov, A. G. Borisov, G. E. Makhmetov, *et al.*, Surf. Sci. **401**, 206 (1998).
29. A. G. Borisov and J. P. Ganyacq, Surf. Sci. **445**, 430 (2000).
30. D. Woodruff and T. Delchar, *Modern Techniques of Space Science* (Cambridge Univ. Press, Cambridge, 1986; Mir, Moscow, 1989).

Translated by G. Skrebtsov

Physics of the Solid State, Vol. 45, No. 5, 2003, pp. 983–989. Translated from Fizika Tverdogo Tela, Vol. 45, No. 5, 2003, pp. 937–943.

POLYMERS AND LIQUID CRYSTALS

Dielectric Relaxation in Polymers and Copolymers of Methacrylates and Methacrylamides with Chromophoric Groups in Side Chains

N. V. Afanas'eva, T. I. Borisova, V. N. Ivanova, V. A. Luk'yashina, G. K. Lebedeva, G. I. Nosova, N. N. Smirnov, N. A. Solovskaya, and V. V. Kudryavtsev

Institute of Macromolecular Compounds, Russian Academy of Sciences, Bol'shoĭ pr. 31, St. Petersburg, 199004 Russia

e-mail: Diel@imc.macro.ru

Received May 16, 2002; in final form, October 1, 2002

Abstract—The dielectric relaxation and molecular motion in polymers and copolymers of methacrylates and methacrylamides with π-conjugated anisodiametric chromophoric groups in the side chains are investigated in the temperature range from –170 to 120–150°C at frequencies of 0.1–100 kHz. It is shown that the motion of chromophoric groups and relaxation transitions in these systems are similar to those in liquid-crystal polymers with side mesogenic chains. The chromophoric groups execute orientational motion of two types: orientational rotations about the long axes in the glass state and orientational rotations about the short axes at temperatures above T_g. The π-conjugation excludes local motion within the chromophoric group. © *2003 MAIK "Nauka/Interperiodica".*

1. INTRODUCTION

Comblike polymers or copolymers with covalently bonded chromophoric groups in the side chains are widely used as polymeric systems with nonlinear optical properties [1–4]. Since these systems offer a number of advantages over other polymers, they are very promising for technical applications. The use of monomers with covalently bonded chromophoric groups makes it possible to prepare polymers with a stable homogeneous distribution of the chromophore over the polymer bulk. In this case, the degree of orientation of chromophoric groups in an electric field (poling) turns out to be higher than that in polymers containing chromophoric groups in the main chains. As a rule, π-conjugated groupings are used as chromophores in side chains of the polymers. Consequently, there appears a nonlinear dependence of the polarization on the applied field. The second-harmonic generation depends on the depolarization of the π-electron system with donor and acceptor properties [5]. Under these conditions, it is possible to achieve maximum nonlinear effects and fast response. Conjugated chromophores also possess relatively large third-order nonlinearity coefficients [6].

The properties of optically nonlinear systems are substantially affected by relaxation of the external field–induced orientation of chromophoric groups, i.e., by the time characteristics of the disorientation (randomization) of the chromophore axes after switching off the external field. These characteristics can exhibit complex behavior depending on the disorientation mechanism. For example, the relaxation proceeding in systems with a chromophore that contains groupings capable of isomerizing involves at least two (fast and slow) stages. According to Buffeteau *et al.* [1] and Ho *et al.* [2], the fast stage of relaxation is associated with *trans–cis* isomerization of azobenzene groups. The slow randomization stage is attributed to a cooperative motion executed by the main chains of polymers at temperatures corresponding to a transition from the glass state to the high-elasticity state. However, there is a great deal of experimental evidence that the slow relaxation can occur at temperatures considerably below the glass transition point T_g [1, 7–9]. For polyimides whose side chains are formed by chromophoric groups introduced through flexible spacers, the relaxation of the orientation of chromophoric groups can be observed at temperatures more than 300 K below the glass transition point T_g [8]. The rate of disorientation of the chromophore axes at temperatures close to T_g increases drastically [8]. It was assumed that, in this case, the slow randomization of the chromophore in the side chain at temperatures below T_g is governed by a local motion without participation or with a limited participation of the main chain. At temperatures close to T_g, the drastic increase in the disorientation rate is caused by an intensive thermal motion of macromolecular chains due to a defreezing of segmental mobility.

It should be emphasized that the external field–induced orientation of chromophoric groups depends on the temperature and reaches the highest degree at temperatures near the glass transition point T_g [10]. These findings indicate that the generation of optical

1063-7834/03/4505-0983$24.00 © 2003 MAIK "Nauka/Interperiodica"

Structures of the homopolymers and random copolymers 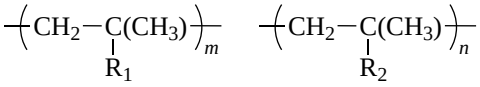

Designations	R_1	R_2	*m*	*n*
P1	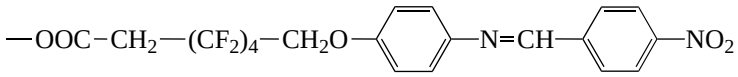		100	0
P2	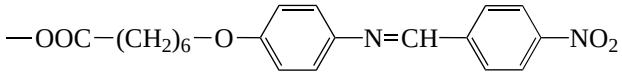		100	0
CP3	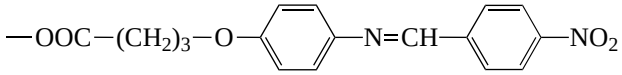	–OOC–CH_2–$(CF_2)_4$H	20	80
CP4	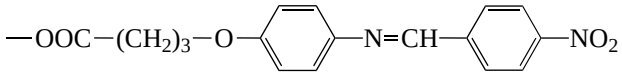	–OOC–CH_2–$(CH_2)_4$H	20	80
CP5	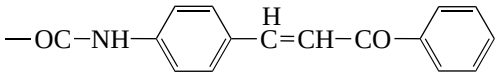	–OOC–CH_2–$(CF_2)_4$H	40	60
CP6	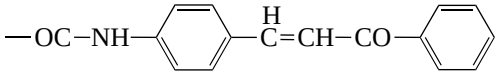	–OOC–CH_2–$(CH_2)_4$H	60	40

nonlinearity is directly related to the relaxation properties of the system not only at temperatures close to T_g (the α relaxation transition) but also at temperatures below T_g at which the relaxation can proceed in small local regions.

The purpose of the present work was to investigate the intrachain dynamics and dielectric relaxation in methacrylate and methacrylamide polymers and copolymers whose side chains contain π-conjugated anisodiametric chromophoric groups, namely, 4'-(4-nitrobenzylideneamino)phenol derivatives [11].

The dielectric relaxation and relaxation phenomena responsible for the slow relaxation stage of nonlinear optical coefficients are similar in nature. These phenomena are associated with the orientation of dipoles in an electric field on the molecular level. In this respect, the methods based on measurements of both the dielectric relaxation and relaxation of nonlinear optical characteristics should provide information on the chain dynamics in polymers [5]. It is believed that, in both cases, the activation characteristics and the relaxation times of the corresponding processes should be close to each other. Therefore, the results of dielectric measurements can be useful in designing the architecture of a monomer unit for the purpose of obtaining optimum temperature–time characteristics of the optical nonlinearity of polymers.

The chemical structures and designations of the homopolymers and random copolymers chosen as the objects of our investigation are given in the table.

The homopolymers differ in the structure of their side chain flexible fragment (spacer), which binds the chromophoric group to the macromolecular backbone. In polymer P1, the spacer includes a $(CF_2)_4$ fragment and contains six carbon atoms. The spacer in polymer P2 consists of six methylene groups. The random copolymers differ in the structure of the chromophore-containing comonomer units and spacers. The chromophores in copolymers CP3 and CP4 contain the –N=CH– azomethine group. In copolymers CP5 and CP6, the chromophores include the –CH=CH– stilbene group. Furthermore, the chromophoric group in copolymers CP3 and CP4 is attached through the kinetically flexible chain $(CH_2)_3O$, whereas the amide group in copolymers CP5 and CP6 extends the conjugated chain and excludes the internal rotation in the side chain. The second comonomer has considerably shorter side chains: $CH_2(CF_2)_4H$ in copolymers CP3 and CP5 and $(CH_2)_5H$ in copolymers CP4 and CP6. In this series of compounds, we determined the screening role of the second chromophore-free comonomer and assessed additional interactions that occur between side chains due to fluorine-containing groupings. Moreover, the local and cooperative chain dynamics can change depending on the flexibility of the spacer attaching the

chromophoric group to the main chain. In this respect, we elucidated how the chemical structure of the homopolymers and copolymers under investigation affects the dynamics of the chromophoric group.

The second purpose of this work was to identify the relaxation transitions occurring at temperatures that correspond either to fast orientation of chromophore dipoles in an external field or to an inverse process, namely, slow relaxation of nonlinear optical characteristics.

2. SAMPLE PREPARATION AND EXPERIMENTAL TECHNIQUE

The homopolymers and copolymers were synthesized through radical polymerization of the corresponding monomers in the bulk (P1) or in a 30 wt % dimethylacetamide solution (P2 and CP3–CP6) with dinitrilazodiizobutyric acid (1 wt %) as an initiating agent at a temperature of 60°C.

All the polymers were refined by reprecipitation from solutions in cyclohexanone to a methanol–water mixture (1 : 3). The characteristic viscosity η of polymers P1 and P2 in acetone was approximately equal to 0.5×10^2 cm^3/g. The characteristic viscosities η of copolymers CP3 and CP4 in cyclohexanone were 1.62×10^2 and 0.4×10^2 cm^3/g, respectively.

The structure and the composition of the synthesized polymers were examined by ^{1}H NMR and UV spectroscopy.

The ^{1}H NMR spectra were recorded on a Bruker AC-200 spectrometer (200.1 MHz) with respect to the solvent signals. In this work, deuterated acetone $(CD_3)_2CO$ and dimethyl sulfoxide (DMSO-d_6) were used as solvents. The absorption electronic spectra were measured on a Specord M-40 spectrophotometer.

The ^{1}H NMR spectra of homopolymers P1 and P2 in deuterated dimethyl sulfoxide and copolymers CP3 and CP4 in deuterated acetone contain the proton signals characteristic of the chromophoric fragment. The chemical shifts δ of the ^{1}H NMR signals with respect to that of a reference sample (tetramethylsilane) are as follows: δ = 1.05–2.20 (H_{aliph}), 3.20–4.50 (CH_2O–Ar), 4.90 (CH_2–CF_2), 6.90–7.80 (H_{arom}), and 8.20–8.60 (H and –N=CH_2) ppm. The relative number of the chromophoric fragments in copolymers CP3 and CP4 was estimated at $m : n = 20 : 80$ from the ratio of the signals in their ^{1}H NMR spectra.

The UV spectra of films prepared from homopolymers P1 and P2 and copolymers CP3 and CP4 exhibit absorption bands characteristic of the chromophore in the range 328–344 nm.

Methacrylates of 4'-(4-nitrobenzylideneamino)phenol derivatives were synthesized according to procedures similar to those described in [12].

The ^{1}H NMR spectra of copolymers CP5 and CP6 in deuterated dimethyl sulfoxide contain the proton signals characteristic of the chromophoric fragment at δ = 0.71–1.52 ($5H_{aliph}$), 9.51–10.000 (H and –NHCO), and 7.41–8.32 (11H, $9H_{arom}$, and CH=CH) ppm. From the ratio of the signals in the ^{1}H NMR spectra of these copolymers, the relative numbers of chromophoric fragments in CP5 and CP6 were estimated at $m : n$ = 40 : 60 and 60 : 40, respectively.

The UV spectra of films of copolymers CP5 and CP6 are characterized by the absorption bands typical of the chromophore in the range 340–350 nm. The *N*-(4-chalcone)methacrylamide monomer was prepared from 4-aminochalcone [13] and methacryloyl chloride in dimethylacetamide at 0°C and had the melting temperature T_m = 152–153°C.

The dielectric losses ($\tan\delta$) were measured using a TR-9701 instrument at frequencies of 0.1–100 kHz in the temperature range from –160 to 150°C. A two-electrode cell with electrodes prepared from chrome-plated brass with a Teflon insulation were used in the experiments. The measurements were performed in a dried air atmosphere after holding the samples at a temperature of 60°C under vacuum. The samples were prepared in the form of films 30–50 μm thick through pressing at temperatures 15–20 K above the glass transition point T_g. The accuracy in measurement of $\tan\delta$ was no less than 1–2%.

3. RESULTS AND DISCUSSION

Dielectric relaxation in polymethacrylates has been studied for polymers with side chains of significantly different structures. Local relaxation in side chains is predominantly associated with the intrachain rotations. This process proceeds either without participation or with insignificant participation of the main chain when its conformation remains unchanged. In the case where the side chains contain groupings that induce strong polar or dispersion interactions or form hydrogen bonds, the relaxation processes and the corresponding local motions are characterized by specific features. Examples are provided by specific types of orientational motion in liquid-crystal polymers with anisodiametric mesogens in the side chains and in crystallizing homologs of comblike polymers [14, 15]. It can be expected that the kinetically rigid, anisodiametric chromophoric groups, which are contained in the side chains of the studied polymers, can also substantially affect the interaction between the side chains. Since the systems considered in the present work are structurally similar to liquid-crystal polymers, the relaxation proceeding in our polymers should be interpreted taking into account the specific features of molecular mobility in liquid-crystal polymers with side mesogenic chains. First, in the dielectric relaxation spectrum, it is necessary to separate the contributions associated with chromophore motions of different types. Then, the relation

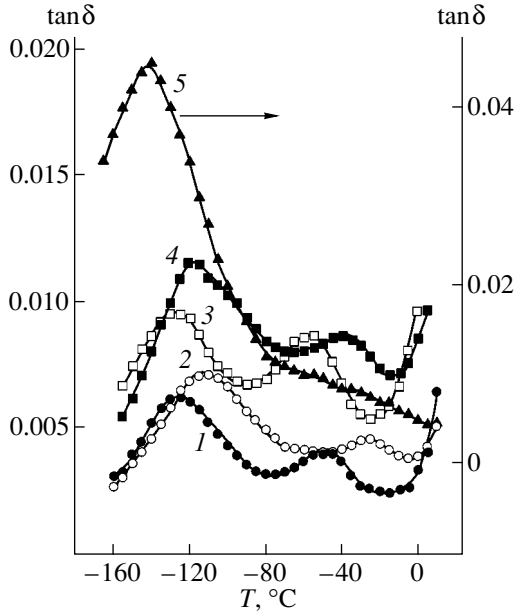

Fig. 1. Temperature dependences of tanδ for (*1*, *2*) P1 and (*3*, *4*) P2 homopolymers and (*5*) poly(fluorobutyl methacrylate). Frequency of measurements, kHz: (*1*, *3*, *5*) 0.1 and (*2*, *4*) 1.

between the polymeric structure and the orientational chromophore motion should be revealed for the series of polymers under investigation.

Figure 1 shows the temperature dependences of tanδ for homopolymers P1 and P2 and, for comparison, a similar dependence for poly(fluorobutyl methacrylate) in the low-temperature range. The dependences of the corresponding relaxation times in the Arrhenius coordinates are depicted in Fig. 2a. A comparison of the results obtained for the chromophore-containing and chromophore-free polymers clearly demonstrates that the number of dipole relaxation regions and their temperature and frequency ranges, and, hence, the relaxation times and activation energies (30–40 kJ/mol), coincide for all three polymers [17].

The dielectric loss peak observed in the range from –130 to –80°C for homopolymer P1 should be assigned to the motion in the $(CF_2)_4$ fragment. Note that dielectric losses in this temperature range also occur for homopolymer P2, in which the $(CH_2)_6$ spacer does not contain fluorine. This indicates that the dipole relaxation of kinetic units involving the ester group and ether oxygen also proceeds in the aforementioned temperature and frequency ranges [17]. The height of the peak in the temperature dependence of tanδ for homopolymer P1 is lower than that for homopolymer P2. This can be explained by the restrictions of the orientation in polymer P1 due to the stronger interactions and the spatial ordering of fluoroalkyl fragments, which is confirmed by the ^{19}F nuclear magnetic relaxation [18, 19].

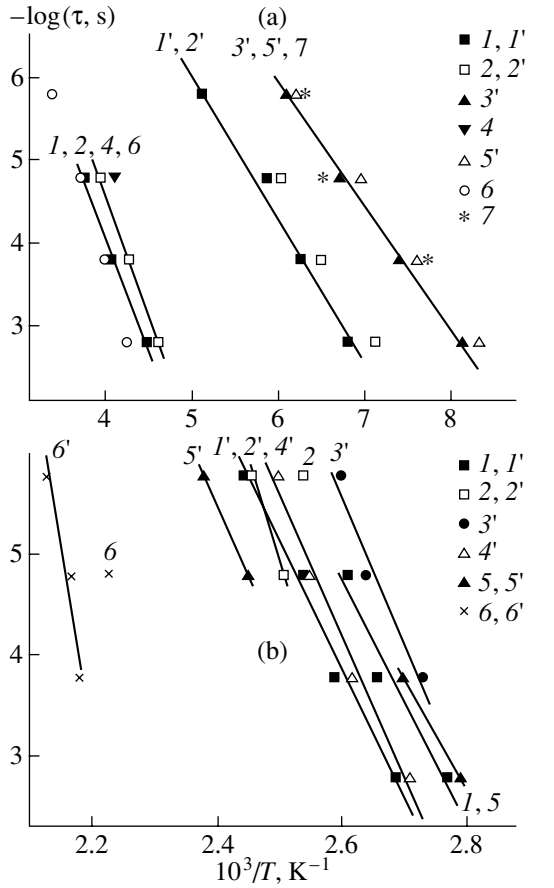

Fig. 2. Dependences of the relaxation time on the reciprocal of the temperature for homopolymers and copolymers (*1*, *1*') P1, (*2*, *2*') P2, (*3*') CP3, (*4*, *4*') CP4, (*5*, *5*') CP5, and (*6*, *6*') CP6 in (a) β (unprimed numerals) and γ (primed numerals) dipole relaxation regions and (b) α (unprimed numerals) and δ (primed numerals) dipole relaxation regions.

At present, the mechanism of motion associated with the relaxation region at temperatures ranging from –50 to 0°C cannot be considered to be established conclusively. Relaxation processes with characteristic times lying in a narrow range in the Arrhenius coordinates are observed in liquid-crystal polymers with mesogenic groups in the main or side chains irrespective of the chemical structure [20]. The corresponding motion is treated as orientational small-angle rotations of mesogenic groups around their long axes, which do not require large volumes.

In our case, the rotation in the side chain can occur owing to CH_2 hinges in homopolymer P1 or ether oxygen in homopolymer P2.

At high temperatures, we failed to observe relaxation phenomena because of the superposition of dielectric losses due to electrical conduction. We succeeded in overcoming this problem by measuring the dielectric losses in mechanical mixtures of the polymers with poly(styrene). Poly(styrene) is dielectrically

transparent at temperatures up to the glass transition point T_g. Above this temperature, the α transition with a small peak in the temperature dependence of tanδ is observed for poly(styrene) (Fig. 3). It is known that, in mixtures whose components are incompatible and form coarse-grained phases, the glass transition points T_g and, hence, the temperatures of the α transitions for each component do not depend on the quantitative composition and coincide with those for homopolymers. Figure 3 illustrates this situation by using the example of a model mixture of poly(styrene) with poly(*p*-chlorostyrene) (10 wt %).

The high-temperature relaxation in the polymers under investigation was examined with the use of mixtures of 10 wt % homopolymer P1 (or P2) with 90 wt % poly(styrene). It can be seen from Fig. 4 that the dielectric losses in poly(styrene) are very small and cannot distort the curves describing the temperature dependences of tanδ for the chromophore-containing polymers. Two transitions with close relaxation times rather than one transition are observed in the glass transition ranges of the chromophore-containing polymers. The α transition has a trivial meaning and is caused by the increase in the rate of segmental motion in the main chains. The origin of the δ transition is associated with orientational rotations of mesogenic groups or, in our case, chromophoric groups about their short axes. Such a rotation requires a large volume and usually becomes possible at a temperature above the glass transition point T_g, i.e., under the conditions of cooperative motion of macromolecular backbones. This accounts for the high degree of orientation of the chromophore axes upon poling and the high rates of their disorientation after switching off the field at high temperatures.

The dipole relaxation processes in the copolymers (Figs. 5, 6) and the homopolymers, in principle, are identical in nature. However, the differences in the structure of the side chains of the chromophore-containing comonomer and in the comonomer structure lead to a change in the quantitative characteristics of the transitions.

In copolymers CP3 and CP4, the chromophoric group is attached to the main chain through the $-(CH_2)_3O-$ spacer. In liquid-crystal polymers, the γ relaxation transition governed by the motion of the flexible fragment in the spacer and its terminal polar groups manifests itself in the range from –130 to –100°C only when the spacer consists of five or more methylene groups [21]. As can be seen from Fig. 5, the γ transition in the range from –130 to –100°C is actually absent in copolymer CP4. For copolymer CP3, the symmetric part of the maximum in the dependence $\tan\delta(T)$ at these temperatures can be assigned to the contribution associated with the dipole polarization in the $(CF_2)_4$ fragment. In this case, the main contribution to the γ relaxation process is determined by the orientational motion in the $(CF_2)_4$ fragment of the second comonomer.

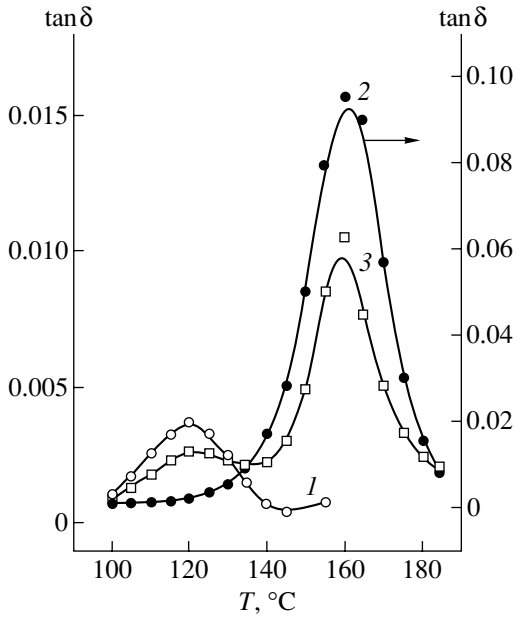

Fig. 3. Temperature dependences of tanδ for (*1*) poly(styrene), (*2*) poly(*p*-chlorostyrene), and (*3*) a mechanical mixture of 90 wt % poly(styrene) with 10 wt % poly(*p*-chlorostyrene). The frequency of measurements is 1 kHz.

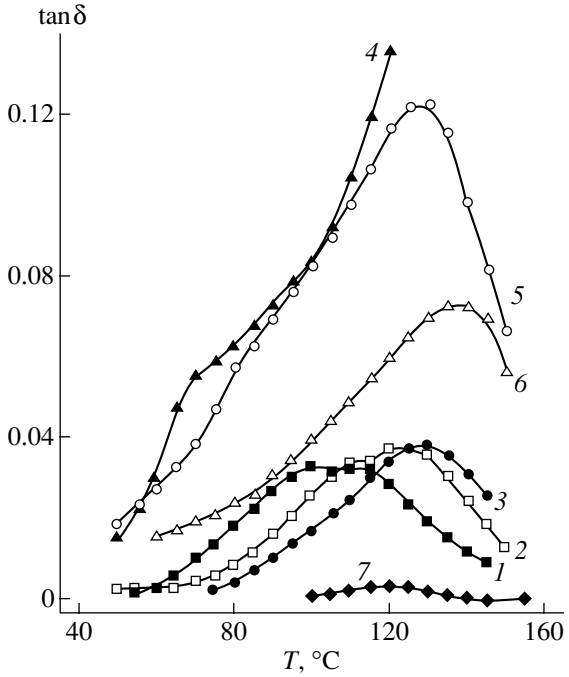

Fig. 4. Temperature dependences of tanδ for mixtures of 90 wt % poly(styrene) with (*1*–*3*) 10 wt % P1 and (*4*–*6*) 10 wt % P2 homopolymers and for (*7*) poly(styrene). Frequency of measurements *f*, kHz: (*1*, *4*, *7*) 1, (*2*, *5*) 10, and (*3*, *6*) 100.

A similar relaxation behavior is observed in copolymers CP5 and CP6 at temperatures below the glass

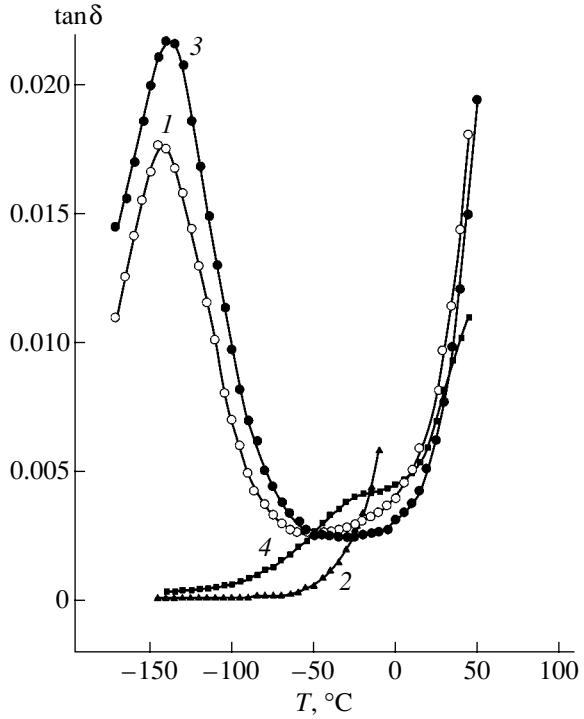

Fig. 5. Temperature dependences of tanδ for (*1*) CP3, (*2*) CP4, (*3*) CP5, and (*4*) CP6 copolymers in the β and γ relaxation regions. The frequency of measurements is 1 kHz.

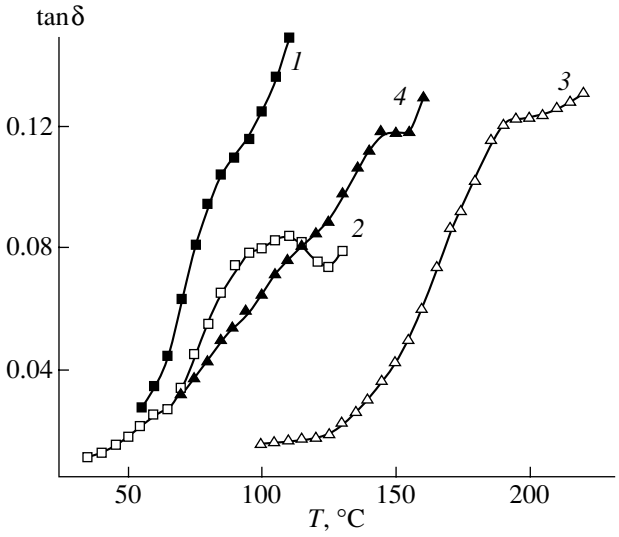

Fig. 6. Temperature dependences of tanδ for (*1*) CP3, (*2*) CP4, (*3*) CP5, and (*4*) CP6 copolymers. Frequency of measurements *f*, kHz: (*1*, *2*) 1, (*3*) 10, and (*4*) 100.

transition point T_g (Fig. 5). The γ transition is absent in copolymer CP6, because the spacer attaching the chromophoric group to the main chain is not flexible and the second comonomer does not contribute to the dielectric losses at low temperatures. The contribution of the $(CF_2)_4$ fragment is similar to that considered for copolymer CP3. Compared to the homopolymers, in the copolymers, the screening of the side fluorine-containing chain fragments by the fluorine-free comonomers decreases the tendency of the $(CF_2)_4$ group to intrachain association. As a consequence, the temperatures of the γ transition in the copolymers are lower than those in the homopolymers (Fig. 2a). It can be seen from Fig. 5 that the β process (in the range from –20 to –40°C) is weakly pronounced in the copolymers. One of the reasons for this circumstance is a lower chromophore content in the copolymers.

The relaxation transitions in copolymers at temperatures above the glass transition point T_g are similar to those observed in homopolymers. The asymmetry revealed in the dependence $\tan\delta(T)$ suggests the occurrence of two processes. This implies that the chromophoric groups in the copolymers, as in the homopolymers, can execute orientational rotations about their short axes at temperatures higher than the glass transition point. Therefore, the shoulder in the ascending portion of the peak in the dependence $\tan\delta(T)$ should be assigned to the α transition. The shape of the dependences indicates that the component associated with the δ transition has a somewhat higher intensity. At high frequencies, the δ transition determines the location of the peak in the temperature dependence of tanδ. It is of interest that the temperatures of the α transitions in both homopolymers and copolymers CP3 and CP4 are very close to each other and differ by no more than 10 K. Moreover, the corresponding relaxation times are also close for the polymers under investigation. These methacrylates have the same main chains and differ only in the structure of the side chains. Consequently, the cooperative segmental motion, in which the ester groups adjacent to the main chain are involved, occurs without participation of the remaining side chain fragments and does not depend on their structure.

In copolymers CP5 and CP6, the chromophoric group is attached to the main chain through the amide group and, hence, the side chain is completely conjugated and rigid.

As was shown in [22], the amide group attaching the side chain to the main chain significantly changes the relaxation behavior of the polymer due to the formation of intrachain hydrogen bonds. There arise regions with a rigid, as if, ladder structure of the macromolecular backbone. In copolymer CP6, additional transitions are revealed at ~30 and 70°C and the temperatures of the α and glass transitions shift to ~150°C (Fig. 2b). The changes observed in copolymer CP5 are less pronounced. This can be explained by the difference in the comonomer structure: owing to strong interactions, the $(CF_2)_4$ fragments prevent the formation of hydrogen bonds.

4. CONCLUSIONS

Thus, the results obtained in the present work allowed us to draw the inference that the orientational motion of anisodiametric rigid chromophoric groups occurs at temperatures slightly above the glass transition point T_g. This motion requires rotations of chromophoric dipole moments about the short axes of the chromophoric groups. In liquid-crystal polymers, the δ transition proceeding through a similar mechanism also occurs at temperatures higher than the glass transition point T_g. The cooperative motion of the main chains is most likely a necessary condition for the appearance of the sufficiently large-volume fluctuations required for orientational motion of the chromophoric groups. In order for the chromophoric groups to be disoriented at temperatures below the glass transition point T_g, the macromolecules must have such a structure that ensures a real probability of occurrence of orientational rotations of the chromophoric groups about their short axes.

A change in the structure and the screening of the interaction between the side chains due to the copolymerization do not noticeably affect the orientational motion of the chromophoric groups.

The mobility of the chromophoric groups in polymethacrylates with sufficiently long side chains containing these groups is similar to that of mesogenic groups in liquid-crystal polymers with side mesogenic chains. In this case, the glass transition temperature T_g is determined by the structure of the main chain and does not depend on the structure of the side chains in the polymers under consideration. The change observed in the glass transition temperature T_g when changing over from the methacrylate chain to the methacrylamide chain is associated with the increase in the rigidity of the macromolecular backbone due to the formation of hydrogen bonds stabilizing the main chain.

ACKNOWLEDGMENTS

This work was supported by the Russian Foundation for Basic Research, project no. 00-15-97-297.

REFERENCES

1. T. Buffeteau, F. L. Labarthet, M. Pezolet, and C. Sourisseau, Macromolecules **31** (21), 7312 (1998).
2. M. S. Ho, A. Natansohn, and P. Rochon, Macromolecules **28**, 6124 (1995).
3. M. S. Ho, A. Natansohn, and P. Rochon, Macromolecules **29**, 44 (1996).
4. D. Broun, A. Natansohn, and P. Rochon, Macromolecules **28**, 6116 (1995).
5. C. Y. Stacey, M. N. Ostrovsky, and H. S. Zackritz, in *Dielectric Spectroscopy of Polymeric Materials: Fundamental and Applications*, Ed. by Y. P. Runt and J. J. Fitzgerald (Am. Chem. Soc., Washington, DC, 1998).
6. M. Sylla, D. Manaiba-Maximea, A. M. Abbu, and J. Delaunau, Polymer **21**, 3507 (2000).
7. H. Müller, J. Müller, O. Nuyhen, and P. Strohriegl, Macromol. Rapid Commun. **13**, 289 (1992).
8. Z. Sokkat, P. Pretre, and A. Knoelson, J. Opt. Soc. Am. B **15** (1), 401 (1998).
9. W. Kim Mee, A. Rastegar, I. D. Olenic, *et al.*, Mol. Cryst. Liq. Cryst. **352**, 407 (2000).
10. A. Dhinojwala, G. K. Wong, and J. M. Torkelson, J. Chem. Phys. **100** (8), 6046 (1994).
11. G. K. Lebedeva, I. M. Sokolova, V. N. Ivanova, *et al.*, Fiz. Tverd. Tela (St. Petersburg) **43** (4), 750 (2001) [Phys. Solid State **43**, 783 (2001)].
12. B. K. Mandal, T. Takahashi, M. Maeda, *et al.*, Macromol. Chem. Phys. **192**, 1019 (1991).
13. W. Davey and I. R. Gwilt, J. Chem. Soc. **3**, 1008 (1957).
14. *Side Chain Liquid Crystal Polymers*, Ed. by C. B. McArdle (Blackie, Glasgow, 1989).
15. T. I. Borisova, L. L. Burshteĭn, V. A. Shevelev, *et al.*, Vysokomol. Soedin., Ser. A **13** (10), 674 (1971).
16. T. I. Borisova, L. D. Budovskaya, V. N. Ivanova, *et al.*, Vysokomol. Soedin., Ser. A **22** (12), 2672 (1980).
17. T. I. Borisova and N. A. Nikonorova, Macromol. Chem. Phys. **199**, 2147 (1998).
18. E. R. Gasilova, V. A. Shevelev, V. N. Ivanova, and M. I. Bitsenko, Vysokomol. Soedin., Ser. A **37** (12), 2013 (1995).
19. Yu. Ya. Gotlib, I. A. Torchinskiĭ, and V. A. Shevelev, Vysokomol. Soedin., Ser. A **39** (12), 2005 (1997).
20. N. Nikonorova, T. Borisova, V. Shibaev, *et al.*, Macromol. Chem. Phys. **8**, 204 (2001).
21. N. Nikonorova, T. Borisova, A. Stakhanov, and V. Shibaev, Mol. Cryst. Liq. Cryst. **331**, 59 (1999).
22. T. I. Borisova, L. L. Burshteĭn, N. A. Nikonorova, and V. P. Shibaev, Vysokomol. Soedin., Ser. A **24** (8), 1669 (1982).

Translated by O. Borovik-Romanova

Physics of the Solid State, Vol. 45, No. 5, 2003, pp. 990–1001. Translated from Fizika Tverdogo Tela, Vol. 45, No. 5, 2003, pp. 944–953.

POLYMERS AND LIQUID CRYSTALS

Fluctuations of Orientational Order in a Uniaxial Nematic Liquid Crystal with Biaxial Molecules and Its Response to an External Field

E. M. Aver'yanov

Kirensky Institute of Physics, Siberian Division, Russian Academy of Sciences, Akademgorodok, Krasnoyarsk, 660036 Russia

e-mail: aver@iph.krasn.ru

Received June 4, 2002; in final form, October 18, 2002

Abstract—Homogeneous thermal fluctuations of the orientational order parameters S and G of biaxial molecules in a uniaxial nematic liquid crystal are investigated in the framework of the molecular–statistical theory. It is demonstrated that the molecular biaxiality significantly affects the order parameters S and G, their temperature dependences in the nematic phase, the amplitude and the temperature dependence of the order parameter fluctuations in the nematic and isotropic phases, and the character of the transition from the nematic phase to the isotropic liquid phase. It is established that the fluctuations of the parameters S and G in the nematic phase are related to the temperature dependences of S and G and the susceptibilities χ_S and χ_G of the nematic liquid crystal to external fields, which leads to a change in the parameters S and G at a fixed director orientation. Explanations are offered for the known experimental data on the orientational ordering of biaxial molecules under the action of external fields in the isotropic phase of nematic liquid crystals. *© 2003 MAIK "Nauka/Interperiodica".*

1. INTRODUCTION

The orientational order of lathlike biaxial molecules with respect to the director **n** in a uniaxial calamitic nematic liquid crystal is characterized by the Saupe matrix elements [1]:

$$S_{ij} = \langle 3\cos\theta_{i\mathbf{n}}\cos\theta_{j\mathbf{n}} - \delta_{ij}\rangle/2, \quad (1)$$

where $\theta_{i\mathbf{n}}$ is the angle between the ith axis of the molecular coordinate system xyz and the director **n** and the brackets $\langle\ldots\rangle$ indicate statistical averaging. In the case of molecules with point symmetry group (C_{2v}, D_2, or D_{2h}), when the intrinsic coordinate system of the matrix S_{ij} is chosen as the molecular coordinate system, there are two independent order parameters, namely, $S = S_{zz}$ and $G = S_{xx} - S_{yy}$.

A number of important aspects of the influence of the molecular shape on the transition from a nematic phase to an isotropic liquid phase (N–I transition) were considered in [2–11] within different variants of the molecular–statistical theory and molecular models. However, the specific features of variations in the parameters S and G and the two-phase region in the vicinity of the N–I transition have not been investigated as a function of the molecular biaxiality. Moreover, it has been found that the N–I transition becomes similar in character to a second-order transition with an increase in the degree of molecular biaxiality [2–10]. The elucidation of the origin of this effect requires analysis of the fluctuations $\overline{\delta S^2}$, $\overline{\delta G^2}$, and $\overline{\delta S \delta G}$ in the range of the N–I transition, which has not been performed to date.

At present, the fluctuations of the macroscopic tensor order parameter $Q_{\alpha\beta}$ in nematic liquid crystals have been studied in detail in the framework of the Landau–de Gennes theory (see [1, 12, 13] and references therein). The molecular–statistical theory of spatially homogeneous and inhomogeneous fluctuations of the order parameter S for uniaxial molecules in the vicinity of the N–I transition was developed in [14–16]. However, the influence of the molecular biaxiality on the amplitude and temperature dependence of the fluctuations $\overline{\delta S^2}$, $\overline{\delta G^2}$, and $\overline{\delta S \delta G}$ in the nematic and isotropic phases remains unclear.

For calamitic and discotic nematic liquid crystals with uniaxial molecules, the relation of the function $S(T)$ to the fluctuations $\overline{\delta S^2}$ and the linear and nonlinear susceptibilities of the nematic phase to external fields, which are thermodynamically conjugate to the magnitude of S, was established in [17, 18]. For nematic liquid crystals with biaxial molecules, the relation of the dependences $S(T)$ and $G(T)$ to the fluctuations $\overline{\delta S^2}$, $\overline{\delta G^2}$, and $\overline{\delta S \delta G}$ is of even greater interest, because the dependence $G(T)$ in the nematic phase exhibits a nonmonotonic behavior [3, 5, 8]. Furthermore, the order parameter G (like the order parameter S

[1]) in the isotropic phase with molecular ordering induced by external fields anomalously increases as the temperature T_{NI} of the N–I transition is approached [19–21]. In this respect, it is important to reveal how the susceptibilities $\chi_S = (\partial S/\partial h)_{T;\, h\to 0}$ and $\chi_G = (\partial G/\partial h)_{T;\, h\to 0}$ of the nematic and isotropic phases to the external fields h are related to the dependences $S(T)$ and $G(T)$ and also to the fluctuations $\overline{\delta S^2}$, $\overline{\delta G^2}$, and $\overline{\delta S \delta G}$.

In this work, the above problems were analyzed in terms of the molecular–statistical theory. Expressions were derived for the free energy of nonequilibrium and equilibrium states of the nematic phase, and the influence of the biaxiality on the N–I transition was investigated. Moreover, the fluctuations $\overline{\delta S^2}$, $\overline{\delta G^2}$, and $\overline{\delta S \delta G}$ in the nematic and isotropic phases were examined. Consideration was given to the response of a nematic liquid crystal with biaxial molecules to external fields, which leads to a change in the parameters S and G. The relation of the susceptibilities χ_S and χ_G to the temperature dependences of the parameters S and G and their fluctuations was revealed. An interpretation was offered for the experimental data obtained in [19–21].

2. FREE ENERGIES OF A NEMATIC LIQUID CRYSTAL IN NONEQUILIBRIUM AND EQUILIBRIUM STATES

In a uniaxial calamitic nematic liquid crystal consisting of molecules with the aforementioned symmetry, the orientation of the molecular coordinate system xyz with respect to the director coordinate system XYZ ($\mathbf{n} \parallel Z$) is characterized by the Euler angles $\Omega(\phi, \theta, \psi)$. Here, ϕ and θ are the azimuthal and polar angles of the long molecular axis z in the coordinate system XYZ, respectively; and ψ is the rotation angle of the molecule about the z axis. With the use of the orientational distribution function of molecules $f(\Omega)$, we can write

$$\begin{aligned} S \equiv \langle P_2 \rangle &= \int P_2(\cos\theta) f(\Omega) d\Omega, \\ G \equiv \langle D(\theta, \psi) \rangle &= \int (1 - P_2)\cos 2\psi f(\Omega) d\Omega, \end{aligned} \tag{2}$$

where $P_2(\cos\theta)$ is the Legendre polynomial. The quantity G characterizes the degree of hindrance to the rotation of molecules about their long axes z. For given parameters S and G, reasoning from the principle of the maximum informational entropy [22] with due regard for formulas (2) and the normalizing condition for $f(\Omega)$, the function $f(\Omega)$ can be represented in the following form [23]:

$$\begin{aligned} f(\Omega) &= \frac{1}{8\pi^2 Z} \exp(\lambda_P P_2 + \lambda_D D), \\ Z &= \frac{1}{8\pi^2} \int \exp(\lambda_P P_2 + \lambda_D D) d\Omega. \end{aligned} \tag{3}$$

The parameters S and G can be defined by the expressions

$$S = \partial \ln Z/\partial \lambda_P, \quad G = \partial \ln Z/\partial \lambda_D, \tag{4}$$

which form a system of equations for determining $\lambda_P(S, G)$ and $\lambda_D(S, G)$.

We will consider the nematic and isotropic phase at a constant volume. The difference between the free energies of the nematic and isotropic phases per molecule can be written in the form

$$\Delta F = E(S, G) + kT \int \ln[8\pi^2 f(\Omega)] f(\Omega) d\Omega, \tag{5}$$

where $E(S, G)$ is the anisotropic part of the internal energy. In the mean-field approximation, with allowance made for the results of analyzing the intermolecular interactions in nematic liquid crystals [5, 8, 23, 24], we can write

$$E(S, G) = -(u/2)(S + \lambda_1 G)^2, \tag{6}$$

where $u > 0$ and the parameter λ_1 is determined by the molecular properties. For anisotropic dispersion intermolecular interactions in the mesophase, this parameter has the form

$$\lambda_1 = (\gamma_{xx} - \gamma_{yy})/(2\gamma_{zz} - \gamma_{xx} - \gamma_{yy}). \tag{7}$$

Here, γ_{ii} are the molecular polarizability tensor components averaged over the entire spectral range. At $0 \le \lambda_1 \le 1$, molecules have polarizability ellipsoids that are either prolate ($\lambda_1 < 1/3$) or oblate ($\lambda_1 > 1/3$) along the z axis and, correspondingly, form either calamitic or discotic nematic phases. Within the approaches developed in [11, 25], the parameter λ_1 for the same form of $E(S, G)$ [expression (6)] can be associated with the sizes of molecules characterized by an ellipsoidal or more complex shape.

Substitution of formulas (3) and (6) into expression (5) gives the functional of the nonequilibrium free energy:

$$\begin{aligned} \Delta F &= -\frac{u}{2}(S + \lambda_1 G)^2 \\ &+ kT[\lambda_P S + \lambda_D G - \ln Z(\lambda_P, \lambda_D)], \end{aligned} \tag{8}$$

where λ_P and λ_D are the functions of the parameters S and G. Then, taking into account relationships (4), we have

$$\begin{aligned}(\partial F/\partial S)_T &= -u(S + \lambda_1 G) + kT\lambda_P,\\ (\partial F/\partial G)_T &= -u\lambda_1(S + \lambda_1 G) + kT\lambda_D.\end{aligned} \tag{9}$$

The conditions of the thermodynamic equilibrium $(\partial F/\partial S)_T = (\partial F/\partial G)_T = 0$ allow us to obtain the relationships

$$\begin{aligned}\lambda_P(S, G) &= \frac{u}{kT}(S + \lambda_1 G),\\ \lambda_D(S, G) &= \frac{u\lambda_1}{kT}(S + \lambda_1 G)\end{aligned} \tag{10}$$

for determining the dependences $S(T)$ and $G(T)$ corresponding to extrema of functional (8). Substitution of relationships (10) into expressions (3) gives the equilibrium distribution function

$$\begin{aligned}f_e(\Omega) &= \frac{1}{8\pi^2 Z_e}\exp\left[\frac{u}{kT}(S + \lambda_1 G)(P_2 + \lambda_1 D)\right],\\ Z_e &= \frac{1}{8\pi^2}\int \exp\left[\frac{u}{kT}(S + \lambda_1 G)(P_2 + \lambda_1 D)\right]d\Omega,\end{aligned} \tag{11}$$

at which functional (5) has an extremum. With the use of relationships (10) in functional (8), we find the equilibrium free energy

$$\Delta F_e = (u/2)(S + \lambda_1 G)^2 - kT\ln Z_e \tag{12}$$

at the extreme points of functional (8). Expression (12) cannot be treated (as was done in monographs [1, 26] and also in [2, 14]) as a functional valid at arbitrary (nonequilibrium) values of S and G and cannot be used for calculating the fluctuations $\overline{\delta S^2}$, $\overline{\delta G^2}$, and $\overline{\delta S \delta G}$. This misinterpretation of expression (12) will be demonstrated below using calculations of $\overline{\delta S^2}$ for a nematic liquid crystal with uniaxial molecules as an example. The difference between the Landau series in the expansions of ΔF [formula (8)] and ΔF_e [formula (12)] in powers of the parameters S and G is shown in Appendix 1, in which the obtained data are also compared with those for uniaxial molecules [26, 27].

3. THE INFLUENCE OF MOLECULAR BIAXIALITY ON THE CHARACTER OF THE N–I TRANSITION

The specific features of the N–I transition with a change in λ_1 in the range $0 \le \lambda_1 < 1/3$ can be revealed using numerical calculations. The relationships

$$\begin{aligned}S &= \int P_2(\cos\theta) f_e(\Omega) d\Omega,\\ G &= \int D(\theta, \psi) f_e(\Omega) d\Omega\end{aligned} \tag{13}$$

represent the system of self-consistent equations, which possesses several solutions. Among them, ΔF exhibits a minimum for the dependences $S_e(T)$ and $G_e(T)$, which satisfy the following conditions:

$$\begin{aligned}(F_{SS})_{T,e} \ge 0, \quad (F_{GG})_{T,e} \ge 0,\\ (F_{SS})_{T,e}(F_{GG})_{T,e} - (F_{SG})^2_{T,e} \ge 0.\end{aligned} \tag{14}$$

Here, the subscript e refers to the derivatives $F_{SS} = \partial^2 F/\partial S^2$, … at thermodynamic equilibrium. For subsequent analysis, we introduce the variances

$$\begin{aligned}\Delta_P = \langle P_2^2\rangle - S^2, \quad \Delta_{PD} = \langle P_2 D\rangle - SG,\\ \Delta_D = \langle D^2\rangle - G^2,\end{aligned} \tag{15}$$

which characterize the nonuniformity of the orientational distribution of molecules in a sample. The variances can be written in the form

$$\begin{aligned}\Delta_P = \partial S/\partial\lambda_P, \quad \Delta_{PD} = \partial S/\partial\lambda_G = \partial G/\partial\lambda_P,\\ \Delta_D = \partial G/\partial\lambda_D.\end{aligned} \tag{16}$$

With the use of these expressions, we obtain the Jacobian

$$J = \partial(S, G)/\partial(\lambda_P, \lambda_D) = \Delta_P\Delta_D - \Delta_{PD}^2, \tag{17}$$

which is positive in the stability region of the calamitic nematic phase. Therefore, with due regard for relationships (16) and (17), we can write the following expressions:

$$\begin{aligned}\partial\lambda_P/\partial S = \Delta_D/J, \quad \partial\lambda_D/\partial G = \Delta_P/J,\\ \partial\lambda_P/\partial G = \partial\lambda_D/\partial S = -\Delta_{PD}/J.\end{aligned} \tag{18}$$

The repeated differentiation of relationships (9) and the use of expressions (18) give

$$\begin{aligned}(F_{SS})_{T,e} &= kT(\Delta_D/J - 1/t),\\ (F_{GG})_{T,e} &= kT(\Delta_P/J - \lambda_1^2/t),\\ (F_{SG})_{T,e} &= -kT(\Delta_{PD}/J + \lambda_1/t),\end{aligned} \tag{19}$$

where $t = kT/u$ and variances (15) are calculated with the distribution function (11) at $S = S_e$ and $G = G_e$. The limiting temperatures of the stability of the isotropic and nematic phases can be obtained from the condition that the left-hand side of the last inequality in relationships (14) becomes zero. These temperatures obey the equation

$$t = \Delta_P + 2\lambda_1\Delta_{PD} + \lambda_1^2\Delta_D \equiv \Delta_A, \tag{20}$$

in which we used the designations

$$\Delta_A = \langle A^2\rangle - \langle A\rangle^2, \quad A = P_2 + \lambda_1 D. \tag{21}$$

In the isotropic phase, we have $\Delta_P = 1/5$, $\Delta_D = 3/5$, and $\Delta_{PD} = 0$ and formula (20) can be rearranged to give the expression

$$t^*(\lambda_1) = (1 + 3\lambda_1^2)/5 \quad (22)$$

for the limiting temperature of the stability of the isotropic phase. By substituting this expression into relationships (11) and (13) at fixed λ_1, we find the parameters $S^* = S_e(t^*, \lambda_1)$ and $G^* = G_e(t^*, \lambda_1)$. The simultaneous solution of the system of equations (13) and (20) at fixed λ_1 gives the limiting temperature $t_1(\lambda_1)$ of the stability of the nematic phase and the parameters $S_1 = S_e(t_1, \lambda_1)$ and $G_1 = G_e(t_1, \lambda_1)$. The simultaneous solution of the system of equations (13) and the equation $\Delta F_e = 0$ in expression (12) at fixed λ_1 enables us to obtain the temperature $t_{NI}(\lambda_1)$ and the parameters $S_{NI} = S_e(t_{NI}, \lambda_1)$ and $G_{NI} = G_e(t_{NI}, \lambda_1)$. The dependences of the above parameters on λ_1 are plotted in Figs. 1 and 2.

As can be seen from Fig. 1, an increase in λ_1 leads to an increase in the ratio $(S^* - S_{NI})/(S_{NI} - S_1)$ from 1.762 at $\lambda_1 = 0$ to 2 in the range corresponding to linear dependences of S^*, S_{NI}, and S_1 on λ_1. In this range, the ratios between S^*, S_{NI}, and S_1 do not depend on λ_1 and are determined by formulas (A1.6)–(A1.10) given in Appendix 1. The dependences of the parameters S_{NI} and G_{NI} on λ_1 are qualitatively similar to those obtained in [4, 6, 7, 10] within other variants of the molecular–statistical theory and different models of biaxial molecules. A characteristic feature of the influence of λ_1 on the N–I transition is that a decrease in the two-phase region $(t_1 - t^*)$ with an increase in λ_1 is attended by a weak change in the ratio $(t_{NI} - t^*)/(t_1 - t_{NI})$ from 7.65 at $\lambda_1 = 0$ to 8 at $\lambda_1 \approx 1/3$. It should be noted that the inclusion of the anisotropy of the orientational distribution of molecules over the angle ϕ results in the appearance of the low-temperature biaxial nematic phase N_b. An increase in λ_1 leads to a decrease in the temperature range of the calamitic nematic phase, and the I–N_b continuous transition occurs at $\lambda_1 = 1/3$ [1–3, 9].

The dependences of the parameters G^*, G_{NI}, and G_1 on λ_1 exhibit a nonmonotonic behavior. The change in the ratios between G^*, G_{NI}, and G_1 as a function of λ_1 is associated with the nonmonotonic dependence of $G(T)$ in the nematic phase. The differentiation of expressions (13) with respect to temperature and the solution of the obtained system of equations with respect to the derivatives $\partial S/\partial T$ and $\partial G/\partial T$ give the relationships

$$\frac{\partial S}{\partial T} = -\frac{\langle A\rangle(\Delta_P + \lambda_1\Delta_{PD})}{T(t - \Delta_A)},$$
$$\frac{\partial G}{\partial T} = -\frac{\langle A\rangle(\Delta_{PD} + \lambda_1\Delta_D)}{T(t - \Delta_A)}. \quad (23)$$

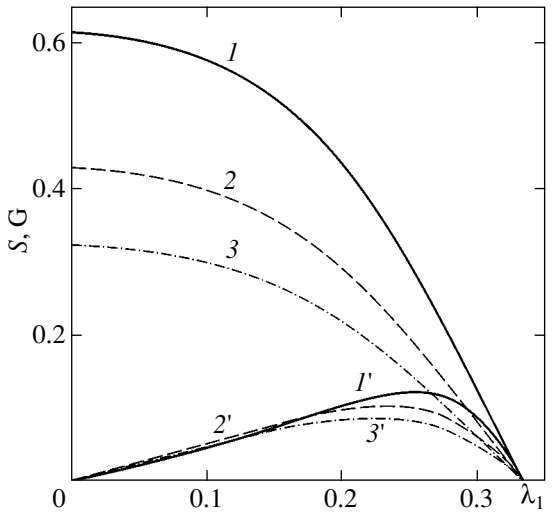

Fig. 1. Dependences of the parameters (*1*–*3*) *S* and (*1'*–*3'*) *G* on λ_1 at t = (*1*, *1'*) t^*, (*2*, *2'*) t_{NI}, and (*3*, *3'*) t_1.

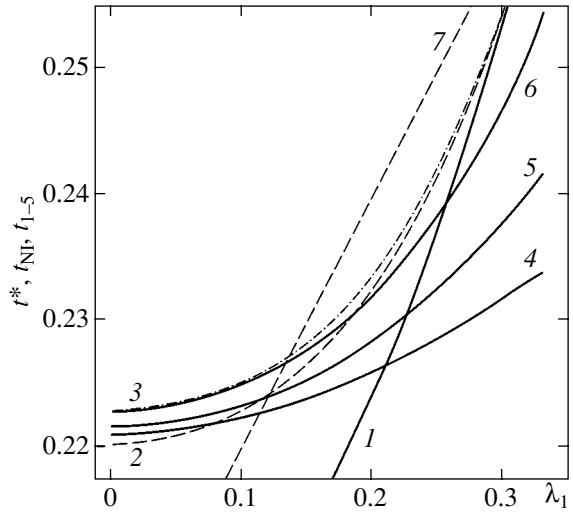

Fig. 2. Dependences of the temperatures (*1*) t^*, (*2*) t_{NI}, (*3*) t_1, (*4*) t_2, (*5*) t_3, (*6*) t_4, and (*7*) t_5 on λ_1. Points (with the abscissas λ_1 = 0.075, 0.111, 0.122, and 0.184) indicate the intersections of the curve $t_{NI}(\lambda_1)$ with the curves $t_2(\lambda_1)$, $t_3(\lambda_1)$, $t_5(\lambda_1)$, and $t_4(\lambda_1)$, respectively.

A comparison of these relationships with formula (20) shows that the derivatives $\partial S/\partial T$ and $\partial G/\partial T$ diverge at $t = t_1$. The derivative $\partial G/\partial T$ is equal to zero when the following condition is satisfied:

$$\Delta_{PD} = -\lambda_1\Delta_D. \quad (24)$$

Since the inequality $\Delta_D \geq 0$ is valid irrespective of the sign of λ_1, the sign of Δ_{PD} is opposite to the sign of λ_1. The solution of the system of equations (13) and (24) at fixed λ_1 gives the quantities $t_2(\lambda_1)$, $S_2 = S_e(t_2, \lambda_1)$, and $G_2 = G_e(t_2, \lambda_1)$ corresponding to the maximum in the

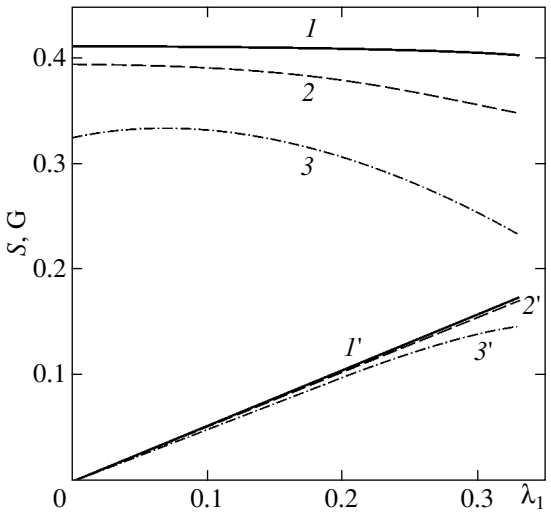

Fig. 3. Dependences of the parameters (*1–3*) *S* and (*1'–3'*) *G* on λ_1 at t = (*1*, *1'*) t_2, (*2*, *2'*) t_3, and (*3*, *3'*) t_4.

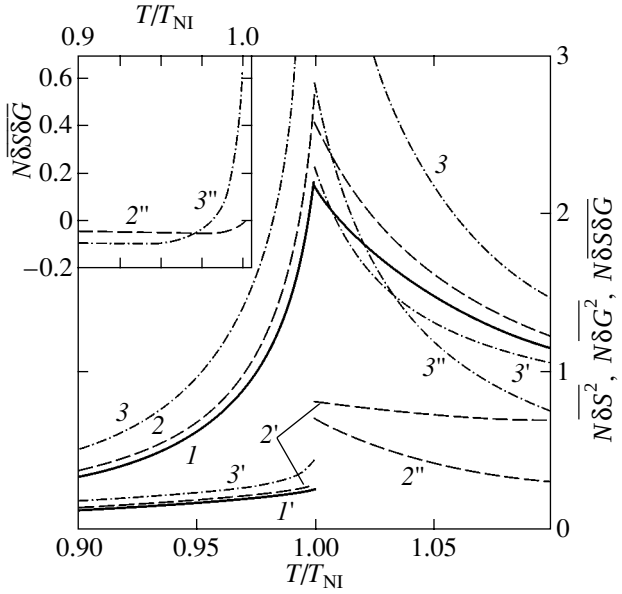

Fig. 4. Dependences of the fluctuations (*1–3*) $N\overline{\delta S^2}$, (*1'–3'*) $N\overline{\delta G^2}$, and (*2"*, *3"*) $N\overline{\delta S \delta G}$ on T/T_{NI} at λ_1 = (*1*, *1'*) 0, (*2*, *2"*) 0.1, and (*3*, *3"*) 0.2.

dependence $G(t)$ at given λ_1. The dependences of these quantities are displayed in Figs. 2 and 3.

It can be seen from Fig. 2 that, at $\lambda_1 \le 0.075$, the inequality $t_{NI}(\lambda_1) \le t_2(\lambda_1)$ is satisfied and the function $G(t)$ monotonically increases with an increase in t over the entire range $t \le t_{NI}$. For molecules with $\lambda_1 > 0.075$, we have $t_{NI}(\lambda_1) > t_2(\lambda_1)$ and an increase in t leads to a nonmonotonic variation in the function $G(t)$. This function increases in the range $t \le t_2$ from zero at $t = 0$ to the maximum value G_2 at $t = t_2$ and then decreases in the range $t_2 < t \le t_{NI}$. The inequality $t^* < t_2$ is valid at $\lambda_1 < 0.212$, and the inequality $t_2 < t^*$ holds at $0.212 < \lambda_1 < 1/3$. The value of S_2 depends weakly on λ_1 and varies from 0.413 to 0.402, which agrees with the experimental data for pure nematic liquid crystals in the absence of low-temperature smectic phases. The dependence $G_2(\lambda_1)$ is nearly linear over the entire range of λ_1 and can be used for estimating the value of λ_1 from the maximum of the experimental dependence $G(t)$ for real liquid crystals.

4. FLUCTUATIONS OF THE ORDER PARAMETERS *S* AND *G*

In a nematic liquid-crystal sample containing N molecules, the homogeneous thermal fluctuations $\delta S = S - S_e$ and $\delta G = G - G_e$ lead to the change in the total free energy of the sample $\delta F = N(\Delta F - \Delta F_e)$, which can be written, correct to terms quadratic in δS and δG, in the form

$$\delta F = \frac{N}{2}[(F_{SS})_{T,e}\delta S^2 + 2(F_{SG})_{T,e}\delta S\delta G + (F_{GG})_{T,e}\delta G^2]. \quad (25)$$

The distribution function $w \sim \exp(-\delta F/kT)$ for the quantities $x_1 = (N)^{1/2}\delta S$ and $x_2 = (N)^{1/2}\delta G$ has the following form:

$$w(x_1, x_2) = \frac{\sqrt{\beta}}{2\pi}\exp\left(-\frac{1}{2}\beta_{ik}x_i x_k\right), \quad i, k = 1, 2, \quad (26)$$

where the matrix elements β_{ik} and the matrix determinant β are defined by the relationships

$$\beta_{11} = \Delta_D/J - 1/t, \quad \beta_{12} = \beta_{21} = -(\Delta_{PD}/J + \lambda_1/t),$$
$$\beta_{22} = \Delta_P/J - \lambda_1^2/t, \quad \beta = (t - \Delta_A)/Jt. \quad (27)$$

According to [28], averaging with the use of function (26) gives

$$\overline{x_i x_k} = \int_{-\infty}^{\infty}\int_{-\infty}^{\infty} x_i x_k w(x_1, x_2)dx_1 dx_2 = \beta_{ik}^{-1}, \quad (28)$$

where β_{ik}^{-1} is the element of the matrix that is inverse to the matrix β_{ik}. As a result, we obtain

$$N\overline{\delta S^2} = \frac{t\Delta_P - \lambda_1^2 J}{t - \Delta_A}, \quad N\overline{\delta G^2} = \frac{t\Delta_D - J}{t - \Delta_A},$$
$$N\overline{\delta S\delta G} = \frac{t\Delta_{PD} + \lambda_1 J}{t - \Delta_A}. \quad (29)$$

The temperature dependences of these fluctuations are depicted in Fig. 4. Let us consider the cases of uniaxial and biaxial molecules.

4.1. Uniaxial Molecules

At $\lambda_1 = \Delta_{PD} = 0$, the fluctuations δS and δG are statistically independent and $\overline{\delta S \delta G} = 0$. For both phases, we have $N\overline{\delta G^2} = \Delta_D$. In the nematic phase, the following relationships are valid:

$$\begin{aligned} \Delta_D &= 3/5 - 6S/7 + 9\langle P_4\rangle/35, \\ \langle P_4\rangle &= (7 + 5S - 35t)/12, \end{aligned} \tag{30}$$

where $P_4(\cos\theta)$ is the Legendre polynomial. With allowance made for these relationships, from formulas (29), we obtain

$$N\overline{\delta G^2} = \Delta_D(S, t) = 3(1 - S - t)/4. \tag{31}$$

As can be seen from Fig. 4, this quantity increases only slightly with an increase in t and remains finite at $t = t_1 = 0.2228$ and $S_1 = 0.3236$, whereas the derivative $d\overline{\delta G^2}/dt$ diverges at this point. Upon the N–I transition, the quantity $N\overline{\delta G^2}$ jumpwise increases from 0.2631 to a value of 3/5, which is independent of temperature. The temperature dependences of the fluctuations

$$\overline{\delta S^2} = \frac{t\Delta_P}{N(t - \Delta_P)} \tag{32}$$

in the nematic and isotropic phases are asymmetric with respect to T_{NI}. In the isotropic phase, we have $\overline{\delta S^2} \sim (T - T^*)^{-1}$ in the vicinity of the temperature T_{NI} and the value of $\overline{\delta S^2}$ approaches $1/(5N)$ at $t \gg \Delta_P = 1/5$. In the nematic phase, we obtain

$$\Delta_P(S, t) = (1 + S - 2S^2 - 3t)/2 \tag{33}$$

and $\overline{\delta S^2}$ more rapidly decreases away from the temperature T_{NI}. This is in qualitative agreement with the experimental data on the temperature dependence of the longitudinal susceptibility for the nematic phase $\chi \sim \overline{\delta S^2}$ [17, 29]. The value of $N\overline{\delta S^2}$ for both phases at $T = T_{NI}$ is considerably larger than $N\overline{\delta G^2}$ and decreases from 2.1991 to 2.1812 upon the N–I transition.

From analyzing the results obtained for the uniaxial molecules, it is clearly seen that the calculation of the fluctuations $\overline{\delta S^2}$ with the use of ΔF_e [defined by expression (12)] instead of ΔF given by formula (8) (as was done in [14]) leads to the relationship

$$\overline{\delta S^2} = \frac{kT}{N}\left(\frac{\partial^2 F_e}{\partial S^2}\right)^{-1}_{S = S_e} = \frac{t^2}{N(t - \Delta_P)}. \tag{34}$$

This relationship differs from expression (32) and gives correct parameters $\overline{\delta S^2}$ only at $t \approx \Delta_P$, which corresponds to the temperatures $t \approx t^*$ ($t \approx t_1$) that cannot be experimentally obtained in the isotropic (nematic) phase. Even at $t = t_{NI}$, from formula (34), we obtain $N\overline{\delta S^2} = 2.4202$ and 2.4010 for the nematic and isotropic phases, respectively. These values differ significantly from the above values calculated from expression (32). In view of the difference between formulas (32) and (34), expression (32) can be derived without recourse to relationship (8) (see Appendix 2).

4.2. Biaxial Molecules

At $\lambda_1 \neq 0$ and a fixed ratio T/T_{NI}, the quantities $\overline{\delta S^2}$ and $\overline{\delta G^2}$ increase with an increase in λ_1 due to a decrease in the two-phase region $T_1 - T^*$. In this case, jumps in $\overline{\delta S^2}$ and $\overline{\delta G^2}$ at $T = T_{NI}$ increase in magnitude. The specific features of the dependence $G(T)$ considerably affect the temperature dependences of the fluctuations $\overline{\delta G^2}$ and $\overline{\delta S \delta G}$. In the nematic phase, at $t = t_2$ and under condition (24), from relationships (29), we obtain

$$N\overline{\delta G^2} = \Delta_D(\lambda_1, t_2), \quad \overline{\delta S \delta G} = -\lambda_1 \overline{\delta G^2}. \tag{35}$$

As a result, we have $\overline{\delta S \delta G} < 0$ in the range $0 < t \leq t_2$ regardless of the value of λ_1. At $t > t_2$ and $\partial G/\partial T < 0$, the values of $\overline{\delta G^2}$ and $\overline{\delta S \delta G}$ increase rapidly. The numerator in formula (29) for $\overline{\delta S \delta G}$ involves two terms with different signs and becomes zero under the condition

$$t\Delta_{PD} = -\lambda_1 J. \tag{36}$$

For fixed λ_1, the solution to the system of equations (13) and (36) gives the quantities $t_3(\lambda_1)$, $S_3 = S_e(t_3, \lambda_1)$, and $G_3 = G_e(t_3, \lambda_1)$ corresponding to the equality $\overline{\delta S \delta G} = 0$. The dependences of the quantities t_3, S_3, and G_3 on λ_1 are represented in Figs. 2 and 3. It can be seen from Fig. 2 that, at $\lambda_1 \leq 0.111$, the inequality $t_{NI}(\lambda_1) \leq t_3(\lambda_1)$ is satisfied and $\overline{\delta S \delta G} < 0$ over the entire range $t < t_{NI}$ (curve *2*" in the inset in Fig. 4). In the range $0.075 < \lambda_1 < 0.111$, the inequality $\overline{\delta S \delta G} < 0$ is valid and the function $G(t)$ decreases with an increase in $t > t_2(\lambda_1)$.

At $\lambda_1 > 0.111$, the values of $\overline{\delta S \delta G}$ are positive in the vicinity of T_{NI}. The dependence $S_3(\lambda_1)$ is weak, whereas the dependence $G_3(\lambda_1)$ exhibits a nearly linear behavior and is very similar to the dependence $G_2(\lambda_1)$.

From formulas (29), it follows that, in the case when the condition

$$t(\Delta_D - \Delta_{PD}) = J(1 + \lambda_1) \tag{37}$$

is satisfied, the equality $\overline{\delta S \delta G} = \overline{(\delta G)^2}$ holds. In the nematic phase, at fixed λ_1, the solution of the system of equations (13) and (37) leads to the dependences $t_4(\lambda_1)$, $S_4 = S_e(t_4, \lambda_1)$, and $G_4 = G_e(t_4, \lambda_1)$, which are shown in Figs. 2 and 3. It can be seen from Fig. 2 that, in the nematic phase, at $\lambda_1 < 0.184$ and $T = T_{NI}$, we have $\overline{\delta S \delta G}(T_{NI}) < \overline{\delta G^2}(T_{NI})$. This situation is illustrated by curves *3*' and *3*'' in Fig. 4. As can be seen from Fig. 3, the dependence $S_4(\lambda_1)$ is nonmonotonic and differs significantly from the dependences $S_{2,3}(\lambda_1)$. On the other hand, the dependence $G_4(\lambda_1)$ exhibits a nearly linear behavior and differs from the dependences $G_{2,3}(\lambda_1)$ only at $\lambda_1 \le 1/3$.

For the isotropic phase, Eq. (37) has the solution

$$t_5 = (1 + \lambda_1)/5. \tag{38}$$

The corresponding dependence is plotted in Fig. 2. The inequality $\overline{\delta S \delta G}(T_{NI}) < \overline{\delta G^2}(T_{NI})$ holds at $\lambda_1 < 0.122$. At $\lambda_1 > 0.184$, the inequality $\overline{\delta S \delta G}(T_{NI}) > \overline{\delta G^2}(T_{NI})$ is satisfied for both phases (see Fig. 4). In the isotropic phase, relationships (29) are reduced to the following formulas:

$$N\overline{\delta S^2} = \frac{5t - 3\lambda_1^2}{25[t - t^*(\lambda_1)]}, \quad N\overline{\delta G^2} = \frac{3(5t-1)}{25[t - t^*(\lambda_1)]},$$
$$N\overline{\delta S \delta G} = \frac{3\lambda_1}{25[t - t^*(\lambda_1)]}, \tag{39}$$

where $t^*(\lambda_1)$ is given by expression (22). Then, at $t \approx t^*(\lambda_1)$ and $N\overline{\delta G^2} \gg 3/5$, we obtain

$$N\overline{\delta S^2} = \frac{1}{25[t - t^*(\lambda_1)]}, \quad \overline{\delta G^2} = 9\lambda_1^2 \overline{\delta S^2},$$
$$\overline{\delta S \delta G} = 3\lambda_1 \overline{\delta S^2}. \tag{40}$$

Note that the last two formulas directly follow from relationship (A1.5) [valid in the vicinity of $t \approx t^*(\lambda_1)$] and the expression $\delta G = (dG/dS)_{S_e = 0}\delta S = 3\lambda_1 \delta S$. In this temperature range, the inequalities $\overline{\delta G^2} \le \overline{\delta S \delta G} \le \overline{\delta S^2}$ are satisfied at $\lambda_1 \le 1/3$. As the difference $[t - t^*(\lambda_1)]$ increases, the quantities $N\overline{\delta S^2}$ and $N\overline{\delta G^2}$ approach their limiting values of 1/5 and 3/5 and the quantity $\overline{\delta S \delta G} \sim [t - t^*(\lambda_1)]^{-1}$ tends to zero. A comparison of formulas (39) and (32) at $\Delta_P(S = 0) = 1/5$ indicates that, at a fixed difference $t - t^*$, the molecular biaxiality leads only to a small decrease in the value of $\overline{\delta S^2}$, whereas the temperature dependences of the quantities $\overline{\delta G^2}$ and $\overline{\delta S \delta G}$ and their divergence at $t = t^*(\lambda_1)$ in the isotropic phase are completely determined by the molecular biaxiality.

The fluctuation effects in the nematic and isotropic phases in the vicinity of the N–I transition differ considerably in character. In the nematic phase, at $\lambda_1 = 0.2$ and $T = T_{NI}$, the values of $N\overline{\delta S^2}$, $N\overline{\delta G^2}$, and $N\overline{\delta S \delta G}$ are equal to 5.7214, 0.4431, and 0.6272, respectively. As a result, we obtain the inequalities $\overline{\delta S^2} \gg \overline{\delta G^2}$ and $\overline{\delta S^2} \gg \overline{\delta S \delta G}$. At $\lambda_1 < 0.2$, an increase in $\overline{\delta S^2}$ in the vicinity of T_{NI} due to molecular biaxiality is not large enough to change the inequality

$$\overline{(\delta S)_V^2} \ll S^2, \tag{41}$$

which follows from the experimental data for typical calamitic nematic liquid crystals, such as MBBA and alkylcyanobiphenyls [17, 29]. In inequality (41), $\overline{(\delta S)_V^2}$ is the homogeneous long-wavelength fluctuation of *S* in the volume $V = 4\pi\xi^3/3$, where ξ is the correlation length of fluctuations of *S*. By virtue of inequality (41), the effect of fluctuations of *S* and *G* on the physical properties dependent on *S* is weak in the calamitic nematic phase of typical mesogenic compounds. On the other hand, condition (41) is the criterion for the applicability of the mean-field approach to the description of the N–I transition [28]. For mesogenic compounds with parameters λ_1 close to 1/3, condition (41) is violated and the values of $\overline{\delta G^2}$ and $\overline{\delta S \delta G}$ become comparable to those of $\overline{\delta S^2}$. In this case, the N–I transition should be described taking into account the fluctuations $\overline{\delta G^2}$ and $\overline{\delta S \delta G}$ in addition to the fluctuations $\overline{\delta S^2}$.

In the isotropic phase, at the transition point T_{NI}, the values of $N\overline{\delta S^2}$, $N\overline{\delta G^2}$, and $N\overline{\delta S \delta G}$ (even at $\lambda_1 = 0.2$) are equal to 4.9059, 2.2941, and 2.8235, respectively; i.e., they are close in order of magnitude. Therefore, the pretransitional effects should be analyzed with due regard for the fluctuations $\overline{\delta S^2}$, $\overline{\delta G^2}$, and $\overline{\delta S \delta G}$. This is particularly true for the description of the response of nematic liquid crystals to external actions.

5. RESPONSE OF A NEMATIC LIQUID CRYSTAL TO EXTERNAL FIELDS

Let us consider the response of a calamitic nematic liquid crystal to an external field h, which leads to a change in the order parameters S and G at a fixed orientation of the director **n**. The susceptibilities serve as a measure of the linear response and are defined by the relationships

$$\chi_S = (\partial S/\partial h)_{T;\, h\to 0}, \quad \chi_G = (\partial G/\partial h)_{T;\, h\to 0}. \quad (42)$$

For magnetic (H) and high-frequency electric [$E(\omega)$] fields parallel to the director, the expressions for h have the form

$$h_H = \frac{\Delta k}{3}H^2, \quad h_E = \frac{\Delta\gamma(\omega) f_\parallel(\omega)}{3}E^2(\omega), \quad (43)$$

where $\Delta k = k_{zz} - (k_{xx} + k_{yy})/2$ and $\Delta\gamma(\omega) = \gamma_{zz}(\omega) - [\gamma_{xx}(\omega) + \gamma_{yy}(\omega)]/2$ are the anisotropies of the diamagnetic and electric molecular polarizabilities, respectively; $f_\parallel(\omega)$ is the component of the tensor of the local field acting on a molecule in the liquid crystal; and $E(\omega)$ is the amplitude of the macroscopic electric field in the liquid crystal. In the presence of the field h, formula (8) takes the form

$$\Delta F = -\frac{u}{2}(S + \lambda_1 G)^2 - h(S + \lambda_2 G) + kT[\lambda_P S + \lambda_D G - \ln Z(\lambda_P, \lambda_D)]. \quad (44)$$

Here, the second term on the right-hand side characterizes the energy of interaction between the liquid crystal and the field per molecule and the parameter λ_2 is defined by expression (7), in which γ_{ii} is replaced either by k_{ii} at $h = h_H$ or by $\gamma_{ii}(\omega)$ at $h = h_E$. In the general case, the values of λ_1 and λ_2 are different, even though they can coincide for particular compounds. The parameters $\lambda_P(S, G)$ and $\lambda_D(S, G)$ are determined from the system of equations (4), in which $S = S(h)$ and $G = G(h)$. Under thermodynamic equilibrium conditions $(\partial F/\partial S)_{T,h} = (\partial F/\partial G)_{T,h} = 0$, with the use of relationships (44), we obtain the system of equations of state for a nematic liquid crystal in the external field h, that is,

$$\lambda_P(S, G) = \frac{u}{kT}(S + \lambda_1 G) + \frac{h}{kT}, \qquad \lambda_D(S, G) = \frac{u\lambda_1}{kT}(S + \lambda_1 G) + \frac{\lambda_2 h}{kT}. \quad (45)$$

Substitution of these expressions into formula (3) gives the equilibrium distribution function of molecules in the presence of the external field:

$$f_{e,h}(\Omega) = \frac{1}{8\pi^2 Z_{e,h}} \times \exp\left[\frac{u}{kT}(S + \lambda_1 G)(P_2 + \lambda_1 D) + \frac{h}{kT}(P_2 + \lambda_2 D)\right], \qquad Z_{e,h} = \frac{1}{8\pi^2} \times \int \exp\left[\frac{u}{kT}(S + \lambda_1 G)(P_2 + \lambda_1 D) + \frac{h}{kT}(P_2 + \lambda_2 D)\right] d\Omega. \quad (46)$$

Differentiation of the equations of state (45) with respect to h at a constant temperature with allowance made for expressions (18) leads to the system of equations in $(\partial S/\partial h)_T$ and $(\partial G/\partial h)_T$. By solving this system, we obtain

$$\left(\frac{\partial S}{\partial h}\right)_T = \frac{1}{kT(t - \Delta_A)}[t\Delta_P - \lambda_1^2 J + \lambda_2(t\Delta_{PD} + \lambda_1 J)], \qquad \left(\frac{\partial G}{\partial h}\right)_T = \frac{1}{kT(t - \Delta_A)}[t\Delta_{PD} + \lambda_1 J + \lambda_2(t\Delta_D - J)]. \quad (47)$$

Here, the parameters described by formulas (15), (17), and (21) are calculated with the distribution function (46) and depend on h. The derivatives $(\partial S/\partial h)_T$ and $(\partial G/\partial h)_T$ diverge at the temperatures $t^*(\lambda_1, h)$ and $t_1(\lambda_1, h)$ obeying the equation

$$t = \Delta_A(h). \quad (48)$$

The parameter Δ_A [expression (21)] is the second-order cumulant, which can be written in the following form:

$$\Delta_A(h) = \frac{\partial^2 \ln Z_{e,h}}{\partial \lambda_A^2} = \langle A|A\rangle, \quad (49)$$

where $\lambda_A = u(S + \lambda_1 G)/kT$. The dependence $\Delta_A(h)$ can be represented as a series:

$$\Delta_A(h) = \sum_{n=0}^{\infty} \frac{\lambda_B^n}{n!}\left(\frac{\partial^{2+n} \ln Z_{e,h}}{\partial \lambda_A^2 \partial \lambda_B^n}\right)_{\lambda_B = 0} \equiv \sum_{n=0}^{\infty} \frac{\lambda_B^n}{n!}\langle A|A|\overbrace{B|\ldots|B}^{n}\rangle_0, \quad (50)$$

where $\lambda_B = h/kT$ and $B = P_2 + \lambda_2 D$. Here, all the cumulant averages $\langle a_1|a_2|\ldots|a_n\rangle_0$ are calculated at $h = 0$ with the distribution function (11). In the approximation linear in h, Eq. (48) for the isotropic phase takes the form

$$T^* = \frac{u}{5k}(1 + 3\lambda_1^2)\left\{1 + \frac{2[1 - 3\lambda_1(\lambda_1 + 2\lambda_2)]}{7kT^*(1 + 3\lambda_1^2)}h\right\}. \quad (51)$$

For uniaxial molecules at $\lambda_1 = \lambda_2 = 0$, with due regard for expressions (43) at $h = h_H$, this expression coincides

with the relationship obtained earlier in [30] in a different way. At $\lambda_1 = \lambda_2 = 1/3$, T^* becomes independent of h.

In the limit $h \longrightarrow 0$, the rearrangement of relationships (47) with allowance made for expressions (29) permits us to obtain susceptibilities (42) in the following form:

$$\chi_S = \frac{N}{kT}[\overline{\delta S^2} + \lambda_2 \overline{\delta S \delta G}],$$
$$\chi_G = \frac{N}{kT}[\overline{\delta S \delta G} + \lambda_2 \overline{\delta G^2}]. \quad (52)$$

A comparison of formulas (23) and (47) at $h = 0$ makes it possible to derive the relationships between the susceptibilities and the temperature dependences of the order parameters S and G in the absence of a field. At $\lambda_1 = \lambda_2$, these relationships are simplified and take the form

$$\chi_S = -\frac{T}{u(S + \lambda_1 G)}\frac{\partial S}{\partial T}, \quad \chi_G = -\frac{T}{u(S + \lambda_1 G)}\frac{\partial G}{\partial T}. \quad (53)$$

From these relationships, we have $\chi_G < 0$ at $t < t_2$ and $\partial G/\partial T > 0$. The contributions of the fluctuations $\overline{\delta S \delta G}$ to the susceptibility χ_S and the fluctuations $\overline{\delta G^2}$ to the susceptibility χ_G are determined by the value of λ_2, which is different for the electric and magnetic fields. At $t = t_3$ and $\overline{\delta S \delta G} = 0$, the susceptibilities χ_S and χ_G are governed only by the fluctuations $\overline{\delta S^2}$ and $\overline{\delta G^2}$, respectively.

In the isotropic phase, substitution of expressions (39) into formulas (52) gives

$$\chi_S^{(i)} = \frac{5t - 3\lambda_1(\lambda_1 - \lambda_2)}{25kT[t - t^*(\lambda_1)]},$$
$$\chi_G^{(i)} = \frac{3(5t\lambda_2 + \lambda_1 - \lambda_2)}{5t - 3\lambda_1(\lambda_1 - \lambda_2)}\chi_S^{(i)}. \quad (54)$$

Since $5t > 1$ and $\lambda_1 - \lambda_2 \ll 1$, from formulas (54), we find

$$\chi_G^{(i)} = 3\lambda_2\chi_S^{(i)}\left[1 + \frac{1}{5t\lambda_2}(\lambda_1 - \lambda_2)(1 + 3\lambda_1\lambda_2)\right] \approx 3\lambda_2\chi_S^{(i)}. \quad (55)$$

In the linear-field approximation, the order parameters $S(h)$ and $G(h)$ induced by the field h in the isotropic phase of the nematic liquid crystal are given by the expressions

$$S(h) = \chi_S^{(i)}h, \quad G(h) = \chi_G^{(i)}h = 3\lambda_2 S(h). \quad (56)$$

The parameters $S(h)$ and $G(h)$ increase proportionally to $[T - T^*(\lambda_1)]^{-1}$ as the temperature T_{NI} is approached. Making allowance for formulas (43) and (54), expressions (56) fit the experimental data obtained in [19–21] for pure nematic liquid crystals fairly well. The interpretation of the dependences $G(h) \sim S(h) \sim (T - T^*)^{-1}$ observed in the constant field h for the order parameters of impurity biaxial molecules with a small concentration in the isotropic phase of the nematic matrix [21] calls for special examination, because the constant λ_m in the expression $G(h) = 3\lambda_m S(h)$ in this case is predominantly determined by the interaction between the impurity and the matrix.

Now, we analyze the possibilities of using formulas (56) to interpret the experimental data on the quadrupole splitting $\Delta\nu_k$ of the ^{2}D NMR lines associated with the C–D$_k$ bonds. The quadrupole splitting $\Delta\nu_k$ depends on the orientation of the C–D$_k$ bond with respect to the axes of the molecular coordinate system xyz and orientational order of molecules and can be represented as

$$\Delta\nu_k = \text{const}(SS_\beta + GG_{\beta\varphi}/3). \quad (57)$$

Here, $S_\beta = (3\cos^2\beta - 1)/2$, $G_{\beta\varphi} = (3/2)\sin^2\beta\cos 2\varphi$ β is the angle between the C–D$_k$ bond and the z axis of the molecular coordinate system xyz, and φ is the angle between the x axis and the projection of the C–D$_k$ bond onto the xy plane. The quadrupole splitting $\Delta\nu_k$ can become zero for a continuum of C–D$_k$ directions. In the molecular coordinate system, the equation $\Delta\nu_k = 0$ can be rearranged to the following form:

$$x^2S_{xx} + y^2S_{yy} + z^2S_{zz} = 0. \quad (58)$$

Among the three parameters S_{ii}, two parameters have the same sign. By designating their magnitudes as S_u and S_v and allowing for the condition Tr$\mathbf{S} = 0$, from Eq. (58), we obtain the expression

$$\bar{u}^2S_u + \bar{v}^2S_v - \bar{w}^2(S_u + S_v) = 0, \quad (59)$$

which is an equation of an elliptic cone with a vertex at the origin of the coordinates and the axis $\bar{w}$. In the section that is perpendicular to the $\bar{w}$ axis and is located at the distance $c = \pm(S_u + S_v)^{-1/2}$ from the origin of the coordinates, the cone directrix is an ellipse with the semiaxes $a = (S_u)^{-1/2}$ and $b = (S_v)^{-1/2}$. The angles β_u and β_v determining the half-aperture of the cone are defined as

$$\beta_u = \arctan(1 + S_v/S_u)^{1/2},$$
$$\beta_v = \arctan(1 + S_u/S_v)^{1/2}. \quad (60)$$

The equality $\Delta\nu_k = 0$ is satisfied for all the C–D$_k$ directions lying on this "magic" cone $C(xyz)$. The diagonals $|\bar{u}| = |\bar{v}| = |\bar{w}|$ of the molecular coordinate system lie on the cone $C(xyz)$ and correspond to $S_\beta = G_{\beta\varphi} = 0$. For uniaxial molecules with the axis $z = \bar{w}$ and $S_u = S_v$, the circular cone $C(xyz)$ is characterized by the half-aperture angle $\beta \approx 54.74°$.

The shape of the cone $C(xyz)$ is specified by the parameters S and G and depends on the mesophase temperature and the ratio between the parameters S_u and S_v. At $S > G$ and $S_{xx} = -(S - G)/2$, $S_{yy} = -(S + G)/2$, and $S_{zz} = S$, we have $\bar{u} = x$, $\bar{v} = y$, $\bar{w} = z$. In the nematic phase, at values of λ_1 close to 1/3, the parameters S and G in the vicinity of the N–I transition are small and are related by the expression $S = 3\lambda_1 G$ [see relationship (A1.5)]. Therefore, the angles

$$\beta_x = \arctan\left(\frac{2}{1-3\lambda_1}\right)^{1/2}, \quad \beta_y = \arctan\left(\frac{2}{1+3\lambda_1}\right)^{1/2} \quad (61)$$

are independent the temperature. As the value of λ_1 approaches 1/3, the semiaxis a increases and tends to infinity at $G = S$. In this case, the cone $C(xyz)$ degenerates into two mutually perpendicular planes which intersect along the x axis and make the angles $\beta_y = \pm 45°$ with the z axis. For particular compounds and C–D_k bonds, one of the parameters S_{ii} in Eq. (58) can change sign with a variation in the mesophase temperature, because the dependence $G(S)$ in the nematic phase exhibits a nonmonotonic behavior. As a consequence, the $\bar{w}$ axis changes its direction from one axis in the system xyz to another axis. The changeover to the inequality $G > S$, which is valid only for biaxial impurity molecules in the calamitic nematic liquid crystal, is accompanied by the transformation of the above planes into the cone $C(xyz)$ with the axes $\bar{u} = x$, $\bar{v} = z$, and $\bar{w} = y$ and the semiaxes of the ellipse $a \gg b$.

In the isotropic phase, when expressions (56) hold true, λ_1 in formulas (61) should be replaced by λ_2 or λ_m for impurity molecules) and the angles $\beta_{x,y}$ do not depend on the parameters $S(h)$ and $G(h)$. This circumstance accounts for the situation where the proportional relationship $\Delta\nu_k \sim S(h)$ is observed for a number of C–D_k bonds in the molecule, whereas the other C–D_k bonds in the same molecule are characterized by $\Delta\nu_n = 0$ [19, 21]. The orientation of the latter bonds is similar to that of the directrix of the cone $C(xyz)$ with parameters (61). This provides the basis for the technique of determining the orientation of C–D_k bonds in the molecular coordinate system.

6. CONCLUSIONS

Thus, the results obtained in the present work demonstrated that the molecular biaxiality substantially affects the dependences $S(T)$ and $G(T)$ and the magnitudes S_{NI} and G_{NI} upon the N–I transition. An increase in the molecular biaxiality parameter λ_1 is attended by a decrease in the values S_{NI} and G_{NI} and a narrowing of the two-phase region. However, the ratio $(T_{NI} - T^*)/(T_1 - T_{NI})$ remains unchanged up to the parameter $\lambda_1 = 1/3$, which is a limiting value for calamitic nematic liquid crystals and corresponds to the I–N_b transition to the biaxial nematic phase. The specific features of the dependence $G(T)$ have a considerable effect on the magnitude and temperature behavior of the fluctuations $\overline{\delta G^2}$ and $\overline{\delta S \delta G}$. The fluctuations $\overline{\delta S \delta G}$ in the nematic phase vary nonmonotonically and can change sign from negative to positive as the temperature T_{NI} is approached. In the nematic phase, the fluctuations $\overline{\delta G^2}$ and $\overline{\delta S \delta G}$ at values $\lambda_1 < 0.2$ typical of mesogenic molecules are appreciably less than the fluctuations $\overline{\delta S^2}$ and do not affect the applicability of the mean-field approach to the description of the N–I transition. At values of λ_1 close to 1/3 and small parameters S_{NI}, the fluctuations $\overline{\delta S^2}$, $\overline{\delta G^2}$, and $\overline{\delta S \delta G}$ are large and comparable to each other, so that the mean-field approximation is inapplicable.

In the isotropic phase, the molecular biaxiality determines the ratios between the fluctuations $\overline{\delta S^2}$, $\overline{\delta G^2}$, and $\overline{\delta S \delta G}$ and their temperature behavior. At $\lambda_1 \approx 0.2$ for real mesogenic molecules, the fluctuations $\overline{\delta S^2}$, $\overline{\delta G^2}$, and $\overline{\delta S \delta G}$ are comparable to each other in the vicinity of the temperature T_{NI}. The inclusion of the molecular biaxiality makes it possible to explain the dependences $G(h) \sim S(h) \sim (T - T^*)^{-1}$, which are experimentally observed for the parameters $G(h)$ and $S(h)$ that are induced by the field h in the isotropic phase of the nematic. Moreover, the specific features of the quadrupole splitting of the NMR lines in the spectra of selectively deuterated mesogenic and impurity molecules in the isotropic phase of nematic liquid crystals can also be interpreted in terms of the molecular biaxiality.

APPENDIX 1

Let us now demonstrate that the expansions of ΔF [defined by formula (8)] and ΔF_e [represented by formula (12)] into a Landau series in powers of the parameters S and G up to fourth-order terms differ significantly. The expansion of the function $Z(\lambda_P, \lambda_D)$ [given by expression (3)] into a power series of $\lambda_{P,D}$ and substitution of this series into relationships (4) give the series $S = S(\lambda_P, \lambda_D)$ and $G = G(\lambda_P, \lambda_D)$ whose inversion makes it possible to obtain the dependences $\lambda_P(S, G)$ and $\lambda_D(S, G)$. With the required precision up to third-order terms, these dependences have the form

$$\lambda_P = 5S - \frac{25}{7}S^2 + \frac{25}{21}G^2 + \frac{425}{49}S^3 + \frac{425}{147}SG^2,$$
$$\lambda_D = \frac{5}{3}G\left(1 + \frac{10}{7}S + \frac{85}{49}S^2\right) + \frac{425}{441}G^3. \quad (A1.1)$$

The dependence $\lambda_P(S, G)$ is the even function and the dependence $\lambda_D(S, G)$ is the odd function of the parameter G. Substitution of formulas (A1.1) into the series $\ln Z(\lambda_P, \lambda_D)$ gives

$$\ln Z = \frac{5}{6}(3S^2 + G^2) - \frac{50}{21}(S^3 - SG^2) + \frac{425}{588}(3S^2 + G^2)^2. \quad \text{(A1.2)}$$

This expansion is a power series of the invariants $I_2 = \mathrm{Tr}(\mathbf{S}^2) = (3S^2 + G^2)/2$ and $I_3 = \mathrm{Tr}(\mathbf{S}^3) = 3(S^3 - SG^2)/4$ of the matrix $\mathbf{S}$ (1). In the diagonal form, this matrix has the following elements: $S_{xx} = -(S - G)/2$, $S_{yy} = -(S + G)/2$, and $S_{zz} = S$. Substitution of formulas (A1.1) and (A1.2) into relationship (8) leads to the sought expansion

$$\Delta F = -\frac{u}{2}(S + \lambda_1 G)^2 + \frac{5}{6}kT(3S^2 + G^2) - \frac{25}{21}kT(S^3 - SG^2) + \frac{425}{1764}kT(3S^2 + G^2)^2. \quad \text{(A1.3)}$$

The minimization of expression (A1.3) with respect to the parameters S and G results in the system of equations (10). From this system of equations, we derive the relationship

$$\lambda_D(S, G) = \lambda_1 \lambda_P(S, G). \quad \text{(A1.4)}$$

Substitution of series (A1.1) into relationship (A1.4) gives the expression

$$G = 3\lambda_1 S - \frac{45}{7}\lambda_1(1 - \lambda_1^2)S^2 + \ldots. \quad \text{(A1.5)}$$

With this expression, the function ΔF described by formula (A1.3) can be reduced to a form $\Delta F(S)$ with coefficients dependent on λ_1. At $G < S$, the third-order term in formula (A1.3) is negative and the N–I transition is a first-order transition. Let us consider the situation at $G \leq S$ when the N–I transition is similar in character to a continuous transition and the parameters S and G are small in its vicinity. Then, in relationship (A1.5), it is possible to retain only the first term. Its substitution into formula (A1.3) leads to the series

$$\Delta F(S) = \frac{1}{2}a(T - T^*)S^2 - \frac{1}{3}bS^3 + \frac{1}{4}cS^4 \quad \text{(A1.6)}$$

with the coefficients

$$a(\lambda_1) = 5k(1 + 3\lambda_1^2), \quad b(\lambda_1, T) = \frac{25}{7}kT(1 - 9\lambda_1^2), \quad c(\lambda_1, T) = \frac{425}{49}kT(1 + 3\lambda_1^2)^2. \quad \text{(A1.7)}$$

At $\lambda_1 = 0$, these coefficients are reduced to the coefficients (4.23) obtained in [27]. The coefficient $b(\lambda_1, T)$ becomes zero at $\lambda_1 = 1/3$, which agrees with the results following from formula (7). The limiting temperature of the stability of the isotropic phase $t^* = kT^*/u$ and the parameter $S^* = S(t^*)$ are defined by the expressions

$$t^*(\lambda_1) = (1 + 3\lambda_1^2)/5, \quad S^* = \frac{7(1 - 9\lambda_1^2)}{17(1 + 3\lambda_1^2)^2}. \quad \text{(A1.8)}$$

The temperature t_{NI} of the N–I transition and the parameter S_{NI} can be written as follows:

$$t_{NI} = \frac{153(1 + 3\lambda_1^2)^3 t^*}{153(1 + 3\lambda_1^2)^3 - 10(1 - 9\lambda_1^2)^2}, \quad S_{NI} = 2S^*/3. \quad \text{(A1.9)}$$

The limiting temperature of the stability of the nematic phase t_1 and the parameter $S_1 = S(t_1)$ are related to parameters (A1.8) through the expression

$$t_1 = \frac{68(1 + 3\lambda_1^2)^3 t^*}{68(1 + 3\lambda_1^2)^3 - 5(1 - 9\lambda_1^2)^2}, \quad S_1 = S^*/2. \quad \text{(A1.10)}$$

In the λ_1 range under consideration, the ratios between the parameters S^*, S_{NI}, and S_1 do not depend on λ_1 and the two-phase region $t_1 - t^*$ decreases with an increase in λ_1. However, the ratio $(t_{NI} - t^*)/(t_1 - t_{NI})$ varies from 7.4 at $\lambda_1 = 0$ to 8 in the limit $\lambda_1 = 1/3$.

Now, expansions similar to those represented by formulas (A1.3) and (A1.6) will be derived for the function ΔF_e given by formula (12). Let us introduce the following designations:

$$\eta = S + \lambda_1 G, \quad A(\theta, \psi) = P_2(\cos\theta) + \lambda_1 D(\theta, \psi). \quad \text{(A1.11)}$$

It can be shown that the two equations $(\partial F_e/\partial S)_T = (\partial F_e/\partial G)_T = 0$ are equivalent to one self-consistent equation for the parameter η; that is,

$$\eta = \langle A \rangle_e \equiv \int A(\theta, \psi) f_e(\Omega) d\Omega. \quad \text{(A1.12)}$$

The expansion of the function ΔF_e [formula (12)] in powers of η has the form

$$\Delta F_e(\eta) = \frac{u}{2T}[T - T^*(\lambda_1)]\eta^2 - \frac{(1 - 9\lambda_1^2)u^3}{105(kT)^2}\eta^3 + \frac{(1 + 3\lambda_1^2)^2 u^4}{700(kT)^3}\eta^4 + \ldots, \quad \text{(A1.13)}$$

where the expression for $T^*(\lambda_1) = u(1 + 3\lambda_1^2)/5k$ coincides with that in relationship (A1.8). Substitution of the first term of expansion (A1.5) into formula (A1.13)

gives the expansion of $\Delta F_e(S)$ in the form of series (A1.6) with the coefficients

$$a_e(\lambda_1, T) = \frac{u}{T}(1 + 3\lambda_1^2)^2,$$

$$b_e(\lambda_1, T) = \frac{(1 - 9\lambda_1^2)(1 + 3\lambda_1^2)^3 u^3}{35(kT)^2}, \qquad \text{(A1.14)}$$

$$c_e(\lambda_1, T) = \frac{(1 + 3\lambda_1^2)^6 u^4}{175(kT)^3}.$$

These coefficients differ from coefficients (A1.7) and, at $\lambda_1 = 0$, coincide with those given in [2, 26]. At $T = T^*(\lambda_1)$, we have $a_e = a$, $b_e = b$, and $c_e = 7c/17$. Therefore, the use of expansion (A1.13) is sufficiently correct only in the isotropic phase at temperatures close to $T^*(\lambda_1)$.

APPENDIX 2

For a nematic liquid crystal with uniaxial molecules at a constant volume, formula (32) can be obtained from the general thermodynamic relations [28]

$$\overline{\delta S^2} = \left(\frac{\partial S}{\partial T}\right)^2_{V;\ \delta T = 0} \overline{\delta T^2}, \quad \overline{\delta T^2} = \frac{kT^2}{C_V} \qquad \text{(A2.1)}$$

under the assumption that the temperature fluctuations are responsible for the fluctuations of $S(T)$. The heat capacity at a constant volume with due regard for expression (6) at $\lambda_1 = 0$ can be written in the form

$$C_V = \left[N\frac{\partial E(S)}{\partial T}\right]_V = -NuS\left(\frac{\partial S}{\partial T}\right)_V. \qquad \text{(A2.2)}$$

Substitution of formula (A2.2) into relations (A2.1) gives the relationship

$$\overline{\delta S^2} = -\frac{kT^2}{Nu}\left(\frac{\partial \ln S}{\partial T}\right)_V \qquad \text{(A2.3)}$$

between the fluctuations $\overline{\delta S^2}$ in the nematic phase and the dependence $S(T)$. By substituting the first expression out of the two expressions in (23) at $\lambda_1 = 0$ into relationship (A2.3), we obtain formula (32).

REFERENCES

1. P. G. de Gennes and J. Prost, *The Physics of Liquid Crystals*, 2nd ed. (Clarendon, Oxford, 1993; Mir, Moscow, 1982).
2. M. J. Freiser, Mol. Cryst. Liq. Cryst. **14** (1–2), 165 (1971).
3. J. P. Straley, Phys. Rev. A **10** (5), 1881 (1974).
4. R. G. Priest, Solid State Commun. **17** (4), 519 (1975).
5. G. R. Luckhurst, C. Zannoni, P. L. Nordio, and U. Segre, Mol. Phys. **30** (5), 1345 (1975).
6. W. M. Gelbart and B. Barboy, Mol. Cryst. Liq. Cryst. **55** (1–2), 209 (1979).
7. N. P. Tumanyan and E. P. Sokolova, Zh. Fiz. Khim. **58** (10), 2444 (1984).
8. B. Bergersen, P. Palffy-Muhoray, and D. A. Dunmur, Liq. Cryst. **3** (3), 347 (1988).
9. B. Mulder, Phys. Rev. A **39** (1), 360 (1989).
10. B. Tjipto-Margo and G. T. Evans, J. Chem. Phys. **94** (6), 4546 (1990).
11. A. Ferrarini, G. Moro, P. L. Nordio, and G. R. Luckhurst, Mol. Phys. **77** (1), 1 (1992).
12. E. F. Gramsbergen, L. Longa, and W. H. De Jeu, Phys. Rep. **135** (2), 195 (1986).
13. Z. H. Wang and P. H. Keyes, Phys. Rev. E **54** (5), 5249 (1996).
14. R. Blinc, S. Lugomer, and B. Zeks, Phys. Rev. **9** (6), 2214 (1974).
15. Lin Lei, Phys. Rev. Lett. **43** (21), 1604 (1979).
16. B. Pouligny and J. Lalanne, Phys. Rev. A **26** (6), 3679 (1982).
17. E. M. Aver'yanov, Zh. Éksp. Teor. Fiz. **97** (3), 855 (1990) [Sov. Phys. JETP **70**, 479 (1990)].
18. E. M. Aver'yanov, Zh. Éksp. Teor. Fiz. **110** (5), 1820 (1996) [JETP **83**, 1000 (1996)].
19. G. S. Attard, P. A. Beckmann, J. W. Emsley, *et al.*, Mol. Phys. **45** (5), 1125 (1982).
20. J. W. Emsley, C. T. Imrie, G. R. Luckhurst, and R. D. Newmark, Mol. Phys. **63** (2), 317 (1988).
21. G. R. Luckhurst, J. Chem. Soc., Faraday Trans. 2 **84** (8), 961 (1988).
22. H. Haken, *Information and Self-Organization: A Macroscopic Approach to Complex Systems* (Springer-Verlag, Berlin, 1988; Mir, Moscow, 1991).
23. E. M. Aver'yanov and A. N. Primak, Liq. Cryst. **10** (4), 555 (1991).
24. E. M. Aver'yanov and A. N. Primak, Liq. Cryst. **13** (1), 139 (1993).
25. A. A. Gerasimov, Ukr. Fiz. Zh. **27** (9), 1314 (1982).
26. S. Chandrasekhar, *Liquid Crystals*, 2nd ed. (Cambridge Univ. Press, Cambridge, 1992; Mir, Moscow, 1980).
27. J. Katriel, G. F. Kventsel, G. R. Luckhurst, and T. J. Sluckin, Liq. Cryst. **1** (4), 337 (1986).
28. L. D. Landau and E. M. Lifshitz, *Statistical Physics*, 3rd ed. (Nauka, Moscow, 1976; Pergamon, Oxford, 1980), Part 1.
29. E. M. Aver'yanov, *Local-Field Effects in Optics of Liquid Crystals* (Nauka, Novosibirsk, 1999).
30. P. Palffy-Muhoray and D. A. Dunmur, Mol. Cryst. Liq. Cryst. **97**, 337 (1983).

Translated by O. Borovik-Romanova